IBIC'20

International Beam Instrumentation Conference

PROCEEDINGS

Foto: Rogério Cassimiro | Escultura: Tomie Ohtake

LNLS CNPEM MINISTRY OF SCIENCE, TECHNOLOGY AND INNOVATIONS PÁTRIA AMADA BRASIL BRAZILIAN GOVERNMENT

IBIC2020

9th International Beam Instrumentation Conference 2020
14–18 September 2020

remote (organized by CNPEM/LNLS, Campinas, Brazil)

ISBN: 978-3-95450-222-6
ISSN: 2673-5350
DOI: 10.18429/JACoW-IBIC2020

JACoW Publishing
Esplanade des Particules 1
1211 Geneva 23
Switzerland
Technical Editor: Volker RW Schaa, GSI, Germany

Content from this work may be used under the terms of the CC BY 3.0 licence (© 2020). Any distribution of this work must maintain attribution to the author(s), title of the work, publisher, and DOI.

IBIC 2020

International Beam Instrumentation Conference

Summary

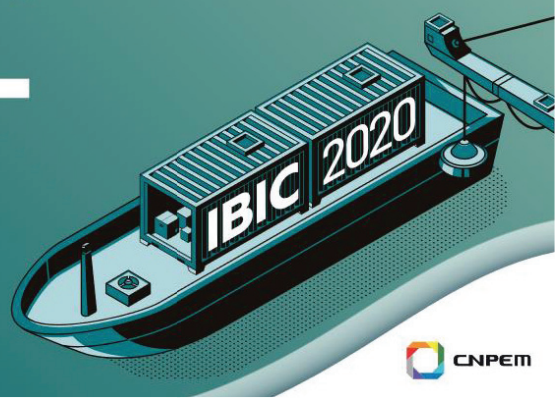

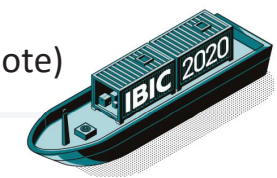

EXHIBITORS

bergoz INSTRUMENTATION

dimtel

JACoW.org

RadiaBeam

UHV D

APS American Physical Society JOURNALS

INSTRUMENTATION TECHNOLOGIES

TELEDYNE SP DEVICES Everywhereyoulook™

Faraday Cup Award:
Faraday-cup.com

CAENels Gear For Science

PHOTONIS Scientific Detectors

OAK RIDGE National Laboratory

iSee

πTEC PI-TECNOLOGIA

CNPEM MINISTRY OF SCIENCE, TECHNOLOGY AND INNOVATIONS PÁTRIA AMADA BRASIL

start time (UTC)	Monday, 14 Sep	Tuesday, 15 Sep	Wednesday, 16 Sep	Thursday, 17 Sep	Friday, 18 Sep	start time (UTC)
12:00		Opening Social Hour (@iSee) *12:00 - 13:00 (UTC)*	Opening Social Hour (@iSee) *12:00 - 13:00 (UTC)*	Opening Social Hour (@iSee) *12:00 - 13:00 (UTC)*	Opening Social Hour (@iSee) *12:00 - 13:00 (UTC)*	12:00
...	MOAO: Overview and Commissioning (@ZOOM) **Moderators:** Steven Lidia (FRIB), Adriana Wawrzyniak (Solaris)	TUAO: Beam Charge, Beam Loss, Machine Protection and Feedback Systems (@ZOOM) **Moderators:** David Gassner (BNL), Kay Wittenburg (DESY)	WEAO: Longitudinal Diagnostics and Synchronization (@ZOOM) **Moderators:** Mario Ferianis (Elettra), Volker Schlott (PSI)	THAO: Transverse Profile, Emittance Monitors and Machine Learning (@ZOOM) **Moderators:** Andreas Jansson (ESS), Changbum Kim (PAL)	FRAO: Beam Position Monitors and Data Acquisition (@ZOOM) **Moderators:** Nicolas Hubert (Soleil), Rhodri Jones (CERN)	...
13:00	Welcome (@ZOOM)	Precise Bunch Charge Measurement Using BPM Pickup Jian Chen (SSRF/SARI)	Novel Trends in Bunch Length Diagnostics Based on Coherent Polarization Radiation Alessandro Curcio (Solaris)	Machine Learning-based Beam Size Stabilization Simon C. Leemann (LBNL)	Developing Electronics for Radiation Environments Salvatore Danzeca (CERN)	13:00
13:10						13:10
13:20	Initial Experiences With Beam Diagnostics During Sirius Commissioning Henrique de O. Caiafa Duarte (LNLS/Sirius)	Investigation of Novel Radiation Hard and Fast Scintillator for Heavy Ions Detection - Maxim Saifulin (GSI)	Terahertz Detection Techniques Overview Francesco Mazzocchi (KIT)	Using Machine Learning Tools to Predict Accelerator Failure Miha Reščič (University of Huddersfield)	Direct Digitization and ADC Parameter Trade-off for Bunch-by-Bunch Signal Processing Irene Degl'Innocenti (University of Pisa / CERN)	13:20
13:30		Diagnostics for Collimator Irradiation Studies in the Advanced Photon Source Storage Ring Jeffrey Dooling (ANL/APS)				13:30
13:40	Beam Instrumentation Performances Through the ESRF-EBS Commissioning Laura Torino (ALBA - formerly at ESRF)		Optimization of Lasers in Electron Accelerator Applications Sharon Vetter (SLAC)	Beam Coupling Impedance Analyze Using Bunch-by-Bunch Measurement - Xingyi Xu (SSRF/SARI)	High Performance Data Acquisition for a Modern Accelerator - Guobao Shen (ANL/APS)	13:40
13:50		The Ionization Chamber Monitor for Electron Beam at Ultra High Dose Rate - Chloe Lahaye (IN2P3/LPC Caen)		Source Size and Emittance Measurements for Low-Emittance Light Sources Nazanin Samadi (CLS) and Xianbo Shi (ANL/APS)	BPM Electronics with Self-Calibration at the ALS Gregory Portmann (LBNL)	13:50
14:00	Beam Diagnostics in the Advanced Plasma Wakefield Experiment AWAKE Anna-Maria Bachmann (MPI Munich / CERN)	System Identification and Stability Considerations for Closed Orbit Feedback at SIS-18 - Rahul Singh (GSI)	Non-invasive Longitudinal Profile Measurements of Electron Bunches Simultaneously to FEL Operation at MHz Rates Nils Lockmann (DESY)			14:00
14:10		Break and Social Interaction (@ZOOM)	Break and Social Interaction (@ZOOM)	Advanced Laser-Driven Plasma Accelerator Electron-Beam Diagnostics with COTR Techniques Alex Lumpkin (FNAL/Fermilab)	Break and Social Interaction (@ZOOM)	14:10
14:20	Break and Social Interaction (@ZOOM)	TUPP: Tuesday Poster Session (@ZOOM) *14:20 - 16:30 (UTC)* + Industrial Exhibition (@Virtual Booths) *14:20 - 16:30 (UTC)*	WEPP: Wednesday Poster Session (@ZOOM) *14:20 - 16:30 (UTC)* + Industrial Exhibition (@Virtual Booths) *14:20 - 16:30 (UTC)*	Features of the Metal Microstrip Detectors for Beam Profile Monitoring - Dmytro Ramazanov (NASU/INR)	Commissioning of the Beam Energy Position Monitor System for the Superconducting RIKEN Heavy-ion Linac Tamaki Watanabe (RIKEN)	14:20
14:30	Commissioning of the CSNS Beam Instrumentation System Jilei Sun (CSNS)			Break and Social Interaction (@ZOOM)		14:30
14:40				THPP: Thursday Poster Session (@ZOOM) *14:40 - 16:30 (UTC)* + Industrial Exhibition (@Virtual Booths) *14:40 - 16:30 (UTC)*	HEPS Storage Ring BPM Development Shu-Jun Wei (IHEP/HEPS)	14:40
14:50	Beam Instrumentation System for Shanghai Soft X-ray FEL Test Facility - Longwei Lai (SSRF/SARI)				IBIC 2020 Summary (@ZOOM)	14:50
15:00	Group Print Screen (@ZOOM)				IBIC 2021 Presentation (@ZOOM)	15:00
15:10	Q&A Virtual Conference (@ZOOM) *15:10 - 16:30 (UTC)* Guidance for Poster Presentation Clarification of Doubts Feedback from Participants ***Moderators:*** *Willem Blokland (ORNL)* *Lorraine Bobb (DLS)* *Gustavo Bruno (LNLS/Sirius)* *Daniel Tavares (LNLS/Sirius)* Industrial Exhibition (@Virtual Booths) *15:10 - 16:30 (UTC)*				Closing Remarks (@ZOOM)	15:10
...					**Tracks:** Overview and Commissioning Beam Charge and Current Monitors Beam Loss Monitors and Machine Protection Feedback Systems and Beam Stability Longitudinal Diagnostics and Synchronization Machine Parameter Measurements Transverse Profile and Emittance Monitors Data Acquisition and Digital Architectures Beam Position Monitors	15:20
16:30 ... 17:30	Beam Instrumentation Community Get-together (@iSee) *16:30 - 18:00 (UTC)*	End Social Hour (@iSee) *16:30 - 17:30 (UTC)*	End Social Hour (@iSee) *16:30 - 17:30 (UTC)*	End Social Hour (@iSee) *16:30 - 17:30 (UTC)*		...
18:00						18:00

IBIC 2020 - 9th International Beam Instrumentation Conference (Remote)

Presented Work

Contribution	Count	Time (pre-recorded)
Invited Orals	16	6 hours 17 minutes
Contributed Orals	10	1 hour 52 minutes
Posters	85	-
Total	**111**	**8 hours 8 minutes**
Papers	**72**	-

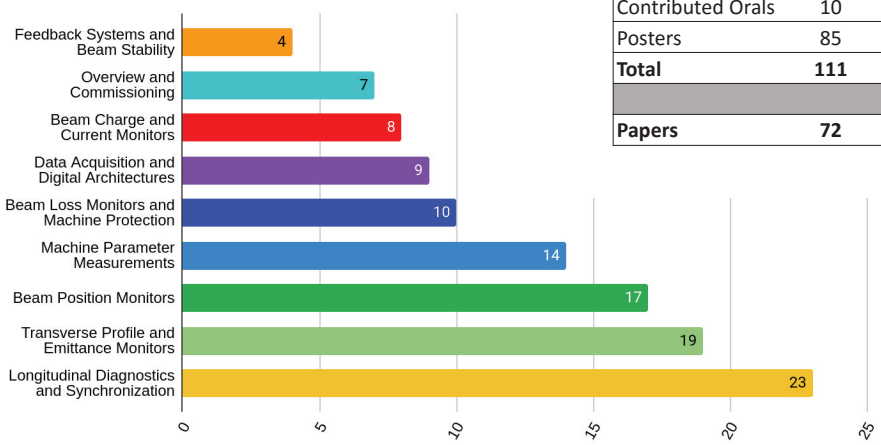

Participation

Attendee	Count
Delegates	220
Students	70
Exhibitors (Delegates)	19
Total	**309**
Exhibitors (Companies)	**9**

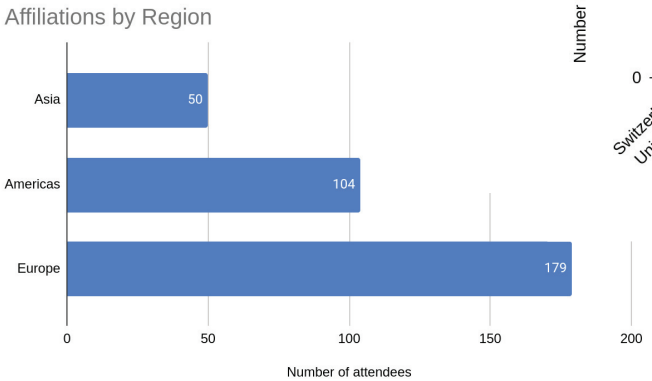

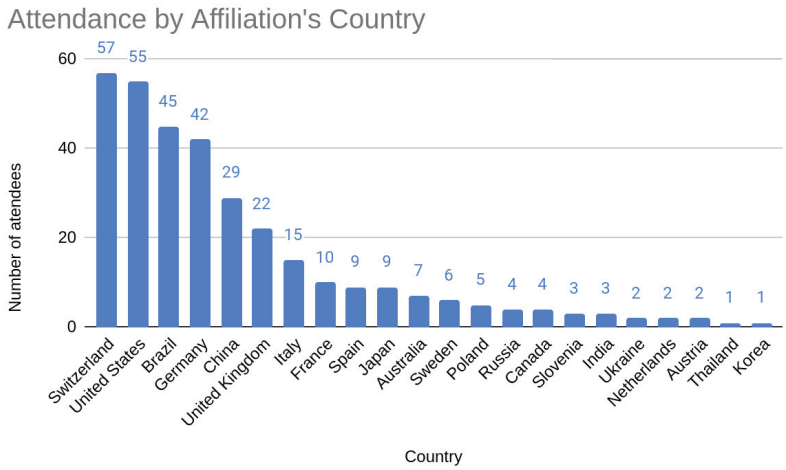

IBIC 2020 - 9th International Beam Instrumentation Conference (Remote)

Interaction

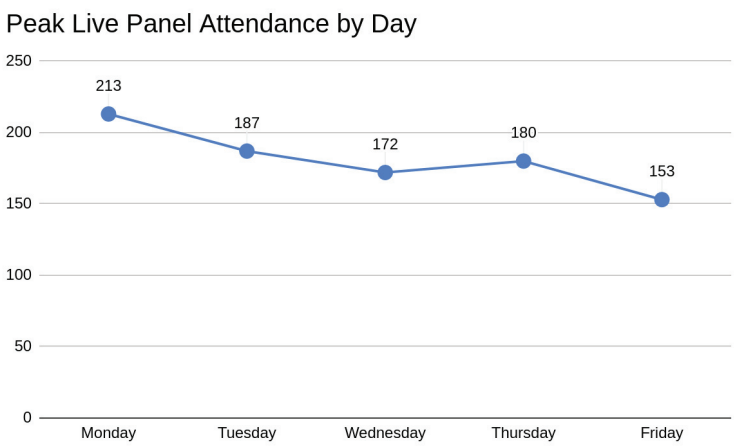

Compiled all entries on chats, Q&A and community boards: **681 raw entries**

Removing comments like "Hi", "Thanks", "Nice", "Here's my email", troubleshooting, Whova automatic messages, LOC messages with Zoom links, etc.:

269 entries of true interaction by written form

In addition:

- direct questions on 5 days of live panels
- discussions on up to 31 parallel poster
- social events in "virtual reality"

THE (REMOTE) JACoW TEAM!

Renan Picoreti
(Editor-in-chief)

Renan Picoreti – CNPEM

Jan Chrin - PSI

Volker RW Schaa - GSI

David Button - ANSTO

Anthony Cuffe - JLab

IBIC 2020 - 9th International Beam Instrumentation Conference (Remote)

- Whova platform, including the Q& communities will be online for several months!
- Feel free to continue asking and answering the Q&A boards and topics of the communities!
- Proceedings will be published on the JACoW website at: https://jacow.org/IBIC2020

IBIC 2020 LOCAL Organizing Committee

Renan Picoteti

Priscila Alves

Lucas Dias

Dora Marques

Santos city

Santos city (before the pandemic)

bergoz INSTRUMENTATION
dimtel
RadiaBeam
UHV D
INSTRUMENTATION TECHNOLOGIES
TELEDYNE SP DEVICES Everywhereyoulook™
CAENels Gear For Science
PHOTONIS Scientific Detectors
πTEC PI-TECNOLOGIA
LNLS
CNPEM
MINISTRY OF SCIENCE, TECHNOLOGY AND INNOVATIONS
PÁTRIA AMADA BRASIL BRAZILIAN GOVERNMENT

THANK YOU!

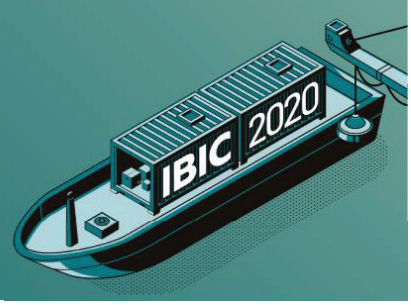

Scientific Program Committee (SPC)

Tonia Batten		CLS	Canada
Willem Blokland		ORNL	USA
Lorraine Bobb		Diamond	Great Britain
Mario Ferianis		Elettra	Italy
David Gassner		BNL	USA
Nicolas Hubert		Soleil	France
Ubaldo Iriso		ALBA	Spain
Andreas Jansson		ESS	Sweden
Rhodri Jones		CERN	Switzerland
Kevin Jordan		JLab	USA
Changbum Kim		PAL	South Korea
Prapong Klysubun		SLRI	Thailand
Patrick Krejcik		SLAC	USA
Yongbin Leng		SSRF/SARI	China
Steven Lidia		FRIB	USA
Hirokazu Maesaka		Spring-8	Japan
Sergio Marques	**Conference Chair**	LNLS	Brazil
Toshiyuki Mitsuhashi		KEK	Japan
Eric Norum		LBNL	USA
Victor Scarpine		FNAL	USA
Volker Schlott		PSI	Switzerland
Nicholas Sereno		ANL	USA
Daniel Tavares	**SPC Chair**	LNLS	Brazil
Adriana Wawrzyniak		Solaris	Poland
Kay Wittenburg		DESY	Germany
Junhui Yue		IHEP	China

Remote Organizing Committee (ROC)

Lorraine Bobb		Diamond	Great Britain
Willem Blokland		ORNL	USA
Gustavo Bruno	**ROC Chair**	LNLS	Brazil
Henrique Caiafa		LNLS	Brazil
Andreas Jansson		ESS	Sweden
Changbum Kim		PAL	South Korea
Sergio Marques		LNLS	Brazil
Toshiyuki Mitsuhashi		KEK	Japan
Takashi Obina		KEK	Japan
Daniel Tavares		LNLS	Brazil

Local Organizing Committee (LOC)

Dora Maria Marques Aquino	**Conference Coordinator**	CNPEM, Brazil
Gustavo Bruno	**LOC/ROC Chair & IT Manager**	CNPEM/LNLS, Brazil
Henrique Caiafa	**Ind. Exhibition & Sponsorship Manager**	CNPEM/LNLS, Brazil
Renan Picoreti	**Editor-in-Chief**	LNLS, Brazil
Sergio Marques	**Conference Chair**	CNPEM/LNLS, Brazil
Daniel Tavares	**SPC Chair**	LNLS, Brazil

JACoW Editorial Team (JET)

Gustavo Bruno		LNLS	Brazil
David Button		ANSTO	Australia
Jan Chrin		PSI	Switzerland
Anthony Cuffe		JLab	USA
Renan Picoreti	**Editor-in-Chief**	LNLS	Brazil
Volker RW Schaa	**Technical Editor**	GSI	Germany

IBIC 2020 group photo (1 / 7)

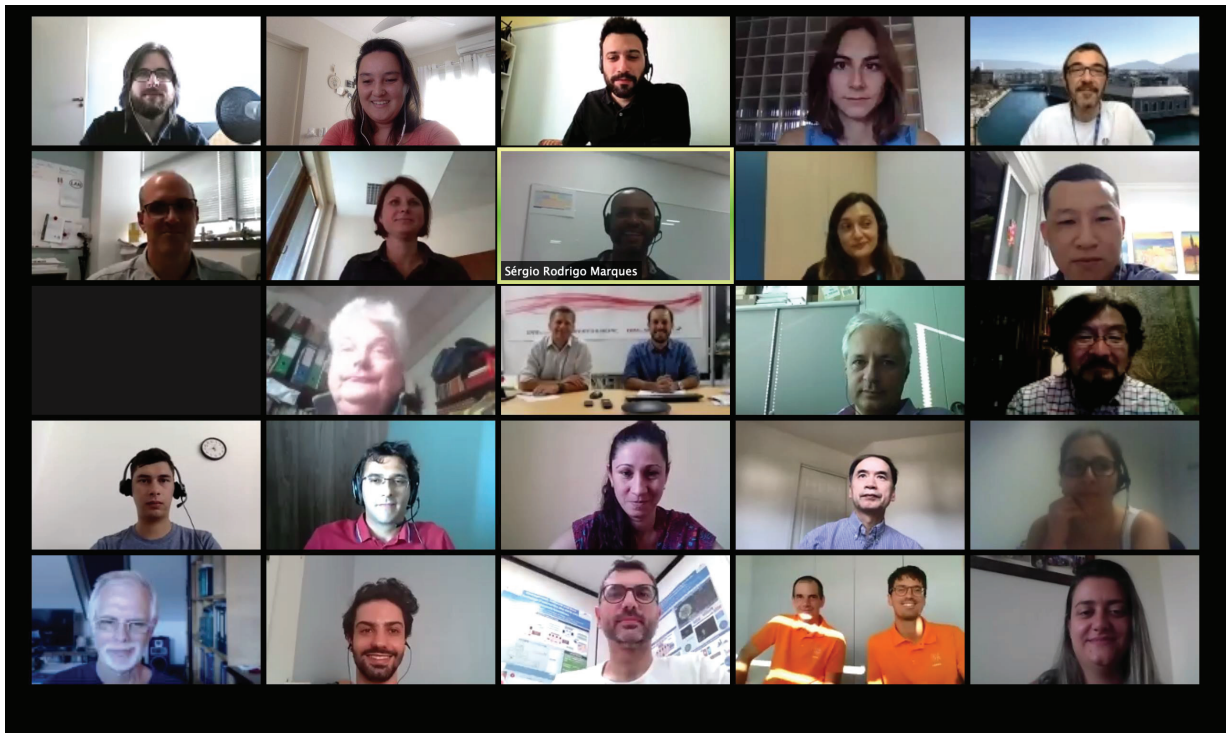

IBIC 2020 group photo (2 / 7)

IBIC 2020 group photo (3 / 7)

IBIC 2020 group photo (4 / 7)

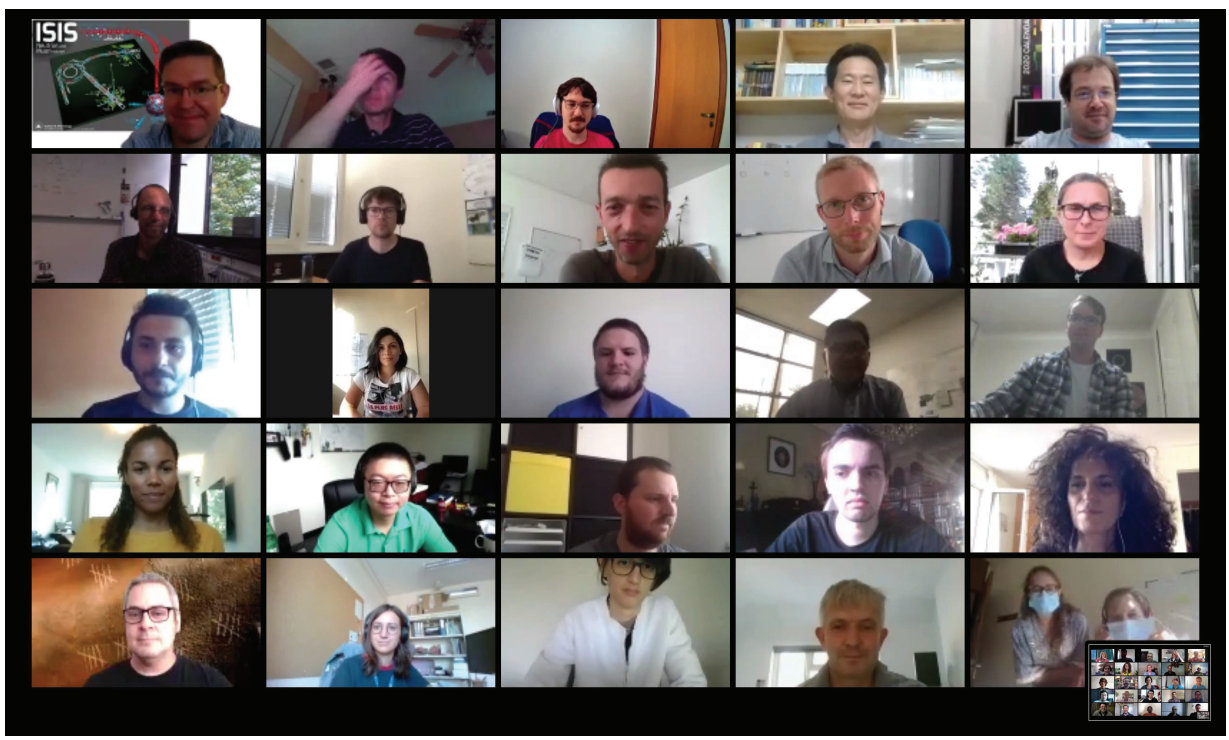

IBIC 2020 group photo (5 / 7)

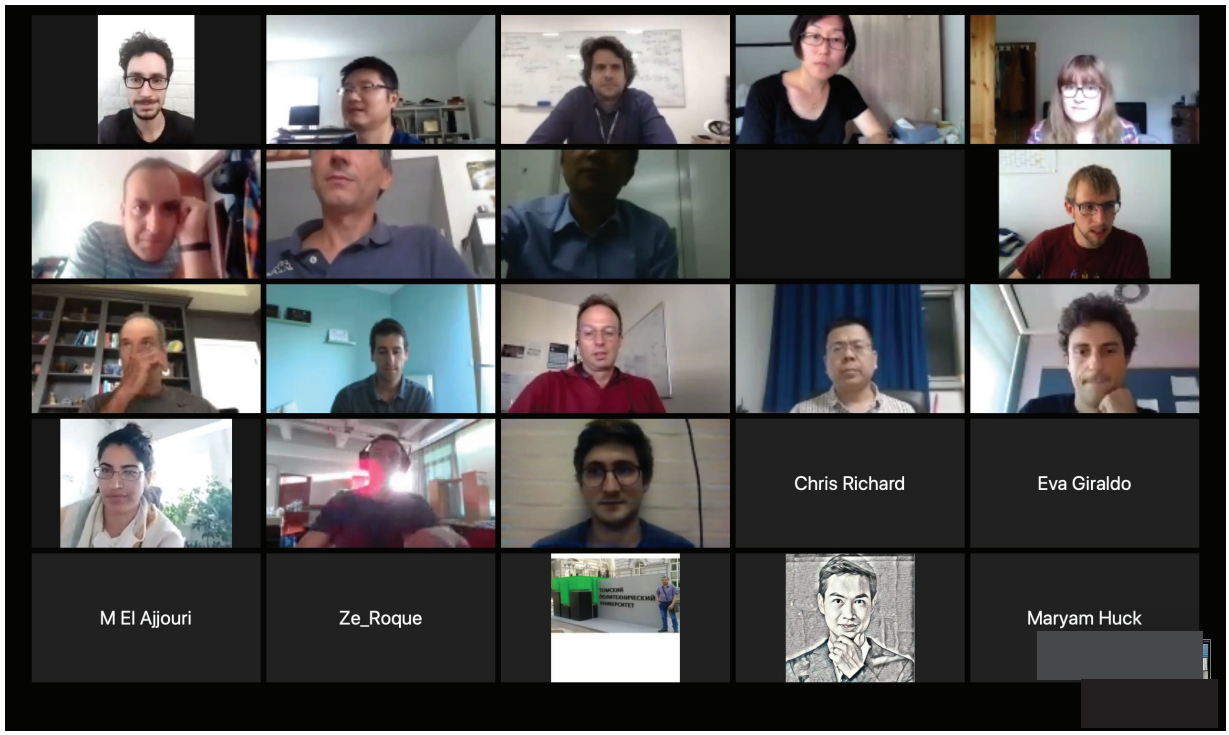

IBIC 2020 group photo (6 / 7)

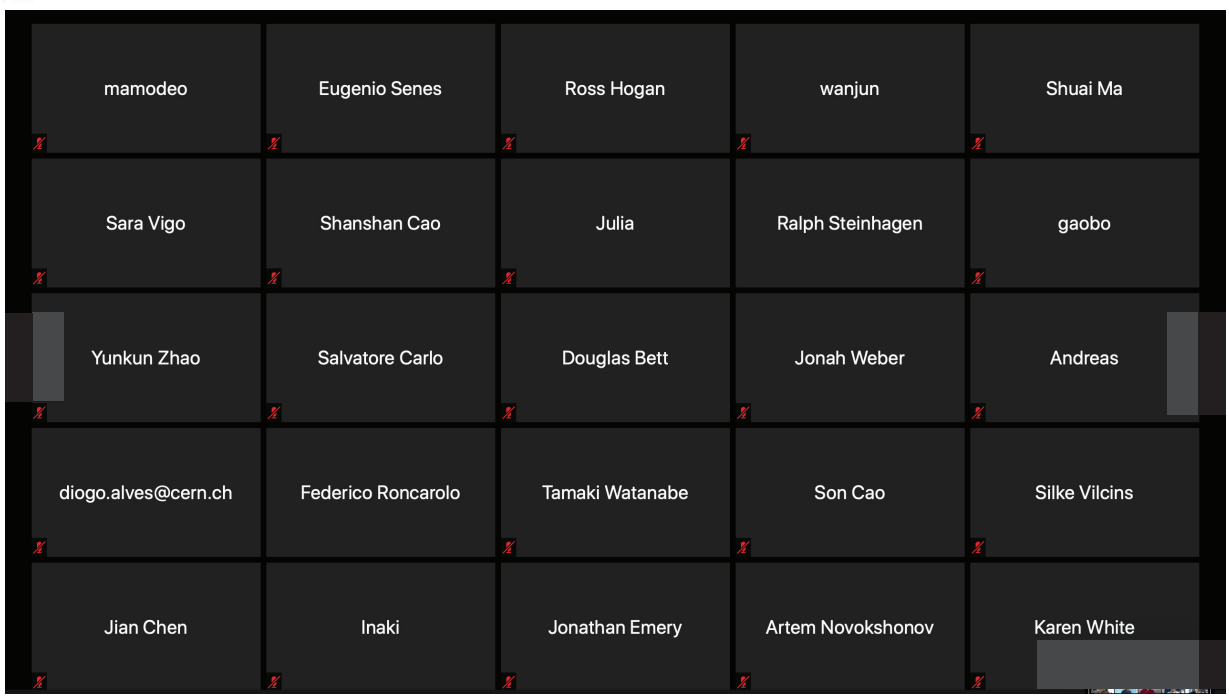

IBIC 2020 group photo (7 / 7)

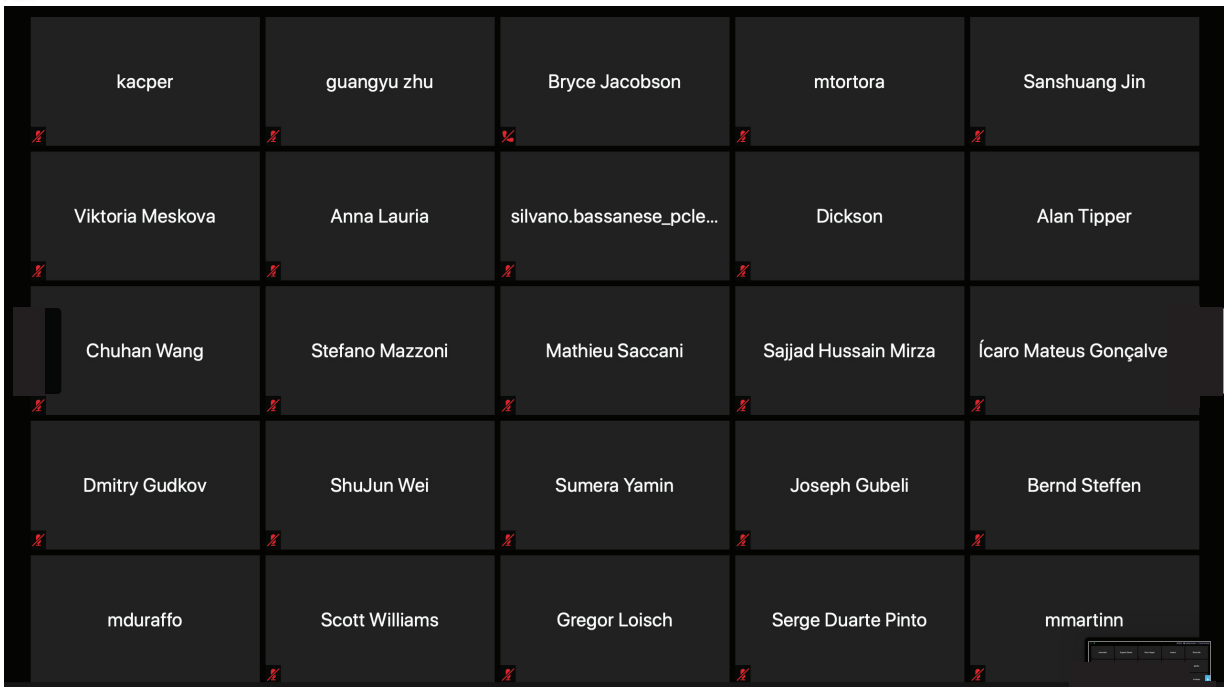

Contents

Preface i
Copyright . . . ii
Summary . . . iii
Committees . . . xi
Group Photos . . . xiii
Contents . . . xvii

Papers 1
MOAO01 – Beam Diagnostics in the Advanced Plasma Wakefield Experiment AWAKE . . . 1
MOAO03 – Commissioning of the Beam Instrumentation System of CSNS . . . 7
MOAO04 – Beam Instrumentation Performances through the ESRF-EBS Commissioning . . . 11
MOAO05 – Beam Instrumentation System for Shanghai Soft X-ray FEL Test Facility . . . 17
TUAO01 – Precise Bunch Charge Measurement Using BPM Pickup . . . 21
TUAO02 – Diagnostics for Collimator Irradiation Studies in the Advanced Photon Source Storage Ring . . . 26
TUPP05 – X-Ray Beam Size Monitor Enclosure for the Advanced Photon Source Upgrade . . . 34
TUPP06 – Inclined X-ray Beam Position Monitors to Reduce Influence of Filling Pattern for the SPring-8 Photon Beamlines . . . 37
TUPP09 – Multiplexer System for the SPEAR3 Booster BPM Upgrade . . . 41
TUPP10 – X-Ray Beam Position Monitor Silicon Photodiode Measurements for the Advanced Photon Source Upgrade . . . 46
TUPP12 – Automated Management of Libera SPARK Module IOCs in SPEAR3 . . . 51
TUPP17 – Direct Observations of Sub-micropulse Electron-beam Effects from Short-range Wakefields in TESLA-type Superconducting RF Cavities . . . 56
TUPP18 – Observations of Optical Synchrotron Radiation from Ultra-low Charges Stored in a Ring Operating at 425 MeV . . . 61
TUPP23 – Streak Camera Measurement of Electron Beam Energy Loss Per Turn in the Advanced Photon Source Particle Accumulator Ring . . . 66
TUPP24 – LOCO Corrections for Beam Trajectory Optimisation on the ISIS Accelerator . . . 70
TUPP28 – Simulation of Cherenkov Diffraction Radiation for Various Radiator Designs . . . 73
TUPP32 – Development of Novel Non-Destructive 2D and 3D Beam Monitoring Detectors at the Bern Medical Cyclotron . . . 78
TUPP35 – Development of a Thermal Response Model for Wire Grid Profile Monitors and Benchmarking to CERN LINAC4 Experiments . . . 82
TUPP37 – A Beam Profile Monitor for High Energy Proton Beams Using Microfabrication Techniques . . . 86
WEAO02 – THz Detection Techniques Overview . . . 90
WEPP01 – Filling Pattern Measurement Using a 500 MHz Digitizer at Soleil and APS Storage Rings . . . 96
WEPP03 – Bunch Purity Measurement for SSRF . . . 99
WEPP04 – Modernization and Operation of Ionization-proportional Gas Counter at INR RAS Proton Linac . . . 103
WEPP05 – Reentrant Cavity Resonator as a Beam Current Monitor (BCM) for a Medical Cyclotron Facility . . . 107
WEPP06 – Investigation of an Optical-Fiber Based Beam Loss Monitor at the J-PARC Extraction Neutrino Beamline 110
WEPP07 – The Insertable Beam Stop in the ESS SPK Section . . . 114
WEPP10 – Proton-Induced SEY From Beam Interceptive Devices in the ESS Linac . . . 117
WEPP12 – Simulation of the Signal Processing for the New Interaction Region BPMs of the High Luminosity LHC 120
WEPP13 – Design and Test of CBPM Prototypes for SHINE . . . 124
WEPP15 – Experiments With a Quadrated Dielectric-Filled Reentrant Cavity Resonator as a Beam Position Monitor (BPM) for a Medical Cyclotron Facility . . . 128
WEPP16 – Advanced Light Source High Speed Digitizer . . . 132
WEPP17 – Upgrade and First Commissioning of Transverse Feedback System for SSRF . . . 136
WEPP20 – Measurements of Ultraviolet FEL Seed Laser Pulse Width Broading in Thin SS-BBO Crystals . . . 140
WEPP21 – Evaluation of a Novel Pickup Concept for Ultra-Low Charged Short Bunches in X-Ray Free-Electron Lasers . . . 145
WEPP22 – Submicropulse Energy-Time Correlations of 40-Mev Electron Beams at Fast . . . 150
WEPP24 – Prototype Design of Bunch Arrival Time Measurement System Based on Cavity Monitor for SHINE . 154
WEPP26 – Effect of phase modulation on the transverse beam size and emittance of the HLS-II ring . . . 158
WEPP27 – An Alternative Processing Algorithm for the Tune Measurement System in the LHC . . . 162

WEPP28 – High-Accuracy Diagnostic Tool for Beam Position Monitor Troubleshooting in SSRF Based on Clustering Analysis . . . 166
WEPP29 – Energy Gain Measurement for Electrons Accelerated in a Single-Cycle THz Structure . . . 170
WEPP31 – Design of the Beam Diagnostic System for the New 3 GeV Light Source in Japan . . . 174
WEPP33 – Progress of Profile Measurement Refurbishment Activities at HIPA . . . 179
WEPP34 – First Beam Profile Measurements by Beam Induced Fluorescence at the J-PARC Neutrino Extraction Beamline . . . 184
WEPP36 – Recent Progress on the Commissioning of a Gas Curtain Beam Profile Monitor Using Beam Induced Fluorescence for High Luminosity LHC . . . 188
WEPP37 – Transverse Phase Portrait Tomography of Proton Beams at INR RAS Linac . . . 193
WEPP38 – Diamond Beam Halo Monitor . . . 197
THAO04 – Beam Coupling Impedance Analyze Using Bunch-by-Bunch Measurement . . . 202
THAO05 – Advanced Laser-driven Plasma Accelerator Electron-beam Diagnostics with COTR Techniques . . . 206
THAO06 – Features of the Metal Microstrip Detectors for Beam Profile Monitoring . . . 211
THPP04 – Testbed Development for the Characterisation of an ASIC for Beam Loss Measurement Systems . . . 215
THPP05 – Properties of Cherenkov Diffraction Radiation as Predicted by the Polarisation Currents Approach for Beam Instrumentation . . . 218
THPP08 – Development of Abnormal Beam State Monitoring Processor on SSRF Storage Ring . . . 223
THPP10 – Influence of a Bellow to a Cavity BPM for SINBAD . . . 226
THPP11 – Study of Multi-Bladed Photon BPM Designs . . . 229
THPP12 – Characterization Study of a Button BPM with an Approach to Automated Measurements . . . 233
THPP16 – Septum Orbit Feedforward Correction at the AS . . . 237
THPP20 – Virtual Slit for Improved Resolution in Longitudinal Emittance Measurement . . . 241
THPP21 – Design and Development of a Novel Stripline Fast Faraday Cup to Measure Ion Beam Profile . . . 246
THPP22 – A THz-Driven Split Ring Resonator for Temporal Characterization of Femtosecond MeV Electron Beam 250
THPP23 – Tracking Frequency Reference Phase Changes at Point of Use Based on BPM Measurements . . . 254
THPP25 – Measurements of Ion Instability and Emittance Growth for the APS-Upgrade . . . 258
THPP26 – Transverse Broad-band Impedance Studies of the New In-vacuum Cryogenic Undulator at Bessy II Storage Ring . . . 263
THPP29 – Application of Wavelet Algorithm in Tune Measurement . . . 268
THPP33 – Simulation Methods for Transverse Beam Size Measurements Using the Heterodyne Near Field Speckles of Hard X-rays . . . 272
THPP34 – Calibration and Image Restoration for the Beam Profile Measurement System . . . 276
THPP35 – Lens Calibration for Beam Size Monitors at ThomX . . . 281
THPP36 – Prototype Design of Wire Scanner for SHINE . . . 285
FRAO02 – Direct Digitization and ADC Parameter Trade-off for Bunch-by-Bunch Signal Processing . . . 288
FRAO04 – Commissioning of the Beam Energy Position Monitor System for the Superconducting RIKEN Heavy-ion Linac . . . 295
FRAO05 – High Performance Data Acquisition for a Modern Accelerator . . . 303

Appendices **307**
List of Authors . . . 307
Institutes List . . . 312

ISBN: 978-3-95450-222-6 ISSN: 2673-5350 doi:10.18429/JACoW-IBIC2020-MOA001

BEAM DIAGNOSTICS IN THE ADVANCED PLASMA WAKEFIELD EXPERIMENT AWAKE

A.-M. Bachmann[1,2*], Max Planck Institute for Physics, Munich, Germany
P. Muggli, Max Planck Institute for Physics, Munich, Germany
[1]also at TU Munich, Munich, Germany
[2]also at CERN, Geneva, Switzerland
on behalf of the AWAKE Collaboration

Abstract

In AWAKE a self-modulated proton bunch drives wakefields in a plasma. Recent experiments successfully demonstrated many aspects of the self-modulation of the drive bunch as well as acceleration of test electrons. Next experiments will focus on producing a multi-GeV accelerated electron bunch with low emittance and low energy spread. The experiment requires a variety of advanced beam diagnostics to characterize the self-modulated proton bunch at the picosecond time scale. These include optical transition radiation and a streak camera for short and long time scale detailed imaging of self-modulation and hosing, coherent transition radiation for modulation frequency measurements in the 100–300 GHz frequency range and multiple fluorescent screens for core and halo measurements. An overview of these diagnostics will be given.

INTRODUCTION

AWAKE operates at one of the lowest plasma densities of all currently available plasma-based accelerator experiments. The plasma electron density n_{e0} determines the fastest time-scale τ of characteristics of the bunch modulation with the plasma electron angular frequency, $\omega_{pe} = \left(n_{e0}e^2/\epsilon_0 m_e\right)^{1/2}$, with $\tau = 2\pi/\omega_{pe}$, where constants have usual meaning: e, charge of the electron: ϵ_0, vacuum permittivity; m_e, mass of the electron; c, the speed of light in vacuum. For $n_{e0} = 10^{14}$–10^{15} cm^{-3} this corresponds to $\tau = 3.5$–11.1 ps. The time resolution needed to directly observe the modulation is thus at the limit of currently commercially available streak cameras (≈ 200 fs). The density also determines the smallest spatial scale through the cold plasma collisionless skin depth c/ω_{pe}. The main phenomena to resolve are the structure of the proton bunch that drives plasma wakefields and of the wakefields themselves. The incoming proton bunch is much longer than the wakefields' period τ. Thus it experiences self-modulation (SM) as it travels through the plasma [1]. The SM process acts on the bunch through the periodic focusing and defocusing transverse wakefields along the bunch, generating a train of micro-bunches with periodicity $\sim \tau$ and shorter than τ.

To study this fundamental beam-plasma interaction process in detail, we acquire time-resolved transverse images of the modulated bunch density distribution measuring the optical transition radiation with a streak camera [2, 3]. With multiple fluorescent screens along the beam path, we acquire time integrated images of the modulated bunch to complement the time-resolved images [4]. Additionally, with heterodyne receivers the frequency of the modulation can be measured independently [5]. We measure energy, energy spread and charge capture of an electron bunch, externally injected and accelerated in the plasma with an electron spectrometer [6, 7].

We describe the diagnostics that were used in the first round of experiments (2016–2018). We also briefly outline the diagnostic challenges for the upcoming experiments (starting 2021) that will focus on the accelerated bunch quality. As with all plasma-based accelerators beam diagnostics must measure small spatial and temporal scales, typically µm and 100 fs, respectively. In addition, diagnostic measurements must be integrated into compact spaces and measure simultaneously properties of very different beams, the high population, long duration and long β-function proton bunch and the low population, short duration and small spatial size electron bunch. Moreover, in these experiments, they must overlap in space and time with $\ll \tau$ and c/ω_{pe} accuracy at the plasma entrance, an overlap that also complicates diagnostics at the plasma exit.

THE AWAKE EXPERIMENT

In the AWAKE experiment the transverse central 2 mm diameter of a 10 m long rubidium (Rb) vapor source is ionized by a 4 TW (peak power) Ti:Sapphire laser pulse. An ≈ 12 cm-long CERN SPS proton bunch propagates through the plasma. The long proton bunch drives wakefields in the plasma. Focusing and defocusing transverse fields alternate along the bunch with the wakefields' period $\sim \tau$. The wake-

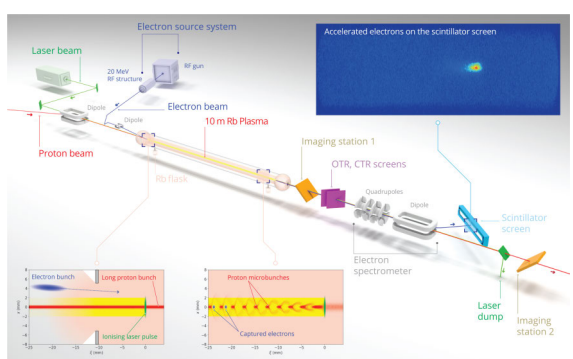

Figure 1: Layout of the AWAKE experiment [6].

* bachmann@mpp.mpg.de

Content from this work may be used under the terms of the CC BY 3.0 licence (© 2020). Any distribution of this work must maintain attribution to the author(s), title of the work, publisher, and DOI

ISBN: 978-3-95450-222-6 ISSN: 2673-5350 doi:10.18429/JACoW-IBIC2020-MOA001

Content from this work may be used under the terms of the CC BY 3.0 licence (© 2020). Any distribution of this work must maintain attribution to the author(s), title of the work, publisher, and DOI

fields act back on the long proton bunch, leading to radial modulation. The modulation is seeded with the ionizing laser-pulse co-propagating within the proton bunch (Seeded Self-Modulation) [8]. In the focusing phase of the wakefields protons remain on axis, while in between in the defocusing phase protons diverge, resulting in micro-bunching. The modulated proton bunch resonantly drives wakefields. The longitudinal wakefields accelerate a short electron bunch, generated on a photo-cathode and externally injected [9]. Beam diagnostics are placed downstream of the plasma to characterize the modulated proton bunch and the accelerated electrons. The fluorescent screens to measure the time integrated transverse distribution of the proton bunch are shown in Fig. 1, referred to as imaging station 1 and 2. The radial extent of defocused proton distribution depends on the transverse wakefields' amplitude they have experienced [4]. Two thin metal screens (OTR, CTR screen in Fig. 1) allow for the measurement of the optical transition radiation (OTR) and coherent transition radiation (CTR) emitted by the protons and micro-bunches, respectively, when entering the screens. The OTR is sent to a streak camera, acquiring a time-resolved image of the transverse distribution of a slice of the modulated proton bunch. The CTR is detected by heterodyne receivers to determine the modulation frequency of the bunch train. The charge and energy of the electron bunch after acceleration in the plasma are measured with the electron spectrometer.

PROTON BUNCH DIAGNOSTICS

In the following we describe the diagnostics used to characterize the modulated proton bunch driving the plasma wakefields and we show some example results.

Optical Transition Radiation and Streak Camera for Time-Resolved Transverse Distribution Measurements

The modulated bunch propagates through a foil (280 µm silicon wafer coated with 1 µm mirror-finished aluminium) where OTR, carrying the spatio-temporal pattern of the proton bunch distribution, is emitted [2]. The screen is placed 3.5 m after the plasma exit (see Fig. 1). The light is relay imaged onto the slit (20 µm) of a streak camera (Hamamatsu C10910-05) acquiring the time-resolved transverse bunch density distribution. These images can display the long time evolution of the self-modulated train and defocused protons. The evolution of the protons leaving the bunch is captured only over a few wakefields' periods due to aperture limitations of the imaging system (field of view $x \approx \pm 4$ mm in Fig. 2).

To reach the best time resolution, the camera must be operated in a speckle regime. The time resolution then reaches ≈ 0.8 ps. However, we image the transverse bunch density distribution and operate with larger intensity images in order to obtain single images of the bunch structure. The OTR signal (equal in duration to that of the proton bunch) lasts for ≈ 1 ns, much longer than the shortest time window (73 ps)

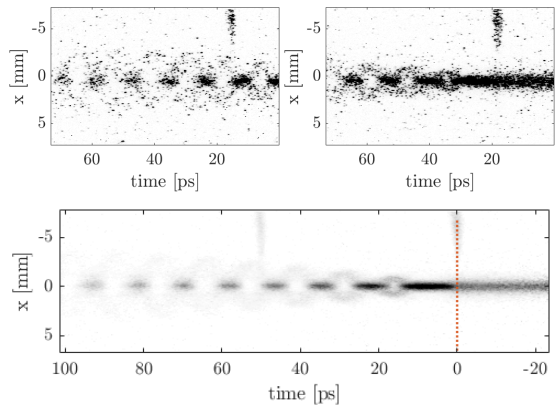

Figure 2: Single streak camera image of the start of the SM (top right), single streak camera image with a 50 ps time delay to the start of the SM (top left) and sets of the two time delays of 20 streak camera images each, stitched together using the timing reference signal (bottom).

with maximum time resolution, potentially further decreasing the time resolution. This typically decreased the time resolution to ≈ 2 ps for the short time window.

To decrease the noise of the images, we average several acquisitions of the same position along the bunch from successive events. This requires a repetitive signal (reproducibility of the modulation) and a very stable trigger for the diagnostic ($< \tau$) or an independent signal tied in time to the modulation itself. The electronic trigger jitters on the tens of picoseconds scale. We therefore send a mirror bleed replica of the laser pulse that ionizes the Rb vapor, and thus starts the self-modulation of the bunch, to the streak camera together with the OTR. We offset it from the OTR signal along the camera slit (see signal at $x \leq -4$ mm in Fig. 2). This time reference signal has an accuracy of 0.6 ps with respect to the ionizing laser pulse and thus with the start of the self-modulation. This replica combined with a tunable delay, serves as a time reference that can be used to average and stitch multiple events [10]. The averaging of multiple events allows for images of the modulated bunch with a much higher signal to noise ratio than with single images. By stitching the images of the shortest time window, i.e. combining a number of image sets taken with various reference signal delays with respect to the start of the self-modulation, we can measure fast time scale details along the bunch, as well as examine modulation structures with greater time resolution over a long time scale (see Fig. 2).

At the location of the OTR screen, the RMS transverse size of the proton bunch is ≈ 580 µm and the transverse size of the micro-bunches is similar [3]. Measurements show that the spatial resolution is on the order of 180 µm.

Figure 2 shows an example of a single image of the proton bunch near the start of the SM (top right), a single image with camera trigger and reference laser pulse shifted by 50 ps (top left) and of two sets of images (20 events each), acquired with a 50 ps trigger delay in between and "stitched"

ISBN: 978-3-95450-222-6 ISSN: 2673-5350 doi:10.18429/JACoW-IBIC2020-MOA001

together (bottom). Here the first reference signal timing is without delay with respect to the ionizing laser pulse, marked with the red dashed vertical line in the stitched image. This corresponds to the start of the plasma, here at time $t = 0$. In this case the plasma electron density is $n_{e0} = 0.9{\times}10^{14}$ cm^{-3} and thus $\tau = 11.7$ ps.

We use the space and time-resolved transverse slice of the modulated proton bunch density mapped from the streak camera images for qualitative and quantitative characterization of the self-modulated bunch. The position, shape and length of the proton micro-bunches is crucial for plasma wakefield acceleration experiments. The driver charge (here protons) should ideally be in the decelerating and focusing phase of the wakefields (one fourth of the plasma period in linear wakefield theory [11]). This would lead to large plasma wakefields' amplitudes and thus large acceleration and focusing of injected particles when placed at the right longitudinal position within the wakefields' period.

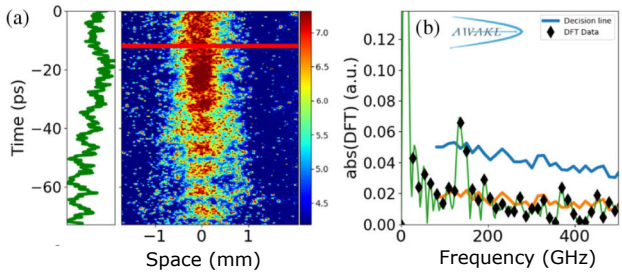

Figure 3: Image a) shows a streak camera image of the self-modulated proton bunch (moving from the bottom to the top) with the plasma starting at the red horizontal line and the projection of the central density distribution with the green curve on the left, b) shows the DFT of the projection, with determined peaks marked with black diamonds and the dominant frequency above the noise threshold determined as 137 GHz with $n_{e0} = 2.5 \times 10^{14}$ cm^{-3} (from [3]).

With the time-resolved bunch density maps the modulation frequency can be determined using the discrete Fourier transform (DFT) of the modulated bunch train [3]. This is shown in Fig. 3, with the streak camera image of a single event and the projection of the central bunch density in green on the left and the DFT and peak determination on the right. With a plasma period of $\tau < 11$ ps and a resolution of ≈ 2 ps, an upper bound of the micro-bunch length can be determined. The relative charge per micro-bunch can be measured, taking into account the effect of the streak camera slit on the transverse distribution [12]. This is particularly important for example when studying the effect of plasma density gradients on the SM process and validate theory and simulation predictions [13]. Competing instabilities of a particle bunch in the plasma, as the hosing instability, can be analyzed by studying the non-axi-symmetric behaviour of the modulated bunch with the time-resolved images [14]. In all studies the 3.5 m of vacuum propagation between the plasma exit and the OTR screen, and thus additional divergence of protons, needs to be taken into account.

Fluorescent Screens for Time Integrated Transverse Distribution Measurements

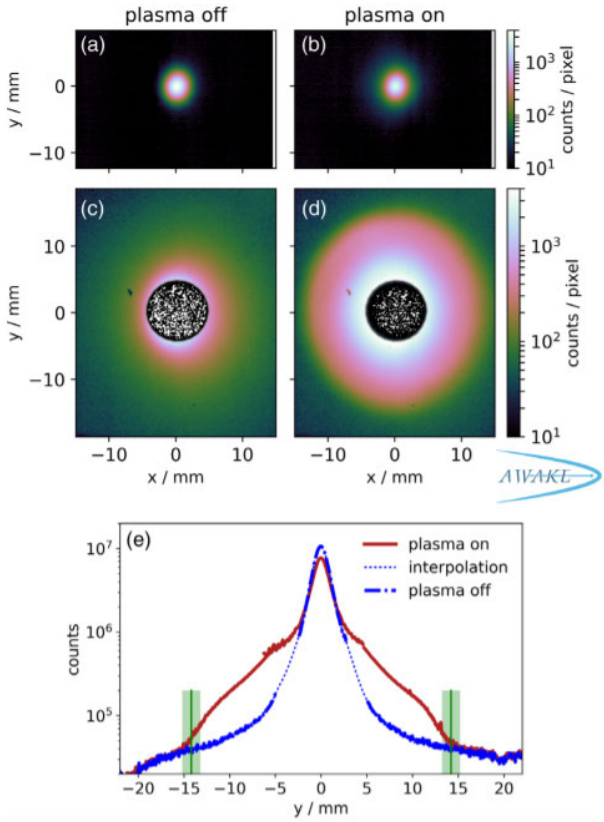

Figure 4: Time integrated transverse proton bunch density distribution acquired with fluorescent screens for the measurement of defocused protons and transverse wakefields' amplitude determination (from [4]). Images a), b) show core images, c), d) halo images for the same events with a), c) plasma OFF and b), d), plasma ON. Image e) shows the reconstructions of the bunch profile from the two cameras, as well as the value determined for the halo radius (green lines) and its uncertainty (green shaded regions). These images were obtained at imaging station 2 ($\approx$ 10 m from the plasma exit). Similar images were obtained at imaging station 1.

Fluorescent screens are placed along the beam line before and after the plasma, measuring the time integrated transverse proton bunch distribution, see Fig. 4. The radial modulation of the bunch in plasma leads to divergence of protons in defocusing regions between the focused regions of the micro-bunches. These protons appear as a halo around the bunch core on the imaging stations $\approx$ 2 m and $\approx$ 10 m after the plasma. The halo's radial extent is a measure of the integrated defocusing wakefields the protons have experienced [4]. At each of the two imaging stations, the light is divided into two light paths with a camera each. One camera measures the entire bunch distribution with parameters adjusted to the high density core of the bunch. This image also gives information about the beam alignment and eventual kicks of the beam by the plasma when beam and plasma are

Content from this work may be used under the terms of the CC BY 3.0 licence (© 2020). Any distribution of this work must maintain attribution to the author(s), title of the work, publisher, and DOI

ISBN: 978-3-95450-222-6 ISSN: 2673-5350 doi:10.18429/JACoW-IBIC2020-MOA001

Content from this work may be used under the terms of the CC BY 3.0 licence (© 2020). Any distribution of this work must maintain attribution to the author(s), title of the work, publisher, and DOI

misaligned. For the second camera the light passes through a mask, blocking the high intensity light from the dense core. Parameters are adjusted to measure the low light level halo. The combination of the two images enables a larger dynamic range measurement of the entire radial bunch distribution, detecting for the same event the significantly lower intensity of the signal from defocused protons (halo) around the core without saturation. The halo measurements have successfully shown that wakefields grow along the proton bunch [4], as predicted by theory and simulation results. SM, an axi-symmetric bunch-plasma mode of interaction produces a circular core and halo, when the finite radius plasma and the proton beam are well aligned. On the contrary, the hosing instability [15] is a non-axi-symmetric mode of interaction that may produce correspondingly asymmetric core and halo. Some of the self-modulation and hosing characteristics can thus be studied from time-integrated and time-resolved images of the proton bunch.

Heterodyne Detectors for Modulation Frequency Measurements Using Coherent Transition Radiation

We obtain an independent frequency measurement of the proton bunch modulation by analysing the CTR emitted when the bunch train enters a foil (Al-coated silicon oxide screen) placed after the plasma (see Fig. 1). The CTR signal is in the $f_{CTR} \approx 100 - 300$ GHz frequency range for plasma electron densities in the $n_{e0} \approx 10^{14}$–10^{15} cm^{-3} range. This microwave signal is transported with waveguides to heterodyne detectors. They consist of a frequency-tunable, local oscillator synthesizer, an amplifier/frequency multiplier chain, a sub-harmonic mixer and an oscilloscope [5]. The signal at f_{CTR} is mixed with a reference signal at approximately the same frequency $f_{ref} \cong f_{CTR}$, guessed from the rubidium, thus plasma density $f_{CTR} \cong f_{pe} \sim n_{e0}^{1/2}$. The difference frequency signal at $f_{IF} = |f_{CTR} - f_{ref}|$ is acquired with a fast, multi-GHz bandwidth oscilloscope. The reference signal is generated by the frequency multiplication of a tunable local low frequency oscillator (f_{LO}) as $f_{ref} = n_{harm} f_{LO}$, with harmonic number n_{harm}. One can then determine $f_{CTR} = n_{harm} f_{LO} \pm f_{IF}$ from measurements of f_{IF} with multiple f_{LO} with small frequency increments, for a fixed f_{CTR}.

In the experiment, the CTR signal is split in three and analyzed with three heterodyne systems covering the entire 100–300 GHz frequency range. For low plasma densities, this diagnostic provides simultaneous information about two or three of the modulation harmonics. Detection of harmonics of the modulation signal indicates deep modulation of the bunch radius and thus formation of a micro-bunch train with $\tau = 1/f_{CTR}$ period. The heterodyne systems provide short (~duration of the proton bunch), low frequency (5–20 GHz) signals on the oscilloscope, consisting of only a few periods. We use DFT to determine f_{IF}.

The modulation frequency of the proton bunch has been measured with this technique and compared to the results obtained from DFT analysis of streak camera images and the plasma frequency expected from the plasma density (when measuring the vapor density and assuming full ionization of the Rb valence electron) [3]. It was also used to measure the modulation frequency as a function of plasma density gradients [13]. There is very good agreement between the modulation frequencies obtained from DFT of streak camera images time profiles and from CTR signals. Moreover, CTR signals at the second harmonic of the modulation frequency were also detected, confirming the deep modulation of the bunch density.

ELECTRON BUNCH DIAGNOSTICS

The electron bunch is externally injected into the wakefields, driven by the proton bunch. We characterize the accelerated electron bunch after the plasma with the spectrometer.

Spectrometer for Charge, Energy and Energy Spread Measurements

For electron injection, temporal synchronization between the self-modulation of the driver and the short electron bunch is ensured by emitting the electrons from a photo-cathode with a frequency-tripled fraction of the ionizing laser pulse. They are accelerated from the RF-cathode through a booster structure and injected into the plasma (oblique or on axis injection) with initially $\approx$ 18 MeV and accelerated up to multiple GeV [6]. At injection, the bunch charge is $\lesssim$ 1 nC and the RMS length estimated to be $\gtrsim$ 5 ps [16], thus on the order of the wakefields' period. This injection scheme thus corresponds to injecting electrons at many phases of the wakefields (2π) and letting the wakefields capture and accelerate a fraction of the incoming bunch population. The electrons may dephase through energy gain and loss.

In the current setup, after the plasma exit the electrons are focused with two quadrupoles and bent with a dipole onto a scintillator screen (see Fig. 1), imaged onto a camera in a dark room [17].

The dipole introduces a correlation between the horizontal position and energy of the electrons on the screen. Thus the peak energy and the energy spread of the accelerated electron distribution can be measured [6, 16].

The relation between light and charge was acquired exposing the screen directly with a beam with known charge [18]. Using the light-charge calibration one can determine the charge after the plasma, and thus capture rate of the injected electrons [6].

DIAGNOSTICS FOR FUTURE EXPERIMENTS

In previous experiments, the goal was to demonstrate and study the self-modulation of the proton bunch in plasma and to show that electrons can be accelerated in wakefields driven by the resulting bunch train. The electron bunch length was comparable to the wakefields' period to ensure covering all phases of the wakefields, ensuring that electrons would

ISBN: 978-3-95450-222-6 ISSN: 2673-5350 doi:10.18429/JACoW-IBIC2020-MOA001

be captured for all events, regardless of the relative timing of electrons with respect to the wakefields. In addition, electrons were injected at an angle with respect to the proton bunch propagation axis.

In upcoming measurements [19], the focus will be on preserving the quality of the accelerated electron bunch, such as high charge, low emittance and low energy spread. Those can only be achieved with a short electron bunch ($\ll \tau$) injected at the right phase of the wakefield, focusing and accelerating. The electron bunch parameters must be tailored such that plasma electron blow-out can be reached with a transverse size matched to the ion column focusing force to preserve slice emittance. Beam loading needs to be reached, to obtain a narrow energy spread and preserve the projected emittance [20].

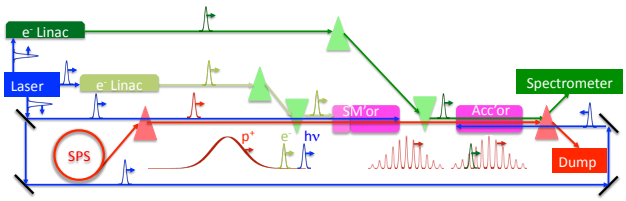

Figure 5: AWAKE setup planned for future measurements.

During the SM growth the phase of the wakefields evolves [21, 22], i.e. their phase velocity is slower than the proton bunch velocity [23]. Electrons will thus be injected after the proton bunch is fully modulated. Therefore two plasma stages, separated by a short gap for electron injection will be used, as shown in Fig. 5. The first plasma stage is for the SM of the long proton bunch, the second plasma stage for the acceleration of the electron bunch in the wakefields driven by the fully modulated proton bunch. The first plasma stage will include a plasma density step for wakefields to maintain amplitudes comparable to that at their saturation value, over long distance [13]. We want to monitor the effect of the density step on the plasma electron density perturbation sustaining wakefields at the end of the plasma with a new THz shadowgraphy diagnostic.

These experiments will bring new diagnostics challenges, both on the entrance and exit side of the plasma. The matched β-function of the $\approx$ 150 MeV electron beam to an ion column of density 10^{14}–10^{15} cm^{-3} is $\beta_{0m} \approx$ 4–13 mm. With a normalized emittance of 2 mm·mrad this corresponds to a waist transverse size of $\sigma_r \approx$ 5–10 µm, very challenging to produce and measure, especially in the Rb vapor environment. The bunch length σ_ξ on the order of 60–100 µm can be measured by electro-optic sampling or CTR interferometry. It can be monitored on a single-event-basis by measuring the CTR energy E_{CTR} and the bunch population N, and using the dependence $E_{CTR} \sim N^2/\sigma_\xi$. The spatial alignment between the two beams will be measured and monitored in the presence of the two bunches with very different parameters (population, β-function, size and length) using conventional (protons) and new Cherenkov diffraction (electrons) beam position monitors [24].

At the plasma exit, the bunch energy spectrum will be measured using a standard imaging magnetic spectrometer (quadrupoles, dipole). The accelerated electron and the modulated proton bunch overlap in space and time. Thus measuring the electron bunch emittance requires a diagnostic that separates the two bunches or the two signals. In the first category, measuring the transverse size in the non-dispersive plane of the magnetic spectrometer, the equivalent of a quadrupole scan in a single or multiple events, can in principle yield emittance [25]. In the second category, measuring the betatron radiation by the accelerated electron bunch can yield an emittance measurement [26]. Also diffraction radiation measurements, taking advantage of the difference in relativistic factor between the accelerated electrons and the protons, may provide an emittance and other bunch measurements [27, 28].

CONCLUSION

AWAKE is the first proton-beam-driven wakefield accelerator [8]. It proved the concept of seeded self-modulation and the acceleration of externally injected electrons up to 2 GeV over 10 m of plasma.

The experiment operates with a low plasma density, putting the typical time scale of observation in the few picoseconds regime. We use OTR and a streak camera with a reference laser signal to obtain detailed images of the proton bunch self-modulation over hundreds of picoseconds while preserving picosecond resolution. Stitching many events together greatly suppresses the noise of the streak camera images. We also use heterodyne detection of CTR emitted by the bunch train to directly measure the modulation frequency, including its harmonics.

Together with more standard beam diagnostics, including screens and energy spectrometer, these diagnostics have allowed for a detailed understanding of the SM process [3, 4, 13, 16] and for the demonstration of acceleration of externally injected electrons to GeV energies [6].

Future experiments will focus on producing an accelerated electron bunch with significant charge, low relative energy spread, while essentially preserving its incoming emittance. These experiments present a number of new challenges for diagnostics, which include: size and alignment measurements at the micron scale; synchronization at the sub-picosecond scale; single-event measurements of all incoming and outgoing parameters, including the emittance of the accelerated bunch.

Because of its typical operating frequency range (100–300 GHz), this accelerator pushes diagnostics typical of RF accelerators, operating in the GHz frequency range, towards those, typical of other plasma-based accelerators, operating at higher plasma densities and thus in the THz frequency range.

Content from this work may be used under the terms of the CC BY 3.0 licence (© 2020). Any distribution of this work must maintain attribution to the author(s), title of the work, publisher, and DOI

ISBN: 978-3-95450-222-6 ISSN: 2673-5350 doi:10.18429/JACoW-IBIC2020-MOA001

Content from this work may be used under the terms of the CC BY 3.0 licence (© 2020). Any distribution of this work must maintain attribution to the author(s), title of the work, publisher, and DOI

REFERENCES

[1] N. Kumar *et al.*, "Self-Modulation Instability of a Long Proton Bunch in Plasmas", *Phys. Rev. Lett.*, vol. 104, p. 255003, 2010. doi:10.1103/physrevlett.104.255003

[2] K. Rieger *et al.*, "GHz modulation detection using a streak camera: Suitability of streak cameras in the AWAKE experiment", *Rev. of Scientific Instruments*, vol. 88, p. 025110, 2017. doi:10.1063/1.4975380

[3] E. Adli *et al.* (AWAKE Collaboration), "Experimental Observation of Proton Bunch Modulation in a Plasma at Varying Plasma Densities", *Phys. Rev. Lett.*, vol. 122, p. 054802, 2019. doi:10.1103/PhysRevLett.122.054802

[4] M. Turner *et al.* (AWAKE Collaboration), "Experimental Observation of Plasma Wakefield Growth Driven by the Seeded Self-Modulation of a Proton Bunch", *Phys. Rev. Lett.*, vol. 122, p. 054801, 2019. doi:10.1103/PhysRevLett.122.054801

[5] F. Braunmueller *et al.*, "Novel diagnostic for precise measurement of the modulation frequency of Seeded Self-Modulation via Coherent Transition Radiation in AWAKE", *Nucl. Instr. and Meth. in Phys. Res. A*, vol. 909, p. 76, 2018. doi:10.1016/j.nima.2018.02.080

[6] E. Adli *et al.* (AWAKE Collaboration), "Acceleration of electrons in the plasma wakefield of a proton bunch", *Nature*, vol. 561, p. 363, 2018. doi:10.1038/s41586-018-0485-4

[7] E. Gschwendtner, M. Turner *et al.* (AWAKE Collaboration), "Proton-driven plasma wakefield acceleration in AWAKE", *Phil. Trans. R. Soc. A.*, vol. 377, p. 20180418, 2019. doi:10.1098/rsta.2018.0418

[8] P. Muggli *et al.* (AWAKE Collaboration), "AWAKE readiness for the study of the seeded self-modulation of a 400 GeV proton bunch", *Plasma Physics and Controlled Fusion*, vol. 60, no. 1, p. 014046, 2017. doi:10.1088/1361-6587/aa941c

[9] K. Pepitone *et al.*, "The electron accelerators for the AWAKE experiment at CERN — baseline and future developments", *Nucl. Instr. and Meth. in Phys. Res. A*, vol. 909, p. 102, 2018. doi:10.1016/j.nima.2018.02.044

[10] F. Batsch *et al.*, "Setup and Characteristics of a Timing Reference Signal with sub-ps Accuracy for AWAKE", *Journal of Physics: Conference Series (JPCS)*, to be published. arXiv:1911.12201

[11] P. Chen *et al.*, "Plasma Focusing for High-Energy Beams", *IEEE Transactions on Plasma Science*, vol. 15, no. 2, pp. 218–225, 1987. doi:10.1109/TPS.1987.4316688

[12] A.-M. Bachmann and P. Muggli, "Determination of the Charge per Micro-Bunch of a Self-Modulated Proton Bunch using a Streak Camera", in *Proc. 4th European Advanced Accelerator Concepts Workshop (EAAC2019)*, La Biodola, Isola d'Elba, Italy, Sep. 2019. arXiv:1912.02162

[13] F. Braunmueller, T. Nechaeva *et al.* (AWAKE Collaboration), "Proton Bunch Self-Modulation in Plasma with Density Gradient", submitted for publication. arXiv:2007.14894

[14] M. Moreira *et al.*, "Signatures of the self-modulation instability of relativistic proton bunches in the AWAKE experiment", *Nucl. Instrum. Meth. A*, vol. 909, p. 343, 2018. doi:10.1016/j.nima.2018.03.014

[15] D. H. Whittum *et al.*, "Electron-hose instability in the ion-focused regime", *Phys. Rev. Lett.*, vol. 67, p. 991, 1991. doi:10.1103/PhysRevLett.67.991

[16] M. Turner *et al.* (AWAKE Collaboration), "Experimental study of wakefields driven by a self-modulating proton bunch in plasma", emphPhys. Rev. Accel. Beams, vol. 23, p. 081302, 2020. doi:10.1103/PhysRevAccelBeams.23.081302

[17] J. Bauche *et al.*, "A magnetic spectrometer to measure electron bunches accelerated at AWAKE", *Nucl. Instrum. Meth. A*, vol. 940, p. 103, 2019. doi:10.1016/j.nima.2019.05.067

[18] F. R. Keeble, "Measurement of the electron energy distribution at AWAKE", Ph.D. Thesis, University College London, London, United Kingdom, 2019.

[19] P. Muggli (AWAKE Collaboration), "Physics to plan AWAKE Run 2", *Journal of Physics: Conference Series 224 (JPCS)*, to be published. arXiv:1911.07534v2

[20] V. K. Berglyd Olsen *et al.*, "Emittance preservation of an electron beam in a loaded quasilinear plasma wakefield", *Phys. Rev. Accel. Beams*, vol. 21, p. 011301, 2018. doi:10.1103/PhysRevAccelBeams.21.011301

[21] A. Pukhov *et al.*, "Phase velocity and particle injection in a self-modulated proton-driven plasma wakefield accelerator", *Phys. Rev. Lett.*, vol. 107, p. 145003, 2011. doi:10.1103/PhysRevLett.107.145003

[22] C. B. Schroeder *et al.*, "Growth and Phase Velocity of Self-Modulated Beam-Driven Plasma Waves", *Phys. Rev. Lett.*, vol. 107, p. 145002, 2011. doi:10.1103/PhysRevLett.107.145002

[23] A. Caldwell and K. Lotov, "Plasma wakefield acceleration with a modulated proton bunch", *Phys. Plasmas*, vol. 18, p. 103101, 2011. doi:10.1063/1.3641973

[24] T. Lefèvre *et al.*, "Cherenkov Diffraction Radiation as a tool for beam diagnostics", presented at the IBIC'19, Malmö, Sweden, Sep. 2019, paper THAO01.

[25] J. Chappell *et al.*, "Progress Towards a Single-Shot Emittance Measurement Technique at AWAKE", in *Proc. IPAC'19*, Melbourne, Australia, May 2019, pp. 3742–3745. doi:10.18429/JACoW-IPAC2019-THPGW067

[26] B. Williamson *et al.*, "Betatron radiation diagnostics for AWAKE Run 2", *Nucl. Instrum. Meth. A*, vol. 971, p. 164076, 2020. doi:10.1016/j.nima.2020.164076

[27] M. Bergamaschi *et al.*, "Noninvasive Micrometer-Scale Particle-Beam Size Measurement Using Optical Diffraction Radiation in the Ultraviolet Wavelength Range", *Phys. Rev. Applied*, vol. 13, p. 014041, 2020. doi:10.1103/PhysRevApplied.13.014041

[28] R. B. Fiorito, C. P. Welsch, H. D. Zhang, and A. G. Shkvarunets, "Novel Single Shot Bunch Length Diagnostic using Coherent Diffraction Radiation", in *Proc. IPAC'15*, Richmond, VA, USA, May 2015, pp. 1150–1152. doi:10.18429/JACoW-IPAC2015-MOPWI004

ISBN: 978-3-95450-222-6 ISSN: 2673-5350 doi:10.18429/JACoW-IBIC2020-MOA003

COMMISSIONING OF THE BEAM INSTRUMENTATION SYSTEM OF CSNS

J.L. Sun#, W.L. Huang, F. Li, P. Li, M. Meng, R.Y. Qiu, J.M. Tian, Z.H. Xu, T. Yang, L. Zeng, T.G. Xu, Institute of High Energy Physics, Chinese Academy of Sciences, China

Abstract

China Spallation Neutron Source (CSNS) accelerator complex consists of a front end, an 80MeV DTL LINAC, and a 1.6GeV Rapid Cycling Synchrotron (RCS). It is designed with a beam power of 100kW in the first phase and reserves upgrade capability to 500kW in the second phase. CSNS has started user operation at 20kW after the initial beam commissioning in 2018, the beam power is quickly up to 50kW and 80kW by two times beam commissioning in between the user beam time 2019, and finally reached 100kW, the design goal, in February 2020. The experiences and most recent status of beam instrumentation system of CSNS during the beam power ramping is introduced.

INTRODUCTION

The CSNS is designed to accelerate proton beam pulses to 1.6 GeV kinetic energy at 25 Hz repetition rate, striking a solid metal target to produce spallation neutrons. The accelerator provides a beam power of 100 kW on the target in the first phase. It will be upgraded to 500kW beam power at the same repetition rate and same output energy in the second phase. A schematic layout of CSNS phase-1 complex is shown in Figure 1. In the phase one, an ion source produces a peak current of 25 mA H- beam. RFQ linac bunches and accelerates it to 3 MeV. DTL linac raises the beam energy to 80 MeV. After H- beam is converted to proton beam via a stripping foil, RCS accumulates and accelerates the proton beam to 1.6 GeV before extracting it to the target [1, 2].

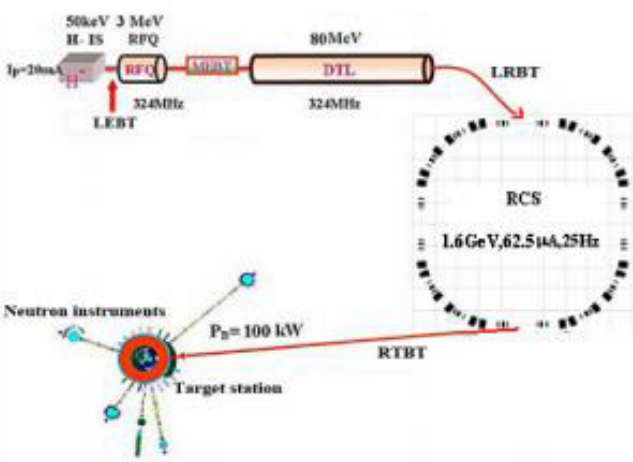

Figure 1: Schematics of the CSNS complex.

#sunjl@ihep.ac.cn

BEAM MONITORS

For the entire beam instrumentation system of CSNS, amounts of beam monitors are installed along the beam line, including beam position monitor (BPM), beam current monitor, beam profile monitor, beam loss monitor (BLM) and so on. Layout of the beam instrumentation system as shown in Figure 2 [3].

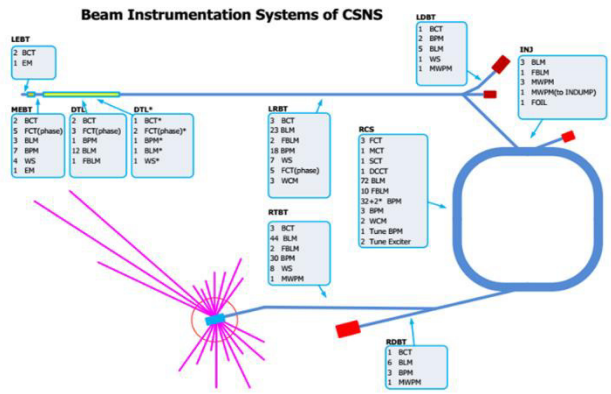

Figure 2: Layout of the beam instrumentation system of CSNS.

Beam Current Monitor

Many current transformer (CT) are used for the current measurement. Part of the magnetic rings of CT purchased from Bergoz and the other developed by our self together with a domestic company. The Cobalt-base alloys with magnetic conductivity around 20,000 to 25,000 at 25 Hz was used for the self-developing ring. Two methods used for the current calculation: 1) Take part of the flat waveform subtract background waveform then averaging; 2) Integrated waveform value as the particle number calculation.

There are two special requests for the current measurement at CSNS. One located at LINAC in front of a beam dump (LDCT), as shown in Figure 3, during normal operation the H- beam goes down to RCS but one of the BLMs along the goes up direction line has an expected high value, which induced by the residual gas stripped proton beam. A new type of electronics for low current measurement was designed for the LDCT and the residual gas stripped proton beam was measured successfully, the H- stripping percentage is ~4‰. The other special CT is located at the injection line for the strip foil efficiency measurement. Most of the H- lose two electrons when pass through the strip foil turn to proton beam and cycling in RCS, very tiny part loses only one electron turn to H0, after the second strip foil fully stripped goes to the beam dump, as Figure 4 up shows.

Content from this work may be used under the terms of the CC BY 3.0 licence (© 2020). Any distribution of this work must maintain attribution to the author(s), title of the work, publisher, and DOI

ISBN: 978-3-95450-222-6 ISSN: 2673-5350 doi:10.18429/JACoW-IBIC2020-MOA003

Content from this work may be used under the terms of the CC BY 3.0 licence (© 2020). Any distribution of this work must maintain attribution to the author(s), title of the work, publisher, and DOI

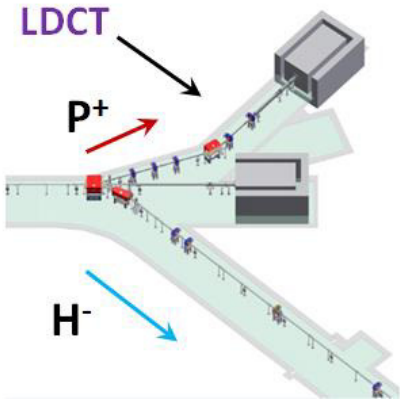

Figure 3: Layout of the LINAC beam dump.

A CT was designed in 2019 for the low current H0 detection and mounted on the beam line during summer shutdown. The history data of H0 CT can be seen in Figure 4 down, the output signal is around 20 μA (beam power 100 kW) when a new strip foil is applied, which corresponding the strip efficiency ~99.7%. The output is decreasing smoothly with the time goes on, mainly because the foil becomes wrinkling and make the H0 scattered, not all H0 passed through the CT. Together with the BLMs at the injection area, the strip foil life time is estimated around 5 weeks.

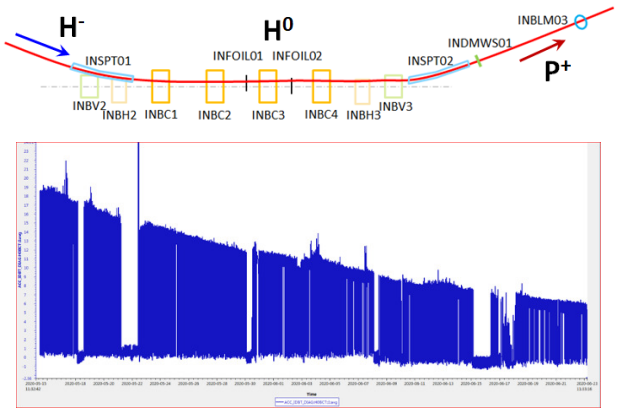

Figure 4: Schematic of the injection line of CSNS (up) and history data of the H0 CT at injection line (down).

Beam Position Monitor

Two type of BPM were designed for the accelerator, stripline for LINAC and shoe-box for the RCS ring and RTBT, as shown in Figure 5. 38 shoe-box BPM are installed in the RCS ring, 32 of them will be used to the orbit measurement, 3 of them will provide the beam position signal to the RF system, 1 for tune measurement, and the last 2 have lower capacitance will be used mainly during commissioning to measure lower signals.

Figure 5: Stripline BPM designed for LINAC (left) and shoe-box BPM for RTBT (right).

The cycling period of the beam bunches is changing from injection to extraction at RCS, two triggers were used for the BPM data acquisition, one from control system (Yellow) to indicate the beam (Pink) is coming soon and the other one from RF system (Green) to tell the electronics to start the data acquisition for each bunch, see Figure 6.

Figure 6: Two triggers of the RCS BPM electronics.

Beam Profile Monitor

Stepper motor driven type wire scanner is used for the beam profile measurement at CSNS-LINAC, mechanical schematic as shown in Figure 7, during the measurement a frame with three wires mounted is driven by a stepper motor scanning through the beam. H- loses 2 electrons on the wire during the interception and the beam profile can be obtained by measure the amount of these electrons during scanning.

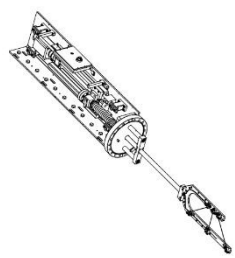

Figure 7: Mechanical schematic of CSNS wire scanner.

Carbon wire with 50 μm diameter is applied at MEBT, as carbon wire has lower energy deposition thus has longer life time than the metal wire. Tungsten wire with

ISBN: 978-3-95450-222-6 ISSN: 2673-5350 doi:10.18429/JACoW-IBIC2020-MOA003

30 μm diameter is applied at LRBT and RTBT, here the energy deposition is not a fatal issue any more since the beam energy has been increased to 80 MeV and 1.6 GeV.

In order to restrain the neutralization, a positive bias is normally applied on the wire to enhance the signal to noise ratio. An experiment aim to find out how much positive bias should be enough for the profile measurement at CSNS-LINAC was carried out at both MEBT and LRBT. Mean time negative bias was applied also, to see how it will influence the measurement.

Figure 8 shows the MEBT horizontal profile measurement results under different bias voltage (varying from -80 V to 100 V) of the 3 MeV H- beam running at 1Hz, 100 μs pulse width, ~5 mA beam current. The total signal on the wire indeed enhanced when positive bias applied, and the bias voltage beyond 20 V, the total signal reaches a plateau, no more enhancement gained even further increase the bias. The beam current goes higher when measuring at 80/100 V bias, that is why the profile curves are higher than the curves at 20~60 V.

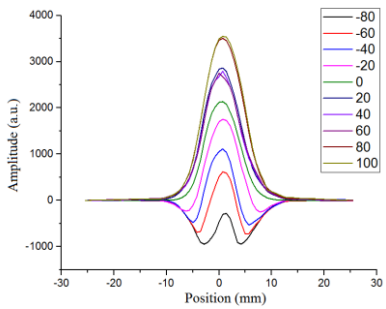

Figure 8: Horizontal profile measurement results under different bias voltage at CSNS-MEBT.

Same experiment as MEBT was performed at LRBT, here the H- beam energy is 80 MeV, which is much higher than MEBT. Figure 9 shows the horizontal beam profile measured by a specific wire scanner while different bias was applied, and beam current was stable at 9 mA during the experiment.

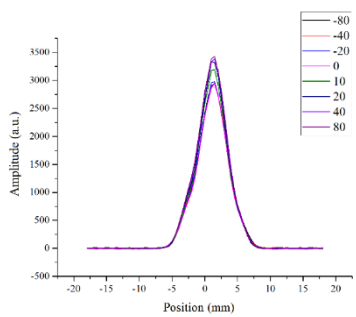

Figure 9: Horizontal profile measurement results under different bias voltage at CSNS-LRBT.

From Figure 9, there was no signal reverse at LRBT even a negative bias was applied. The measurement results are almost the same when negative bias and no bias applied, the main reason is the reaction cross section between residual gas and H- beam at 80 MeV is much lower than 3 MeV [4], the amount of the positive ions induced by the ionization become negligible. For the positive bias, it does improve the signal to noise ratio, and 20 V bias should be satisfying the profile measurement also at LRBT, same as MEBT.

Beam Emittance Measurement System

Double slits system was set up for the low energy section beam emittance measurement, mainly for LEBT@50 keV, MEBT@3 MeV and DTL1@20 MeV. Graphite plate is welded in front of the copper plate for the one mounted after RFQ and DTL1 in order to protect the copper from the thermal deposition. The first slit of all 3 sets are with water cooling to protect the copper plate from the beam damage. One of the measurement results as shown in Figure 10 of the beam after RFQ, left figure shows the simulated result ε_x=0.152 π mm·mrad and the right figure shows the measured result ε_x=0.160 π mm·mrad, which show good agreement with each other.

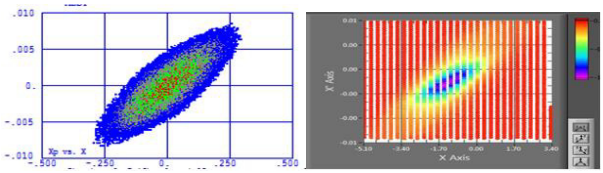

Figure 10: Emittance measurement result of the beam after RFQ (X plane).

Beam Loss Monitor

Ionization chamber filled with Argon and Nitrogen plus self-developed electronics is the main solution at CSNS for beam loss measurement for gamma ray detection. The schematic of the BLM as shown in Figure 11. All ion chambers were calibrated through a Cobalt-60 plus Keithley-6517 system after manufacturing, the sensitivity of the ion chamber is ~19 pA/rad/h. Beside the ion chamber, plastic scintillator together with photomultiplier is used for fast beam loss detection at some key positions, e.g. injection area and downstream of the bending magnets.

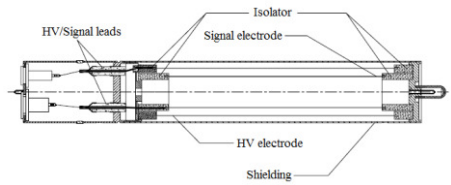

Figure 11: Schematic of the BLM at CSNS.

Beside the gamma ray ion chamber, neutron ion chamber was also developed mainly for low energy section beam loss detection since 2016. The ion chamber is filled with BF3 and with 7.5 cm thick PE covered as the fast neutrons' moderator. One neutron detector and a gamma detector were mounted in the same location at DTL1 for cross comparison, as shown in Figure 12. Through beam test the BF3 signal is ~1757 times higher than Ar+N2, agrees well with theoretical calculation

Content from this work may be used under the terms of the CC BY 3.0 licence (© 2020). Any distribution of this work must maintain attribution to the author(s), title of the work, publisher, and DOI

ISBN: 978-3-95450-222-6 ISSN: 2673-5350 doi:10.18429/JACoW-IBIC2020-MOA003

Content from this work may be used under the terms of the CC BY 3.0 licence (© 2020). Any distribution of this work must maintain attribution to the author(s), title of the work, publisher, and DOI

(~1600). Optimization of the thickness of the moderator is now on going to increase the response time of the neutron detector.

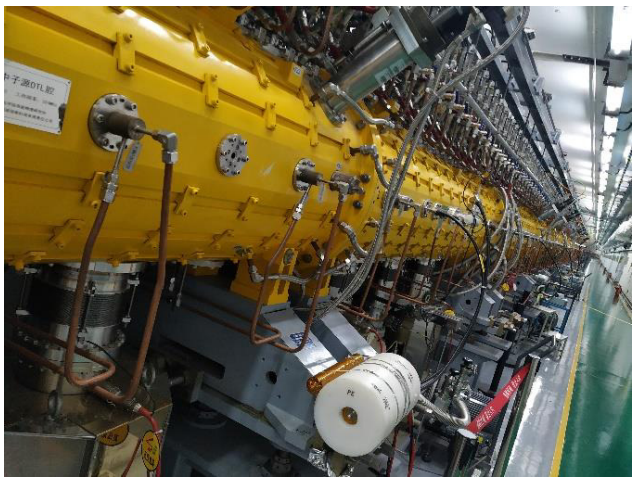

Figure 12: Beam test layout of the neutron detector and gamma detector.

SUMMARY

CSNS has achieved its design goal of 100 kW, in February 2020, 18 months ahead of schedule, and running at 100 kW stably since then. For beam instrumentation system all subsystems perform well, we are keep developing, improving and updating.

REFERENCES

[1] S. Fu *et al.*, "Status and Challenges of the China Spallation Neutron Source", in *Proc. 2nd Int. Particle Accelerator Conf. (IPAC'11)*, San Sebastian, Spain, Sep. 2011, paper TUXA01, pp. 889-893.

[2] S. Fu *et al.*, "Status of the China Spallation Neutron Source Project", in *Proc. 23rd Particle Accelerator Conf. (PAC'09)*, Vancouver, Canada, May 2009, paper TH1GRI02, pp. 3053-3057.

[3] J. L. Sun *et al.*, "Status of the Beam Instrumentation System of CSNS", in *Proc. 57th ICFA Advanced Beam Dynamics Workshop on High-Intensity and High-Brightness Hadron Beams (HB'16)*, Malmö, Sweden, Jul. 2016, pp. 95-97. doi:10.18429/JACoW-HB2016-MOPR017

[4] Glenn F. Knoll, Radiation Detection and Measurement, 4th Edition, Hoboken, New Jersey, USA: John Wiley & Sons, Inc., 2010.

ISBN: 978-3-95450-222-6 ISSN: 2673-5350 doi:10.18429/JACoW-IBIC2020-MOA004

BEAM INSTRUMENTATION PERFORMANCES THROUGH THE ESRF-EBS COMMISSIONING

L. Torino*, ALBA-CELLS, Cerdanyola del Vallès, Spain
N. Benoist, F. Ewald, E. Plouviez, J.L. Pons, B. Roche, K.B. Scheidt, F. Taoutaou, F. Uberto,
European Synchrotron Radiation Facility, Grenoble, France

Abstract

The upgrade of the European Synchrotron Radiation Facility (ESRF) storage ring has lead to the construction of a new machine called the Extremely Brilliant Source (EBS). EBS has been successfully commissioned in less than three month and reached the targeted parameters for user mode. The success of the EBS commissioning also depended on the performances and the reliability of the beam instrumentation used to monitor the beam. In this paper a summary of the EBS commissioning is presented with a special focus on the beam instrumentation performances.

INTRODUCTION

After one year of shutdown during which the old ESRF storage ring has been completely dismantled, the new Extremely Brilliant Source (EBS) has been successfully commissioned and it is currently running in user mode.

The innovative Hybrid Multi-Bend Achromate lattice allows to achieve horizontal and vertical emittances of respectively 150 and 5 pm [1]. Thanks to the reduction of emittances, in particular in the horizontal plane, the 6 GeV electron beam is able to produce a more brilliant and coherent synchrotron radiation beam.

User mode beam parameters have been reached in three month.

The commissioning started on November 28th 2019, few days ahead of schedule thanks to the time saved in the installation phase and the quick commissioning of the linac and the booster. The first turn was achieved straight away thanks to the outstanding work done on the machine alignment. The beam was stored for the first time on December 5th with on-axis injection. In this period two obstacles were found and removed and problems related with magnets calibration and cross-talking were spotted and solved. On December 15th off-axis injection was established and accumulation occurred. After one moth shutdown on January 17th 2020 the commissioning started again and it ended exactly on time on March 2nd when 200 mA were achieved and the hand was let to the commissioning of beamlines.

The whole commissioning period can be divided into two main phases:

- First turns and storage;
- Accumulation and current ramp-up.

These results have been quickly achieved also thanks to a well functioning beam instrumentation system which has been able to monitor the beam from day one. Most of the commissioning work for the beam instrumentation in fact was performed on the old ESRF machine, as presented in [2].

In this paper, the performances of the main beam instrumentation systems and their relevance in reaching each of the milestones will be presented.

BEAM POSITION MONITORS

The EBS Beam Position Monitor (BPM) system is composed by 320 BPMs blocks (10 per cells) equipped with a hybrid Libera electronics system for data acquisition and processing [3]. This hybrid readout system is composed by 6 Libera Brilliance, capable to provide stream of data at 10 kHz which are used by the Fast Orbit Feedback, and 4 Libera Spark.

The BPM system was essential during the commissioning not only for orbit measurements and for allowing the machine tuning but also to see the beam during first turns at very low current, thanks to its high sensitivity.

First Turns and Storage

During this phase, BPMs were used mostly in ADC or in Turn-By-Turn (TBT) mode. Liberas Spark naturally work in time domain processing: this makes it rather easy to switch the system to TBT mode. For Liberas Brilliance the anti-smearing algorithm has been used to reduce the effect of the narrow digital filter embedded in the electronics [4].

For the first turns, the most used feature of the BPM system was the the signal "Sum" providing the sum of the signals coming from the four BPM buttons. This signal is proportional to the current and a plot of the its value versus the BPM number provides a clear indication of the presence of the beam along the machine. The intensity of the signal being proportional to the current, a drop of the of intensity represents a drop in current: this feature can clearly reveal the presence of obstacles on the trajectory.

Figure 1 shows one of the first injections in the storage ring during November 28, first day of commissioning. The horizontal axis corresponds to the Libera ADC samples: 304 samples represent one revolution period. On the vertical axis, the BPMs are shown ordered in the direction of the beam propagation: one column represents one machine turn. The data is triggered 7 revolution periods before the beam arrival time. It is clear that the beam was able to perform more than one turn, already at the first injection. Also, it is possible to notice that a drop of beam intensity is present somewhere around 2/3 of the machine (cell 23). This was the first identification of the presence of an obstacle in the

* ltorino@cells.es

Content from this work may be used under the terms of the CC BY 3.0 licence (© 2020). Any distribution of this work must maintain attribution to the author(s), title of the work, publisher, and DOI

ISBN: 978-3-95450-222-6 ISSN: 2673-5350 doi:10.18429/JACoW-IBIC2020-MOA004

Content from this work may be used under the terms of the CC BY 3.0 licence (© 2020). Any distribution of this work must maintain attribution to the author(s), title of the work, publisher, and DOI

storage ring, which indeed was confirmed by other systems and removed straight after.

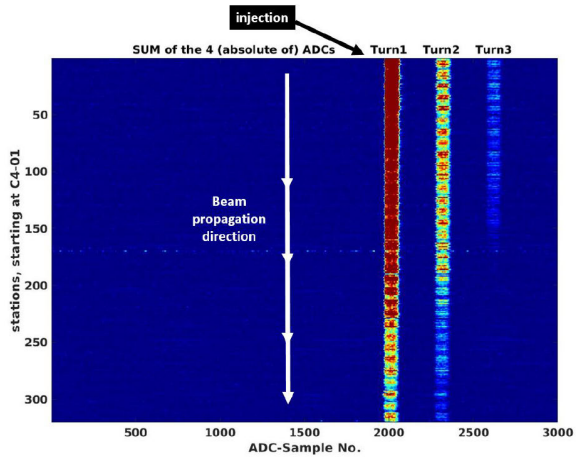

Figure 1: One of the first injection in the EBS storage ring, seen by the BPM system in ADC mode. One turn corresponds to 304 ADC samples, the beam is moving from the top to the bottom.

The BPM system has also been able to measure the beam first turn trajectory from day one. Figure 2 shows the orbit of the beam over the first two turns (one turn corresponds to 320 BPMs). Due to the large excursion of the beam path, a polynomial model has been used to obtain the transverse beam position online instead of the standard Delta-over-Sum formula [5].

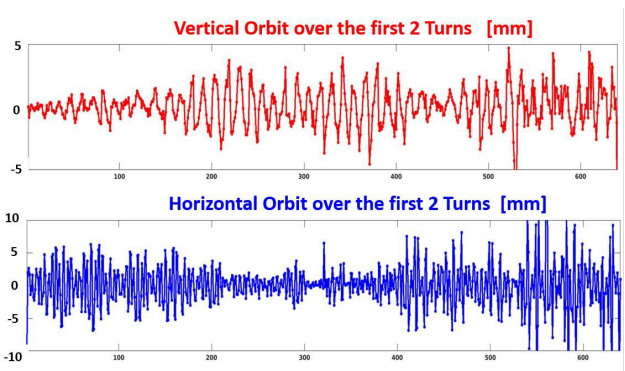

Figure 2: Horizontal and vertical orbit over two turns during one of the first injections in the EBS machine.

Beam orbits obtained in this way have been used since the beginning to compute and implement corrections and adjust the machine parameters.

The BPM sum signal has also been used as rough, not calibrated, turn-by-turn current monitor when trying to store the beam via RF capture. The sum turn-by-turn signal from one of the BPM was used to spot the number of turns performed by the beam. When RF-capture happened the signal did not go back to the noise level but stayed higher, as shown in Fig. 3.

Moreover, the injection efficiency was very low at the beginning, only a small amount of electrons was entering

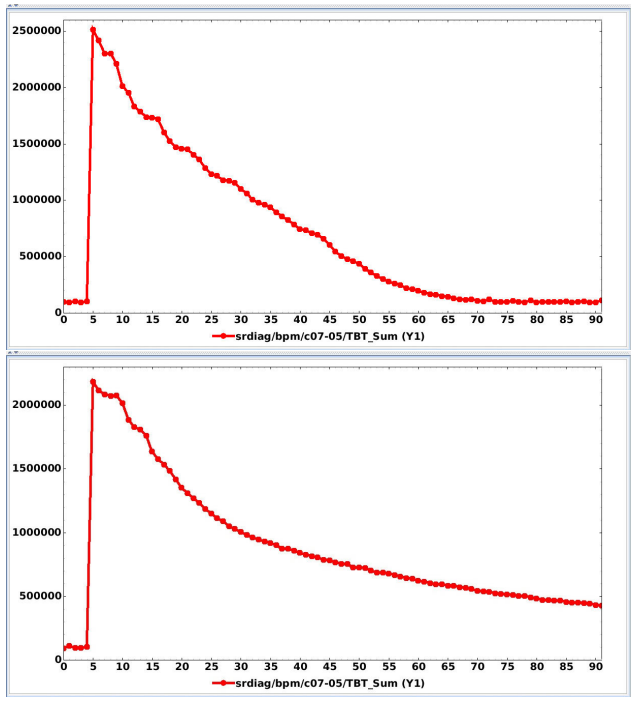

Figure 3: Turn-by-turn sum signal from BPM 5 of cell 7. Each sample represent one turn. No RF-capture (top), beam stored (bottom): the signal stays on top of the noise level.

in the storage ring and the standard current transformer was not sensitive enough to measure such a small current. To cope with this lack of information, slow data from BPM sum signals was displayed at a sampling rate of 1 Hz and this allowed to see the first stored beam even if its current was lower than 1 µA.

Accumulation and Current Ramp-Up

Throughout all the process of achieving accumulation and then current ramp-up, BPMs have been constantly used to measure the orbit before and after applying corrections.

In order to guarantee a better precision, Beam Based Alignment (BBA) has been performed as soon as 5 mA of stored beam were reached. The rms of the offsets yielded values of 170 µm on the horizontal plane and 142 µm on the vertical.

The vertical beam stability measured with 20 Hz SA data was found to be 32 nm without orbit correction and it went down to 12 nm (rms) when corrections were applied.

Orbit measurements using the optimized BPM system were able to spot problems with the scale factor of lattice magnets, calibration errors, unexpected magnetic cross-talk between quadrupoles and dipoles. Of course, these measurements are still very important even after the commissioning period, in order to permanently monitor the beam and to provide an input to the feedback system.

ISBN: 978-3-95450-222-6 ISSN: 2673-5350 doi:10.18429/JACoW-IBIC2020-MOA004

BEAM LOSS MONITORS

In 2018, an upgrade of the ESRF Beam Loss Monitor (BLM) system has been performed [6]. The system was installed and fully commissioned with the old machine.

The EBS BLM system is composed by 128 Beam Loss Detectors (BLDs, 4 per cell), and 32 Libera-BLM electronics (1 per cell), each one capable of control and readout 4 detectors. The BLDs are calibrated relative to each other to ensure consistency between the readings of different units.

The BLM system has been of great importance during all the commissioning, mainly thanks to its high sensitivity and its versatility in acquiring easily fast and slow data. The fast-data configuration has been mainly used during the First turn phase, while the slow data acquisition has been of great help to monitor the vacuum conditioning and for machine optimization.

First Turns

In order to obtain useful signals, during this phase, the BLM system was set in "Fast acquisition" mode. In this mode, the electronics input impedance is set to 50 Ω in order to be able to acquire almost bunch by bunch losses. Two possible operation settings could be selected and could be checked in parallel:

- ADC mode: raw data from the ADC at 125 MHz;
- Turn by turn: sum of the ADC signal in order to integreat the losses in one turn (≃333 kHz).

The ADC data has been used since the first moment to spot the real number of turns the beam was performing. It is natural that during first injections the beam get lost. The most of the losses will be concentrated in the first turns but the residual beam will continue circulating for longer. This could be easily observed using one of the BLDs and looking at ADC data comprehending a temporal span of several turns, as shown in Fig. 4. The raw ADC data from one of the first injection showed that most of the beam was lost in the first 3 turns, here the beam still provided enough signal to be seen also by the BPMs (Fig. 1), but some more turns were actually performed.

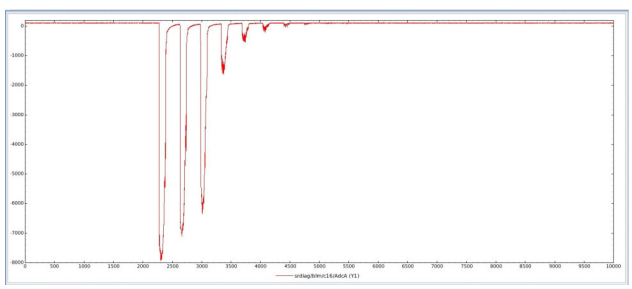

Figure 4: ADC data of one of the first injections (as in Fig. 1), showing that the beam actually performs more than three turns.

With the BLM system being distributed all around the machine (as the BPM system), it was possible to follow the longitudinal position of the beam and spot the location in which it was mainly lost. Since the very first injection it was in fact clear that the beam was performing more than one turn and that it was mainly lost before the first BLD of cell 23, i.e. at the straight section. This, together with the data from the BPM, made clear the identification of the first obstacle that was found in the storage ring. Figure 5 shows the distribution of losses at the first turn, peaking at the first BLD of cell 23.

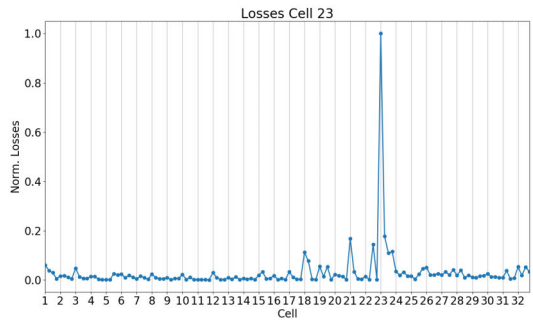

Figure 5: Distribution of the losses of the first turn of one of the very first injection in EBS. The losses are concentrated at the first BLD of cell 23.

In the same way, a mis-installed vacuum vessel in cell 8 and a second obstacle in cell 5 have been identified.

The obstacle in cell 5 was the reason for the low initial injection efficiency. Cell 5 is in fact the first cell after injection (happening in cell 4). A small residual aluminium foil was trapped there generating some losses some turns after injection. The amount of losses on turn by turn base was not so high after few turns though and nothing clear was observed neither by the BPM system. However, after storage, when switching the BLDs to slow acquisition mode, a huge spike was observed in cell 5. In order to verify the presence of an obstacle, bumps at the supposed obstacle location were performed, showing a clear indication of its presence, as depicted in Fig. 6. The removal of this obstacle drastically improved the injection efficiency allowing accumulation and current ramp-up.

Current Ramp-Up

The BLM system has been heavily used during the current ramp-up phase for two main scopes: machine optimization and vacuum conditioning monitoring.

In the first case the sum of the slow signal (1 MΩ impedance, 1 Hz repetition rate) has been used to optimize the beam lattice: a reduction of the signal (i.e. total losses) is related with a better configuration of the machine at a given emittance. This signal has been preferred to the one of the lifetime, used for the old machine, being more sensitive and responding faster to the setting modifications. An example of optics optimization using the total losses is presented in Fig. 7: during the beam decay, the lattice was tuned in order to minimize the losses maintaining the emittance constant.

Content from this work may be used under the terms of the CC BY 3.0 licence (© 2020). Any distribution of this work must maintain attribution to the author(s), title of the work, publisher, and DOI

ISBN: 978-3-95450-222-6 ISSN: 2673-5350 doi:10.18429/JACoW-IBIC2020-MOA004

Content from this work may be used under the terms of the CC BY 3.0 licence (© 2020). Any distribution of this work must maintain attribution to the author(s), title of the work, publisher, and DOI

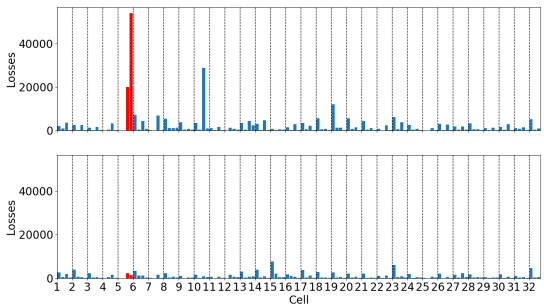

Figure 6: Slow losses around the ring before (top) and after (bottom) the bump in cell 5. The peak reduction due to the bypassing of the obstacle is evident.

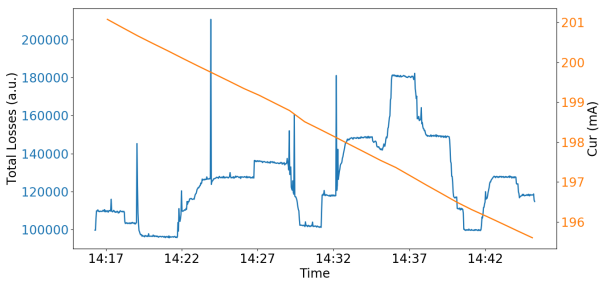

Figure 7: Total losses used to perform beam optimization (in blue) and beam current (in orange).

The other main usage of the BLM system during the commissioning was the monitoring of the vacuum conditioning especially at the insertion device chamber positions. These chambers are typically very small and constantly heated by synchrotron radiation and thus degassing at least during the first period of exposition. Also, a small misalignment of the chamber might result in damages due to the high flux of hard X-rays impinging on the chamber surface. The expected behavior is a reduction of losses after some time of vacuum conditioning at a given current. Mostly, this has been the behavior of all the insertion device chambers but two that were promptly replaced. After chambers were removed the normal conditioning behavior of the machine was recovered.

ELECTROMAGNETIC DEVICES

Electromagnetic devices such as current monitors and striplines have been very useful during machine commissioning. In particular, a large use of striplines to monitor the fill pattern and for tune measurement have been of great help.

First Turn

The fill pattern monitor system, developed in the old machine [7], guarantees a high dynamic range and a good bandwidth. To see the first turn, attenuators connected to the stripline used as pickup were removed in order to extract the largest possible signal. This indeed allowed to see the presence of beam since the very beginning of the commissioning. Figure 8 shows a snapshot of the fill pattern over several turns during one of the very first injections. The injected fill pattern was 1/3 of the storage ring and it is clear that the beam current was reducing after each turn.

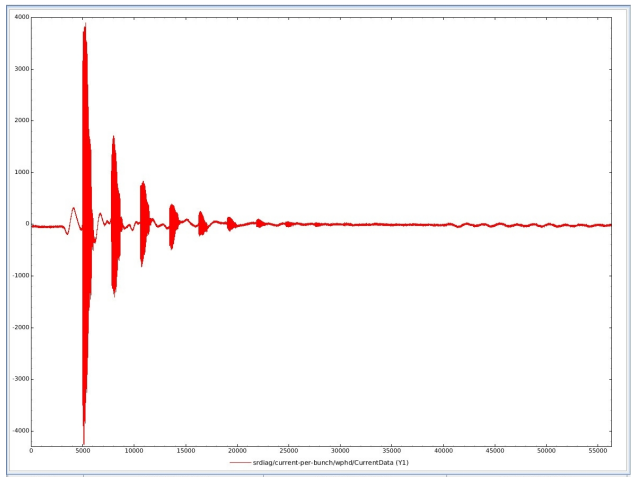

Figure 8: Snapshot of the device server of the oscilloscope used for fill pattern measurement during one of the very first injections.

As soon as the beam was stored the tune monitor started to be of great importance. At EBS, the tune monitor system [8] consists of a shaker to excite the beam, four BPM buttons from one of the 20 button chambers, a Libera Spark to read the data and a device server for data processing. Attenuators used to reduce the signal intensity were removed for in order to be able to perform measurements at very small current.

A snapshot of the tune monitor application obtained the first day of stored beam is presented in Fig. 9. Note that the estimated current at that moment was 50 µA.

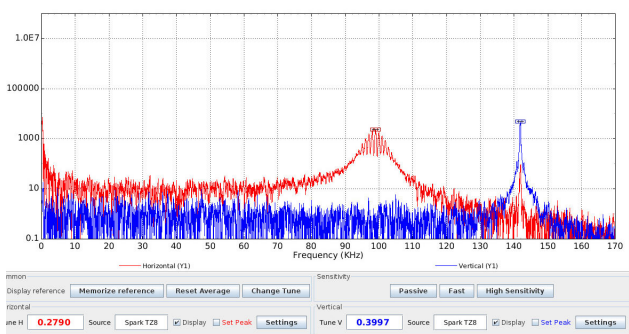

Figure 9: Snapshot of the tune monitor application. In red the horizontal tune and in blue the vertical one.

Current Ramp-Up

During the current ramp-up, the tune monitor and the fill pattern measurements have been used in a standard way to routinely monitor tune and fill pattern. In particular this last one has been used also to check the synchronization between

ISBN: 978-3-95450-222-6 ISSN: 2673-5350 doi:10.18429/JACoW-IBIC2020-MOA004

the injector and storage ring, such to verify the timing and improve the injection efficiency.

Once accumulation was established standard current monitors as the Parametric Current Transformer (PCT) and the Integrated Current Transformer (ICT) have been successfully put in operation showing outstanding resolution. Figure 10 shows the beam current over two days just after accumulation was established. In order to condition the machine the maximum amount of current was let circulating into the machine during night, while during day-time, commissioning work was carried out.

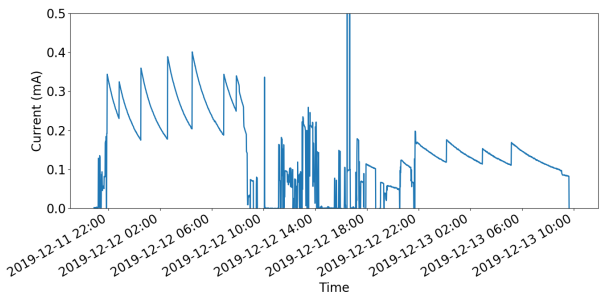

Figure 10: Current evolution during two days just after accumulation was established.

FEEDBACK

Feedback systems are used to improve beam orbit stability (orbit feedback [9]) and avoid coupled-bunch or single-bunch instabilities (bunch-by-bunch feedback [10]). Both systems were developed and commissioned on the old ESRF storage ring.

Current Ramp-Up

The orbit feedback consists in a mixed slow-fast feedback. The orbit perturbations were already minimized by the machine design. Figure 11 presents a comparison of the beam motion with and without the orbit feedback. When the feedback is off the beam looks already quite stable (less then 1 µm rms), when the feedback is on, the beam motion is further reduced to less then 0.5 µm rms.

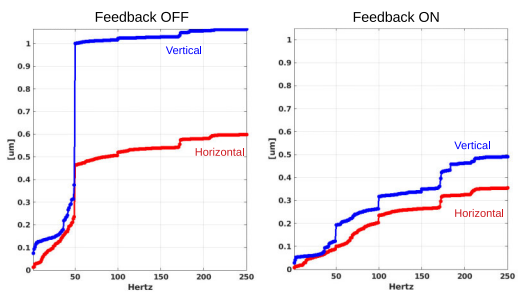

Figure 11: Beam motion with the beam off (left) and on (right) in the horizontal (red) and vertical (blue) plane.

The importance of bunch by bunch feedback became obvious at higher current, where beam instabilities started to arise due to ion trapping. EBS is running from day one of user mode with the same fill pattern of the old machine, most of these fill patterns foresee at least a single bunch filled with high current (from 1 to 8 mA). In order to cope with single bunch instabilities the multi-bunch feedback is operational and reducing blow up effects.

EMITTANCE MONITORS

The emittance monitor of EBS is composed by five pinhole systems taking light from two different source types in order to allow energy spread measurement [11].

Stored Beam

As soon as the beam was stored, the first sychrotron light was observed at the pinholes stations. In order to get an image of the beam at very low current, all filters were removed. The pinhole can be aligned remotely with four degree of freedom. Figure 12 shows the first image of the EBS light. At the time 12 µA of current were present in the storage ring.

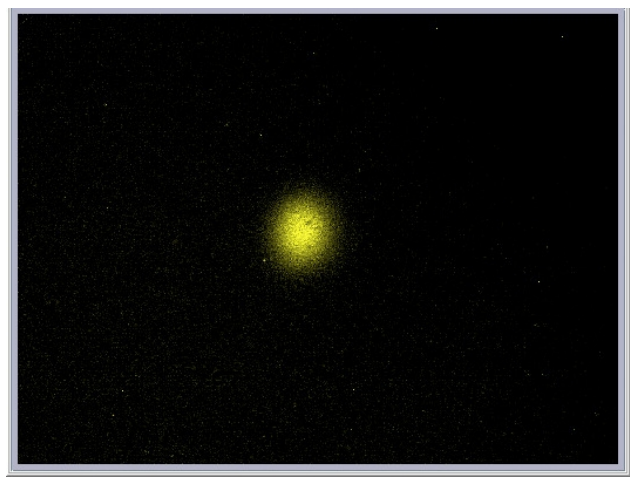

Figure 12: First EBS synchrotron light observed at one of the pinhole locations.

Current Ramp-Up

Once accumulation was achieved, emittance measurements have been used to optimize the machine lattice to achieve the ultimate performances. An example of emittance measurement used during beam optimization is presented in Fig. 13.

OUTLOOK

The role of beam instrumentation in the commissioning of EBS has been primary. All the instruments has been fulfilling all the expectations since day one mainly thanks to the experience gained in commissioning and operating them in the old ESRF machine. This experiences and a

Content from this work may be used under the terms of the CC BY 3.0 licence (© 2020). Any distribution of this work must maintain attribution to the author(s), title of the work, publisher, and DOI

ISBN: 978-3-95450-222-6 ISSN: 2673-5350 doi:10.18429/JACoW-IBIC2020-MOA004

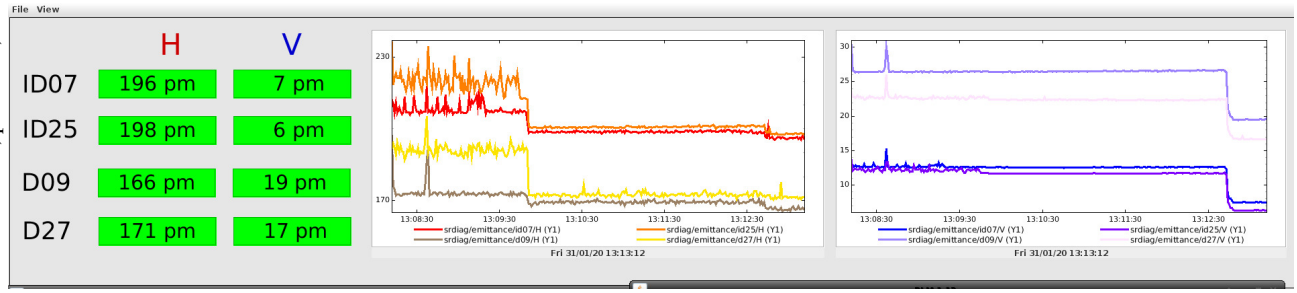

Figure 13: Emittance evolution when tuning quadrupoles.

deep knowledge of the equipment have also permitted a non-conventional use for many of them allowing to speed up the full commissioning process.

REFERENCES

[1] J. Biasci *et al.*, "A low emittance lattice for the ESRF", in *Synchrotron Radiation News*, vol. 27, no. 6, pp. 8–12 2014. doi:10.1080/08940886.2014.970931

[2] L. Torino *et al.*, "Overview on the Diagnostics for EBS-ESRF", in *Proc. 8th Int. Beam Instrumentation Conf. (IBIC'19)*, Malmö, Sweden, Sep. 2019, pp. 9–13. doi:10.18429/JACoW-IBIC2019-MOA003

[3] K. B. Scheidt, "Complete Test Results of New BPM Electronics for the ESRF New LE-Ring", in *Proc. 7th Int. Beam Instrumentation Conf. (IBIC'18)*, Shanghai, China, Sep. 2018, pp. 257–260. doi:10.18429/JACoW-IBIC2018-TUPB02

[4] K. B. Scheidt, "Increased Performance and Functionality of the Libera BPMs in the ESRF Storage Ring", presented at European Synchrotron Light Sources (ESLS 2016), Trieste, Italy, November 2016.

[5] A. A. Nosych, U. Iriso, and J. Olle, "Electrostatic Finite-element Code to Study Geometrical Nonlinear Effects of BPMs in 2D", in *Proc. 4th Int. Beam Instrumentation Conf. (IBIC'15)*, Melbourne, Australia, Sep. 2015, pp. 418–422. doi:10.18429/JACoW-IBIC2015-TUPB047

[6] L. Torino and K. B. Scheidt, "New Beam Loss Detector System for EBS-ESRF", in *Proc. 7th Int. Beam Instrumentation Conf. (IBIC'18)*, Shanghai, China, Sep. 2018, pp. 346–352. doi:10.18429/JACoW-IBIC2018-WEOB01

[7] L. Torino, B. Roche, and B. Vedder, "Current Per Bunch Distribution Measurement at ESRF", in *Proc. 8th Int. Beam Instrumentation Conf. (IBIC'19)*, Malmö, Sweden, Sep. 2019, pp. 59–62. doi:10.18429/JACoW-IBIC2019-MOPP002

[8] B. Roche, E. Plouviez, F. Uberto, "Improved Tune Monitor", presented at Diagnostics Experts for European Light Sources (DEELS 2017), Soleil Synchrotron, France, June 2017.

[9] E. Plouviez and F. Uberto, "The Orbit Correction Scheme of the New EBS of the ESRF", in *Proc. 5th Int. Beam Instrumentation Conf. (IBIC'16)*, Barcelona, Spain, Sep. 2016, pp. 51–54. doi:10.18429/JACoW-IBIC2016-MOPG09

[10] B. Roche, "Experience on the integration of Diamond MBF-2 @ ESRF", presented at Joint ARIES Workshop on Electron and Hadron Synchrotrons, Bellaterra, Spain, November 2018.

[11] F. Ewald, "Comparison of beam size monitoring using x-rays at ESRF", presented at Topical Workshop on "Emittance Measurements for Light Sources and FELs, Cerdanyola del Valles, Spain, Jan. 2018.

Content from this work may be used under the terms of the CC BY 3.0 licence (© 2020). Any distribution of this work must maintain attribution to the author(s), title of the work, publisher, and DOI

ISBN: 978-3-95450-222-6 ISSN: 2673-5350 doi:10.18429/JACoW-IBIC2020-MOA005

BEAM INSTRUMENTATION SYSTEM FOR SHANGHAI SOFT X-RAY FEL TEST FACILITY*

L.W. Lai, L.Y.Yu, Y.B. Leng†, R.X.Yuan, J.Chen, Y.B.Yan, W.M.Zhou, J.Chen, S.S.Cao, L.H.Hua, B.Gao, N.Zhang, T.Shen, F.Z.Chen, R.T.Jiang, W.C.Fang, C.Feng
SSRF, Shanghai Advanced Research Institute, Chinese Academy of Sciences, Shanghai, China

Abstract

Shanghai Soft-Xray FEL (SXFEL) test facility was designed and built to demonstrate EEHG and HGHG schemes and verify key technologies for the future hard x-ray FEL facility (SHINE). After three years commissioning 8.8 nm FEL radiation with peak power of 1 MW had been achieved at the end of 2019. The design, fabrication, commissioning and operation of BI system including stripline-BPM, Cavity-BPM, screen monitor, bunch length monitor, beam arrival monitor, bunch energy monitor, will be introduced in this paper. Several lessons learned during design stage and beam commissioning stage, such as radiation damage of CCDs and step-motors, bad choice of CBPM working frequency, thermal drift of BAM and so on, will be addressed as well.

INTRODUCTION

SXFEL Test Facility (SXFEL-TF) was initiated in 2006 and founded in 2014. Its 0.84GeV linac and undulators were installed through 2016 to 2018, it is for testing the cascaded seeding schemes. The main parameters are listed in Table 1. The SXFEL-TF commissioning has completed this year, and the SXFEL user facility (SXFEL-UF) is under construction. The layout of SXFEL-TF and SXFEL-UF are shown in Figure 1.

Table 1: SXFEL-TF Parameters

Parameter	Value
Total length	293m
Electron energy	0.84 GeV
Bunch charge	0.5 nC
Repetition rate	10 Hz
FEL output	8.8 nm
FEL scheme	HGHG/EEHG
FEL pulse	100-200 fs
FEL power	>100 MW

*Work supported by Youth Innovation Promotion Association, CAS (Grant No. 2019290); The National Key Research and Development Program of China (Grant No. 2016YFA0401903).
† lengyongbin@zjlab.org.cn

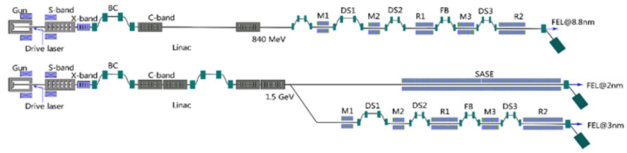

Figure 1: Layout of SXFEL-TF (top) and SXFEL-UF (bottom).

In order to maintain high FEL gain, high performance beam instrumentation system is required for the SXFEL-TF. Measured beam parameters including bunch charge, beam position (BPM), beam profile, beam arrival time (BAM) and bunch length (BLM). Table 2 lists the beam diagnostic devices included and the required resolution.

Table 2: Requirements of SXFEL-TF Diagnostic System

	Quantity	Resolution
Bunch charge	7	1%
Beam position (injector and linac)	28	10μm
Beam position (undulator)	17	1μm
Beam profile	56	20μm
Arrival time	4	100fs
Bunch length (CSR)	1	100fs
Bunch length(deflector)	1	100fs

The system control and data acquisition are based on the EPICS platform, which enables bunch-by-bunch measurement.[1]

BEAM INSTRUMENTATION SYSTEM DESIGN AND PERFORMANCE

Bunch Charge Measurement

Integrated current transformers (ICT) from Bergoz are adopted to monitor the bunch charge along the accelerator. Instead of using analog integrator BCM-IHR-E from Bergoz and a digitizer to sample the bunch charge result, we using an oscilloscope to sample the signal from ICT directly and perform the integral calculation in the digital zone. The ADC of the oscilloscope is 10 bits, bandwidth is 600 MHz, and maximum sampling rate is 5GSPS. An embedded EPICS soft-IOC has been developed on the oscilloscope to get the sampled data and calculate the charge.

One of the advantages of this solution is avoiding the interference of noise signal to the analog circuit. Another advantage is that digital signal processing algorithms can be

Content from this work may be used under the terms of the CC BY 3.0 licence (© 2020). Any distribution of this work must maintain attribution to the author(s), title of the work, publisher, and DOI

ISBN: 978-3-95450-222-6 ISSN: 2673-5350 doi:10.18429/JACoW-IBIC2020-MOA005

Content from this work may be used under the terms of the CC BY 3.0 licence (© 2020). Any distribution of this work must maintain attribution to the author(s), title of the work, publisher, and DOI

applied in the oscilloscope to improve the measurement performance. For example, Fig. 2(top) is the output signal of ICT on linac coupling a high frequency noise signal. This is hard to find and hard to remove in the traditional solution. However, the noise signal is displayed on the oscilloscope directly and can be removed perfectly by applying PCA algorithm in the soft-IOC(Fig. 2 (bottom)).

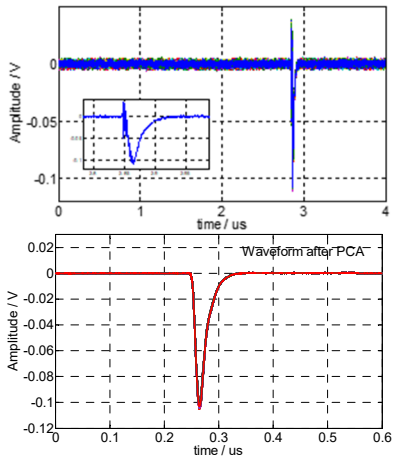

Figure 2: PCA algorithm applied on oscilloscope.

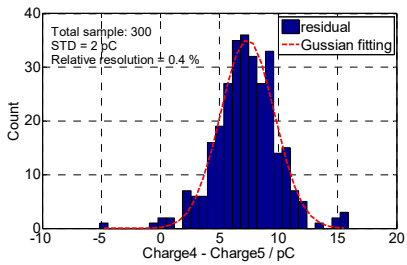

Figure 3: Bunch charge measurement resolution evaluation with PCA.

The system relative resolution is 0.7%, and improved to 0.4% after applying PCA algorithm (Fig. 3). This is better than the 1.0% requirement.

Beam Position Measurement

Accurate beam trajectory measurement and control are the foundation of XFEL success radiation. There have two different types of transverse BPM monitors on the XFEL. Stripline BPMs are applied in the injector and linac section. The electrode length is 150mm, and the stripline BPM total length is 250mm. The electrode K=5.24mm. Figure 4 is the design of the BPM.

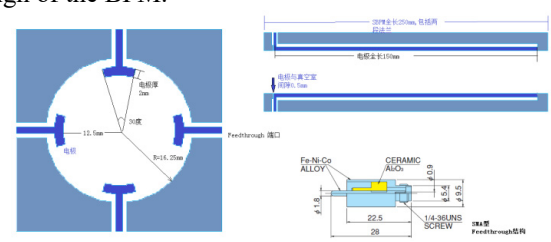

Figure 4: Stripline BPM design.

The strongest frequency of the stripline output RF signal is 500MHz. The RF signals are fed into an in-situ developed Digital BPM signal processor (DBPM) directly. RF signals firstly passing through a serial of conditioning components, including 500MHz IF, 20MHz BW Band Pass Filters (BPF), Low Pass Filters (LPF), amplifiers and 31dB configurable attenuator, then sampled by 16bits, 125MSPS ADCs on the DBPM[2]. The output signal amplitude of each pick-up is calculated by implementing $\sqrt{\sum_{i=1}^{N} x_i^2}$ calculation in the FPGA on the DBPM, x_i is the sampled N points BPM signal. Then Δ/Σ algorithm is applied to get beam position. An EPICS IOC is developed on the ARM, which communicate with FPGA through PCIE bus. Figure 5 shows the BPM pickup installed in tunnel (up left), the DBPM in cabinet (up right) and DBPM OPI control panel(bottom).

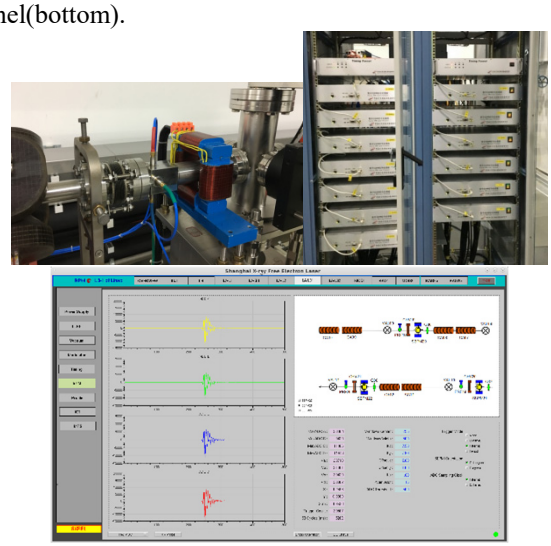

Figure 5: Stripline BPM and DBPM.

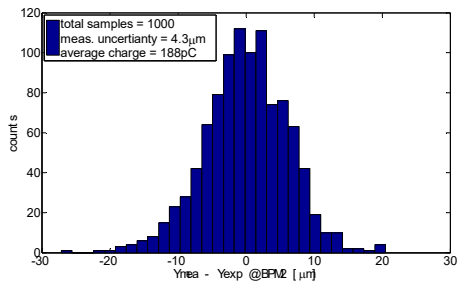

Figure 6: Stripline BPM system performance.

The stripline BPM system performance is evaluated by applying three adjacent BPM in a straight section. Figure 6 shows the resolution is 4.3μm@188pC, which is much better than the required 10μm @500pC.

Cavity BPMs are used in the undulator section to meet the 1μm high resolution requirement. The cavity BPM structure refers to the SCALA design. Table 3 shows the frequency and loaded Q value of each cavity.

ISBN: 978-3-95450-222-6 ISSN: 2673-5350 doi:10.18429/JACoW-IBIC2020-MOA005

Table 3: Cavity BPM Parameters

Cavity	Frequency	Loaded Q
Reference	4693 ± 3MHz	2250 +-10%
Horizontal	4681 ±3MHz	4500 +-10%
Vertical	4688 ± 3MHz	4500 +-10%

There is no tuner for the cavities, and the frequency of the three cavities are separated to avoid the possible cross-talk between cavities.

The same narrow band DBPM is applied for the cavity BPM signal DAQ because of time rush and lack of experience. The sampling clock is 119MHz synchronized with machine. Then a complex analog LO signal generator is designed to down convert the output RF signals of the three cavities to around 500MHz. Figure 7 shows the cavity BPM pickup and pre-amplifier installed in tunnel(left) and the LO, down-mixing front-end and the DBPM installed in cabinet (right).

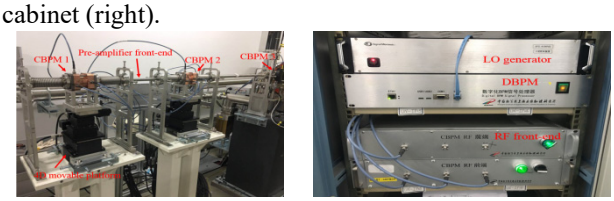

Figure 7: Cavity BPM and the electronics.

FFT algorithm is applied in the FPGA to get the amplitude and phase of each cavity signal. Phase difference calculation and direction judgement algorithm is developed in FPGA, and each BPM has been calibrated by beam experiment.

Figure 8 shows the three adjacent BPM evaluation test result. The resolution is 880nm@±800μm, which is better than the required 1μm@±500μm.

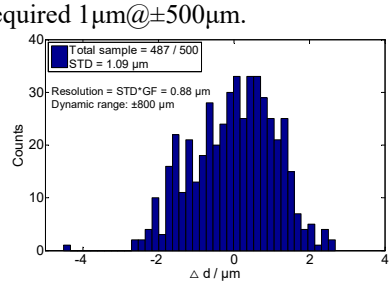

Figure 8: Cavity BPM system performance.

Beam Profile Measurement[3]

An Ce:YAG/OTR and CCD based beam profile system is designed for the measurement of beam size and emittance on SXFEL-TF. By using GigE Vision bus cameras (JAI and Basler) and network-based step-servo motors (MOONS SSM24Q-3RG), image data and motors can be accessed via TCP/IP protocol. IOCs deployed on servers (IBM System x3550 series) are responsible for the image processing and system control. Figure 9 is the system scheme. This DAQ scheme simplifies the system structure, also used on the measurement of beam energy and bunch length.

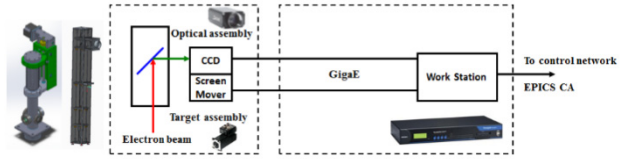

Figure 9: Beam profile measurement system.

The image horizontal and vertical RMS resolution is 13μm@41μm, 15μm@50μm respectively.

Beam Arrival Time Measurement[4]

There have four RF cavity based beam arrival time (BAM) measurement systems deployed on the SXFEL-TF. The BAM pickup consists of two monopole cavities. Table 4 lists the parameters.

Table 4: BAM Pickup Parameters

Parameters	Cavity #1	Cavity #2
Frequency/MHz	4685	4720
Bandwidth/MHz	1	1
Decay time/ns	318	318
Q_{load}	4671	4716

The BAM cavity #1 output signal is down converted to around 500MHz by mixing with synchronized 4184.5MHz LO signal. The down converted IF signal is sampled and processed by the narrow band DBPM as cavity BPM solution.

Figure 10 shows the best beam test uncertainty of the system is 45 fs over 20 minutes.

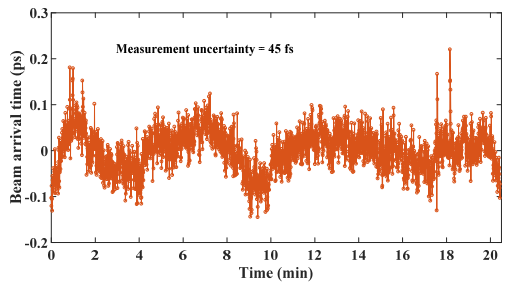

Figure 10: BAM system performance.

Time-of-Flight (ToF) Measurement

Two dual-cavity BAMs are installed at the upstream and downstream ends of chicane section respectively to measure the TOF in the chicane section. Figure 11 is the system diagram. The output signals from cavity#1 of BAM#1 and cavity#2 of BAM#2 are mixed together and down converted to about 35M, then sampled with a wide bandwidth DBPM to get the TOF. When the electron bunch passes through the chicane structure, the difference in beam energy will be converted into different beam paths, resulting in different beam flight times. This design can be used to measure the beam energy.

Content from this work may be used under the terms of the CC BY 3.0 licence (© 2020). Any distribution of this work must maintain attribution to the author(s), title of the work, publisher, and DOI

ISBN: 978-3-95450-222-6 ISSN: 2673-5350 doi:10.18429/JACoW-IBIC2020-MOA005

Content from this work may be used under the terms of the CC BY 3.0 licence (© 2020). Any distribution of this work must maintain attribution to the author(s), title of the work, publisher, and DOI

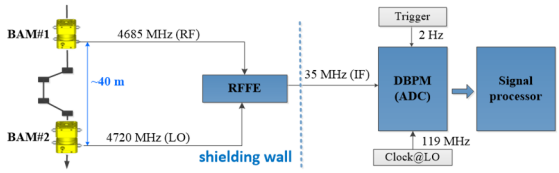

Figure 11: TOF system.

Figure 12 shows the best result of measurement uncertainty in is 38 fs and 53 fs in 20 minutes and 18 hours respectively.

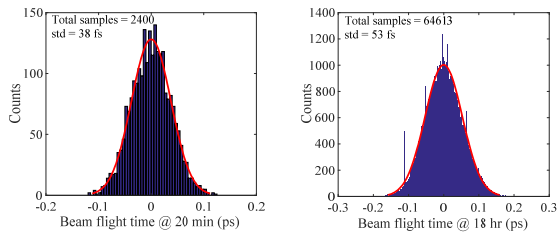

Figure 12: TOF performance.

Bunch Length Measurement

In order to measure the bunch length, a system based on X-band radio-frequency deflector system is established in the end of undulator. Table 5 lists the design parameters.

Table 5: Deflector Parameters

Parameters	Value
Frequency	11.424GHz
Phase advance	120Deg.
Maximum power	20MW
Transverse voltage	0~30MV
Total length	0.6m
Filling time	60ns
Repetition frequency	50Hz
Parameters	Value

The deflector makes the single FEL pulse reconstruction possible, including FEL profile, FEL pulse energy, relative timing jitter, correlation between two stages FEL pulse.

A non-destructive bunch length monitor using Coherent Synchrotron Radiation (CSR) is installed after linac chicane section to get relative bunch length. Figure 13 shows the system diagram.

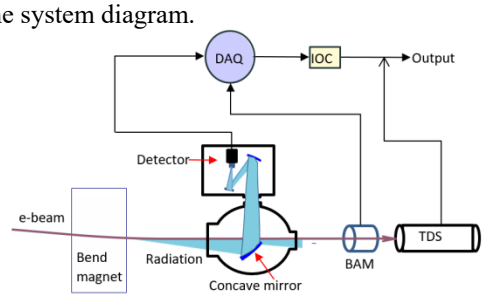

Figure 13: CSR bunch length measurement system.

Pyroelectric detector from QMC INSTRUMENTS is used as signal detector. BAM cavity output signal is used to monitor the bunch charge and normalize the pyroelectric output signal. The DAQ is NI PXI-5122, it consists of 2 channels, 14 bits, 100MSPS ADCs. The deflector is used to calibrate the system. Figure 14 is the calibration between CSR and deflector. The test results show the resolution is better than 30fs.

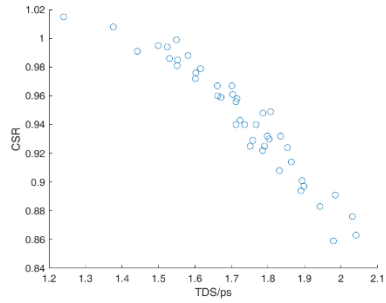

Figure 14: Bunch length calibration between CSR and deflector.

SUMMARY

The beam diagnostic system in SXFEL-TF has been introduced briefly in this paper. Each subsystem meets the performance requirement, thus assisting FEL commissioning to the designed radiation successfully. However, some lessons are learned on SXFEL-TF. For example, because of the frequency of the cavity BPM's three cavities is inconsistent and the DBPM is narrow band, the two restrictions make the RF front-end module complex. CCD lack of radiation protection and there have high dose radiation during commissioning, resulting in a lot of CCDs are damaged at that time. The lessons learned from SXFEL-TF will help to improve the BI system in SXFEL-UF.

REFERENCES

[1] Y. B. Yan *et al.*, "Data Acquisition System for Beam Instrumentation of SXFEL and DCLS", in *Proc. 7th Int. Beam Instrumentation Conf. (IBIC'18)*, Shanghai, China, Sep. 2018, pp. 137-139. doi:10.18429/JACoW-IBIC2018-MOPC11

[2] L. W. Lai, F. Z. Chen, Y. B. Leng, T. Wu, Y. B. Yan, and J. Chen, "Upgrade of Digital BPM Processor at DCLS and SXFEL", in *Proc. 9th Int. Particle Accelerator Conf. (IPAC'18)*, Vancouver, Canada, Apr.-May 2018, pp. 4807-4810. doi:10.18429/JACoW-IPAC2018-THPML071

[3] L. Y. Yu, J. Chen, Y. B. Leng, K. R. Ye, and W. M. Zhou, "Design of the Beam Profile Monitors for the SXFEL Facility", in *Proc. 1st Int. Beam Instrumentation Conf. (IBIC'12)*, Tsukuba, Japan, Oct. 2012, paper TUPB81, pp. 534-536.

[4] S. S. Cao, J. Chen, Y. B. Leng, and R. X. Yuan, "The Application of Beam Arrival Time Measurement at SXFEL", in *Proc. 7th Int. Beam Instrumentation Conf. (IBIC'18)*, Shanghai, China, Sep. 2018, pp. 342-345. doi:10.18429/JACoW-IBIC2018-WEOA04

ISBN: 978-3-95450-222-6 ISSN: 2673-5350 doi:10.18429/JACoW-IBIC2020-TUA001

PRECISE BUNCH CHARGE MEASURMENT USING BPM PICKUP*

J. Chen†, Y.B. Leng#, L.W. Lai, B. Gao, S.S. Cao, F.Z. Chen, Y.M. Zhou, T. Wu, X.Y. Xu, R.X. Yuan

Shanghai Advanced Research Institute, CAS, Shanghai, China

Abstract

Precise bunch charge measurement is the fundamental of charge feedback, beam lifetime measurement, beam loss monitor, as well as the basis of the related interlocking work. Beam position monitor (BPM) is often used for high-resolution bunch charge measurement due to its superior performance. In this paper, the pros and cons of Stripline BPM, Button BPM, and Cavity BPM for measurement of bunch charge in storage ring and FEL will be discussed. The related simulations and beam experiment results are also mentioned, the results show that the relative bunch charge resolution of the Button BPM can reach 0.2‰ in SSRF, 0.73‰ and 0.21‰ of the SBPM and CBPM in SXFEL, respectively. Besides, based on the method of beam experiments, we systematically studied the position dependence of BPM pickup for bunch charge measurement and related compensation algorithms.

INTRODUCTION

Shanghai Synchrotron Radiation Facility (SSRF) is a low emittance 3rd-generation light source consisting of a 3.5 GeV storage ring, a full energy booster and a 150 MeV linac, as well as dozens of beam lines and experimental stations. The Shanghai soft X-ray free electron laser (SXFEL) is a test facility for exploring key FEL schemes (EEHG/HGHG) and technologies, which adopt FEL frequency doubling of ultraviolet band seeded laser of 265 nm to achieve output wavelength of 9 nm, 100 fs pulse duration, 10 HZ repetition rate, and 100 MW peak power[1]. The overall length of SXFEL is about 300 meters and the nominal electron beam energy of the linac is 0.84 GeV. And it will be upgrade to a user facility in 2021. In addition, SHINE, a hard X-ray FEL facility with high energy, high repetition rate, is also under pre-research. The total length of the SHINE is about 3.1 Km，located near SSRF and SXFEL, the goal is to build a superconducting linear accelerator with an energy of 8 GeV, 3 undulator lines, 3 light speed lines, and the first batch of 10 experimental stations. Together with SSRF and SXFEL to build a photonic science center in China.

For high quality electron beams, accurate measurement of beam charge and its stability is one of the most important parameters for stable operation of accelerator. For example, for SHINE, so as to avoid damage the cryogenic superconducting undulator caused by beam loss, a requirement that the beam loss measurement accuracy is better than 0.01% in key areas is proposed. Therefore, research on this topic has great significance to the efficient operation of these facilities.

BPM picks up the electromagnetic field excited when the bunch passes through the vacuum chamber, which carries the information of the bunch, which is widely used in the measurement of a variety of bunch parameters. Its unique characteristics are also one of the methods to achieve high-precision bunch charge measurement.

This paper focuses on the motivation of using BPM probes for high-precision bunch charge measurement, introduces the principle of BPM for bunch charge measurement. The dependence of the horizontal and vertical parameters for high-precision bunch charge measurement is simulated, and some simulation results are verified by beam experiments. In addition, the system signal conditioning and data acquisition schemes and digital signal processing algorithms are also mentioned.

MEASUREMENT PRINCIPLE

For the electrostatic induction BPM, when the beam passes through the vacuum chamber, the electrode generates an induced charge under the action of electrostatic induction, and the induced signal contains the position and charge amount information of the bunch. In electron accelerators, typical probes are SBPM and Button BPM. The output signal can be expressed by Eq.(1) and (2), respectively.

$$V(t)=\frac{\phi Z}{4\pi}\left[e^{-\frac{t^2}{2\sigma^2}}-e^{-\frac{(t-\frac{2l}{c})^2}{2\sigma^2}}\right]\cdot\frac{Q}{\sqrt{2\pi}\sigma}. \quad (1)$$

$$V_B(t)=\frac{Q}{2\pi^{\frac{3}{2}}}\cdot\frac{\varphi lR}{\beta_b c}\cdot\frac{t}{\sigma_t^{3}}\cdot e^{-\frac{t^2}{2\sigma_t^2}}. \quad (2)$$

For Cavity BPM, when the bunch passes through the cavity, various characteristic modes of the electromagnetic field will be excited due to the tail field effect. For a standard cylindrical cavity, the excited TM_{010} mode which contains the bunch charge message can be represented by Eq. (3) :

$$V_p^{010}=\frac{q\omega_{010}}{2}\cdot\sqrt{\frac{Z}{Q_{ext}^{010}}\cdot\frac{2LT^2}{\varepsilon\omega_{010}\pi a^2 J_1^2(\chi_{01})}}\cdot J_0^2\left(\frac{\chi_{01}}{a}\rho\right)\cdot e^{-\frac{t}{\tau_{010}}}\cdot e^{-\frac{\omega_{010}\sigma_z^2}{2c^2}}\cdot\sin(\omega_{010}t+\varphi) \quad (3)$$

It can be seen from the above expression that the BPM pickups for bunch charge measurement still has the dependent factors such as bunch length, position offset, etc.

*Work supported by National Natural Science Foundation of China (2016YFA0401903) and Ten Thousand Talent Program and Chinese Academy of Sciences Key Technology Talent Program
†chenjian@zjlab.org.cn
#lengyongbin@sinap.ac.cn

Content from this work may be used under the terms of the CC BY 3.0 licence (© 2020). Any distribution of this work must maintain attribution to the author(s), title of the work, publisher, and DOI

ISBN: 978-3-95450-222-6 ISSN: 2673-5350 doi:10.18429/JACoW-IBIC2020-TUA001

Content from this work may be used under the terms of the CC BY 3.0 licence (© 2020). Any distribution of this work must maintain attribution to the author(s), title of the work, publisher, and DOI

Therefore, in order to accurately measure the bunch charge, the dependence of transverse and longitudinal parameters needs to be studied.

SIMULATION

In order to simulate the influence of the horizontal and vertical parameter dependence on BPM for charge measurement, CST (Computer Simulation Technology) was used to build the BPM probe model and simulate the relevant parameters.

Based on the SBPM structure and size parameters which used in SXFEL, a simulation model is established by CST, as shown in Fig. 1. The electrode length was designed at 150mm, and the corresponding frequency is 500 MHz and its integer multiples. To reduce the crosstalk between the electrodes, the electrode opening angle was designed at 30° and the vacuum tube diameter is 25mm.

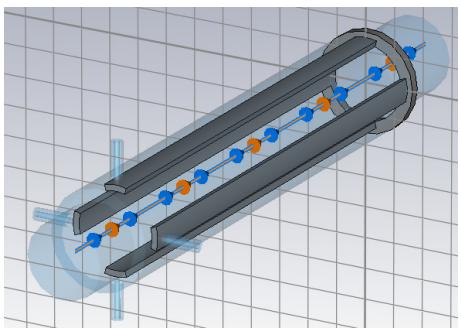

Figure 1: CST model of the SBPM.

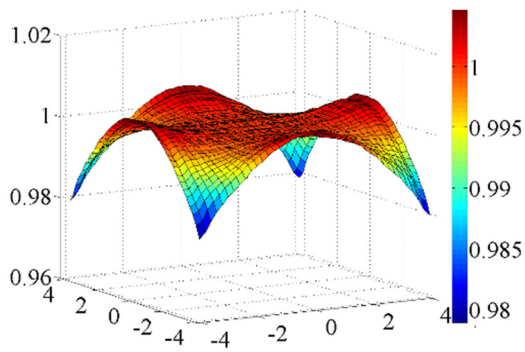

Figure 2: Simulation results of the SBPM @ 10 ps bunch length.

Figure 2 shows the dependence of the electrode and signal simulated by CST on the position of the bunch when the bunch length is 10ps. The simulation results show that in the case of position offset (1mm, 1mm), the deviation of the electrode sum signal relative to (0mm, 0mm) is about 0.01%.

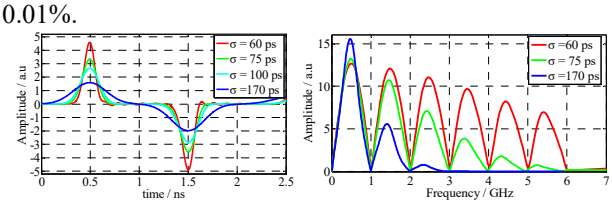

Figure 3: The relationship between SBPM electrode output signal and bunch length.

Figure 3 shows the time-domain waveform and frequency spectrum of the SBPM electrode signal simulated by CST under different bunch lengths.

The results show that with the increase of the bunch length, the peak amplitude of the bipolar pulse gradually decreases, and the spectrum energy gradually concentrates toward the low frequency.

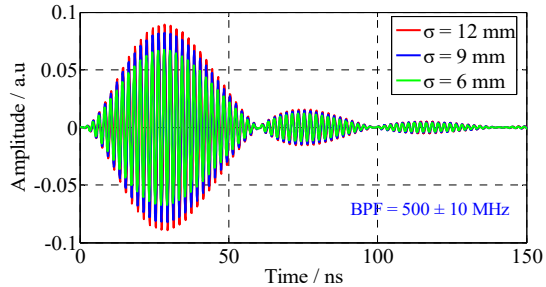

Figure 4: Waveforms after narrowband filtering under different bunch lengths.

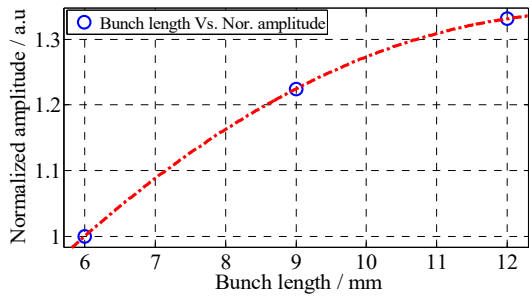

Figure 5: Dependence of SBPM signal and bunch length.

A 500±10MHz narrow-band digital filter on the simulated waveforms with different bunch lengths. The filtered waveforms are shown in Fig. 4. The signal amplitude is extracted to verify the dependence of SBPM on bunch charge measurement and bunch length, As shown in Fig. 5. Base on the results, the output signal changes about 4% when the bunch length changes 0.5ps around 2ps was estimated

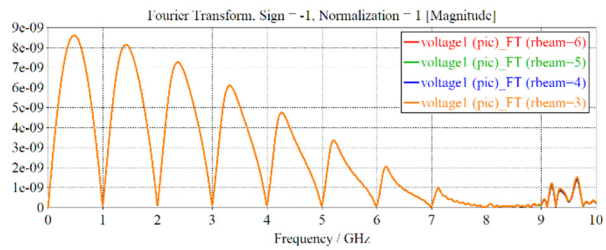

Figure 6: Dependence of SBPM signal and cross-sectional size.

Similarly, a simple simulation of the dependence of the cross-sectional size of the bunch has been done, as shown in Fig. 6. The simulation results show that when the operating frequency < 10 GHz, the impact of the cross-sectional size on the measurement of the bunch charge is negligible.

ISBN: 978-3-95450-222-6 ISSN: 2673-5350 doi:10.18429/JACoW-IBIC2020-TUA001

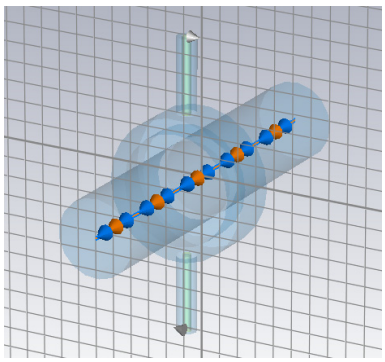

Figure 7: CST model of the Cavity BPM (TM_{010}).

For the cavity BPM with TM_{010} mode as the main mode, is often used in the FEL device for the relative measurement of the bunch charge and the beam arriving time measurement. Therefore, in accordance with the existing CBPM parameters of SXFEL, a model was established in CST to simulate the bunch position dependence and bunch length dependence, as shown in Fig. 7.

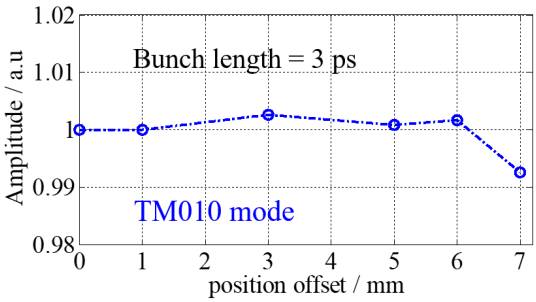

Figure 8: Position dependence of TM_{010} cavity.

Figure 8 shows the dependence of the TM_{010} mode signal simulated by CST on the position of the bunch when the bunch length is 3ps. The simulation results show that in the case of position offset < 6 mm, the deviation of the signal is less than 0.1%.

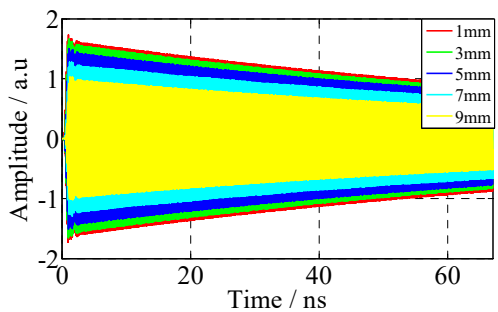

Figure 9: Bunch length dependence of TM_{010} cavity.

Figure 9 shows the time-domain waveform after digital filter of the TM010 mode signal simulated by CST under different bunch lengths. The dependence of TM_{010} mode signal and bunch length was shown in Fig. 10, the results are in good agreement with the theoretical formula.

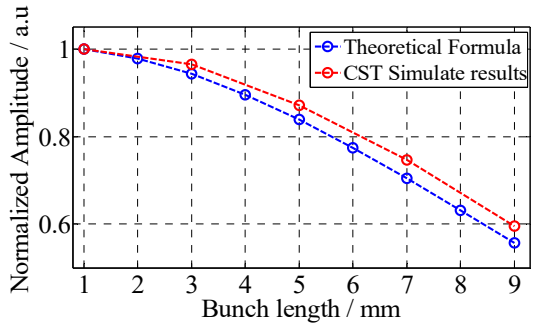

Figure 10: Dependence of TM_{010} mode signal and bunch length.

BEAM EXPERIMENT

Based on the modeling and simulation of CST, the relationship between the beam position dependence and the bunch length dependence of the BPM pickups were obtained. On this basis, we did some experiments in SSRF and SXFEL for preliminary verification.

In the laboratory, we used the method of pulling a copper beryllium wire through the SBPM and scan the two-dimensional position to verify the relationship between the electrode sum signal and the position. The experimental platform is shown in Fig. 11, and the scanning results are shown in Fig. 12. The qualitative results are consistent with the simulation results.

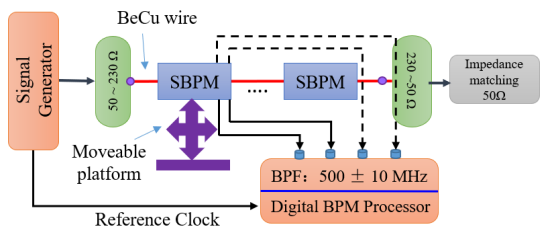

Figure 11: Diagram of the experiment platform.

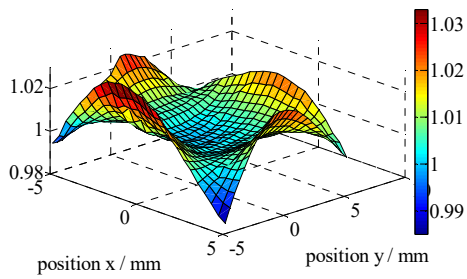

Figure 12: Dependence between electrode sum signal and position.

During the injection transient of SSRF, the beam position oscillation process can be used to analyze the relationship between the bunch charge and the position dependence. As shown in Fig. 13, under ± 0.4mm position oscillation, the bunch charge depends on the measurement position. The slope is about 0.0005 / mm.

Content from this work may be used under the terms of the CC BY 3.0 licence (© 2020). Any distribution of this work must maintain attribution to the author(s), title of the work, publisher, and DOI

ISBN: 978-3-95450-222-6 ISSN: 2673-5350 doi:10.18429/JACoW-IBIC2020-TUA001

Content from this work may be used under the terms of the CC BY 3.0 licence (© 2020). Any distribution of this work must maintain attribution to the author(s), title of the work, publisher, and DOI

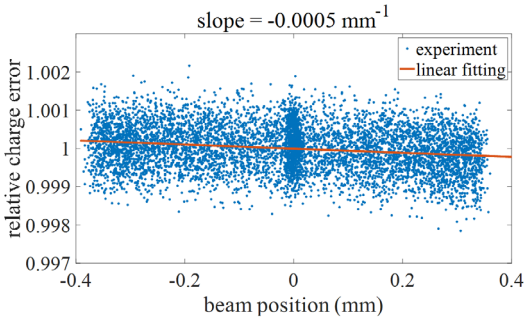

Figure 13: Dependence between electrode sum signal and bunch position.

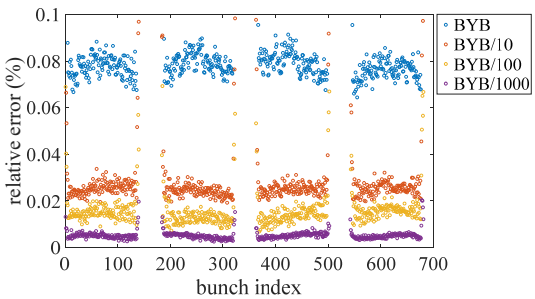

Figure 14: Resolution of bunch-by-bunch charge measurement.

In SSRF, the relative bunch charge of bunch-by-bunch is measured, and the relative uncertainly under different data refresh rates are obtained by data averaging, as shown in Fig. 14. Compared with the closed orbit measurement, the beam position stability is on the order of micrometers (< 2 μm), and the relative charge measurement error is about 1E-6 based on the position-dependent slope. For Turn-by-Turn beam position measurement, with 10 times σ (~20 μm) to evaluation, the relative charge measurement error is about 1E-5. Therefore, for the synchrotron radiation source, under normal operating conditions, the error introduced by the position dependence is basically negligible. Apart from this, assuming that the beam life time is 10 hours, the amount of charge in 1 second is reduced by 3E-5, so the beam life time can be measured in the order of 10s or minutes.

Regarding the beam position dependence of cavity of TM_{010} mode, two adjacent reference cavities of CBPM are used in the SXFEL for experiments. The experimental platform is shown in Fig. 15. The first Cavity is fixed as a reference, and a moving platform is used to move the adjacent cavity to simulate the beam offset.

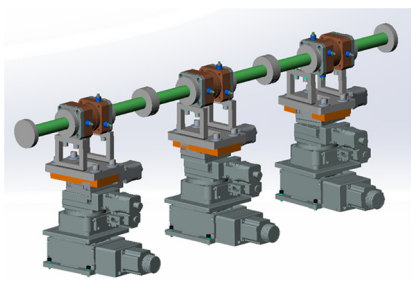

Figure 15: Experimental platform setup in SXFEL.

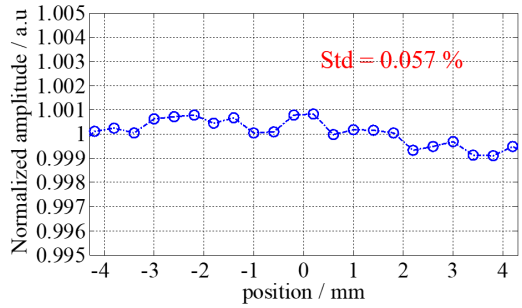

Figure 16: Results of position dependence of the TM_{010} cavity.

Due to the limitation of the movable platform, the moving range can only be moved within ±4.2mm. According to the experimental results, within the range of ±4.2mm, the reference cavity position dependence is not obvious, which is consistent with the CST simulation results, as shown in Fig. 16, and the relative amplitude extraction difference at different positions is better than 0.1%.

SIGNAL PROCESSING METHOD

Since the bipolar pulse signal output by the SBPM electrode is a wideband signal, there are two processing solutions for the signal conditioning and signal acquisition of the SBPM system, broadband and narrowband.

According to the results of simulation analysis, when the SNR the output signal of the pickups higher than the effective bit of the ADC under a large bunch of charges, a narrow-band filtering scheme is used to broaden the waveform, so as to obtain more processing gain. In the choice of system internal / external clock or internal / external trigger, a test system was setup in SXFEL for comparison. The experimental comparison results are shown in Fig 17. The results show that for SBPM / Button BPM, under the narrowband filtering scheme, the configuration of external clock and external trigger has limited improvement in resolution.

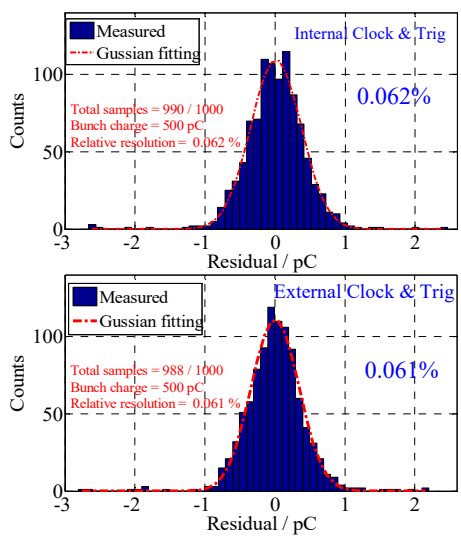

Figure 17: Relative error of the SBPM system by Internal Clock and Internal Trigger (Top). By External Clock and External Trigger (Bottom).

ISBN: 978-3-95450-222-6 ISSN: 2673-5350 doi:10.18429/JACoW-IBIC2020-TUA001

On the other hand, for systems that require phase-locked sampling (for example, BPM in the storage ring is used to acquire bunch-by-bunch signals). In this case, the jitter of the sampling phase will seriously deteriorate the performance of the system. Based on this, we propose the Two-phase sampling based peak seeking method to minimize the impact of sampling phase jitter, so as to extract the peak-value accurately. The diagram is shown in Fig. 18, the phase of the two points sampled at the time can be derived from the ratio of the two points with a fixed delay, and the value of the peak point can be obtained from the ratio of the normalized curve[2 3].

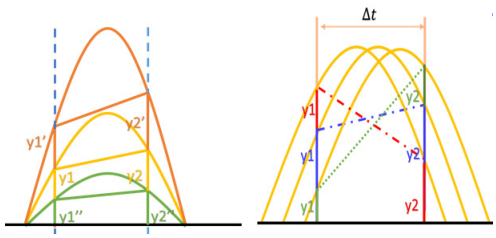

Figure 18: Diagram of method of two-phase sampling based peak seeking.

Based on this data acquisition scheme, it is applied in the SSRF bunch-by-bunch charge measurement. As shown in Fig. 19, it compares the std value of single-point peak extraction method and the two-phase sampling based peak seeking method to extract the peak. It can be seen that two-phase sampling based peak seeking method basically minimized the influence of sampling phase jitter. Under the average of more than 1W sets of data, the resolution of bunch charge measurement better than 0.02%, as shown in Fig. 20.

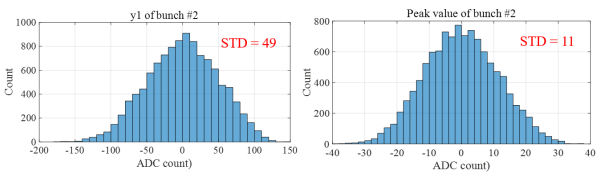

Figure 19: The std value of single-point peak extraction method (Left) and the two-phase sampling based peak seeking method (Right) to extract the peak.

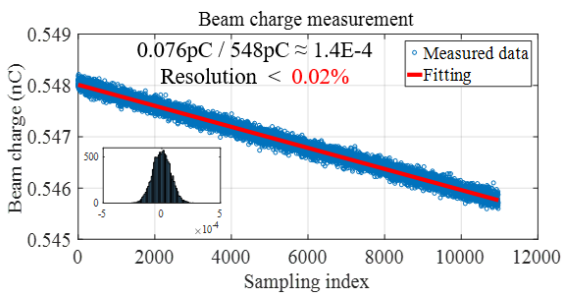

Figure 20: Resolution of bunch charge measurement.

For cavity pickup, it couples a narrowband signal. For low-Q cavity pickup, because the decay time is very small, the analog IQ demodulation to baseband is used to demodulate the amplitude and phase information of the signal. For high-Q cavity pickup, because the decay time is large, the ADC can collect more effective data points in the effective waveform section, so the method of down-conversion to low IF is often adopted. In digital signal processing, high-Q cavity signals have more processing methods [4]. To balance the signal processing gain and the relative signal to noise ratio, the data interception algorithm can improve the resolution of the system to a certain degree. Through simulation, when the signal processing length is about twice the decay time, the relative uncertainty of processing can reach the minimum value. The Cavity data on SXFEL is processed. When the data processing length is 2.18 times decay time, the relative uncertainty is reduced from 0.044% to 0.021%.

CONCLUSION

The BPM pickups has a high amplitude extraction accuracy due to its unique characteristics, so it is often used for accurate bunch charge measurement. The dependence of the horizontal and vertical parameters for high-precision bunch charge measurement is simulated, and some simulation results are verified by beam experiments. In addition, the system signal conditioning and data acquisition schemes and digital signal processing algorithms for SBPM / Button BPM and cavity BPM also are mentioned, which can minimize the uncertainly of measurement.

REFERENCES

[1] Shanghai Soft X-ray FEL (SXFEL) Conceptual Design Report. 2015.

[2] Y.B. Leng, Y.B. Yan and W.M. Zhou, "Precise beam current measurement for storage ring using beam position monitor", *High Pow Las Part Beam,* vol. 22, pp. 2973-2978, 2010, doi:10.3788/HPLPB20102212.2973

[3] F.Z. Chen *et al.*, "Touschek lifetime study based on the precisely bunch-by-bunch BCM system at SSRF", *Nuclear Science and Techniques,* vol. 30, Issue (9): 144, 2019, doi: 10.1007/s41365-019-0655-6

[4] V. Sargsyan, "Comparison of stripline and cavity beam position monitor", TELSA, Hamburg, Germany, Rep. TESLA Report 2004-03, Mar. 2004.

Content from this work may be used under the terms of the CC BY 3.0 licence (© 2020). Any distribution of this work must maintain attribution to the author(s), title of the work, publisher, and DOI

ISBN: 978-3-95450-222-6 ISSN: 2673-5350 doi:10.18429/JACoW-IBIC2020-TUA002

DIAGNOSTICS FOR COLLIMATOR IRRADIATION STUDIES IN THE ADVANCED PHOTON SOURCE STORAGE RING*

J. Dooling†, M. Borland, W. Berg, J. Calvey, G. Decker, L. Emery, K. Harkay, R. Lindberg, G. Navrotksi, V. Sajaev, J. Stevens, Y. P. Sun, K. P. Wootton, A. Xiao,
Argonne National Laboratory, Lemont, USA
A. H. Lumpkin, Argonne Associate of Global Empire, LLC,
Argonne National Laboratory, Lemont, USA

Abstract

The Advanced Photon Source (APS) is building a fourth-generation storage ring (4GSR), replacing the present double-bend achromat lattice with a multibend achromat system thereby allowing the production of ultra-bright x-ray beams. The new lattice enables a two-order-of-magnitude reduction in horizontal beam emittance and a factor of two increase in beam current. The result is an electron beam of very high energy- and power-densities. Initial predictions suggest virtually any material struck by the undiluted electron beam will be damaged. Two experimental beam abort studies have been conducted on collimator test pieces in the present APS SR to inform the design of a fully-functional machine protection system for APS 4GSR operations at 200 mA. A comprehensive suite of diagnostics were employed during the studies. The diagnostics used in these experiments are not new, but employed in different ways to obtain unique data sets. With these data sets now in hand, we are developing new numerical tools to guide collimator design.

INTRODUCTION

The Advanced Photon Source Upgrade (APS-U) project centers on the construction of a fourth generation storage ring (4GSR) [1]. The ultra-low emittance lattice operating at 6 GeV and 200 mA will result an electron beam of very high energy- and power-densities. MARS [2] simulations indicated virtually any material struck by the undiluted, primary beam will be damaged. The objective of this work is to conduct experimental studies which informs the design and construction of a robust, fully-functional collimator system for 200 mA APS-U beam operations. A variety of diagnostics play a key role in observing and evaluating the effects of whole beam dumps on candidate collimator materials which is the subject of these studies.

Two beam-loss studies have been performed thus far, the first in May 2019 and the second in January 2020. Conducting these experiments successfully requires a diverse set of diagnostics such as Turn-By-Turn (TBT) Beam Position Monitors (BPMs), cameras, DC Current Transformers (DCCTs), and beam loss monitors (BLMs). A different set of diagnostic techniques are used after the study to examine the collimator test pieces including microscopy and metallurgy.

* Work supported by the U.S. Department of Energy, Office of Science, Office of Basic Energy Sciences, under Contract No. DE-AC02-06CH11357.
† dooling@aps.anl.gov

EXPERIMENTAL METHODS

Both irradiation studies were conducted at the beginning of run periods during start-up machine studies in order to extract the collimator test pieces before user operations began. This approach is somewhat risky since this time may be necessary to condition new vacuum components or other hardware; for example, the collimator/scraper assembly. A plan view of the assembly is presented in Fig. 1. This location is just downstream of the fourth rf cavity in this Sector 37 (S37) long straight section.

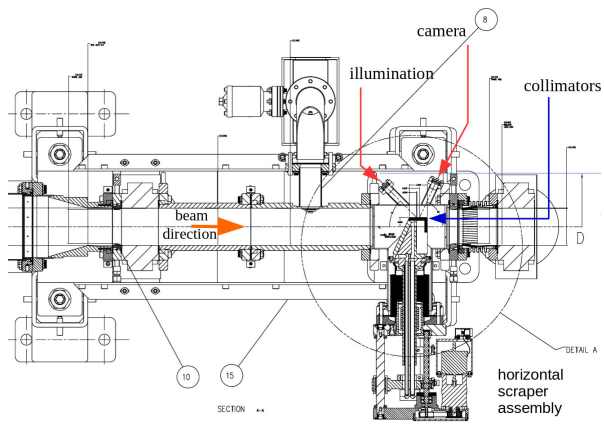

Figure 1: Collimator/scraper assembly plan view in the APS SR S37 long straight section. The location is just downstream of the fourth rf cavity.

Diagnostic Camera

For both experiments, a diagnostic camera was built in the SR tunnel to view the collimator surfaces. The camera hardware was then disassembled and removed at the end of each study. The collimators are viewed through a 65° port and illuminated through a 45° port as indicated in Fig. 1. The angles are measured from the beam axis. The depth of field (DOF) for the optical system is 2 mm at the collimator surface. The resolution is approximately 50 µm and the field of view is 11 mm. Radiation protection for the camera is provided first by moving the unit approximately 0.5 m below the beam centerline, and second by shielding with Pb bricks. A photograph of the camera assembly and image of the installed collimator pieces prior to the first irradiation experiment are shown in Fig. 2. In the first experiment, two collimator materials were tested: titanium alloy Ti6Al4V and aluminum alloy T6061. In this image the darker titanium

Content from this work may be used under the terms of the CC BY 3.0 licence (© 2020). Any distribution of this work must maintain attribution to the author(s), title of the work, publisher, and DOI

ISBN: 978-3-95450-222-6 ISSN: 2673-5350 doi:10.18429/JACoW-IBIC2020-TUA002

(a) Diagnositc Camera assembly.

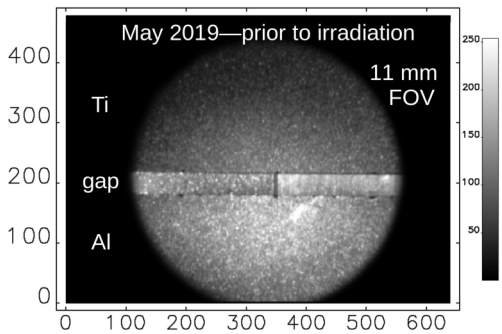

(b) Pre-Irradiation collimator image.

Figure 2: a) Diagnostic Camera hardware and b) collimator image prior to the first irradiation experiment. The field of view is approximately 11 mm and gap between collimator pieces is 1 mm.

alloy is on top; however, the image is flipped vertically so that actually the aluminum piece is above the beam centerline.

In addition to frame grabber software used to capture still images, a digital video recorder (DVR) was employed to capture images from the Diagnostic Camera during beam strikes. The DVR operated at a 30 frames per second (fps) rate with a resolution of 360 x 240. DVR playback allowed the viewing of the one video frame that had the flash of light and a 33 ms snapshot of the dynamic scene after the beam-abort trigger.

Linear Variable Differential Transformer Calibration

The position and motion of the scraper assembly needed to be accurately known for proper placement of the collimator test pieces once mounted and inside the vacuum chamber. Horizontal position placement was made using a linear variable differential transformer (LVDT). Total linear travel of the collimators was 4.747 cm. Survey and Alignment scribed the location when the collimator apex was located at the beam centerline. The distance from a fully retracted or withdrawn position to the beam centerline was measured to be 2.774±0.005 cm.

Collimator Measurements

Two collimator test pieces are mounted on the end of the horizontal scraper shown in Fig. 1. The surface facing the beam is machined to have large radius (0.8 m) creating an apex near the center of the collimator. The apex is where we expect the beam to strike first as it loses energy after rf muting. An oblique drawing of the collimator test piece is presented in Fig. 3. The radius machined into the beam-facing surface yields an apex approximately 0.3 mm above the chord connecting the upstream and downstream ends of the collimator. A microscope system provides both a view of the machined radius as well as surface roughness. An anamorphic image of the collimator surface magnified in the horizontal direction 3000 times is also shown in Fig. 3. The measurement was made on the aluminum test piece installed for the May 2019 experiment; the surface roughness was found to be 2.7 µm. The aluminum test pieces used in the January 2020 study had a significantly reduced surface roughness value of 0.45 µm.

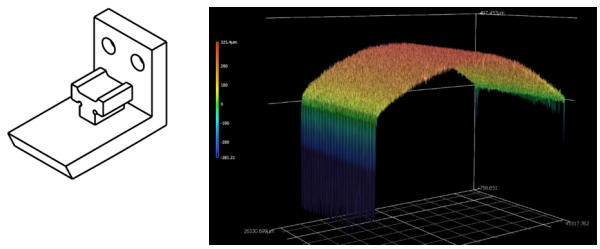

(a) Coll. test piece. (b) Collimator surface, anamorphic view.

Figure 3: Collimator test piece a) oblique view and b) a 3000X magnification of the beam-facing surface in horizontal direction. In a), the beam-facing surface is out of view, below the image.

Temperature and Pressure

Temperature and pressure sensors played an important role during conditioning of the collimator/scraper assembly. Temperature measurements were made with resistance temperature detectors (RTDs) and thermocouples (TCs); additional detectors were placed on the exterior of the vacuum chamber, near the beam end of the scraper. The two detectors with the highest readings from both RTDs and TCs sets are presented in Fig. 4 for the period over which all 11 200 mA beam dumps occurred. This time period occurred between two beam dumps with nominal beam currents of 150 mA. The highest readings occurred on the scraper vacuum chamber where the rf fingers are located internally, close to where the two tubes join (see Fig. 1). The number of bunches chosen for the 150 mA cases was 324 (every fourth rf bucket filled). Because of significant wakefield heating for this case, the number of bunches was increased to 972 for the 200 mA

Content from this work may be used under the terms of the CC BY 3.0 licence (© 2020). Any distribution of this work must maintain attribution to the author(s), title of the work, publisher, and DOI

ISBN: 978-3-95450-222-6 ISSN: 2673-5350 doi:10.18429/JACoW-IBIC2020-TUA002

Content from this work may be used under the terms of the CC BY 3.0 licence (© 2020). Any distribution of this work must maintain attribution to the author(s), title of the work, publisher, and DOI

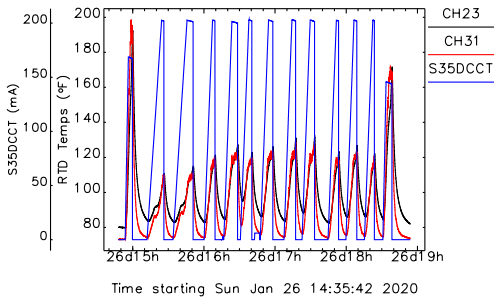

(a) RTD readings.

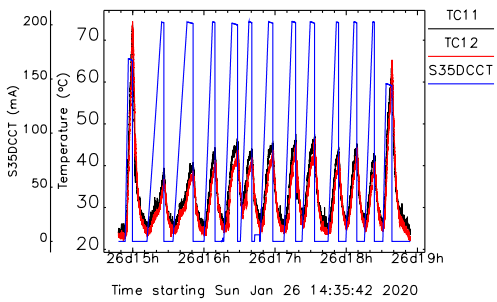

(b) TC readings.

Figure 4: The two highest a) RTD and b) TC readings of all nominal 200 mA beam aborts and the 150 mA cases immediately proceeding and following.

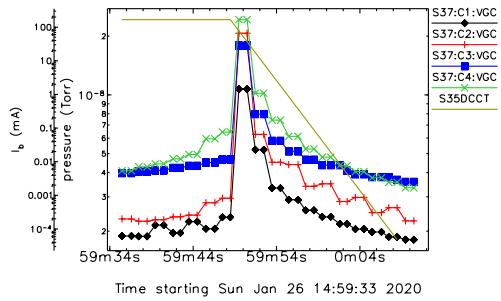

(a) 150 mA.

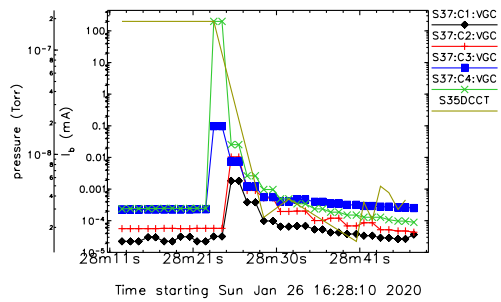

(b) 200 mA.

Figure 5: Pressure transients in the S37 rf cavities from beam dumps at a) 150 and b) 200 mA.

beam aborts. Wakefield heating scales approximately as MI^2 where M is the number of bunches and I is the current of a single bunch. With this scaling, the heating at 200 mA with charge spread equally over 972 bunches should be only 59% of that at 150 mA with 324 bunches.

Vacuum pressure was also of concern due to the proximity of the collimator/scraper assembly to the S37 rf cavities. Pressure in the cavities are monitored with cold cathode gauges. During conditioning on the day prior to the irradiation study, we found pressure spikes were reduced by leaving the scraper parked with the apex of the collimator surfaces 3.7 mm inboard ($x = -3.7$ mm) of the nominal beam centerline during injection. The surfaces were then moved to $x = -2.0$ mm for beam aborts. At the highest currents, modest pressure rise was observed as beam current was injected and stored for beam aborts; however, more substantial transients occurred as the beam was dumped. The collimator/scraper assembly is located 1.6 m downstream of the fourth rf cavity in the S37 long straight section. The other three cavities are located further upstream equidistantly spaced approximately 1 m apart. Figure 5 compares the the pressures recorded in the four S37 rf cavities during the first beam dump from 150 mA and a later beam abort from 200 mA. For the 150 mA case, peak pressure was recorded in chamber 4 (C4) at approximately 20 nTorr; however, at 200 mA, the peak pressure in C4 is an order of magnitude higher. As expected, peak pressures fell for cavities further away from the strike location.

A pressure limit of 1 µTorr was established prior to studies as a trip level. Though exceeded during early conditioning, no trips were recorded during the collimator irradiation studies.

Gap Localization

The change of stored current with time monitored with the DCCT provides a measure of beam lifetime. Beam lifetime also allowed us to localize the center of the collimator assembly by identifying the location of the gap between the two collimator test pieces. Gap localization was accomplished by step-wise scanning a 10 mA beam vertically past the gap while measuring beam lifetime; the beam was positioned approximately 0.9 mm from the collimator surface. A sketch of the geometry and gap localization results are presented in Fig. 6.

COLLIMATOR IRRADIATION MEASUREMENTS

One of the January 2020 collimator irradiation study goals was to reach 200 mA. As mentioned above, we accomplished this goal by increasing the number of bunches from 324 to 972.

Emittance, Charge, and Current Density

Emittance is determined using a pinhole camera assuming Gaussian spatial distributions. Beam size and current density are calculated from beam emittance and lattice functions

ISBN: 978-3-95450-222-6 ISSN: 2673-5350 doi:10.18429/JACoW-IBIC2020-TUA002

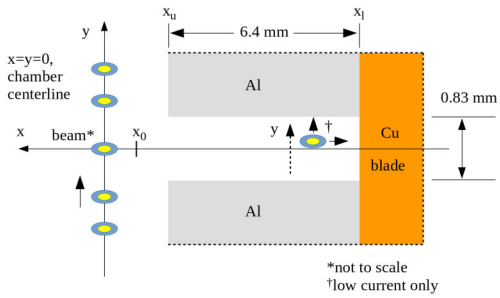

(a) Collimator gap schematic.

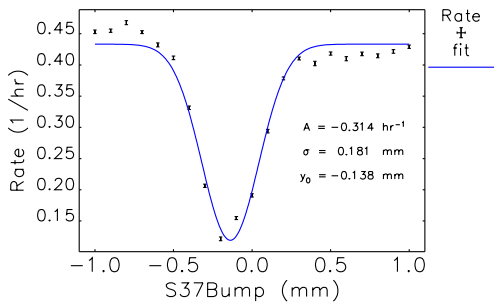

(b) Lifetime measurements.

Figure 6: a) Collimator gap geometry schematic with vertical beam scanning and b) lifetime measurements indicating the center of the gap. The beam was positioned 0.9 mm from the collimator surface.

at the scraper location assuming $\beta_x = 4.0$ m, $\beta_y = 6.0$ m, $\eta_x = 0.059$ m, $\eta_y = \eta'_x = \eta'_y = 0$, and $\Delta p/p = 10^{-3}$. The current density is calculated as $j_b = I_b/(2\pi\sigma_x\sigma_y)$. A triple reduced horizontal beamsize (RHB) lattice was developed to minimize the spot size at the S37 scraper location. The lattice was modeled with the beam dynamic code `elegant` [3].

Variation in vertical emittance with scraper position is observed prior to beam dumps; whereas, horizontal emittance essentially shows no change. Horizontal and vertical emittances are plotted in Fig. 7 along with scraper position for the $y_{\text{bump}} = 2.6$ mm, 200 mA beam dump case. A position of 2.57 cm corresponds to the apex of the collimators at $x = -2.0$ mm from the nominal beam centerline.

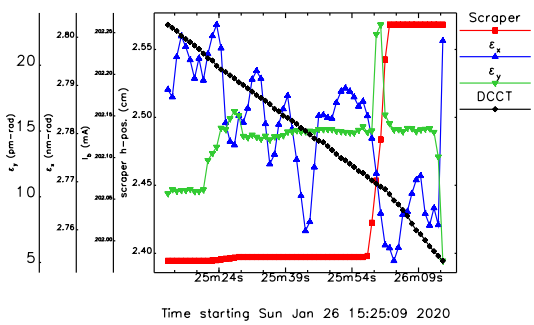

Figure 7: Beam emittances, scraper position, DCCT at 200 mA for a 2.6 mm vertical bump. Note the change in DCCT slope (reduction in lifetime) as the scraper is inserted to its final position. Also the vertical emittance transient may indicate an ion instability.

Diagnostic Camera Images

Visible light emission was observed down to the lowest current levels, approximately 2 mA during the May 2019 study. At low currents, emission is likely due to scintillation or optical transition radiation; at high currents, black body radiation is dominant. During our May 2019 experiment, we were limited to maximum currents of 65 mA. Emission images from this earlier study have been previously reported [4]. The final image recorded with the diagnostic camera at the end of the study is shown in false color in Fig. 8.

Visible light emission from a pair of beam dumps from the January 2020 experiment are presented in Fig. 9. Surprisingly in our January 2020 experiment, where only aluminum test pieces were used, significantly more ejecta features were observed in the 65 mA range; see Fig. 9a. As mentioned above, the Diagnostic Camera DOF is 2 mm; therefore, the linear features seen in Fig. 9a must be close to the collimator surface. At 200 mA, the emission is much brighter while linear features, though present, are less pronounced; see Fig. 9b. The collimator surfaces are strongly affected by beam dumps; surface images and a summary of the beam dump parameters are presented in the next section.

PHOTOGRAPHY AND MICROSCOPY

Images from the May 2019 experiment showed damage to the titanium alloy test piece was significantly greater than to the aluminum for the same current [4]. Irradiation effects in titanium were observed down to 16 mA; whereas, the minimum current for surface damage in aluminum was 32 mA. One additional complication was that the titanium test piece became activated during the experiment. For these reasons, we decided not to do further testing with titanium.

In early February 2020, after the second experiment, photographs were taken of both aluminum collimator pieces while still attached to the scraper assembly; an example is presented in Fig. 10. The sequence number and times

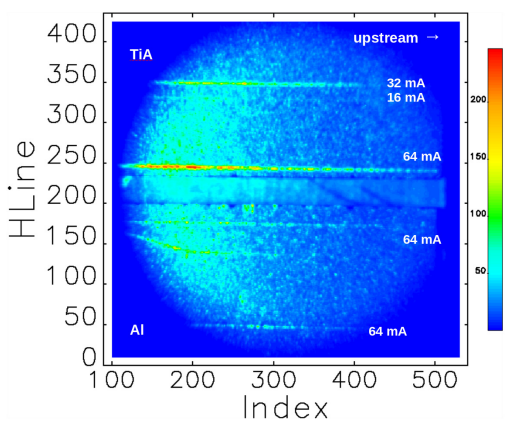

Figure 8: Last image of the collimator surfaces after the final beam dump of the May 2019 study, shown in false color.

Content from this work may be used under the terms of the CC BY 3.0 licence (© 2020). Any distribution of this work must maintain attribution to the author(s), title of the work, publisher, and DOI

ISBN: 978-3-95450-222-6 ISSN: 2673-5350 doi:10.18429/JACoW-IBIC2020-TUA002

Content from this work may be used under the terms of the CC BY 3.0 licence (© 2020). Any distribution of this work must maintain attribution to the author(s), title of the work, publisher, and DOI

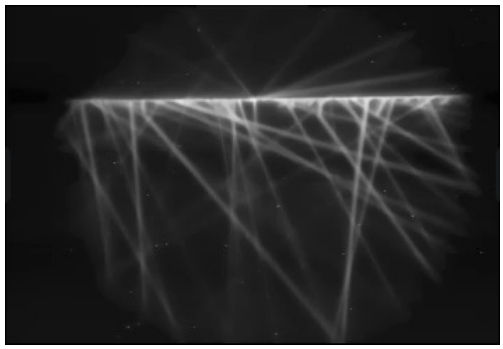

(a) Beam strike recorded at 69.4 mA.

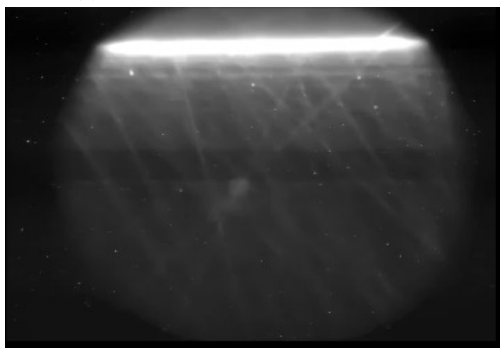

(b) Beam strike recorded at 201 mA.

Figure 9: Visible light emission from beam dumps at a) 69.4 mA and b) 201 mA. The beam moves from right to left.

struck are indicated on the left side of Fig. 10 while nominal current is indicated on the right side. Once the collimator pieces were removed from the scraper body, better resolution images of the irradiation surfaces were obtained.

Table 1 lists the beam dumps in sequential order along with current, emittances, rms spot sizes, and estimated dose levels. Gaussian transverse profiles are assumed. At 200 mA, calculated current densities reach 39 A mm^{-2}, approximately 5 times the damage threshold observed in aluminum. Dose

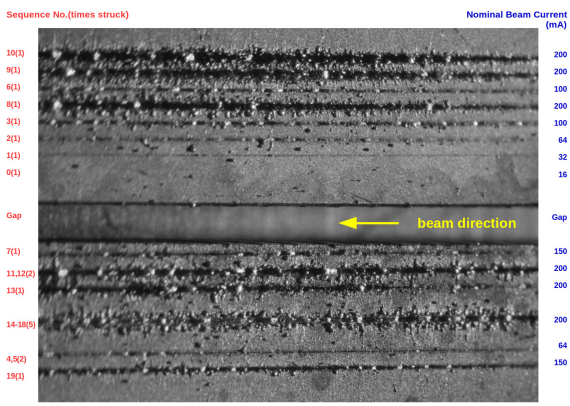

Figure 10: Higher resolution photograph of the January 2020 collimator test pieces. The pieces are still attached to the scraper body. Sequence number and times struck are shown on the left; nominal currents are listed on the right.

is calculated as,

$$D = S_{pc} \frac{N_q}{2\pi\sigma_x\sigma_y} \tag{1}$$

where S_{pc} is the collisional stopping power for 6 GeV electrons in aluminum [5] and N_q is the total number of circulating electrons. At 6 GeV, the collisional stopping power in Al is 2.153 MeV cm^2 g^{-1} (note: the radiative stopping power is 246.7 MeV cm^2 g^{-1}).

The upper collimator piece from the January 2020 study received only a single beam dump at each vertical position. Examining this piece under a microscope with different lighting orientations reveals some of the structure of the beam strike damage. Figure 11 presents a micrograph of the upper collimator piece. Starting from the bottom of the images,

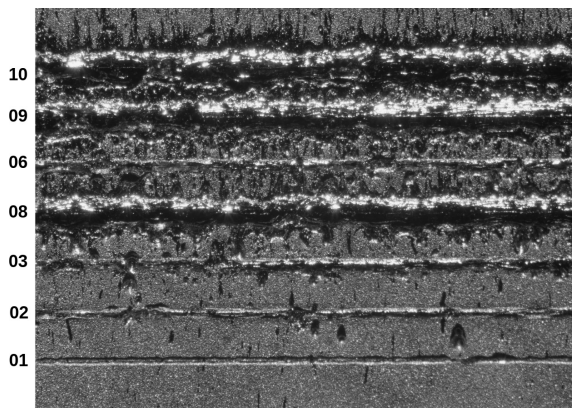

Figure 11: Microscopy image of the upper collimator piece from the January 2020 study. Starting from the bottom of the image, beam strike currents increase from 34.6 to 202.1 mA. The vertical separation between each beam strike position is 0.4 mm. Illumination is from the bottom of the image. Sequence numbers are given on the left.

the beam dump currents were 34.6, 69.4, 99.1, 202.0, 100.0, 201.2, and 202.1 mA. The nominal separation between each strike is 0.4 mm.

TURN-BY-TURN BPMS AND FAST BLMS

Beam dumps were monitored by both TBT BPMs and fast BLMs. TBT BPMs are fast enough to resolve beam position turn by turn. Fast BLMs are based on high-purity fused silica fibers as well as small cylindrical fused-silica radiators. A comparison of the differentiated TBT BPM sum signal peak times and peak loss intensity time since rf muting ("Arrival Time") from several BLMs versus current is presented in Fig. 12 for data collected during the January 2020 beam abort study. A systematic difference of approximately 2 turns (7 µs) is observed between the TBT BPMs and the fast BLM data with the fast BLM peaks appearing first. This difference may be due to the TBT BPM data being generated as the log of the sum signals, whereas the fast BLM signals are linear. Large loss signals can saturate the BLM photomultipler tubes, so care must be exercised here.

ISBN: 978-3-95450-222-6 ISSN: 2673-5350 doi:10.18429/JACoW-IBIC2020-TUA002

Table 1: Chronological Sequence Number (SN), No. of Bunches, Y-Offset, Beam Current, Charge per Bunch, Emittance, Spot Size, Current Density, and Dose During the January 2020 S37 Collimator Study; Gray Backgrounds Represent Locations of Repeated Beam Dumps

SN	No. bun.	y-off. (mm)	I_b (mA)	Q_b (nC)	ϵ_x (nm)	ϵ_y (pm)	σ_x (mm)	σ_y (μm)	j_e ($\frac{A}{mm^2}$)	D (MGy)
0	27	1.0	18.1	2.18	1.831	6.00	0.1039	6.00	4.61	3.65
1	54	1.4	34.6	2.18	1.829	5.28	0.1039	5.63	9.42	7.47
2	108	1.8	69.4	2.18	1.972	7.58	0.1066	6.74	15.36	12.18
3	324	2.2	99.1	1.13	2.088	13.36	0.1088	8.95	16.20	12.84
4	108	-3.4	73.1	2.18	2.012	7.51	0.1074	6.71	16.14	12.80
5	108	-3.4	66.6	2.18	1.965	7.88	0.1065	6.88	14.47	11.47
6	324	3.0	100.0	1.13	2.023	13.74	0.1076	9.08	16.29	12.92
7	324	-1.0	166.8	1.7	2.120	9.58	0.1094	7.58	32.02	25.39
8	972	2.6	202.0	0.76	2.765	14.91	0.1206	9.46	28.18	22.35
9	972	3.4	201.2	0.76	2.094	17.85	0.1089	10.35	28.41	22.53
10	972	3.8	202.1	0.76	2.104	15.51	0.1091	9.65	30.56	24.23
11	972	-1.4	199.8	0.76	2.140	9.52	0.1097	7.56	38.33	30.39
12	972	-1.4	201.9	0.76	2.132	9.55	0.1096	7.57	38.74	30.71
13	972	-1.8	201.4	0.76	2.112	9.54	0.1092	7.57	38.79	30.76
14	972	-2.6	201.9	0.76	2.117	10.71	0.1093	8.02	36.68	29.08
15	972	-2.6	201.4	0.76	2.102	10.42	0.1090	7.91	37.18	29.48
16	972	-2.6	201.9	0.76	2.108	10.44	0.1091	7.92	37.19	29.49
17	972	-2.6	201.8	0.76	2.112	10.61	0.1092	7.98	36.86	29.22
18	972	-2.6	202.2	0.76	2.124	10.36	0.1094	7.88	37.31	29.58
19	324	-3.8	143.6	1.7	2.087	11.49	0.1088	8.30	25.32	20.07

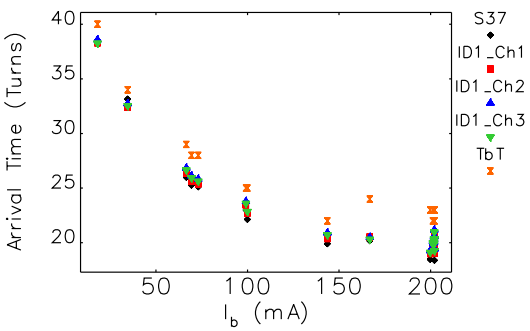

Figure 12: Comparison of arrival times of the loss signals determined from the fast BLMS and TBT BPMs.

Loss intensity signals observed on one of the fast BLMs in ID1 shows good agreement with elegant simulations. The elegant data consists of differentiated particles remaining with respect to time in Turns since rf muting. These data are plotted in Fig. 13, again from the January 2020 abort study. ID1 BLMs are 110 m downstream of the S37 scraper location.

METALLURGY

Metallurgical analysis was performed on the aluminum test piece used in the May 2019 experiment. A transverse cross section was cut from the test piece, polished, then prepared with Barker's etch. A comparison of cross sections struck by 33.1 and 67.4 mA beams is presented in Fig. 14. The expansion in the affected area as the current is increased from 33.1 to 67.4 mA appears to be greater than a factor of two, especially in the partial melt zone. Based on the effects of higher current irradiation during the January 2020 experiment, these cases are viewed as being transitional from no-damage to plastic flow to melt and finally vaporization. Table 1 shows dose rates of 30 MGy were attained, a factor of 2 higher than that required for hydrodynamic behavior [6].

The reason that a metallurgical analysis of the titanium alloy piece was not conducted was its activation and the production of mixed waste cutting and polishing would have generated. After the January 2020 experiment, both of the aluminum tests pieces were found to be activated. Gamma spectroscopy conducted on March 13, 2020 showed the nuclide responsible for the largest count rate was beryllium-7. Be-7 is generated by high-energy events such as spallation or cosmic ray impacts on nitrogen or oxygen in the atmosphere.

DISCUSSION

Over the range of currents and bunch patterns selected to conduct these experiments, particularly in the January study, a wide range of material behavior has been observed. Surface roughness may play a role when comparing the effects of 65 mA beam aborts in May 2019 and January 2020,

Content from this work may be used under the terms of the CC BY 3.0 licence (© 2020). Any distribution of this work must maintain attribution to the author(s), title of the work, publisher, and DOI

ISBN: 978-3-95450-222-6 ISSN: 2673-5350 doi:10.18429/JACoW-IBIC2020-TUA002

Content from this work may be used under the terms of the CC BY 3.0 licence (© 2020). Any distribution of this work must maintain attribution to the author(s), title of the work, publisher, and DOI

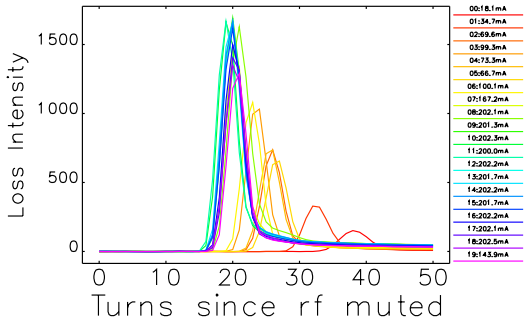

(a) ID1, Ch. 3 fast BLM.

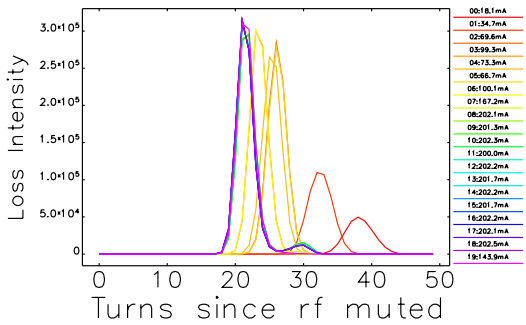

(b) elegant.

Figure 13: Comparison of a) fast BLM loss intensity with b) elegant modeling for the 20 beam abort cases.

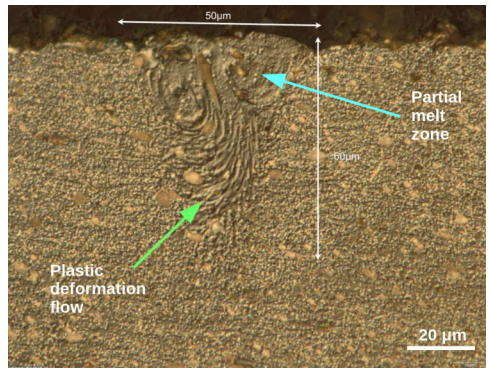

(a) 33.1 mA.

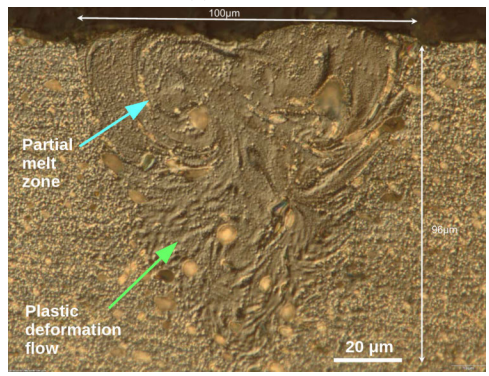

(b) 67.4 mA.

Figure 14: Cross sections of the aluminum test piece showing regions of a) 33.1 mA and b) 67.4 mA beam strikes. Regions of plastic flow and partial melt are identified. The beam direction is out of the page.

suggesting wakefield effects could be involved. However another explanations could exist such as material composition or current density. At 16 mA, no damage is detectable on the aluminum collimators; however, at 32 mA plastic deformation and partial melting take place. At 65 mA, material expulsion begins; however the transverse extent of the damage is relatively small. At 100 mA and above, the region of damage grows significantly. At 200 mA, the beam strike area is strongly evacuated leaving a clear trench even after a single dump; this is most likely a region of strong hydrodynamic activity. The large light output at high currents is ascribed as predominately black body radiation. The melting temperature of the T6061 aluminum alloy is 858 K and 2345 K for the thin aluminum oxide layer on the surface. In the May 2019 experiment, the oxide layer remained largely intact up to 65 mA; this was not the case in the January 2020 study. The fact that the heated region can be cleared in a single strike indicates the beam can propagate further downstream as it is dumped. Coupled modeling between particle-matter interaction, hydrodynamic, and beam dynamics codes (multiphysics) is required to adequately address this behavior.

SUMMARY

Two experiments have been conducted in the APS SR to reproduce expected whole-beam dump conditions in the APS-U. In the first experiment, transitions from solid to plastic/partial-melt states in Al and Ti-alloy target collimators were observed. In the second experiment, 200 mA was attained on aluminum targets; transitions to a fully hydrodynamic behavior were observed. Beam dynamics predictions by elegant show good agreement with measurements of beam arrival time and temporal pulse compression with current. Our suite of diagnostics has provided important data to allow benchmarking of coupled-code multiphysics investigations.

ACKNOWLEDGMENTS

Thanks to R. Soliday and H. Shang for assistance with analysis scripts.

REFERENCES

[1] M. Yabashi and H. Tanaka, “The next ten years of X-ray science”, *Nature Photonics*, vol. 11, no. 1, pp. 12–14, Jan. 2017. doi:10.1038/nphoton.2016.251

[2] N. V. Mokhov et al., “MARS15 Overview”, *AIP Conf. Proc.*, vol. 896, no.1, pp. 50-60, 2007. Rep. Fermilab-Conf-07/008-AD. doi:10.1063/1.2720456

[3] M. Borland, “elegant: A Flexible SDDS-Compliant Code for Accelerator Simulation”, presented at the 6th International Computational Accelerator Physics Conference, ICAP2000,

ISBN: 978-3-95450-222-6 ISSN: 2673-5350 doi:10.18429/JACoW-IBIC2020-TUAO02

Darmstadt, Germany, Sep. 2000. Rep. ANL/APS LS-287. doi:10.2172/761286

[4] J. C. Dooling *et al.*, "Studies of Beam Dumps in Candidate Horizontal Collimator Materials for the Advanced Photon Source Upgrade Storage Ring", presented at the NAPAC'19, Lansing, MI, USA, Sep. 2019, paper MOPLM14.

[5] ESTAR, https://physics.nist.gov/PhysRefData/Star/Text/ESTAR.html

[6] D. C. Wilson, R. P. Godwin, J. C. Goldstein, N. V. Mokhov, and C. A. Wingate, "Hydrodynamic Calculations of 20-TeV Beam Interactions with the SSC Beam Dump", in *Proc. PAC'93*, Washington D.C., USA, Mar. 1993, pp. 3090–3093.

Content from this work may be used under the terms of the CC BY 3.0 licence (© 2020). Any distribution of this work must maintain attribution to the author(s), title of the work, publisher, and DOI

ISBN: 978-3-95450-222-6 ISSN: 2673-5350 doi:10.18429/JACoW-IBIC2020-TUPP05

X-RAY BEAM SIZE MONITOR ENCLOSURE FOR THE ADVANCED PHOTON SOURCE UPGRADE*

K. P. Wootton†, W. Cheng, G. Decker, S. H. Lee, B. X. Yang
Argonne National Laboratory, Lemont, USA

Abstract

Confirmation of pm rad scale emittances from the Advanced Photon Source Upgrade electron storage ring necessitates direct measurement of the electron beam size. In the present work, we motivate design choices for the X-ray beam size monitor shielding enclosure for the Advanced Photon Source Upgrade. Particular emphasis is given to outlining design choices from the perspectives of safety, overall project construction schedule and eventual beamline operations.

INTRODUCTION

As a high average brightness source of X-ray photons, the storage ring for the Advanced Photon Source Upgrade (APS-U) is designed to operate with ambitious transverse emittances on the order of ~42 pm [1, 2]. In order to utilise the high brightness X-ray beams, a range of accelerator diagnostic instruments are planned to provide beam position stability and accelerator control [3]. In particular, to quantify the horizontal and vertical emittances, beam size monitors are planned for APS-U [4].

In the present work, we outline the enclosure design for the APS-U storage ring electron beam size monitor beamline.

BEAM SIZE MONITOR

Hard X-ray synchrotron radiation beam size monitors are planned for APS-U to quantify the transverse emittances of the stored electron beam [4, 5]. For an operating storage ring such as the Advanced Photon Source (APS), this is an important online diagnostic of the beam in the accelerator [6, 7]. A key performance parameter for successful completion of the APS-U project is that the horizontal emittance $\varepsilon_x \leq 130$ pm rad [1]. The beam size monitor is the principal instrument for confirming the emittances.

The principal functional requirement for absolute beam size measurement is that the contribution of system resolution σ_r to the measured electron beam size σ_e is not larger than 10% when added in quadrature. For the proposed timing and brightness operating modes of APS-U, the functional requirements of the absolute beam size monitor are summarised in Table 1 [1].

Table 1: APS-U Electron Beam Sizes at Bending Magnet A:M1.1 in Timing and Brightness Operating Modes

Parameter	Value	Units
Timing Mode	–	–
Horizontal beam size	7.2	µm
Vertical beam size	25.1	µm
Brightness Mode	–	–
Horizontal beam size	7.2	µm
Vertical beam size	9.1	µm

BEAMLINE LOCATION

Measurement of emittance based on the beam size is optimised where the contribution to the beam sizes is dominated by the emittance. For APS-U, the horizontal dispersion η_x is zero by design in the insertion straights, and so the nominal bending magnet source for the beam size monitor is the first longitudinal gradient bending magnet in an arc cell A:M1.1 [1].

The beam size monitor beamline will be located in Sector 38 of the APS-U storage ring. A schematic illustration of the beamline is shown in Fig. 1. This location was selected because the nominated photon source A:M1.1 bending magnet was only available in the radiofrequency cavity insertions. We will extract the bending magnet radiation through an unused insertion device photon beam extraction chamber, because user beamlines will occupy all the APS-U insertion device front ends.

There are several challenges that arise in the construction of a beamline in this location. The storage ring tunnel shield-

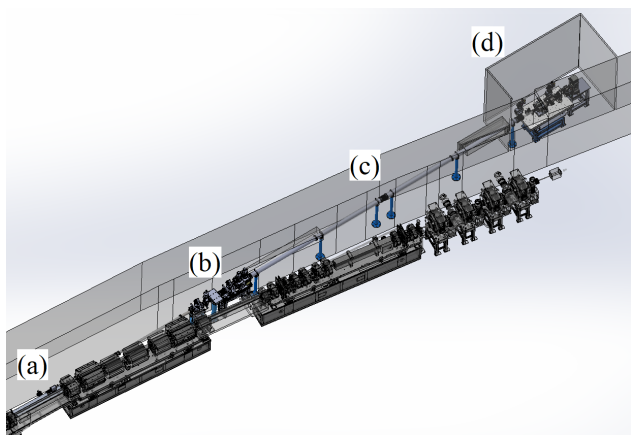

Figure 1: Schematic overview of Sector 38 beam size monitor beamline for APS-U. In this figure, the beam direction is from left to right. (a) Synchrotron radiation absorbers and pinhole mask. (b) Bending magnet beamline front end components (photon shutter, safety shutters and lead collimator). (c) Photon beam vacuum chamber through accelerator shield wall. (d) Endstation instruments and beamline enclosure.

* Work supported by the U.S. Department of Energy, Office of Science, Office of Basic Energy Sciences, under Contract No. DE-AC02-06CH11357.
† kwootton@anl.gov

Content from this work may be used under the terms of the CC BY 3.0 licence (© 2020). Any distribution of this work must maintain attribution to the author(s), title of the work, publisher, and DOI

ISBN: 978-3-95450-222-6 ISSN: 2673-5350 doi:10.18429/JACoW-IBIC2020-TUPP05

ing wall is not a ratchet wall geometry in this location, and is instead uniformly 1.1 m radial thickness concrete. Connecting the enclosure to the storage ring necessitates drilling a hole through the shield wall of approximately 8 m length. A similar dimension hole (albeit in the backwards-going direction) was drilled through the shield wall for a previous normal incidence diffraction (NID-X) beamline at the APS [8, 9].

ENCLOSURE DESIGN CHOICES

The principal requirement of the enclosure is to provide radiation protection to personnel in the vicinity of the enclosure when the beam is permitted to enter. Several design choices impacted the design of the enclosure. Some of the principal considerations are summarised.

Image Magnification and Beamline Length

For the X-ray pinhole camera, the distance from the A:M1.1 bending magnet source to the pinhole is 6.6 m. To achieve an optical magnification of 3, the camera is positioned 20 m downstream of the pinhole assembly.

Safety

The principal function of the enclosure is to shield against prompt radiation from the accelerator. For the particular beamline geometry and beam energy of 6 GeV, this is anticipated to be synchrotron radiation photons, gas bremsstrahlung and electromagnetic showers resulting from injected beam losses [10].

Earlier designs of the beamline envisioned the use of a new concrete shielded enclosure. Nominally, this was selected to match the existing storage ring shielding. However this introduced new concerns into design and construction, specifically the need to determine the structural capacity of the footing for the existing technical floor.

Based on Monte Carlo simulations of the beamline geometry, we have found that we can achieve the required radiological protection performance using an enclosure composed of lead panels, following the standard guidelines for hard X-ray white beam enclosures at the APS [11, 12].

Construction Schedule

In order to minimise disruption to the synchrotron light user community, APS-U construction and accelerator commissioning are planned to occur within a period of one calendar year. In order to meet this proposed schedule for accelerator removal and installation, we aim to maximise opportunities for construction activities during APS operation.

Choosing an enclosure construction type that is well-characterised (lead panelling) affords us the experience of previous beamline design and construction activities at APS. Construction activities for the enclosure can also begin during routine user operations.

It is anticipated that siting the endstation instruments in an enclosure may ease both the construction and commissioning schedules for the beamline. At APS-U, sector 38 is the furthest point in the accelerator tunnel from the nearest adjacent equipment access door ('super door'), making it beneficial to minimise the volume of equipment to be moved in to the accelerator tunnel at this location. The narrow aisle in the accelerator tunnel may also restrict the upright transport of an optical table with endstation instruments pre-assembled (or else limit the width of the table).

Beamline Operations

Locating the endstation equipment within a dedicated enclosure allows for the long-term benefit of access to the instruments for maintenance. During user runs, access to instruments located within the accelerator enclosure is necessarily limited to maintenance and machine studies periods.

SUMMARY

The physics requirements of the beam size monitors for APS-U motivate the construction of a beamline in an unusual location in the storage ring.

In the present work, we have summarised design choices for the X-ray beam size monitor shielding enclosure for the APS-U. Particular emphasis is given to outlining design choices from the perspectives of safety, overall project construction schedule and eventual beamline operations.

ACKNOWLEDGEMENTS

The submitted manuscript has been created by UChicago Argonne, LLC, Operator of Argonne National Laboratory ("Argonne"). Argonne, a U.S. Department of Energy Office of Science Laboratory, is operated under Contract No. DE-AC02-06CH11357. The U.S. Government retains for itself, and others acting on its behalf, a paid-up nonexclusive, irrevocable worldwide license in said article to reproduce, prepare derivative works, distribute copies to the public, and perform publicly and display publicly, by or on behalf of the Government. The Department of Energy will provide public access to these results of federally sponsored research in accordance with the DOE Public Access Plan. http://energy.gov/downloads/doe-public-access-plan

REFERENCES

[1] T. E. Fornek, "Advanced Photon Source Upgrade Project Final Design Report", Argonne National Laboratory, Lemont, IL, USA, Rep. APSU-2.01-RPT-003, May 2019. doi:10.2172/1543138

[2] M. Borland, T. G. Berenc, R. R. Lindberg, V. Sajaev, and Y. P. Sun, "Lower Emittance Lattice for the Advanced Photon Source Upgrade Using Reverse Bending Magnets", in *Proc. North American Particle Accelerator Conf. (NAPAC'16)*, Chicago, IL, USA, Oct. 2016, pp. 877–880. doi:10.18429/JACoW-NAPAC2016-WEPOB01

[3] N. Sereno *et al.*, "Beam Diagnostics for the APS MBA Upgrade", in *Proc. 9th Int. Particle Accelerator Conf. (IPAC'18)*, Vancouver, Canada, Apr.-May 2018, pp. 1204–1207. doi:10.18429/JACoW-IPAC2018-TUZGBD3

Content from this work may be used under the terms of the CC BY 3.0 licence (© 2020). Any distribution of this work must maintain attribution to the author(s), title of the work, publisher, and DOI

ISBN: 978-3-95450-222-6 ISSN: 2673-5350 doi:10.18429/JACoW-IBIC2020-TUPP05

Content from this work may be used under the terms of the CC BY 3.0 licence (© 2020). Any distribution of this work must maintain attribution to the author(s), title of the work, publisher, and DOI

[4] B. X. Yang, S. H. Lee, J. W. Morgan, and H. Shang, "High-Energy X-Ray Pinhole Camera for High-Resolution Electron Beam Size Measurements", in *Proc. 5th Int. Beam Instrumentation Conf. (IBIC'16)*, Barcelona, Spain, Sep. 2016, pp. 504–507. doi:10.18429/JACoW-IBIC2016-TUPG66

[5] B. X. Yang and S. H. Lee, "Planned x-ray diffraction diagnostics for APS Upgrade emittance measurements", presented at Topical Workshop on Emittance Measurements for Light Sources and FELs, Barcelona, Spain, Jan. 2018, unpublished.

[6] M. Borland, L. Emery, A. H. Lumpkin, N. Sereno, and B. X. Yang, "Recent Observations on the APS Storage Ring Using Synchrotron Radiation Monitors", in *Proc. 6th European Particle Accelerator Conf. (EPAC'98)*, Stockholm, Sweden, Jun. 1998, paper WEP01G, pp. 1556–1558.

[7] B. Yang, A. H. Lumpkin, L. Emery, and M. Borland, "Recent developments in measurement and tracking of the APS storage ring beam emittance", *AIP Conf. Proc.*, vol. 546, pp. 622–630, 2000. doi:10.1063/1.1342639

[8] Y. Shvyd'ko, "X-ray resonators and other applications of Bragg backscattering", Ph.D. Thesis, Universität Hamburg, Hamburg, Germany, 2001. doi:10.3204/DESY-THESIS-2002-028

[9] A. T. Macrander and P. M. Platzman, "Alternative Methods for Sub-eV Resolution Inelastic X-ray Scattering", *Rev. Sci. Instrum.*, vol. 67, p. 3380, 1996. doi:10.1063/1.1146932

[10] K. C. Harkay *et al.*, "High-Charge Injector for on-Axis Injection Into A High-Performance Storage Ring Light Source", in *Proc. 10th Int. Particle Accelerator Conf. (IPAC'19)*, Melbourne, Australia, May 2019, pp. 3423–3426. doi:10.18429/JACoW-IPAC2019-THYYPLM3

[11] P. Fernandez and S. Davey, "Guidelines for Beamline and Front-End Radiation Shielding Design at the Advanced Photon Source", Argonne National Laboratory, Lemont, IL, USA, Rep. ANL/APS/TB-44 (Rev. 5), Sep. 2014. doi:10.2172/1177556

[12] S. Chitra, private communication, May 2020.

ISBN: 978-3-95450-222-6 ISSN: 2673-5350 doi:10.18429/JACoW-IBIC2020-TUPP06

INCLINED X-RAY BEAM POSITION MONITORS TO REDUCE INFLUENCE OF FILLING PATTERN FOR THE SPring-8 PHOTON BEAMLINES

H. Aoyagi†, Y. Furukawa, S. Takahashi
Japan Synchrotron Radiation Research Institute (JASRI), Hyogo, Japan

Abstract

Influence of bunch filling patterns on X-ray beam position monitors (XBPMs) increased year by year as the bunch current of the storage ring increased. We have performed a systematic evaluation of the influence of the filling patterns. As a result, the cause of the influence was to be found to be suppression of the XBPM current signal due to the space charge effect, and was able to be quantified by observing the behavior of the current signal while changing the applied voltage to a photoelectron collecting electrode. On the other hand, we have designed a new blade-shaped detection element having inclined configuration for the purpose of mitigating the space charge effect. It has been demonstrated that the influence of filling patterns is reduced to a few μm. We also report that, as a result of a series of efforts against the existing XBPMs for all insertion device beamlines, the influence has been reduced to approximately 5 μm RMS.

INTRODUCTION

The X-ray beam position monitors (XBPMs) at the SPring-8 storage ring works in a photoemission mode that is equipped with four blade-shaped detection elements made of tungsten as photocathodes [1]. The XBPMs are installed at insertion devise beamlines (ID-BLs) and bending magnet beamlines (BM-BLs), and have a stable operation record for over 20 years. Monitoring photon beam axes with the XBPMs, which have been fully evaluated for their performances, ensures the stable supply of the photon beam to beamline users. The rf-BPM of the storage ring excels in global diagnosis of closed orbit distortions, while the XBPM is suitable for accurate diagnosis of photon beams of individual beamlines.

SPring-8 constantly provides various several-bunch mode operations, which combine single bunches (isolated bunces) and train bunches (partial full-filling) [2] to perform the time-division experiment. The bunch current has been gradually increasing, and reached up to 5 mA/bunch in a single bunch and 0.38 mA/bunch in partial full-filling. The bunch current of 1 mA/bunch corresponds to 4.8 nC in the storage ring. As the bunch current increased, the influence of bunch filling patterns on XBPM performance increased year by year.

INFLUENCE OF FILLING PATTERN

The XBPM readouts in five types of several-bunch modes systematically were evaluated using the readouts in multi-bunch mode as the reference data to quantitatively understand the phenomenon that affects the XBPMs by changing the filling pattern. The multi-bunch mode, a type of a filling pattern, has the least impact on the accelerator beam operation. This measurement is performed in the same procedure as for the fixed point observation that is regularly conducted before the beginning of each user operation cycles with setting the ID gap of each ID-BL to a certain fixed value. As shown in Fig. 1 (a), it was found that different filling patterns have different effects on XBPMs.

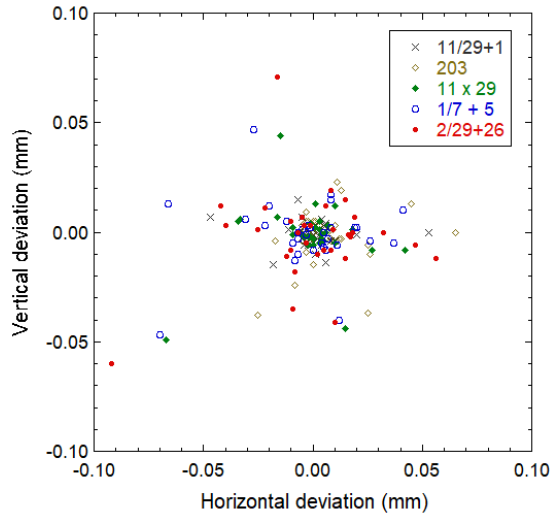

(a) Before the series of measures

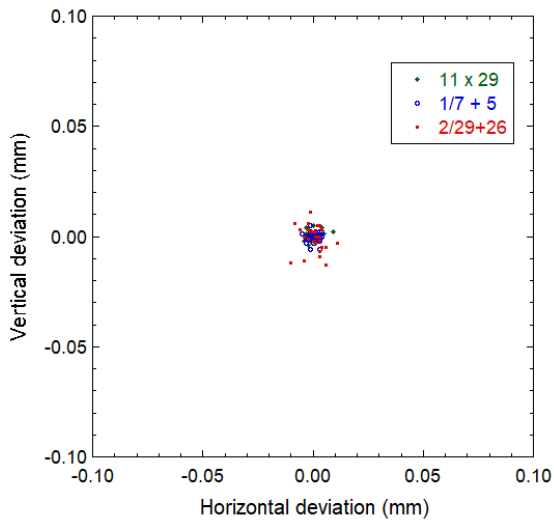

(b) After the series of measures

Figure 1: Deviations of XBPM readouts from the reference positions (multi-bunch) due to variations of five different filling patterns of the storage ring.

† aoyagi@spring8.or.jp

Content from this work may be used under the terms of the CC BY 3.0 licence (© 2020). Any distribution of this work must maintain attribution to the author(s), title of the work, publisher, and DOI

ISBN: 978-3-95450-222-6 ISSN: 2673-5350 doi:10.18429/JACoW-IBIC2020-TUPP06

Content from this work may be used under the terms of the CC BY 3.0 licence (© 2020). Any distribution of this work must maintain attribution to the author(s), title of the work, publisher, and DOI

Table 1: Bunch Current and the Deviation of the Readouts of Existing XBPMs

Filling pattern	Bunch current (mA/bunch)		Deviation of XBPM readouts (μm RMS)	
	Train	Isolated	Horizontal	Vertical
Multi	0.05	—	3.6	2.0
11/29 + 1	0.10	5.0	13.9	5.8
203	—	0.5	17.6	12.6
11 x 29	0.31	—	27.7 → **2.7** *	14.6 → **2.0** *
1/7 + 5	0.24	3.0	33.5 → **2.4** *	15.2 → **2.1** *
2/29 + 26	0.38	1.4	40.3 → **4.3** *	20.5 → **5.6** *

* after taking a series of measures

Table 1 shows the bunch current value in each filling pattern and the deviation of XBPM readouts in root mean square (RMS). The most significant effect was seen in 2/29 filling + 26 bunches mode, where the maximum horizontal and vertical displacements are approximately 40 μm RMS and approximately 20 μm RMS, respectively [3]. We verified the cause of the influence by changing the applied voltage to photoelectron collecting electrodes (normal applied voltage HV = +100 V). In the significantly affected XBPMs, current signals of the blade-shaped detection elements were greatly attenuated in the several-bunch modes, and were sensitive to the change in the applied voltage. We presumed that the cause should be space charge effect of photoelectrons near the surface of the detection elements. Therefore, we changed the operating conditions of the fixed point observation to confirm whether the influence of the filling pattern could be reduced. The major changes were 1) increasing the applied voltage to the collecting electrodes, 2) widening the ID gaps for the fixed point observations. As a result, as shown in Fig. 1(b), we succeeded in suppressing the influences of changing the filling pattern to less than several μm in RMS [4, 5]. Table 1 shows the deviation of XBPM readouts in RMS after taking a series of measures.

However, as long as the XBPMs having the existing detection elements are used, the ID gaps for fixed point observation must be widened. Therefore, we attempted to solve the problem of the space charge effect of the detection elements by newly designing and manufacturing.

STRUCTURE OF INCLINED-XBPM

We designed a new XBPN aiming at generating a high electric field between the detection elements and the collecting electrodes to mitigate the space charge effect. Since the existing detection elements are placed parallel to the beam axis, actual irradiated spots were concentrated on the edge of the blade tip (t = 0.2 mm). Therefore, the effective electric field was not efficiently applied to the detection elements. In the new design, we have devised a way for the broad side area of the blades to be the irradiated spots by adopting an inclined configuration arranged at an inclination of 1/60 to the beam axis [5]. Accordingly, it is expected that the effect of extracting photoelectrons by the electric field applied between the blades and the collecting electrode will be improved, resulting in mitigation of the space charge effect. In addition, as an additional function, concentration of heat load on the tips of the blades can be reduced by introduction of a curved forming of the blades. Furthermore, the location of the maximum heat load moves to the central of the blades, so that the cooling effect could be improved. Figure 2 shows the difference in shape and configuration between the existing and newly designed detection elements.

Figure 3 shows a photograph of the blade-shaped detection elements mounted with the inclined configuration [6]. Collecting electrodes are provided on both sides of the detection elemenct. Since the actual irradiated spots are the outer surface of the curved forming tip, the emitted photoelectrons are efficiently extracted to the collecting electrode (positive potential). In the existing design, the distances between the tips of the four detection elements were 6 mm in horizontal and 4 mm in vertical, but the new design adopted 7 mm in horizontal and 6 mm in vertical from the viewpoint of heat resistance. As a result, the output current signal of each detection elements decreases, and it can be also expected that the space charge effect will be mitigated. Figure 4 shows schematics of newly designed detection elements, a water-cooled blade holder and a monitor vacuum chamber that conforms to the design of th existing XBPM.

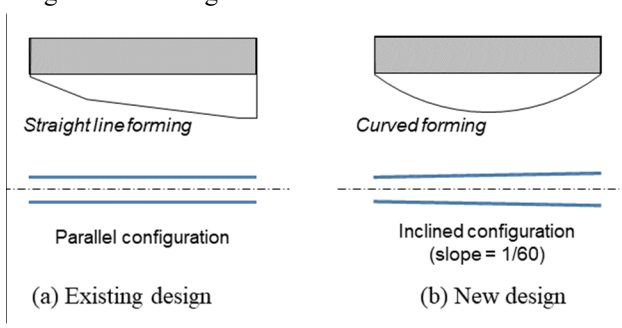

Figure 2: Schematics of blade-shaped detection elements. The difference in shape (top) and the difference in configuration (bottom) between (a) existing design and (b) new design are shown. The size of the tungsten plates are 60x20x0.2t. The shaded parts are sprayed by ceramic (60x10x0.1t).

ISBN: 978-3-95450-222-6 ISSN: 2673-5350 doi:10.18429/JACoW-IBIC2020-TUPP06

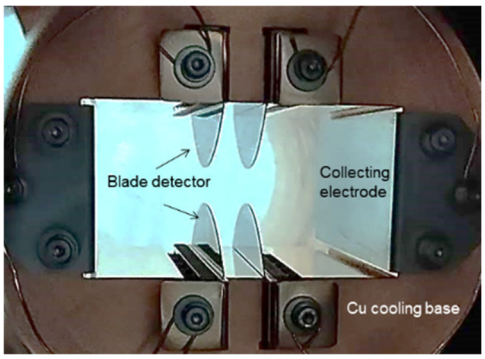

Figure 3: Photograph of detector heads.

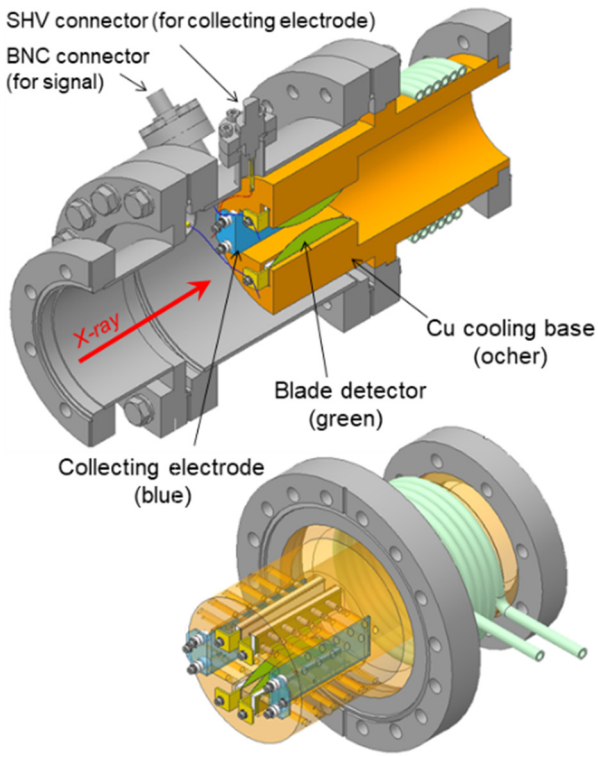

Figure 4: Schematics of an inclined-XBPM, a view of the internal configuration along a vertical cross-section (top) and a perspective view (bottom).

APPLIED VOLTAGE TO COLLECTING ELECTRODES

The dependences of the each blade current signal on the applied voltage to the collecting electrodes was measured to evaluate the influence of the space charge effect on the inclined-XBPM. The operation mode consists of the multi-bunch mode ("160 bunch train x 12") as the reference and two several-bunch modes ("11/29-filling + 1 bunch" and "2/29-filling + 26 bunches"). ID gap is set to 8.1 mm (minimum gap) and 13.0 mm (fixed point observation gap). The average values of four blade current signals were plotted in Fig. 5. In the multi-bunch mode, a lower limit voltage of the plateau region appears below the applied voltage of +100 V even under the condition of Gap = 8.1 mm. On the other hands, in the several-bunch mode ("2/29-filling + 26 bunches"), the lower limit voltage of the plateau region appears at +100 V under the condition of Gap = 13.0 mm, while the plateau region appeared at approximately +200 V under the condition of Gap = 8.1 mm. In other words, the lower limit voltage of the plateau region increases as the impact of the operation mode on the beam operation is greater (several-bunch mode) and as the ID gap becomes narrower, resulting in the increase in the blade current signal.

For comparison, the data of the existing XBPM ("parallel" configuration) in the several-bunch mode ("2/29-filling + 26 bunches") are also plotted. In the existing XBPM, the plateau region is clearly above +200 V or higher, even though the ID gap is set wider. This suggests that the inclined-XBPM in more effective than the existing XBPM in terms of reducing the influence of the filling pattern.

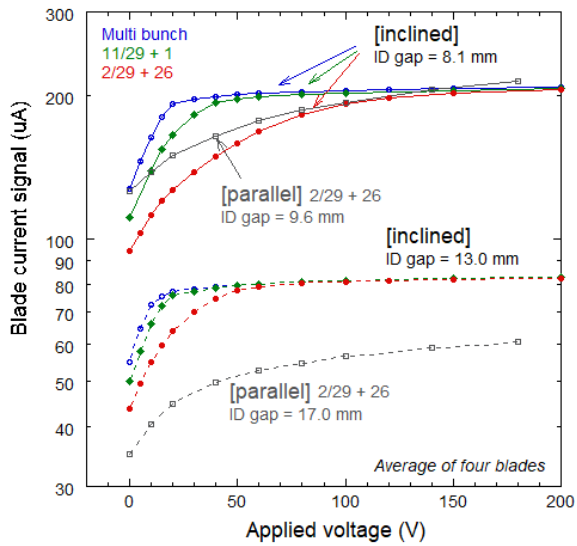

Figure 5: Applied voltage curves of blade current signal (average of four detection elements).

DEMONSTRATION BY FIXED POINT OBSERVATION

Beam position measurements in the operation mode of "2/29-filling + 26 bunches", having the most significant impact on the beam operation, were performed with the inclined-XBPM to directly evaluate the influence of the filling patterns using the same procedure as the fixed point observation. The differences in XBPM readouts from those in the multi-bunch mode were evaluated under four condition consisting of two different applied voltage to the collecting electrode (+100 V and +500 V) and ID Gaps (13.0 mm and 8.1 mm) combination. As shown in Table 2, the differences in horizontal of approximately 5 µm were observed, when the applied voltage to the collecting electrodes was +100 V. It can be seen that the influence of changing the filling pattern is small enough when the applied voltage is +500 V.

Content from this work may be used under the terms of the CC BY 3.0 licence (© 2020). Any distribution of this work must maintain attribution to the author(s), title of the work, publisher, and DOI

ISBN: 978-3-95450-222-6 ISSN: 2673-5350 doi:10.18429/JACoW-IBIC2020-TUPP06

Content from this work may be used under the terms of the CC BY 3.0 licence (© 2020). Any distribution of this work must maintain attribution to the author(s), title of the work, publisher, and DOI

Table 2: Fixed Point Observation Results for the Inclined-XBPM

Condition		Difference in Readouts	
ID Gap (mm)	XBPM HV (V)	Δx (μm)	Δy (μm)
13.0	100 V	4.5	1.0
	500 V	-1.5	1.0
8.1	100 V	-5.0	-1.5
	500 V	0.0	1.0

CONCLUSION

We succeeded in suppressing the filling pattern dependency of the existing XBPM to less than several μm in RMS by taking a series of measures, such as, 1) increasing the applied voltage to the collecting electrodes, 2) widening the ID gaps for the fixed point observations.

To essentially solve the filling pattern dependency problem, a newly designed inclined-XBPM, whose detection elements were arranged with inclined configuration to mitigate the space charge effect, was manufactured. The dependence of each blade current signal on the applied voltage to the collecting electrodes was measured, and it was shown that the lower limit voltage of the plateau region decreases. In addition, we performed evaluation tests using the same procedure as for the fixed point observation, and demonstrated that the influence of filling pattern can be reduced.

REFERENCES

[1] H. Aoyagi, T. Kudo, H. Kitamura, "Blade-type X-ray beam position monitors for SPring-8 undulator beamlines", *Nucl. Instrum. Meth. A*, vol. 467-468, pp. 252-255, 2001.

[2] SPring-8 operation schedule, http://www.spring8.or.jp/ja/users/operation_status/schedule/bunch_mode/

[3] H. Aoyagi, Y. Furukawa, and S. Takahashi, "Performance of the X-ray beam position monitors and observation of beam drifts in the SPring-8 storage ring", in *Proc. 15th Annual Meeting of Particle Accelerator Society of Japan (PASJ'18),* Aug. 2018, Nagaoka, Japan, paper WEOL06 (5 pages), in Japanese.

[4] H. Aoyagi, Y. Furukawa, and S. Takahashi, "Evaluation and reduction of influence of filling pattern on x-ray beam position monitors for SPring-8", *in Proc. 10th Int. Particle Accelerator Conf. (IPAC'19)*, Melbourne, Australia, May 2019, pp. 2526--2528. doi:10.18429/JACoW-IPAC2019-WEPGW027

[5] H. Aoyagi and S. Takahashi, "X-ray beam position monitor to mitigate influence of filling pattern at SPring-8", in *Proc. 16th Annual Meeting of Particle Accelerator Society of Japan (PASJ'18),* Jul.-Aug. 2019, Kyoto, Japan, paper THPI029 (4 pages), in Japanese.

[6] Vacuum and Optical Instruments; http://www.shinku-kogaku.co.jp/

ISBN: 978-3-95450-222-6 ISSN: 2673-5350 doi:10.18429/JACoW-IBIC2020-TUPP09

MULTIPLEXER SYSTEM FOR THE SPEAR3 BOOSTER BPM UPGRADE*

F. Toufexis†, L. Campana‡, P. Boussina, J.J. Sebek, J. Corbett, SLAC, Menlo Park, CA 94025, USA

Abstract

BPM measurements in booster synchrotrons are often only critical during accelerator commissioning or when a problem occurs. As a result, many facilities do not make large investments in booster BPM signal processors; they either have very few BPMs and/or use older generation processors. The SPEAR3 booster BPM processor system, for instance, has operated since 1990 with commercial multiplexers to switch between BPM button signals into a single dated analog BPM processor that was developed at SLAC. This system has reached its end-of-life so we are in the process of upgrading to modern multiplexers that feed a pair of turn-by-turn Libera SPARK-ERXR processors. This low-cost solution gives us the ability to arbitrarily multiplex between BPM signals during the energy ramp with modern BPM processors. The system can either measure 2 BPMs turn-by-turn in parallel during the entire energy ramp, or sequentially measure all BPMs (2 at a time) at different time slices within the ramp. Here we show measurements of the MiniCircuits switch we chose as well as our architecture for the upgrade.

INTRODUCTION

The SPEAR3 injector was commissioned in 1990 [1], and includes a 120 MeV linac injector with a thermionic RF gun [2], the booster synchrotron [3] and the Transport Lines. The entire injector, including the Transport Lines, is equipped with stripline-style Beam Position Monitors (BPMs). The original booster synchrotron BPM electronics used a commercial multiplexer to switch between BPM button signals into an in-house built analog BPM processor [4]. Out of the 40 booster BPMs, 20 are connected to long-haul cables that come out of the ring and are connected to the legacy BPM processor system. In this system, the 20 BPMs are connected to three slow multiplexer modules (referred to as the R10Ts). The output of these three multiplexers is connected to a faster multiplexer. The output of this multiplexer is filtered and then connected to an in-house BPM processor. Two different software systems can obtain the orbit from the booster: one system can get the average position in a number of time slots per booster ramp for one BPM, while the other system can get the position in several time slots for all BPMs in the same ramp.

At the time of this writing two (plus a spare) Instrumentation Technologies Libera SPARK-ERXR Turn-by-Turn (TbT) BPM processors have been installed at the booster and have gone through preliminary testing. We are also building two new multiplexer chassis that will connect the 20 connected booster BPMs into the SPARK processors to measure the orbit on a TbT basis during a booster ramp. We have investigated commercial switch options to replace the R10Ts; there are several option with sub-microsecond switching time but cost upwards of $7,000 for a 10-input switch that is not financially attractive. The Mini-Circuits USB-1SP16T-83H was the lowest cost option we found, had adequate specifications for our needs, and was readily available to purchase. The specifications are summarized in Table 1.

This work is organized as follows: we begin with time-domain and frequency domain measurements of the switch in the lab. Then we show measurements with the actual BPM signals from the booster. Finally we show the overall architecture of the new system we are building.

TIME-DOMAIN LAB MEASUREMENTS

The MiniCircuits switch provides both a TTL and USB interface. The USB interface can be used for slow switching on the order of milliseconds according to the manual; therefore we use the TTL interface. The unit has a DB9 connector to provide power and TTL signals if USB is not being used. We made a custom cable; one end had a DB9 connector, and the other had two banana plugs to connect ground and power as well as 5 coaxial cables with BNC connectors to connect the TTL signals to a delay generator for testing. The measurement setup is shown in Figure 1.

First we tested with one RF input signal at 400 MHz and −10 dBm. We programmed the delay generator to toggle 1 channel as shown in Figure 2a, switching between the signal and an unconnected input. We noticed that the gating on/off of the output signal jittered with respect to the signal generator. We subsequently connected a second RF input signal, now switching between two inputs. Figure 2b shows the transition of the output. The whole transition itself takes less than 5 µs as specified; however, the transition time with respect to the delay generator signal again showed jitter of about 10 µs. We suspect this is due to the microprocessor on the switch that internally controls the switching; most likely the microprocessor periodically checks the input TTL

Table 1: Mini-Circuits USB-1SP16T-83H Switch Specs

Frequency	1 MHz – 8 GHz
Isolation	63 dB Min (0 GHz – 3 GHz)
Transition Time	5 µs
Power Handling	30 dBm
Insertion Loss	7.5 dB Max (0 GHz – 3 GHz)
Interface	USB & TTL
Inputs	16
Price	$1,835

* Work sponsored by US Department of Energy Contract DE-AC02-76SF00515.
† ftouf@slac.stanford.edu
‡ Currently at Dipartimento di fisica, Sapienza università di Roma, Rome, Italy

Content from this work may be used under the terms of the CC BY 3.0 licence (© 2020). Any distribution of this work must maintain attribution to the author(s), title of the work, publisher, and DOI

ISBN: 978-3-95450-222-6 ISSN: 2673-5350 doi:10.18429/JACoW-IBIC2020-TUPP09

Content from this work may be used under the terms of the CC BY 3.0 licence (© 2020). Any distribution of this work must maintain attribution to the author(s), title of the work, publisher, and DOI

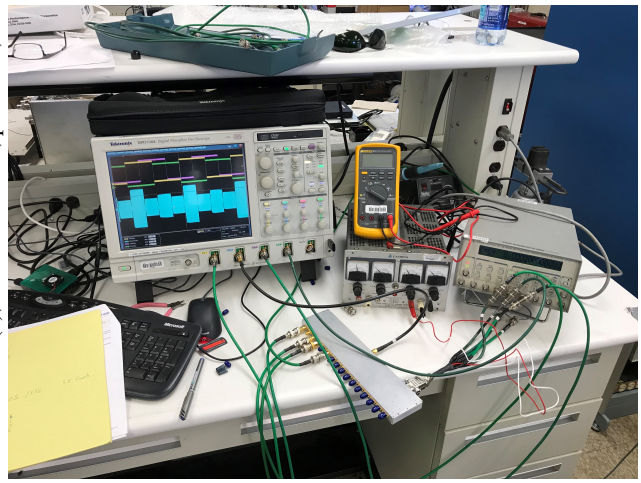

Figure 1: Measurement setup. The scope shows the continuous switching between 4 channels of different frequency and amplitude.

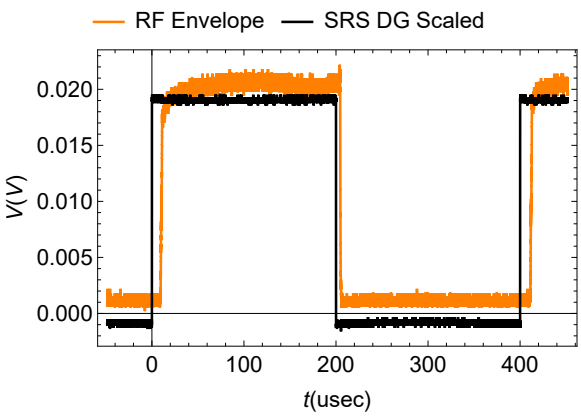

(a) On/off characteristics

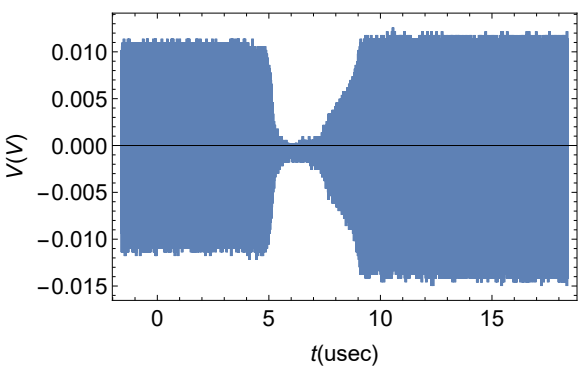

(b) Switching between two RF input signals.

Figure 2: Transition data.

signals and decides how to modify the switch configuration. Therefore we consider the effective dead time of a transition to be 20 µs.

Finally, we tested a configuration with continuous switching between four channels. We programmed the delay generator to toggle 3 control TTL signals in a pattern that would cause the switch to alternate between 4 channels. We connected signals with frequencies between 250 MHz and 500 MHz, and power between −20 dBm and −10 dBm. The resulting output signal is shown in Figure 1. As expected, the switching characteristics appeared the same as in the two-channel case.

VNA MEASUREMENTS

We next connected port 1 of a Vector Network Analyzer (VNA) to channel 1 of the switch and port 2 to the COM port. Without changing this setup, we measured S-parameters for 3 cases: a) channel 1 enabled, b) channel 2 enabled, and c) channel 16 enabled. The different channels were enabled through EPICS using a prototype controller based on a Raspberry Pi and an Arduino.

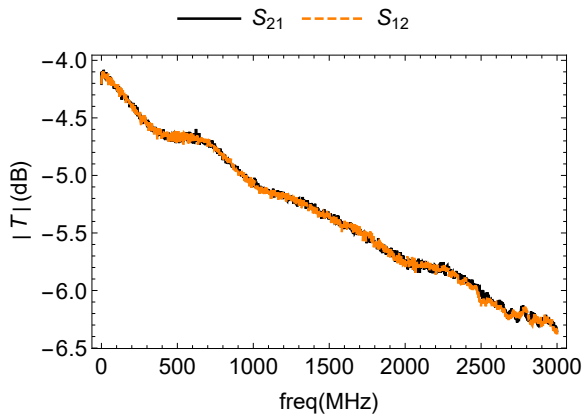

(a) Attenuation through the switch.

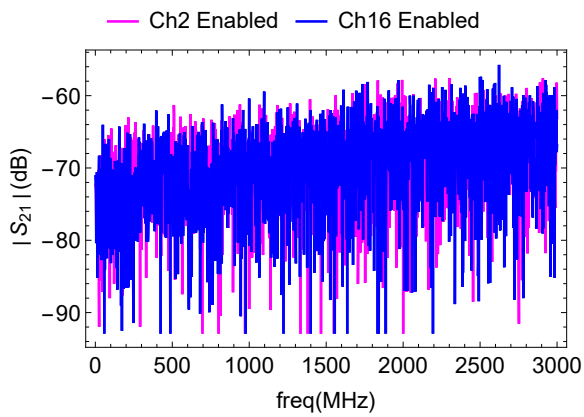

(b) Isolation when a different channel is enabled.

Figure 3: Attenuation and isolation data.

Figure 3a shows the transmission from channel 1 to the COM port and reverse when channel 1 is activated. The switch is near perfectly reciprocal. Attenuation increases almost linearly with increased frequency from about 4.2 dB at near DC frequencies to about 6.4 dB at 3 GHz. This is a much improved response when compared to the existing system. Figure 3b shows the isolation from channel 1 to the COM port when a different channel is enabled. The switch has around 60 dB isolation.

ISBN: 978-3-95450-222-6 ISSN: 2673-5350 doi:10.18429/JACoW-IBIC2020-TUPP09

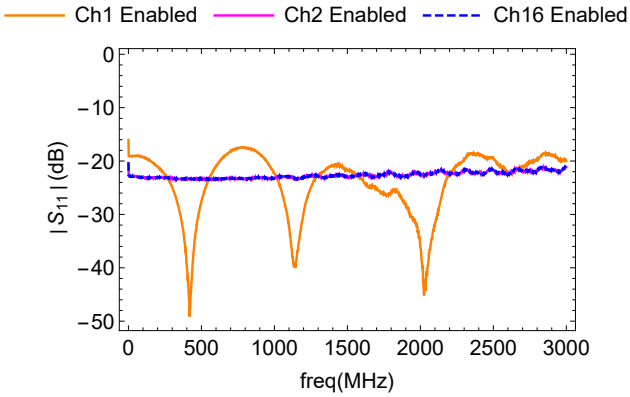

(a) Reflection from channel 1.

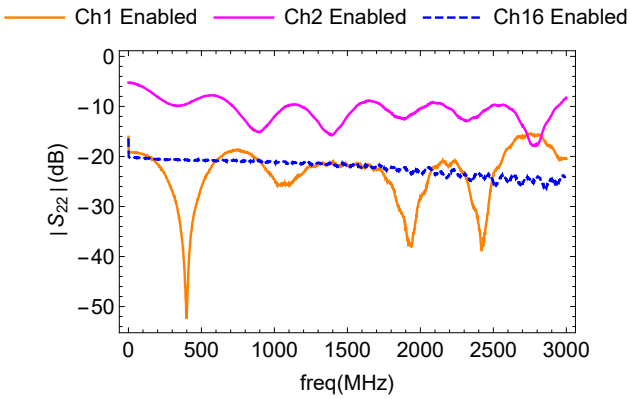

(b) Reflection from the COM port.

Figure 4: Reflection data.

Figure 4 shows the reflection from channel 1 and the COM port for different enabled channels. The input is always well-matched irrespective of the enabled channel. The output is not always well-matched; we are not sure why, but we do not expect it to be an issue as the output of the switch will be connected to a BPM processor that is not generating signals.

BEAM-BASED MEASUREMENTS

We further performed a number of measurements with the booster beam and the actual BPM signals to see how the switch affects the waveforms. Figure 5 shows a single-pass BPM waveform directly on the scope and through the switch. As expected from the attenuation of the switch, the amplitude is roughly half. We see an additional reduction at the positive part of the waveform, but overall the switch does not appear to substantially degrade the waveform.

We then connected one BPM button signal on channel 1 and set the switch on that channel. Figure 6 shows the BPM waveform through the switch for multiple turns while channel 1 was activated. We can observe oscillations on the envelope. We further connected a second BPM to channel 2 through a 6 dB attenuator and set the switch to alternate between channel 1 and 2. Figure 7 shows the transition from channel 2 to channel 1. From this data we believe that we can post-process the BPM data by identifying transitions

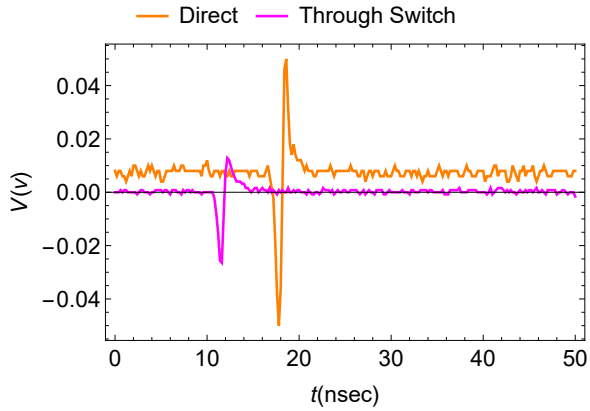

Figure 5: Direct BPM waveform and through the switch.

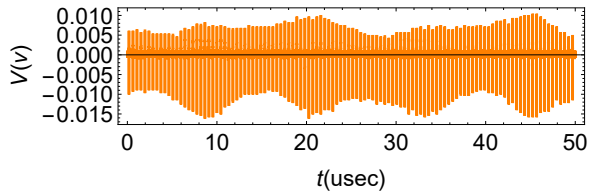

Figure 6: BPM waveform of several turns through the switch.

from the signal amplitude in software. Once we identify transitions, since we know the transition time and sequence, we can discard the data points close to the transitions.

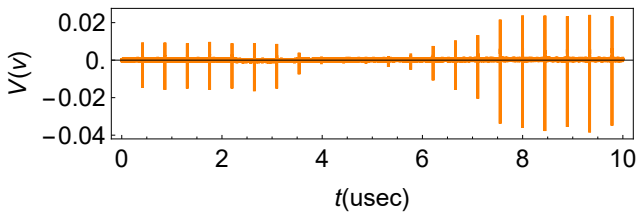

Figure 7: BPM waveform during a transition between two channels.

BPM SWITCH ARCHITECTURE & PROTOTYPE

Figure 8a shows an overview of the BPM multiplexer system. The inputs of four MiniCircuits switches are connected to the ABCD buttons coming from the synchrotron. The outputs are connected to the inputs of one SPARK-ERXR module. The switches are controlled through the DB9 TTL interface. A microcontroller Printed Circuit Board (PCB) is used to control the four switches. We have chosen the Infineon XMC4800 microcontroller since it is an industrial part with long support lifetime and has a simple software environment to configure its peripherals and program it, and can receive commands through a USB serial interface. An EPICS IOC can then send commands to the microcontroller using EPICS `SteamDevice`. The microcontroller can be directly connected on the USB port of a computer (such as a RaspberryPi) that hosts the IOC. Alternatively, the microcontroller can be connected to a terminal server; the IOC

Content from this work may be used under the terms of the CC BY 3.0 licence (© 2020). Any distribution of this work must maintain attribution to the author(s), title of the work, publisher, and DOI

ISBN: 978-3-95450-222-6 ISSN: 2673-5350 doi:10.18429/JACoW-IBIC2020-TUPP09

Content from this work may be used under the terms of the CC BY 3.0 licence (© 2020). Any distribution of this work must maintain attribution to the author(s), title of the work, publisher, and DOI

will reside on a server and send commands over the network. The 10 Hz injector trigger is also supplied to the microcontroller. We developed a proof-of-concept prototype shown in Fig. 8b. In the protype we used the XMC4700 development board connected to a vector board with DB9 connectors for the switches and BNC trigger input. The microcontroller is connected to the USB port of a Raspberry Pi that hosts an EPICS IOC.

This system can operate in two modes: a) static, and b) alternating. In the static mode the switches are set to one BPM and the SPARK reads only this BPM. In the alternating mode the microcontroller cycles through the connected BPMs constantly through the booster ramp. In this case the SPARK reads positions from a number of time slices from all the connected BPMs during the booster ramp. The 10 Hz injection trigger is used to signal the beginning of booster ramp. A software script then postprocesses the SPARK data and assigns different portion of the TbT data to different BPMs; the switch between BPMs can be identified by looking when the sum signal falls bellow a certain threshold. Additionally we can connect one of the switch inputs to the RF signal of the booster to act a fiducial.

Figure 9 shows measured data from the SPARK while switching between four BPMs. In the x position we can see jumps in the data points around the BPM transitions. However, in the same transitions we can see the sum signal becomes low as expected from the switch characteristics. We can identify the transition times using the sum information and then discard the data points around the switch transitions.

We are building two multiplexer chassis with the Mini-Circuits switch in order to connect the 20 booster BPMs to the two SPARK-ERXR TbT Processors. Each chassis will have internally 4 switches for the 4 BPM buttons. The booster ramp is approximately 30 ms. If we have 10 BPMs connected to each chassis, then we can measure each BPM for 3 ms during the ramp. If we further split this in 30 time slices, then a time slice for one BPM is 100 µs. Subtracting the 20 µs of dead time during a BPM switch, we can sample 80 µs or approximately 150 turns per BPM per time slice.

SUMMARY

In this work we showed proof-of-concept measurements for a low-cost BPM multiplexer system for the SPEAR3 booster synchrotron. Instead of having one BPM processor per physical BPM we will use a set of commercial multiplexers that feed two Libera SPARK-ERXR TbT BPM processors. The existing system also used multiplexers but has reached its end of life. We have evaluated a commercial switch and showed testing results both in the lab and with the actual BPM signals from the booster. From the data we collected, the unit has an average dead time due to switching of about 20 µs. The performance of this switch is adequate for the replacing the R10Ts in the booster BPM system. Finally we described the architecture for the upgrade. The system can either measure 2 BPMs TbT during the entire energy ramp, or sequentially measure all BPMs (2 at a time) at different time slices within the ramp.

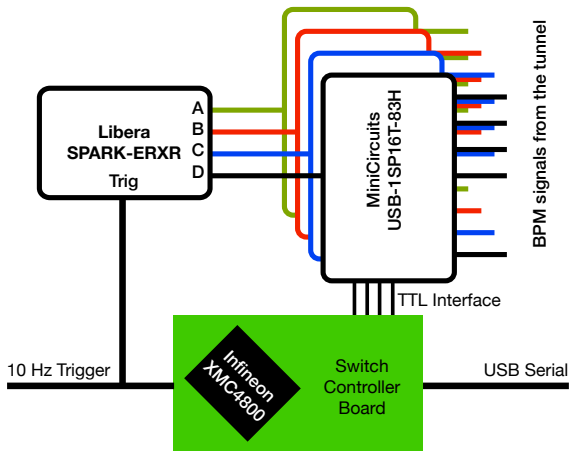

(a) Schematic of the proposed system upgrade.

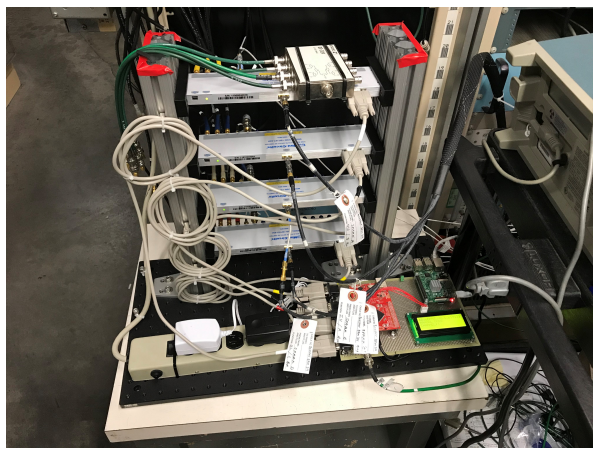

(b) Picture of the proof-of-concept prototype.

Figure 8: BPM multiplexer system.

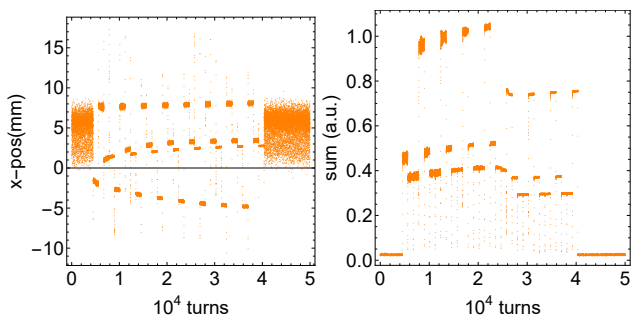

Figure 9: Measured data from the SPARK while switching between four BPMs.

ACKNOWLEDGMENTS

The authors would like to thank Shantha Condamoor, Scott Wallters, Kevin Helms, and the SPEAR3 operations staff for technical assistance.

ISBN: 978-3-95450-222-6 ISSN: 2673-5350 doi:10.18429/JACoW-IBIC2020-TUPP09

REFERENCES

[1] S. Baird and J. Safranek, "Commissioning the SSRL injector," in *Conference Record of the 1991 IEEE Particle Accelerator Conference*, vol. 5, May 1991, pp. 2865–2867. DOI: 10.1109/PAC.1991.165129.

[2] M. Borland, "A High Brightness Thermionic Microwave Electron Gun," Ph.D. dissertation, Stanford University, Feb. 1991.

[3] H. Weidemann, M. Baltay, J. Voss, K. Zuo, C. Chavis, R. Hettel, J. Sebek, H. D. Nuhn, J. Safranek, L. Emery, M. Horton, J. Weaver, J. Haydon, T. Hostetler, R. Ortiz, M. Borland, S. Baird, W. Lavender, P. Kung, J. Mello, W. Li, H. Morales, L. Baritchi, P. Golceff, T. Sanchez, R. Boyce, J. Cerino, D. Mostowfi, D. F. Wang, D. Baritchi, G. Johnson, C. Wermelskirchen, B. Youngman, C. Jach, J. Yang, and R. Yotam, "The 3 GeV synchrotron injector for SPEAR," in *Conference Record of the 1991 IEEE Particle Accelerator Conference*, vol. 5, May 1991, pp. 2688–2690. DOI: 10.1109/PAC.1991.165072.

[4] W. Lavender, S. Baird, S. Brennan, M. Borland, R. Hettel, H. D. Nuhn, R. Ortiz, J. Safranek, J. Sebek, C. Wermelskirchen, and J. Yang, "The SSRL injector beam position monitoring systems," in *Conference Record of the 1991 IEEE Particle Accelerator Conference*, vol. 2, May 1991, pp. 1151–1153. DOI: 10.1109/PAC.1991.164563.

Content from this work may be used under the terms of the CC BY 3.0 licence (© 2020). Any distribution of this work must maintain attribution to the author(s), title of the work, publisher, and DOI

ISBN: 978-3-95450-222-6 ISSN: 2673-5350 doi:10.18429/JACoW-IBIC2020-TUPP10

Content from this work may be used under the terms of the CC BY 3.0 licence (© 2020). Any distribution of this work must maintain attribution to the author(s), title of the work, publisher, and DOI

X-RAY BEAM POSITION MONITOR SILICON PHOTODIODE MEASUREMENTS FOR THE ADVANCED PHOTON SOURCE UPGRADE*

K. P. Wootton†, H. P. Cease, M. J. Erdmann, S. Oprondek, M. Ramanathan, B. X. Yang
Argonne National Laboratory, Lemont, IL, USA

Abstract

To best leverage the orders of magnitude average brightness increase of multi-bend achromat synchrotron radiation storage rings, ambitious beam stability requirements are imposed. One system that will be employed at the Advanced Photon Source Upgrade in support of photon beam stability will be X-ray beam position monitors. In the present work, electrical characterisation of several types of photodiodes are evaluated for potential use in X-ray beam position monitors.

INTRODUCTION

In order to meet demanding photon beam stability requirements of the Advanced Photon Source – Upgrade (APS-U) [1], hard X-ray beam position monitors are planned [2–4]. Several geometries of x-ray beam position monitors for different insertion device beamlines are foreseen, based upon the grazing-incidence insertion device hard x-ray fluorescence BPM (GRID XBPM) detector geometry [2–11].

In the present work, electronic performance testing of silicon photodiodes for X-ray beam position monitors is presented.

PHOTODIODES TESTED

The photodiodes tested in these studies were Luna Opto-Electronics solderable silicon photodiodes. The diodes are intended to be operated either in a photoconductive ('C') or photovoltaic ('V') mode. These solderable photodiodes are compatible with operation in an ultrahigh vacuum environment. Diode types tested in the present work included:

- PDB-C612-2,
- PDB-C613-2,
- PDB-V615-2.

METHOD

We consider here electrical tests that can be performed throughout stages of detector assembly, cleaning and installation. During all measurements in the present work, the photodiode under test was positioned within a light-tight box.

Shunt Resistance

Shunt resistance is defined to be the average slope of the voltage-current V–I curve about 0 V. The accepted practice for the measurement of diodes is to measure the current across the diode at voltages of ±10 mV [12].

For measurement of shunt resistance, the DC power supply and picoammeter were connected in series with the photodiode. The current through the diode was measured using the picoammeter. The power supply was set to output either +10 mV, 0 mV or −10 mV.

The sequence of measurement was to measure at 0 mV, +10 mV, 0 mV, −10 mV. Three observations of the current at each voltage setpoint were made. It took some time for the picoammeter current measurement to reach equilibrium. During these tests it took approximately 30 s per voltage step for the current measurement to stabilise. In practice, this was the slowest measurement to make.

Two-Wire Resistance

One technique to measure resistance of the diode is to perform a two-wire resistance measurement [13]. The average forward resistance is measured with a digital multimeter (Keysight 34465A 6 1/2 digit multimeter) used as an ohmmeter. The measurement current is 500 nA [14]. Due to the nonlinear I–V curve of the photodiode, this resistance value is expected to change with the measurement current. This measurement only returns a value for the voltage with the leads connected in forward bias across the diode. For a normal diode measured in reverse bias, the multimeter returned an 'overload' response.

Each two-wire resistance measurement took less than one second to measure. Three observations were made at each setting.

Diode Test

A diode test is commonly included on multimeters [13]. It is a voltage measurement at a nominal current. In the present work, the current used was ∼1 mA.

Each diode test took less than one second to measure. Three observations were made at each setting.

Photocurrent

Photodiodes in the GRID XBPM are illuminated by X-ray fluorescence from a cerium-doped yttrium aluminium garnet (YAG) scintillator crystal. As a performance characteristic, we evaluate the uniformity of DC photocurrent produced by these photodiodes when illuminated by a green LED.

To evaluate the photocurrents of photodiodes, the photodiode was illuminated by a InGaAlP light emitting diode

* Work supported by the U.S. Department of Energy, Office of Science, Office of Basic Energy Sciences, under Contract No. DE-AC02-06CH11357.
† kwootton@anl.gov

ISBN: 978-3-95450-222-6 ISSN: 2673-5350 doi:10.18429/JACoW-IBIC2020-TUPP10

(LED) with a central emission wavelength of 571 which closely matches the central emission wavelength of 550 nm of the YAG scintillator. The diode was powered by a DC power supply with a 500 Ω resistor in series. The power supply for the LED was configured to operate in voltage-controlled mode. The voltage was set at each setpoint between 0 – 12 V, in steps of 2 V.

RESULTS

For each model of photodiode tested, histograms of the measured distribution of properties are presented.

PDB-C612-2

The measured shunt resistance of the PDB-C612-2 photodiodes is plotted in Fig. 1.

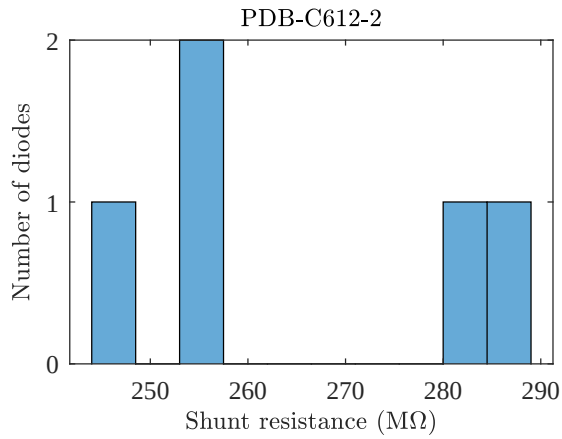

Figure 1: PDB-C612-2 shunt resistance measurements.

The measured two-wire resistance of the PDB-C612-2 photodiodes is plotted in Fig. 2.

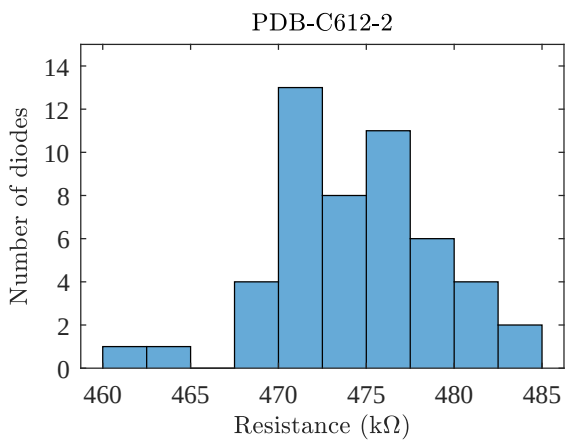

Figure 2: PDB-C612-2 two-wire resistance measurements.

The measured diode test of the PDB-C612-2 photodiodes is plotted in Fig. 3.

The photocurrent response of the PDB-C612-2 photodiodes is plotted in Fig. 4.

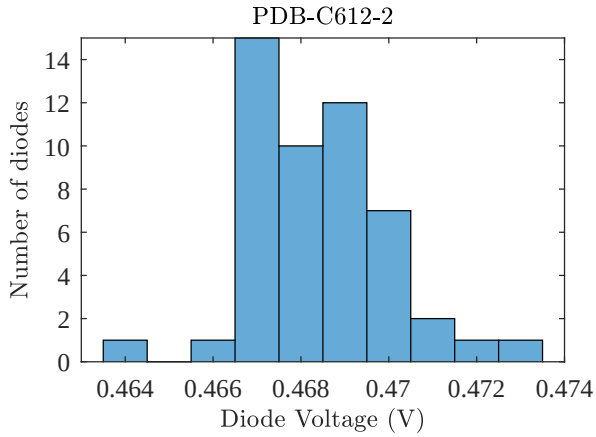

Figure 3: PDB-C612-2 diode measurements.

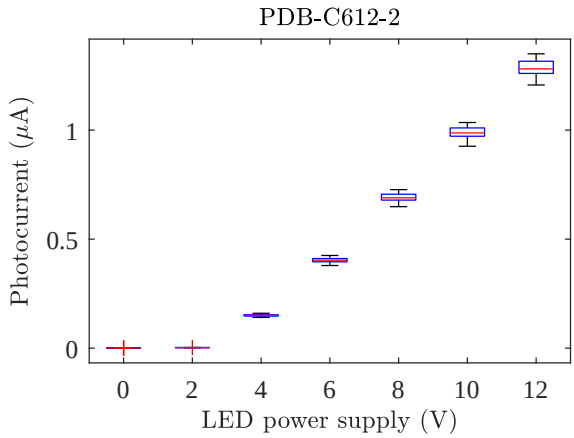

Figure 4: PDB-C612-2 photocurrent measurements.

PDB-C613-2

The measured shunt resistance of the PDB-C613-2 photodiodes is plotted in Fig. 5.

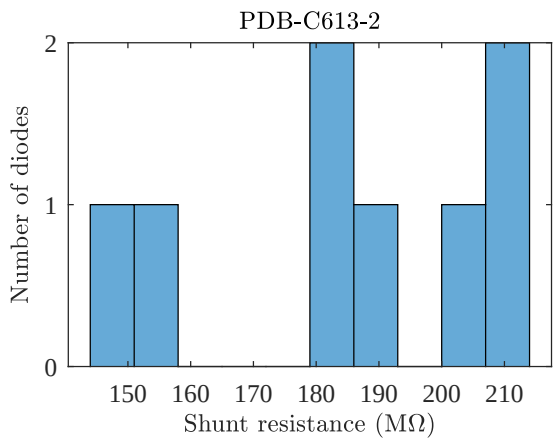

Figure 5: PDB-C613-2 shunt resistance measurements.

The measured two-wire resistance of the PDB-C613-2 photodiodes is plotted in Fig. 6.

The measured diode test of the PDB-C613-2 photodiodes is plotted in Fig. 7.

Content from this work may be used under the terms of the CC BY 3.0 licence (© 2020). Any distribution of this work must maintain attribution to the author(s), title of the work, publisher, and DOI

ISBN: 978-3-95450-222-6 ISSN: 2673-5350 doi:10.18429/JACoW-IBIC2020-TUPP10

Content from this work may be used under the terms of the CC BY 3.0 licence (© 2020). Any distribution of this work must maintain attribution to the author(s), title of the work, publisher, and DOI

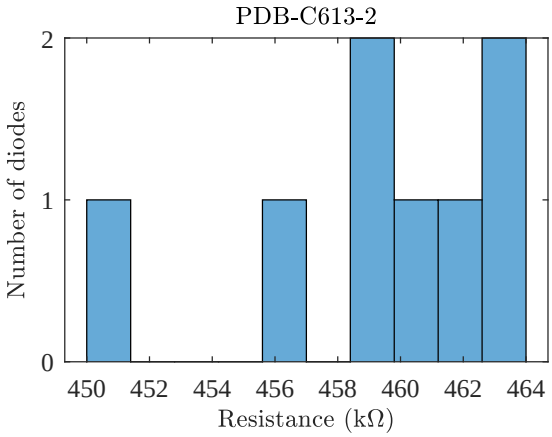

Figure 6: PDB-C613-2 two-wire resistance measurements.

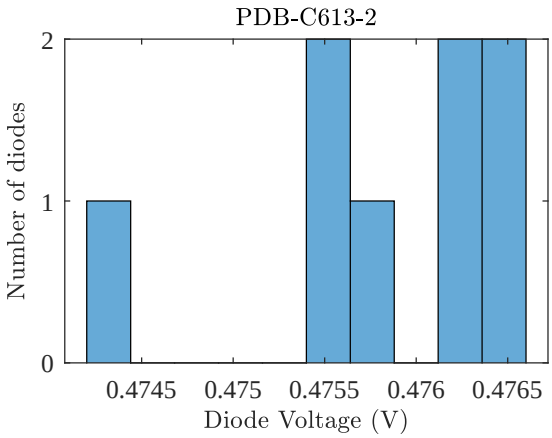

Figure 7: PDB-C613-2 diode measurements.

The photocurrent response of the PDB-C613-2 photodiodes is plotted in Fig. 8.

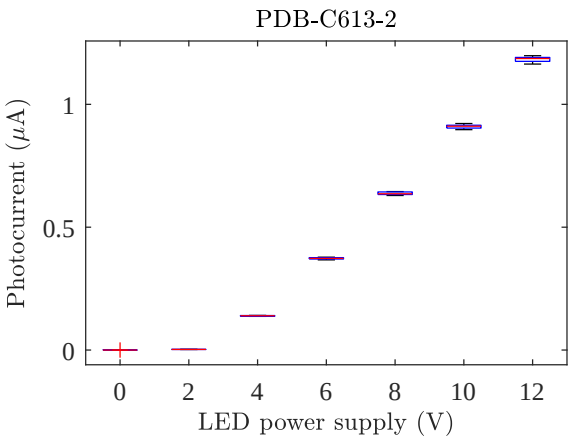

Figure 8: PDB-C613-2 photocurrent measurements.

PDB-V615-2

The measured shunt resistance of the PDB-V615-2 photodiodes is plotted in Fig. 9.

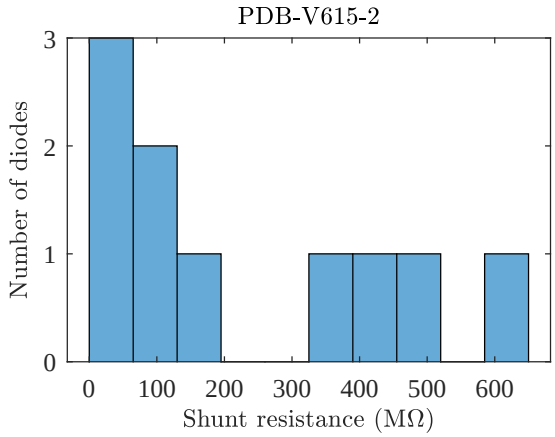

Figure 9: PDB-V615-2 shunt resistance measurements.

The measured two-wire resistance of the PDB-V615-2 photodiodes is plotted in Fig. 10.

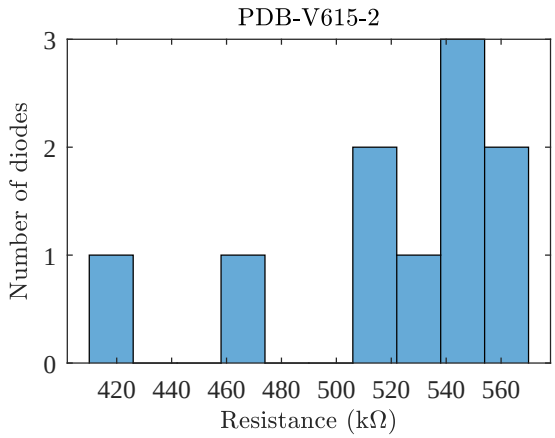

Figure 10: PDB-V615-2 two-wire resistance measurements.

The measured diode test of the PDB-V615-2 photodiodes is plotted in Fig. 11.

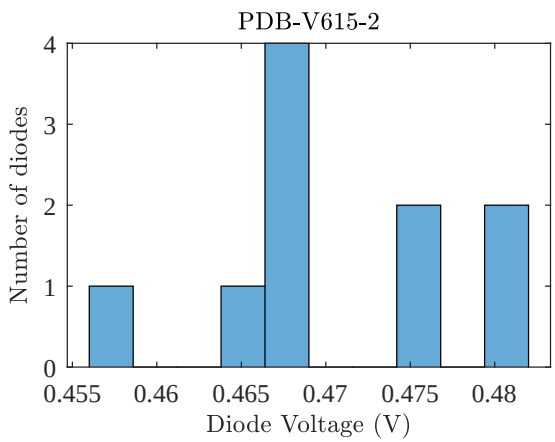

Figure 11: PDB-V615-2 diode measurements.

The photocurrent response of the PDB-V615-2 photodiodes is plotted in Fig. 12.

ISBN: 978-3-95450-222-6 ISSN: 2673-5350 doi:10.18429/JACoW-IBIC2020-TUPP10

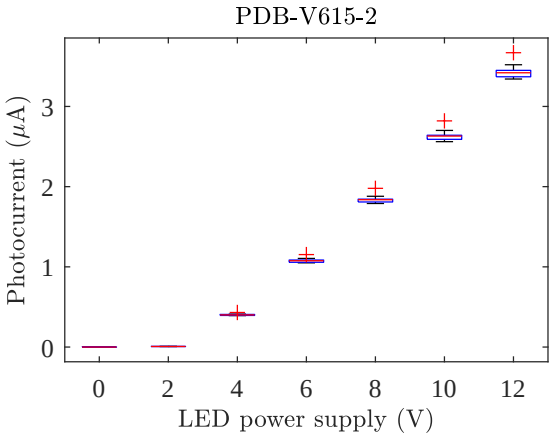

Figure 12: PDB-V615-2 photocurrent measurements.

DISCUSSION

We compared the electrical measurements of various diodes. A summary of the mean and standard deviation of these measurements is given in Table 1. The spread of photocurrent results for each type of photodiode was evaluated for the given condition of 12 V excitation of the illuminating LED.

Table 1: Mean (μ) and Standard Deviation (σ) of Batch Measurements of Photodiodes

Property	**Units**	μ_{C612}	σ_{C612}	$\frac{\sigma_{C612}}{\mu_{C612}}$ (%)
Shunt resistance	MΩ	265	19	7.1
2-wire resistance	kΩ	466	3.1	0.67
Diode voltage	V	0.465	0.001	0.28
Photocurrent	μA	1.29	0.03	2.6
Property	**Units**	μ_{C613}	σ_{C613}	$\frac{\sigma_{C613}}{\mu_{C613}}$ (%)
Shunt resistance	MΩ	186	26	14
2-wire resistance	kΩ	459	4.4	0.96
Diode voltage	V	0.476	0.001	0.16
Photocurrent	μA	1.18	0.01	0.95
Property	**Units**	μ_{V615}	σ_{V615}	$\frac{\sigma_{V615}}{\mu_{V615}}$ (%)
Shunt resistance	MΩ	220	225	100
2-wire resistance	kΩ	520	46	8.8
Diode voltage	V	0.471	0.007	1.6
Photocurrent	μA	3.44	0.10	2.8

We evaluated the statistical distribution of the diode properties using a ratio of the standard deviation over the mean (σ_i/μ_i), where i is the identifier of the photodiode model. For the PDB-V615-2 diode, the ratio (σ_i/μ_i) for the shunt resistance, two-wire resistance and diode voltage is more than an order of magnitude larger than the ratio for the PBD-C612-2 or PDB-C613-2 diodes. The statistical distribution of photocurrents appears similar for all three diode types, at about 1–3%. In future, other diode properties could additionally be measured, such as the dark current at a reverse bias of 5 V.

CONCLUSION

Electronic performance testing of silicon photodiodes for X-ray beam position monitors was presented. For the V615 diode, the statistical spread of shunt resistance, two-wire resistance and diode voltage is more than an order of magnitude larger than the ratio for the C612 or C613 diodes. The statistical distribution of photocurrents appears similar for all three diode types, within 1–3%.

ACKNOWLEDGEMENTS

The submitted manuscript has been created by UChicago Argonne, LLC, Operator of Argonne National Laboratory ("Argonne"). Argonne, a U.S. Department of Energy Office of Science Laboratory, is operated under Contract No. DE-AC02-06CH11357. The U.S. Government retains for itself, and others acting on its behalf, a paid-up nonexclusive, irrevocable worldwide license in said article to reproduce, prepare derivative works, distribute copies to the public, and perform publicly and display publicly, by or on behalf of the Government. The Department of Energy will provide public access to these results of federally sponsored research in accordance with the DOE Public Access Plan.
http://energy.gov/downloads/doe-public-access-plan

REFERENCES

[1] T. E. Fornek, "Advanced Photon Source Upgrade Project Final Design Report", Argonne National Laboratory, Lemont, IL, USA, Rep. APSU-2.01-RPT-003, May 2019. doi:10.2172/1543138

[2] G. Decker, B. X. Yang, R. M. Lill, and H. Bui, "APS Beam Stability Studies at the 100-Nanoradian Level", in *Proc. 14th Beam Instrumentation Workshop (BIW'10)*, Santa Fe, NM, USA, May 2010, paper TUCNB02, pp. 74–78.

[3] R. M. Lill, N. Sereno, and B. X. Yang, "BPM Stabiltiy Studies for the APS MBA Upgrade", in *Proc. 5th Int. Beam Instrumentation Conf. (IBIC'16)*, Barcelona, Spain, Sep. 2016, pp. 55–58. doi:10.18429/JACoW-IBIC2016-MOPG10

[4] N. S. Sereno *et al.*, "Beam Diagnostics for the APS MBA Upgrade", in *Proc. 9th Int. Particle Accelerator Conf. (IPAC'18)*, Vancouver, Canada, Apr.-May 2018, pp. 1204–1207. doi:10.18429/JACoW-IPAC2018-TUZGBD3

[5] B. X. Yang, G. Decker, P. K. Den Hartog, and S.-H. Lee, "High-Power Hard X-ray Beam Position Monitor Development at the APS", in *Proc. 14th Beam Instrumentation Workshop (BIW'10)*, Santa Fe, NM, USA, May 2010, paper TUPSM043, pp. 233–237.

[6] B. X. Yang, G. Decker, P. K. Den Hartog, S.-H. Lee, and K. W. Schlax, "Progress in the Development of a Grazing-incidence Insertion Device X-ray Beam Position Monitor", in *Proc. 24th Particle Accelerator Conf. (PAC'11)*, New York, NY, USA, Mar.-Apr. 2011, paper MOP189, pp. 441–443.

[7] B. X. Yang *et al.*, "High-Power Beam Test of the APS Grazing-Incidence Insertion Device X-ray Beam Position Monitor", in *Proc. 15th Beam Instrumentation Workshop (BIW'12)*, Newport News, VA, USA, Apr. 2012, paper WECP01, pp. 235–237.

Content from this work may be used under the terms of the CC BY 3.0 licence (© 2020). Any distribution of this work must maintain attribution to the author(s), title of the work, publisher, and DOI

ISBN: 978-3-95450-222-6 ISSN: 2673-5350 doi:10.18429/JACoW-IBIC2020-TUPP10

Content from this work may be used under the terms of the CC BY 3.0 licence (© 2020). Any distribution of this work must maintain attribution to the author(s), title of the work, publisher, and DOI

[8] B. X. Yang *et al.*, "Advanced X-ray Beam Position Monitor System Design at the APS", in *Proc. North American Particle Accelerator Conf. (NAPAC'13)*, Pasadena, CA, USA, Sep.-Oct. 2013, paper WEPSM14, pp. 1079–1081.

[9] B. X. Yang *et al.*, "Design and Development for the Next Generation X-ray Beam Position Monitor System at the APS", in *Proc. 6th Int. Particle Accelerator Conf. (IPAC'15)*, Richmond, VA, USA, May 2015, pp. 1175–1177. doi:10.18429/JACoW-IPAC2015-MOPWI014

[10] B. X. Yang *et al.*, "Performance Test of the Next Generation X-Ray Beam Position Monitor System for the APS Upgrade", in *Proc. 5th Int. Beam Instrumentation Conf. (IBIC'16)*, Barcelona, Spain, Sep. 2016, pp. 78–81. doi:10.18429/JACoW-IBIC2016-MOPG17

[11] B. X. Yang, "State of the Art X-Ray Photon BPMs for Next Generation Storage Ring Light Sources", presented at North American Particle Accelerator Conf. (NAPAC'16), Chicago, IL, USA, Oct. 2016, paper FRA1IO02, unpublished.

[12] P. C. Thompson and T. C. Larason, "Method of Measuring Shunt Resistance in Photodiodes", in *Proc. Measurement Sci. Conf. 2001*, Anaheim, CA, USA, 2001.

[13] T. R. Kupholdt, "Lessons in Electric Circuits, Volume III – Semiconductors," 5th Ed., 2009. http://www.ibiblio.org/kuphaldt/electricCircuits/

[14] *Keysight Truevolt Series Digital Multimeters Operating and Service Guide (Part Number: 34460-90901)*, Keysight Technologies, Inc., Loveland, CO, USA, Version 7, Mar. 2020, p. 166.

ISBN: 978-3-95450-222-6 ISSN: 2673-5350 doi:10.18429/JACoW-IBIC2020-TUPP12

AUTOMATED MANAGEMENT OF LIBERA SPARK MODULE IOCs IN SPEAR3*

F. Toufexis†, S. Condamoor, D. A. Morataya Campos, C. S. Ramirez, J. J. Sebek, C. Wermelskirchen, J. Corbett, SLAC, Menlo Park, CA 94025, USA
P. Leban, M. Znidarcic, Instrumentation Technologies, Solkan, Slovenia

Abstract

We are actively upgrading BPM processors in the SPEAR3 accelerator complex as several of the existing systems are reaching end-of-life. To consolidate the resources required for development and maintenance we have evaluated and installed several processors from the Libera SPARK hardware series. We found that two common deployment methods typically used with these modules, micro-SD card and network boot, are either hard to maintain or lack flexibility. Instead we have developed an automated method based on a network boot scheme where an external EPICS soft IOC manages the assignment of specific SPARK modules to physical BPMs in the accelerator. Each module queries the soft IOC at boot time to determine which BPM it is assigned to and then starts its IOC with the appropriate BPM prefix for the PV names. This deployment method allows for quick, seamless swapping of SPARK modules by machine operators or physicists. It addition, it allows us to bring additional modules online for testing, or to move modules to different locations with a different PV prefix for the new location. This method is applicable to other EPICS-enabled devices where the device hardware also hosts an IOC.

INTRODUCTION

SPEAR3 is a 3 GeV, 500 mA, 3rd generation synchrotron light source, commissioned in 2004 [1]. It operates with beam current distributed in four bunch trains and a single isolated timing bunch for pump-probe experiments. Top-up occurs at 5-minute intervals. Each top-up event requires about 50 single-bunch charge pulses into targeted SPEAR3 buckets at a 10 Hz rate. The SPEAR3 storage ring contains 18 lattice cells each with 6 button-style Beam Position Monitors (BPMs). Three BPMs per cell are connected to Bergoz processors for fast orbit control and beam inter-lock purposes. Several more BPMs are connected to the Echotek processors [2] to provide Turn-by-Turn (TbT) orbit information at discrete locations. The Echotek processors were developed in-house and produced commercially when SPEAR3 was commissioned; they are used for accelerator physics programs and not for operations. The Echotek have reached their and of life and we have evaluated commercial alternatives for replacement. A Libera Brilliance+ was first tested in SPEAR3 in 2017 [3]. Since TbT studies for accelerator physics programs do not require the long-term stability capability of the Brilliance+, and additionally the fast orbit feedback is implemented in the Bergoz BPM system, a SPARK-ERXR processor [4] was purchased and installed for accelerator physics applications. Additionally we are in the process of installing and testing Beam Loss Monitors (BLMs) for Libera that have the same base hardware and software infrastructure as the SPARKs.

The SPEAR3 injector was commissioned in 1990 [5], and includes the 120 MeV linac injector with a thermionic RF gun [6], the booster synchrotron [7] and the Transport Lines. The entire injector, including the Transport Lines, is equipped with stripline-style BPMs. The original booster synchrotron BPM electronics used a commercial multiplexer to switch between several BPM signals into an in-house built analog BPM processor [8]. In the Linac-To-Booster (LTB) and Booster-To-SPEAR (BTS) Transport Lines 1990's-era Bergoz BPM processors have provided reliable shot-by-shot single-pass data at 10 Hz with limited resolution [8]. As an upgrade to the original Transport Line BPM processors, two smaller-diameter stripline BPMs connected to two SLAC-built uTCA-based BPM processors replaced the last two BPMs at the end of the BTS in 2015 (BTS BPMs 8 and 9). This system has proven hard to maintain and we have evaluated single-pass SPARK-EL processors as a replacement. The units were tested in the BTS and LTB Transport Lines demonstrating comparable position resolution to the uTCA processors at the small-diameter striplines, as well as substantially improved resolution at the large-diameter striplines.

Since these BPM processors, as well as the BLMs, have the same base hardware and software, we wanted a unified architecture of deploying and managing these modules. We aim for an architecture that allows for easy swaps in the event of a module failure, but additionally gives us the flexibility to bring modules online for testing or to relocate modules and change the EPICS Process Variable (PV) prefix they publish appropriately. All these requirements come down to having the ability to dynamically change the EPICS PV prefixes. We perform this through an external EPICS soft Input/Output Controller (IOC) that manages the information for the prefixes and settings. Each module runs a shell script that acquires all this information and starts its IOC with the appropriate prefix and settings. This work is organized as follows: we begin by explaining our considerations for choosing this deployment architecture and then give a high-level description of our solution. Subsequently we describe the infrastructure that is needed to implement this architecture and the details of how a module boots and acquires its PV prefixes. Finally, in the appendix we show certain important code snippets.

* Work sponsored by US Department of Energy Contract DE-AC02-76SF00515.
† ftouf@slac.stanford.edu

Content from this work may be used under the terms of the CC BY 3.0 licence (© 2020). Any distribution of this work must maintain attribution to the author(s), title of the work, publisher, and DOI

ISBN: 978-3-95450-222-6 ISSN: 2673-5350 doi:10.18429/JACoW-IBIC2020-TUPP12

Content from this work may be used under the terms of the CC BY 3.0 licence (© 2020). Any distribution of this work must maintain attribution to the author(s), title of the work, publisher, and DOI

CONSIDERATIONS FOR DEPLOYMENT

SPEAR3 operates with a very small accelerator team; typically only one person is an expert on any given system, with a second person having some knowledge about it. As a result in deploying new electronics systems we are aiming for architectures that if a module fails, an operator can swap the failed module with a spare with only minimal guidance.

When a SPARK BPM processor boots up, it requires the following information in order to operate inside the control system: the PV prefixes that identify the physical BPM it is assigned to and settings that are specific to that BPM (e.g. gains and offsets). There are two straightforward approaches in deploying the SPARKs: using the micro-SD (uSD) card or perform a network boot.

Using the uSD card involves hard-coding the PV prefixes and settings in the card. Note that the uSD card can itself become corrupted. Therefore for each physical BPM we need to maintain two uSD cards. The cards themselves are small and labeling them is very hard, thus making management difficult. In addition, it is time consuming to upgrade the firmware in the event of a software update from Libera; we would need to update all the uSD cards including the spares. Alternatively we could have one uSD card template where someone would have to clone during a module swap and change the settings. Most operators, however, do not have the skills to perform this task. Additionally in the BTS the different BPMs are physically different and need different configuration, thus increasing the chances of an error during a module swap.

The alternative to the uSD card is a network boot. In this case a linux boot image is stored in the Trivial File Transfer Protocol (TFTP) server and is supplied to the module during boot time. The IOC files are stored in the Network File System (NFS) server. The Dynamic Host Configuration Protocol (DHCP) server assigns a hostname based on the Media Access Control (MAC) address that is linked to the physical BPM the specific module is connected to, i.e. `BTS-BPM08`. This allows for easy firmware upgrade as all the files are located in a central server; all that is required to happen is update them and reboot the modules. However, in the event of a module swap the Network Group needs to update the entry in the DHCP server with the MAC address of the spare module and restart the DHCP server that could cause other issues in the network. To handle restoring the settings for a physical BPM, either EPICS `autosave` or simply a MATLAB script could be used.

SOLUTION OVERVIEW

To solve the aforementioned issues, we developed a new deployment architecture based on the network boot with the addition of a database that manages assignment of BPM processors to physical BPMs. In our architecture the network hostnames for the SPARK modules are based simply on the module model and some identification number, i.e. `spark-el-04`; the hostname has no connection to a physical BPM. The mapping of a BPM processor to a physical BPM is handled by a soft IOC that resides in central server and an Extensible Display Manager (EDM) panel is used to enter the settings. For example this soft IOC will maintain the information that module `spark-el-04` is connected to `BTS-BPM08`. When module `spark-el-04` boots up, before starting the IOC, it will query the soft IOC "which BPM am I assigned?" based on its hostname. The result of this query will be `BTS-BPM08` and the module will start the BPM IOC with `BTS-BPM08` as the prefix for its PVs.

In the event of a module failure the following steps need to be taken to recover:

1. The Operator assigns one of the spare BPM processors to the physical BPM the failed module was connected to in the soft IOC EDM panel.

2. The Operator physically swaps the modules and powers up the new module.

3. The Network Group updates a repaired module information in DHCP during normal business hours when convenient.

An advantage of this approach is that we can bring spare modules online in the control system to test them without affecting operations, i.e conflicting PV names. Additionally we can move modules around. This is important as in SPEAR we only plan to have a few SPARK TbT processors and want to be able to move them to different BPMs as needed. The same would apply to BLMs.

INFRASTRUCTURE

Figure 1 summarizes the infrastructure required for this deployment scheme: On the network side a number of services are needed: A TFTP server is used to supply the boot image to the SPARK modules when they are powered on. DHCP is used to assign IP addresses and hostnames to the modules. Each module's MAC address (including spares) needs to be entered to the DHCP server database along with a specific hostname for that MAC address. The DHCP server additionally points the module to the TFTP server to download the boot image and the NFS server for file storage. The NFS server is used to supply a file system that the module mounts. The SPARK IOC files reside in the NFS space. Additionally we create directories for each SPARK module and for each physical BPM. The module mounts these directories once it has its hostname and BPM assignment, and uses them for log or temporary files.

A soft IOC is needed to hold the mapping between each SPARK module and the physical BPM it is assigned. This soft IOC resides in one of our servers. For each SPARK module we create a PV; the hostname is part of that PV name, while the PV value is the physical BPM assignment. The PV value can additionally be `UNASSIGNED` to denote that the module is not connected to a BPM, or `TEST` in the case we want to bring a module online for testing. In our case for the Transport Lines we use two PVs: one for the Transport Line, `LTB` or `BTS`, and a second for the

ISBN: 978-3-95450-222-6 ISSN: 2673-5350 doi:10.18429/JACoW-IBIC2020-TUPP12

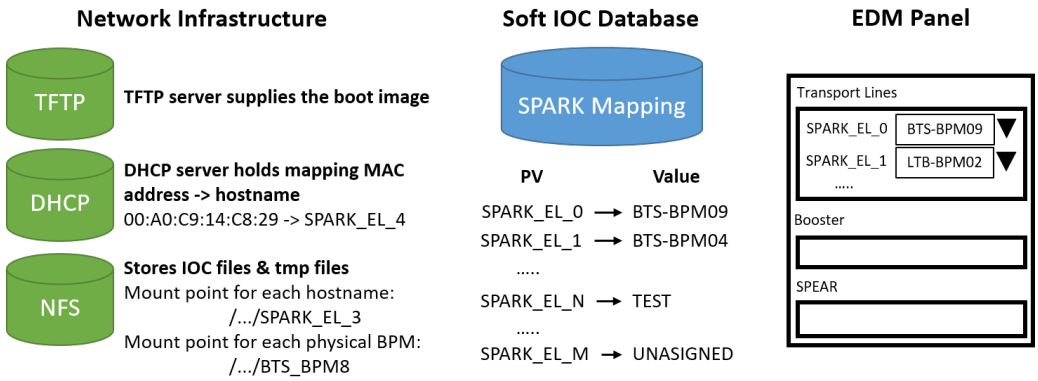

Figure 1: Overview of the Infrastructure needed to perform Network Boot with a Hostname/PV prefix Soft IOC database.

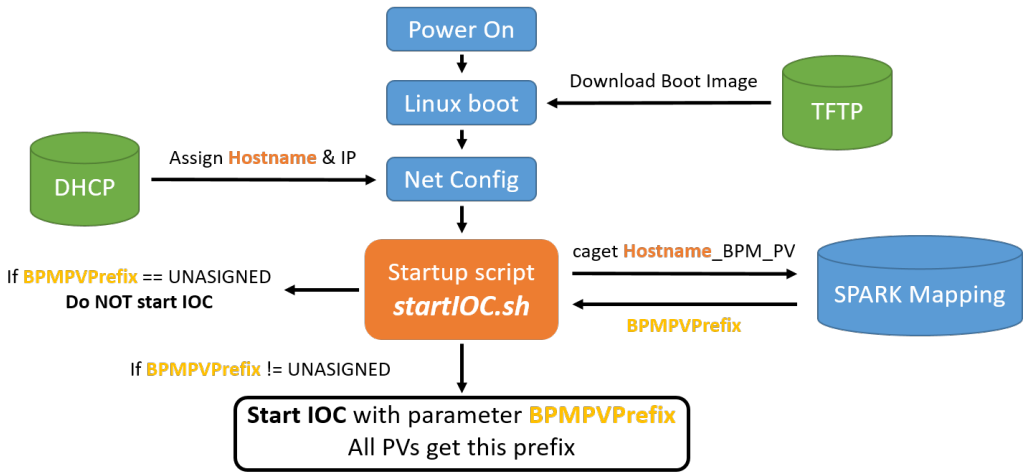

Figure 2: Simplified boot sequence of a SPARK module.

BPM number within the Transport Line, i.e. `BPM08`. In our implementation these two PVs for module with hostname `$UNITNAME` are `SPARKMngr:$UNITNAME:BPM:TL` and `SPARKMngr:$UNITNAME:BPM:BPM`. The options for `SPARKMngr:$UNITNAME:BPM:TL` are `LTB`, `BTS`, `TEST`, and `UNASSIGNED`, while for `SPARKMngr:$UNITNAME:BPM:BPMN` the options are `BPM01` through `BPM09`. At boot time a script in the module will querry these two PVs and determine the BPM prefix, i.e. `SPARK-BTS-BTS08`. We further use this soft IOC to hold the settings for each BPM, such as gains and offsets. We do this with another set of PVs per BPM, i.e. `SPARKMngr:SPARK-BTS-BTS08:Kx`.

Finally a set of EDM panels are needed as an interface to this system. One EDM panel shows the list of SPARK modules and for each module the assignment of Transport Line and BPM number within that Transport Line, and similarly for the Booster and SPEAR3. Another EDM panel holds the settings for each physical BPM.

MODULE BOOT SEQUENCE

Figure 2 illustrates the boot sequence of each SPARK module. When the unit powers on it announces itself to the network and TFTP supplies the linux Boot Image. Then linux starts running and it gets from DCHP the hostname and IP based on its MAC address.

Eventually the `startIOC.sh` scripts executes. We have modified this script from what was supplied from Libera to perform the following steps:

1. Query PVs on the soft IOC based on its hostname and calculate the PV prefix for the module's IOC.

2. Perform a series of checks that this PV prefix is valid in the accelerator, and additionally that there is no other IOC on the network running with it. This PV prefix is written in a temporary file read by the `st.cmd`.

3. Query PVs on the soft IOC based on the PV prefix to obtain the settings for the physical BPM, i.e. gains and offsets. These settings are written in another temporary file as EPICS `dbpf` commands read by the `st.cmd` after the `iocInit()`.

4. Start the IOC with `procServ` and a modified `st.cmd` to read the PV prefix and settings.

Content from this work may be used under the terms of the CC BY 3.0 licence (© 2020). Any distribution of this work must maintain attribution to the author(s), title of the work, publisher, and DOI

ISBN: 978-3-95450-222-6 ISSN: 2673-5350 doi:10.18429/JACoW-IBIC2020-TUPP12

Content from this work may be used under the terms of the CC BY 3.0 licence (© 2020). Any distribution of this work must maintain attribution to the author(s), title of the work, publisher, and DOI

SUMMARY

We have presented an automated method for deploying Libera SPARK modules other EPICS-enabled devices where the device hardware also hosts an IOC. This method is based on a network boot scheme where an external EPICS soft IOC manages the assignment of specific SPARK modules to physical BPMs in the accelerator. Each module queries the soft IOC at boot time to determine which BPM it is assigned to and then starts its IOC with the appropriate BPM prefix for the PV names. This deployment method allows for quick, seamless swapping of SPARK modules by machine operators or physicists. It addition, it allows us to bring additional modules online for testing, or to move modules to different locations with a different PV prefix for the new location. Most importantly though, since a script automates the process and performs various checks for errors, this method minimizes the chances of making a mistake when bringing a module online, whether that is using different settings or having the same PV prefix as an already running IOC.

ACKNOWLEDGMENTS

The authors would like to thank the SPEAR3 operations staff, Scott Wallters, and Kevin Helms for technical assistance.

APPENDIX

Here we show some code snippets from the `startIOC.sh` script for the Transport Lines. To assemble the PV prefix for the Transport Lines we have two PVs, one to assign the Transport Line (`LTB`, `BTS`, `TEST`, `UNASSIGNED`), and one for the BPM number within the Transport Line. We start by getting the hostname:

```
UNITNAME=`hostname`
```

This will return `spark-el-01`. Then we query the PV `SPARKMngr:spark-el-01:BPM:TL` in the soft IOC to get the Transport Line assignment and write the result to a temporary file:

```
exec $CAGET -t SPARKMngr:$UNITNAME:
    BPM:TL |& tee $IOC_CONFIG/
    transportLineName
```

We need to check that `caget` did indeed return the value of the PV by measuring the number of words in the temporary file; if there is only one word then that word is the value we asked, otherwise the soft IOC was not accessible and the script should exit without starting the IOC:

```
cat $IOC_CONFIG/transportLineName |
    wc -w > $IOC_CONFIG/
    transportLineNameWC

if [ ! "$(head -n 1 $IOC_CONFIG/
    transportLineNameWC)" -eq 1 ]
then
        echo "SPARKManager soft IOC
            not accessible" |& tee -a
            $STARTUP_ERROR
        exit 1
fi
```

Assuming no error we get the Transport Line assignment:

```
TRANSPORTLINE="$(head -n 1
    $IOC_CONFIG/transportLineName)"
```

that is `BTS`. We use the same procedure and query another PV to get the BPM number within that Transport Line:

```
BPMNUMBER="$(head -n 1 $IOC_CONFIG/
    bpmName)"
```

that is `BPM08`. We can now calculate the PV Prefix:

```
BPM_PREFIX="SPARK-$TRANSPORTLINE-
    $BPMNUMBER"
```

that is `SPARK-BTS-BPM08`. Now we need to perform a series of checks to ensure this PV prefix is valid; for example there is no `BPM08` in our `LTB`:

```
if [ "$BPM_PREFIX" == "SPARK-LTB-
    BPM08" ]
then
        CAPUT_EXIT_STATUS=$(exec
            $CAPUT -t SPARKMngr:
            $UNITNAME:STATUS.VAL "
            Error: SPARK-LTB-BPM08
            doesn't exist")
        exit 1
fi
```

If there is an error at this point we log it to a status PV. Assuming the PV prefix is valid we need to check that no other IOC already started on the network with this BPM prefix by checking a PV that the SPARK should publish:

```
exec $CAGET -t $BPM_PREFIX:input:
    max_adc |& tee -a $IOC_CONFIG/
    iocAlreadyRunning
```

If `caget` returns more that one word, then then IOC was not accessible, therefore not running.

To handle the settings for a particular physical BPM we use the same procedure: the soft IOC has a number of settings PVs for each physical BPM. The `startIOC.sh` continues to query the values of these PVs and writes a set of EPICs `dbpf` commands in an temporary file that will be loaded in the `st.cmd` after the `iocInit()` command:

```
echo "dbpf(\"$BPM_PREFIX:dsp:
    pickup_orientation_sp\",\"
    $PICKUPORIENTATION\")" >
/tmp/BPMSettings.env
```

Once all these steps have occurred successfully the `startIOC.sh` starts the module's IOC using `procServ`.

ISBN: 978-3-95450-222-6 ISSN: 2673-5350 doi:10.18429/JACoW-IBIC2020-TUPP12

REFERENCES

[1] "SPEAR 3 Design Report," SLAC, CA, USA, Tech. Rep. SLAC-R–609, Dec. 2002.

[2] J. J. Sebek, D. J. Martin, T. Straumann, and J. V. Wachter, "Design and performance of SSRL beam position electronics", in *Proc. 14th Beam Instrumentation Workshop (BIW'10)*, Santa Fe, NM, USA, May 2010, paper TUPSM029, pp. 182–186.

[3] S. Condamoor *et al.*, "Machine studies with Libera instruments at the SLAC SPEAR3 accelerators," in *Proc. 7th Int. Beam Instrumentation Conf. (IBIC'18)*, Shanghai, China, Sep. 2018, pp. 284–288.

[4] P. Leban, "Libera SPARK-ERXR User Manual," Tech. Rep., 2017.

[5] S. Baird and J. Safranek, "Commissioning the SSRL injector," in *Proc. 1991 IEEE Particle Accelerator Conf. (IPAC'91)*, San Francisco, CA, USA, May 1991, vol. 5, pp. 2865–2867.

[6] M. Borland, "A High Brightness Thermionic Microwave Electron Gun," Ph.D. dissertation, Stanford University, CA, USA, Feb. 1991.

[7] H. Wiedemann *et al.*, "The 3 GeV synchrotron injector for SPEAR", in *Proc. 1991 IEEE Particle Accelerator Conf. (IPAC'91)*, San Francisco, CA, USA, May 1991, vol. 5, pp. 2688–2690.

[8] W. Lavender *et al.*, "The SSRL injector beam position monitoring systems," in *Proc. 1991 IEEE Particle Accelerator Conf. (IPAC'91)*, San Francisco, CA, USA, May 1991, vol. 2, pp. 1151–1153.

Content from this work may be used under the terms of the CC BY 3.0 licence (© 2020). Any distribution of this work must maintain attribution to the author(s), title of the work, publisher, and DOI

ISBN: 978-3-95450-222-6 ISSN: 2673-5350 doi:10.18429/JACoW-IBIC2020-TUPP17

Content from this work may be used under the terms of the CC BY 3.0 licence (© 2020). Any distribution of this work must maintain attribution to the author(s), title of the work, publisher, and DOI

DIRECT OBSERVATIONS OF SUBMICROPULSE ELECTRON-BEAM EFFECTS FROM SHORT-RANGE WAKEFIELDS IN TESLA-TYPE SUPERCONDUCTING RF CAVITIES *

A. H. Lumpkin†, R. M. Thurman-Keup, D. R. Edstrom Jr., P. Prieto, J. Ruan,
Fermi National Accelerator Laboratory, Batavia, IL, USA
B. T. Jacobson, A. L. Edelen, J. A. Diaz-Cruz, F. Zhou,
SLAC National Accelerator Laboratory, Menlo Park, CA, USA

Abstract

Experiments were performed at The Fermilab Accelerator Science and Technology (FAST) facility to elucidate the effects of short-range wakefields (SRWs) in TESLA-type rf cavities. FAST has a unique configuration of a photocathode rf gun beam injecting two TESLA-type single cavities (CC1 and CC2) in series prior to the cryomodule. To investigate short-range wakefield effects, we have steered the beam to minimize the signals in the higher-order mode (HOM) detectors of CC1 and CC2 for a baseline, and then used a vertical corrector between the two cavities to steer the beam off axis at an angle into CC2. A Hamamatsu synchroscan streak camera viewing a downstream OTR screen provided an image of y-t effects within the micropulses with ~10-micron spatial resolution and 2-ps temporal resolution. At 500 pC/b, 50 b, and 4 mrad off-axis steering into CC2, we observed an ~100-micron head-tail centroid shift in the streak camera image y(t)-profiles. This centroid shift value is 5 times larger than the observed HOM-driven centroid oscillation within the macropulse, and it is consistent with a calculated short-range wakefield effect using ASTRA simulations.

SUBMISSION OF PAPERS

The preservation of the low emittance of electron beams during transport through the accelerating structures of large facilities is an ongoing challenge. In the cases of the TESLA-type superconducting rf cavities currently used in the European X-ray Free-electron Laser (FEL) [1] and the currently-under-construction Linac Coherent Light Source upgrade (LCLS-II XFEL) [2], off-axis beam transport may result in emittance dilution due to transverse long-range (LRW) and short-range wakefields (SRW) [3-5]. To investigate such effects, experiments were performed at the Fermilab Accelerator Science and Technology (FAST) facility with its unique two-cavity configuration after the photocathode rf gun [6]. We used optical transition radiation (OTR) imaging with a UV-visible synchroscan streak camera to display sub-micropulse y-t effects in the 41-MeV beam.

We report effects on beam transverse position centroids and sizes correlated with off-axis beam steering in TESLA-type cavities. We used a 3-MHz micropulse repetition rate and targeted diagnostics for these tests. Our initial data from an OTR imaging source indicated our streak camera can provide ~10-micron spatial resolution with 1-2 ps (σ) temporal resolution depending on the bandpass filter employed. Since the observed bunch lengths were 10-20 ps (σ), we had sufficient resolution for up to 20 time slices in the 4σ profile. In this sense we also obtained slice-emittance information (with β-function information). We used the higher-order mode (HOM) detectors and rf BPMs to establish first the desired off-axis steering and then evaluated the short-range wakefield effects on the beam dynamics.

EXPERIMENTAL ASPECTS

The IOTA Electron Injector Linac

The Integrable Optics Test Accelerator (IOTA) electron injector at the FAST facility (Fig. 1) begins with an L-band rf photoinjector gun built around a Cs2Te photocathode (PC). When the UV component of the drive laser, described elsewhere [7] is incident on the PC, the resulting electron bunch train with 3-MHz micropulse repetition rate exits the gun at <5 MeV. Following a short transport section with a pair of trim dipole magnet packages (H/V100 and H/V101), the beam passes through two superconducting rf (SCRF) capture cavities denoted CC1 and CC2, and then a transport section to the low-energy electron spectrometer, D122. Diagnostics used in these studies include the rf BPMs, the imaging screens at X107, X108, X121, and X124, and HOM couplers at the upstream and downstream ends of each SCRF cavity. The HOM signals were processed by the HOM detector circuits with the Schottky diode output provided online though ACNET, the Fermilab accelerator controls network [4]. The HOM detectors' bandpass filters were optimized for two dipole passbands from 1.6 to 1.9 GHz, and the 1.3-GHz fundamental was reduced with a notch filter. The rf BPMs' electronics were configured for bunch-by-bunch capability with optimized system attenuation. At 2 nC per micropulse, the rms noise was found to be 25 μm in the horizontal axis (x) and 15 μm in the vertical axis (y) at B101 in the test with 4.5-MeV beam from the gun. However, for these studies on short-range transverse wakefields, we relied on a streak camera to provide the sub-micropulse spatial information.

* This manuscript has been authored by Fermi Research Alliance, LLC under Contract No. DE-AC02-07CH11359 with the U.S. Department of Energy, Office of Science, Office of High Energy Physics.
† lumpkin@fnal.gov

ISBN: 978-3-95450-222-6 ISSN: 2673-5350 doi:10.18429/JACoW-IBIC2020-TUPP17

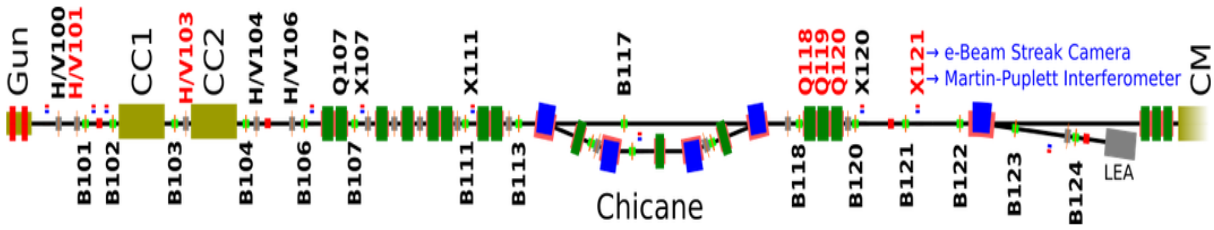

Figure 1: Schematic of the FAST beamline layout showing the PC rf gun, capture cavities (CCn), correctors (H/Vnnn), rf BPMs (Bnnn), chicane, OTR and YAG:Ce screens (Xnnn), the spectrometer dipole bend magnet (D122), and the beginning of the cryomodule (CM).

The Streak Camera System

We utilized a C5680 Hamamatsu streak camera with an S20 PC operating with the M5675 synchroscan vertical deflection unit that was phase locked to 81.25 MHz as shown in Fig. 2. In addition, we used a phase-locked-loop C6878 delay box that stabilizes the streak image positions to about 1 ps temporal jitter over 10s of minutes. These steps enabled the synchronous summing of 50-150 micropulses or bunches (b) generated at 3 MHz by the photoinjector or the offline summing of 10-100 images to improve statistics in the sum images. We applied the principle to optical transition radiation (OTR) generated from an Al-coated Sisubstrate at the X121 screen location (see Fig. 1) with subsequent transport to the beamline streak camera. Commissioning of the streak camera system was facilitated through a suite of controls centered around ACNET. This suite includes operational drivers to control and monitor the streak camera as well as Synoptic displays to facilitate interface with the driver. Images were captured from the streak camera using the readout camera, Prosilica 1.3-Mpixel cameras with 2/3" format, and were analyzed both online and with an offline MATLAB-based ImageTool processing program [8]. Bunch-length measurements using these techniques have been reported previously from the A0 Facility [9] and FAST first system streak camera commissioning at 20 MeV [10].

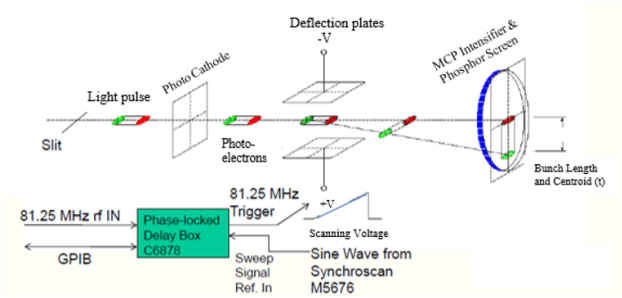

Figure 2: Schematic of the C5680 synchroscan streak camera with phase locking at 81.25 MHz.

EXPERIMENTAL RESULTS

Initial Streak Camera Data

In order to investigate the short-range, wakefield-driven submicropulse effects, we used the HOM detector signals as a measure of how far off axis the beam was in the cavities. We minimized the HOMs in CC1 and CC2 as the reference point, and then stepped the V103 corrector magnet current values. For the 24-MeV post-CC1 beam energy, a change of 1 A in corrector current corresponded to a 2-mrad angular steering change into CC2. The transport optics rotated the image 90° so we observed the vertical spatial information on the horizontal display axis in the streak image from X121. The changes in projected vertical beam profile size are shown in Fig. 3a. Beam size dilution is clearly seen at 650 μm compared to the 400-μm cases. In Fig. 3b, the head-tail kick directions follow the corrector steering polarity as expected. These

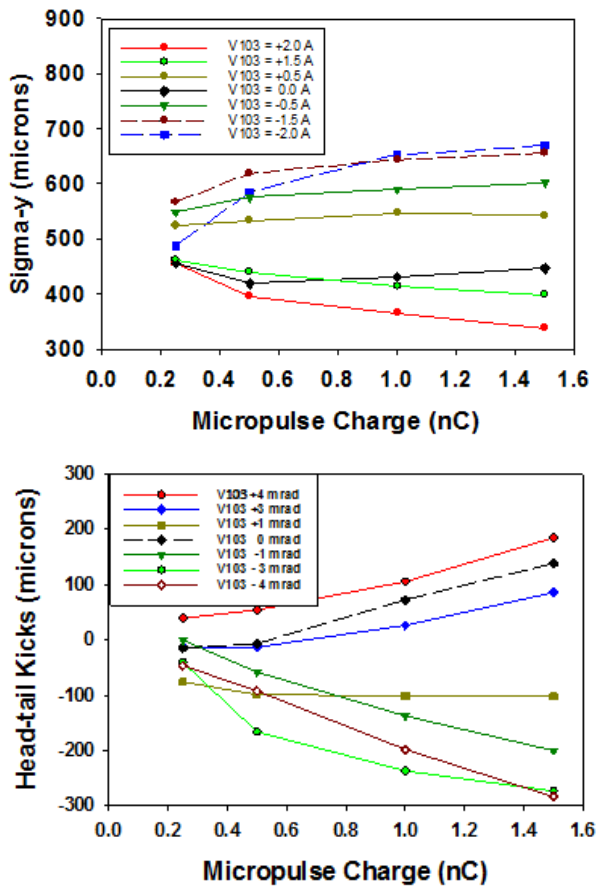

Figure 3: (a) Projected vertical beam profiles for X121 streak camera images versus charge at various V103 corrector values. (b) Observed head-tail centroid kicks for the same images as a function of charge and V103 corrector values. A 1-A corrector current change corresponds to a 2-mrad angular steering change into CC2.

Content from this work may be used under the terms of the CC BY 3.0 licence (© 2020). Any distribution of this work must maintain attribution to the author(s), title of the work, publisher, and DOI

ISBN: 978-3-95450-222-6 ISSN: 2673-5350 doi:10.18429/JACoW-IBIC2020-TUPP17

Content from this work may be used under the terms of the CC BY 3.0 licence (© 2020). Any distribution of this work must maintain attribution to the author(s), title of the work, publisher, and DOI

data exhibit the direction the beam is off axis while the HOMs with the electronics used indicate only the offset magnitude. These combined effects may be used in a future machine learning training application to mitigate emittance dilution effects.

Space-Charge-Driven Bunch Elongation Effects

The streak images when projected to the time axis provide the electron bunch profile and length. With an initial laser pulse length of 4 ps, we observed the significant electron bunch elongation due to space-charge forces as seen in Fig. 4. In this case the laser spot size was ~ 0.45 mm by 0.56 mm so at 250 pC/b and above the space-charge forces dominated the distributions.

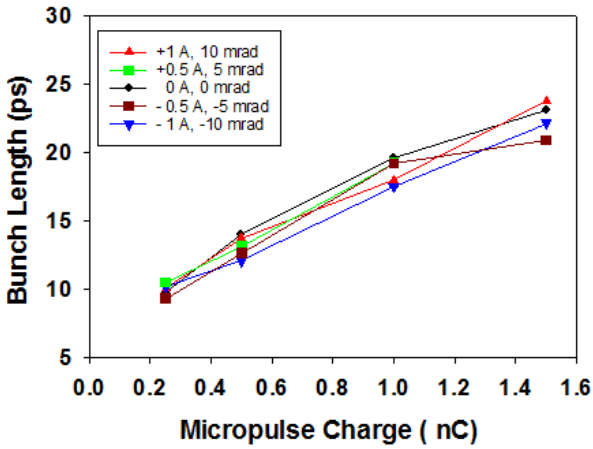

Figure 4: Streak camera bunch length versus charge results during the V101 corrector scan from -1.0- to +1.0-A values. At 4.5 MeV, a 1-A current change corresponds to a 10-mrad angular change into CC1. The transverse laser spot is ~ 0.5 mm in x and y in this case.

Bunch by Bunch RF BPM Data

We also evaluated the potential long-range wakefield or HOM effects on the beam centroid by using the rf BPM data. An example of the centroid motion *within* the 50- micropulse train of a macropulse is shown in Fig. 5 with both noise-reduction and bunch-by-bunch capabilities implemented. The 100-kHz oscillation seen in the B117 data is a difference frequency between HOM mode 14 in CC2 and a beam harmonic [4]. The field oscillations kicked different micropulses according to the amplitude at that point in time, resulting in the submacropulse effects. The quadrupole triplet Q118-120 was used to focus the beam smaller horizontally while leaving the vertical size at ~ 800 µm at the X121 YAG:Ce station. The beam centroid oscillation amplitude is much reduced to <20 µm at B121 downstream of this triplet, and thus the main competing mechanism identified does not account for the observed y-t effect in the streak image. Since the ASTRA simulation for the FAST setup indicated a 400-µm head-tail kick for 500 pC/b and a 5-mm offset at 41 MeV, we attribute the 100-µm head-tail effects for a 2-3 mm offset seen in Fig. 3 to such short-range wakefields [11].

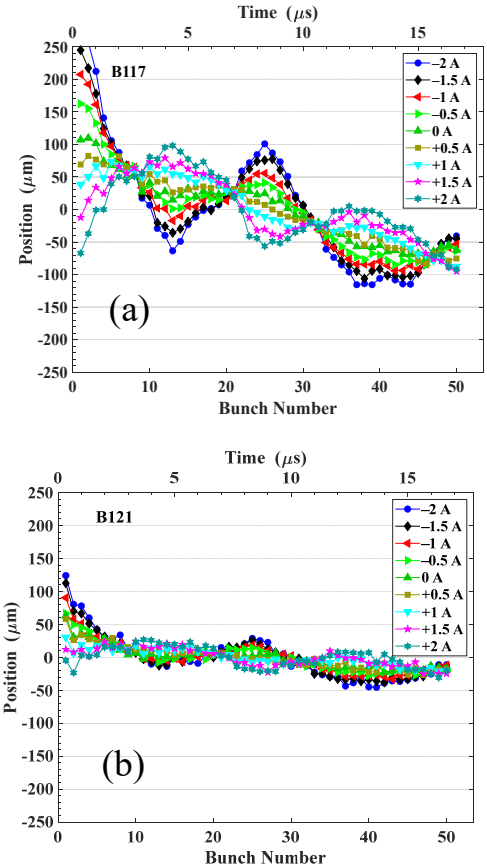

Figure 5: Examples of the variation of the beam vertical centroids bunch by bunch for 50 micropulses at B117 (a) and B121 (b) for V103 settings of ±2A from the reference. These were 100-shot averages to show the 100-kHz oscillation effects generated in CC2.

ASTRA Simulations of the Short-range Wakefield

The ASTRA simulations used the nominal FAST linac input deck with the laser bunch length of 4 ps sigma, a laser transverse spot size of 1.2 mm in x and y, an injection phase of 45o, a gun gradient of 45 MV/m, and the capture cavity gradients of 21 and 14 MV/m for CC1 and CC2, respectively. In particular, the program utilizes the 3D fields of the TESLA-type cavities to produce realistic simulations of the beam through the cavities for comparison to the observations. The simulations were for a single micropulse with 500 pC of charge transiting the two cavities with 0 mm and 5 mm offsets as shown in Fig. 6.

The time-sliced vertical distributions at the head and tail of the micropulse are shown. The simulation shows a tear-drop shape in y-t space (envision later time upward) as reported previously [5] and an approximately 400-µm head-tail kick for the 5-mm offset in Fig. 6b.

In Fig. 7 the elongation of the electron bunch is calculated as σ_t = 11.2 ps compared to the 4-ps laser pulse. This is attributed to space-charge forces acting before acceleration in CC1. The charge dependence of the bunch length

ISBN: 978-3-95450-222-6 ISSN: 2673-5350 doi:10.18429/JACoW-IBIC2020-TUPP17

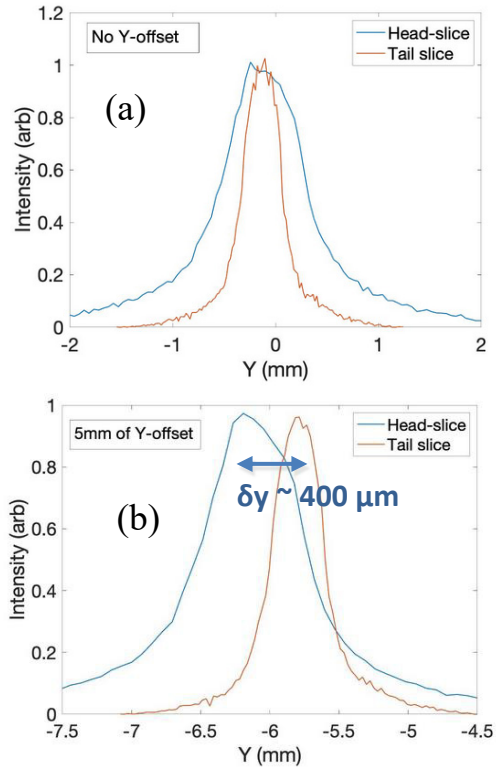

Figure 6: ASTRA simulation results of the head-tail kick for (a) no y offset and (b) 5-mm y offset through the cavities with a calculated ~400-µm head-tail kick.

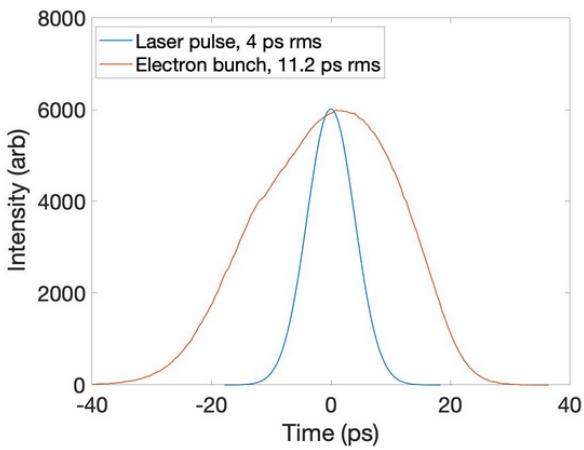

Figure 7: ASTRA simulation results for the electron-beam bunch length at 500 pC/b compared to the initial laser pulse length.

from ASTRA is shown in Fig. 8 for the laser transverse spot size of 1.2 mm and the initial laser pulse of 4-ps duration. The electron beam rms bunch length varies from ~10 to 14 ps for 0.25 to 1.5 nC/b, respectively. There would be an expected increase in this effect for a smaller laser spot size of 0.5 mm as seen in the Fig. 4 data.

SUMMARY

In summary, observations of short-range wakefield effects on beam dynamics were made using the streak camera to obtain y-t images at the submicropulse time scale.

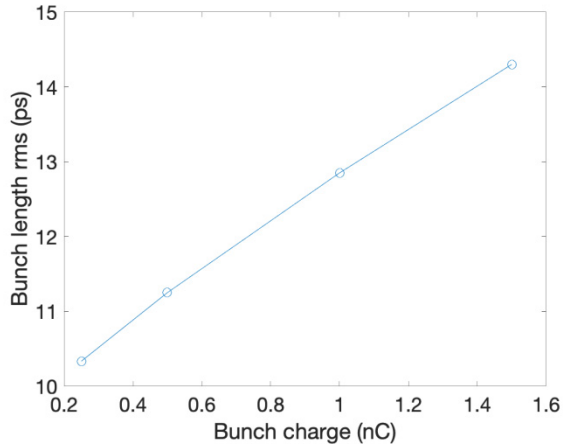

Figure 8: ASTRA simulation results for the charge dependence of the observed bunch length after CC2. The laser pulse length was 4 ps.

The HOM detectors and rf BPMs were used to evaluate off-axis steering related to these tests, and the HOM-induced sub-macropulse centroid motion was shown to be much smaller than the observed effects. Moreover, the head-tail centroid kicks were consistent with short-range wakefield results from ASTRA for the TESLA-type superconducting rf cavity and attributed to that effect.

ACKNOWLEDGMENTS

The Fermilab authors acknowledge the support of C. Drennan, A. Valishev, D. Broemmelsiek, G. Stancari, and M. Lindgren, all in the Accelerator Division at Fermilab. The SLAC/NAL authors acknowledge the support of J. Schmerge (Superconducting Linac Division, SLAC).

REFERENCES

[1] H. Weise, "Commissioning and First Lasing of the European XFEL", in *Proc. FEL'17*, Santa Fe, NM, USA, Aug. 2017, pp. 9-13. doi:10.18429/JACoW-FEL2017-MOC03

[2] P. Emma, "Status of the LCLS-II FEL Project at SLAC", presented at the 38th Int. Free Electron Laser Conf. (FEL'17), Santa Fe, NM, USA, Aug. 2017, paper MOD01, unpublished.

[3] J. T. Seeman *et al.*, "Transverse wakefield control and feedback in the SLC linac", SLAC National Accelerator Laboratory Rep. SLAC-Pub-4182, 1987.

[4] A. H. Lumpkin *et al.*, "Submacropulse electron-beam dynamics correlated with higher-order modes in Tesla-type superconducting rf cavities", *Phys. Rev. Accel. and Beams* vol. 21, p. 064401, 2018. doi:10.1103/PhysRevAccelBeams.21.064401

[5] A.H. Lumpkin, R.M. Thurman-Keup, D. Edstrom, and J. Ruan, "Submicropulse electron-beam dynamics correlated with short-range wakefields in Tesla-type superconducting rf cavities", *Phys. Rev. Accel. and Beams*, vol. 23, p. 054401, 2020. doi:10.1103/PhysRevAccelBeams.23.054401

[6] P. H. Garbincius *et al.*, "The ASTA User Facility Proposal", FNAL, Batavia, IL, USA, Rep. Fermilab-TM-2568, October 2013.

Content from this work may be used under the terms of the CC BY 3.0 licence (© 2020). Any distribution of this work must maintain attribution to the author(s), title of the work, publisher, and DOI

ISBN: 978-3-95450-222-6 ISSN: 2673-5350 doi:10.18429/JACoW-IBIC2020-TUPP17

Content from this work may be used under the terms of the CC BY 3.0 licence (© 2020). Any distribution of this work must maintain attribution to the author(s), title of the work, publisher, and DOI

[7] J. Ruan, M. D. Church, D. R. Edstrom, T. R. Johnson, and J. K. Santucci, "Commission of the Drive Laser System for Advanced Superconducting Test Accelerator", in Proc. IPAC'13, Shanghai, China, May 2013, paper WEPME057, pp. 3061-3063.

[8] R. Thurman-Keup, FNAL, off-line MATLAB-based ImageTool, 2011.

[9] A. H. Lumpkin, J. Ruan, and R. Thurman-Keup, "Synchroscan streak camera imaging at a 15-MeV photoinjector with emittance exchange", *Nucl. Instrum. Methods Phys. Res., Sect. A*, vol. 687, pp. 92-100, 2012. doi:10.1016/j.nima.2012.05.068

[10] A. H. Lumpkin, D. Edstrom, and J. Ruan, "Initial Demonstration of 9-MHz Framing Camera Rates", in Proc. NA-PAC16, Chicago, IL, USA, Oct. 2016, pp. 333-336 doi:10.18429/JACoW-NAPAC2016-TUPOA25

[11] V. Lebedev, private communication, May 2016.

ISBN: 978-3-95450-222-6 ISSN: 2673-5350 doi:10.18429/JACoW-IBIC2020-TUPP18

OBSERVATION OF OPTICAL SYNCHROTRON RADIATION FROM ULTRA-LOW CHARGES STORED IN A RING OPERATING AT 425 MeV*

A. H. Lumpkin†, Argonne Associate, Argonne National Laboratory, Lemont, IL, USA
K. P. Wootton, Argonne National Laboratory, Lemont, IL, USA

Abstract

The initial observations of optical synchrotron radiation (OSR) emitted over millions of passes from a few electrons circulating in the Particle Accumulator Ring (PAR) at the Advanced Photon Source have been done with a digital CMOS camera and a synchroscan streak camera operating at 117.3 MHz. The discrete changes of integrated counts in the CMOS image region of interest are ascribed to single electron steps at ~3500 counts per e^-. Circulations of a single electron at 375 MeV and at 425 MeV were demonstrated in the 12 bit digital FLIR USB3 camera images. The Hamamatsu C5680 streak camera operating at the 12th harmonic of the fundamental revolution frequency at 9.77 MHz was used to measure the bunch length from 0.5 nC circulating charge down to tens of electrons or < 10 aC. The latter cases were performed with 6 ps temporal resolution for the first time anywhere, to our knowledge. We report a preliminary effective bunch length of 276±36 ps for 57 electrons (9.1 aC) stored based on a fit to a single Gaussian peak. The results will be compared to the standard zero-current model for the ring.

INTRODUCTION

Investigations into the probability of photon emission via the optical synchrotron radiation (OSR) mechanism from single electrons circulating in small storage rings have been done with spatially-integrating and light-intensity-monitoring photo multiplier tubes (PMTs) or photodiodes in the past [1, 2] and more recently with PMTs and digital CCD cameras [3]. These gave the intensity effect vs stored electron number and transverse size. However, mapping of the longitudinal distribution of photons emitted by a few electrons circulating in a ring has only been done at the 10 ns level [1–4].

We employ for the first time a synchroscan streak camera that is phase locked to 117.3 MHz, the 12th harmonic of the fundamental revolution frequency at 9.77 MHz of the Particle Accumulator Ring (PAR) at the Advanced Photon Source (APS). This provided temporal resolution of about 6 ps on the slowest streak range. In this case electrons circulate at 1/12th the streak camera vertical deflection frequency so no turns are missed, and the phase locking of the instrument to the radiofrequency (rf) means the camera phase is nearly the same to a few ps over hundreds of seconds. The streak camera sees every turn, and its phosphor screen integrates the arrival times of the photo-electron events on the deflection axis (one photon is emitted per electron per 137 turns, the reciprocal of the fine structure constant α). The readout CCD sensor accumulates the phosphor image over 33 ms, and the analogue image is then readout at 30 Hz and digitized.

We also obtained digital CMOS camera images for the single electron emissions averaged over the acquisition range of 0.1–10 s on the chip, as demonstrated by the discrete or quantized steps in the integrated intensity of the OSR-based beam image over 97.7 million turns. These data provided the critical online assessment of the number of stored electrons in the ring in parallel with the streak camera studies.

EXPERIMENTAL ASPECTS

The APS Accelerators

The schematic of the linac and PAR is shown in Fig. 1 [5]. The small ring is designed to accumulate charges injected from the S-band linac which can operate at up to 30 Hz macropulse rate. Usually, the thermionic cathode rf gun is used to generate a short ~10 ns pulse train of 28 micropulses at 2.86 GHz. Operations at a 30 Hz rate allow the generation of 1–1.8 nC per macropulse. This is far more than we need, so for the low-charge studies up to 5 beam profile screens were inserted in the beam line to attenuate the number of electrons actually captured in the PAR. As we stepped in the screens, we compensated for the input signal loss in the digital camera with increased exposure times from 100 µs up to 10 s. We roughly demonstrated an ultra-low charge monitor operating at 6 orders of magnitude below the rf BPM sum signal monitor used normally as a beam intensity monitor. These experiments were done at 375 MeV in the July 2019 injector studies period and 425 MeV in the November 2019 studies period.

The Optical Diagnostics

The OSR was transported from the PAR West dipole magnet source through a quartz window and via Al mirrors out of the accelerator enclosure up to a shrouded optics table on the mezzanine above [6]. This configuration (Fig. 2) provided access to the detectors in use, the digital CMOS camera and the Hamamatsu C5680 streak camera. (The PMT on the East dipole source was not optimized for these tests, but it did provide some medium-intensity level data.) The OSR signal was split by a mirror that was inserted halfway into the light path. Approximately half of the signal went to the digital camera and half to the Hamamatsu C5680 streak camera with an UV-IR transmitting input optics and S20 photocathode. This camera's vertical sweep unit was phase

* Work supported by the U.S. Department of Energy, Office of Science, Office of Basic Energy Sciences, under Contract No. DE-AC02-06CH11357.
† lumpkin@anl.gov

Content from this work may be used under the terms of the CC BY 3.0 licence (© 2020). Any distribution of this work must maintain attribution to the author(s), title of the work, publisher, and DOI

ISBN: 978-3-95450-222-6 ISSN: 2673-5350 doi:10.18429/JACoW-IBIC2020-TUPP18

Content from this work may be used under the terms of the CC BY 3.0 licence (© 2020). Any distribution of this work must maintain attribution to the author(s), title of the work, publisher, and DOI

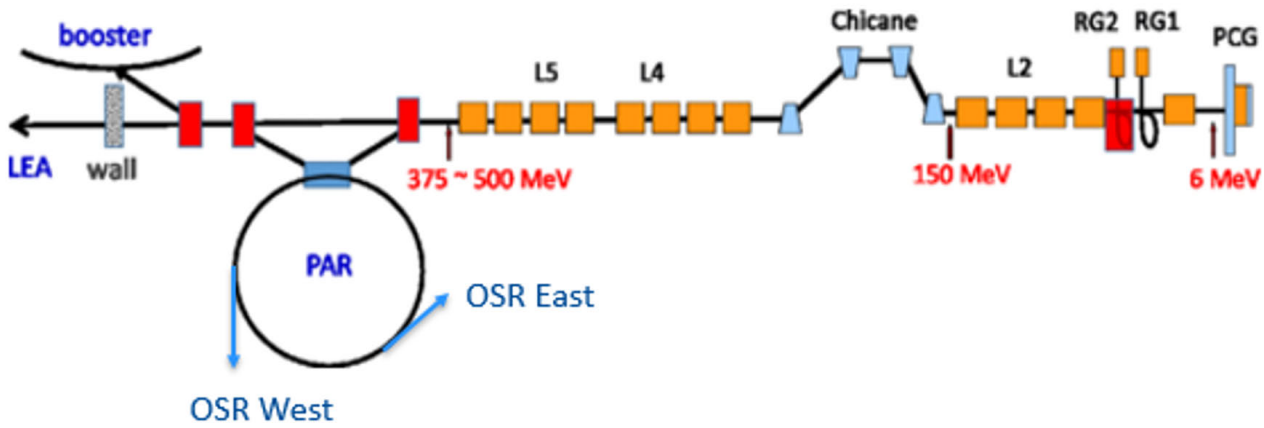

Figure 1: Schematic layout of the APS linac and PAR injector chain. (Adapted under Creative Commons license CC-BY 4.0 from Ref. [5]).

locked to the 117.3 MHz sine wave input that was amplified in the synchroscan unit to generate the sinusoidal sweep voltage. Arrival times of the different photons from the different turns were synchronously summed, giving the time-averaged *x-t* images. The image shape and projections of these two planes provide the unique information on several-electron OSR emission.

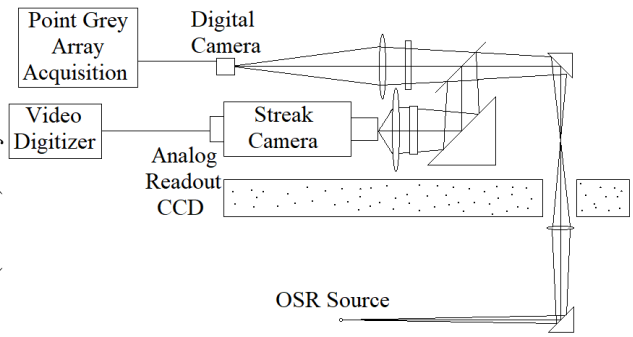

Figure 2: Schematic illustration of the PAR West optics table with the CMOS camera and the streak camera.

The 12-bit digital CMOS camera was a FLIR Grasshopper3 USB3 camera. It allowed designations of a region of interest (ROI) and output of the integrated counts. This was very useful in tracking the intensity changes with electron number and establishing the 3500 counts per e- steps in the ROI online. The high quantum efficiency (~58% at 500 nm) for visible wavelengths was advantageous for these studies. The calibration factor was 31.8 µm per pixel (in both *x* and *y* axes).

EXPERIMENTAL RESULTS

Initially, we considered a PMT to look for OSR intensity changes at low charge. This proved to be problematic at about 100 fC. The digital camera, however, was able to track the average ROI intensity signals down to the few-electron range ($Q \approx 1$ aC) and even to a single electron stored. The streak camera data in focus mode and streak mode also showed results at the 10 electron level for the first time, to our knowledge.

Digital Camera Data

The experimental CMOS results were exemplified by the recognition of the discrete steps in the intensity as we lost individual electrons as shown in Fig. 3. This plot shows the intensity changes in the ROI in the 4 to 1 electron (s) stored cases. Insertion of ND 5.0 filters at selected times including at 03:57 and 04:19 checked the baseline which did drift over time. The 1 e^- intensity level at 04:25 is bracketed by the ND test at 04:19 and the purposeful dump of the single electron at 04:28. The single electron was stored for ~15 minutes, or 8.7 billion turns at 375 MeV.

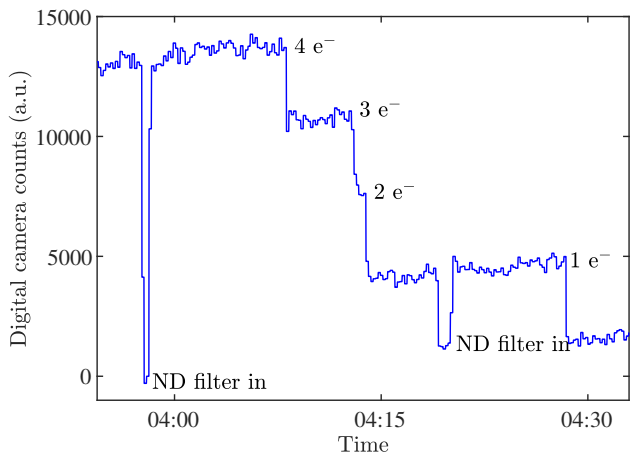

Figure 3: OSR intensity in the west synchrotron light monitor (PAR:SLM1) versus run time. The discrete intensity steps are at 3,500 counts/e^-. At 04:19, the ND filters were inserted briefly to show the background level while a single electron was stored. This electron was purposely lost at 04:28.

Another way to assess the digital CMOS data involved using the images obtained during the run for different electron numbers and subtracting the background image obtained

ISBN: 978-3-95450-222-6 ISSN: 2673-5350 doi:10.18429/JACoW-IBIC2020-TUPP18

with zero electrons. Examples are shown in Fig. 4 where the background subtracted images for 4, 3, 2, and 1 electron are shown. The 2D image is shown in all four cases.

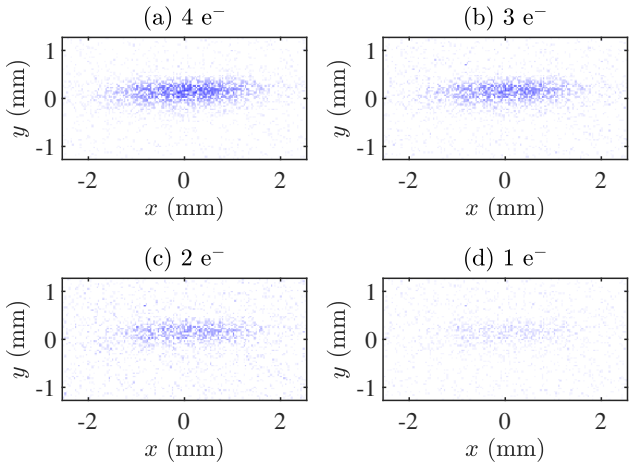

Figure 4: A set of 4 CMOS camera 2D images. These are background subtracted for the four stored-electron-number cases indicated, 4 to 1. This is at 375 MeV.

Streak Camera Results

The streak camera results are partly constrained by the Hamamatsu fiber-optically-coupled analogue readout CCD camera that was Peltier cooled to 0°C to reduce dark current and used with an 8-bit video digitizer running at 30 Hz. We acquired a reference nominal-charge streak image with 0.32 nC stored using the streak range 4 (R4) with ~1.5 ns time coverage and 3.0 ps per pixel temporal calibration factor. The calibration factor was from the data sheet for this synchroscan unit. Figure 5 shows an example focus mode image (a) with a focus y-size of σ = 1.7 pixels in Fig. 5b. The entrance slit was opened so the small vertical beam size set the streak axis resolution limit. Fig. 6 shows the streak camera image and a measured bunch length of 124 ± 4 pixels or 372 ± 12 ps based on a fit to a single Gaussian peak, respectively. These are screen captures from the ImageTool MATLAB program [7]. This latter bunch length value is consistent with the zero-current bunch length for the PAR model at 425 MeV with the 12th harmonic rf powered on [8–10] and recent photodiode bunch length data [11].

We reduced the stored charge controllably by using the PAR injection kickers down to the single electron circulating. On the way, we obtained 100s of streak camera images at different charge levels. In Fig. 7 we show the accumulated image for 57 e$^-$ (< 9 aC) circulating. The fitted value to the projected time profile is 276 ± 36 ps, 25% lower than the observed 0.32 nC case in Fig. 6 and ~17% lower than the calculated equilibrium bunch length of 331 ps at 1 aC using the impedance model for the PAR at 425 MeV [12].

The high frequency noise in the images was addressed with a sliding 9-channel average routine available in the MATLAB processing program [7]. In Fig. 8a we show the raw temporal profile for 57 e$^-$ data compared to the smoothed

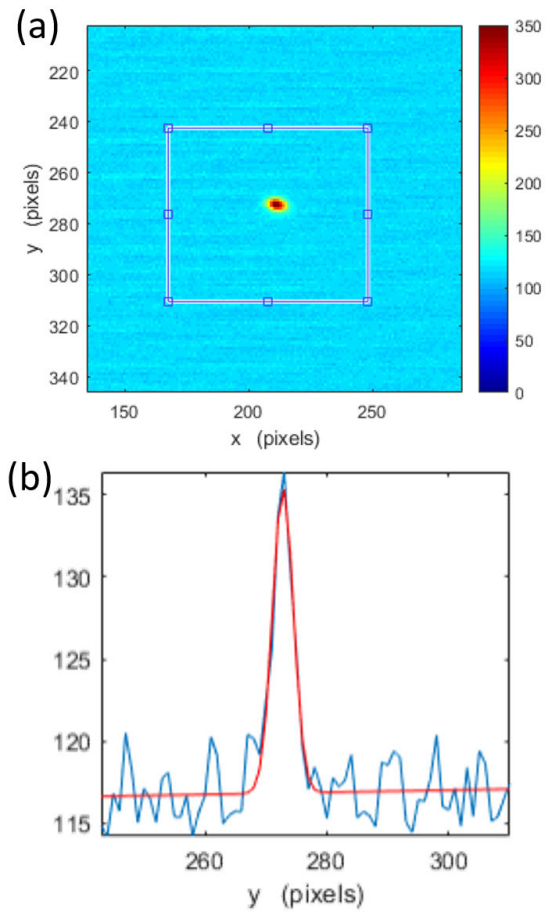

Figure 5: (a) Focus mode image and (b) projected time-axis profile with σ = 1.7 pixels at 0.32 nC.

background. This smoothing then was applied to both the data profile and the summed background image (200 images) as shown in Fig. 8b. It is clear the OSR data are far above the background, and there appear to be some residual localized structures. The interpretation of these is still to be done, although weak background noise bands are a candidate. This temporal profile is in principle the probability distribution of the emission of OSR photons over ~65 million turns. Localizations might occur in statistically starved conditions. This will be explored in the future using onboard averaging in the digitizer board to reduce the digitizing readout noise role. Improved noise filtering algorithms will also be considered.

SUMMARY

In summary, we performed initial investigations of OSR emissions from a few electrons stored in the PAR at 375 and 425 MeV with a digital CMOS camera and with a synchroscan streak camera. We measured a bunch length of 285 ps at 0.5 nC stored charge as a reference at 325 MeV and 372 ps at 425 MeV. We were able to identify OSR from a single electron stored using the CMOS camera and OSR from 10s of electrons stored using a streak camera for the first time. The latter bunch length for 57 e$^-$ stored was observed

Content from this work may be used under the terms of the CC BY 3.0 licence (© 2020). Any distribution of this work must maintain attribution to the author(s), title of the work, publisher, and DOI

ISBN: 978-3-95450-222-6 ISSN: 2673-5350 doi:10.18429/JACoW-IBIC2020-TUPP18

Content from this work may be used under the terms of the CC BY 3.0 licence (© 2020). Any distribution of this work must maintain attribution to the author(s), title of the work, publisher, and DOI

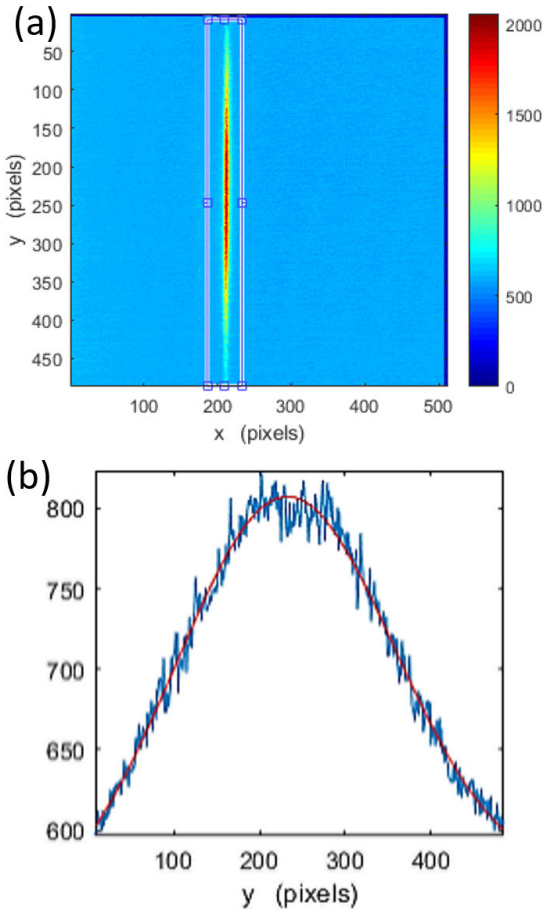

Figure 6: (a) Streak mode Range 4 image and (b) time profile with bunch length of 372 ± 12 ps at 0.32 nC. The vertical scale time range is 1500 ps.

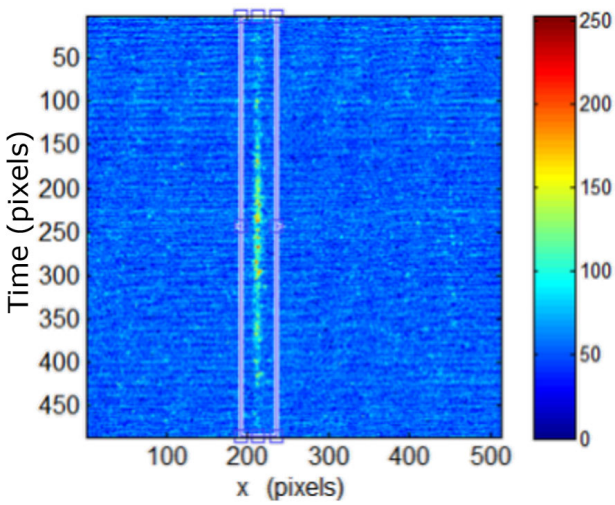

Figure 7: Streak camera sum image (200 images) at 425 MeV for 57 e⁻ circulating in the ring. The vertical scale time range is 1500 ps. The projected time profile with the single Gaussian peak fit gives the bunch length σ_t = 276 ± 36 ps. The digitizer background noise adds to the variance.

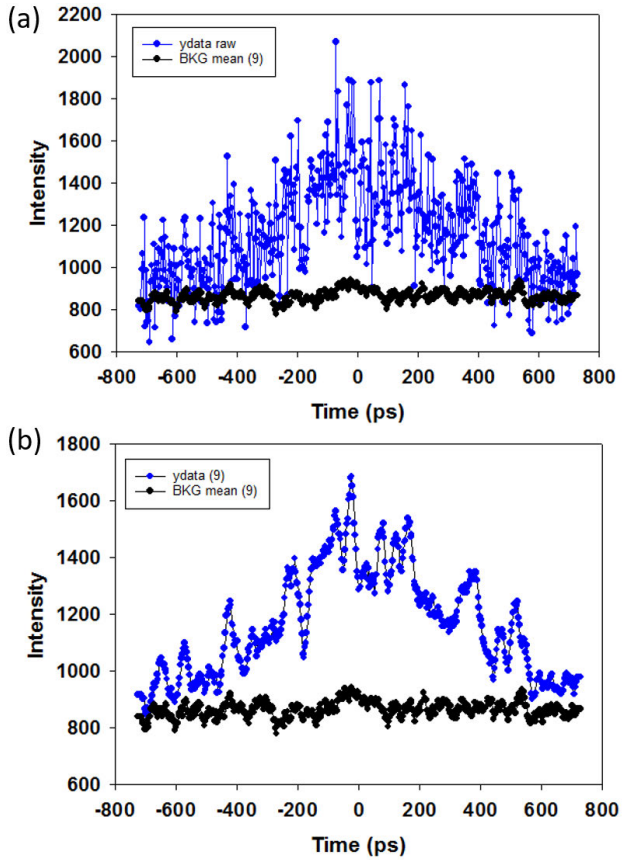

Figure 8: Comparisons of the 57 e⁻ data (a) *y* raw data vs. smoothed background and (b) smoothed data (blue) profile from Fig. 7 and the smoothed, independently summed background profile. A sliding 9-channel smoothing routine for the mean in MATLAB was used to reduce the fluctuations in both.

to be 25% shorter than the reference at 425 MeV. We are reviewing our results in the context of existing models on the PAR [12], OSR, and streak tubes. Further investigations and data processing are planned to elucidate the effect.

ACKNOWLEDGEMENTS

The authors acknowledge the support of J. Byrd and M. Borland of the Accelerator Systems Division and R. Hettel of APS-U at ANL.

REFERENCES

[1] F. Riehle, S. Bernstorff, R. Fröhling, and F.P. Wolf, "Determination of electron currents below 1 nA in the storage ring BESSY by measurement of the synchrotron radiation of single electrons", *Nucl. Instrum. Methods Phys. Res. A*, vol. 268, pp. 262–269, 1988. doi:10.1016/0168-9002(88)90616-X

[2] I. V. Pinayev, V. M. Popik, T. V. Shaftan, A. S. Sokolov, N. A. Vinokurov, and P. V.Vorobyov, "Experiments with undulator radiation of a single electron", *Nucl. Instrum. Methods. Phys. Res. A*, vol. 341, pp. 17–20, 1994. doi:10.1016/0168-9002(94)90308-5

ISBN: 978-3-95450-222-6 ISSN: 2673-5350 doi:10.18429/JACoW-IBIC2020-TUPP18

[3] N. Kuklev, J. D. Jarvis, Y. K. Kim, A. L. Romanov, J. K. Santucci, and G. Stancari, "Synchrotron Radiation Beam Diagnostics at IOTA - Commissioning Performance and Upgrade Efforts", in *Proc. 10th Int. Particle Accelerator Conf. (IPAC'19)*, Melbourne, Australia, May 2019, pp. 2732–2735. doi:10.18429/JACoW-IPAC2019-WEPGW103

[4] R. Klein *et al.*, "Operation of the Metrology Light Source as a primary radiation source standard", *Phys. Rev. Spec. Top. Accel. Beams*, vol. 11, p. 110701, 2008. doi:10.1103/PhysRevSTAB.11.110701

[5] S. Shin, Y. Sun, J. Dooling, M. Borland, and A. Zholents, "Interleaving lattice for the Argonne Advanced Photon Source linac", *Phys. Rev. Accel. Beams*, vol. 21, p. 060101, 2018. doi:10.1103/PhysRevAccelBeams.21.060101

[6] W. Berg, B. Yang, A. Lumpkin, J. Jones, "Design and Commissioning of the Photon Monitors and Optical Transport Lines for the Advanced Photon Source Positron Accumulator Ring", *AIP Conf. Proc.*, vol. 390, pp. 483–490, 1997. doi:10.1063/1.52325

[7] R. M. Thurman-Keup, A. S. Johnson, A. H. Lumpkin, and J. Ruan, "Transverse Emittance and Phase Space Program Developed for Use at the Fermilab A0 Photoinjector", in *Proc. 24th Particle Accelerator Conf. (PAC'11)*, New York, NY, USA, Mar.-Apr. 2011, paper MOP226, pp. 528–530.

[8] M. Borland, "Update on the Argonne Positron Acumulator Ring", in *Proc. 15th Particle Accelerator Conf. (PAC'93)*, Washington D.C., USA, Mar. 1993, pp. 2028–2031. doi:10.1109/PAC.1993.309211

[9] C.-Y. Yao, B. Yang, and H. Shang, private communication, Jul. 2009.

[10] B. X. Yang, A. H. Lumpkin, M. Borland, K. Harkay, and A. Nassiri, "Characterization of Beam Dynamics in the APS Injector Rings Using Time-Resolved Imaging Techniques", in *Proc. 17th Particle Accelerator Conf. (PAC'97)*, Vancouver, Canada, May 1997, paper 5P040, pp. 2052–2054. doi:10.1109/PAC.1997.751104

[11] J. C. Dooling, J. R. Calvey, K. C. Harkay, B. X. Yang, and C. Yao, "Fast Photodetector Bunch Duration Monitor for the Advanced Photon Source Particle Accumulator Ring", in *Proc. 9th Int. Particle Accelerator Conf. (IPAC'18)*, Vancouver, Canada, Apr.-May 2018, pp. 1819–1822. doi:10.18429/JACoW-IPAC2018-WEPAF006

[12] K. Harkay, private communication, Dec. 2019.

Content from this work may be used under the terms of the CC BY 3.0 licence (© 2020). Any distribution of this work must maintain attribution to the author(s), title of the work, publisher, and DOI

ISBN: 978-3-95450-222-6 ISSN: 2673-5350 doi:10.18429/JACoW-IBIC2020-TUPP23

Content from this work may be used under the terms of the CC BY 3.0 licence (© 2020). Any distribution of this work must maintain attribution to the author(s), title of the work, publisher, and DOI

STREAK CAMERA MEASUREMENT OF ELECTRON BEAM ENERGY LOSS PER TURN IN THE ADVANCED PHOTON SOURCE PARTICLE ACCUMULATOR RING*

K. P. Wootton†, J. R. Calvey, J. C. Dooling, K. C. Harkay, Y. Sun, B. X. Yang
Argonne National Laboratory, Lemont, IL 60439, USA
A. H. Lumpkin, Argonne Associate of Global Empire, LLC,
Argonne National Laboratory, Lemont, IL 60439, USA

Abstract

Relativistic electron beams in storage rings radiate a significant fraction of beam energy per turn. As demonstrated in previous experiments, with the radiofrequency accelerating structures off, the turn-by-turn time of arrival of the electron bunch can be observed from the synchrotron radiation that it produces using a streak camera. In the present work, we present measurements of the energy loss per turn of an initially short electron bunch (~1 ps RMS) from a photocathode electron gun in the Advanced Photon Source Particle Accumulator Ring (375 MeV, 102 ns revolution period). With the streak camera synchroscan locked to the twelfth harmonic of the revolution frequency (117.3 MHz), we observe an injection transient in the horizontal direction.

INTRODUCTION

Injecting and accumulating charge in an electron storage ring is a dynamic process. It relies upon the emission of incoherent synchrotron radiation to damp the beam phase space to an equilibrium distribution. The energy loss per turn due to incoherent synchrotron radiation has previously been observed at GeV-scale electron storage rings [1, 2]. In those experiments, the electron beam was injected into the storage ring with the radiofrequency (RF) cavities switched off.

In the present work, dual-sweep streak camera measurements were performed which uniquely show inherent energy spread effects on the bunch length per turn, electron beam energy loss per turn, and the injection transverse transient for the initial ~1 ps duration bunch injected at 375 MeV.

THEORY

Energy Loss per Turn

In the absence of an accelerating RF voltage, an electron loses energy U_0 each turn due to incoherent synchrotron radiation [3]. The energy loss per turn can be calculated using the second synchrotron radiation integral I_0 [4]. Due to the non-zero momentum compaction factor α_c of the ring [4], the electron follows a dispersive orbit and arrives earlier each turn. At at a time t following injection, the change in arrival time of the electron bunch relative to the synchronous arrival time is given by [1]:

$$\Delta T_{\text{tot}} = \frac{1}{2}\frac{f_0}{E}\alpha_c U_0 t^2, \tag{1}$$

where f_0 is the revolution frequency, and E is the electron beam energy.

Injection Transient

Injection transients have previously been observed using turn-by-turn optical measurements at other laboratories [5–10]. For beams injected transversely off-axis for accumulation in a storage ring, the beam centroid is observed to oscillate at the betatron frequency in the plane of the orbit offset. In the Particle Accumulator Ring (PAR), electrons are injected with a horizontal offset from the central beam axis.

Beam centroid oscillations are observed at the betatron frequency if there is a dispersion mismatch, and oscillate at twice the betraton frequency if there is a beta function mismatch [11]. The observation of such transverse effects are deducible from dual-sweep streak camera images.

METHOD

A chain of injectors is used to accelerate electrons at the Advanced Photon Source (APS). The injector chain is illustrated schematically in Fig. 1 [12]. In the present work, we utilise electron beams from the photocathode gun (PCG) [13] and RF thermionic gun 2 (RG2) [14]. These beams are accelerated using the main linac accelerating structures (L2, L4 and L5), and injected into the PAR.

The PAR is operated as an electron damping ring [15]. In normal operation, beams injected from the linac are accumulated over multiple linac cycles and damped before injection as a single bunch into the booster synchrotron. The PAR RF system features two cavities with the fundamental RF cavity operating at the revolution frequency 9.77 MHz, and a 12$^{\text{th}}$ harmonic bunch compressing cavity operating at 117.2 MHz [16]. Calculated parameters of the PAR are summarised in Table 1.

To observe the electron beam arrival on a turn-by-turn basis, we used a streak camera installed at the PAR West synchrotron light port: a location in the lattice with non-zero horizontal dispersion [17–19]. The Hamamatsu model C5680 streak camera was operated in the dual-sweep configuration. A synchroscan module was used as the deflector

* Work supported by the U.S. Department of Energy, Office of Science, Office of Basic Energy Sciences, under Contract No. DE-AC02-06CH11357.
† kwootton@anl.gov

ISBN: 978-3-95450-222-6 ISSN: 2673-5350 doi:10.18429/JACoW-IBIC2020-TUPP23

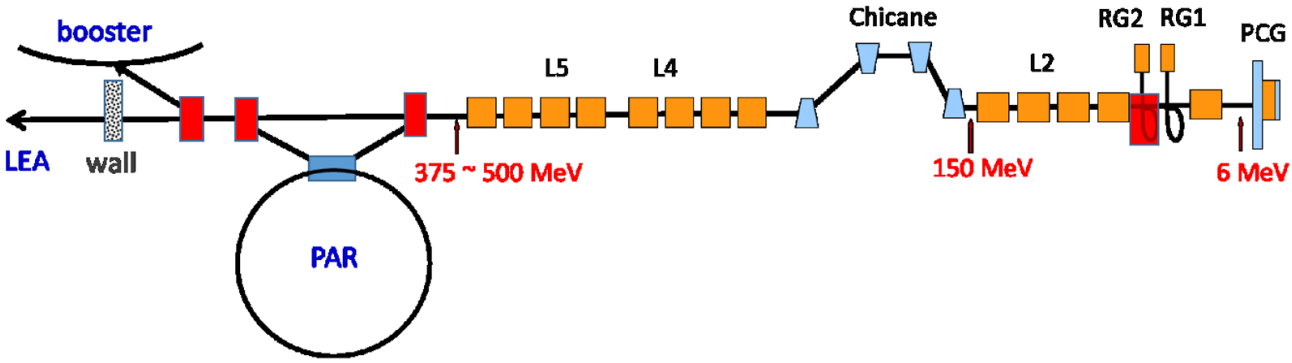

Figure 1: Schematic layout of the APS linac and PAR injector chain. In the present work, we utilise electron beams from the photocathode gun (PCG) and RF thermionic gun 2 (RG2). These beams are accelerated using the main linac accelerating structures (L2, L4 and L5), and injected into the Particle Accumulator Ring (PAR) at 375 MeV. (Reproduced under Creative Commons license CC-BY 4.0 from [S. Shin *et al.*, *Phys. Rev. Accel. Beams*, vol. 21, p. 060101, 2018], Ref. [12])

Table 1: PAR Parameters for the Present Experiment

Parameter	Symbol	Value	Units
Beam energy	E	0.375	GeV
Revolution period	T	102	ns
Betatron tune (x)	ν_x	2.177	–
Betatron tune (y)	ν_y	1.211	–
Momentum compaction factor	α_c	0.244	–
Second synchrotron radiation integral	I_2	6.16	m^{-1}
Energy loss per turn	U_0	1.72	keV

in the vertical plane (synchronised with the 117.1 MHz RF signal), on sweep range 4 (1.48 ns full scale, 3.0 ps per pixel). A slow dual axis unit was used as the horizontal deflector, varying the sweep range between 1-10 µs (10-100 turns of the PAR).

RESULTS

Stored Beam at Equilibrium

The longitudinal profile of the electron beam over several turns at equilibrium with both the fundamental and the 12th harmonic RF cavities powered [15] is plotted in Fig. 2.

From Fig. 2, we confirmed that the damped electron bunches arrive at an equal revolution period of 102 ns, and we validated the horizontal time axis calibration. The equilibrium bunch length was determined to be ~300 ps from the vertical axis image signal distribution.

Photocathode Gun Beam

To observe longitudinal electron beam dynamics at injection, we accelerate a single ~1 ps electron bunch from the photocathode gun using the linac, and inject it into the PAR. This is illustrated in Fig. 3 over the first 1 µs following injection (the first ~8 turns), and Fig. 4 over a timescale of the first 2 µs following injection (the first ~16 turns).

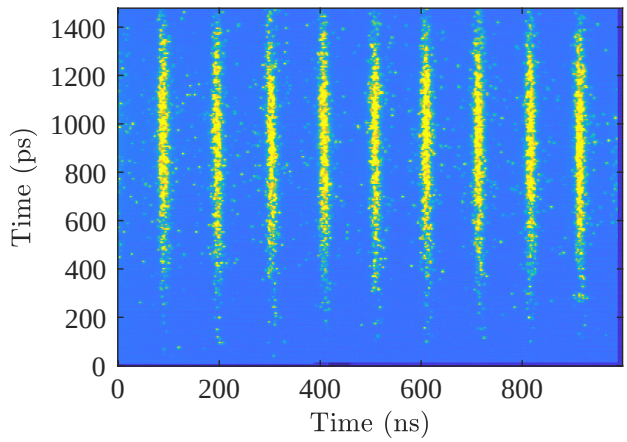

Figure 2: Observation over 9 turns of the PAR of a single electron bunch stored beam at equilibrium, with both the fundamental and 12th harmonic RF cavity on.

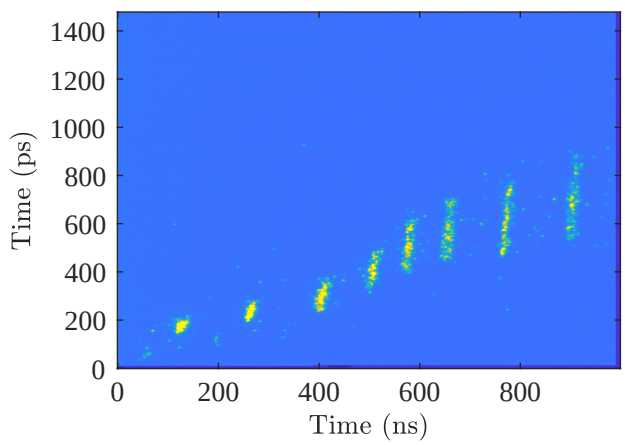

Figure 3: Observation over the first eight turns of a single electron bunch from the photocathode RF gun injected into the PAR. The slow streak range (horizontal axis) of the streak camera was 1 µs. Both the fundamental and 12th harmonic RF cavity were off.

Content from this work may be used under the terms of the CC BY 3.0 licence (© 2020). Any distribution of this work must maintain attribution to the author(s), title of the work, publisher, and DOI

ISBN: 978-3-95450-222-6 ISSN: 2673-5350 doi:10.18429/JACoW-IBIC2020-TUPP23

Content from this work may be used under the terms of the CC BY 3.0 licence (© 2020). Any distribution of this work must maintain attribution to the author(s), title of the work, publisher, and DOI

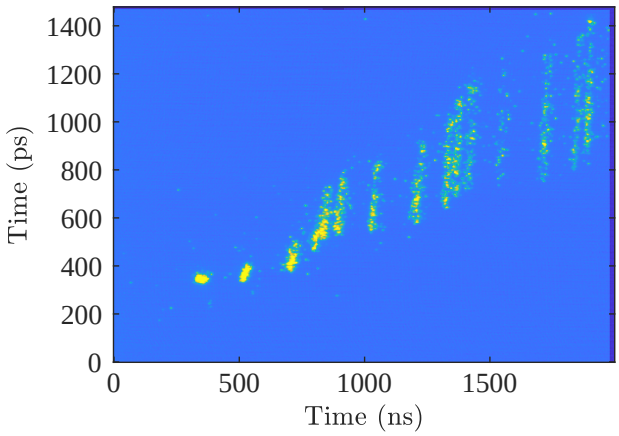

Figure 4: Observation over the first sixteen turns of a single electron bunch from the photocathode RF gun injected into the PAR. The slow streak range (horizontal axis) of the streak camera was 2 µs. Both the fundamental and 12th harmonic RF cavity were off.

Thermionic Gun Beam

Another option for injecting into the linac is to use the RF thermionic guns. We accelerated a ∼10 ns duration electron bunch train from RF thermionic gun 2 gun using the linac [14], and injected it into the PAR. This is illustrated in Fig. 5 over the first 1 µs following injection.

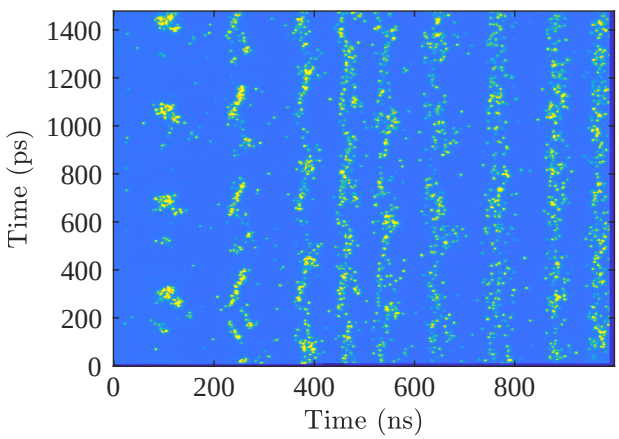

Figure 5: Observation over the first nine turns of a ∼12 ns duration electron bunch train from the thermionic RF gun injected into the PAR. Electron bunches in the train are separated along the vertical axis by 350 ps corresponding to the RF frequency of the electron gun (2856 MHz). Both the fundamental and 12th harmonic RF cavity were off.

DISCUSSION

Since the streak camera horizontal axis has both spatial and slow temporal information, the transverse injection transient results in the shift of the peak positions away from the regular temporal spacings along the slow (horizontal) time axis of Fig. 2. This means that in principle the amplitude of the horizontal oscillation could be extracted from the images with further analysis.

Unlike in Fig. 2, for the injected beam in Figs. 3–4, it appears that the beam arrival time observed on the horizontal (slow) axis of the streak camera is oscillating in time, with a period of about six turns. Based on the period of oscillation corresponding approximately with the fractional horizontal betatron period, we associate this oscillation with a mismatched horizontal injection transient, rather than a temporal oscillation. Another possible mechanism to consider is the effect of coherent synchrotron radiation in the THz frequency scale on the energy loss per turn.

Parabolic fits for the energy loss per turn are presented in Fig. 6, bounding the time of arrival of the electron beam envelope in time. One possibility for the discrepancy between the observed and calculated energy loss per turn could be a mismatch of the beam energy with the ring at injection [2].

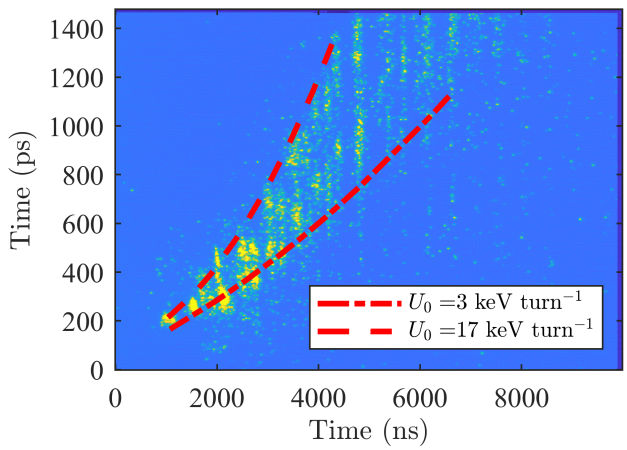

Figure 6: Observation over the first turns of a single electron bunch from the photocathode RF gun injected into the PAR. The slow streak range (horizontal axis) of the streak camera was 10 µs. Both the fundamental and 12th harmonic RF cavity were off. Parabolic fits for the maximum and minimum energy loss per turn observed are plotted.

CONCLUSION

Using a streak camera, we have observed the time of arrival and bunch lengthening of a ∼1 ps electron bunch for the turns immediately following injection into the PAR electron damping ring. With the streak camera synchroscan unit locked to the twelfth harmonic of the revolution frequency (117.3 MHz), we observe an injection transient in the horizontal direction. An energy loss per turn of the electron beam was observed to be 3 keV turn^{-1} $< U_0 <$ 17 keV turn^{-1} compared to the model of U_0 = 1.7 keV turn^{-1}.

ACKNOWLEDGEMENTS

The submitted manuscript has been created by UChicago Argonne, LLC, Operator of Argonne National Laboratory ("Argonne"). Argonne, a U.S. Department of Energy Office of Science Laboratory, is operated under Contract No.

ISBN: 978-3-95450-222-6 ISSN: 2673-5350 doi:10.18429/JACoW-IBIC2020-TUPP23

DE-AC02-06CH11357. The U.S. Government retains for itself, and others acting on its behalf, a paid-up nonexclusive, irrevocable worldwide license in said article to reproduce, prepare derivative works, distribute copies to the public, and perform publicly and display publicly, by or on behalf of the Government. The Department of Energy will provide public access to these results of federally sponsored research in accordance with the DOE Public Access Plan.
http://energy.gov/downloads/doe-public-access-plan

REFERENCES

[1] J. M. Byrd and S. De Santis, "Longitudinal injection transients in an electron storage ring", *Phys. Rev. ST Accel. Beams*, vol. 4, p. 024401, 2001. doi:10.1103/PhysRevSTAB.4.024401

[2] A. A. Nosych, B. Bravo, and U. Iriso, "Energy Loss Measurements with Streak Camera at ALBA", in *Proc. 7th Int. Beam Instrumentation Conf. (IBIC'18)*, Shanghai, China, Sep. 2018, pp. 548–551. doi:10.18429/JACoW-IBIC2018-THOB02

[3] J. Schwinger, "On the Classical Radiation of Accelerated Electrons", *Phys. Rev.*, vol. 75, pp. 1912–1925, 1949. doi:10.1103/PhysRev.75.1912

[4] R. H. Helm, M. J. Lee, P. L. Morton, and M. Sands, "Evaluation of Synchrotron Radiation Integrals", *IEEE Trans. Nucl. Sci.*, vol. 20, pp. 900–901, 1973. doi:10.1109/TNS.1973.4327284

[5] J. C.Bergstrom and J. M. Vogt, "The optical diagnostic beamline at the Canadian Light Source", *Nucl. Instrum. Methods Phys. Res. Sect. A*, vol. 562, pp. 495–512, 2006. doi:10.1016/j.nima.2006.02.200

[6] A. S. Fisher, M, Petree, R. Kraus, Y.-S. Au, and B. Chan, "Turn-by-Turn Imaging of the Transverse Beam Profile in PEP-II", *AIP Conf. Proc.*, vol. 868, pp. 303–312, 2006. doi:10.1063/1.2401418

[7] W. X. Cheng *et al.*, "Fast-Gated Camera Measurements in SPEAR3", in *Proc. 23rd Particle Accelerator Conf. (PAC'09)*, Vancouver, Canada, May 2009, paper TH6REP032, pp. 4015–4017.

[8] W. J. Corbett, W. X. Cheng, A. S. Fisher, and W. Y. Mok, "Injection Beam Dynamics in SPEAR3", in *Proc. 14th Beam Instrumentation Workshop (BIW'10)*, Santa Fe, NM, USA, May 2010, paper TUPSM065, pp. 318–322.

[9] J. Corbett, W. Cheng, A. S. Fisher, W. Mok, and S. Westerman, "Visible Light Diagnostics at SPEAR3", *AIP Conf. Proc.*, vol. 1234, pp. 637–640, 2010. doi:10.1063/1.3463286

[10] M. J. Boland, T. M. Mitsuhashi, and K. P. Wootton, "Turn-by-turn Observation of the Injected Beam Profile at the Australian Synchrotron Storage Ring", in *Proc. 1st Int. Beam Instrumentation Conf. (IBIC'12)*, Tsukuba, Japan, Oct. 2012, paper MOPB83, pp. 276–278.

[11] M. G. Minty and W. L. Spence, "Injection Envelope Matching in Storage Rings", in *Proc. 16th Particle Accelerator Conf. (PAC'95)*, Dallas, TX, USA, May 1995, paper RAA06, pp. 536–538. doi:10.1109/PAC.1995.504711

[12] S. Shin, Y. Sun, J. Dooling, M. Borland, and A. Zholents, "Interleaving lattice for the Argonne Advanced Photon Source linac", *Phys. Rev. Accel. Beams*, vol. 21, p. 060101, 2018. doi:10.1103/PhysRevAccelBeams.21.060101

[13] Y.-E. Sun *et al.*, "Commissioning of the Photo-Cathode RF Gun at APS", in *Proc. 36th Int. Free Electron Laser Conf. (FEL'14)*, Basel, Switzerland, Aug. 2014, paper THP039, pp. 803–806.

[14] J. W. Lewellen *et al.*, "Operation of the APS RF Gun", in *Proc. 19th Int. Linac Conf. (LINAC'98)*, Chicago, IL, USA, Aug. 1998, paper TH4042, pp. 863–865.

[15] E. A. Crosbie, "A Positron Accumulator Ring for APS", Argonne National Laboratory, Argonne, IL, USA, Rep. LS-109, Mar. 1988. doi:10.2172/90005

[16] Y. W. Kang, A. Nassiri, J. F. Bridges, T. L. Smith, and J. J. Song, "RF Cavities for the Positron Accumulator Ring (PAR) of the Advanced Photon Source (APS)", in *Proc. 16th Particle Accelerator Conf. (PAC'95)*, Dallas, TX, USA, May 1995, paper WPP16, pp. 1693–1695. doi:10.1109/PAC.1995.505330

[17] A. H. Lumpkin, "Advanced, time-resolved imaging techniques for electron-beam characterizations", *AIP Conf. Proc.*, vol. 229, pp. 151–179, 1991. doi:10.1063/1.40746

[18] A. Lumpkin and B. Yang, "Status of the synchrotron radiation monitors for the APS facility rings", in *Proc. 16th Particle Accelerator Conf. (PAC'95)*, Dallas, TX, USA, May 1995, paper MPQ09, pp. 2470–2472. doi:10.1109/PAC.1995.505587

[19] W. Berg, B. Yang, A. Lumpkin, and J. Jones, "Design and Commissioning of the Photon Monitors and Optical Transport Lines for the Advanced Photon Source Positron Accumulator Ring", *AIP Conf. Proc.*, vol. 390, pp. 483–490, 1997. doi:10.1063/1.52325

Content from this work may be used under the terms of the CC BY 3.0 licence (© 2020). Any distribution of this work must maintain attribution to the author(s), title of the work, publisher, and DOI

ISBN: 978-3-95450-222-6 ISSN: 2673-5350 doi:10.18429/JACoW-IBIC2020-TUPP24

Content from this work may be used under the terms of the CC BY 3.0 licence (© 2020). Any distribution of this work must maintain attribution to the author(s), title of the work, publisher, and DOI

LOCO CORRECTIONS FOR BEAM TRAJECTORY OPTIMISATION ON THE ISIS ACCELERATOR

E.J. Brookes, H.V. Cavanagh, B. Jones, ISIS, Rutherford Appleton Laboratory, Oxfordshire, UK

Abstract

The ISIS facility at the Rutherford Appleton Laboratory, UK, produces neutron and muon beams for condensed matter research. Its 50 Hz, 800 MeV proton synchrotron delivers a mean beam power of 0.2 MW to two tungsten spallation targets.

The beam optics correction technique implemented in this work is Linear Optics from Closed Orbits (LOCO). LOCO modifies existing accelerator models according to a measured orbit-response matrix (ORM). This correction technique identifies imperfections in the machine lattice, and discrepancies between the machine and model.

The identification of erroneous elements through analysis of the measured ORM is demonstrated in this paper. In comparison to the operational settings achieved through the existing correction techniques, the initial test of the LOCO code demonstrates a 17 % improvement to the RMS trajectory deviation in the horizontal plane. It also shows an 11 % horizontal and 30 % vertical decrease to the standard deviation of trajectory measurements.

INTRODUCTION

The ISIS synchrotron accelerates pulses of 3×10^{13} protons from 70 MeV to 800 MeV at 50 Hz. Particles orbit the ring 12,000 times in the 10 ms acceleration cycle. The 163 m circumference ring contains 32 beam position monitors (BPMs), 14 steering magnets and 20 trim quadrupoles, to measure and adjust the beam optics. Errors in the lattice can result in deviations from the optimal orbit which are difficult to correct empirically. In order to minimise beam loss while maximising beam intensity and use of the available aperture, it is vital to be able to accurately manipulate the beam dynamics throughout the machine.

The Linear Optics from Closed Orbits (LOCO [1]) correction technique, implemented successfully on accelerators worldwide (Fermilab and CERN Boosters [2], Swiss Light Source (SLS) [3]), monitors the behaviour of the beam due to magnet perturbations in an orbit-response matrix (ORM). It then fits perturbations in a simulated version of the ORM, created using existing models in the accelerator design software MAD-X [4] to the measurements. After successful fitting, the resulting matrix is an accurate representation of the machine performance. The modifications made to the model are then reversed and implemented on the machine in order to locate and counteract errors identified by the fitting procedure.

EXISTING CORRECTION PROCEDURE

A model of the accelerator was created in order to predict and study beam optics throughout the machine. This provides the ability to build up a matrix of the ideal responses of all magnets throughout the acceleration cycle.

Originally, the correction technique used was based on the linear equation

$$x_i = R_{ij}\theta_j$$

where x_i is the measured position at monitor i, R_{ij} is the element in the response matrix and θ_j is the kick to magnet j. The matrix was minimised through Singular Value Decomposition in order to determine solutions for θ_j [5].

Later the model was rewritten in MAD-X and its orbit correction capabilities exploited. These corrections directly take measured positions from the machine and vary the N most efficient steering magnets in the model to fit this trajectory. The opposite changes can then be applied to the machine to centre the beam [6].

Though a measured ORM was recorded to aid with steering magnet strength calibration, the MAD-X model and subsequent calculations do not include the ORM in calculations and is therefore not a perfect correction. The constant evolution of real errors on the machine reduces the effectiveness of this method. By measuring a response matrix on the machine and using this in the calculations, the locations of alignment and field errors can be acknowledged and minimised in the correction. Another advantage to the LOCO method is that it uses only response measurements and magnet settings in calculations to determine adjustments to operational magnet settings.

ORBIT-RESPONSE MATRIX

The LOCO method relies on the measurement of the ORM. This is measured by recording the beam position response on the same pulse at all BPMs for a change in current applied to each individual magnet. Each element in the matrix is formed by taking the gradient of three points measured in this fashion. In order to accurately represent the real machine dynamics, the statistical error taken at the 95% confidence level is included in calculations.

The ORM measurements begin with the machine operational setup with a reasonably well-centred beam. The initial measurements from the BPMs are recorded before magnets are individually varied twice, in turn. On each current change, the beam loss was checked around the ring to ensure the beam remained in the vacuum chamber.

During these measurements, it is important to ensure that the current adjustments are large enough to record a measurable change at the BPMs, but small enough that the beam remains within the vacuum chamber. Therefore, the choice of measurement timing and kick strength are important factors. Measurements at ISIS are taken at 4 ms in the acceleration cycle with a total current range of 40 A per magnet. This allows a balance between available aperture and magnetic rigidity.

Since the measured ORM relates to a specific setup of the machine, the response matrix should be re-measured

ISBN: 978-3-95450-222-6 ISSN: 2673-5350 doi:10.18429/JACoW-IBIC2020-TUPP24

before each correction attempt. Measuring a 1,088-element ORM for the entire synchrotron takes roughly 3 hours so is a viable option for a setup shift. Due to the design of the monitors in the High Energy Drift Space (HEDS) at injection, measuring an equivalent 132-element ORM takes 16 hours and is therefore not reasonable for correction shifts.

The existing MAD-X model has been modified to extract the Twiss parameters for orbit response calculations at a monitor (x_i) due to the kick at a magnet (θ_j):

$$\frac{\Delta x_i}{\Delta \theta_j} = \frac{\sqrt{\beta_i \beta_j}}{2\sin(\pi \nu_x)} \cos\left(|\psi_i - \psi_j| - \pi \nu_x\right)$$

where $\beta_{i,j}$ is the beta function and $\psi_{i,j}$ is the phase at the monitor or magnet respectively, and ν_x is the horizontal betatron tune [2]. By individually simulating a change in all variable parameters (currents, misalignments and tilts), the ORM is built up similarly to the machine measurements.

New calibration values for conversion between dipole current and kick strength were calculated from the ORM data for each individual magnet, to improve the balance between variables and constraints over.

For comparison, the operational model and measured response elements are plotted against each other in Fig.1, where a slope of 1 indicates a perfect agreement.

All linear best fits in Fig. 1, lie within 0.1 mm/A below ideal agreement, indicating that the model expects larger responses. This may be a consequence of magnet field errors, systematic BPM calibration errors or the model itself.

The measurements indicate an RMS error of 0.2 mm, suggesting good agreement between model and machine.

The largest discrepancy originates from the measurements for the steering magnet R5HD1, shown in light blue in Fig. 1. The deviations are most prevalent in monitors directly after the magnet and only in the same-plane measurements. Further investigation revealed a discrepancy in the azimuthal location of the magnet. The model had defined R5HD1 ~5 m later than its actual location on the machine.

The response matrix shows negligible coupling in magnet behaviours, so the choice was made to use only same-plane magnets to correct for horizontal and vertical errors.

LOCO CODE

The existing model is written in MAD-X and returns the Twiss parameters at all elements. A Python script was written to collect these data and create an ORM with 147,968 elements (1,088 elements for each variable parameter).

The measured ORM is loaded into a vector and the artificial ORM is loaded into a matrix where each column is an ORM measured for a varied parameter.

During this development stage, Microsoft Excel was used as a front-end to the code, providing a readily accessible version of the measured and calculated ORMs, and the measurements taken to create them. Future work could create a LabVIEW interface for integration with existing beam physics software.

An error vector (equivalent to the chi^2) is calculated and minimised via Singular Value Decomposition to create the modifications needed to represent the real machine dynamics. This is an iterative fitting procedure as not all errors are linear with respect to the magnetic fields.

The modifications made to the artificial ORM are reversed and implemented on the machine.

When the LOCO code was tested on operational beam pulses, the code completed in under 10 seconds and was shown to converge to final values in 3 iterations, shown in Fig. 2.

The minimisation in this technique is under-constrained, as more monitors are used than relevant-plane magnets. The choice of singular values in the fitting is therefore important. Too few singular values will create changes which are too small to be implemented, and too many will produce changes too large for the magnets to manage. The Python code automatically selects the number of singular values to use and has used six in the fitting in Fig. 2.

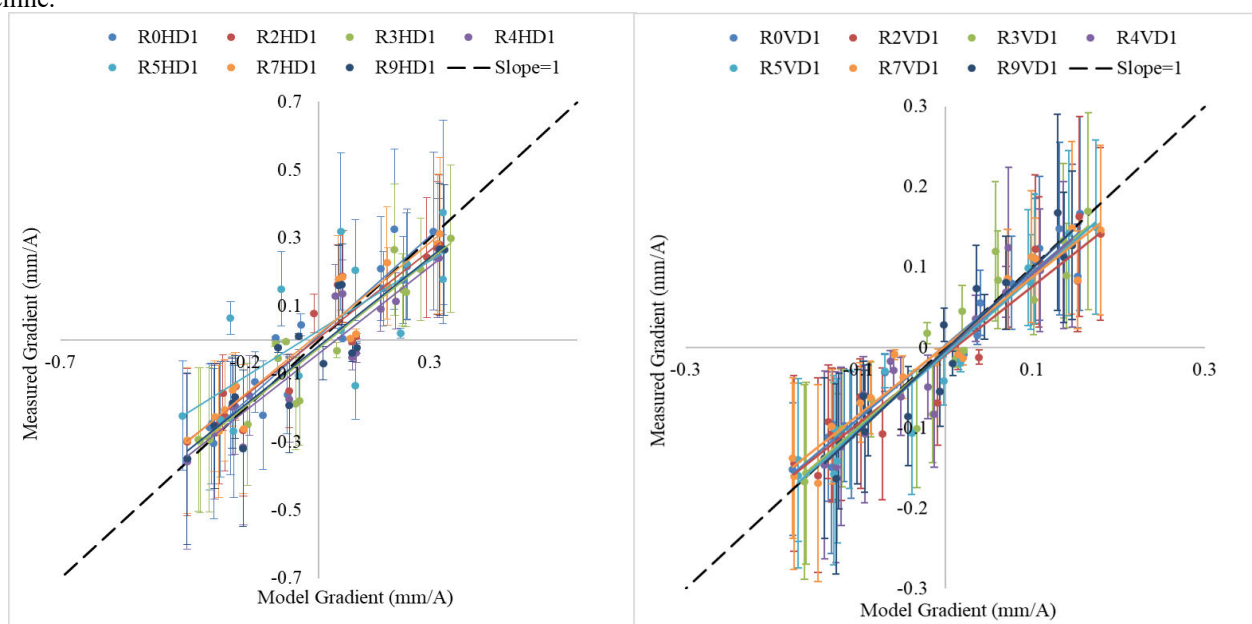

Figure 1: Model and measured matrix elements for comparison for horizontal dipoles (HD) and vertical dipoles (VD).

Content from this work may be used under the terms of the CC BY 3.0 licence (© 2020). Any distribution of this work must maintain attribution to the author(s), title of the work, publisher, and DOI

ISBN: 978-3-95450-222-6 ISSN: 2673-5350 doi:10.18429/JACoW-IBIC2020-TUPP24

Content from this work may be used under the terms of the CC BY 3.0 licence (© 2020). Any distribution of this work must maintain attribution to the author(s), title of the work, publisher, and DOI

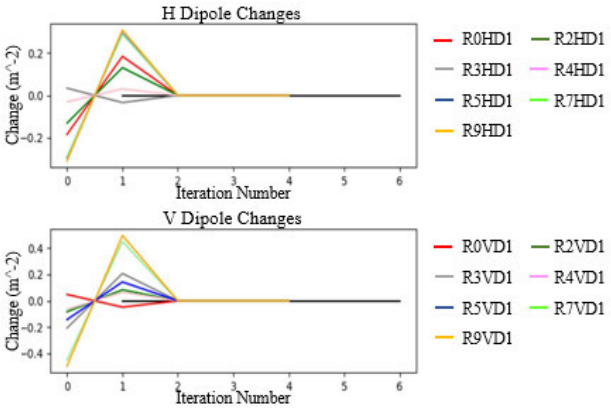

Figure 2: Current changes converge within 3 iterations during iterative fitting procedure.

CORRECTIONS

After collecting the magnet settings from the operational machine, already treated via the existing correction technique, a LOCO correction was attempted on the machine and the results are shown against the operational positions in Fig. 3.

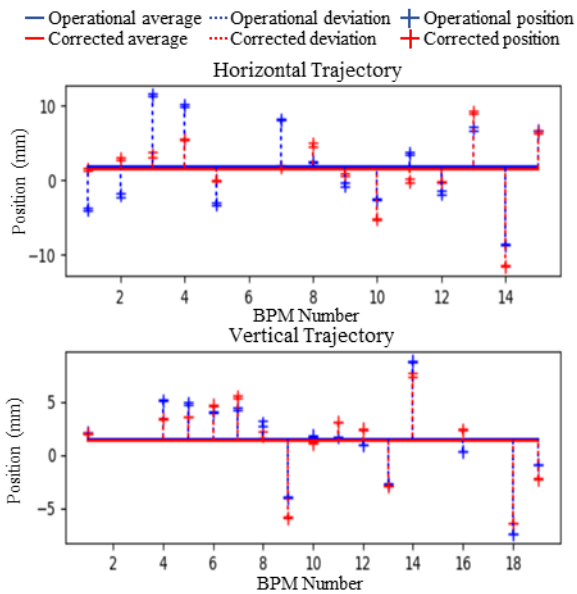

Figure 3: Operational trajectory and trajectory after basic correction plotted for comparison

From the operational average position, the uncorrected RMS deviations were 6.13 mm and 4.19 mm in the horizontal and vertical planes respectively, with pulse-to-pulse standard deviations of 0.23 mm and 0.12 mm. These standard deviations indicate a stable beam, allowing for repeatable measurements.

After the LOCO code had run, the results were implemented on the machine. The misalignment errors indicated fell well within acceptable limits (set to 0.5 mm) in both planes and beam loss remained reasonable. The horizontal RMS deviations reduced to 5.12 mm with a standard deviation of 0.17 mm. The vertical RMS deviations showed negligible change at 4.11 mm, but standard deviation was improved to 0.07 mm.

The LOCO code succeeded in smoothing the trajectory of the beam horizontally by 17 % whilst retaining the vertical RMS value which was already well-centred and improved the standard deviations at 4 ms by 11 % and 30 % horizontally and vertically respectively, making an improvement to the level of stability reached by operational techniques. This was also achieved with reduced steering magnet currents which is beneficial for power consumption and equipment lifetime.

CONCLUSIONS

The LOCO method builds on the correction technique currently used for beam optics correction on the ISIS accelerator. Through the inclusion of real machine errors, the calculations produce an improvement to beam trajectory fluctuations and the stability of the machine, in comparison to the current technique. This correction is limited by the compactness of the ring and the ability to adjust individual magnets. The minimisation is under-constrained as there are more monitors than magnets, so careful consideration should be given to the choice of elements included. The main magnets in the synchrotron are not individually adjustable and therefore cannot be included in this technique.

The machine matches the ideal model very well, revealing few large errors in the machine. Small errors were corrected with respect to their effects on beam position and indicate that the method is a positive contribution to machine tuning and can also be used as a diagnostic tool to monitor element degradation or adjustments.

Further work to include beam envelope and tune corrections can be incorporated, extending the effect of the measured ORM in setup shifts. Measurements have been taken to include quadrupole corrections in the code and can be included in these future correction attempts.

REFERENCES

[1] J. Safranek, “Linear Optics from Closed Orbits (LOCO): an introduction”, in *ICFA Beam Dyn. Newsl.*, vol. 44, pp. 43-49, Dec. 2007.

[2] M. J. McAteer, “Linear optics measurements in the Fermilab booster and the CERN PS booster”, Ph.D. thesis, Phys. Dept, The University of Texas at Austin, USA, 2014.

[3] M. Aiba and M. Böge, “Local orbit response matrix measurement at SLS”, in *Proc. 6th Int. Particle Accelerator Conf. (IPAC’15)*, Richmond, VA, USA, May 2015, pp. 1713-1715. doi:10.18429/JACoW-IPAC2015-TUPJE044

[4] Methodical Accelerator Design, http://madx.web.cern.ch

[5] D. J. Adams, K. Tilley and C. M. Warsop, “The ISIS synchrotron beam control and study programme”, in *Proc. 1999 Particle Accelerator Conf. (Cat.No.99CH36366)*, New York, NY, USA, 1999, pp. 2199-2201 vol.3. doi:10.1109/PAC.1999.794419

[6] B. Jones, D. Adams, B. Pine, H. Smith and C. Warsop, “Progress on beam measurement and control systems for the ISIS synchrotron”, in *Proc. 5th Int. Particle Accelerator Conf. (IPAC’14)*, Dresden, Germany, June 2014, pp. 3700-3702. doi:10.18429/JACoW-IPAC2014-THPME181

ISBN: 978-3-95450-222-6 ISSN: 2673-5350 doi:10.18429/JACoW-IBIC2020-TUPP28

SIMULATION OF CHERENKOV DIFFRACTION RADIATION FOR VARIOUS RADIATOR DESIGNS

K. Lasocha*[1], T. Lefevre, N. Mounet, A. Schloegelhofer[2], CERN, Geneva, Switzerland
D. M. Harryman, JAI, Royal Holloway, University of London, Egham, Surrey, UK
[1]also at Institute of Physics, Jagiellonian University, Krakow, Poland
[2]also at TU Wien, Vienna, Austria

Abstract

Studies performed during the last few years at different facilities have indicated that the emission of Cherenkov Diffraction Radiation (ChDR) can be exploited for a range of non-invasive diagnostics. The question remains of how to choose an optimal dielectric material and which radiator shapes give the most promising results. This contribution presents a semi-analytical framework for calculating the electromagnetic field of a charged particle beam, taking into consideration its interaction with surrounding structures. It allows us to directly compute ChDR at arbitrary probe positions inside the radiator. Several configurations will be discussed and presented, including flat and cylindrical radiators of various dimensions and electrical properties, as well as multilayer structures obtained by adding coatings of metallic nanolayers.

INTRODUCTION

A decade after the discovery of Cherenkov radiation [1], Ginzburg and Frank [2] studied the radiation emitted by a particle moving along the axis of an infinitely long evacuated tunnel surrounded by a dielectric medium. During the following decades Linhart [3] and Ulrich [4] described a similar phenomenon associated with a particle moving parallel to the surface of a dielectric half space. These two are the initial examples of Cherenkov Diffraction Radiation (ChDR), which describes the emitted radiation of a charged particle passing in the close vicinity of a dielectric medium and having a velocity greater than the phase velocity of light in that medium.

Recently, the possibilities which ChDR brings to non-invasive beam diagnostics have been extensively investigated, with the first observation of incoherent radiation, using GeV electrons and positrons at Cornell [5, 6]. What followed were designs of beam position monitors [7] as well as bunch length monitors [8] based on the coherent radiation from short bunches. In parallel more refined radiation models have been developed [9, 10]. In addition, several accelerator facilities across the world have confirmed the feasibility of observing ChDR [11–13].

All this interest motivates the need of developing a tool for quantitative description of ChDR for real case scenarios. Most analytic models serve well only in a limited spectrum of cases, due to the simplicity of the considered radiators. On the other hand, more flexible numerical simulations are very time consuming, especially if the radiator components differ significantly in size. The aim of this contribution is to present a semi-analytical approach, which is based on numerical calculations of the beam field propagating across surrounding materials, according to constraints set by the Maxwell equations. The presented procedure describes radiators infinite in the direction of beam propagation, but gives the possibility of studying complex multilayer structures orthogonal to the direction of beam propagation. The proposed method should be treated as a natural extension of a framework for beam impedance calculations, developed at CERN [14].

CYLINDRICAL GEOMETRY

We shall start by considering the geometry presented in Fig. 1 which is described using cylindrical coordinates r, θ and s. A charged particle travels with the velocity $v = \beta c$ along the s axis in the centre of an axisymmetric structure, consisting of an arbitrary number of layers. Each layer has its own permittivity ϵ_i and permeability μ_i, which may be frequency dependent. The central layer is constrained to be vacuum, but the subsequent layers may be any material, with the outermost layer extending to infinity.

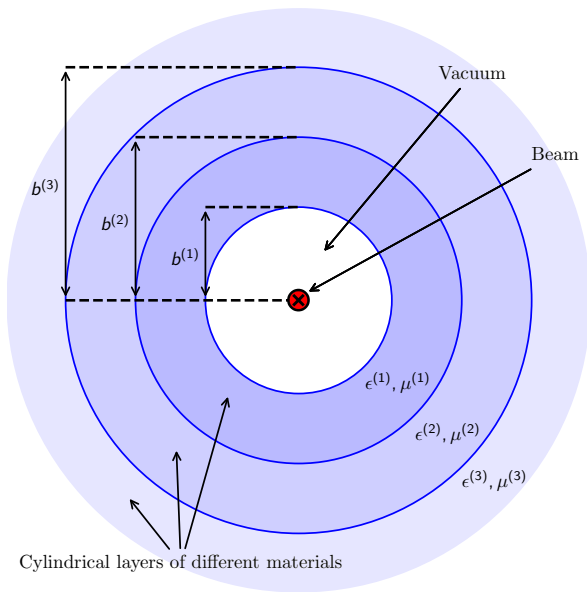

Figure 1: Cylindrical geometry with concentric layers of different materials. The beam travels along the axis perpendicular to the page.

* kacper.lasocha@cern.ch

Content from this work may be used under the terms of the CC BY 3.0 licence (© 2020). Any distribution of this work must maintain attribution to the author(s), title of the work, publisher, and DOI

ISBN: 978-3-95450-222-6 ISSN: 2673-5350 doi:10.18429/JACoW-IBIC2020-TUPP28

Content from this work may be used under the terms of the CC BY 3.0 licence (© 2020). Any distribution of this work must maintain attribution to the author(s), title of the work, publisher, and DOI

The longitudinal component of the electric and magnetic field ($E_s^{(p)}$ and $H_s^{(p)}$) in a probe point at a distance r from the axis, located in layer p, have the following explicit form in frequency domain:

$$E_s^{(p)} = e^{-jks}\left[C_{Ie}^{(p)} I_0(\nu^{(p)} r) + C_{Ke}^{(p)} K_0(\nu^{(p)} r)\right], \quad (1)$$

where I_0 and K_0 are zero-order modified Bessel functions of first and second kind respectively, $k = \frac{\omega}{v}$ is a wave number and $\nu^{(p)} = |k|\sqrt{1-\beta^2\epsilon_p\mu_p}$ is a radial propagation constant. This follows from [14, Eq. (1.85)] by noting that for a centered beam all modes apart from $m = 0$ do not contribute to the field. The complex coefficients $C_{Ie}^{(p)}$ and $C_{Ke}^{(p)}$ depend on frequency, particle velocity and the considered structure. Their explicit calculation is thoroughly shown in [14, Ch. 1.4]. What should be emphasized, is that their computation involves only a small number of Bessel function evaluations and matrix multiplications, and is therefore very fast. The longitudinal component of the magnetic field can be expressed in a similar manner, but it turns out that $H_s^{(p)} = 0$.

Based on Maxwell's equations we can also derive the transverse component of both fields [14, Appx. E.1.1]. The only non-zero transverse components will be E_r and H_θ. In order to derive the time integrated radiated energy, we define

$$\vec{P}(\omega) = \Re\left[\vec{E}(\omega) \times \vec{H}^*(\omega)\right],$$

where $\vec{H}^*$ is the complex conjugate of the magnetic field $\vec{H}$ and $\Re[\cdot]$ denotes the real part of a vector. The energy radiated outside a given volume V that contains the beam, is given by

$$\Delta E = \frac{1}{2\pi}\int d\omega \oiint_{\mathbf{A}=\partial V} \vec{P}(\omega)\cdot d\mathbf{A}, \quad (2)$$

as a consequence of the Poynting theorem.

FLAT GEOMETRY

The next geometry considered is a flat geometry described using Cartesian coordinates x, y and s. This consists of a series of infinitely long (in s direction) and wide (in x direction) plates, each having its own thickness, permittivity ϵ_i and permeability μ_i. A charged particle travels in the s direction inside the central layer, which again we constraint to be vacuum. It is also assumed that the top and bottom outermost layers are infinitely thick. An example of such a structure is presented in Fig. 2.

Let us pick a probe point $P = (x, y, s)$ placed in layer p. The longitudinal component of the electric and magnetic field are of the form [14, Eq. (1.180,1.181)]:

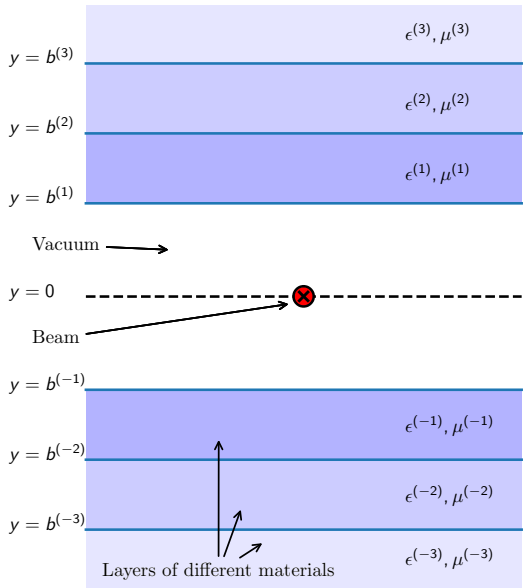

Figure 2: Flat geometry with parallel layers of different materials. The beam travels perpendicular to the page in the plane $y = 0$.

$$E_s^{(p)} = e^{-jks} \times \int_0^\infty dk_x \cos(k_x x)\left[C_{e+}^{(p)}(k_x)e^{k_y^{(p)}y} + C_{e-}^{(p)}(k_x)e^{k_y^{(p)}y}\right],$$

$$H_s^{(p)} = e^{-jks} \times \int_0^\infty dk_x \sin(k_x x)\left[C_{h+}^{(p)}(k_x)e^{k_y^{(p)}y} + C_{h-}^{(p)}(k_x)e^{k_y^{(p)}y}\right],$$

where $k_y^{(p)} = \sqrt{k_x^2 + \nu^{(p)2}}$ is the vertical wave number, with $\nu^{(p)}$ defined as in the previous section. Coefficients $C_{e\pm}, C_{h\pm}$ again depend on k_x, frequency and the properties of all the layers, but this time their calculation requires a time-consuming matrix inversion (all the related details can be found in [14, Ch. 1.5]). On top of that, due to the complicated form of the integrand, the integration needs to be performed numerically. This all results in much slower field calculations than in the case of cylindrical geometry. The transverse components of the electromagnetic field can be derived from the longitudinal ones in the classical way, see [14, Appx. E.2.1]. Having all the components we can calculate the radiated energy in the same way as in the previous section.

CHERENKOV DIFFRACTION RADIATION

The geometries discussed in the two previous sections are suitable to study the properties of ChDR. To do this we choose the outermost layer to be a dielectric and place the

ISBN: 978-3-95450-222-6 ISSN: 2673-5350 doi:10.18429/JACoW-IBIC2020-TUPP28

probe point at a given depth inside this layer. The dielectric layer is set to be infinitely thick in order to avoid reflections from its outermost surface. By creating a grid of probe points, we are able to estimate either a total radiated energy, using Eq. (2), or the spatial distribution of the radiation.

Figure 3 shows the spectral distribution of the energy emitted by a point particle with a charge equivalent to 1 C, which travels a distance of 1 m along the axis of a vacuum cylinder of radius r. The cylinder is surrounded by an infinite dielectric with a refractive index of $n = 2$. The velocity of the point particle corresponds to $\gamma = 10$. As a reference, we plot the distribution for Cherenkov radiation emitted by a particle passing directly through the medium, obtained from the classical Frank-Tamm formula [15]:

$$\frac{dE}{dx} = \frac{q^2}{4\pi} \int_{v > \frac{c}{n(\omega)}} \mu(\omega)\omega\left(1 - \frac{c^2}{v^2 n^2(\omega)}\right) d\omega.$$

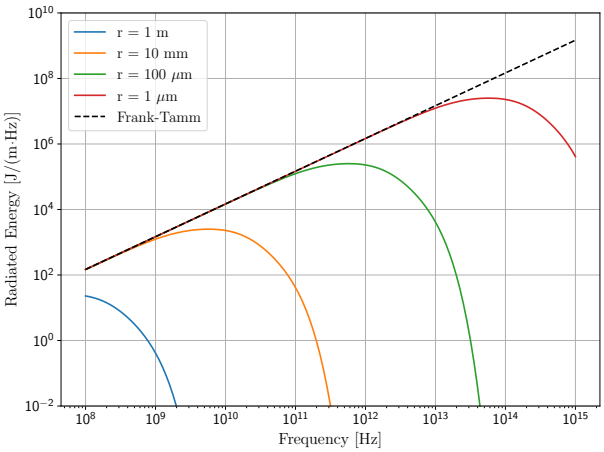

Figure 3: Comparison between Frank-Tamm formula (Cherenkov radiation) and Eq. (2) with decreasing chamber radii (ChDR).

As can be seen in Fig. 3 the calculated distributions follow the Frank-Tamm formula for $\omega \ll \frac{\gamma c}{r}$. On the other hand, for $\omega \gg \frac{\gamma c}{r}$ the amount of radiated energy drops abruptly. This is in agreement with the notion of effective radius, that is the distance over which the particle's field interacts with the surrounding medium, determined in [10] to be $r_{\text{eff}} = \frac{\gamma c}{\omega}$. The presented model based on beam field calculations yields not just qualitative, but quantitative results, which coincide with the well-established Frank-Tamm formula.

SPATIAL DISTRIBUTION OF CHDR

A dense grid of probe points, in which we calculate EM field components, allows us to estimate the spatial distribution of the radiation and monitor which parts of the radiator interact with the beam. To illustrate such an analysis we take the example of one of the experiments reported in [5]. A flat radiator made of fused silica ($n = 1.45$) mounted above of the beam is considered, with a parallel bunched beam of velocity corresponding to $\gamma \approx 10373$. We consider four different vertical impact parameters, that is to say the distance between the axis of the beam and radiator surface: 0.9 mm, 1.08 mm, 1.32 mm and 1.38 mm. A series of probes is placed 2 mm inside the dielectric at different x offset with respect to the beam. For every probe we calculate the vector $\vec{P}(\omega)$ in order to estimate the radiation intensity. The y component of this vector is convoluted with the transverse bunch profile, which is assumed to be a 2-D Gaussian with $\sigma_x = 1.7$ mm, $\sigma_y = 170\,\mu$m. These values correspond to the beam parameters of [5]. Note that in order to convolute the results from this particle distribution, simulations are run with impact parameters different from the four mentioned above. The results are plotted in Fig. 4 for $\omega = 600$ THz and can be compared with [5, Fig. 4].

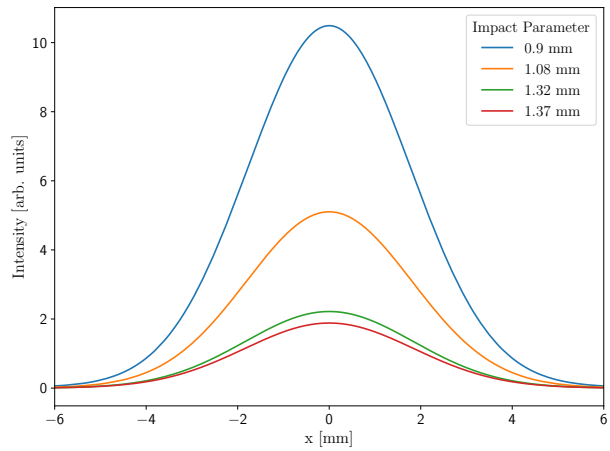

Figure 4: Horizontal profile of ChDR (600 THz) at a depth of 2 mm inside the flat dielectric.

It is interesting to see how the width of the discussed distribution increases with the impact parameter, as this can be compared with the experimental observations [6]. The corresponding values are given in terms of Full Width at Half Maximum (FWHM) in Table 1.

Table 1: Full Width at Half Maximum of ChDR (600 THz) Horizontal Profile at a Depth of 2 mm Inside the Flat Dielectric

Impact Par. [mm]	FWHM [mm]
0.9	4.19
1.08	4.25
1.32	4.33
1.37	4.35

METALLIC NANOLAYERS

The presence of a thin metallic layer between the beam and the dielectric may lead to the excitation of Surface Plasmon Polaritons (SPP) on the metal-vacuum and metal-dielectric intersection. As a consequence, one observes the creation

Content from this work may be used under the terms of the CC BY 3.0 licence (© 2020). Any distribution of this work must maintain attribution to the author(s), title of the work, publisher, and DOI

ISBN: 978-3-95450-222-6 ISSN: 2673-5350 doi:10.18429/JACoW-IBIC2020-TUPP28

Content from this work may be used under the terms of the CC BY 3.0 licence (© 2020). Any distribution of this work must maintain attribution to the author(s), title of the work, publisher, and DOI

of monochromatic Cherenkov radiation with significantly enhanced intensity for particular frequencies [16].

We shall demonstrate this effect with the following setup: a point particle with a charge of 11 fC travels with a velocity corresponding to $\gamma \approx 118.42$ inside a thin silver cylinder surrounded by an infinite layer of a dielectric with a refractive index of $n = 1.45$. The cylinder radius is 200 nm and the silver layer is 80 nm thick. The radius and beam properties correspond to typical beam parameters and dimensions of a Dielectric Laser Accelerator (DLA), reported in [17]. Considering a point charge instead of a distributed electron bunch is a simplification which will require further correction depending on the bunch profile.

As Eq. (1) requires knowledge of the permittivity of silver, we adopt the Drude model [18]

$$\epsilon = \epsilon_\infty - \frac{\omega_p^2}{\omega^2 - j\gamma\omega},$$

where for silver $\epsilon_\infty = 5.3$ (high-frequency permittivity limit), $\omega_p = 1.39 \times 10^{16}$ rad/s (plasma frequency) and $\gamma = 3.2 \times 10^{13}$ Hz (damping constant), as given in [16].

In Fig. 5 we present the spectral distribution of the energy radiated in the case of just the bare dielectric, calculated as described in the previous sections, and in the case of an added 80 nm thick silver coating. As we see, the presence of the metallic layer has transformed a broad ChDR spectrum into a monochromatic visible radiation of significantly higher intensity at that wavelength. The thickness of the metal layer was chosen in order to maximize this effect.

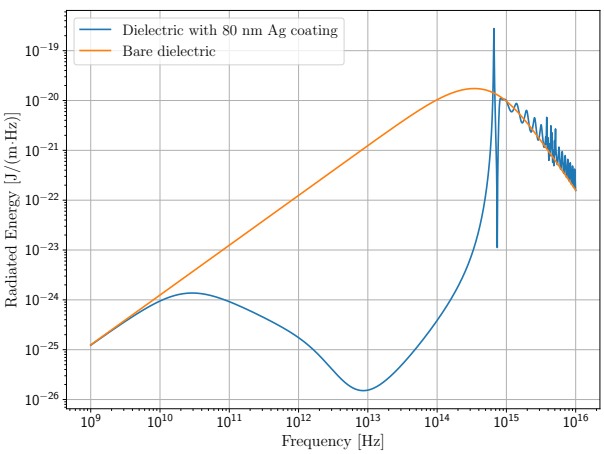

Figure 5: Surface Plasmon Polariton resonance at 660 THz in the geometry compatible with Dielectric Laser Accelerator described in [17].

CONCLUSION

The described theory has been implemented in the form of C++ code with a Python wrapper included. In addition, actions toward integrating it with Polarisation Currents Approach (PCA) [19] to form a single, independent simulation package are ongoing. In the course of this integration a comparison between PCA and the presented approach will be performed to validate the spectral properties of the radiation.

The approach presented in this contribution facilitates calculation of ChDR spectral distributions. In particular, it enables the effect of using multilayer radiators composed of various materials (metals, dielectrics, lossy media) to be studied. The parameters of these layers may be then tuned in order to either maximize the expected radiation output or reshape the spectral distribution. Contrary to previous models, this method provides the spatial, rather than angular, distributions of the radiation. This allows investigating how, and over which volume, the beam field interacts with the materials in different layers and generates radiation.

For applications in beam instrumentation, depending on the accelerator parameters and environment, coating the surface of the dielectric with metallic layers might be useful. It can for example prevent the building up of electron cloud on the dielectric in circular machines. Thin metallic layers, as discussed in this paper would also provide a way to produce a more monochromatic Cherenkov emission through the generation of surface plasmonic wave. In addition, within the model's capabilities is evaluating the expected photon flux, assessing beam position monitors sensitivity, or testing the impact of unsought oxidation of radiator elements.

ACKNOWLEDGEMENTS

The authors would like to express their gratitude for the stimulating discussions with D. Alves.

REFERENCES

[1] P. Čerenkov, "Visible radiation produced by electrons moving in a medium with velocities exceeding that of light", *Physical Review*, vol. 52, no. 4, p. 378, 1937.

[2] V. L. Ginzburg and I. M. Frank, *Doklady Akad. Nauk S.S.S.R.*, vol. 56, no. 699, 1947.

[3] J. G. Linhart, "Čerenkov Radiation of Electrons Moving Parallel to a Dielectric Boundary", *Journal of Applied Physics*, vol. 26, no. 5, pp. 527–533, 1955.

[4] R. Ulrich, "Zur Cerenkov-Strahlung von Elektronen dicht über einem Dielektrikum", *Zeitschrift fur Physik*, vol. 194, pp. 180–192, 1966.

[5] R. Kieffer *et al.*, "Direct Observation of Incoherent Cherenkov Diffraction Radiation in the Visible Range", *Phys. Rev. Lett.*, vol. 121, p. 054802, 2018. doi:10.1103/physrevlett.121.054802

[6] R. Kieffer *et al.*, "Generation of incoherent cherenkov diffraction radiation in synchrotrons", *Phys. Rev. Accel. Beams*, vol. 23, p. 042803, 2020. doi:10.1103/PhysRevAccelBeams.23.042803

[7] T. Lefevre *et al.*, "Cherenkov Diffraction Radiation as a tool for beam diagnostics", in *Proc. IBIC'19*, Malmö, Sweden, Sep. 2019, paper THAO01, pp. 660. doi:10.18429/JACoW-IBIC2019-THAO01

ISBN: 978-3-95450-222-6 ISSN: 2673-5350 doi:10.18429/JACoW-IBIC2020-TUPP28

[8] A. Curcio *et al.*, "Noninvasive bunch length measurements exploiting Cherenkov diffraction radiation", *Phys. Rev. Accel. Beams*, vol. 23, p. 022802, 2020. doi:10.1103/PhysRevAccelBeams.23.022802

[9] M. Shevelev and A. Konkov, "Peculiarities of the generation of Vavilov-Cherenkov radiation induced by a charged particle moving past a dielectric target", *J. Exp. Theor. Phys.*, vol. 118, pp. 501–511, 2014. doi:10.1134/S1063776114030182

[10] D. V. Karlovets and A. P. Potylitsyn, "Universal description for different types of polarization radiation", 2009. arXiv:0908.2336

[11] D. M. Harryman *et al.*, "First Measurements of Cherenkov-Diffraction Radiation at Diamond Light Source", in *Proc. IBIC'19*, Malmö, Sweden, Sep. 2019, paper WEPP037, pp. 624. 10.18429/JACoW-IBIC2019-WEPP037

[12] K. V. Fedorov, Y. M. Saveliev, A. N. Oleinik, P. Karataev, A. Potylitsyn, and T. H. Pacey, "Experimental Observation of Submillimeter Coherent Cherenkov Radiation at CLARA Facility", in *Proc. IBIC'19*, Malmö, Sweden, Sep. 2019, paper TUCO02, pp. 261. doi:10.18429/JACoW-IBIC2019-TUCO02

[13] S. Ninomiya *et al.*, "Measurement of Cherenkov Diffraction Radiation from a Short Electron Bunches at t-ACTS", in *Proc. IPAC'19*, Melbourne, Australia, May 2019, pp. 2536–2538. doi:10.18429/JACoW-IPAC2019-WEPGW031

[14] N. Mounet, "The LHC Transverse Coupled-Bunch Instability", Ph.D. Thesis, École Polytechnique Fédérale de Lausanne, Lausanne, Switzerland, 2012.

[15] I. Frank and I. Tamm, "Coherent visible radiation of fast electrons passing through matter", *Compt. Rend. Acad. Sci. URSS*, vol. 14, no. 3, pp. 109–114, 1937.

[16] S. Liu *et al.*, "Surface Polariton Cherenkov Light Radiation Source", *Phys. Rev. Lett.*, vol. 109, p. 153902, 2012. doi:10.1103/PhysRevLett.109.153902

[17] E. Peralta *et al.*, "Demonstration of electron acceleration in a laser-driven dielectric microstructure", *Nature*, vol. 503, p. 91, 2013. doi:10.1038/nature12664

[18] P. Drude, "Zur Elektronentheorie der Metalle; II. Teil. Galvanomagnetische und thermomagnetische Effecte", *Annalen der Physik*, vol. 308, pp. 369–402, 1900.

[19] D. M. Harryman *et al.*, "Properties of Cherenkov Diffraction Radiation as Predicted by the Polarisation Currents Approach for Beam Instrumentation", presented at the IBIC'20, Santos, Brazil, Sep. 2020, paper THPP05, this conference.

Content from this work may be used under the terms of the CC BY 3.0 licence (© 2020). Any distribution of this work must maintain attribution to the author(s), title of the work, publisher, and DOI

ISBN: 978-3-95450-222-6 ISSN: 2673-5350 doi:10.18429/JACoW-IBIC2020-TUPP32

Content from this work may be used under the terms of the CC BY 3.0 licence (© 2020). Any distribution of this work must maintain attribution to the author(s), title of the work, publisher, and DOI

DEVELOPMENT OF NOVEL NON-DESTRUCTIVE 2D AND 3D BEAM MONITORING DETECTORS AT THE BERN MEDICAL CYCLOTRON*

C. Belver-Aguilar†, T. S. Carzaniga, A. Gsponer, P. Häffner, P. Scampoli[1],
M. Schmid, S. Braccini, Albert Einstein Center for Fundamental Physics (AEC),
Laboratory of High Energy Physics (LHEP), University of Bern, Bern, Switzerland
G. Molinari, TERA Foundation, Novara, Italy
[1]also at Department of Physics "Ettore Pancini", University of Napoli Federico II, Naples, Italy

Abstract

The Laboratory for High Energy Physics (LHEP) at the University of Bern is developing novel beam monitoring detectors for the 18 MeV medical cyclotron in operation at the Bern University Hospital (Inselspital). A 2D non-destructive beam monitor — named π^2 — was developed, based on a thin aluminium foil coated with P47 scintillating material and a camera. It measures the transverse position, shape, and intensity of the beams for several applications, as radiation hardness or radioisotope production studies. This detector allows the processing of data in real time and a reconstruction of the transverse phase space. Based on the π^2, a first prototype of a 3D beam monitoring detector — named π^3 — was conceived, constructed, and tested. It is based on the same scintillating foil mounted on a movable support with a miniaturized camera. The π^3 detector allows for the study of the beam evolution along a beam line, even inside a magnet, and the reconstruction of the beam envelope. In this paper, we report about the design, construction and beam tests performed with these two detectors. Further developments will be also presented and discussed.

INTRODUCTION

Beam monitoring plays a crucial role in both the commissioning and operation of particle accelerators. For some medical cyclotron applications, like the irradiation of small and expensive solid targets [1], non-destructive beam monitors are essential.

At the Bern medical cyclotron, three different beam monitors have been developed by the LHEP. The first one, named UniBEaM [2], is used to measure the beam transverse profile by means of a moving scintillating fiber. The second one is the π^2, a detector based on a fixed scintillating foil and a camera, which allows to measure the beam spot in 2D. The third one is the first prototype of an evolution of the π^2 detector, called π^3, where both the scintillating foil and the camera are mounted in a moving support to allow assessing the beam evolution along the beam path.

In this paper, the main features and beam tests of the π^2 and π^3 beam monitors are reported. Beam tests were performed using the 6 m long Beam Transfer Line (BTL) [3] and the 18 MeV proton beam delivered by the Bern medical cyclotron.

* Work partially supported by the Swiss National Science Foundation (SNSF). Grants: 200021_175749, CRSII5_180352, CR23I2_156852
† carolina.belver@lhep.unibe.ch

THE π^2 BEAM MONITOR

The π^2 hardware, based on a phosphor screen and a camera, is a common design which was already used in some other accelerator facilities, for example at the Korean Institute of Radiological and Medical Sciences [4]. However, the pre-processing and analysis software that has been implemented in our detector represents a step forward in the analysis of the images provided by this type of detectors: it is being developed to perform real-time measurements of beam position, size and current, but also phase space representation and beam emittance measurement, as well as tuning of the BTL magnet currents.

The π^2 detector, as shown in Fig. 1, consists of a cerium- and terbium-doped yttrium orthosilicate (Y_2SiO_5:Ce,Tb) phosphor screen (P47) and a camera, to control the beam position and beam size during a proton irradiation. This detector can monitor beam currents in the range between pA and several μA.

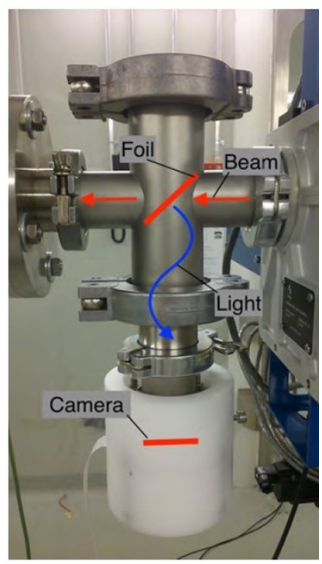

Figure 1: The KF40 four way pipe that supports the π^2 detector. The positions of the scintillating foil and camera are shown in red.

The scintillating screen is placed at the center of a KF40 four way pipe with a tilt angle of 45° with respect to the beam path. It has a diameter of 20 mm, and consists of a 0.8 μm aluminum foil coated with a 1 μm layer of P47. An optimal heat dissipation is achieved by gluing the thin

ISBN: 978-3-95450-222-6 ISSN: 2673-5350 doi:10.18429/JACoW-IBIC2020-TUPP32

aluminum foil onto an aluminum support with SikaPower 1548 glue. A remotely controlled pneumatic system is used for inserting and extracting the phosphor screen from the beam path during beam operations [5].

The camera used for this detector is a Raspberry Pi Camera Module V2 [6], which is equipped with a 8 megapixel CMOS sensor [7]. It is placed inside a cylinder made of polyoxymethylene (POM) for neutron shielding, as shown in Fig. 1. The size of the camera is 4.6 mm (diagonal). The camera can capture images with a resolution of 3280 × 2464 pixels. It can also record videos with a resolution of 1920 × 1080 pixels and a maximum frame rate of 90 FPS.

The π^2 software

A Python program has been developed for image preprocessing and data analysis. The integrated software allows for monitoring on-line several beam parameters. The main functions are:

Real-time view of the 2D beam spot This mode is very useful when tuning the beam, and has the possibility of streaming the camera output over the network. A computer connected to the LAN receives the video stream with a latency of about 2–3 seconds.

Evaluation of beam position, beam size and beam current The analysis software allows for the correction of the perspective of the captured image due to the tilted position of the scintillating foil with respect to the beam. It also converts pixels to mm. Furthermore, a brightness value, between 0 and 255, is assigned to each image pixel to assess the total intensity, which is then normalized to the camera gain and exposure time in order to determine the beam current. In particular, the range of beam currents at which a linear response of the π^2 can be expected was studied at the BTL of the Bern cyclotron. Results are shown in Fig. 2, where a good linearity was found from ~ 500 nA to ~ 2 µA. A Graphical User Interface (GUI), shown in Fig. 3, has been developed to measure beam position, beam size and beam current in real-time. It allows to start a live view, capture and show an image by setting an automatic or manual exposure time, and show the Gaussian fit of the projections in both the horizontal and vertical plane. A measurement of the total and normalized intensities, as well as the mean and FWHM of both fits are also shown.

Tuning of the BTL magnet currents with the π^2 When performing experiments at the BTL, setting up the 4 quadrupole currents is usually very time consuming. In order to ease the tuning of the BTL optics, a machine learning library of Python (scikit-learn) has been used to train a multi-output linear regression model providing the optics configuration required for a given beam width in both the horizontal and vertical planes. The beam transport matrix through a drift space is used to predict the optics configuration at any point along the BTL. This first model has been tested for beam sigmas between 2 mm and 10 mm, with promising results.

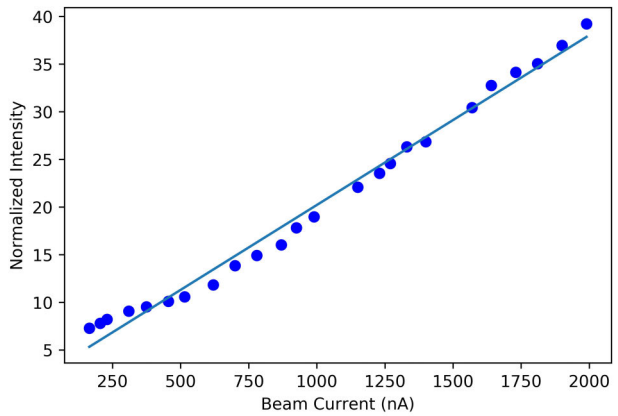

Figure 2: Normalized intensity measured with the π^2 as a function of the beam current.

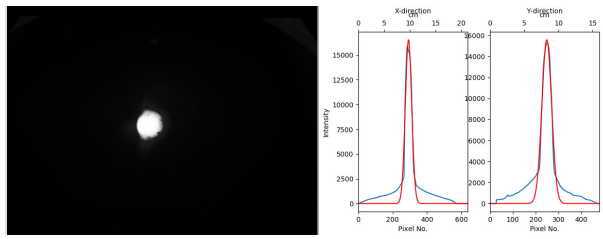

Figure 3: Screenshot of the π^2 GUI, showing the 2D beam cross-section (left) and the projections in both the horizontal and vertical planes (right).

Phase space reconstruction A study on the reconstruction of the transverse beam phase space based on the projections of the 2D beam spot is ongoing. The tomography method is used in the software. Phase space tomography is based on the reconstruction of the transverse phase space in each plane by using several projections at different angles. The quadrupole scan method is used for taking beam projections at different rotation angles, and the filtered back projection technique reconstructs back the phase space.

THE π^3 BEAM MONITOR

The π^3 beam monitor is based on a scintillating foil mounted on a moving support together with a miniaturized camera, which allows to reconstruct the beam distribution along the beam path, providing either an online video or a graphical reconstruction of the beam envelope. At the Bern medical cyclotron, the π^3 first prototype has been used to characterize the beam inside the PET-Mini Beamline (MBL) [8]. The MBL consists of a movable ensemble of one quadrupole doublet and two embedded steering magnets, mounted on a beamline of ~ 1 m long. This compact instrument will be used to irradiate solid targets and produce non-standard radioisotopes for medical and nuclear physics using a solid target.

Content from this work may be used under the terms of the CC BY 3.0 licence (© 2020). Any distribution of this work must maintain attribution to the author(s), title of the work, publisher, and DOI

ISBN: 978-3-95450-222-6 ISSN: 2673-5350 doi:10.18429/JACoW-IBIC2020-TUPP32

Content from this work may be used under the terms of the CC BY 3.0 licence (© 2020). Any distribution of this work must maintain attribution to the author(s), title of the work, publisher, and DOI

The main components of the π^3 detector are shown in Fig. 4. The scintillating foil is placed in one of the edges of the movable support. As in the case of the π^2, it consists of an aluminium foil coated with P47 and a camera. The camera used for this first prototype is a KKMoon 5 mm 2 m Mini Digital USB Endoscope Inspection Camera, with a diameter of 5 mm. The resolution of this camera is 640×480 pixels and it can record videos at 8 frames/second. The USB port of the camera is connected via a vacuum feedthrough to a Raspberry Pi computer, which is used for data acquisition. A pulley system is used to pull the cable of the miniaturized camera when it moves backwards along the MBL.

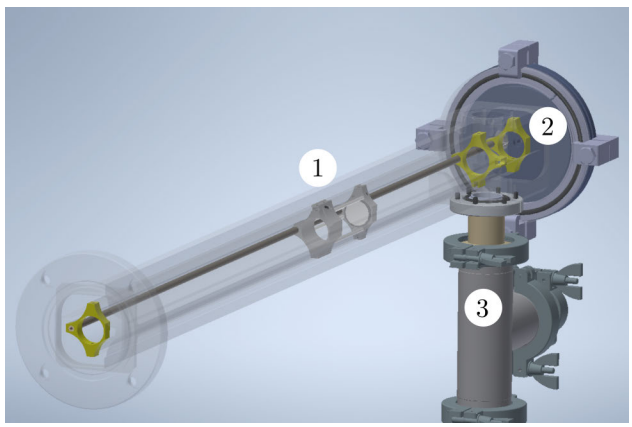

Figure 4: 3D view of the π^3 detector mounted inside of the MBL beampipe. The moving support (1), the motor (2) and the tube for the pulley system (3) are visible.

The movable support featuring the scintillating foil and the camera is connected to a long endless screw located all along the beam pipe of the MBL. This screw is linked to a stepper motor, which moves the support 1 mm per revolution and can perform very small steps down to 1/100 rotation. A thermal gap filler pad has been used between the camera and the support to allow heat conduction and prevent image degradation due to overheating of the camera.

The π^3 software

During a measurement, the support is moved for a given distance and the camera view is recorded at the same time. Images can be analyzed by the π^3 software after pre-processing is applied, including a perspective correction and the application of a circular mask to cut off parts of the image which are not on the sensitive area of the scintillating screen, therefore reducing image noise. The goal of the analysis program, written in Python, is to fit a Gaussian distribution to all the individual images to reconstruct the beam shape at each acquired position inside the MBL. This Gaussian distribution describes the beam by means of the beam center and the covariance matrix. From the diagonal of the covariance matrix, the standard deviation σ in both the horizontal and vertical planes can be calculated, which are directly connected to the β-function commonly used in beam dynamics.

First Beam Tests

The π^3 prototype was installed in the BTL of the Bern cyclotron. The π^2 detector was also used to study the beam before entering to the MBL, as it shown in Fig. 5.

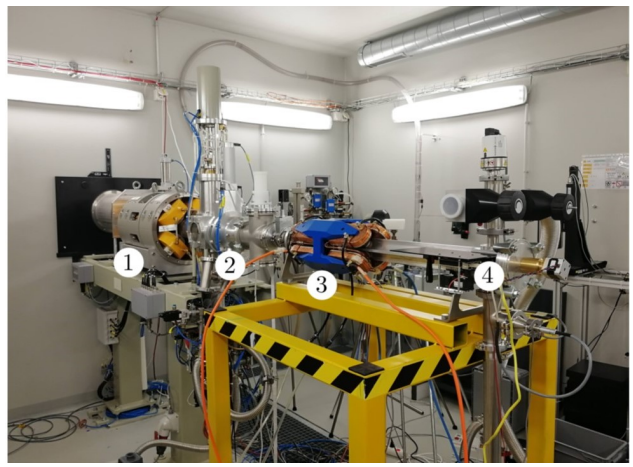

Figure 5: The setup for beam tests of the π^3 detector at the BTL of the Bern medical cyclotron: (1) one of the two BTL quadrupole doublets, (2) the π^2 detector, (3) the integrated magnets of the MBL, and (4) the controller and motor of the π^3 detector are visible.

The first tests were devoted to study the performance of the detector considering different optics configurations: (1) disabling the MBL, which is equivalent to move the π^3 detector along a drift space, (2) when a focalized beam enters the MBL, and (3) when a flat beam enters the MBL. In case (3), the two quadrupoles of the MBL are used to focalize the beam at the end of the line. The results are shown in Fig. 6.

The π^3 beam monitor has been able to measure the evolution of the beam width along the MBL, for a length of 660 mm, in several magnet configurations. For the first configuration (Fig. 6, left), the beam was focused by the BTL magnets, whereas the MBL magnets were disabled. In this configuration, the foil and the camera were moved along a drift space, and the sigma increase in both planes as expected from the transport matrix along a drift space. In the second case (Fig. 6, center), the beam is focused at the MBL entrance by the BTL magnets and refocused by the MBL magnets. In this case, the sigma inside the MBL shows the effect of the MBL quadrupoles, both with a current of 40 A. The net effect of the two quadrupoles is a small focusing of the beam in the vertical plane, as compared with the drift space, whereas in the horizontal plane it remains the same. In the third case, when a flat (not focalized) beam enters the MBL, the MBL magnets are able to slightly reduce the beam sigma in both planes, when the first quadrupole is disabled and the second one has a current of 75 A.

CONCLUSIONS AND OUTLOOK

Two types of beam monitoring detectors have been developed at the LHEP, both using a scintillating foil and a

ISBN: 978-3-95450-222-6 ISSN: 2673-5350 doi:10.18429/JACoW-IBIC2020-TUPP32

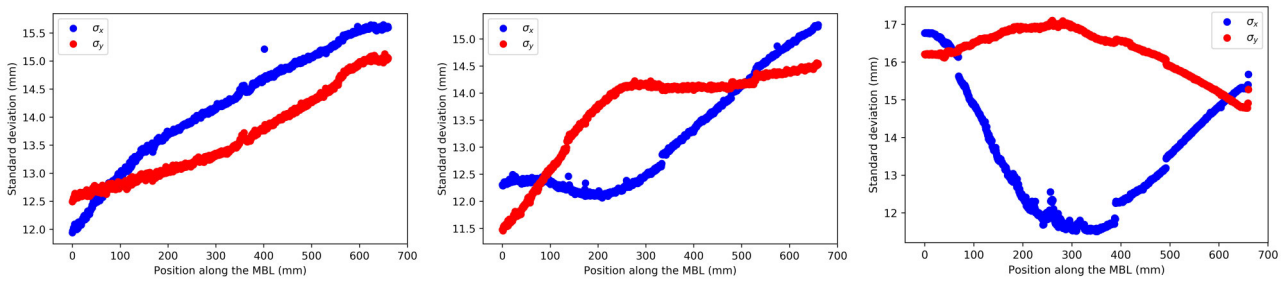

Figure 6: The sigma of the beam measured in both horizontal (red) and vertical (blue) planes, along the MBL length, for three different BTL and MBL magnet configuration: (1) when considering the MBL as a drift space (left), when focusing with the BTL and re-focusing with the MBL magnets (center), and when a flat beam enters the MBL (right).

camera to image the beam cross-section and measure beam position, size and current. The first detector, named π^2, is already used in a daily basis at the BTL of the Bern medical cyclotron. It is used to control the beam in experiments where beam currents from about hundred nA to a few µA are required. A complete Python software and a GUI have been developed for this detector, allowing additional features such as the tuning of the BTL magnet currents on-line and reconstruction of the transverse phase space. The second detector, named π^3, is a first prototype that has been tested with the BTL. The main differences between the π^2 and the π^3 detectors are the movable support of the π^3, which holds together the scintillating foil and the camera, and allowed to study the beam evolution along the MBL, and the location of the camera outside and inside the vacuum chamber, respectively. The results of the first beam tests show that the π^3 monitor can successfully be used to study and understand the effects of the optics of a beam line on an ion beam. Further developments of these two detectors are ongoing.

REFERENCES

[1] S. Braccini, C. Belver-Aguilar, T. S. Carzaniga, G. Dellepiane, P. Haeffner, and P. Scampoli, "Novel Irradiation Methods for Theranostic Radioisotope Production With Solid Targets at the Bern Medical Cyclotron", in *Proc. Cyclotrons'19*, Cape Town, South Africa, Sep. 2019, pp. 127–131. doi:10.18429/JACoW-CYCLOTRONS2019-TUA02

[2] M. Auger, S. Braccini, T. S. Carzaniga, A. Ereditato, K. P. Nesteruk, and P. Scampoli. "A detector based on silica fibers for ion beam monitoring in a wide current range", *Journal of Instrumentation*, vol. 11, p. P03027, 2016. doi:10.1088/1748-0221/11/03/p03027

[3] S. Braccini, "The new Bern PET cyclotron, its research beam line, and the development of an innovative beam monitor detector", *AIP Conference Proceedings*, vol. 1525, p. 144–150, 2013. doi:10.1063/1.4802308

[4] S. Y. Noh, S. D. Chang, J. G. Hwang, G. Hahn, and T. K. Yang, "The Development of Scintillating Screen Detector for Beam Monitoring at the KHIMA Project", in *Proc. IPAC'16*, Busan, Korea, May 2016, pp. 244–247. doi:10.18429/JACoW-IPAC2016-MOPMR010

[5] T. S. Carzaniga, "Study of Scandium Radio-Isotope Production for Theranostics with Medical Cyclotrons", Ph.D. Thesis, University of Bern, Bern, Switzerland, 2019.

[6] Raspberry Pi Camera Module v2, https://www.raspberrypi.org/products/camera-module-v2

[7] CMOS Sensor, https://www.sony-semicon.co.jp/e/products/IS/industry/product.html

[8] M. P. Dehnel, D. E. Potkins, and T. M. Stewart, "An Integrated Self-Supporting Mini-Beamline for PET Cyclotrons", in *Proc. Cyclotrons'13*, Vancouver, Canada, Sep. 2013, paper TUPSH014, pp. 251–253.

Content from this work may be used under the terms of the CC BY 3.0 licence (© 2020). Any distribution of this work must maintain attribution to the author(s), title of the work, publisher, and DOI

ISBN: 978-3-95450-222-6 ISSN: 2673-5350 doi:10.18429/JACoW-IBIC2020-TUPP35

DEVELOPMENT OF A THERMAL RESPONSE MODEL FOR WIRE GRID PROFILE MONITORS AND BENCHMARKING TO CERN LINAC4 EXPERIMENTS

A. Navarro*, F. Roncarolo, CERN, Geneva, Switzerland
M. Sapinski, TERA Fundation

Abstract

The operation of wire grids as beam profile monitors, both in terms of measurement accuracy and wire integrity, can be heavily affected by the thermal response of the wires to the energy deposited by the charged particles. A comprehensive model to describe such interaction has been implemented including beam induced heating, all relevant cooling processes and the various phenomena contributing to the wire signal such as secondary emission and H^- electron scattering. The output from this model gives a prediction of the wire signal and temperature evolution under different beam conditions. The model has been applied to the wire grids of the CERN LINAC4 160 MeV H^- beam and compared to experimental measurements. This successful benchmarking allowed the model to be used to review the beam power limits for operating wire grids in LINAC4.

INTRODUCTION

Wire Grid Profile monitors [1] are extensively used for transverse beam profile measurements in linacs and transfer lines. They consist of a series of thin wires supported on a frame, as shown in Fig. 1. The signal on each wire, used to reconstruct the beam profile, is generated by a combination of different phenomena occurring after the beam-wire interaction, such as direct charge deposition (e.g. stripped electrons stopped in the wire in the case of H^- beams), secondary emission of electrons, thermionic emission of electrons, etc. In most cases these wire grids are movable devices that are inserted into the beam line only when needed.

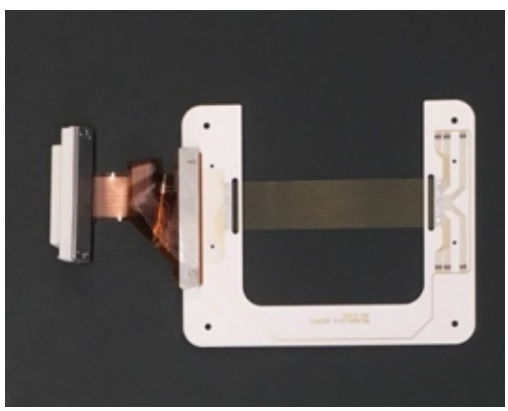

Figure 1: Example of a Wire Grid recently installed in the CERN LINAC4, featuring 40 µm tungsten wires separated by 0.5 mm.

* araceli.navarro.fernandez@cern.ch

For a given wire grid detector design and materials, the beam power density, defined by beam intensity, transverse size and longitudinal structure, can generate high wire temperatures, which may perturb the measurement accuracy or even damage the detector. An example of such an issue is shown in Fig. 2, where a LINAC4 grid suffered overheating of the wires after operation at 160 MeV. This prompted the need for a thorough understanding of the wire temperature evolution in order to correctly retrieve the transverse beam characteristics and set operational limits on the beam power allowed for grid use.

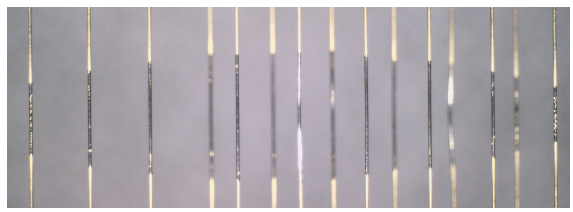

Figure 2: Effect of wire gird heating as observed with an optical microscope, with the individual wires visible over the grey background. The evaporation of the gold coating (dark central area on each wire) is clearly visible, from which one can even infer the beam density profile in the plane of measurement.

The original LINAC4 wire grid design was already supported by theoretical calculations of the thermal response [2, 3]. However, the operational limits defined by this approach clearly did not take into account all phenomena. We therefore adopted and applied another model, initially developed for fast wire scanners [4], with the aim of bench-marking dedicated beam measurements and defining operational limits.

Measuring the temperature evolution of thin wires as they interact with particle beams is challenging. Firstly, the temperature range is broad, from 300 K up to 3000 K, which excludes the use of contact thermometers [5]. Secondly, the small wire diameters makes the use of optical methods [6] very difficult. Bench-marking of the simulations is therefore based on the observation of thermionic currents, occurring at well know temperatures, similar to the studies presented in [7] for measuring stripping foil temperatures.

HEATING MODEL

During operation, the wire temperature increase due to particles energy deposition is accompanied by various cooling processes occurring both during and after the beam passage.

Content from this work may be used under the terms of the CC BY 3.0 licence (© 2020). Any distribution of this work must maintain attribution to the author(s), title of the work, publisher, and DOI

ISBN: 978-3-95450-222-6 ISSN: 2673-5350 doi:10.18429/JACoW-IBIC2020-TUPP35

These include radiative, conductive, thermionic and sublimation cooling. The instantaneous temperature variation during a beam pulse can be written as:

$$\Delta T_{Tot} = \Delta T_{Ht} - \Delta T_{Rd} - \Delta T_{Con} - \Delta T_{Th} - \Delta T_{Sub} \quad (1)$$

Each term of this equation will be discussed in the following subsections.

Wire Heating

The temperature increase generated by N_i particles in a detector volume ΔV can be expressed as:

$$\Delta T_{Ht} = \frac{N_i}{\Delta V \cdot Cp(T) \cdot \rho} \cdot \frac{dE}{dx} \quad (2)$$

where dE/dx is the single particle energy deposition normally well described by the Bethe-Bloch formula [8], and simulated with GEANT4 [9] for these studies. ρ the wire material density and C_p the specific heat capacity (temperature dependent).

Radiative Cooling

Black body radiation, usually the dominant cooling effect in a vacuum, is described by the Stephan-Boltzmann law:

$$\Delta T_{rd} = \frac{\Delta S \cdot \sigma_{SB} \cdot \epsilon(T) \cdot (T^4 - T_0^4)}{C_p(T) \cdot \Delta V \cdot \rho} \cdot \Delta t \quad (3)$$

where σ_{SB} is Stephan-Boltzmann constant , ϵ the emissivity of the material (temperature dependent) and ΔS is the surface of the volume ΔV which radiates during the time Δt.

Thermionic Cooling

Thermionic electron emission occurs when the energy transferred to the electrons by thermal excitation exceeds their work function. The electron emission contributes both to the signal on the wire and to the cooling. The Richardson-Dushman equation describes the current density, J_{Th}, generated in the wire due to thermionic emission:

$$J_{Th} = A_R \cdot T^2 \cdot exp\left(-\frac{\phi}{k_B T}\right) \quad (4)$$

where ϕ is the work function of the material, A_R the Richardson constant and k_b Bolzmann's constant. The resulting cooling contribution, ΔT_{Th} can be written as:

$$\Delta T_{Th} = \Delta S \cdot (\phi + 2\sigma_B T) \cdot \frac{J_{Th}}{C_p(T) \cdot \Delta V \cdot \rho} \cdot \Delta t \quad (5)$$

Conductive Cooling

Thermal conduction is the transfer of heat within a body. The one dimensional heat equation is described as

$$\frac{\partial T}{\partial t} = \alpha(T)\frac{\partial^2 T}{\partial x} \qquad 0 \le x \le L \qquad t \ge 0 \quad (6)$$

where α(T) is related to the thermal conductivity by $\alpha(T) = \lambda(T)/\rho C_p(T)$. In our model, this equation is integrated over the wire length L, with the boundary condition $T(0,t) = T(L,t)$ =300 K.The numerical solution is implemented via a Forward Time Centered Space (FTCS) approximation [10].

Sublimation Cooling

At high temperatures, another cooling term can appear due to energy transfer during the material sublimation process. Without considering the variation in the wire diameter and thus the change in mass and heat capacity, the temperature variation due to sublimation can be written as:

$$\Delta T_{Sub} = -H_{sub} \cdot W(T) \quad (7)$$

where H_{sub} is the enthalpy of sublimation and W(T) the material sublimation rate [11].

INTENSITY MODEL

In addition to the signal generated by thermionic emission according to Eq. (4), which can be significant at high temperatures, each charged particle deposited in the wire also generates a net charge. The electric charge per incident particle ($Q\left(\frac{e}{Proj}\right)$) can be simplified as:

$$Q\left(\frac{e}{Proj}\right) = Q_{dep} + Q_{SE} \quad (8)$$

with Q_{dep} the direct charge deposition and Q_{SE} the contribution from secondary electrons emission.

Charge Deposition

In the general case of accelerated ions with N_p the number of protons in the nucleus and N_e the number of electrons hitting the wire the deposited charge can be estimated as:

$$Q_{dep} = N_p \cdot (1 - BS_p) \cdot (1 - \eta) - N_e \cdot (1 - BS_e) \cdot \mu \quad (9)$$

where BS_p and BS_e refer to the proportion of back-scattered protons and electrons respectively, η the proportion of protons that traverse the wire and μ the proportion of incident electrons that are stopped. For our model, all these parameters were calculated using GEANT4.

Charge due to Secondary Emission

Each charged particle entering or exiting the detector surface has a certain probability of generating secondary electrons (SE) that escape the wire. The model adopted can be summarized as follows:

$$Q_{SE} = N_p \cdot (SEY_{p1} + \eta \cdot SEY_{p2}) \quad (10)$$
$$+N_e \cdot (SEY_{e1} + SEY_{e2} \cdot (1 - \mu)) +$$
$$N_p \cdot BS_p \cdot SEY_{BS_{p1}} + N_e \cdot BS_e \cdot SEY_{BS_{e1}} + Y_D$$

The Secondary Emission Yield (SEY) gives the average number of electrons emitted per incident particle [12]. SEY_p refers to SE generated due to incident protons, while SEY_e refers to SE generated due to incident electrons. The sub indices 1 and 2 represent the wire surfaces, 1 being the first surface encountered by the beam particles and 2 the exiting surface. Y_D is the proportion of SE generated by these secondary electrons themselves and SEY_{BS} accounts for the SE generated by back-scattered particles.

Content from this work may be used under the terms of the CC BY 3.0 licence (© 2020). Any distribution of this work must maintain attribution to the author(s), title of the work, publisher, and DOI

ISBN: 978-3-95450-222-6 ISSN: 2673-5350 doi:10.18429/JACoW-IBIC2020-TUPP35

Content from this work may be used under the terms of the CC BY 3.0 licence (© 2020). Any distribution of this work must maintain attribution to the author(s), title of the work, publisher, and DOI

BENCH MARKING METHOD

Bench-marking of the model is based on the comparison between the wire signals and the beam current measurement from dedicated beam current transformers, for LINAC4 pulses of variable length. The measurements presented here were performed with one of the wire grids located in the 160 MeV LINAC4 section and consisted of 32 wire of 40 µm diameter, made of Tungsten coated with Gold. The main beam parameters are summarized in Table 1.

Table 1: Measured Beam Parameters at the Wire Grid Location, Used as Input for the Simulations

Parameter	Value
Particle	H^- ($N_p = 1$, $N_e = 2$)
Energy	160 MeV
Repetition Rate	0.83 Hz
Beam Position	X_0 = -2.69 Y_0 = −2.64 mm
Beam Size	σ_x = 0.31 σ_y = 2.64 mm

Under the assumption that the beam position and size do not significantly change during the pulse, something verified for the measurements used for the bench-marking, the signal on each wire is proportional to the beam current until the wire temperature increase is high enough (about 2000 K) to make Thermionic emission (Eq. (4)) significant.

The experiment consisted of increasing the beam pulse length in a controlled way in order to gradually reach a beam power on the wires that made thermionic emission evident. This would allow bench-marking of the the model under such a scenario, and use it to predict the wire temperature.

RESULTS AND DISCUSSION

An example of some measurement results is shown in Fig. 3. This shows the signal from a single wire intercepting the beam core over 3 consecutive LINAC4 pulses of 450 µs duration. This signal is compared to the beam current evolution measured by a Beam Current Transformer, which gave similar results for all 3 pulses. The data has been scaled to allow a direct comparison between the two instruments. The intensity modulation during the pulse and the pulse interruptions reflect the real beam properties during these measurements, arising from the source and chopper settings respectively. The plot shows two main characteristics of the wire signal that are fundamental for bench-marking the model:

1. During a pulse the wire heats up due to Thermionic emission, as seen by the divergence of the signal with respect to the intensity measured by the BCT. This effect increases slightly pulse after pulse due to the higher initial wire temperature.
2. In the 1.2 s periods between pulses the wire cools down with thermionic electrons still emitted while the wire is hot directly after the pulse leading to a slightly positive signal.

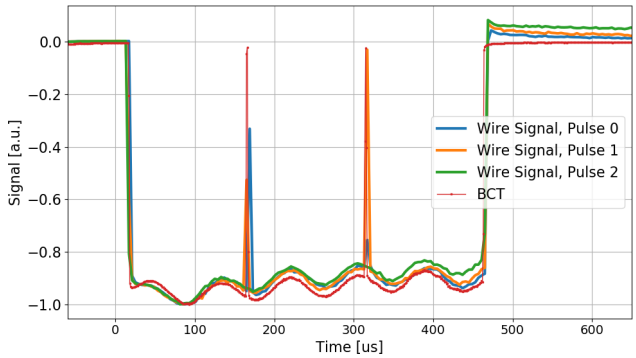

Figure 3: Signal as measured on the wire intercepting the beam core over 3 consecutive LINAC4 pulses of 450 µs duration scaled for comparison with the beam current signal as measured by a beam current transformer.

The wire signal and BCT signals (with the chopper 'holes' removed to make the results clearer) are shown again in Fig. 4, this time together with the output from the model.

The simulation does not currently include a variable beam intensity during the pulse, which is why the modulation caused by the source is not visible. Despite this, the example shows how the model successfully reproduces both of the experimental features described above, namely the divergence from the BCT signal during the pulse and the continued emission of thermionic electrons after the beam passage.

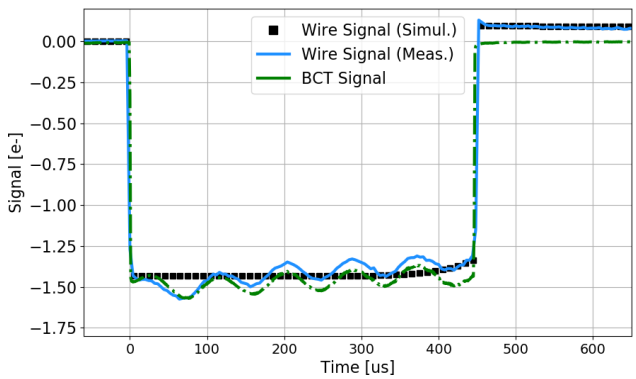

Figure 4: Signal generated in the wire intercepting the beam core as a function of time. Simulated data in black, experimental data in blue.

The agreement between the model and experiment in terms of wire signal versus beam current evolution, is well within 10 % after averaging for the LINAC4 source intensity modulations. Although more experiments and simulation tuning will be needed to fully validate the model, this first result at LINAC4 gives a high degree of confidence that such a model can be used to accurately simulate wire temperatures. Figure 5 shows the simulated maximum temperature reached by the wire during 6 consecutive LINAC4 pulses. A very fast temperature increase can be observed during the beam passage, followed by a comparatively slow cooling. The repetition rate of the beam is currently low enough for the maximum temperature to stabilize after six pulses, to

ISBN: 978-3-95450-222-6 ISSN: 2673-5350 doi:10.18429/JACoW-IBIC2020-TUPP35

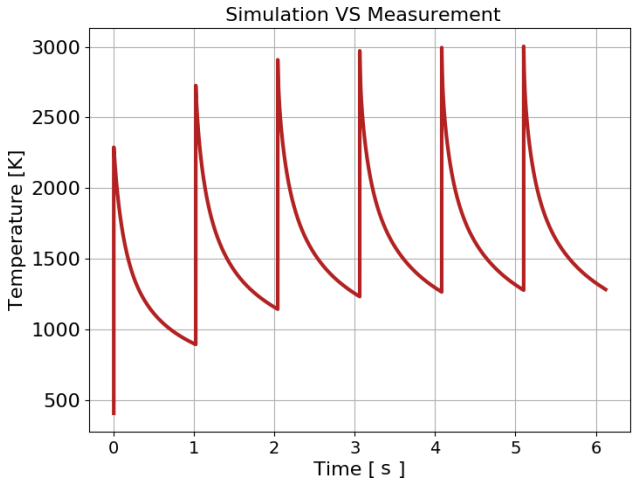

Figure 5: Maximum wire temperature as inferred from the simulation of the bench-marking experiment

about $T_{max} = 3000$ K. This is compatible with the observed evaporation of the wire gold coating without damage to the tungsten core, as confirmed by the visual inspection of the grid after the experiment.

SIMULATION OF LINAC4 BEAM POWER LIMITS FOR GRIDS OPERATION AT 160 MeV

The model can be applied to a variety of beam parameters and wire characteristics, and has allowed a re-calculation the LINAC4 beam power limits at 160 MeV to minimize the risk of overheating and damaging the tungsten wires. This results in plots like the one in Fig. 6 for all wire grids that maintains the maximum temperature reached below 1400 K (the limit for gold coating evaporation), for a variety of beam characteristics in terms of pulse length and total current.

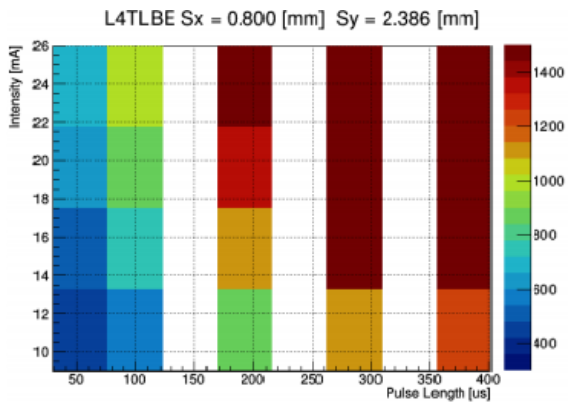

Figure 6: Maximum temperature reached by wire grid detectors for several intensity and pulse length combinations.

OUTLOOK

A first version of a comprehensive model simulating wire grid electrical signal generation and thermal evolution induced by intense ion beams has been bench-marked with beam based experiments using the LINAC4 H^- beam at 160 MeV. The model has been proven to reproduce well the onset of thermionic emission, which can then be used as an indirect wire temperature measurement. The results obtained give a high degree of confidence in the simulation of the beam power limits for the safe operation of the high energy wire grids in LINAC4. As a continuation of this work, the model will be applied to other wire grids and beams in the CERN complex, as well as to fast wire scanners.

In parallel, it is planned to experimentally enhance the accurate determination of some key input parameters, such as the material surface emissivity, that for the moment are only inferred from literature.

REFERENCES

[1] U.Raich, "Beam Diagnostics", Geneva, CERN, pp. 503-514, 2014. https://cds.cern.ch/record/1693047/files/p503.pdf

[2] B. Cheymol, "Development of beam transverse profile and emittance monitors for the CERN LINAC4", Geneve, LPC, 2011. http://cds.cern.ch/record/1503551

[3] F. Zocca *et al.*, "Profile and Emittance Measurements at the CERN LINAC4 3MeV Test Stand", in *Proc. IBIC'13*, Oxford, UK, paper WEPF09, pp. 826-829, 2013.

[4] M. Sapinski, "Model of Carbon Wire Heating in Accelerator Beam", Geneva, CERN, 2008. https://cds.cern.ch/record/1123363

[5] A. J. Onnink *et al.*, "How hot is the wire: Optical, electrical, and combined methods to determine filament temperature", *Thin Solid Films*, vol. 674, pp. 22-32, 2019. doi:10.1016/j.tsf.2019.02.003

[6] P. Antunes *et al.*, "Thin bonding wire temperature measurement using optical fiber sensors', *Measurement*, vol. 44, no. 3, pp. 554-558, March 2011. doi:10.1016/j.measurement.2010.11.016

[7] T. Spickermann *et al.*, "Stripper Foil Temperatures and Electron Emission at the Los Alamos Proton Storage Ring", in *Proc. PAC'03*, Portland, OR, USA, paper FPAB083, pp. 3455–3457, 2003.

[8] K. Nakamura *et al.*, "Passage of particles through matter", Particle Data Group, JP G37, 075021 (2010) and 2011 partial update for the 2012 edition, pp. 1–42, Feb. 2012. https://pdg.lbl.gov/2011/reviews/rpp2011-rev-passage-particles-matter.pdf

[9] GEANT4, https://geant4.web.cern.ch/

[10] G. W. Recktenwald, "Finite-Difference Approximations to the Heat Equation", *Mechanical Engineering*, vol. 10, pp. 1–27, 2004.

[11] S. Dushman, *Scientific Foundations of Vacuum Technique*, John Wiley & Sons, Inc., New York, 1962 (second edition).

[12] J. Allison *et al.*, "Recent developments in GEANT4", *Nucl. Instrum. Methods Phys. Res., Sect. A*, vol. 835, pp. 186-225, 2016. doi:10.1016/j.nima.2016.06.125

Content from this work may be used under the terms of the CC BY 3.0 licence (© 2020). Any distribution of this work must maintain attribution to the author(s), title of the work, publisher, and DOI

ISBN: 978-3-95450-222-6 ISSN: 2673-5350 doi:10.18429/JACoW-IBIC2020-TUPP37

Content from this work may be used under the terms of the CC BY 3.0 licence (© 2020). Any distribution of this work must maintain attribution to the author(s), title of the work, publisher, and DOI

A BEAM PROFILE MONITOR FOR HIGH ENERGY PROTON BEAMS USING MICROFABRICATION TECHNIQUES*

Wilfrid Farabolini, Antonio Gilardi, Blerina Gkotse, Alessandro Mapelli, Isidre Mateu†, Viktoria Meskova†, Giuseppe Pezzullo, Federico Ravotti, Ourania Sidiropoulou, European Organization for Nuclear Research (CERN), Geneva, Switzerland
Didier Bouvet, Jean-Michel Sallese
École Polytechnique Fédérale de Lausanne (EPFL), Lausanne, Switzerland

Abstract

In High Energy Physics (HEP) experiments it is a common practice to expose electronic components and systems to particle beams, in order to assess their level of radiation tolerance and reliability when operating in a radiation environment. One of the facilities used for such tests is the Proton Irradiation Facility (IRRAD) at the European Organization for Nuclear Research (CERN). In order to properly control the 24 GeV/c proton beam and guarantee reliable results during the irradiation tests, Beam Profile Monitor (BPM) devices are used. The current BPMs are fabricated as standard flexible PCBs featuring a matrix of metallic sensing pads. When exposed to the beam, secondary electrons are emitted from each pad, thus generating a charge proportional to the particle flux crossing the pads. The charge is measured individually for each pad using a dedicated readout system, and so the shape, the position and the intensity of the beam are obtained. The beam profile determination with this technique requires thus the usage of non-invasive and radiation tolerant (~10^{18} p/cm^2/y) sensing elements. This study proposes a new fabrication method using microfabrication techniques in order to improve the BPMs performance while greatly reducing the device thickness, thus making them also appropriate for the monitoring of lower energy and intensity particle beams. The fabricated prototypes were tested at the CERN CLEAR facility with 200 MeV electrons.

INTRODUCTION

Beam monitoring instrumentation is essential for the IRRAD proton facility, where about a thousand samples are irradiated every year, with a total accumulated proton fluence typically exceeding 10^{18} p/cm^2. To successfully perform these tests, a precise monitoring of the proton beam profile is essential. Therefore, flexible Printed Circuit Boards (PCBs) patterned with a matrix of sensing pixels, have been used as Secondary Electron Emission (SEE) Beam Profile Monitors (BPMs) since several years [1]. These devices were manufactured with a standard flex-PCB technology, composed of multiple copper layers sandwiched with epoxy glue. These stacked layers were originally considered to multiply the signal, but had the drawback of making a rather thick device (~0.6 mm). Moreover, radiation-induced damage effects were observed in the sensing region of the device and, sometimes, induced its failure during operation. These effects were attributed to the epoxy not resisting the levels of radiation at which the BPMs are exposed.

This article presents a series of working prototypes based on a newly developed microfabrication process with nanometre aluminium (Al) layers on thin polymeric substrates. Compared to the old BPMs, the new prototypes are thinner (20 times the substrate, and one order of magnitude the metal), and therefore less invasive when interacting with the beam. They are expected to present an enhanced radiation tolerance thanks to the employed microfabrication technology (which avoids gluing) and have a higher sensitivity because of the usage of Aluminium (Al) as sensing material which has, intrinsically, higher secondary electron yield (SEY) than copper.

The validation of their functionality with experiments in dedicated test-benches and a particle beam, is also presented in this paper. These experiments are the prerequisite to have operational BPM devices for the IRRAD facility after the CERN Long Shutdown 2, as well as, to investigate their usability in very low energy beams as of interest for more general-purpose applications (e.g. industry, medicine).

STATE OF THE ART

The standard beam instrumentation for secondary beam area at CERN is generally not designed to be used in an irradiation beam-line. To cope with this problem, custom-made standard BPM devices consisting on rectangular-shaped, flexible PCBs, patterned with a matrix of metallic sensing pads on the one end, and a multi-pin connector on the opposite one, have been developed for the IRRAD facility at CERN (see Fig. 1 (left)).

Secondary Electron Emission (SEE), on which the BPMs working principle is based, occurs when a high-intensity beam impinges on a metallic foil and electrons of the energy below 50 eV (Secondary Electrons (SE)) are produced. The number of SEs ejected from the foil is proportional to the local beam intensity [2]. The SEs are then converted into an electrical signal, which is measured and recorded by a dedicated electronics. An online web application, finally displays the current from every metallic pad resulting in two-dimensional beam profiles.

*Work supported by the European Union's Horizon 2020 research and innovation programme under grant agreement No 777222 (ATTRACT Phase-1 project).
†e-mail address: isidre.mateu@cern.ch, viktoria.meskova@cern.ch.

ISBN: 978-3-95450-222-6 ISSN: 2673-5350 doi:10.18429/JACoW-IBIC2020-TUPP37

These monitoring devices are installed on every irradiation system of the IRRAD facility and are exposed to the beam together with the samples to be irradiated. Although they have proven to work well during the run 2014 to 2018 of IRRAD, multiple drawbacks has been identified about their functionality.

The standard IRRAD BPMs have shown damages (detaching, burning and bumps) on the region traversed by the beam, because of the usage of epoxy glue between the sensing and isolating layers. Moreover, when all the irradiation systems of IRRAD are positioned in beam, the sum of all BPMs can add almost 2 mm of copper and 8 mm of polyimide to the total material budget, thus significantly contributing to the multiple scattering in the beam-line. Other than the damage, the devices become highly radioactive after long time exposure, something of special concern when the facility staff needs to access the irradiation area or replace a broken device.

The main challenge that the devices are facing is the high radiation levels that they should withstand, particle fluences equivalent, at least, to one year of operation in the facility (~10^{18} protons). Moreover, the beam monitoring in IRRAD must be permanent and real time, because these data are also used by the CERN Control Centre (CCC) to tune the beam extraction parameters (e.g. shape, position, charge).

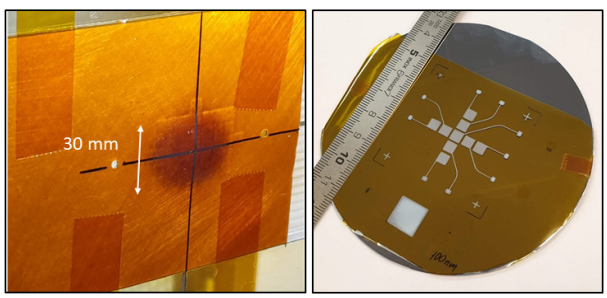

Figure 1: On the left, old BPM device, consisting of a PCB patterned with a matrix of sensing pads from copper in multiple layers. The footprint of the beam can be observed. One the right, the new BPM device, consisting of aluminium sputtered on polyimide substrate.

MICRO-BPM DESIGN & FABRICATION

Based on the experience with the old BPMs, the following requirements were identified for a new generation of devices: they should withstand the expected radiation cumulated during, at least one year of IRRAD operation, they should be made of materials that have short radioactivity, in order to minimize the exposure of the operators and users. Moreover they should be, on the one hand, thin to avoid the multiple scattering and any interference with the projectile beam, while on the other hand thick enough to allow easy handling. Relatively low cost and easy manufacturing are also desired.

Microfabrication techniques allow to meet the above mentioned requirements. Deposition of thin films down to the nanometre scale on rigid substrates can be easily achieved with standard techniques. Thus, initial production runs started in the Centre of Micro and Nano technology (CMi) of EPFL in 2018, and confirmed the perspective of microfabrication [3].

These first devices were produced on standard Si/SiO_2 wafer substrates and were tested methodically to study different configurations of the metal layers and thus, serving as guideline for optimizing later productions. More specifically, the experimental results showed that multiple metal layers nor isolation of the sensing material influence the signal intensity. Suspicion of contribution from the silicon substrate to the total signal suggested to move forward and focus our research on the manufacturing on insulating substrates. Subsequent productions were therefore realized using polyimide as substrate. Polyimide (Kapton) was chosen because of its thermal and chemical stability, low dielectric constant, high electrical resistivity, possibility of getting very thin films and most important increased radiation tolerance.

The field of microfabrication related to metal deposition on polymeric substrates is still very much in its infancy, which led us to a careful selection of each step of the manufacturing process: e.g. deposition techniques and equipment, sensing material and substrate, were chosen after strict validation. This included new studies about the quality of the adhesion between the sensing and the supporting material, the effects of oxide to the SEY, the homogeneity of the metal deposition and the electrical connections.

For the microfabrication of the new devices (Fig. 1 (left)), shadow masks were produced. To engrave the substrate with the desirable pattern, aluminium was sputtered on polyimide substrate under vacuum pressure, as shown in Fig. 2. Restrictions related to the cleanroom production such as mask fragility, target (metal) thickness limit, thin polyimide film manipulation, mask fixation on the substrate, machine power modes (burning issues) and support size (usually wafer shaped), emerged and have been solved by optimizing subsequent production runs.

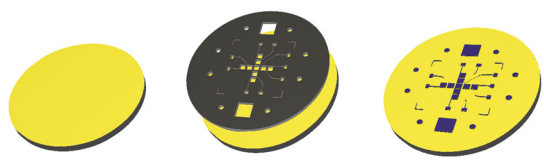

Figure 2: Shadow mask deposition technique. (a) Thin polyimide film on a silicon wafer support. (b) Shadow mask put on the top on the polyimide. (c) BPM design patterned on the top on polyimide after aluminium sputtering process.

Aluminium was chosen as sensing material because of its availability, low cost and higher SEY (δ_{max}=3.5, see Fig. 3) compared to Copper (δ_{max}=2.4 [4]). The polyimide substrate was treated with oxygen plasma and titanium under vacuum pressure before the metal deposition, in order to improve the adhesion properties between the two materials, as experimentally tested.

Content from this work may be used under the terms of the CC BY 3.0 licence (© 2020). Any distribution of this work must maintain attribution to the author(s), title of the work, publisher, and DOI

ISBN: 978-3-95450-222-6 ISSN: 2673-5350 doi:10.18429/JACoW-IBIC2020-TUPP37

Content from this work may be used under the terms of the CC BY 3.0 licence (© 2020). Any distribution of this work must maintain attribution to the author(s), title of the work, publisher, and DOI

The new BPMs feature improved characteristics with respect to the older version. They are thinner (less invasive) and more durable, because of material processing. Last, but not least, during the irradiation of both old and new BPM devices at the CERN CLEAR electron facility, a higher response to the beam was also observed.

As mentioned in theory [5], and confirmed by a surface analysis performed at CERN (Fig. 3), the SEY of Al in vacuum is rather independent of the thickness of the metal. Layers 10 nm, 50 nm, 100 nm and 400 nm thick showed roughly the same results, especially at increasing primary particle energy, while coating the Al with an extra oxide layer (in this case 10 nm) increased the yield by 23%. This effect, observed in vacuum, could be used as a method to easily increase the SEY and hence, the sensitivity of the BPM devices to particle beams. Unfortunately, this finding was proven not to be valid when the emitting surface is surrounded by air at atmospheric pressure, as shown by the experimental test at CLEAR (next section).

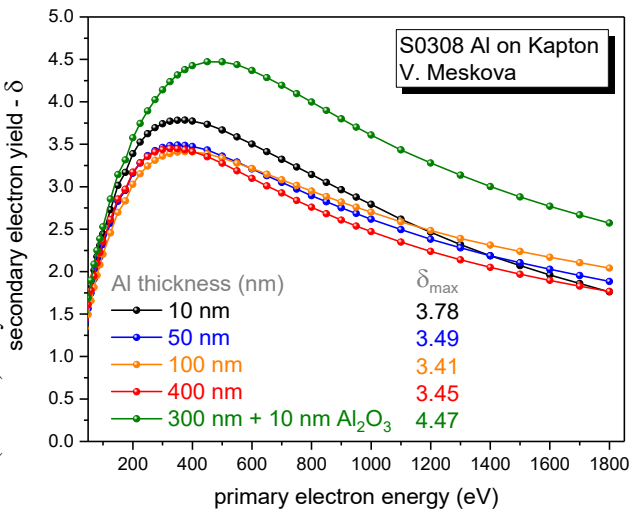

Figure 3: SEY spectra of metallized Kapton samples with different metal layer thickness. Tests were performed in a vacuum enclosure and bombardment by low energy electrons.

EXPERIMENTAL DETERMINATION OF SECONDARY ELECTRON YIELD UNDER 200 MeV ELECTRON IRRADIATION

With the objective of determining their Secondary Electron Yield (SEY), the produced devices were tested under a 200 MeV electron beam at the CERN CLEAR facility [6].

PCB frames were designed to support the BPMs during the CLEAR irradiations (Fig. 4). These frames hosted also the electrical connection between the detector and the DAQ. The connections from the BPM to the PCB were done using silver glue. Figure 4 shows the experimental setup, with three BPMs mounted on their respective PCBs, and attached to a Plexiglas support. A motorized stage was used to remotely move the support and position the different BPMs in and out the beam spot.

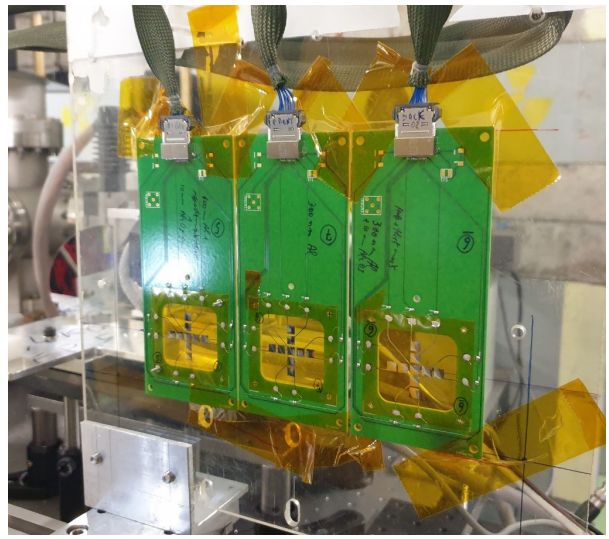

Figure 4: Experimental setup for the CLEAR irradiation tests. The BPMs were mounted on dedicated PCBs and attached to a Plexiglas support. The support, in turn, was mounted to a motorized stage which allowed positioning the devices under the beam spot.

The beam spot was focused enough to be practically fully contained in the central pad of the BPM. Beam intensity scans were performed for each of the tested BPMs in order to verify the linearity of the response and determine the SEY.

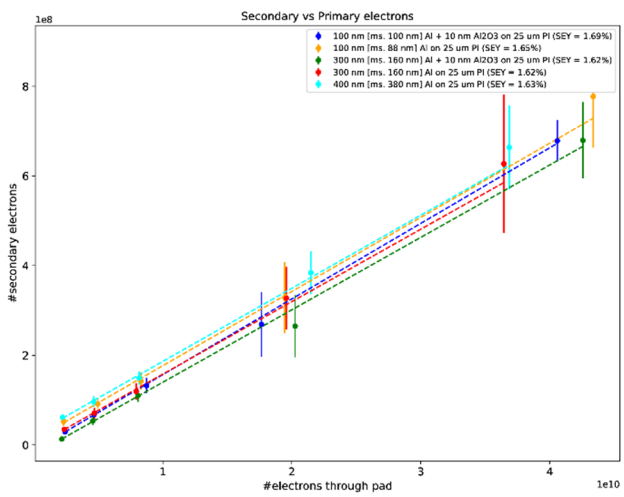

Figure 5: SEY measured for the different BPMs tested at the CLEAR facility.

Figure 5 shows the obtained results for BPMs with different aluminium layer thickness, ranging from 100 nm to 400 nm. The obtained SEY is around 1.6% in all cases, with no observed dependency on the aluminium thickness. Moreover, some of the devices featured a 10 nm Al_2O_3 layer on top of the Al layer, which did not look to have any impact on their performance.

ISBN: 978-3-95450-222-6 ISSN: 2673-5350 doi:10.18429/JACoW-IBIC2020-TUPP37

The obtained yield is in very good agreement with the values in Figure 3 when extrapolating them to hundreds of MeV primary particle energy. Irradiation of old standard BPMs in the same conditions at CLEAR, resulted in an experimental SEY in air for copper lower than 1 % proving the increased sensitivity of the new devices.

Table 1 summarizes the tested devices and the obtained results. The measured thickness (second column of Table 1), refers to Focused Ion Beam (FIB) measurements [7] that were done to cross-check the Al thickness deposited by sputtering and to analyse the homogeneity of the deposition (see an example in Fig. 6).

Table 1: SEY from the Aluminium Pads on 25 µm Polyimide, After Electron Irradiation at CLEAR

Expected Al thickness [nm]	Measured Al thickness [nm]	Extra Al_2O_3 [nm]	SEY [%]
100	100	10	1.69
100	88	-	1.65
300	160	10	1.62
300	160	-	1.62
400	380	-	1.63

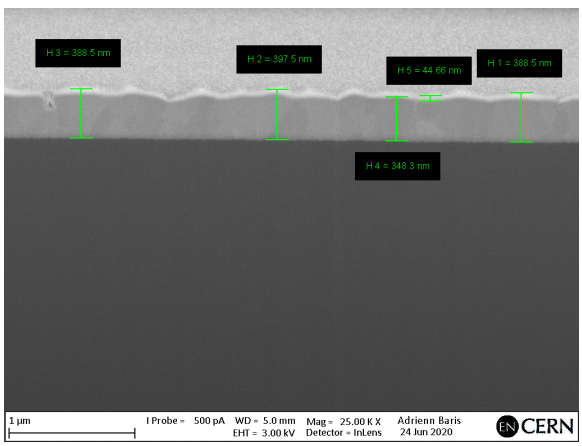

Figure 6: Focused Ion Beam (FIB) analysis on a 400 nm samples, confirming an average thickness of 380 nm.

CONCLUSION

The new devices have overall shown to work reliably and feature improved parameters related to their thickness (material budget) and SEY (sensitivity). Although extensive radiation tolerance tests were not possible in the scope of this study, in the investigated fluence range, degradation effects were not observed. A SEY of around 1.6% was experimentally determined for all the devices, when irradiated by a 200 MeV electron beam. This represents an increase with respect to the SEY measured for the old BPMs under the same beam, which was below 1%, and is in line with the theoretical expectation of aluminium having a higher yield than copper.

These initial results, together with the intrinsic improvement in the fabrication process (see Table 2 for a performance comparison with the old devices), confirm the sputtering of thin metal films on polyimide substrate as a viable fabrication method for the next generation of BPMs in the IRRAD facility.

Table 2: Summary Table Comparing the Performance of the Old and New BPM Devices

Device Parameters	Old device (2018)	New device (2020)
Metal	Cu	Al
Metal Thickness	100 µm	100 nm
Substrate thickness	475 µm	25 µm
Total material budget in IRRAD	8 mm	0.5 mm
Theoretical SEY (maximum)	2.4	3.5
Measured SEY (200 MeV e^-)	<1%	1.6%
Radiation-induced degradation	observed	not observed with electrons

ACKNOWLEDGEMENTS

The authors wish to thank the staff of the Center of Micronanotechnology (CMi) of the École Polytechnique Fédérale de Lausanne (EPFL) for providing their assistance during the cleanroom production. In addition, we would like to express our thanks to the colleagues of the TE and EN department at CERN for the SEY and the Focused Ion Beam (FIB) measurements respectively.

REFERENCES

[1] F. Ravotti *et al.*, "The Beam Profile Monitoring System for the CERN IRRAD Proton Facility", in *Proc. 5th Int. Beam Instrumentation Conf. (IBIC'16)*, Barcelona, Spain, Sep. 2016, pp. 825-828. doi:10.18429/JACoW-IBIC2016-WEPG75

[2] H. Seiler, "Secondary electron emission in the scanning electron microscope", *J. Appl. Phys.*, vol. 54, no. 11, pp R1-R18, 1983. doi:10.1063/1.332840

[3] J. Bronuzzi *et al.*, "Beam profile monitor devices using microfabricated metal thin-films", CERN, Geneva, Switzerland, AIDA-2020-NOTE-2019-003, 2019.

[4] V. Baglin *et al.*, "The Secondary Electron Yield of Technical Materials and its Variaton with Surface Treatments", in *Proc. 7th European Particle Accelerator Conf. (EPAC'00)*, Vienna, Austria, Jun. 2000, paper THXF102, pp. 217-221.

[5] L. Jiangtao *et al.*, "Secondary electron emission influenced by oxidation on the aluminum surface: the roles of the chemisorbed oxygen and the oxide layer", *Plasma Sources Sci. T.*, vol. 27, no. 4, pp. 044002, 2018. doi: 10.1088/1361-6595/aab74b

[6] D. Gamba *et al.*, "The CLEAR user facility at CERN", *Nucl. Inst. and Meth. In Phys. Res., A,* vol. 909, pp 480-583, 2018. doi: 10.1016/j.nima.2017.11.080

[7] A. Korsunsky *et al.*, "Residual stress evaluation at the micrometer scale: Analysis of the thin coating by FIB milling and digital image correlation", *Surf. Coat. Tech.*, vol. 205, pp. 2393-2403, 2010. doi:10.1016/j.surfcoat.2010.09.033

Content from this work may be used under the terms of the CC BY 3.0 licence (© 2020). Any distribution of this work must maintain attribution to the author(s), title of the work, publisher, and DOI

ISBN: 978-3-95450-222-6 ISSN: 2673-5350 doi:10.18429/JACoW-IBIC2020-WEA002

THz DETECTION TECHNIQUES OVERVIEW

F. Mazzocchi, D. Strauß, T. Scherer, KIT IAM-AWP, Eggenstein Leopoldshafen, Germany
A. S. Müller, E. Bründermann, KIT IBPT, Eggenstein Leopoldshafen, Germany

Abstract

In the following work, we present a general overview of the various techniques that can be employed to detect and characterize THz waves. The overview will take into consideration several technologies based on different physical principia, capable of both broadband and narrowband detection.

INTRODUCTION

In recent years, the THz part of the electromagnetic spectrum has attracted special attention due to the broad range of possible applications deriving from it and its presence in multiple natural phenomena. T-rays are able to pass almost unobstructed through a wide range of non-polar materials such as fabrics, paper, wood, ceramics, plastics and plasma. Radioastronomy, spectroscopy, molecular sensing, plasma diagnostics, security and biomedical imaging are only a few possible uses of the THz spectrum. Such wide range of applications demands a similarly wide range of detection techniques and devices. The methods presented in this overview have been organized in four groups, based on the physical principia they rely on: thermal, direct, heterodyne and sampling detection. For each of the techniques, the operational limits and the most frequent applications are also presented.

THERMAL DETECTORS

Conceptually speaking, thermal detectors represent the simplest sensors employed for power measurements in the THz region, and can be thought as composed by three distinct parts: the radiation absorber, the heat sink and the thermal link between them (Fig. 1).

Radiation impinging on the absorber determines a rise in temperature $\Theta(T)$ given by [1]

$$\Theta = \frac{\eta P_\omega}{\sqrt{\omega^2 C^2 + G^2}} \tag{1}$$

where C and G are, respectively, the thermal capacity and conductivity. η is the detection efficiency and P_ω the power related to the incoming radiation. We can define the response time of the detector as

$$\tau = C/G \tag{2}$$

that is minimized for small thermal masses and high conductivities. For room temperature detectors, we can expect response time ranging from as few seconds to a few milliseconds. Examples of thermal detectors include pyroelectrics, thermopiles, Golay cells and bolometers. Nowadays, bolometers are the most widespread of these kind of

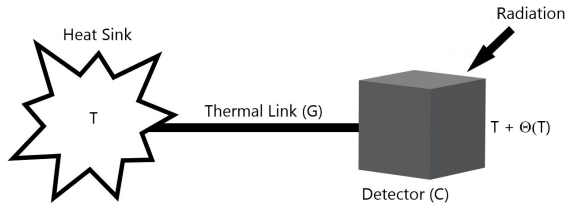

Figure 1: Schematic representation of a thermal detector main elements.

detectors, and will be the main subject of the section. The reader interested in the other aforementioned devices can refer to [1] for a more extensive treatment. In 1961 Low [2] described a popular bolometer based on germanium, that consisted in a doped semiconductor absorber suspended in vacuum by wires that function as both thermal and electrical contacts. The semiconductor is biased with a constant current, and the change in temperature induced by the absorbed radiation determines a detectable change in the electrical resistance of the device. We can introduce the generalized resistance temperature coefficient α as:

$$\alpha = R^{-1}\,(dR/dT) \tag{3}$$

where R and T are the resistance and temperature. α represents the steepness of the R/T curve. Of course the higher the voltage response of the detector to a given signal, the better. This is achieved by cooling the device down to liquid helium temperatures or lower. The obtained reduced thermal capacitance determines therefore a faster and more sensitive detector. Given that bolometers are operated with a current bias, there is an additional varying electrical power that leads to an effective thermal time constant $G_{Eff} = G - \alpha P_E = G - I^2 R\alpha$. Semiconductor bolometers typically require heavy doping, in order for them to have a more metal like behaviour of the resistance, avoiding thermal runaways. The main conduction mechanism is, in this case, performed by charge carriers passing from one donor atom to the other. The resistance temperature coefficient takes the explicit form of

$$\alpha = -\frac{1}{2}\sqrt{\frac{T_0}{T^3}} \tag{4}$$

with T_0 in the order of 2–10 K. Semiconductor bolometers can reach Noise Equivalent Power (NEP) in the order of 10^{-12}–10^{-13} W/Hz$^{1/2}$ in a 0.15–15 THz frequency range and response times of roughly 10 µs. Applications in astrophysics are the most widespread, with notable instru-

Content from this work may be used under the terms of the CC BY 3.0 licence (© 2020). Any distribution of this work must maintain attribution to the author(s), title of the work, publisher, and DOI

ISBN: 978-3-95450-222-6 ISSN: 2673-5350 doi:10.18429/JACoW-IBIC2020-WEA002

ments like SPIRE [3] in the Herschel Space Observatory and SCUBA [4] inside the Maxwell Mauna Kea Observatory.

Higher sensitivities in bolometers can be achieved by taking advantage of the very narrow superconducting transitions. Materials like tantalum [5], niobium nitride [6] and niobium [7] are regularly used in the form of superconducting thin films in such devices. Since they have a positive temperature coefficient, they require a constant voltage bias instead of a constant current, in order to avoid thermal runaways. When the voltage is kept constant, absorbed radiation power determines a decrease of the bias current (electrothermal feedback), that cannot therefore exceed the limit $G_{Eff} = 0$ that determines the runaway. Since with these devices we tend to work close to the superconducting transition, where the R/T curve is steeper, they are commonly referred also as Transition Edge Sensors (TES). They reach extremely small NEP values, around 10^{-19} W/Hz$^{1/2}$ at $10^{-15} W$ of background illumination [8] and response times in the order of microseconds. SCUBA2 [9] is an example of instrument using such detectors. For the detection of low energy photons, typically below 1.5 THz, lower effective mass carriers are needed in order to be sensitive to lower ionization levels. Hot Electron Bolometers [10] (HEBs) also require the use of superconductors. At cryogenic temperatures, the electrons are only weakly coupled with the phonon system and even small energies can break this bond, generating the hot electrons referred by the device's name. The phonons of the thin film represent the thermal reservoir of the bolometer, and the heat capacitance involved in the detection mechanism is the one of the electrons. The electron phonon relaxation time represents, therefore, the relevant thermal conductance of the whole system. HEBs are typically capable of NEPs in the order of 10^{-18} W/Hz$^{1/2}$ and response time around the 10 ps range, making them adapt to detecting the bunch dynamics of a synchrotron storage ring.

DIRECT DETECTORS

Direct detectors include a large range of very different devices, including rectifiers, superconducting vortex assisted and kinetic inductance detectors, to name a few. Schottky diodes are the most prominent examples of the rectifiers family. In such devices, the impinging electro-magnetic radiation acting on the sensor induces an AC at the radiation frequency and, given a non linear voltage - current curve of the device, a DC component rises, that is related to the amplitude of the input. The Schottky barrier [11] is formed by the junction of a metal with a semiconductor, and presents a very low forward voltage drop when compared to other kind of diodes. This aspect, together with the fact that Schottky diodes are majority carrier devices, allows for very fast switching, with time constants lower than 10 ps. They can be operated at room temperature and bias free, which limits the noise level. Typical zero-bias NEP values are in the 10^{-12} W/Hz$^{1/2}$ range. Recent development in the fabrication techniques have allowed very wide band devices, with the detectable frequencies range as wide as 50 GHz–5 THz. They are regularly employed, as an example, in microbunching measurements [12], where time resolutions in the order of a nanosecond are required. Another device pertaining to the family of rectifiers is the Superconducting Tunnel Junction (STJ), also know as superconductor-insulator-superconductor (SIS) tunnel junction. As the name suggests, it consists of twin layers of superconductors separated by a very thin (around tens of Angstrom) insulator membranes. When cooled down below their critical temperature, Cooper pairs start to form, with binding energy 2Δ that is also the gap of the density of states. The gap voltage is defined as:

$$V_G = \frac{2\Delta}{e} \tag{5}$$

A bias voltage equal to the gap voltage will make the densities of states at both sides of the insulator to overlap, and Cooper pairs will break down back to single electrons. These quasiparticles can tunnel through the insulating barrier, if it is thin enough, and recombine into Cooper pairs on the other side of it. This results in a steep increase of current in the I-V curve of the device. During normal operation, the DC bias will be kept below the gap limit, and incoming photons will break down Cooper pairs into normal electrons, that then tunnel through the barrier in the direction of the applied voltage. The tunnelling current is proportional to the energy of the photons, since more energetic quanta will generate more quasiparticles. Devices of these kind dedicated to photons detection in the submillimeter range operate mostly between 0.7 and 2.4 THz, with NEPs in the order of 10^{-18} W/Hz$^{1/2}$ at 1 THz [13]. They are extensively used in the astrophysics field as single photon detectors in a wide range of frequencies, from IR to X-rays. Another technology that has been first developed in the astrophysics [14] field and that is being adapted only recently to other applications, such as fusion plasma diagnostics [15], is the Kinetic Inductance Detector, or KID. Such a device consists of an array of superconducting microresonators, each with a natural resonance frequency equal to

$$\nu_R = \frac{1}{\sqrt{LC}} \tag{6}$$

with L and C representing the inductance and capacitance of the resonator. The kinetic inductance derives from the inertial mass of the charge carriers (again a mixture of Cooper pairs and electrons) when they are subject to high frequency alternating electrical fields. Photons striking the detector can break down Cooper pairs if their energy is bigger than the 2Δ gap, generating quasi particles. At this point, the kinetic part of the microresonator inductance increases, resulting in a shift of the complex scattering transmission parameter S_{21} peak toward lower frequency values, in addition to a change in phase. One of the biggest advantages of this technology is the ease with which it can be read out. By tuning each microresonator to a unique resonance, arrays of hundreds of pixels can be easily multiplexed with a single feed line, either a microstrip or a co-planar waveguide.

Content from this work may be used under the terms of the CC BY 3.0 licence (© 2020). Any distribution of this work must maintain attribution to the author(s), title of the work, publisher, and DOI

ISBN: 978-3-95450-222-6 ISSN: 2673-5350 doi:10.18429/JACoW-IBIC2020-WEA002

Content from this work may be used under the terms of the CC BY 3.0 licence (© 2020). Any distribution of this work must maintain attribution to the author(s), title of the work, publisher, and DOI

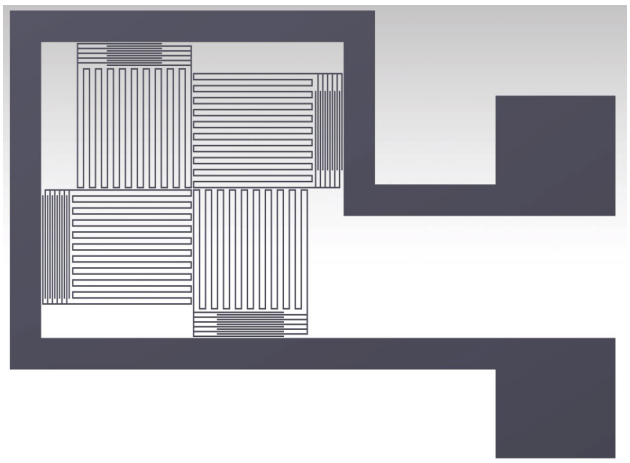

Figure 2: 2D model of the KID array developed as polarimetric fusion plasma diagnostic at KIT IAM-AWP [15]. The pixels are two by two sensitive to only one plane of polarization, in virtue of their orientation. The meandering line of each resonator represents their inductance L and it's the same for all the pixels, while the capacitors are different in number and length of their digit to tune the resonance frequency.

Additionally, the fabrication is very simple, since only single layer deposition is needed and photolithography allows very fast production times. The detectors used in astrophysics are normally made of aluminium thin films (T_C = 1.2 K) and operated in the 250–300 mK range. The use of superconductors with higher critical temperatures like niobium and niobium nitride, with T_C in the 9–15 K range, allows the use of normal liquid He cryostats instead of more expensive closed refrigerators system, at the cost of a reduced sensitivity. These detectors can easily reach values of 10^{-18} W/Hz$^{1/2}$ for the NEP, with record values toward 10^{-19} W/Hz$^{1/2}$ [16], maximum energy resolution of 100 meV and a rise time around 50 ps. The bandwidth can be tuned to cover detection from the radiofrequency range up to the X-rays, and they can be made intrinsically polarization sensitive. The instrument NIKA2 [17] is a good application example of such technology.

Most of the detectors treated so far require cooling down to liquid helium temperatures or even below, to guarantee their optimal operation. While LHe cryogenic techniques are well developed and reliable, they add a degree of complexity to the systems equipped with these technologies. Additionally, few of them reach the required response time to fully resolve, for example, the dynamics of a storage ring bunch. With these premises in mind, an innovative device in the form of a high temperature superconductor detector has been recently developed for measurements at the Karlsruhe Research Accelerator (KARA). It consists of microbridges of $YBa_2Cu_3O_7$ (or YBCO) from 30 nm thick films [18] on a R-cut sapphire substrate. YBCO has a T_C of around 83 K, making the use of liquid nitrogen temperatures feasible. The fast (< 15 ps) photoresponse of these detectors at THz ranges has been demonstrated to be vortex-assisted rather than bolometric in nature [19]. Type II superconductors are characterized by the formation of what are called Abriksov vortices, especially when an external magnetic field is applied to it. These vortices are composed by supercurrent loops circulating around a non superconducting core, and are therefore sensitive to electric and magnetic fields. The electric field from a storage ring generates a current pulse across the microbridge. This pulse causes the vortices to rearrange in a line, creating a channel that facilitates the crossing of the bridge. One interesting aspect of this innovative device is that in virtue of the detecting mechanism, it can be operated bias free, simplifying the experimental setup. Additionally, it has a very high responsivity (700 V/W), enabling it to be embedded directly into an ultra fast readout system like KAPTURE [20] without the use of an amplifier.

HETERODYNE DETECTION

Heterodyne detection is an extremely widespread technique, since it is at the base of modern day TV, Radio and wireless telecommunication. Two signals of similar frequency that coexist in the same circuit will generate additional frequencies determined by their sum and difference. The receiver is optimized for the detection of the difference frequency, since it's value is orders of magnitudes (GHz for THz signals) lower than the beat frequency. Such a receiver can be divided into two main building blocks: front and back end. The front end is responsible for the collection of the THz radiation, while the back end task is to collect the signal from the front end, to amplify it and to detect it. The front end itself contains two main elements, in the form of a Local Oscillator (LO) and a mixer. The local oscillator is responsible for the generation of the reference signal to be subtracted to the incoming radiation, and at THz ranges can take the form of multiplied microwave emitters for frequencies below 2 THz, or Quantum Cascade Lasers (QCLs) at shorter wavelengths. The generation of the additional frequencies is then performed in the mixer, a nonlinear electrical circuit. The nonlinearity is a required characteristic, since the additional frequencies are generated by the higher order terms of the expansion of the I-V curve:

$$I(V) = k_0 + k_1 V + k_2 V^2 + \cdots = \sum_{i=0}^{\infty} k_i V^i \qquad (7)$$

given an input voltage of the form:

$$V = V_{LO} \sin(\omega_{LO} t) + V_S \sin(\omega_s t) \qquad (8)$$

The power of the harmonics decreases with the square of the harmonic number, therefore only the sum and difference (or intermediate frequency ν_{IF}) are transferred to the back end in a significative quantity, in the case of double sideband (DSB) mixers. The mechanism described above is proper of the so called square law mixers, since the device responds to the square of the sum of the waveforms fields. If the mixer was to react individually to the signals, then it would function more as a switch, acting on the voltage waveform

ISBN: 978-3-95450-222-6 ISSN: 2673-5350 doi:10.18429/JACoW-IBIC2020-WEA002

induced by the LO field, with his action dictated by the radiation signal. The resulting output in this case is the product of the switching and signal waveform, and, when its duty cycle is not 50%, contains all the superior harmonics that therefore need to be filtered out. Slow mixers with detection mechanism unable to follow the fast dynamics of the fields, respond to the total power of the incoming radiation and fall into the first category that includes the hot electron bolometers. Fast devices like the Schottky diode or the SIS junctions can be used as switching mixers. In heterodyne detection, a good indication of the noise level of the device is given by the receiver noise temperature T_{REC} that in the end determines the sensitivity of the device, the minimum detectable power in a given integration time:

$$\Delta T_{MIN} = \frac{k_{REC} T_{REC}}{\sqrt{\tau \Delta \nu}} \tag{9}$$

where k_{REC} is a receiver dependent constant, $\Delta\nu$ is the detection bandwidth and τ the integration time. Generally speaking, Schottky diodes present higher noise figures compared both HEBs and SIS mixers (Fig. 3), and the noise temperature raises for higher frequencies. Heterodyne systems are widely used, as an example, in the Electron Cyclotron Emission (ECE) diagnostics installed in nuclear fusion machines, like Wendelstein 7X [21], to determine the electron temperature. It consists of a 32 channel radiometer, capable of covering the second harmonic of the ECE, in a range from 126 to 160 GHz, donwnconverting it to 4–40 GHz. There's a notch filter installed at 140 GHz, since the Electron Cyclotron Resonance Heating (ECRH) system operates at that frequency and would overload the radiometer if its radiation was allowed to pass through. Each of the 32 channels refers to a precise flux surface (constant magnetic field) of the plasma, since the emission frequency is dependent on the magnetic field strength that itself is a function of the radial coordinate inside the toroidal vacuum chamber. The radiometer uses a single broadband diode mixer and a local oscillator at 122 GHz [22].

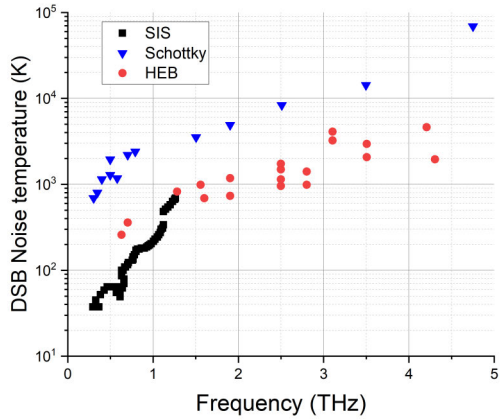

Figure 3: Noise figures for different kind of mixers. Data extracted from Fig. 5.35 in Ref. [1].

SAMPLING DETECTION

The development of fs-lasers in the last 25 years led, among other things, to advancement in both generation and detection of THz radiation. Sampling detection uses either a gated photoconductive antenna (Auston Switch [23]) or non linear optical crystal like ZnTe (Electro Optical Sampling, EOS [24]) to sample and extract information from a THz pulse. In the first of these techniques, light from the fs-laser impinges on the antenna, exciting the charge carriers. The conductivity changes abruptly, supported by the newly photogenerated electrons. The incoming THz radiation act as a voltage bias, driving a current in the antenna. Since the fs pulse is much shorter than the THz one, the change in conductivity can be considered as a delta function, and the induced current has the same pulse shape as the THz electrical field [1]. Electro Optical Sampling is based on the Pockels effect present in many crystals that lack inversion symmetry, like ZnTe [25]. These crystals show birefringency when a voltage is present across their section. The magnitude of the difference between the ordinary and extraordinary refractive indices depends linearly on the magnitude of the electric field, therefore this phenomenon is also known as linear electro-optical effect. In this frame, the THz radiation acts as modulation signal for the crystal, changing the birefringency according to its pulse shape. A concurrent ultrafast fs-laser pulse will see its polarization status modified accordingly with the temporal profile of the modulation. At this point, a Wollaston prism is used to separate the extraordinary and ordinary components of the fs pulse with the encoded information, each one impinging on a separate balanced detector. The difference in signal between the P and S detectors allows to reconstruct the amplitude of the THz waveform. Both techniques are widely employed in Time Domain Spectroscopy (TDS) [26], that consists in a pump-probe kind of technique where the pump signal is used to generate the THz radiation and the probe signal to gate the detector or modulate the polarization status of the THz pulse to be detected. The generation methods mirror the detection ones, with, respectively, photoemission from a voltage biased antenna or optical rectification by a non linear crystal [27]. Auston switch-based systems are limited by the parameters of the antenna to, typically, a maximum of 6 THz although recently bandwidths in excess of 70 THz have been achieved [28] through Au-implanted Ge emitters. The antenna structure, together with the materials properties determine also the response time, that can be around 300 fs with InGaAs emitters [29]. In EOS, the bandwidth is limited mainly by the length of the fs pulse and by the thickness and the absorption of the crystal. It can have an extreme extension, from 100 GHz to 37 THz [30]. As an example, EOS has been employed as longitudinal diagnostics for single-shot electron bunch profiling at the KARA facility in Karlsruhe [31]. Strong THz radiation bursts can be produced by short electron bunches [32] as result of in-

Content from this work may be used under the terms of the CC BY 3.0 licence (© 2020). Any distribution of this work must maintain attribution to the author(s), title of the work, publisher, and DOI

ISBN: 978-3-95450-222-6 ISSN: 2673-5350 doi:10.18429/JACoW-IBIC2020-WEA002

Content from this work may be used under the terms of the CC BY 3.0 licence (© 2020). Any distribution of this work must maintain attribution to the author(s), title of the work, publisher, and DOI

stabilities patterning. The bunch length was in the order of few picoseconds, with a repetition rate of 2.72 MHz. The laser pulse itself is stretched from femtoseconds length up to picoseconds through a fiber optics stretcher and a compressor, to make it overlap with the bunch pulse and allow single shot acquisition. The electro optical crystal is made out from gallium phosphide. At the end of the system, an ultrafast Si photodiode detector array (KALYPSO [33]) with the repetition rate also set at 2.72 MHz, extracts the encoded bunch profiles on a turn by turn basis.

CONCLUSION

We presented a review of several techniques that can be employed in the field of THz waves detections. The devices presented have been divided into four main categories, spanning from thermal detectors, to direct detection methods, to heterodyne and finally sampling detection. The most sensitive room temperature detector is the normal bolometer, closely followed by the Schottky diode. The latter gains an edge on the former in response time thanks to its very fast switching action. If noise level is a priority, then the superconducting devices here presented present absolutely the best performances, with NEPs for KIDs, HEBs and TES reaching the 10^{-18}–10^{-19} W/Hz$^{1/2}$. Heterodyne systems are capable of extremely wide dynamic ranges (above 100 dB) and present also very good noise figures, especially when equipped with a cryogenic mixer like STJs. Electro optical sampling systems offer an extremely wide bandwidth and the single shot measurement capability, but require very precise synchronization and overlap with the THz pulse.

REFERENCES

[1] E. Bründermann *et al.*, *Terahertz Techniques*, Berlin, Germany: Springer-Verlag Berlin Heidelberg, 2012. doi:10.1007/978-3-642-02592-1

[2] , F. J. Low, "Low-Temperature Germanium Bolometer", *J. Opt. Soc. Am.*, vol. 51, p. 1300, 1961. doi:10.1364/josa.51.001300

[3] M. J. Griffin *et al.*, "The Herschel-SPIRE instrument and its in-flight performance", *A&A*, vol. 518, p. L3, 2010. doi:10.1051/0004-6361/201014519

[4] W. S. Holland *et al.*, "SCUBA: a common-user submillimetre camera operating on the James Clerk Maxwell Telescope", *Mon. Not. R. Astron. Soc.*, vol. 303, pp. 659–672, 1999. doi:10.1046/j.1365-8711.1999.02111.x

[5] A. Skalare *et al.*, "Speed measurements of diffusion-cooled tantalum bolometers", *IEEE Trans. Appl. Supercond.*, vol. 13, pp. 160–163, 2003. doi:10.1109/TASC.2003.813670

[6] R. Romestain *et al.*, "Fabrication of a superconducting niobium nitride hot electron bolometer for single-photon counting", *New J. Phys.*, vol. 6, p. 129, 2004. doi:10.1088/1367-2630/6/1/129

[7] D. F. Santavicca *et al.*, "Antenna Coupled Niobium Bolometers for Terahertz Spectroscopy", *IEEE Trans. Appl. Supercond.*, vol. 17, pp. 412–415, 2007. doi:10.1109/TASC.2007.898191

[8] A. J. Miller *et al.*, "Demonstration of a low-noise near-infrared photon counter with multiphoton discrimination", *Appl. Phys. Lett.*, vol. 83, pp. 791–793, 2003. doi:10.1063/1.1596723

[9] W. S. Holland *et al.*, "SCUBA-2: the 10 000 pixel bolometer camera on the James Clerk Maxwell Telescope", *Mon. Not. R. Astron. Soc.*, vol. 430, pp. 2513–2533, 2013. doi:10.1093/mnras/sts612

[10] F. C. Wellstood *et al.*, "Hot-electron effects in metals", *Phys. Rev. B*, vol. 49, pp. 5942–5955, 1994. doi:10.1103/physrevb.49.5942

[11] R. T. Tung, "The physics and chemistry of the Schottky barrier height", *Appl. Phys. Rev.*, vol. 1, p. 011304, 2014. doi:10.1063/1.4858400

[12] M. Brosi *et al.*, "Fast mapping of terahertz bursting thresholds and characteristics at synchrotron light sources", *Phys. Rev. Accel. Beams*, vol. 19, p. 110701, 2016. doi:10.1103/PhysRevAccelBeams.19.110701

[13] S. Ariyoshi *et al.*, "Terahertz detector based on a superconducting tunnel junction coupled to a thin superconductor film", *Appl. Phys. Lett.*, vol. 95, p. 193504, 2009. doi:10.1063/1.3263711

[14] S. Doyle *et al.*, "Lumped Element Kinetic Inductance Detectors", *J. Low Temp. Phys.*, vol. 151, pp. 530–536, 2008. doi:10.1007/s10909-007-9685-2

[15] F. Mazzocchi *et al.*, "THz multi-line of sight polarimeter for fusion reactors", *Fusion Eng. Des.*, vol. 130, pp. 1–5, 2018. doi:10.1016/j.fusengdes.2018.02.089

[16] P. de Visser *et al.*, "Fluctuations in the electron system of a superconductor exposed to a photon flux", *Nat. Commun.*, vol. 5, p. 3130, 2014. doi:10.1038/ncomms4130

[17] M. Calvo *et al.*, "The NIKA2 Instrument, A Dual-Band Kilopixel KID Array for Millimetric Astronomy", *J. Low Temp. Phys.*, vol. 184, pp. 816–823, 2016. doi:10.1007/s10909-016-1582-0

[18] P. Thoma *et al.*, "Highly Responsive Y–Ba–Cu–O Thin Film THz Detectors With Picosecond Time Resolution", *IEEE Trans. Appl. Supercond.*, vol. 23, p. 2400206, 2013. doi:10.1109/TASC.2012.2233851

[19] P. Probst*et al.*, "Nonthermal response of Y–Ba_2–Cu_3–O_7 thin films to picosecond THz pulses", *Phys. Rev. B*, vol. 85, p. 174511, 2012. doi:10.1103/PhysRevB.85.174511

[20] M. Caselle *et al.*, "KAPTURE-2. A picosecond sampling system for individual THz pulses with high repetition rate", *JINST*, vol. 12, p. C01040, 2017. 10.1088/1748-0221/12/01/C01040

[21] S. Schmuck *et al.*, "Design of the ECE diagnostic at Wendelstein 7-X", *Fusion. Eng. Des.*, vol. 84, pp. 1739–1743, 2009. doi:10.1016/j.fusengdes.2008.12.094.

[22] J. Nührenberg*et al.*, "Overview on Wendelstein 7-X Theory", *Fusion Technol.*, vol. 27, pp. 71–78, 1995. doi:10.13182/FST95-A11947048

[23] B. Di Bartolo and O. Forte (Eds.), "Advances in Spectroscopy for Lasers and Sensing". Netherlands: Springer Netherlands, 2006. doi:10.1007/1-4020-4789-4

[24] B. Pradarutti *et al.*, "Electrooptical sampling of ultra-short THz pulses by fs-laser pulses at 1060 nm", *Appl. Phys. B*, vol. 85, pp. 59-–62, 2006. doi:10.1007/s00340-006-2303-1

ISBN: 978-3-95450-222-6 ISSN: 2673-5350 doi:10.18429/JACoW-IBIC2020-WEA002

[25] J-P. Caumes*et al.*, "Kerr-Like Nonlinearity Induced via Terahertz Generation and the Electro-Optical Effect in Zinc Blende Crystals", *Phys. Rev. Lett.*, vol. 89, p. 047401, 2002. doi:10.1103/PhysRevLett.89.047401

[26] M. Hangyo *et al.*, "Terahertz Time-Domain Spectroscopy of Solids: a Review", *Int. J. Infrared Millimeter Waves*, vol. 26, pp. 1661-–1690, 2005. doi:10.1007/s10762-005-0288-1

[27] A. Rice *et al.*, "Terahertz optical rectification from 110 zinc-blende crystals", *Appl. Phys. Lett.*, vol. 64, pp. 1324–1326, 1994.

[28] A. Singh *et al.*, "Up to 70 THz bandwidth from an implanted Ge photoconductive antenna excited by a femtosecond Er:fibre laser", *Light Sci. Appl.*, vol. 9, p. 30, 2020. doi:10.1038/s41377-020-0265-4

[29] E. R. Brown *et al.*, "State-of-the-art in 1.55 µm ultrafast InGaAs photoconductors, and the use of signal-processing techniques to extract the photocarrier lifetime", *Semicond. Sci. Technol.*, vol. 20, pp. S199–S204, 2005. doi:10.1088/0268-1242/20/7/009

[30] P. Y. Han *et al.*, "Coherent, broadband midinfrared terahertz beam sensors", *Appl. Phys. Lett.*, vol. 73, pp. 3049–3051, 1998. doi:10.1063/1.122668

[31] S. Funkner *et al.*, " Revealing the dynamics of ultrarelativistic non-equilibrium many-electron systems with phase space tomography", 2019. arXiv:1912.01323

[32] E. Roussel *et al.*, "Observing microscopic structures of a relativistic object using a time-stretch strategy", *Sci. Rep.*, vol. 5, p. 10330, 2015. doi:10.1038/srep10330

[33] L. Rota, C. M. Caselle, N. Hiller, A.-S. Mueller, and M. Weber, "An Ultrafast Linear Array Detector for Single-Shot Electro-Optical Bunch Profile Measurements", in *Proc. IBIC'14*, Monterey, CA, USA, Sep. 2014, paper TUPD10, pp. 435–437.

Content from this work may be used under the terms of the CC BY 3.0 licence (© 2020). Any distribution of this work must maintain attribution to the author(s), title of the work, publisher, and DOI

ISBN: 978-3-95450-222-6 ISSN: 2673-5350 doi:10.18429/JACoW-IBIC2020-WEPP01

FILLING PATTERN MEASUREMENT USING A 500 MHz DIGITIZER AT SOLEIL AND APS STORAGE RINGS

D. Bisiach, M. Cargnelutti, P. Leban, M. Žnidarčič, Instrumentation Technologies doo, Solkan, Slovenia
N. Hubert, D. Pedeau, SOLEIL, Gif-sur-Yvette, Paris, France
A. Brill, N. Sereno, ANL, Lemont-Illinois, USA

Abstract

Filling pattern was measured at SOLEIL and APS storage ring using a 500 MHz digitizer. Various filling patterns were measured: from a single bunch to a multi-bunch hybrid fill. The digitizer has 14-bit granularity and locks the sampling clock to exact RF frequency (352 MHz). Signals were sampled from the standard BPM pickup and APD diode. Data were retrieved using Matlab and Labview interfaces and compared to existing systems.

INTRODUCTION

An essential part of the synchrotron diagnostics system involves the investigation of the bucket distribution during the operation.

Modern light sources allow to operate with different filling pattern modes (e.g. single bunch, multi-bunch, hybrid patterns), and knowledge of the real-time bunch charge longitudinal distribution can help to tune the beam stability and performance [1].

Digitizers with high ADC resolution and wide dynamic range are an alternative to the existing high sampling rate oscilloscopes that are commonly used in combination with BPM pick-up or APD diode detectors.

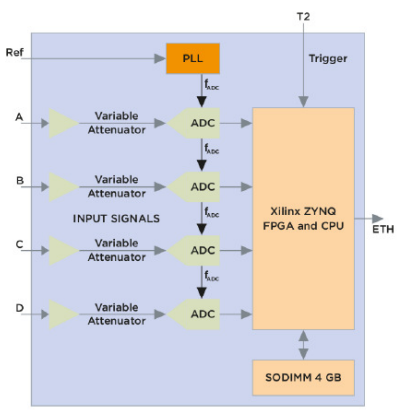

Figure 1: Libera Digit 500 block schematics.

The Libera Digit 500 is a 500 MHz/14-bit ADC digitizer based on the CavityBPM hardware [2] with the possibility to customize the frontend (e.g. input bandwidth, additional filters…). The sampling clock is locked to an external reference input to lock the internal PLL (maximum jitter 10 ps) on the machine RF clock. Data from the ADC are di-rectly sent to a Xilinx Zynq 7035 based SOC which runs both the signal processing and the OS.

The total dynamic range is 90 dB which is achieved with the use of the 0-31 dB frontend attenuators. The instrument is triggerable with a maximum trigger frequency of 1kHz (see Fig. 1).

The Libera Digit 500 DC version has an analog bandwidth of 0-250 MHz, the Libera Digit 500 AC version used during the testing at Soleil, and APS has a 250 MHz-2 GHz analog bandwidth.

The purpose of these measurements was to confirm that the Libera Digit 500 could be used as a filling pattern monitoring device in case of BPM pickups and to evaluate its behavior also using diode detectors [3].

Access to the interface can be performed using a TANGO client, Labview, or the SSH interface.

MEASUREMENTS – SOLEIL

The fill pattern monitoring testing consisted of testing two setups, the first using a BPM pickup as a bunch detector and the second using an APD diode setup.

Fill Pattern Monitor Using BPM

The original filling pattern monitoring instrumentation at Soleil consists of an Agilent Digitizer with 8 GS/s-8 bit resolution.

The setup with the Libera Digit 500 AC is illustrated in Fig.2 and it was implemented to retrieve the signal directly from a pickup using attenuators and phase shifters to tune the signal delays and the bunch flat top.

The pickup outputs (A, B, C, and D) were connected to fixed attenuators. Each attenuator output entered a mechanical phase shifter (API Technologies – Weinschel, bandwidth DC-3GHz). Since the signal power was still too high some additional attenuators were placed before the signal splitter-combiner (Mini-Circuits ZFRSC-4-842-S+, DC-8400 MHz). The combined signal then entered an additional mechanical phase shifter (4428C from ARRA, bandwidth DC-4 GHz).

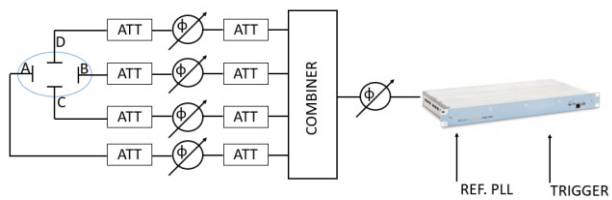

Figure 2: Setup schematics.

Content from this work may be used under the terms of the CC BY 3.0 licence (© 2020). Any distribution of this work must maintain attribution to the author(s), title of the work, publisher, and DOI

ISBN: 978-3-95450-222-6 ISSN: 2673-5350 doi:10.18429/JACoW-IBIC2020-WEPP01

Before the measurement, every single channel delay was set equal with the first mechanical phase shifter (maximizing each signal amplitude having the three other channels disconnected). This trick allows us to set the same time delay on all the 4 channels, resulting in a sync sum signal from the pickup to the Libera Digit 500.

Once all the 4 channels had the same time delay set the second mechanical phase shifter was used to reach the maximum signal amplitude which assured the sampling point to be on the flat top of the measured pulse.

The signal from the BPM was tested with different filling patterns and at different currents: single bunch, 8 bunches, and 1 quarter filling (reported in Fig. 3).

The signal level was adjusted with the frontend attenuators.

The length of the acquisition buffer was 650000 data points which correspond to 1562 turns. The acquisition noise is pretty constant over the input scale.

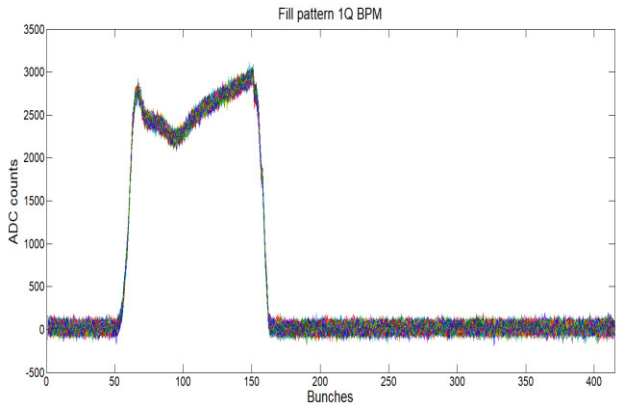

Figure 3: BPM fill pattern for a 1Q filling. The x-axis reports the bunches number while the y-axis the relative ADC counts.

During the 8 bunches machine operation mode, the flat top acquisition point was shifted in the slope direction reaching the 75% and 50% of the original maximum amplitude, RMS noise did not increase.

The AC Libera Digit 500 gives identical results in term of resolution compared to the initial SOLEIL setup on a BPM signal and is an appropriate system for filling pattern monitoring on such signal.

Fill Pattern Monitor Using an APD

The Libera Digit 500 was connected to an existing setup using an APD diode. The original setup was monitoring the signal with an oscilloscope (an Agilent Digitizer with 8 GS/s-8 bit resolution, 1 GHz bandpass frequency).

The Libera Digit 500 was connected to the diode output. The measurement with the diode is more delicate because its linearity range is too small to cover the current full scale. We kept the diode output amplitude constant at ~0.3 V adjusting for each current optical densities at the input. With 21 dB attenuation in the Libera Digit 500, it corresponds to ~7000 counts on the ADCs.

The effect of the AC coupling on the Libera Digit 500 can be seen and consists in a recovery effect due to the DC component (which was not present on the BPM setup), this is reported for a one quarter filling in Fig. 4:

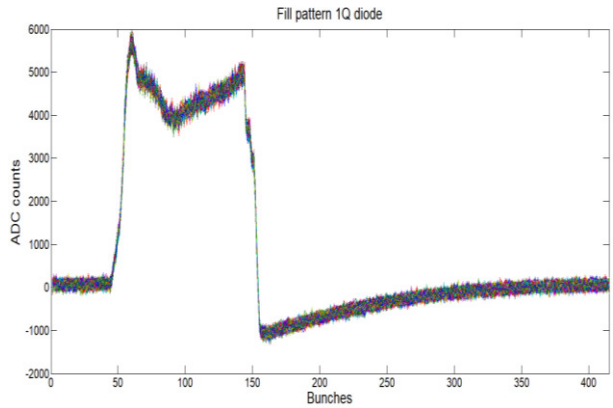

Figure 4: Diode DC recovery effect with 1Q filling.

The same recovery effect is reported in Fig. 5 with a 2Q fill pattern, leaving to an offset between Q1 and Q2:

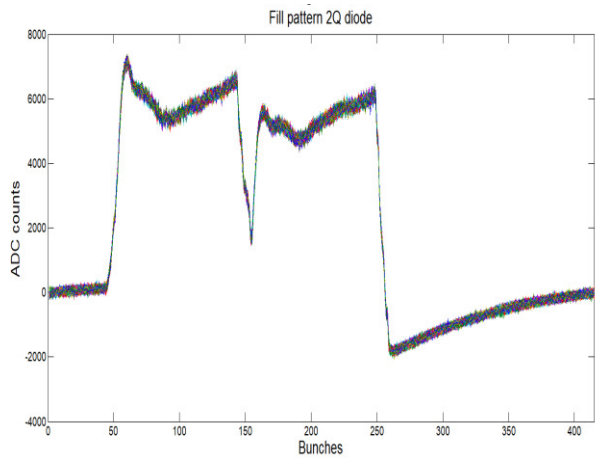

Figure 5: Diode DC recovery effect with 2Q filling.

The AC version of the Libera Digit 500 is not adapted to an APD diode signal. The DC version (with extended bandwidth) has not been tested.

MEASUREMENTS – SOLEIL

The BCM used for the reference measurement is a Xilinx FPGA-based device developed by the Advanced Light Source (ALS). It uses a Virtex-6 FPGA, with an FMC104 14-bit 250MSPS ADC. Interleaved sampling is used to obtain 46 sample points per bucket, and 1024 turns are averaged to determine the charge for each bunch. An EPICS IOC converts ADC counts into bunch current using the SR DCCT value.

The Libera Digit 500 was connected to a spare set of bpm buttons. These bpm cables were connected directly to

Content from this work may be used under the terms of the CC BY 3.0 licence (© 2020). Any distribution of this work must maintain attribution to the author(s), title of the work, publisher, and DOI

ISBN: 978-3-95450-222-6 ISSN: 2673-5350 doi:10.18429/JACoW-IBIC2020-WEPP01

Content from this work may be used under the terms of the CC BY 3.0 licence (© 2020). Any distribution of this work must maintain attribution to the author(s), title of the work, publisher, and DOI

the buttons and phase-matched with mechanical phase shifters, and then combined with a ZN4PD1-50-S+ combiner (500-5000 MHz). An attenuator was used on the combined signal to bring the output signal to a safe range for the Digit 500 input. The input RF clock phase was adjusted with phase shifters to maximize the ADC counts of the signal of the Digit 500. For the 'scaled' plot, the BCM units were in mA (positive peaks), while the Libera Digit 500 units were ADC counts (negative peaks). The mean of each was calculated to find the scaling factor to plot them both together.

Figure 6 reports a comparison between the Libera Digit 500 and the existing BCM device. The storage ring was filled with 324 bunches.

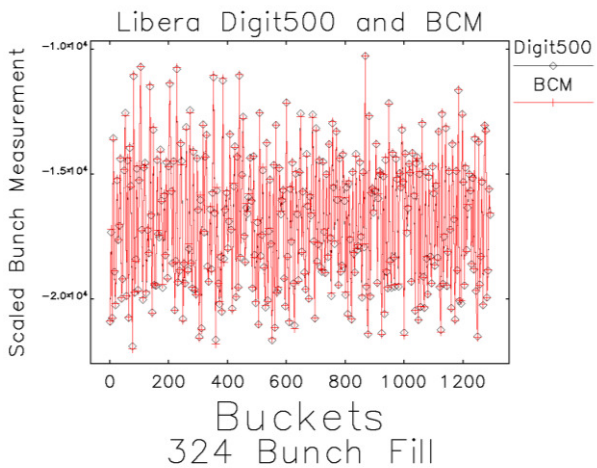

Figure 6: BCM and Libera Digit 500 comparison.

It is possible to see that the peaks corresponding to the BCM readout (in red) are well aligned with the peaks detected by the Libera Digit 500 (grey dots).

CONCLUSIONS

The performed measurements proved the capability of the Libera Digit 500 to perform as an efficient fill pattern monitoring system for light source storage rings.

The module works perfectly for acquiring the BPM signal. This behavior is supported by the results from both testings at SOLEIL and APS storage ring.

When connected to the photodiode detector the AC coupling distorts the signal due to the DC component coming from the diode.

ACKNOWLEDGEMENTS

The authors are grateful to SOLEIL and APS storage rings for providing a testbench for various measurements.

REFERENCES

[1] C. Y. Wu, J. Chen, K. T. Hsu, K. H. Hu, and C. H. Kuo, "Filling Pattern Measurement for the Taiwan Light Source", in *Proc. 11th European Particle Accelerator Conf. (EPAC'08)*, Genoa, Italy, Jun. 2008, paper TUPC038, pp. 1137-1139.

[2] M. Cargnelutti *et al.*, "Design and Simulations of the Cavity BPM Readout Electronics for the ELI-NP Gamma Beam System", in *Proc. 7th Int. Particle Accelerator Conf. (IPAC'16)*, Busan, Korea, May 2016, pp. 264-266. doi:10.18429/JACoW-IPAC2016-MOPMR017

[3] P. Leban, S. Bassanese, G. Brajnik, and R. De Monte, "Evaluation of a New 500 MHz Digitizer at Elettra and Fermi", in *Proc. 10th Int. Particle Accelerator Conf. (IPAC'19)*, Melbourne, Australia, May 2019, pp. 2635-2637. doi:10.18429/JACoW-IPAC2019-WEPGW071

ISBN: 978-3-95450-222-6 ISSN: 2673-5350 doi:10.18429/JACoW-IBIC2020-WEPP03

BUNCH PURITY MEASUREMENT FOR SSRF*

B.Gao, L.W.Lai†, X.Q.Liu, S.S.Cao, Y.B.Leng

Shanghai Advanced Research Institute, Chinese Academy of Sciences, Shanghai, China

Abstract

SSRF is currently working on the beam line phase-II project, which has moved toward laser/X-ray pump-probe experiments. To quantify the bunch filling pattern and purity of the timing bunch, high precision beam charge measurement is necessary. Therefore, a bunch purity monitor based on the time-correlated single-photon counting techniques has been installed. A series of tests to evaluate the system have been carried out, according to these results, it is able to predict the system performance. The system has exceptionally good time resolution (a few pico seconds) and high dynamic range (more than seven orders of magnitude).

INTRODUCTION

Shanghai synchrotron radiation facility (SSRF) is a third-generation synchrotron radiation light source. It has completed a lot of research work in the 11 years since its establishment. The ongoing SSRF beamline phase-II project, the main construction content includes the construction of 16 beam lines and experimental stations, experimental auxiliary systems, light source performance expansion, etc. The project focuses on major scientific and technical issues in the fields of energy, environment, materials, condensed matter physics, earth sciences, chemistry and life sciences, with the goal of greatly improving the overall experimental capabilities of SSRF. It also has a lot of technology goals. To realize the third-generation synchrotron radiation light source experimental technology with near-limit resolution (time/space/energy/momentum), realize the innovative combination of photon energy regions and ultra-long station hall experimental technology, and realize online/offline comprehensive experimental capabilities [1].

At SSRF storage ring 720 RF buckets are available be populated with electrons. At the primary operational mode, 200 buckets are left empty, only 520 bunches in 4 bunch trains are injected to the storage ring. During the construction of the SSRF beamline phase-II project, the requirements for time-resolved experiments and special time structure filling modes are proposed. In order to meet this requirement, SSRF will be operated in hybrid mode. In the future, one of the buckets in the dark place will be populated with the timing bunch.

For the time-resolved experiment, in the detection window, there expects no other interference except for the synchronization light emitted by the probe bunch, that is, it is necessary to ensure that there are no electrons in the buckets around the timing bunch. These experiments typically require the pattern to be as exact as possible, with ideally no electrons in unwanted bucket/bunch positions: a typical ratio of 10^5 :1 between wanted/unwanted populations is desired this ratio often being referred to as the bunch purity [2]. However, in actual operation after the bunch is excited from the electron gun, due to acceleration errors during acceleration, part of the electrons will be captured by the RF buckets adjacent to the timing bunch, resulting in poor bunch purity; In addition, due to the effect of intra-beam scattering, there will also has a small amount of electrons in the adjacent buckets. Therefore, the users want to get more accurate bunch pattern, the purity measurement concept is born from this. Therefore, the injector and X-Y kicker magnets must be optimized to eliminate unwanted charges. At this time, the measurement of the bunch pattern provides a very important basis.

Historically, a dedicated BPM was used to monitor the filling pattern at SSRF and other light sources [3-6]. Although the beam charge monitor based on the BPM provides a rough monitoring of the bunch pattern, the resolution can reach to 0.02% (average measurement), this method is far from the requirement of purity measurement. Therefore, a more precise system is needed to measure the bunch purity of the timing bunch.

A bunch purity measurement system based on the photomultiplier tube and time-correlated single photon counter has been established at SSRF. This article introduces the construction of this system, the verification and optimization of system performance, and the related beam experiment results.

TIME-CORRELATED SINGLE PHOTON COUNTING

Time-correlated single photon counting (TCSPC) has the advantages of good time resolution, high sensitivity, high measurement accuracy, and large dynamic range. Photon counting technology is a digital technology that measures discrete photon pulses [7 ,8]. The intensity of the detected photocurrent is lower than the thermal noise level (10^{-14}W) of the photodetector itself at room temperature. It is difficult to use the usual DC detection method Extract it out. The photon counting method takes advantage of the natural discrete characteristics of the photon detector's output electrical signals under weak light irradiation, and uses pulse discrimination technology and digital counting technology to identify and extract extremely weak signals. The photomultiplier tube (PMT) outputs a fluctuating direct current when the input light intensity is relatively strong, and when the light is weak, the output photocurrent is no longer continuous, and when the input light is extremely

* Work supported by Youth Innovation Promotion Association, CAS (Grant No. 2019290); SSRF-II beamline project
† lailongwei@zjlab.org.cn

Content from this work may be used under the terms of the CC BY 3.0 licence (© 2020). Any distribution of this work must maintain attribution to the author(s), title of the work, publisher, and DOI

ISBN: 978-3-95450-222-6 ISSN: 2673-5350 doi:10.18429/JACoW-IBIC2020-WEPP03

Content from this work may be used under the terms of the CC BY 3.0 licence (© 2020). Any distribution of this work must maintain attribution to the author(s), title of the work, publisher, and DOI

weak, it will output discrete pulses. The output pulse of the multiplier tube can be identified and extracted by the single photon counter.

For the bunch purity measurement, the TCSPC techniques are common used in storage rings [2] [9-11]. The photon arrival time is measured relative to a clock pulse which is synchronized to the bunch revolution frequency via the storage ring RF system. The TCSPC system gives a histogram of the longitudinal distribution of the beam in the storage ring.

SYSTEM CONFIGURATION

Hardware

The TCSPC based bunch purity monitor was installed in the optics hunch of the SSRF diagnostic beamline. The whole hardware system includes: synchrotron radiation (SR) light extraction end, optical front end, photomultiplier tube, electronics front end, photon counter, etc.

The optics hutch of SSRF diagnostics beamline at about 17m from the source point, the wavelength of the extracted SR light is 532 nm ±5%. The purity measurement system is installed at the end of the beamline.

The front end includes: diaphragm, narrowband filter, and attenuator. The main purpose is to attenuate the synchronized light to be extremely weak to ensure that the PMT output signal is a pulse signal that can be recognized by the photon counter, the counting rate always be set to around 1 count per turn (1.44 μs). The beam current of SSRF is about 300 mA, the visible beam power is about 0.3mW or about 10^{15} photons/s. To reduce the counting rate, the power of SR light must be attenuated by 10 orders of magnitude.

The SR light will hit the PMT after being attenuated by the optical front end. The PMT of this system uses Hamamatsu's E3059-500 photomultiplier tube. The front end of its electronics is an amplifier.

The single photon counter uses the PicoHarp 300 (PicoQuant—http://www.pico-quant.com), bunch revolution frequency (694 kHz) signal generated by the storage ring timing system as its trigger signal. The interval between the photon reaching the detector and the trigger signal can be measured and counted. After a period of time (seconds or Minute level) to obtain the photon distribution curve, that is, the bunch charge distribution curve in the storage ring.

Schematic diagram of Bunch Purity Measurement System at SSRF is showed in Fig.1.

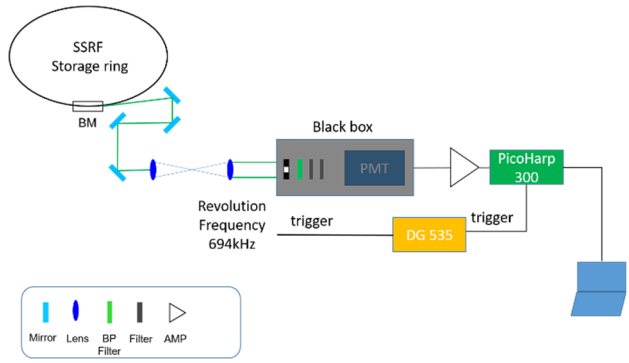

Figure 1: Schematic diagram of Bunch Purity Measurement System at SSRF.

A very important work in the single photon counting method based on time resolution is the removal of background light noise. Synchronous light needs to be attenuated to a single photon before entering the PMT. The presence of background light will directly affect the accuracy of purity measurement. Therefore, it is necessary to shield the background light. This system builds a black box on the optical platform to shield the background noise, as shown in the figure below in Figure 2.

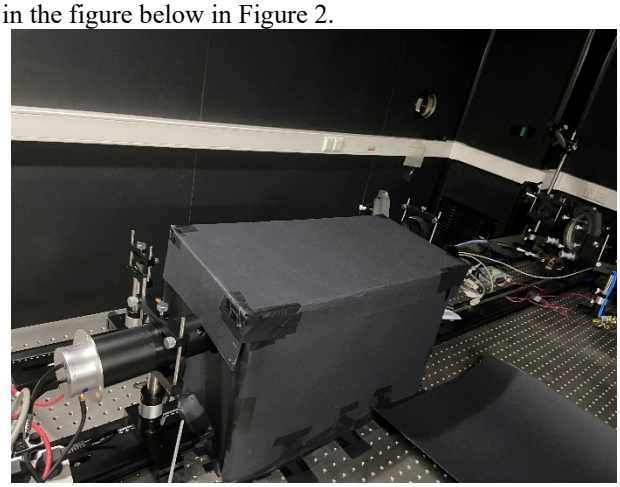

Figure 2: Black box to screen out the background light noise.

Software

The main function of the software is to set the photon counter parameters, data reading, data processing, and EPICS-based IOC and user interface.

The most important parameter setting of the photon counter is the time resolution. TCSPC system generates a histogram of binned arrival time measurements, the minimum binning window of “Pico-Harp 300” is 2ps and the maximum number of longitudinal binned windows in one trigger period is 65536. The trigger frequency of this system is 694 kHz (1.44 μs), so the time resolution of this system is set to 32 ps.

The data processing needs to extract the charge distribution. Since the longitudinal phase (arrival time) jitter of the SSRF under normal mode is a few ps, the bunch peak will be distributed in a single counting interval. Therefore the peak value extraction method is used to extract the charge

ISBN: 978-3-95450-222-6 ISSN: 2673-5350 doi:10.18429/JACoW-IBIC2020-WEPP03

of a single bunch. At the same time, in order to calibrate the beam charge, the system synchronously acquires the value of DCCT to realize the real-time calibration of the bunch charge.

In order to realize the connection with the main control network of the storage ring, the system builds an IOC based on EPICS, and builds a user interface control terminal in the control room, which can display the bunch charge distribution and purity data, as well as the configuration of system parameters, the interface is shown as Fig 3.

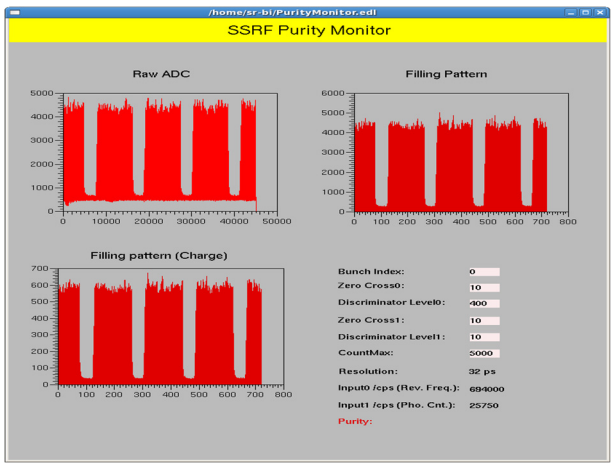

Figure 3: OPI of SSRF bunch purity measurement system.

SYSTEM PERFORMANCE EVALUATION

At present, the Shanghai Light Source has not been working in Hybrid mode, only 500 bunches distributed in 4 bunch trains. Bunch pattern measured by the purity monitor is showed in Fig 4.

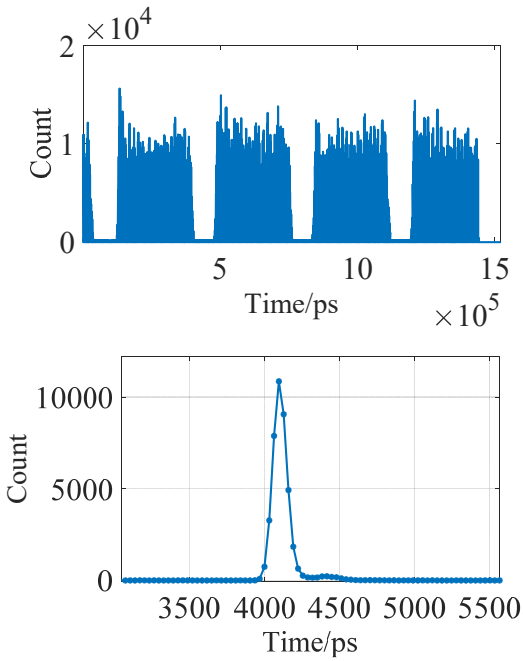

Figure 4: Bunch pattern measured by the SSRF bunch purity monitor at SSRF. Up: Filling pattern; Bottom: Charge distribution of a single bunch.

The SSRF bunch purification system has not been activated, hence the bunch purity cannot be guaranteed. Therefore, in order to evaluate the purity measurement resolution, this article applied for a special machine research time. Only two or three bunches were injected into the storage ring, so that electrons would not appear far away from the stored bunches. Bunch pattern (30 seconds accumulation) is showed in Fig.5.

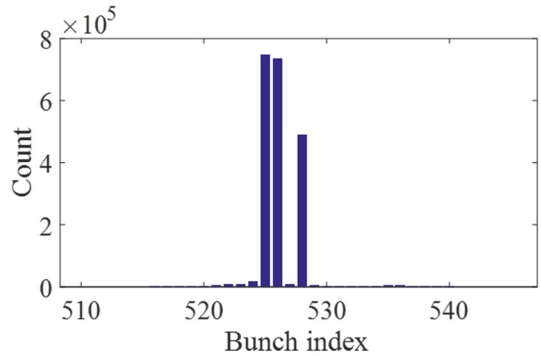

Figure 5: Bunch pattern from Bunch Purity Measurement System after only a few bunches have been injected into the storage ring.

Bunch purity is expressed by the ratio of the count of the highest bunch charge to the lowest count in the storage ring. After about 2 minutes of cumulative counting, the measured purity (ratio of wanted and unwanted populations) can reach $4*10^6$; after about 5 minutes of cumulative counting, the measured purity can reach $2*10^7$ level. According to this, time accumulation will make the purity measurement more accurate, and the data refresh time is a few minutes or even tens of seconds.

CONCLUSION

In this paper, the bunch purity measurement system is built based on the SSRF diagnostic line and time-correlated single photon counting technology. And through the performance evaluation experiment to complete the system performance evaluation. After evaluation, the time resolution of this system can reach to 32 ps; the bunch purity resolution can reach the order of 10^6 under the accumulation of 2 minutes, and the order of magnitude 10^7 under the accumulation of 5 minutes.

In the future, after the hybrid mode is realized, direct purity measurement will be achieved, and thanks to the time resolution bunch length measurement is planned to be studied based this new system.

ACKNOWLEDGEMENTS

Thanks to Dr. Jun He from the Institute of High Energy Physics, Chinese Academy of Sciences and Dr. Jeff Corbett from the SLAC National Laboratory in the United States for their guidance and help.

REFERENCES

[1] Shanghai synchrotron radiation facility and its beam line project, *Bulletin of the Chinese Academy of Sciences*, 2019,34(Z2): 50-53.

Content from this work may be used under the terms of the CC BY 3.0 licence (© 2020). Any distribution of this work must maintain attribution to the author(s), title of the work, publisher, and DOI

ISBN: 978-3-95450-222-6 ISSN: 2673-5350 doi:10.18429/JACoW-IBIC2020-WEPP03

Content from this work may be used under the terms of the CC BY 3.0 licence (© 2020). Any distribution of this work must maintain attribution to the author(s), title of the work, publisher, and DOI

[2] C.A. Thomas, G. Rehm, H.L. Owen, "Bunch purity measurement for Diamond", *Nuclear Inst & Methods in Physics Research A*, 2006, 566(2):762-766.

[3] Yan Yingbing, Leng Yongbin, Lai Longwei, "Beam lifetime measurement using beam position monitor in SSRF" *High Power Laser and Particle Beams*, 2012, 24(1): 189-192.

[4] Zhang Baichun, Leng Yongbin, "Simulation of beam bunch charge measurement using BPM pickup", *Nuclear techniques*, 2009，32(4):256-259.

[5] Y. Yang, Y.B. Leng, Y.B. Yan, *et al.* "Development of the bunch-by-bunch beam position acquisition system based on BEEcube", *Nucl. Sci. Tech.*, no. 27, p. 47, 2016. doi:10.1007/s41365-016-0035-4

[6] F.Z.Chen., Z.C.Chen, Y.M.Zhou, *et al.*, "Touschek lifetime study based on the precise bunch-by-bunch BCM system at SSRF", *Nucl. Sci.Tech.*, no. 30, p. 144, 2019. doi:10.1007/s41365-019-0655-6

[7] D.V.O'Conor.Philips, *Time-correlated Single Photon Counting*, Academic Press, New York, 1984.

[8] W.Becker, "Correlated Single Photon Counting Techniques", vol.81, Springer Series in Chemical Physics, 2005.

[9] B. Xu, E. Carranza, A. Chen, S. Condamoor, W. J. Corbett, and A. S. Fisher, "Electron Bunch Pattern Monitoring via Single Photon Counting at SPEAR3", in *Proc. 6th Int. Beam Instrumentation Conf. (IBIC'17)*, Grand Rapids, MI, USA, Aug. 2017, pp. 168-171. doi:10.18429/JACoW-IBIC2017-TUPCC09

[10] W. J. Corbett, W. Y. Mok, and K. Tian, "Bunch Pattern Measurement via Single Photon Counting at SPEAR3", in *Proc. 3rd Int. Beam Instrumentation Conf. (IBIC'14)*, Monterey, CA, USA, Sep. 2014, paper MOPD21, pp. 195-198.

[11] J.He, J.H.Yue, J.S.Cao, "Bunch purity measurement system for BEPCII", *Nuclear Techniques*, 2015, 38(5): 50103-050103. doi:10.11889/j.0253-3219.2015.hjs.38.050103

ISBN: 978-3-95450-222-6 ISSN: 2673-5350 doi:10.18429/JACoW-IBIC2020-WEPP04

MODERNIZATION AND OPERATION OF IONIZATION-PROPORTIONAL GAS COUNTER AT INR RAS PROTON LINAC

A. Melnikov†, S. Gavrilov[1]
Institute for Nuclear Research of the Russian Academy of Sciences, Troitsk, Moscow, Russia
[1]also at Moscow Institute of Physics and Technology (National Research University), Moscow, Russia

Abstract

Multianode gas counter is used as a detector for low intensity proton beam diagnostics at INR RAS linac. The device consists of ionization chamber to measure beam current and two proportional chambers, based on stripe geometry, to measure beam profiles. The data is processed with Labview software. The models and methods predicting operational characteristics of the counter in ionization and proportional mode are presented. An analytical model of recombination was tested to predict the saturation voltage for ionization mode. Beam test results and operational characteristics of the counter are presented as well as results of investigations of counter degradation under the beam. A new design of a gas filled counter is also discussed.

INTRODUCTION

A proton irradiation facility (PIF) at INR RAS linac is used to study radiation effects in electronic components. This facility is characterized with operational parameters: proton energy - 20÷210 MeV; particles per pulse - 10^7÷10^{12}; pulse duration - 0.3÷180 μs; pulse repetition rate - 1÷50 Hz.

Partially diagnostics is realized with a beam current transformer (BCT) installed in the beam pipe. The BCT provides absolute nondestructive measurements of beam pulse current with the amplitude > 25 μA. To measure beam current and profiles for less intensive beams MGC based on gas ionization is foreseen.

MULTIANODE GAS COUNTER

Multianode gas counter (MGC) [1] consists of 5 plates (Fig. 1) which are printed-circuit boards made of FR4 with 0.5 mm width. The metal covering is 18 μm nickel, plated with 0.05 μm immersive gold.

Three central plates form a dual gap ionization chamber. Electrons of primary ionization are collected at the middle anode plate by a quasi-uniform electrostatic field. This part of the detector allows to measure beam current in an ionization mode.

Lateral regions are proportional chambers for beam position and profile measurements. Electrons are collected at the multichannel anode structure, which consists of 25 stripes with 100 μm width, 100 mm length and 4 mm spacing. Strong nonuniform field around stripes leads to electron avalanches, increasing the signal.

† alexei.a.melnikov@gmail.com

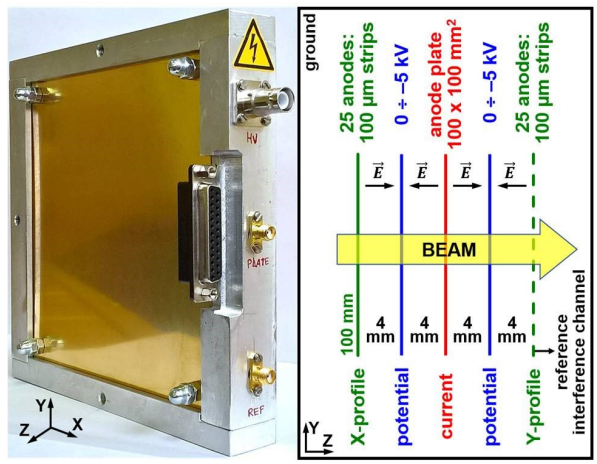

Figure 1: MGC photo and layout.

The total assembly of the counter is not sealed. The filling gas is atmospheric air.

The information about readout electronics and data acquisition system can be found elsewhere [2].

IONIZATION MODE

The number of primary ionization electrons defines the plateau level of ionization mode. The computed signal level based on dE/dx agrees with experimental results with 10% precision [2]. The gas composition was assumed as 80% N_2 and 20% O_2 molecules at standard conditions.

The measured signal from ionization chamber electrodes is caused by induced currents due to the moving electrons and ions: $i^{e,+,-}$ [3].

$$i^e(t) = \frac{Q_0}{t_{de}}\left(1 - \frac{t}{t_{de}}\right) exp\left(-\frac{t}{T_a}\right).$$

$$i^+(t) = \frac{Q_0}{t_{d+}}\left(1 - \frac{t}{t_{d+}}\right).$$

$$i^-(t) = \frac{Q_0}{t_{d-}}\left[1 - \frac{t}{t_{d-}} - \frac{T_a}{t_{de}}\left\{1 - exp\left(-\frac{t_{de}}{T_a}\left(1 - \frac{t}{t_{d-}}\right)\right)\right\}\right],$$

where Q_0 is the total charge of primary particles, $t_{de,+,-}$ is the drift time of electrons or ions of corresponding sign, T_a is an attachment time.

Content from this work may be used under the terms of the CC BY 3.0 licence (© 2020). Any distribution of this work must maintain attribution to the author(s), title of the work, publisher, and DOI

ISBN: 978-3-95450-222-6 ISSN: 2673-5350 doi:10.18429/JACoW-IBIC2020-WEPP04

Content from this work may be used under the terms of the CC BY 3.0 licence (© 2020). Any distribution of this work must maintain attribution to the author(s), title of the work, publisher, and DOI

Electrons are involved in two- or three-body attachment reactions with O_2 molecules with subsequent formation of negative O^- or O_2^- ions [4,5]. The total induced charge in ionization regime does not depend on the number of electrons attached [3].

The time structure of induced current by a pulsed beam can be obtained with the help of convolution operation of pulse time structure with induced currents (Fig. 2). The nonzero tail at the back front of MGC signal for long beam pulses is caused by the cumulative effect of physical degradation of the counter – Malter effect [6] (see also Fig. 9).

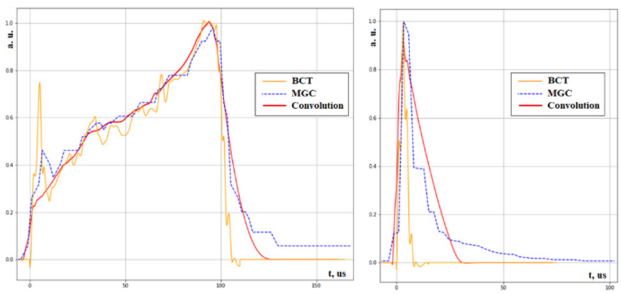

Figure 2: BCT measured signals from a proton macropulse, MGC measured signals from stripes in ionization mode and reconstructed signals with convolution method. Left picture – data for 100 μs beam pulse, right – for 1 μs beam pulse. MGC voltage is 2 kV, the graphs are normalized.

RECOMBINATION MODE

For beam pulses longer than ion collection time charge collection efficiency $f(\xi)$ [7] is:

$$f = \frac{2}{1+\sqrt{1+\frac{2}{3}\,\xi^2}},$$

$$\xi = \frac{md^2\sqrt{q}}{V},$$

where d is electrode spacing, $q\ [C/m^3 s]$ is ionization density, m is a constant depending on gas properties, V-applied voltage.

The formula for collection efficiency can fit the experimental saturation curves to find necessary value of m. After it can predict the shape of a signal curve and saturation threshold voltage. It can be done for different values of particles in the beam pulse N_b proportional to q (Fig. 3). The theoretical scaling of saturation voltage comes from the fact that ξ_{sat} is a dimensionless constant and therefore:

$$V_{sat} = const * \sqrt{q}.$$

Or in logarithmic coordinates $V_{sat}(N_b)$ is a line with a slope 0.5 predicted by the theory. The experiment also gives a line, the slope is 0.38 ± 0.01 (Fig. 4).

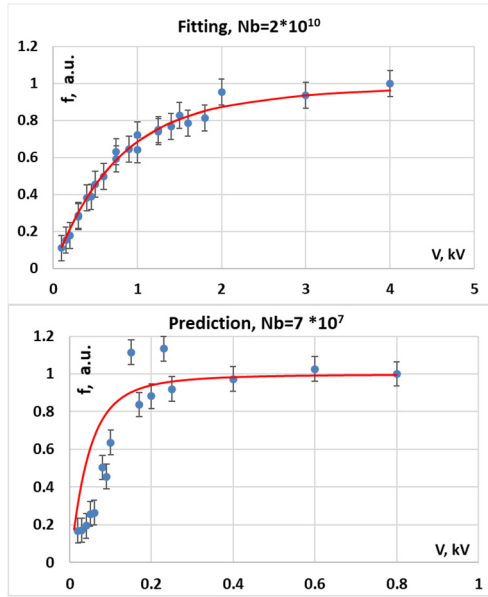

Figure 3: Experimental (blue circles) signal from the ionization chamber and theoretical model (red line). The upper picture is to find parameter m from fitting.

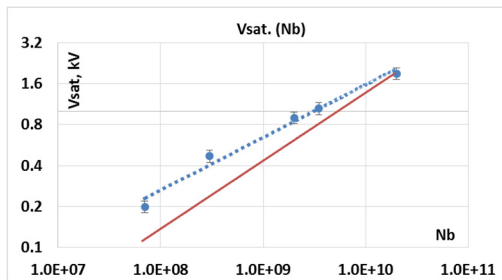

Figure 4: Experimental values (blue dots) and theoretical prediction (red line) of saturation voltage at 0.9 plateau level in a double logarithmic scale.

Another important consequence of the fact that ξ_{sat} is a constant - relation of $V_{sat}(d)$ which helps to find the proper size of a gas gap:

$$V_{sat} = const * d^2.$$

PROPORTIONAL MODE

MGC plates with stripes operate in proportional mode. In this chapter the model to predict gain–voltage properties of a proportional chamber is presented. First the electric field distribution around the stripes was calculated in COMSOL (Fig. 5). The electric field strength along a single line $E(s)$ is of further interest. The result strongly depends on a stripe geometry. This factor mainly defines the error of simulation. Information about detailed stripe shape after etching was needed.

The change in electron (n) and positive ion (m) concentration after passage of ds is:

$$dn = (\alpha - \eta)\, n\, ds.$$

$$dm = \alpha\, n\, ds,$$

ISBN: 978-3-95450-222-6 ISSN: 2673-5350 doi:10.18429/JACoW-IBIC2020-WEPP04

where α and η are townsend ionization and attachment coefficients. A simple integration can be done to get the avalanche plus primary ionization gain. After substitution of $E(s)$, $\alpha(E)$ and $\eta(E)$ in the derived formula one can obtain gain-voltage properties of a proportional chamber (Fig. 6).

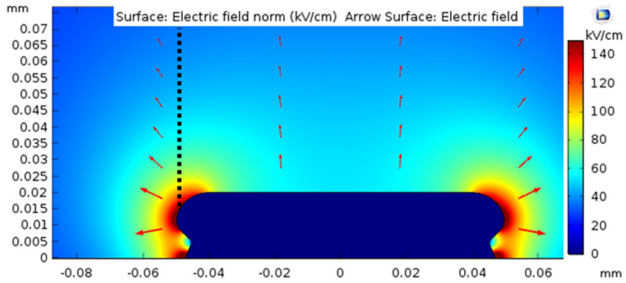

Figure 5: Distribution of electric field near a stripe for 4 kV voltage. The black line is for obtaining $E(s)$.

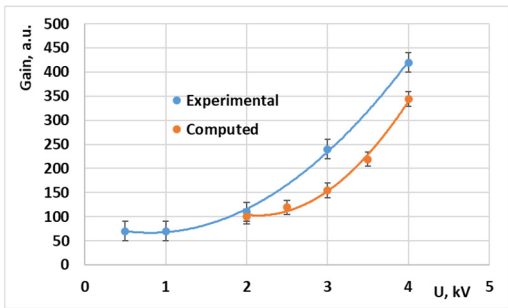

Figure 6: Experimental and computed gain-voltage curves for 94 MeV proton energy for proportional chamber.

MGC EXPLOITATION AND DEGRADATION EFFECTS

The experimental operational range of MGC is $10^7 \div 10^{11}$ p/pulse with pulse duration about 130 μs. Usage of beams less intensive than 10^7 p/pulse decreases the signal below the sensitivity threshold of MGC electronics.

It was found out, that intensive beams (density $>10^{10}$ p/cm^2) lead to oxidation of MGC stripes. Temper colors are visible in Fig. 7.

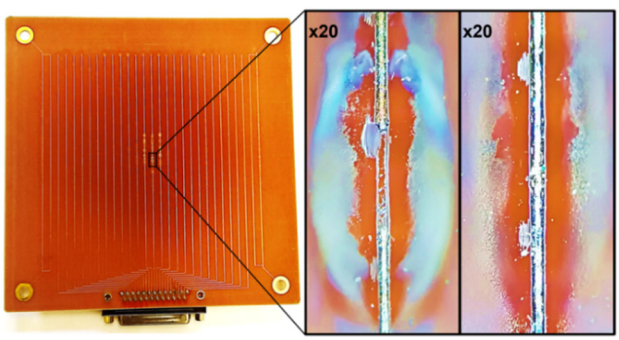

Figure 7: Ageing effects of MGC: stripe destruction and oxidation.

Dielectric oxide film reduces the field strength exerted on particles in avalanche region near stripes and decreases the signal [8]. As an example, profile signal amplitudes in Fig. 8 are almost identical after an irradiation. The way to solve the problem is to use O_2-free gas filling or measure beam profile without gas amplification. The stripes are subjected to physical degradation and destruction because of high ionization near the electrodes.

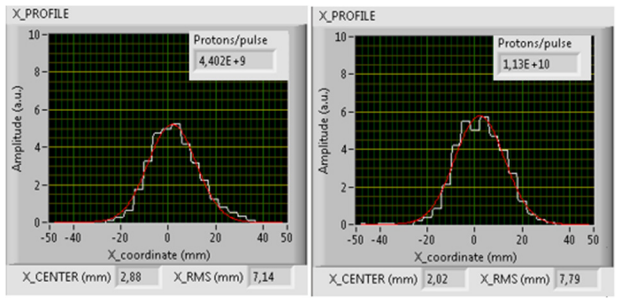

Figure 8: X profiles for a symmetric beam. Left – for $4.4*10^9$ protons/pulse; right – after $2.5*10^{15}$ protons passed for $1.13*10^{10}$ protons/pulse.

Plane chamber electrodes, which are mounted in front of the stripes, are also subjected to degradation (Fig. 9). Cathode deposits are also visible. They cause positive charge build-up and electron emission - Malter effect [6].

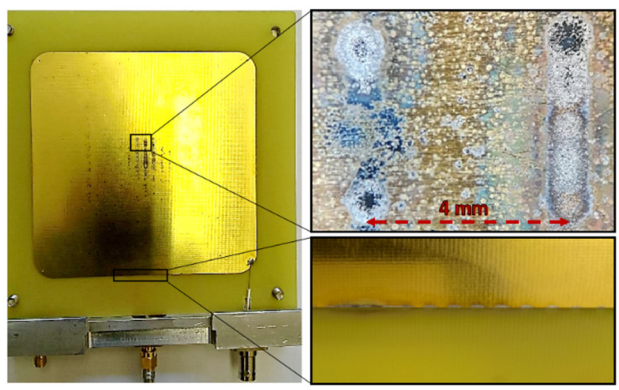

Figure 9: Photo of plane electrodes of proportional chamber subjected to degradation.

The lower limit for incident beam energy is ~ 20 MeV. Protons with this energy do not reach the last air gap of the counter [2].

NEW DESIGN OF A GAS COUNTER

The new design of MGC consists of only 3 printed-circuit boards instead of 5. The total volume is divided in two parts: segmented ionization chambers, measuring beam current and X, Y profiles in ionization mode. Beam current is obtained by summing the profile signals from stripes in the software.

The material, width, metal coating and active area are the same as in the previous version. One plate with uniform square electrodes on both sides is mounted in the middle of a metal housing and connected to a high voltage terminal (Fig. 10). The remaining two plates have 25 signal stripes with 3.9 mm width and 0.1 mm spacing (Fig. 11). There are also two additional stripes at the edges of the active area at zero potential to form a more homogenous electric field in the active volume. The multichannel plates have a dielectric mask covering to

Content from this work may be used under the terms of the CC BY 3.0 licence (© 2020). Any distribution of this work must maintain attribution to the author(s), title of the work, publisher, and DOI

ISBN: 978-3-95450-222-6 ISSN: 2673-5350 doi:10.18429/JACoW-IBIC2020-WEPP04

Content from this work may be used under the terms of the CC BY 3.0 licence (© 2020). Any distribution of this work must maintain attribution to the author(s), title of the work, publisher, and DOI

protect electrical connections. These plates in combination with metal coverings serve as caps to make the total assembly sealed (Fig. 12).

The metal housing has a ring-shaped rubber to prevent a gas leakage. Two screw ports for a gas pumping and pits for electric contacts in the shell of the counter are also visible. The spacing between plates is 8 mm. It was chosen because of mechanical reasons and in order to increase the signal level to compensate partially lack of the gas amplification. The supposed gas filling is N_2.

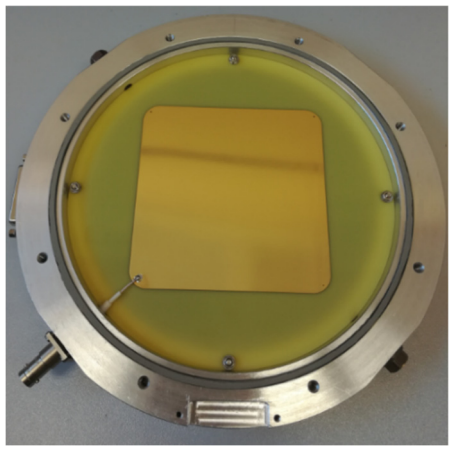

Figure 10: New MGC shell with HV plate.

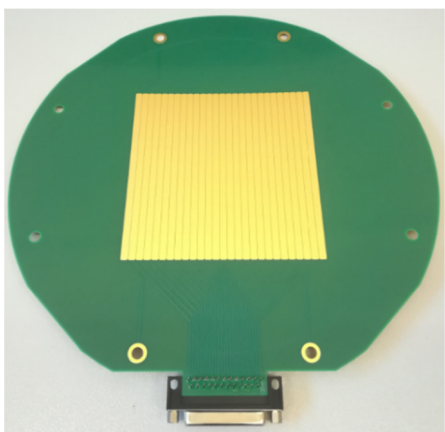

Figure 11: Multichannel plate.

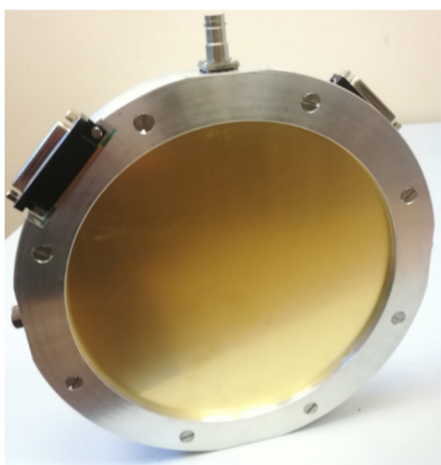

Figure 12: New MGC total assembly.

CONCLUSION

The operational range of MGC was defined during the experiment – $10^7 \div 10^{11}$ p/pulse with pulse duration in range about 50÷100 μs. The relative precision of current determination by MGC is about 10%. Analytical models are consistent with experimental data and help to predict the voltage for gas amplification in proportional mode.

The shift of threshold voltage for ionization regime depending on beam current was tested in the experiment and explained. The results show, that the operational voltage of ionization chamber must be set for the beams of highest possible intensity from a working range of a counter. In case of MGC it is 10^{11} protons/pulse and about 2.5 kV threshold voltage. The influence of a gas gap size on the value of saturation voltage of ionization regime is also discussed.

Based on the exploitation experience of MGC, a new device was developed. The new assembly of the detector is sealed and allows to use O_2-free gas filling to prevent stripe oxidation. The new device works in ionization mode to avoid intense avalanches near thin stripes and their destruction. The gas counter is now thin enough to work in the lower limit of energy range ~ 20 MeV.

REFERENCES

[1] G. Charpak, F. Sauli, "Multiwire Proportional Chambers and Drift Chambers", CERN, Geneva. Switzerland (1979).

[2] A. Melnikov, S. Gavrilov, "Multianode Gas Counter For Low Intensity Beam Diagnostics At The INR LINAC", in *Proc. XXVI Russian Particle Accelerator Conference (RuPAC'18)*, Protvino, Russia.

[3] G. Boissonnat et al., "Measurement of ion and electron drift velocity and electronic attachment in air for ionization chambers", arXiv:1609.03740v1.

[4] Biagi database, www.lxcat.net, copyright 2010.

[5] G.J.M. Hagelaar and L.C. Pitchford, "Solving the Boltzmann equation to obtain electron transport coefficients and rate coefficients for fluid models", *Plasma Sci Sources and Tech 14, 722 (2005)*.

[6] J. Va'vra, "Wire Aging", DESY workshop, October 2, 2001.

[7] J. W. Boag and T. Wilson, "The saturation curve at high ionization intensity", *Br. J. Appl. Phys. 3, p. 222, 1952.*

[8] T. Z. Kowalski and B. Mindur, "Manifestation of Aging Effect in Gas Proportional Counters", DESY workshop on wire aging, University of Mining and Metallurgy, Cracow, Poland.

ISBN: 978-3-95450-222-6 ISSN: 2673-5350 doi:10.18429/JACoW-IBIC2020-WEPP05

REENTRANT CAVITY RESONATOR AS A BEAM CURRENT MONITOR (BCM) FOR A MEDICAL CYCLOTRON FACILITY*

S. Srinivasan†, P.-A. Duperrex, J. M. Schippers
Paul Scherrer Institut, 5232 Villigen PSI, Switzerland

Abstract

At PSI, a dedicated proton therapy facility, with a superconducting cyclotron, delivers 250 MeV beam energy, pulsed at 72.85 MHz. The measurement of beam currents (0.1-10 nA) is generally performed by ionisation chambers (ICs), but at the expense of reduced beam quality, and scattering issues. There is a strong demand to have accurate signal with a minimal beam disturbance. A cavity resonator, on fundamental resonance mode, has been built for this purpose. The cavity, coupled to the second harmonic of the pulse rate, provides signals proportional to the beam current. It is installed in a beamline to measure for the energy range 238-70 MeV. Good agreement is reached between the expected and measured sensitivity of the cavity. The cavity delivers information for currents down to 0.15 nA with a resolution of 0.05 nA when integrated over one second. Its application is limited to a machine-safety monitor to trigger interlocks, within the existing domain of the proton therapy due to the low beam current limits. With new advancements in proton therapy, especially FLASH, the cavity resonator's application as an online beam-monitoring device is feasible.

INTRODUCTION

In proton radiation therapy at PSI, proton beams of low intensities (0.1-10 nA) are traditionally measured with ICs [1]. We face a strict regulation of their use due to scattering issues. A non-invasive BCM, is modelled as a lumped element LC circuit, such that its fundamental mode of resonance is at 145.7 MHz as described in [2]. The induced electric and magnetic fields are concentrated in the capacitive (region 2) and the inductive zones (region 3) of the BCM, as shown in Figure 1. Here, we report on its beamline measurements for the energy range 238-70 MeV.

BCM LOCATION

The proton therapy facility, PROSCAN, is a temperature-controlled environment (28.5±0.5 °C), to have stable operating conditions for its beamline elements. The energy degradation (238-70 MeV), is achieved with the help of a degrader [3], which results in growth of emittance and energy spread [4-6]. An Energy Selection System (ESS), along with a pair of collimators, maintains the beam quality at patient location by limiting the energy spread. An elongation of the proton bunch length and an energy dependent decrease in the bunch amplitude downstream of the degrader is the consequence. This affects the BCM's sensitivity as it is coupled to the second harmonic of the pulse repetition rate, which is located at sixteen meters from the degrader exit as shown in Figure 2.

A Sinc function normalised to average beam current and at multiple energies is given in Table 1, represents the BCM's expected second harmonic amplitude factor, A_2, proportional to the sensitivity.

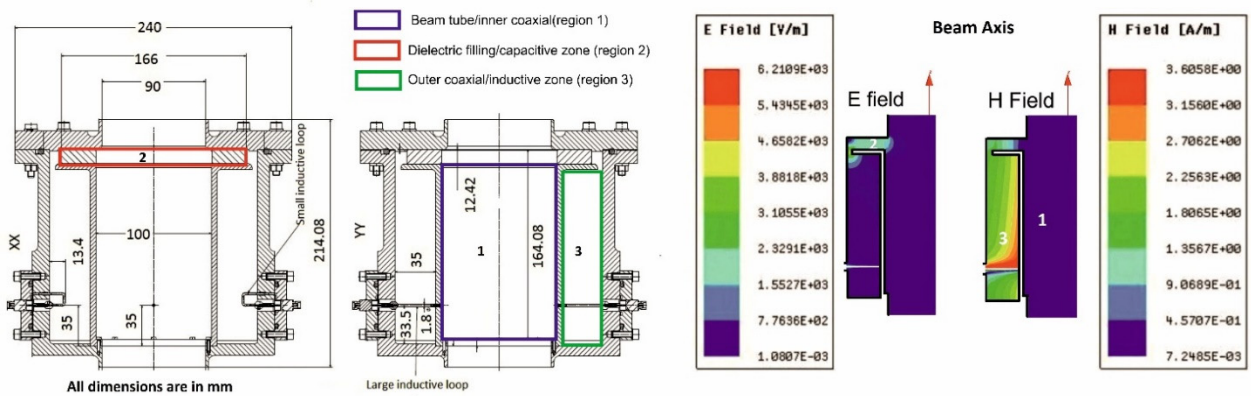

Figure 1: Cut-section of the reentrant cavity resonator (XX and YY) with dimensions correpsonding to TM_{010} frequency at 145.7 MHz. Region 1, 2 and 3 represent the inner coaxial (or beam tube), dielectric filling in the reentrant gap (capacitive zone), and the outer coaxial (inductive zone). The E fields and H fields excited within the resonator shows the separation of the capacitive (marked as 2) and inductive zones (marked as3) in this resonator (right).

* This project has received funding from the European Union's Horizon 2020 research and innovation programme under the Marie Skłodowska-Curie grant agreement No 675265.
† sudharsan.srinivasan@psi.ch

Content from this work may be used under the terms of the CC BY 3.0 licence (© 2020). Any distribution of this work must maintain attribution to the author(s), title of the work, publisher, and DOI

ISBN: 978-3-95450-222-6 ISSN: 2673-5350 doi:10.18429/JACoW-IBIC2020-WEPP05

Content from this work may be used under the terms of the CC BY 3.0 licence (© 2020). Any distribution of this work must maintain attribution to the author(s), title of the work, publisher, and DOI

Table 1: Estimate of the Second Harmonic Amplitude Factor for a Rectangular Bunch Shape [7] at the Resonator Location for Different Beam Energies. Bunch length of 2 ns at the degrader exit is assumed as reference for the calculation. Only for energies lower than 180 MeV, the ESS helps in minimising the momentum spread to ± 1%. Energy spread is calculated as per [8] and is within acceptable range of the measurement as given in [9].

Energy, MeV	Energy Spread, MeV	Momentum Spread, %	Bunch Length at Resonator, ns	2nd Harmonic Amplitude Factor (A_2)
79	4.4	1.0	3.24	0.67
109	4.2	1.0	3.08	0.69
139	3.9	1.0	2.97	0.71
171	3.3	1.0	2.91	0.73
201	2.7	0.84	2.71	0.76
231	1.7	0.70	2.56	0.79

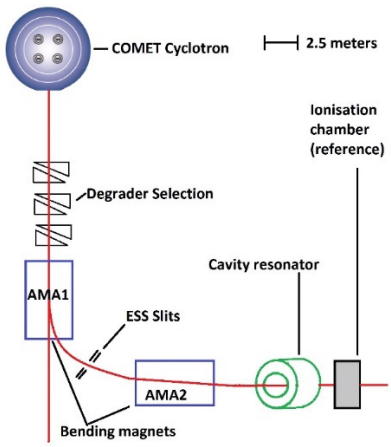

Figure 2: Location of the cavity resonator in the PROSCAN layout. Marked are the COMET cyclotron, degrader selection, ESS for momentum spread, bending magnets, cavity resonator and the IC which is used as beam current reference.

MEASUREMENT CHAIN

A PSI developed measurement system, VME MESTRA, as shown in Figure 3, is used for beam current measurements [10]. The measurement system is configured at 145.7 MHz and starts with a large inductive loop of the BCM. The other large inductive loop is connected to a resonance trombone for tuning capabilities. The pair of the small inductive loops are terminated with 50 Ω.

The cavity signal is amplified with a low-noise amplifier [11] and bandpass filtered with a customized cavity type filter from KL microwave. The centre frequency of the bandpass filter is 145.0 MHz with a 3dB bandwidth of 8.24 MHz. The filtered signal is amplified further with a FEMTO wideband low-noise amplifier [12]. This signal is digitized with the help of a 16-bit Digitizer [13] at 50.0 MSamples/s. The digitized signal is down-converted through a Field Programmable Gate Array (FPGA) on the Digital Down Converter (DDC). The DDC results in an output signal, Res DDC, with 50 k samples/s. The DDC filters the input noise power of the digitized signal with its 18 kHz (3 dB) bandwidth in order to get a high attenuation for the stop band and a flat pass band. The signal integration time of the measurement chain is one second.

RESULTS

No Beam System-response

Prior to beam measurements, the no beam response of the system is measured without the BCM and with the BCM (scenario 1 and 2 in Figure 3) with the cyclotron RF turned on. The measurement without the BCM and with the BCM were recorded as 40000 counts and 63007 counts respectively, with a standard deviation of 1.26%. This value is the measurement offset, $I_{measoff}$, that represents the noise floor of the measurement chain and its RF interference.

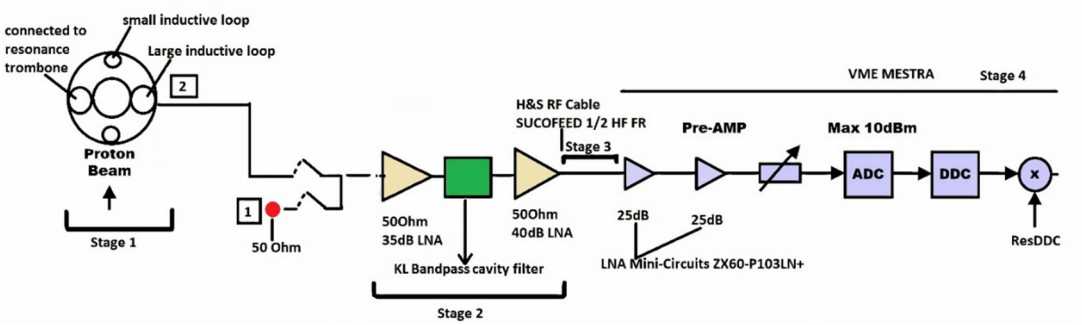

Figure 3: Measurement chain representation from the resonator until the electronic cubicle. The small inductive loops are terminated with 50 Ω. Scenario 1 represents 50Ω on the input of the measurement chain represents Stage 2-4. Scenario 2 represents the resonator connected to the measurement chain represents Stage 1-4.

ISBN: 978-3-95450-222-6 ISSN: 2673-5350 doi:10.18429/JACoW-IBIC2020-WEPP05

Table 2: Measurement Summary for Resonator at Different Energies. The fractional uncertainty of the evaluated measurement offset and the resonator calibration factor are derived from the in-beam measurements through error propagation. The value of the normalizing term, C=212042 Counts/Na. A_2, is taken from Table 1.

Proton Beam Energy (MeV)	Measured Resonator Sensitivity, k_meas (±1.35%) (Counts/nA)	Expected Resonator Sensitivity, k (=A_2*C) (Counts/nA)	Measurement Offset, $I_{measoff}$ (±1.26%) (Counts)
79	138202	142068	62418
109	139821	146309	63008
139	151327	150550	62737
171	153493	154791	62169
201	161152	161152	62104
231	168434	167513	60308

Beam Measurements

The BCM response is measured for beam current sweeps in the range 0-2.5 nA at different energies. The calibration of the BCM is performed with respect to an IC as shown in Figure 2, immediately behind the BCM to have similar beam current values. For the low beam current range a linear relationship exists between the beam current power and the measured signal power, which is given by

$$I^2_{\mathrm{Re}sDDC} = I^2_{measoff} + k^2 I^2_{beam} \quad (1)$$

where the individual power of the measurement offset ($I^2_{measoff}$) and the power of the beam current response ($k^2I^2_{beam}$) are uncorrelated, with k as the BCM sensitivity. The measurement results are summarised in Table 2 and are in good agreement with the expected sensitivity and the measurement offset from the no beam response. The measurement from the BCM is considered position independent as its position dependence is 0.03%/mm measured at 60% of the beam pipe radius.

The lowest detectable beam current, is 0.15 nA, which is defined by a signal level higher than the measurement offset by three σ. The resolution derived from the measurement is 0.05 nA.

The cavity BCM will be used as a beam operation safety monitor as well as in controlling the operation parameters within the normal ranges. With recent trend towards FLASH therapy, the cavity BCM can be used for online beam monitoring as the beam current is in the range of hundreds of nA [14].

CONCLUSION

In this work, to our knowledge, we have demonstrated the first successful non-invasive beam current measurements at a proton therapy facility in the range 0.1-10 nA.

ACKNOWLEDGMENT

The authors like to thank the vacuum group and the PROSCAN maintenance group for installation in the beamline.

REFERENCES

[1] R. Dölling, "Progress of the diagnostics at the PROSCAN beam lines," in *Proc. 8th European Workshop on Beam Diagnostics and Instrumentation for Particle Accelerators (DIPAC'07)*, Venice, Italy, May 2007, pp. 361–363.

[2] S. Srinivasan and P.-A. Duperrex, "Dielectric-filled reentrant cavity resonator as a low-intensity proton beam diagnostic," *Instruments*, vol. 2, no. 4, article no. 24 (17 pages), 2018. doi:10.3390/instruments2040024

[3] V. Rizzoglio *et al.*, "Evolution of a beam dynamics model for the transport line in a proton therapy facility," *Phys. Rev. Accel. Beams*, vol. 20, no. 12, pp. 1–12, 2017. doi:10.1103/PhysRevAccelBeams.20.124702

[4] F. J. M. Farley, "Optimum strategy for energy degraders and ionization cooling," *Nucl. Instrum. Meth.. A*, vol. 540, pp. 235–244, 2005. doi:10.1016/j.nima.2004.11.034

[5] V. Anferov, "Energy degrader optimization for medical beam lines," *Nucl. Instrum, Meth. A*, vol. 496, no. 1, pp. 222–227, 2003. doi:10.1016/S0168-9002(02)01625-X

[6] J. Petzoldt *et al.*, "Characterization of the microbunch time structure of proton pencil beams at a clinical treatment facility," *Phys. Med. Biol.*, vol. 61, no. 6, pp. 2432–2456, 2016. doi:10.1088/0031-9155/61/6/2432

[7] R. E. Shafer, "Beam position monitoring," *AIP Conf. Proc.*, vol. 212, pp. 26–58, 1990. doi:10.1063/1.39710

[8] P. Vavilov, "Ionization losses of high-energy heavy particles," *Sov. Phys. JETP*, vol. 5, no. 4, pp. 749–751, 1957.

[9] M. J. Van Goethem, R. Van Der Meer, H. W. Reist, and J. M. Schippers, "Geant4 simulations of proton beam transport through a carbon or beryllium degrader and following a beam line," *Phys. Med. Biol.*, vol. 54, no. 19, pp. 5831–5846, 2009. doi:10.1088/0031-9155/54/19/011

[10] E. Johansen, "VME MESTRA Rev C Specification," 2020. doi:10.5281/zenodo.3887550 [11]"R&K-LA100-0S Low Noise Amplifier," http://www.rk-microwave.com/jp/products/pdf/LA101-0S_01.pdf (accessed Jan. 16, 2020).

[12] FEMTO, "Datasheet Ultra-Wideband Voltage Amplifier DUPVA-1-70 Variable-Gain," http://www.femto.de (accessed Jan. 15, 2020).

[13] "ADC _ 3110 / 3111 – Eight Channel 16-bit ADC Data Sheet," https://www.ioxos.ch/produit/adc-3110-3111/ (accessed Jan. 15, 2020).

[14] A. Patriarca *et al.*, "Experimental Set-up for FLASH Proton Irradiation of Small Animals Using a Clinical System," *Int. J. Radiat. Oncol. Biol. Phys.*, vol. 102, no. 3, pp. 619-626, 2018. doi:10.1016/j.ijrobp.2018.06.403

Content from this work may be used under the terms of the CC BY 3.0 licence (© 2020). Any distribution of this work must maintain attribution to the author(s), title of the work, publisher, and DOI

ISBN: 978-3-95450-222-6 ISSN: 2673-5350 doi:10.18429/JACoW-IBIC2020-WEPP06

INVESTIGATION OF AN OPTICAL-FIBER BASED BEAM LOSS MONITOR AT THE J-PARC EXTRACTION NEUTRINO BEAMLINE*

S. Cao†, M. Friend, High Energy Accelerator Research Organization (KEK), Tsukuba, Japan

Abstract

Optical fibers, which at once generate and guide Cherenkov light when charged particles pass through them, are widely used to monitor the beam loss at accelerator facilities. We investigate this application at the J-PARC extraction neutrino beamline, where a 30 GeV proton beam with eight bunches of ~13 ns (1σ) bunch width and 581 ns bunch interval, is extracted from the Main Ring, transported, and hit onto a graphite target to produce a highly intense beam of neutrinos. Three 30 m-length 200 µm-core-diameter optical fibers, which are arranged flexibly to form 60 m- or 90 m-length fibers, were installed in the beamline. The beam loss signal was observed with the Muti-Pixel Photon Counters. We discuss the result and prospects of using optical fibers for monitoring and locating the beam loss source.

J-PARC EXTRACTION NEUTRINO BEAMLINE

J-PARC extraction neutrino beamline, detailed in [1], provides one of the most intense beams of $\nu_\mu(\overline{\nu}_\mu)$ for the research concerning neutrino particles, whose its massiveness is the only experimental evidence so far beyond the description of the Standard Model of elementary particles. To extract the 30 GeV proton beam from Main Ring and transport it toward a graphite target for neutrino production, the 238 m-length beamline is instrumented with 21 normal magnets (eight steering, four dipole, and nine quadrupole magnets) and 14 doublets of superconducting combined function magnets. The neutrino beamline receives a beam in a so-called fast-extraction mode, where each beam spill consists of eight bunches of ~13 ns (1σ) bunch width and 581 ns bunch interval. In 2020, J-PARC operates stably at around 515 kW with an intensity of 2.65×10^{14} protons-per-pulse (ppp). J-PARC accelerator and neutrino beamline [2] plan to upgrade to MW-power beam by reducing the cycle repetition from 2.48 s to 1.16 s and increasing the beam intensity to 3.2×10^{14} ppp. To realize the MW beam, equipment robustness against high intensity, beam loss tolerability, handling the radioactive waste, and precisely and continuously monitoring the beam profile are essential. This work concerns merely the beam loss monitor (BLM), including the experience of operating the gas-based BLM system and investigation of using optical fiber-based BLM (O-BLM) as a complementary option for monitoring the beam loss.

GAS-BASED BLM

Proportional counter with a mixture of Ar and CO_2 (Canon Electron Tubes & Devices E6876-400) [3] was chosen to monitor the spill-by-spill beam loss. There are 50 BLMs distributed along 238 m-length beamline, one shown in Fig. 1, and they are integrated into the Machine Protection System (MPS), allowing us to abort the next beam spill in case the spill-integrated BLM signal with the latest spill is higher than a pre-defined threshold.

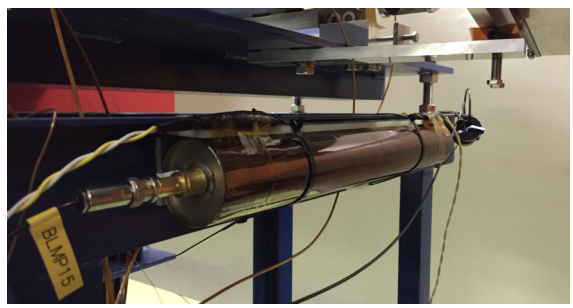

Figure 1: A gas-based BLM installed under the magnet.

Figure 2 shows the beam loss distribution along the beamline. The beam loss is high near the extraction point (at ~0 m position), a collimator (at ~45 m position), and at the most downstream due to backscattering of proton beams on the beam window, production target, and intercepting beam profile monitor. The beam loss is quiet along the superconducting magnet section (from 54 m to 201 m positions).

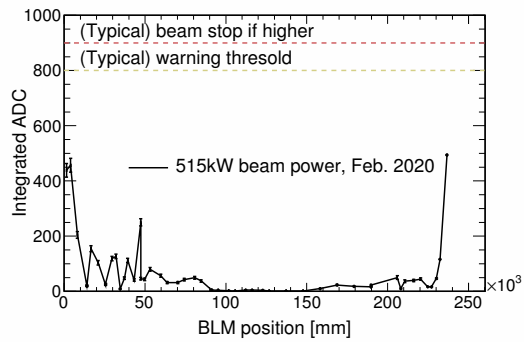

Figure 2: Beam loss distribution with the gas-based BLMs along the 238 m-length extraction neutrino beamline.

With more than ten year operation of BLM, it is well-established that the gas-based BLM functions stably and reliably. The most downstream BLM placed in the highest radioactive area comparing to other BLMs, has signals linearly proportional to the beam power, providing us a useful beam-based calibration to check BLM response regularly and no degrading indication observed. For semi-offline monitoring and analysis, the BLM signal is sampled 30 MHz with

* Work supported by the J-PARC/KEK Neutrino Group
† cvson@post.kek.jp

Content from this work may be used under the terms of the CC BY 3.0 licence (© 2020). Any distribution of this work must maintain attribution to the author(s), title of the work, publisher, and DOI

ISBN: 978-3-95450-222-6 ISSN: 2673-5350 doi:10.18429/JACoW-IBIC2020-WEPP06

a Analog-to-Digital convertor (ADC), providing a measure of the beam (in)stability and thus feedback to the accelerator experts. The beam loss measurement near the extraction point is particularly useful for beam commissioning and optic tuning since it allows us to predict the loss coming from the extraction system. Besides, it is found that the integrated signal of BLM is proportional to the residual dose which is measured directly a few hours after the beam stop.

There are additional features which we wish to have in a complete BLM system, including but not limited to (i) bunch-by-bunch (in)stability monitor, (ii) capability to locate the loss source, (iii) sensitivity to thermal and fast neutrons, and (iv) beam halo detection. Those motivate us to investigate the usage of optical fibers and fast-response photosensor as an alternative method to monitor the beam loss.

OPTICAL FIBER-BASED BLM

Using optical fiber for monitoring the beam loss is well-established method in many facilities where the beam of a charged particle (proton, electron) is delivered in a few ns or shorter pulse [4–6]. With long-pulsed beam such as J-PARC extraction neutrino beamline (~13 ns), the possibility to take advantage of the optical fiber as a beam loss monitor needs further investigation.

General concept and specification

Fundamentals of the optical fiber used as the electromagnetic and hadronic calorimeter can be found in [7]. Charged particles generate Cherenkov light when passing through the optical fiber, which also plays a role as a light guider to the fast photosensor. The number of observed photons is essentially proportional to the flux of charged particles, i.e beam loss. A concept of optical fiber-based BLM (O-BLM) is shown in Fig. 3. While the speed of protons closes to the speed of light, 3.3 ns/m, the speed of photon propagation in the fiber is about 5.0 ns/m. For the loss signal separation, it is important to arrange the fiber-photosensor system such that particles incident on the fiber earlier produce Cherenkov light which reaches the photosensor earlier. The optimal arrangement can achieve a signal separation of up to 8.3 ns/m. Considering a proton beam bunch width of ~13 ns and signal readout resolution in a few ns, a simple simulation shows that the two loss sources are well-separated if two signal-induced positions separated by a physical gap of ~7 m. One can lift this limit by adding more fiber segment between the two loss sources to effectively increase the time separation.

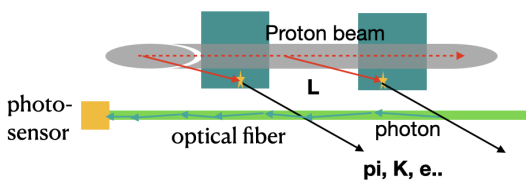

Figure 3: Concept of optical fiber-based BLM to monitor and locate the beam loss.

We use the multimode pure-silica high-OH optical fibers [8] with a core diameter of 200 µm and a numerical aperture (NA) of 0.22 for the measurement setup. Although each batch fiber is 30 m in length, it is flexible to extend the fiber length by using the optical coupling. The optical fiber is an insulator, which allows us to safely lay the fiber on the magnet or directly attach to the beam duct, as shown in Fig. 4. For ns-level response and invulnerable to the strong

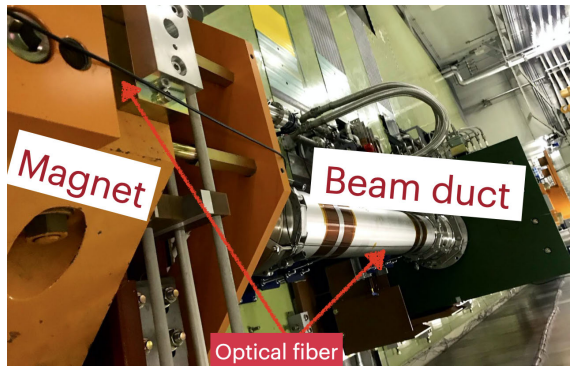

Figure 4: Optical fibers are attached on top of the magnet and the beam duct.

magnetic fields in the beamline, Hamamatsu Multi-Pixel Photon Counter (MPPC) is chosen to read out the signal from the optical fibers. However, MPPC is not radiation-hard enough to operate in a highly radioactive area near the beamline. Guiding the optical fiber to a lower radioactive area, where the MPPC can be placed, is introduced as a solution. The low afterpulse S12571-025 MPPC type [9] has a sensitive size of 1.0 mm×1.0 mm. To position the fiber on the MPPC precisely, we mount MPPC on a round PCB which are housed in a plate with built-in FC-coupler connector. Figure 5 shows detail of the measurement setup for investigating the possibility of loss location.

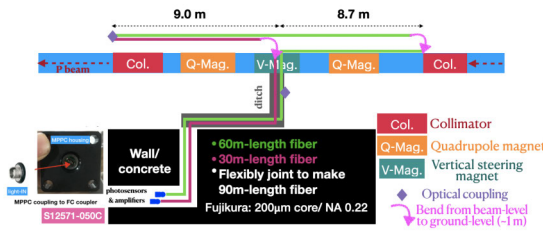

Figure 5: Measurement setup for locating the beam loss source with the optical fiber-based BLM prototype.

In the measurement setup, there are three 30 m-length fiber which is laid out in the way such that we can easily joint to make 60 m- and 90 m-length fibers. The whole setup covers a range of 17.7 m of the beamline, placing between two collimators and passing over two quadrupole magnets and one vertical-steering magnet. In a nominal setup, we consider two readouts for 60 m- and 30 m-length fibers. Relative electronic latency between two readouts is ~ a few ns. A 17.7 m-length segment of the first fiber is placed at the

Content from this work may be used under the terms of the CC BY 3.0 licence (© 2020). Any distribution of this work must maintain attribution to the author(s), title of the work, publisher, and DOI

ISBN: 978-3-95450-222-6 ISSN: 2673-5350 doi:10.18429/JACoW-IBIC2020-WEPP06

Content from this work may be used under the terms of the CC BY 3.0 licence (© 2020). Any distribution of this work must maintain attribution to the author(s), title of the work, publisher, and DOI

beam-level; the rest is placed on the ground or the ditch, which is about 1 m lower. For the second fiber, a 9 m-length segment is placed at the beam-level. Although it is expected that a significantly higher amount of loss particles would be incident on the beam-level segment, the signal can also be generated in the ground-level segment.

O-BLM signal and conventional functionalities

MPPC signal, amplified by a stand-alone amplifier board in the tunnel, is sent ~ 130 m to the electronic rack located on the ground level and read out by oscilloscope or 30 MHz-sampling ADC[1], which is identical to the gas-based BLM. The beam loss signals with an O-BLM and a gas-based BLM are shown in Fig. 6. The bunch structure is observed more clearly with the O-BLM. We take data with the O-BLM

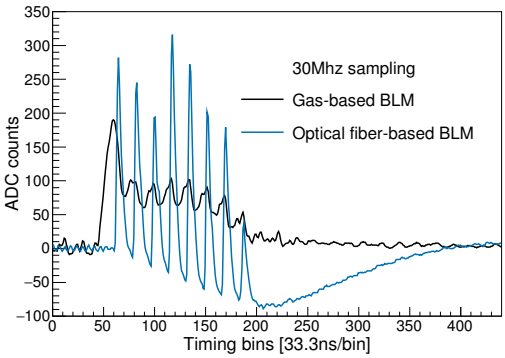

Figure 6: The signals with gas-based BLM and optical fiber-based BLM with 30 MHz sampling DAQ.

and the nearby gas-BLM at the same period with the same DAQ and check the correlation of the signal amplitude between them. The result, shown in Fig. 7, presents a strong correlation between the O-BLM signals and nearby BLMs (BLM-01,10,16)[2] but reduced with faraway (~190 m) BLM-50 indicating that the O-BLM are accepting the same loss source as the gas-based BLM. We also check the stability of the signal of the O-BLM in comparison to the gas-based BLM. This is very important, particularly when one considers integrating the system into MPS since the instability of the signal amplitude can reduce the reliability of the system. In Fig. 8, we compare the stability of the signal of the first peak for two gas-BLM and two O-BLM. It is showed that the stability of the O-BLM amplitude is not as good as that of the BLM. Also, the signal of the 60 m-length fiber seems less stable than the 30 m-length fiber. Those needs further investigation.

Loss source location

The O-BLM, taking advantage of the fast responses from both light production in the optical fiber and MPPC, essentially provides a very good time resolution (a few ns), and thus spatial resolution (1 m more or less). However, the

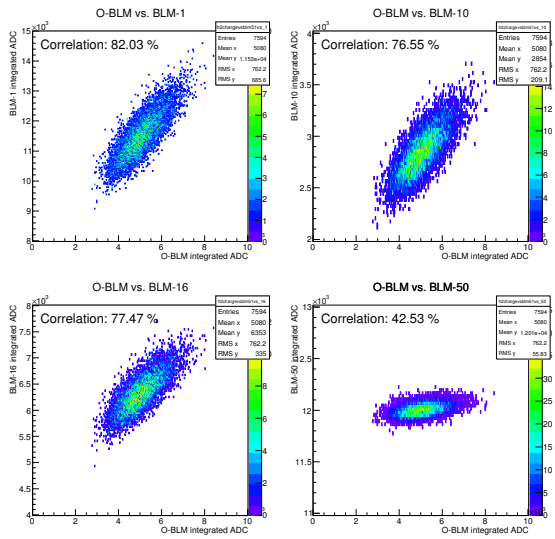

Figure 7: Correlation between the 60 m-length O-BLM with four gas-based BLM placed at four different locations: BLM-10 and BLM-16 are at the most upstream and the most downstream of the 60 m-length O-BLM respectively. BLM-01 and BLM-50 are 30 m upstream away and 190 m downstream from the O-BLM respectively.

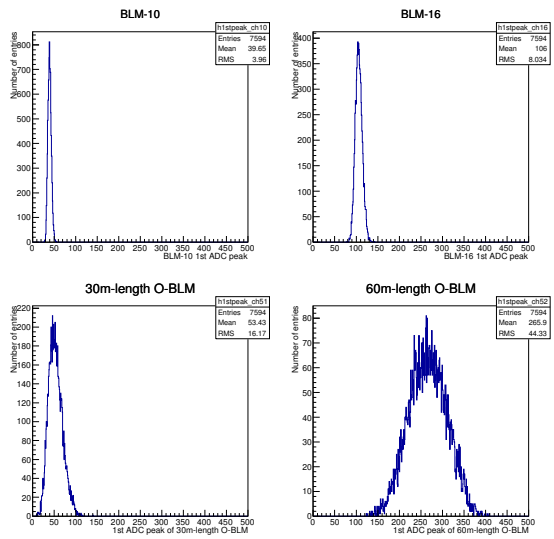

Figure 8: Stability of the signal observed with gas-based BLM and O-BLMs for more than 5 hours beam delivering. BLM-10 and BLM-16 are at the most upstream and the most downstream of the 60 m-length O-BLM respectively.

O-BLM adopted here for the measurement is limited by a relatively long beam bunch width (~13 ns) and complexity of fiber guiding referred to Fig. 5. The MPPC signals recorded with the oscilloscope coming from different fibers is shown in Fig. 9. Signals from both 30 m- and 60 m-length fibers seem to have a two-peak structure for each bunch. The peak-to-peak interval for 60 m-length fiber is ~ 151 ± 10ns, while that of the 30 m-length fiber is just ~ 52 ± 15ns. When two fibers are joined to form 90 m-length fiber and the sig-

[1] To take advance of the O-BLM, faster sampling ADC is needed.
[2] There are strong correlation among BLMs indexed from 01 to 16

ISBN: 978-3-95450-222-6 ISSN: 2673-5350 doi:10.18429/JACoW-IBIC2020-WEPP06

nal is read out in the same end as the original 60 m-length fiber, the second peak of the signal is enhanced significantly due to the contribution of 30 m-length fiber. This suggests that both original 30 m- and 60 m-length fibers receives the same loss source which makes the second peak in their waveform. Using the peak timing information, we estimate that one loss source is near the downstream collimator sketched in Fig. 5. The signal waveform recorded with 90 m-length fiber is fitted with double Gaussian distribution for each bunch. The peak-to-peak interval, shown in Fig. 10, is found to be 156.8 ± 9.8 ns and the withs of the first and second peaks are 42.2 ± 7.5 ns and 46.2 ± 8.3 ns respectively. These peak-to-peak intervals allow us to locate the second loss source, which is either (i)~18.9 m upstream from the previously found loss source, i.e close to the upstream collimator sketched in Fig. 5 or (ii) physically near the vertical steering magnet and charged particles generate the light near the ditch in Fig. 5. That the O-BLM signal widths are larger than the proton beam width may indicate that the loss source is not a point source but a fairly long segment of fiber is fired.

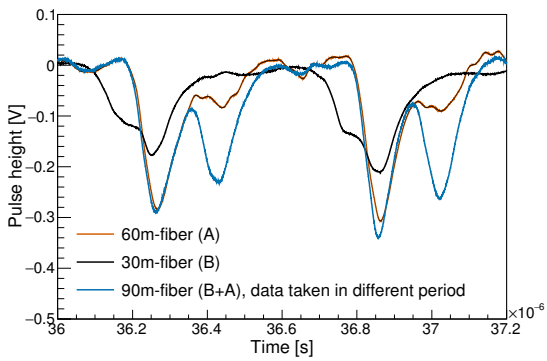

Figure 9: Beam loss, zoomed into first two bunches, observed with three fiber configurations. Data with 90 m-length fiber is taken in not the same period as other data.

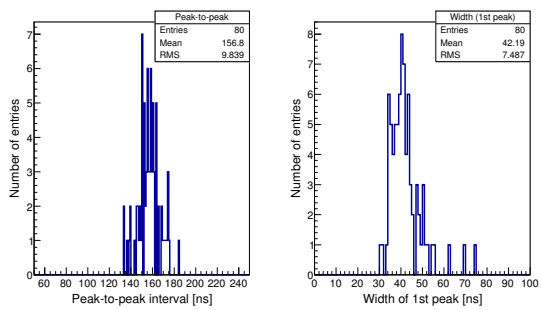

Figure 10: The peak to peak interval and the width of the first peak resulted from the double Gaussian fit per each bunch in the signal waveform with 90 m-length O-BLM.

SUMMARY AND PROSPECTS

We observed the beam loss using the optical fibers with a clear beam bunch structure thanks to the fast response of both optical fiber and MPPC. The portability of fiber allows us to install the fiber easily on the magnet and can attach directly to the beam duct. The signals observed with different fiber configurations indicate that the beam loss at the instrumented section may come from at least two loss sources. In short, O-BLM is a promising and economic option to (i) monitor the beam (in)stability on the bunch basic, and (ii) locate the beam loss source.

One of the most important tasks to realize the O-BLM in our beamline is to simplify the fiber layout to interpolate the loss sources intuitively from the signal waveform. It is ideal to put the fibers along with the beamline without guiding them to the sub-tunnel. In this direction, it is interesting to investigate other types of photosensors which are required to be radiation-hard, magnetic-invulnerable, fast-response, and wide dynamic range. To cover entire the 238 m-length beamline, one may need at least 4 fibers of 60 m-length since the fiber length is limited to a length of ≤ 60 m along the beamline due to the bunch interval. For the loss source locating purpose, it is important to determine precisely (in a few ns levels) the time where the proton beam arrives at a specific point in the beamline. Since it is almost impossible to use the beam trigger with such precision, one needs to determine it basing on the beam signal on a bunch-by-bunch basis. An economic approach is to read signals on each fiber in both ends and calibrate the electronic latency among the channels precisely. If those tasks can be overcome, such an O-BLM system can provide a great tool for beam diagnostics.

REFERENCES

[1] K. Abe *et al.*, "The T2K Experiment", *Nucl. Instrum. Meth. A*, vol. 659, p. 106, 2011. doi:10.1016/j.nima.2011.06.067

[2] K. Abe *et al.*, "J-PARC Neutrino Beamline Upgrade Technical Design Report". arXiv:1908.05141

[3] Canon Electron Tubes and Devices Co.,Ltd, https://etd.canon/en/product/use/science/neutron.html

[4] F. Wulf and M. Körfer, "Local Beam Loss and Beam Profile Monitoring with Optical Fibers", in *Proc. DIPAC'09*, Basel, Switzerland, May 2009, paper WEOA01, pp. 411–417.

[5] T. Obina and Y. Yano, "Optical-Fiber Beam Loss Monitor for the KEK Photon Factory", in *Proc. IBIC'12*, Tsukuba, Japan, Oct. 2012, paper TUPA10, pp. 351–354.

[6] S. Mallows, E. B. Holzer, and J. W. van Hoorne, "Fiber Based BLM System Research and Development at CERN", in *Proc. HB'12*, Beijing, China, Sep. 2012, paper THO3C05, pp. 596–600.

[7] P. Gorodetzky *et al.* , "Quartz fiber calorimetry", *Nucl. Instrum. Meth. A*, vol. 361, pp. 161–179, 1995. doi:10.1016/0168-9002(95)00295-2

[8] Fujikura Ltd., https://www.fujikura.co.jp/eng/products/optical/appliedoptics/01/2050108_12901.html

[9] Hamamatsu Photonics K.K., http://hamamatsu.com.cn/UserFiles/DownFile/Product/s12571-025_etc_kapd1042e03.pdf

Content from this work may be used under the terms of the CC BY 3.0 licence (© 2020). Any distribution of this work must maintain attribution to the author(s), title of the work, publisher, and DOI

ISBN: 978-3-95450-222-6 ISSN: 2673-5350 doi:10.18429/JACoW-IBIC2020-WEPP07

THE INSERTABLE BEAM STOP IN THE ESS SPK SECTION

E. M. Donegani*, T. Grandsaert, T. Shea, C. A. Thomas
European Spallation Source ERIC, Lund, Sweden

Abstract

This paper deals with the Insertable Beam Stop (IBS) to be installed at the transition between the normal conducting and superconducting sections of the ESS linac. The IBS will be used to avoid beam losses in the cryogenic cavities during tuning and commissioning of the ESS linac. The IBS will stop protons in the energy range from 73 MeV to 92 MeV. The proton beam has a current up to 62.5 mA, and 5 and 50 µs long pulses at a rate of 14 or 1 Hz, respectively. Firstly, the IBS was designed in MCNPX/ANSYS to withstand thermal and structural stresses, while minimizing neutron production and limiting the deposited power in the cryogenic cavities below 0.2 W/m. Secondly, the prompt background and residual dose in the vicinity of the IBS were computed, as well as the activation of the IBS components themselves. Finally, a feasibility study was performed to determine if the IBS can be profitably used as a beam-profile monitor. The results will serve as input for calculations of the expected signal in beam loss monitors. Moreover, they will enable the design of the nearby shielding limiting the activation of surrounding structures and allowing maintenance works.

INTRODUCTION

The European Spallation Source (ESS) in Lund (Sweden) is currently one of the largest science and technology infrastructure projects being built today. The facility will rely on the most powerful linear proton accelerator ever built, a rotating spallation target, 22 state-of-the-art neutron instruments, a suite of laboratories, and a supercomputing data management and software development centre [1].

The ESS accelerator high-level requirements are to provide a 2.86 ms long proton pulse at 2 GeV at repetition rate of 14 Hz. This represents 5 MW of average beam power with a 4% duty cycle on the spallation target [2].

A comprehensive suite of beam instrumentation and diagnostics [3] has started to support the commissioning and operation of the normal-conducting linac (NCL) section of the ESS linac. Additional devices are going to be deployed in the superconducting linac (SCL) section, and in the transport lines to the tuning dump and to the spallation target.

At the transition between the NCL and the SCL sections, an Insertable Beam Stops (IBS) will be installed in order to avoid beam losses in the cold cavities during tuning up and commissioning of the ESS linac.

In the following three paragraphs, the main studies that are ongoing and devoted to the design of the IBS will be summarized:

1. MCNPX/ANSYS studies to perform thermo-mechanical simulations,

2. MCNPX/CINDER'90 studies for activation calculation and shielding design,

3. Feasibility studies of utilizing the IBS as a beam-profile monitor.

THERMO-MECHANICAL ANALYSIS

The IBS must guarantee that the proton beam is fully stopped and the beam power is safely dissipated as waste heat. The maximum proton beam current is 62.5 mA and the maximum beam energy is 92 MeV, leading to a peak power of 5.75 MW.

In order to withstand the high power, to minimize the heat transfer to the cold linac section and also the residual radioactivity, the only possible choice for the IBS core is graphite (with a density of 1.8 g/cm^3). Further challenges are posed by the limited space available in the Linac Warm Unit (LWU, see Fig. 1), and its particle-free environment. Therefore, the graphite core is embedded in a tungsten shielding, surrounded in turn by a 3 mm thick layer of titanium, allowing vacuum cleaning and avoiding particle generation.

The outer IBS radius is 5.5 cm and the total IBS length is 8 cm. The IBS is water cooled and the pipes of the circuit system are made of SSL. Energy deposition calculations

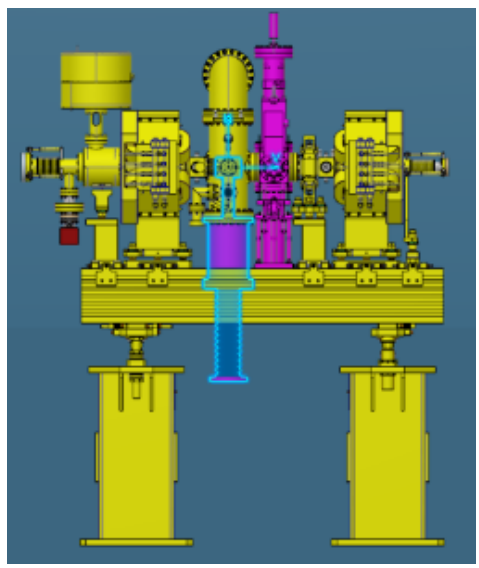

Figure 1: The Linac Warm Unit (LWU) in the ESS spoke (SPK) section, holding the IBS (highlighted in blue). The beam goes from right to left. (Courtesy of STFC and the ESS Vacuum section).

* elena.donegani@ess.eu

Content from this work may be used under the terms of the CC BY 3.0 licence (© 2020). Any distribution of this work must maintain attribution to the author(s), title of the work, publisher, and DOI

ISBN: 978-3-95450-222-6 ISSN: 2673-5350 doi:10.18429/JACoW-IBIC2020-WEPP07

were performed in MCNPX [4], assuming two possible commissioning modes:

- Fast tuning (5 µs, 14Hz, 62.5 mA),
- Slow tuning (50 µs, 1Hz, 62.5 mA).

An asymmetric gaussian beam was simulated with dimensions of (1.8 mm × 2.4 mm). The beam energy was varied in the [73, 92] MeV range. The position of the Bragg peaks within the IBS are reported in Fig. 2 for reference just in the minimum and maximum energy cases. The peak maximum is reduced by 20% when comparing the 92 MeV case to the 73 MeV one. The maximum value of the energy deposition in the graphite bulk is 350 MeV/cm^3/p at the lowest proton energy.

The corresponding temperature rise was obtained via ANSYS [5], using the temperature-dependent heat capacity of each material. The most demanding case is posed by the slow tuning mode, leading to a maximum temperature of 450°C after one single pulse with 73 MeV protons. At the highest energy of 92 MeV, the graphite temperature is below 350°C. In all the considered cases, the maximum temperature of the Ti surface remains below 200°C.

Further ANSYS calculations are ongoing in order to compute the von Mises stress and to optimize the water cooling system.

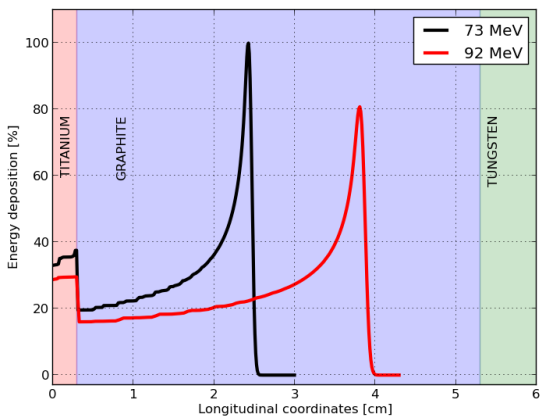

Figure 2: Energy deposition due to 73 MeV and 92 MeV protons, as a function of the longitudinal coordinate of the IBS. The three sections indicate the different structural materials intercepted by the beam. Values are scaled to the maximum value of the Bragg curve for 73 MeV protons.

ACTIVATION AND SHIELDING

Another set of simulations were performed in CINDER'90 [6] to determine the IBS activation after relevant irradiation and cooling periods for the ESS linac commissioning. In general, soon after irradiation, the outer layer of titanium is found to be the most activated component. The total IBS activity saturates at nearly 10^{11} Bq after 12 h of continuous irradiation, for both the two proton energy that were analyzed (73 MeV and 92 MeV).

After irradiation times longer than 8 h and cooling times longer than 100 h, it was noticed that the most activated component is the tungsten bulk instead. A Python script was developed to automatically run CINDER'90 calculations and process the output files; this will be helpful in case information at specific irradiation and/or cooling times will be needed during the ESS linac commissioning.

The activation calculations serve also as input for the design of the IBS shielding. In fact, the dose rate at 30 cm from a surface of the shielding shall not exceed 100 µSv/h after 120 h of irradiation at the maximum average power and 4 h of cooling. Therefore, the IBS and a simplified geometry of the LWU was implemented in MCNPX. As previsously shown in Fig. 1, two quadrupoles and one corrector magnet, two Beam Position Monitors, a Beam Shape Monitor, a vacuum pump were included in the simulations. Downstream of the LWU, a simplified spoke cryomodule is simulated, too. As a reference value, the map of residual dose in the vicinity of the IBS is reported in the left plot of Fig. 3, after an hypothetical irradiation for 120 h and 4 cooling hours at with 93 MeV protons. Further analysis will provide an estimation of the dose received by each LWU components and the power dissipated in the cryogenic components. These information will enable the selection of the shielding material(s) in the tight LWU space. The first investigated material is lead; its impact is notable in the right plot of Fig. 3. Further improvements will enable the reduction of the dose not only sideways but also downstream with respect to the IBS. To further reduce the dose to staff, the installation of a concrete or temporary shielding wall parallel to the beam propagation axis is being considered. A separate set of calculations is

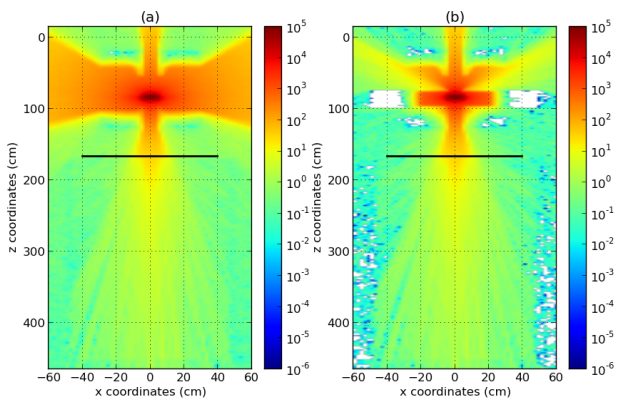

Figure 3: Residual dose distribution in the IBS surroundings (in µSv/h) after irradiation for 120 h with 93 MeV protons and cooling for 4 h. The black horizontal lines indicates for reference the end of the LWU and the start of the SPK crymodoule. The IBS is located in the hot spot. (a) Without shielding and (b) with a compact lead shielding around the IBS.

Content from this work may be used under the terms of the CC BY 3.0 licence (© 2020). Any distribution of this work must maintain attribution to the author(s), title of the work, publisher, and DOI

ISBN: 978-3-95450-222-6 ISSN: 2673-5350 doi:10.18429/JACoW-IBIC2020-WEPP07

Content from this work may be used under the terms of the CC BY 3.0 licence (© 2020). Any distribution of this work must maintain attribution to the author(s), title of the work, publisher, and DOI

planned in order to compute airborne radioactivity and the cooling water activation.

A BEAM PROFILE MONITOR?

To avoid melting any of the IBS components due to a too high power density, the feasibility of embedding a beam-profile monitor is being investigated. The inclusion of such feature is at an early design phase and highly constrained by several requirements. Firstly, the system must be ISO-5 qualified, i.e. particle free. Secondly, the system must fit within the allocated space, as no modification of the vacuum vessel is permitted. With these constraints, several possible diagnostics have been considered: an imaging system, a multi-wire grid or a silicon sensor. In the following paragraphs these three options are outlined.

An imaging system would be composed of two elements: the light source (chromium-doped alumina), which would be flame coated on the Ti layer of the IBS. The material is luminescent and radiation tolerant. This coating materials was already selected for the imaging system of the ESS target [7]. The luminescence is high, in excess of 1000 to 10000 photons per MeV deposited in the material. Samples have been produced and are being tested for ISO-5 cleanness qualification. The image from the beam would be produced by a standard industrial camera and lens, designed to get a field of view of about 100 mm. The camera and lens would be positioned outside of vacuum, looking through a viewport on an upstream vessel that supports also the Bunch Shape Monitor. The optical path contains a single flat mirror, reflecting the light from the IBS to the lens. The system performance is expected to image a probe beam pulse in single shot, and with resolution in the 0.1 mm range.

As a second option, a multi-wire grid could be composed of a grid of tungsten wires, assembled on a ceramic frame, and connected on both sides to a triax connector, so that the shielded ground and signal can be read by an AMC pico4 current ADC. The wire diameter should be thick enough to enhance the signal as well as thin enough to withstand beam-induced heat loads. Based on previous studies [8], a 40 µm tungsten wire would satisfy the requirements. One may note that this system is not a full 2D diagnostics, but it may be sufficient for reporting beam sizes smaller than 1 mm. Assuming a wire spacing of 2 mm, the system would be composed of 100 wires, positioned both in the vertical and horizontal axes of the proton beam.

As a third option, a multi-strip silicon detector on top of the entrance IBS face could serve as beam position, profile and also halo monitor. Moreover, it could potentially monitor the beam intensity if absolutely calibrated e.g. with an upstream Faraday cup or Beam Current Monitor. On one hand this latter solution would be the most compact and radiation-hard one, but on the other hand it is expected to be the most expensive one.

CONCLUSIONS AND OUTLOOK

The first steps for the design of the SPK IBS were presented. Firstly, MCNPX/ANSYS calculations were performed to investigate the thermo-mechanical properties. Further calculations will determine the von-Mises stress and optimize the water cooling system.

Another set of simulations in MCNPX/CINDER'90 were performed to assess the activation of the IBS components and the residual doses after relevant irradiation and cooling times during the ESS linac commissioning. These results will be the starting point for designing the shielding needed to limit the dose to surrounding linac components and to minimize the power deposition in the cryomodules. Moreover, they will serve as input for dedicated calculations of the expected signal in beam loss monitors closed to the IBS.

A self-protection capability would make possible to avoid melting any of the IBS components; therefore the possibility of embedding an imaging system, a multi-wire grid or a silicon sensor on the IBS entrance face is being considered. Exploiting the IBS as a beam-profile monitor would certainly provide a useful diagnostics tool during the commissioning of the ESS linac.

REFERENCES

[1] ESS Website 2020, https://europeanspallationsource.se/about

[2] R.Garoby *et al.*, "The European Spallation Source Design", *Phys. Scr.*, vol. 93, p. 014001, 2018. doi:10.1088/1402-4896/aa9bff

[3] T. J. Shea *et al.*, "Overview and Status of Diagnostics for the ESS Project", in *Proc. IBIC'17*, Grand Rapids, MI, USA, Aug. 2017, pp. 8–15. doi:10.18429/JACoW-IBIC2017-MO2AB2

[4] D. B. Pelowitz, Ed., "MCNPX Users Manual Version 2.7.0", LA-CP-11-00438, 2011.

[5] ANSYS, Inc., http://www.ansys.com/

[6] F.X. Gallmeier et al., "The CINDER90 transmutation code package for use in accelerator applications in combination with MCNPX", in *Proc. 19th Meeting of the International Collaboration on Advanced Neutron Sources (ICANS-XIX)*, Grindelwald, Switzerland, Mar. 2010.

[7] E. Adli *et al.*, "The ESS Target Proton Beam Imaging System as in-Kind Contribution", in *Proc. IPAC'17*, Copenhagen, Denmark, May 2017, pp. 3422–3425. doi:10.18429/JACoW-IPAC2017-WEPVA066

[8] B. Cheymol, "Estimation of the Thermal Load and Signal Level of the ESS Wire Scanner", in *Proc. LINAC'14*, Geneva, Switzerland, Aug.-Sep. 2014, paper MOPP036, pp. 137–139.

ISBN: 978-3-95450-222-6 ISSN: 2673-5350 doi:10.18429/JACoW-IBIC2020-WEPP10

PROTON-INDUCED SEY FROM BEAM INTERCEPTIVE DEVICES IN THE ESS LINAC

E. M. Donegani*
European Spallation Source ERIC, Lund, Sweden

Abstract

During the ESS linac commissioning, a wealth of beam-interceptive devices will be exposed to protons with nominal and non-nominal energies spanning from 75 keV to 2 GeV. Therefore, a database of proton-induced Secondary Emission Yield (SEY) values was prepared for the structural materials of devices insertable into the ESS linac. The database relies on calculations of collision stopping powers in MCNPX and the Sternglass theory applied to protons in the [0.001, 2000] MeV energy range. Results are reported for relevant materials to wire scanners, bunch shape monitors and target imaging systems: Cu, Ti, Ni, W, SiC, TZM and graphite. In the future, the novel method can be used also for determining the impact of secondaries on emittance or beam-current measurements with Emittance Monitor Units or Faraday cups of the ESS linac, respectively. Moreover, the database can be extended to critical structural materials of the ESS linac itself, in order to estimate the impact of secondary electrons on the overall beam quality.

INTRODUCTION

The European Spallation Source (ESS) in Lund (Sweden) is currently one of the largest science and technology infrastructure projects being built today. The facility will rely on the most powerful linear proton accelerator ever built, a rotating spallation target, 22 state-of-the-art neutron instruments, a suite of laboratories, and a supercomputing data management and software development centre [1]. The ESS accelerator high-level requirements are to provide a 2.86 ms long proton pulse at 2 GeV at repetition rate of 14 Hz. This represents 5 MW of average beam power with a 4% duty cycle on the spallation target [2].

A comprehensive suite of beam instrumentation and diagnostics [3] has started to support the commissioning and operation of the normal-conducting linac (NCL) section of the ESS linac. Additional devices are going to be deployed in the superconducting linac (SCL) section, and finally in the transport lines to the tuning dump and to the spallation target. Therefore, a wealth of beam-interceptive devices will be exposed to protons with nominal and non-nominal energies, spanning from 75 keV to 2 GeV:

- Wire Scanners (WS) [4] and Bunch Shape Monitors (BSM) [3] to determine the transverse and the longitudinal charge distribution, respectively;
- Target imaging systems [5] to detect small fractions of the proton beam that are outside a defined aperture, and to measure the horizontal and vertical beam profiles.

* elena.donegani@ess.eu

The WS, BSM and target imaging systems rely on secondary emission from thin wires or grids, from which a current proportional to the beam intensity is measured. The structural materials of such wires and grids are reported in Table 1.

Table 1: List of beam-interceptive devices in the ESS linac, with the corresponding main structural materials and the proton energy range E_P they are exposed to.

Device	E_P [MeV]	Material
EMU	[0.075, 3.6]	TZM, Cu, W
FC	[0.075, 74]	C, Cu, TZM
BSM	[3.6, 90]	C, W
WS	[3.6, 2000]	C, W
IBS	[73, 360]	Ti
Target imaging	[800, 2000]	Ni, SiC, W

There is another set of beam-interceptive devices whose performance can be severely limited by secondary electrons:

- Faraday cups (FC) [6] whose ability to measure the beam current depends on the capability of recapturing the ejected electrons;
- Emittance Monitor Units (EMU) for measuring the emittance, which can rely either on an internal FC [7] or on slit and grid combination [8];
- Insertable Beam Stops (IBS) [9] which is used to safely stop the beam in a particle-free vacuum environment.

Therefore, a database of SEY values was developed for all the structural materials relevant to the beam-interceptive devices in the ESS linac. The newly developed method for calculating Secondary Emission Yields (SEY), induced by protons in the [0.001, 2000] MeV range, is described in the following paragraph.

METHOD

The novel method for calculating the SEY is based on quick calculations of stopping powers in MCNPX [10] and the Sternglass theory [11]. As a first step, a cylindrical rod of the material of interest is simulated in MCNPX; the radius is set equal to two Molière radius, while the length is set long enough to fully contain a beam of 2 GeV protons.

The proton beam is defined as a monoenergetic source of 2 GeV protons, with a Gaussian distribution having σ=0.6 cm. The beam is perpendicularly impinging on the base of the cylindrical rod. In addition to protons, also electrons, neutrons and photons are transported. One single run

Content from this work may be used under the terms of the CC BY 3.0 licence (© 2020). Any distribution of this work must maintain attribution to the author(s), title of the work, publisher, and DOI

ISBN: 978-3-95450-222-6 ISSN: 2673-5350 doi:10.18429/JACoW-IBIC2020-WEPP10

Content from this work may be used under the terms of the CC BY 3.0 licence (© 2020). Any distribution of this work must maintain attribution to the author(s), title of the work, publisher, and DOI

with 1E5 proton histories takes approximately 10 minutes on a standard laptop and provides the collision, radiation and total stopping powers for protons from 2 GeV down to 1 keV. Since in proton-induced SEY calculations it is important to compute the amount of energy lost by protons, the collision stopping power dE/dx is considered (in MeV·cm^2/g).

As a second step, the number of electrons per primary proton (i.e. the SEY) is computed according to the Sternglass formula:

$$SEY = \frac{P \cdot \rho \cdot t}{25\ eV} \cdot \frac{dE}{dx}, \quad (1)$$

where $P = 0.5$ is the probability that an electron escapes from the material surface, ρ is the material density (in g/cm^3) and t is the mean free path of secondary electrons which is set equal to 1 nm. Since the average energy of the secondary electrons is estimated to be in the 20 eV-30 eV range by Sternglass [11], the value of 25 eV appears at the denominator of Eq. (1). The SEY values calculated for the materials and compounds of current interest are summarized in the following paragraph.

RESULTS

The presented method was validated with four elements for which dE/dx values were available from NIST [12]: Al, Cu, Fe and W. The novel method was therefore applied also to all the materials and compounds previously listed in Table 1. As representative example, the calculated SEY values are plotted in Fig. 1 in the case of nickel, for which no data were found available from NIST throughout the proton energy range of interest for the present work.

As expected from Eq. (1), the SEY curve in Fig. 1 follows the trend of the dE/dx distribution, spanning over three orders of magnitude for proton energies in the [0.001, 2000] MeV range. A peak is usually observed around 100 keV, then the SEY values monotonically decrease for increasing proton energies up to 2 GeV. This is an important aspect to be considered for insertable devices in the NCL linac, where the SEY is maximal. The SEY values at relevant energies in the ESS NCL are reported in Table 2. The maximum SEY value is found after 75 keV protons on TZM - a molybdenum alloy which is used in the LEBT EMU and in the energy degrader of a DTL FC.

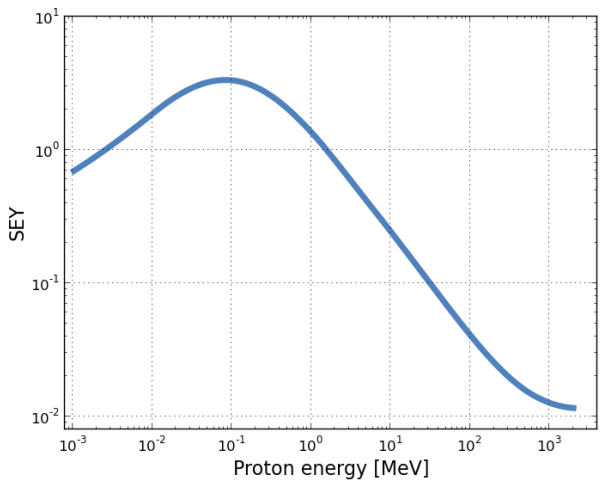

Figure 1: Calculated SEY values by protons in nickel.

The SEY values at relevant energies in the ESS SCL are reported in Table 3. The energies of 800 MeV and 2 GeV are the initial and final intended energy of the beam on target, respectively. At the highest energy considered, the maximum SEY values is found for protons on tungsten.

Any other SEY value at any non-nominal beam energy can be easily inferred from the available dataset.

Table 2: Calculated SEY values for relevant proton energies and structural materials of beam-interceptive devices in the ESS NCL section.

E_P [MeV]	0.075	3.6	21	74
C	2.238	0.315	0.080	0.029
Ti	2.527	0.551	0.152	0.058
Ni	2.695	1.033	0.293	0.113
Cu	2.560	0.982	0.280	0.108
W	2.971	1.339	0.432	0.175
TZM	3.400	0.960	0.285	0.113
SiC	1.604	0.537	0.137	0.050

Table 3: Calculated SEY values for relevant proton energies and structural materials of beam-interceptive devices in the ESS SCL section.

E_P[MeV]	90	360	800	2000
C	0.025	0.010	0.008	0.006
Ti	0.050	0.021	0.015	0.013
Ni	0.098	0.041	0.030	0.027
Cu	0.094	0.039	0.029	0.026
W	0.154	0.067	0.050	0.045
TZM	0.098	0.042	0.031	0.028
SiC	0.044	0.018	0.013	0.011

CONCLUSIONS AND OUTLOOK

The method for calculating SEY values in key structural materials of the devices insertable into the ESS linac was presented. The results are based on fast yet reliable MCNPX calculations and on the Sternglass theory. Proton-induced SEY values were calculated over six orders of magnitude i.e. from 1 keV up to 2 GeV. The lookup tables serve for beam-current estimations, both at nominal and non-nominal beam energies during the ESS linac commissioning. The possibilities offered by the newly developed method are manifold. Since it's virtually possible to define in MCNPX any density, isotope and chemical composition, the method is useful for selecting novel materials and compounds which may be needed for detectors upgrades. Moreover, it enables to explore the impact of oxides on metallic surfaces. In addition, the presented method can help in investigating the

ISBN: 978-3-95450-222-6 ISSN: 2673-5350 doi:10.18429/JACoW-IBIC2020-WEPP10

impact of secondaries on key linac components that could be affected by e.g. the multipacting effect. In the future, it would be useful to further develop the presented method to account for temperature and radiation-induced effects on SEY.

ACKNOWLEDGMENTS

The author is grateful to Dr. Cyrille Thomas and the colleagues working on the ESS target imaging system for having triggered the work presented in this paper. In fact, the presented method was initially developed just for the key materials of the aperture monitor and grid system for the beam on the ESS target, recognized to be universally useful and thus applied to the structural materials of all the other beam-interceptive devices in the ESS linac.

REFERENCES

[1] ESS, https://europeanspallationsource.se/about

[2] R. Garoby *et al.*, "Corrigendum: the European Spallation Source design", *Phys. Scr.*, vol. 93, p. 014001, 2018. doi:10.1088/1402-4896/aaecea

[3] T. J. Shea *et al.*, "Overview and status of diagnostics for the ESS project", in *Proc. 6th Int. Beam Instrumentation Conf. (IBIC'17)*, Grand Rapids, MI, USA, Aug. 2017, pp. 8–15. doi:10.18429/JACoW-IBIC2017-MO2AB2

[4] S. Grulja, S. Cleva, R. De Monte, and M. Ferianis, "Wire scanner diagnostic system", in *Proc. 8th Int. Beam Instrumentation Conf. (IBIC'19)*, Malmö, Sweden, Sep. 2019, pp. 326–327. doi:10.18429/JACoW-IBIC2019-TUPP015

[5] C. A. Thomas *et al.*, "J-PARC test of ESS beam on target diagnostics prototypes aperture monitor and GRID", in *Proc. 8th Int. Beam Instrumentation Conf. (IBIC'19)*, Malmö, Sweden, Sep. 2019, pp. 387–391. doi:10.18429/JACoW-IBIC2019-TUPP032

[6] E. M. Donegani, I. Bustinduy, C. S. Derrez, T. J. Grandsaert, A. Rodríguez Páramo, and T. J. Shea, "Status of the Faraday Cups for the ESS Linac", in *Proc. 8th Int. Beam Instrumentation Conf. (IBIC'19)*, Malmö, Sweden, Sep. 2019, pp. 205–208. doi:10.18429/JACoW-IBIC2019-MOPP044

[7] O. Tuske *et al.*, "ESS emittance measurements at INFN CATANIA", in *Proc. 8th Int. Particle Accelerator Conf. (IPAC'17)*, Copenhagen, Denmark, May 2017, pp. 123–125. doi:10.18429/JACoW-IPAC2017-MOPAB023

[8] B. Cheymol and A. Ponton, "High power and high duty cycle slit and grid system for hadron accelerator commissioning", in *Proc. 57th ICFA Advanced Beam Dynamics Workshop on High-Intensity and High-Brightness Hadron Beams (HB'16)*, Malmö, Sweden, Jul. 2016, pp. 226–231. doi:10.18429/JACoW-HB2016-MOPL017

[9] E. M. Donegani, T. J. Grandsaert, T. J. Shea, and C. A. Thomas, "The insertable beam stop in the ESS SPK section", presented at the 9th Int. Beam Instrumentation Conf. (IBIC'20), Santos, Brazil, Sep. 2020, paper WEPP07, this conference.

[10] D. B. Pelowitz, Ed., "MCNPX Users Manual Version 2.7.0", LA-CP-11-00438, 2011.

[11] E. J. Sternglass, "Theory of secondary electron emission by high-speed ions", *Phys. Rev.*, vol. 108, p. 1, 1957. doi:10.1103/PhysRev.108.1

[12] "Stopping-Power and Range Tables for Electrons, Protons, and Helium Ions", NIST Standard Reference Database 124, https://physics.nist.gov/PhysRefData/Star/Text/PSTAR.html

Content from this work may be used under the terms of the CC BY 3.0 licence (© 2020). Any distribution of this work must maintain attribution to the author(s), title of the work, publisher, and DOI

ISBN: 978-3-95450-222-6 ISSN: 2673-5350 doi:10.18429/JACoW-IBIC2020-WEPP12

SIMULATION OF THE SIGNAL PROCESSING FOR THE NEW INTERACTION REGION BPMs OF THE HIGH LUMONSITY LHC

D. R. Bett*, University of Oxford, UK
M. Wendt, M. Krupa, A. Boccardi, CERN, Geneva, Switzerland

Abstract

New stripline beam position monitors (BPMs) will be installed at the Interaction Regions of the ATLAS and CMS experiments as part of the High-Luminosity upgrade to the LHC. These BPMs will be located in sections of the beamline where the two counter-propagating proton beams co-exist within a single pipe, such that the signal observed on each output port is a combination of the signals generated by each beam. The use of the BPMs as the input for a possible luminosity feedback system places a demanding requirement on the long-term accuracy of the BPMs. Accurate measurement of the position of each beam requires a method for isolating the individual beam signals. A simulation framework has been developed covering all stages of the measurement process, from generation of the signals expected for beams of a given intensity and orbit through to digitization, and has been used to evaluate several candidate methods for extracting the position of each beam in the presence of the unwanted signal from the other.

INTRODUCTION

The High Luminosity LHC is an upgrade of the LHC with a target luminosity five times larger than the current nominal value of 10^{34} cm^{-2}s^{-1}. As part of this upgrade, the beam position monitors (BPMs) in interaction region (IR) 1 and 5 will be replaced, corresponding to the vicinity of the ATLAS and CMS detectors respectively.

The layout of the right side of IR1 and IR5 is illustrated in Fig. 1. Far from the interaction point (IP) the proton beams exist in their own individual pipes and the BPMs need only measure the position of the one beam. Close to the IP, the two beams travel within the same pipe and the BPMs in that region are required to measure the position of both beams. Six new octagonal stripline BPMs of two different types will be installed either side of each of the two IPs, with the BPM closest to the IP being of type A and the remainder of type B. The two types have slightly different apertures and will be installed with different orientations of the electrodes; type A BPMs will have the electrodes oriented at 0° and 90° in the lab frame and the type B BPMs will be rotated by 45° due to the tungsten shielding at those locations. The longitudinal location of each BPM, s, determines the difference in arrival time of the two beams, Δt (Table 1).

BPM MODEL

The CST Microwave Studio [1] model of the type A BPM is shown in Fig. 2. I_1 and I_2 represent beams entering the BPM from opposite directions and V_1 to V_8 the signals observed at each end of the four striplines designated right (R), top (T), left (L) and bottom (B). Stripline BPMs are highly directive [2]; in the ideal case, there is perfect cancellation at the downstream ports between the signal induced in the direction of the beam as the beam enters the BPM, and the signal induced as the beam exits the BPM. The resulting bipolar signal is therefore only observed at the upstream port.This allows such a BPM to be used to distinguish the signal generated by beams travelling in opposite directions.

Table 1: BPM distance from the IP (s) and difference in the arrival time of the two beams (Δt).

BPM Type	s [m]	Δt [ns]
A	21.853	3.92
B	33.073	3.92
B	43.858	6.82
B	54.643	9.72
B	65.743	10.52
B	73.697	7.36

In practice the cancellation is not total and a small amount of signal is observed at the downstream end, combining with main signal from the opposite beam. Figure 3 shows the voltages calculated at each end of each stripline when a simulated beam with the indicated current profile travels along the BPM axis. The first beam to arrive is designated “beam 1” and induces a large (“coupled”) signal at upstream ports 1-4 and a much smaller (“isolated”) signal at downstream ports 5-8, while the reverse is true for “beam 2” which enters the other end of the BPM after time Δt. Each beam distorts the signals that will be used to measure the position of the other beam, and this distortion must be taken into account in order to obtain accurate measurements of the position of each individual beam.

SIMULATION

The numerical computation software GNU Octave [3] was used to simulate the process of obtaining beam position measurements from the stripline signals. The CST predictions of the signals induced at each end of the stripline are scaled according to the position and charge of each beam and the signals from beam 2 are delayed as appropriate in order to form the set of stripline waveforms V_1 to V_8. As the BPMs are located in a very high-radiation environment, long (> 100 m) cables will be used to transport the signals to a digital processor able to operate at a sample frequency of ~ 4 GHz. Given the pulses themselves are only a few

* douglas.bett@physics.ox.ac.uk

Content from this work may be used under the terms of the CC BY 3.0 licence (© 2020). Any distribution of this work must maintain attribution to the author(s), title of the work, publisher, and DOI

ISBN: 978-3-95450-222-6 ISSN: 2673-5350 doi:10.18429/JACoW-IBIC2020-WEPP12

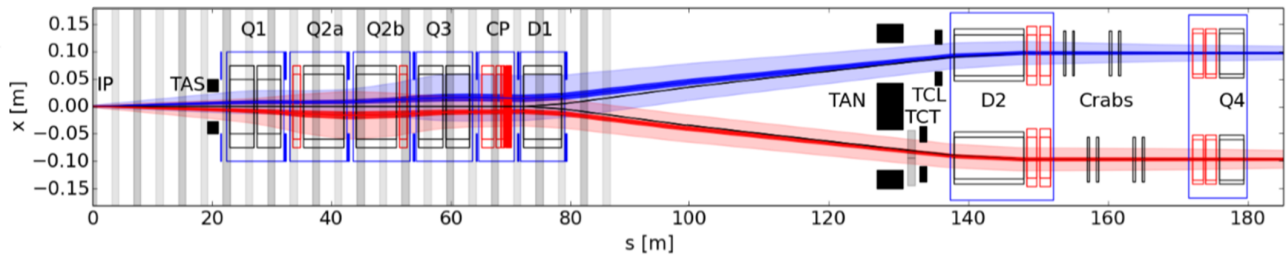

Figure 1: Beam optics in the interaction regions [4]. The dark blue and red strips correspond to the 2σ envelope of the beams and the vertical blue bars either side indicate the locations of the BPMs.

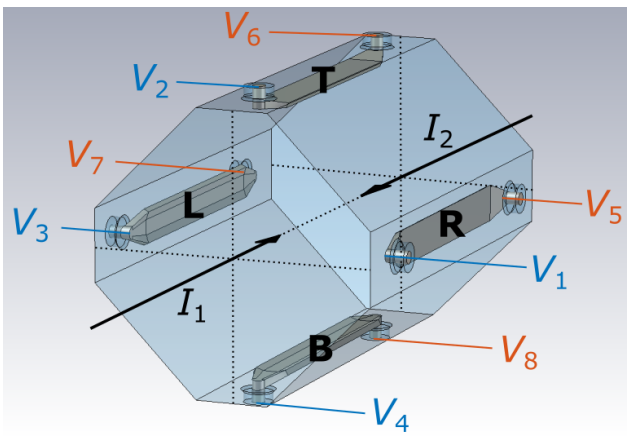

Figure 2: 3D model of the type A BPM in CST Microwave Studio with annotation indicating the beam inputs I_1 and I_2 and the stripline outputs V_1 through V_8.

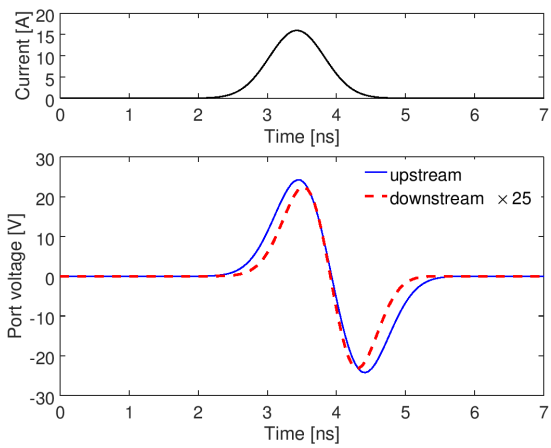

Figure 3: Input beam current profile (top) and voltage induced at the upstream end (solid) and the downstream end (dashed and magnified x25).

nanoseconds long (Fig. 3), the 25 ns bunch spacing between HL-LHC bunches motivates the use of a low-pass filter to make more efficient use of the ADCs by stretching the signals in the time domain. As both ends of the stripline are monitored, a reflectionless filter was implemented [5]. Figure 4 shows how the port 5 (downstream) signals are expected to appear at the stripline itself and at the input to the digitizer. The situation depicted is an extreme case where the charge of beam 1 is ten times higher than that of beam 2, but it serves to illustrate that a small signal from beam 1 is followed $\Delta t = 3.92$ ns later by a larger signal from beam 2. Table 2 lists the values used for the relevant simulation properties; the beam orbits correspond to the pre-squeeze orbits of the beams at the IR1 type A BPM.

Table 2: Simulation Parameters

Property	Value
(x_1, y_1)	$(0.75, -6.45)$ mm
(x_2, y_2)	$(-0.75, 6.15)$ mm
Δt	3.92 ns
Beam 1 population	2.3×10^{11} charges
Beam 2 population	2.3×10^{10} charges
Bunch profile	Gaussian, FWHM = 0.95 ns (both)
Cable attenuation	7.19 dB/100 m @ 1 GHz
Cable velocity	$0.88c$
Cable length	100 m
Cut-off frequency	273 MHz

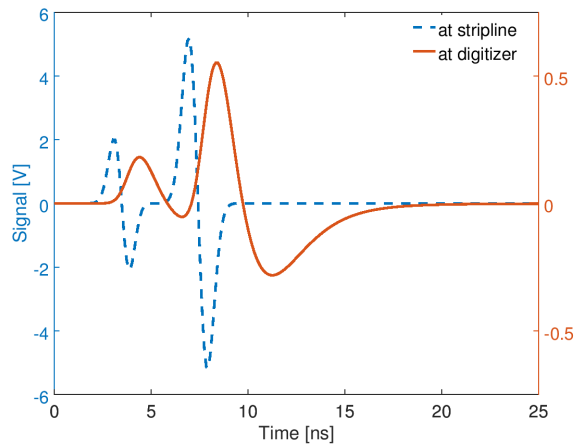

Figure 4: Appearance of V_5 at the stripline (dashed; left axis) and after low pass filtering at the digitizer (solid; right axis) for the simulation parameters given in Table 2.

Variable attenuators are also included in order to match the levels of the analogue stripline signals to the range of the digitizer. The digitization process itself is assumed to

Content from this work may be used under the terms of the CC BY 3.0 licence (© 2020). Any distribution of this work must maintain attribution to the author(s), title of the work, publisher, and DOI

ISBN: 978-3-95450-222-6 ISSN: 2673-5350 doi:10.18429/JACoW-IBIC2020-WEPP12

Content from this work may be used under the terms of the CC BY 3.0 licence (© 2020). Any distribution of this work must maintain attribution to the author(s), title of the work, publisher, and DOI

be asynchronous with respect to the beam and to inject a realistic amount of random noise into the system based on measurements taken with a candidate digitizer. The digital waveforms are then ready to be processed in order to calculate the beam positions.

COMPENSATION

Several methods of compensating the waveforms to account for the signal from the other beam were considered. These included explicit sample-by-sample subtraction of a reference waveform (scaled according to the observed amplitude of the waveform from the other end of the stripline) and a frequency domain approach that assumed the response of the BPM and the other hardware could be measured well enough to be able to recover the image current induced by each beam on each stripline.

An ensemble of 2,760 pulses at the same position was generated by digitizing the set of eight stripline signals generated in the previous section at 12-bit resolution with a 4 GHz sample clock. The clock phase varied uniformly and 1.5 bits of randomly distributed noise was added to each sample. Each set of eight waveforms was then used to perform a position measurement and Fig. 5 shows the results with the "ideal" position that would be measured by the stripline subtracted (note that this position differs from the true position of the beam as the non-linearity of the BPM is not taken into account). The frequency domain method clearly performs the worst and, for the beam conditions outlined here, is in fact worse than not compensating at all, as the offset of the measured mean position is 25 µm compared to less than 3 µm for no compensation. Both the sample-by-sample and power methods reduce this offset to less than half a micron. The single-pass error is approximately 10 µm regardless of whether compensation is performed or not. Power compensation is thus the preferred method as it requires by far the smallest amount of digital processing power.

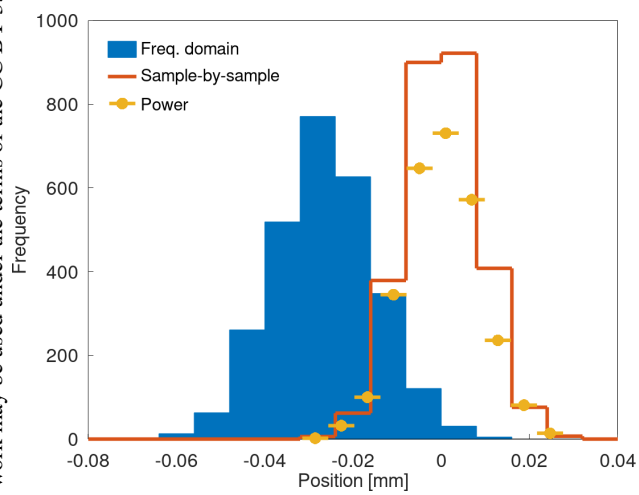

Figure 5: Histograms of the estimated horizontal position of beam 2 for several different methods of compensating for the other beam: frequency domain (solid), sample-by-sample (outline) and power (points).

Power Compensation Method

Consider the signal induced at the upstream end of the R stripline:

$$V_1 = \kappa_{1R} V_{1c} + \kappa_{2R} V_{2i} \tag{1}$$

where:

- V_{1c} is the signal induced at the upstream end of each stripline by a reference beam 1 with some nominal intensity and bunch length that travels on axis.
- V_{2i} is the signal induced by a reference beam 2 which has the same intensity and bunch length as the reference beam 1 and likewise travels on axis.
- The κ scale factors set the amplitude of each term of the stripline signal according to the intensity of each beam and its position in the BPM. $\kappa_{ij} = \rho_{ij} \cdot q_i$, where q_i is the intensity of the actual beam i (expressed as a multiple of the intensity of the reference beam) and ρ_{ij} is the angle subtended by beam i on stripline j (expressed as a multiple of the angle subtended from the center of the BPM).

Taking the sum of the samples squared for both sides:

$$\sum V_1^2 = \kappa_{1R}^2 \sum V_{1c}^2 + 2\kappa_{1R}\kappa_{2R} \sum V_{1c} \cdot V_{2i} + \kappa_{2R}^2 \sum V_{2i}^2 \tag{2}$$

Let $\sum V_i^2 = \psi_i$ and $\sum V_i \cdot V_j = \chi_{ij}$; then Eq. 2 can be rearranged so as to resemble a quadratic equation:

$$\kappa_{1R}^2 + 2\frac{\chi_{1c2i}}{\psi_{1c}}\kappa_{1R}\kappa_{2R} + \left(\frac{\psi_{2i}}{\psi_{1c}}\kappa_{2R}^2 - \frac{\psi_1}{\psi_{1c}}\right) = 0 \tag{3}$$

By making the approximation $\kappa_{2R} \sim \sqrt{\frac{\psi_5}{\psi_{2c}}}$, the coefficients of this quadratic equation can be expressed solely in terms of a set of scalars that can be calculated in advance from the reference waveforms (ψ_{1c}, ψ_{2i}, χ_{1c2i}) and a pair of scalars that must be calculated in real time from the measured waveforms (ψ_1, ψ_5). A similar equation can be derived to give a solution for κ_{1L}, and the beam position can then be calculated in the usual way (difference over sum) to give the horizontal position of beam 1.

CONCLUSION

The new BPMs in the ATLAS and CMS interaction regions must be able to accurately recover the individual position of each beam from a set of stripline signals that are sensitive to the position of both. The response of the BPMs to a beam stimulus was simulated in CST Microwave Studio and used to generate ensembles of waveforms that could be used to assess the performance of different compensation schemes. The initial simulations suggest a pulse-by-pulse approach is likely to deliver sufficient performance without requiring an unfeasible amount of digital processing.

Future studies will investigate the use of a pilot-tone scheme in order to compensate for differences in the behaviour of each channel.

ISBN: 978-3-95450-222-6 ISSN: 2673-5350 doi:10.18429/JACoW-IBIC2020-WEPP12

REFERENCES

[1] CST Microwave Studio, http://www.cst.com

[2] M. Wendt, "BPM systems: A brief introduction to beam position monitoring", arXiv:2005.14081

[3] J. W. Eaton, D. Bateman, S. Hauberg, and R. Wehbring, "GNU Octave version 5.2.0 manual: a high-level interactive language for numerical computations", http://www.gnu.org/software/octave/doc/interpreter

[4] R. De Maria, S. D. Fartoukh, and M. Fitterer, "HLL-HCV1.1: optics version for the HL-LHC upgrade", in *Proc. 6th Int. Particle Accelerator Conf. (IPAC'15)*, Richmond, VA, USA, May 2015, pp. 2090–2093. doi:10.18429/JACoW-IPAC2015-TUPTY037

[5] M. Morgan, "Synthesis of a new class of reflectionless filter prototypes", arXiv:1008.3502

Content from this work may be used under the terms of the CC BY 3.0 licence (© 2020). Any distribution of this work must maintain attribution to the author(s), title of the work, publisher, and DOI

ISBN: 978-3-95450-222-6 ISSN: 2673-5350 doi:10.18429/JACoW-IBIC2020-WEPP13

Content from this work may be used under the terms of the CC BY 3.0 licence (© 2020). Any distribution of this work must maintain attribution to the author(s), title of the work, publisher, and DOI

DESIGN AND TEST OF CBPM PROTOTYPES FOR SHINE*

S. S. Cao†, Y. B. Leng*, R. X. Yuan, R. T. Jiang
Shanghai Advanced Research Institute, Chinese Academy of Sciences, Shanghai, China

Abstract

SHINE (Shanghai High repetition rate XFEL aNd Extreme light facility) is designed to be an extremely high performance hard X-ray free electron laser facility located at Zhangjiang, Shanghai. As one of the key parameters of the facility, the resolution of the beam position measurement in the undulator section is required to be under 200 nm at a low bunch charge of 100 pC and better than 10 μm at 10 pC. To achieve this, a pre-study based on cavity beam position monitors is under development. Four sets of cavity monitors with different frequencies or load quality factors have been designed and are now manufactured by four different companies. It aims to select the cavity with the best performance and select the most capable company. This paper will briefly introduce the motivation, cavity design considerations, and cold test results.

INTRODUCTION

SHINE is a newly proposed high-repetition-rate X-ray FEL facility, which is designed to become one of the most efficient and advanced free electron laser user facilities in the world, providing a tool for cutting-edge research subjects. The facility includes a superconducting linear accelerator with an energy of 8 GeV, 3 underlines, 3 optical beam lines, and the first 10 experimental stations [1,2]. The fundamental parameters of SHINE are presented in Table 1.

Table 1: The Fundamental Parameters of SHINE

Parameters	Values	Units
Beam energy	8	GeV
Bunch charge	100	pC
Max rep-rate	1	MHz
Pulse length	20-50	fs
Peak brightness	5×10^{32}	~

The construction of such a high-level FEL facility has strict requirements for each subsystem. Beam position as one of the key parameters can be used to monitor the electron beam orbital changes. For SHINE, the position resolution requirement at the undulator is better than 200 nm. To achieve that, the high-resolution and high-sensitivity cavity beam position monitor (CBPM) is utilized to extract the beam position [3,4]. The principle is that the intensity of the TM110 mode excited by the beam is proportional to the beam position. By extracting the signal of TM110 mode, the beam position can be obtained. Moreover, the signal of TM_{110} mode is also related to the bunch charge, thus it is essential to use a reference cavity to normalize the bunch charge.

Four different types of CBPM are currently under development. The reason for developing four types of CBPM is based on the following considerations. Firstly, the higher the cavity frequency, the more compact the cavity, and the higher sensitivity and higher the ratio of signal-to-noise (SNR) of the output signal is expected. Thus the C-band and X-band CBPM are proposed. Secondly, the higher the Q_{load}, the longer the signal length, the higher the signal processing gain and the greater the crosstalk between the bunches. Thus the cavities with different Q_{load} are also proposed. Thirdly, it is also necessary to cooperate with several manufacturers and evaluate the processing capabilities so as to select the most capable one. At present, some CBPMs have been fabricated and are awaiting acceptance checks, while others are still under development.

The following subsections will introduce this in detail.

DEVELOPMENT OF FEEDTHROUGH

As an indispensable part of all beam position monitors (BPMs), feedthrough is used to couple the energy stored inside the cavity to the outside to the cavity and convert it to an electrical signal for subsequent electronic processing. Previously, the feedthroughs are purchased from companies. However, the bandwidth of purchased feedthrough is only about 8 GHz, which cannot meet the requirements of X-band CBPM, while the customized feedthroughs are too expensive. Therefore, we decided to independently develop high-bandwidth feedthroughs. Since Dr. Yuan has successfully completed the design of the high-bandwidth N-type feedthrough, we decided complete the design of the SMA-type feedthrough based on the N-type feedthrough.

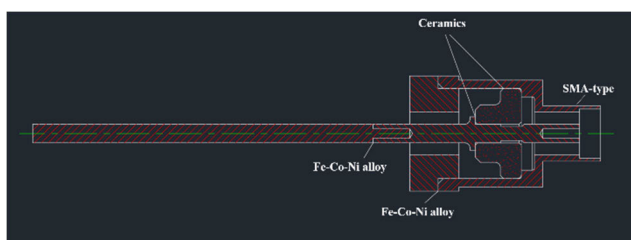

Figure 1: Structure of the SMA-type feedthrough.

The structure of the SMA-type feedthrough is shown in Fig. 1. The first batch of 20 prototypes have been developed, as shown in Fig. 2, including 8 dual-port SMA prototypes and 12 SMA-type feedthroughs. The dual-port SMA prototypes are used to evaluate the bandwidth of the feedthrough and the processing consistency. To improve the connection stability of the SMA interface, a gold-

* Work supported by National Key Research and Development Program of China under Grant 2016YFA0401903.
† lengyongbin@sinap.ac.cn

ISBN: 978-3-95450-222-6 ISSN: 2673-5350 doi:10.18429/JACoW-IBIC2020-WEPP13

plated test was performed. The test results show that gold plating can significantly improve the connection stability of the interface, and none of the feedthrough prototypes shows the poor connection.

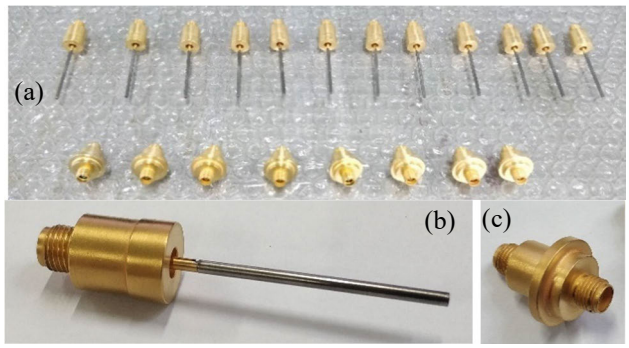

Figure 2: Prototypes of the SMA-type feedthrough:(a) 20 feedthrough prototypes; (b) SMA-feedthrough; (c) dual-port SMA-feedthrough.

Moreover, the S21 parameters of dual-port SMA-feedthroughs and S11 parameters of single-port SMA-feedthrough with a high-bandwidth network analyzer have been tested, as presented in Fig. 3. Among them, the bandwidth results of the 8 prototypes can be obtained through the S21 parameters. The test results show that all 8 prototypes can satisfy the design requirement and can be used in X-band CBPM. Except for the first prototype, the bandwidths of the other 7 prototypes are better than 15.5 GHz. The S11 parameters of the other 12 prototypes produced in the same batch are generally the same, and no prototypes with an obvious deviation of S11 are found.

In general, the high-bandwidth feedthroughs have been successfully developed this time, and they also have a good consistency.

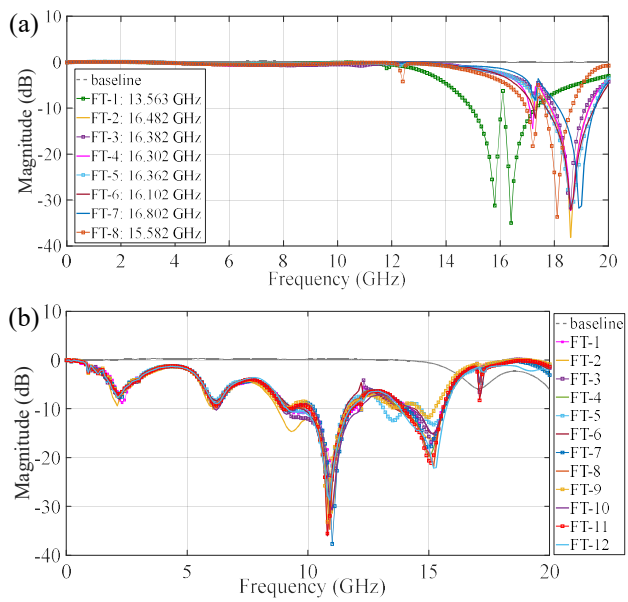

Figure 3: The S parameter tests: (a) S21 test of dual-SMA-feedthroughs; (b) S11 test of single-SMA-feedthroughs.

DEVELOPMENT OF CBPM

As described above, the development of four types of CBPMs with different frequencies and Q_{load} are the key task of this research. To evaluate the impact of frequency on system performance, the frequencies of the C-band and X-band CBPM are specific to be 5771.5 MHz and 11483.5 MHz. And to evaluate the impact of decay time constant (τ) on system performance, CBPM-100, CBPM-200, and CBPM-300 with a decay time (τ) of 100 ns, 200 ns, and 300 ns are going to be developed. The design parameters of the CBPMs are listed in Table 2.

Table 2: Design Parameters of the CBPMs

Parameters	CBPM-100	CBPM-200	CBPM-300	X-CBPM
Freq./MHz	5771.5	5771.5	5771.5	11483
τ/ns	100	200	300	100~200
Qload	1813	3626	5440	3611~7222
BW/MHz	3.18	1.59	1.06	1.59~3.18

With respect to cavity radius of TM_{mnp} mode, it is related to the cavity frequency f_{mnp} and it can be expressed as:

$$r_{mnp} = \frac{cj_{mn}}{2\pi f_{mnp}}$$

where c is the light speed, j_{mn} is the root of Bessel function, especially $j_{01} = 2.405$, $j_{11} = 3.832$. Normally, the tolerance of lathes machining is about 20 μm, which will cause a large frequency difference. The following Table (see Table 3) summarizes the cavity radius and the frequency sensitivity to radius of the C- and X-band CBPMs. The results in the table show that X-band CBPM has higher processing requirements, so we have to pay more attention on it.

Table 3: Radius and Frequency Sensitivity of CBPMs

Cavities	Radius /mm	$\Delta f/\Delta r$ (MHz/μm)	Δf @20 μm
C-CBPM Ref.	19.9	-0.3	6 MHz
C-CBPM Pos.	31.7	-0.2	4 MHz
X-CBPM Ref.	10	-1.1	22 MHz
X-CBPM Ref.	15.9	-0.7	14 MHz

Design of CBPMs

Basically, the design of the reference cavity is relatively simple compared to the position cavity. The C-band reference cavity adopts a re-entrant structure to facilitate frequency tuning and be convenient for cable connection, as shown in Fig. 4 (a). However, for the X-band cavity, due to the limitation of the cavity size and the size of the beam pipe, two rectangular waveguides are added on both sides of the cavity to extend the distance between the

Content from this work may be used under the terms of the CC BY 3.0 licence (© 2020). Any distribution of this work must maintain attribution to the author(s), title of the work, publisher, and DOI

ISBN: 978-3-95450-222-6 ISSN: 2673-5350 doi:10.18429/JACoW-IBIC2020-WEPP13

Content from this work may be used under the terms of the CC BY 3.0 licence (© 2020). Any distribution of this work must maintain attribution to the author(s), title of the work, publisher, and DOI

feedthrough and the beam pipe to facilitate the installation of feedthroughs, as shown in Fig. 4 (b).

The structure of the pillbox-position cavity is relatively complicated, and it can be divided into the following two types, as shown in Fig. 5. To compare the pros and cons of the two structures in design and fabrication, CBPM-100 and CBPM-200 adopt the first structure, as shown in Fig. 5 (a), and CBPM-300 and X-CBPM adopt the second structure, as shown in Fig. 5 (b).

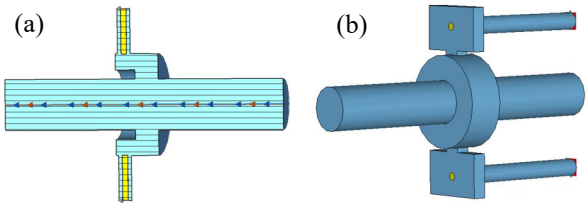

Figure 4: The 3D simulation model: (a) The C-band reference cavity; (b) The X-band reference cavity.

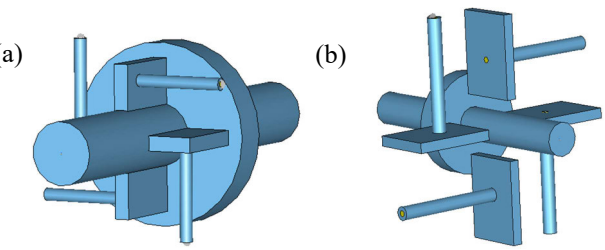

Figure 5: Two types of CBPM position structure.

Based on the above structures, an electromagnetic field simulation software is applied to attain the final cavity size as well as the simulation results. The simulation results can be found in Table 4. Generally, the simulation result of frequency is consistent with the design goal, the simulation result of τ is slightly different from the design goal, but it does not affect our evaluation purpose.

Table 4: Simulation Results of CBPM Reference Cavities

Cavities	Freq. /GHz	τ/ns	Q_{load}	BW /MHz	Vp/ (V/nC)
CBPM100Ref	5.771	101	1831	3.15	12
CBPM100Pos	5.771	109	1976	2.92	2
CBPM200Ref	5.771	211	3825	1.51	4
CBPM200Pos	5.772	203	3681	1.57	0.8
CBPM300Ref	5.772	262	4751	1.21	6
CBPM300Pos	5.773	245	443	1.30	1.1
XCBPM_Ref	11.483	164	5916	1.94	14
XCBPM_Pos	11.483	176	6349	1.81	2

Cold Test

Currently, three sets of CBPM-200 have been fabricated and welded, as shown in Fig. 6. The cold tests with a network analyzer have been performed. The results have also been presented in Table 5. The frequency results of three sets of CBPM with 6 cavities show that the maximum frequency difference between two cavities is 9 MHz, and the maximum frequency difference from the design frequency is 6 MHz. And the maximum bandwidth difference between two cavities is 0.26 MHz, and the maximum frequency difference from the design frequency is less than 0.2 MHz. The preliminary results show that the three sets of cavities have good consistency, but they can be further improved in the future.

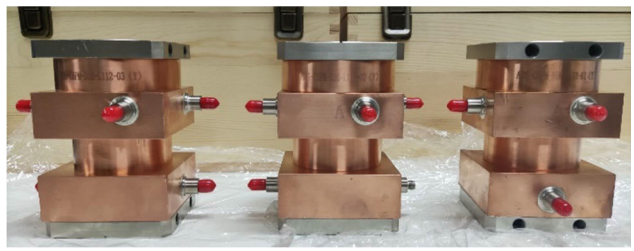

Figure 6: Photo of CBPM-200.

Table 5: Cold Test Results of CBPM-200

Cavities	Freq /GHz	BW /MHz	XY Crosstalk
CBPM#1 Ref.	5.769	1.54	~
CBPM#1 X	5.775	1.67	-60 dB
CBPM#1 Y	5.77	1.52	
CBPM#2 Ref.	5.773	1.49	~
CBPM#2 X	5.774	1.55	-53 dB
CBPM#2 Y	5.768	1.46	
CBPM#3 Ref.	5.776	1.56	~
CBPM#3 X	5.77	1.46	-54 dB
CBPM#3 Y	5.777	1.41	

CONCLUSION

The first version of the four sets of CBPM has been designed. In addition, the pre-research cavity of CBPM-200 has been processed, welded and tested. The test results are in good agreement with the simulation results, but it can be further improved.

Reviewing the entire development process, we still need to pay attention to the mode interference problem during the design process, either remove other interference modes, or move them to a frequency far away from the tested mode; on the other hand, we also need to pay special attention to the XY crosstalk problem. The cavity structure and manufacturing method can be optimized.

In the future, we will further optimize the unreasonable parts of the cavity design and monitor each process of manufacturing to lay the foundation for subsequent mass production.

REFERENCES

[1] C. Feng and H. Deng, "Review of fully coherent free-electron lasers", *Nucl. Sci. Tech.*, vol. 29, p. 160, 2018. doi:10.1007/s41365-018-0490-1

[2] Z. Zhu, Z. T. Zhao, D. Wang, Z. H. Yang, and L. Yin, "SCLF: An 8-GeV CW SCRF Linac-Based X-Ray FEL Facility in Shanghai", in *Proc. 38th Int. Free Electron La-*

ISBN: 978-3-95450-222-6 ISSN: 2673-5350 doi:10.18429/JACoW-IBIC2020-WEPP13

ser Conf. (FEL'17), Santa Fe, NM, USA, Aug. 2017, pp. 182-184. doi:10.18429/JACoW-FEL2017-MOP055

[3] Lorenz R. *et al*., "Cavity-type beam position monitors for the SASE FEL at the TESLA Test Facility", Rep. TESLA-FEL-2003-03, Rep. CM-P00042566, 2003.

[4] Lee S., Ko I. S., Kim C. et al., "Design of the X-band cavity beam position monitor", *Journal of the Korean Physical Society*, vol. 63, no. 7, p.1322-1326, 2013. doi: 10.3938/jkps.63.1322

Content from this work may be used under the terms of the CC BY 3.0 licence (© 2020). Any distribution of this work must maintain attribution to the author(s), title of the work, publisher, and DOI

ISBN: 978-3-95450-222-6 ISSN: 2673-5350 doi:10.18429/JACoW-IBIC2020-WEPP15

Content from this work may be used under the terms of the CC BY 3.0 licence (© 2020). Any distribution of this work must maintain attribution to the author(s), title of the work, publisher, and DOI

EXPERIMENTS WITH A QUADRATED DIELECTRIC-FILLED REENTRANT CAVITY RESONATOR AS A BEAM POSITION MONITOR (BPM) FOR A MEDICAL CYCLOTRON FACILITY*

S. Srinivasan†, P.-A. Duperrex, J. M. Schippers
Paul Scherrer Institut, 5232 Villigen PSI, Switzerland

Abstract

Low beam currents (0.1-10 nA) are used for tumour treatment in the proton radiation therapy facility at PSI. The facility houses a superconducting cyclotron with an extraction energy of 250 MeV pulsed at 72.85 MHz. Online measurement of the beam position is traditionally performed with the help of ionisation chambers (ICs), however, at the expense of reduced beam quality and scattering issues. There is a strong demand to have this measurement performed with minimal beam disturbance, since the beam position is directly associated with the dose-rate applied. A cavity resonator, working on the principle of an electric dipole mode resonance, whose frequency is coupled to the second harmonic of the pulse rate, has been built to measure beam position in a purely non-invasive manner. Followed by a reasonable agreement between the test-bench and the simulation results, the cavity is installed in one of the beamlines. Here, we report on the measurement of the cavity BPM as a function of beam current and position and its shortcomings. When measured with a spectrum analyser, the cavity BPM can deliver position information within the accuracy and resolution demands of 0.50 mm.

INTRODUCTION

Proton beams of low beam currents (0.1-10 nA) are used for radiation therapy at PSI, and its position is traditionally measured with multi-strip ionisation chambers (ICs) [1]. Due to a strict demand for minimal disturbance of the beam, a non-invasive BPM, modelled as four LC cavities within a ground cylinder with a common dielectric is described in [2] as a potential replacement to ICs. It is designed to work on the dipole mode (TM_{110}) of resonance at 145.7 MHz for off-centered beams. The BPM prototype is characterised on a test-bench and its position dependence is in good agreement with the simulation expectation as seen in [2]. The TM_{110} mode frequencies of the horizontal and the vertical polarisations, localised in horizontal and vertical cavities, are at 146.0 MHz and 148.1 MHz due to cavity asymmetries from reassembling to correct for sensitivities as described in [2]. Hence, for validation of the BPM prototype with beam measurements, only horizontal plane cavities are studied due to its proximity to the design TM_{110} mode frequency demand.

* This project has received funding from the European Union's Horizon 2020 research and innovation programme under the Marie Skłodowska-Curie grant agreement No 675265.
† sudharsan.srinivasan@psi.ch

BEAMLINE MEASUREMENTS

The BPM, as shown in Figure 1 [3] , is installed in the temperature-controlled (28.5±0.5 °C) proton therapy facility, PROSCAN, at six meters from the degrader exit (Figure 2).

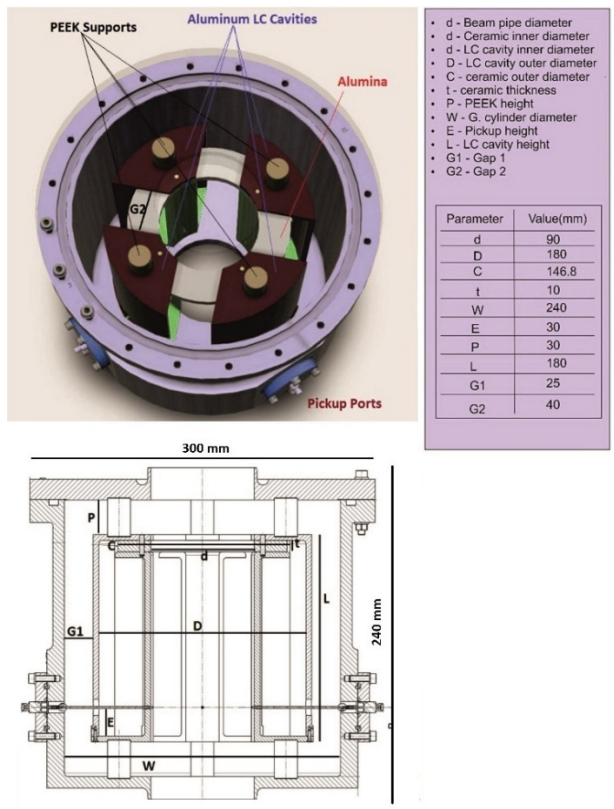

Parameter	Value(mm)
d	90
D	180
C	146.8
t	10
W	240
E	30
P	30
L	180
G1	25
G2	40

Figure 1: Geometry of the four-quadrant reentrant cavity BPM with its design TM_{110} mode frequency at 145.7 MHz and its design monopole mode frequency (TM_{010}) at 127.1 MHz.

The sensitivity of the BPM is expected to be nearly constant for different energies since the influence of energy spread from the degrader on bunch length elongation at the BPM location will be minimal unlike for the BCM location as described in [4].

The measurement reference is an IC located within a meter behind the BPM. The measurement chain, as shown in Figure 2, consists of a single stage amplification of 36 dB each for the horizontal plane cavities and a spectrum analyser. The pickups of the vertical plane cavities of the BPM are terminated with 50 Ω. The beam position response of the BPM prototype is verified at different beam currents and energies.

ISBN: 978-3-95450-222-6 ISSN: 2673-5350 doi:10.18429/JACoW-IBIC2020-WEPP15

The beam current response is measured at two different beam positions: 2.4 mm and 4.8 mm for a 200 MeV beam. The beam energy dependency is tested for 200 MeV and 138 MeV at 4.8 mm. The beam position response is measured at two beam currents: 2.6 nA and 12.2 nA for a 138 MeV beam. Also, the horizontal cavity response for a vertical offset is investigated. The IC used as reference monitor has a beam current and position uncertainty of 1% and 5%.

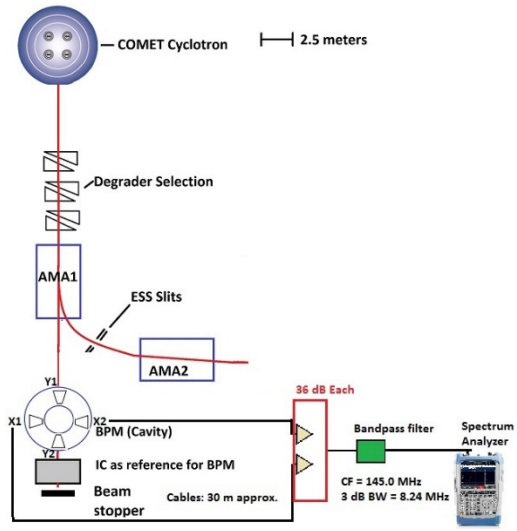

Figure 2: BPM located at six meters from the degrader exit. The measurement chain consists of two low noise-amplifier with 36 dB gain each, followed by a bandpass filter. A spectrum analyser provides amplitude measurement of the BPM for beam position offsets.

Beam Current and Energy Response

The BPM signal is proportional to beam current and beam position. For a given position offset, the BPM's beam current response is linear and the beam current sensitivity is higher for larger position offsets as expected and as seen in Figure 3.

The beam current sensitivity of the X1 cavity, shown in Figure 4, is only 3% lower at 138 MeV compared to 200 MeV, which is in close agreement with the 4% difference in bunch length for the two energies at the BPM location.

Beam Position Response

The 30% higher position sensitivity of the X2 cavity compared to the X1 cavity could be due to the induced cavity asymmetries as discussed in [2]. Consequently, the beam-pickup coupling coefficients of the cavities are affected as indicated by different saturation of the different cavities (encircled in red and purple in Figure 5). As a result, the linear response of the X2 cavity is existent over a position range of - 10.0 mm to +10.0 mm, but for the X1 cavity, it exists over a smaller range from -10.0 mm to +3.0 mm. Similarly, relative to measurements with 2.6 nA beam current, the position sensitivity of the X1 and X2 cavities is improved by approximately 14% and 11% when using 12.2 nA.

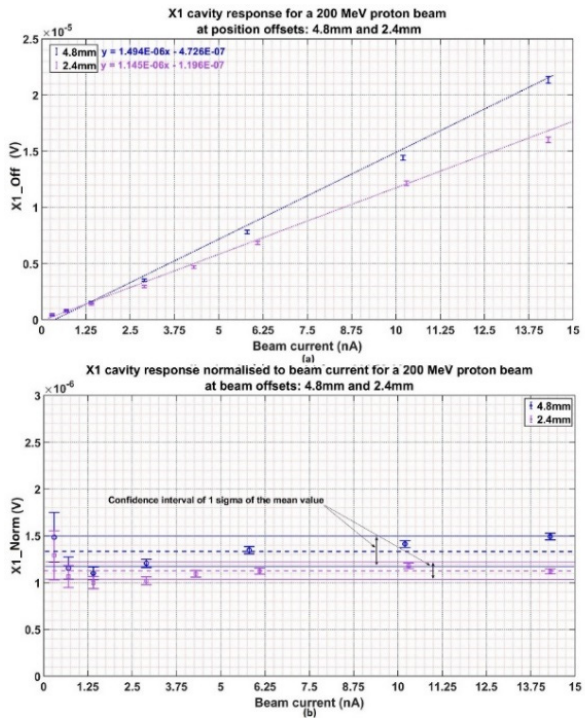

Figure 3: (a) X1 cavity response after measurement-offset correction. (b) After beam current normalisation. The error bars constitute two σ measurement uncertainty.

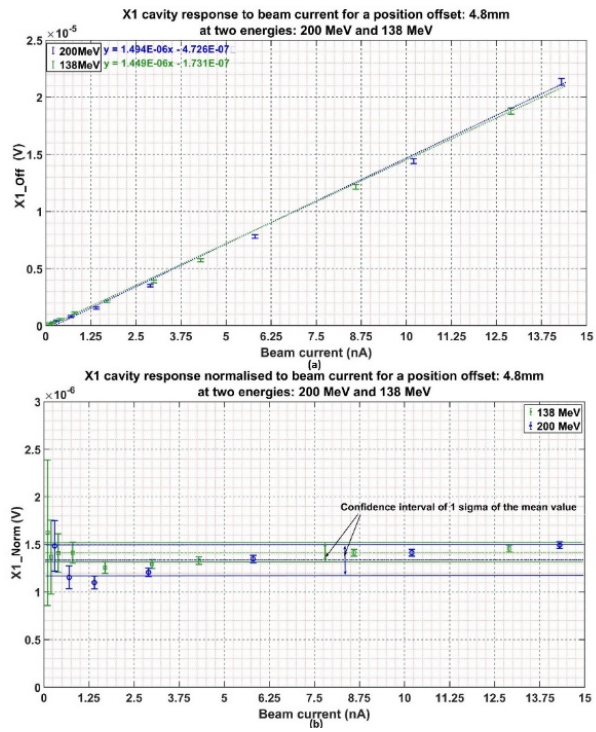

Figure 4: (a) X1 cavity response with measurement-offset correction for a 200 MeV and 138 MeV proton beam at 4.8mm towards X1. (b) After beam current normalisation. The error constitute two σ measurement uncertainty.

For a beam shift along the Y-axis, the TM_{110} mode's horizontal polarisation is unexcited and the signals from the horizontal cavities remain constant as expected (Figure 6).

Content from this work may be used under the terms of the CC BY 3.0 licence (© 2020). Any distribution of this work must maintain attribution to the author(s), title of the work, publisher, and DOI

ISBN: 978-3-95450-222-6 ISSN: 2673-5350 doi:10.18429/JACoW-IBIC2020-WEPP15

Content from this work may be used under the terms of the CC BY 3.0 licence (© 2020). Any distribution of this work must maintain attribution to the author(s), title of the work, publisher, and DOI

The measurement plots represented are after measurement-offset correction and beam current normalisation. The measurement-offset for the beam current and the beam energy studies represent RF interferences and for the beam position study, is the zero position information. The measurement-offset is assumed invariant in time and in phase with positive polarisation of the induced dipole mode.

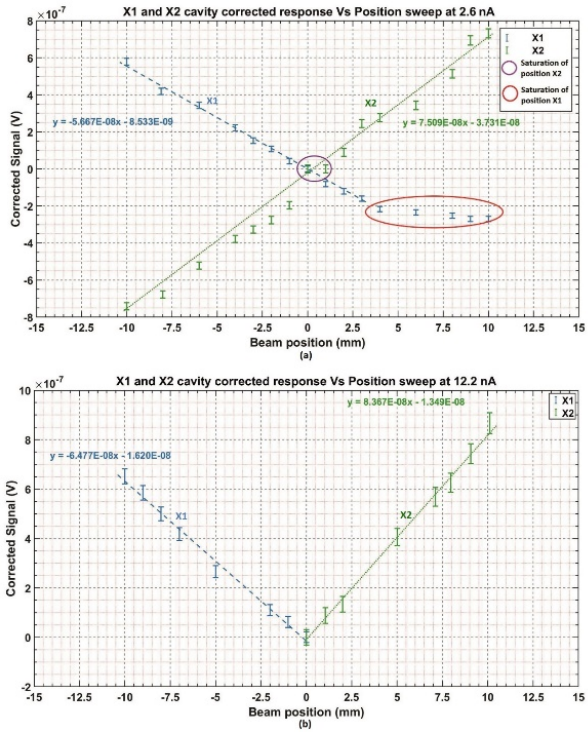

Figure 5: Beam current normalised response of both the horizontal cavities with two σ measurement uncertainty. (a) 2.6 nA beam current. (b) 12.2 nA beam current.

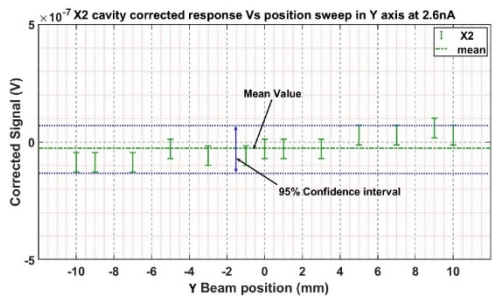

Figure 6: Beam current normalised response of the X2 cavity for position sweep in Y axis in the range -10.0 mm to +10.0 mm. The error bars constitute two σ measurement uncertainty.

The position sensitivity, the position error and the position resolution from the measurement for both the horizontal plane cavities are summarised in Table 1. The slope of the linear-fit equations in Figure 5 gives the position sensitivity of the horizontal plane cavities. The absolute difference between the calculated position and the reference positon from the IC gives the position error. This total position error includes systematic error due to alignment, measurement-offset, and the random error of the measurement, which represents the position resolution and is given by the σ of the calculated position.

Table 1: Measurement Summary of X1 and X2 Cavities

Position Parameters	2.6 nA		12.2 nA	
	X1	X2	X1	X2
Sensitivity, nV/mm	56.7	75.1	64.8	83.7
Error, mm	0.21	0.54	0.27	0.18
Resolution, mm	0.17	0.26	0.18	0.14

DISCUSSIONS

In both the beam current and beam energy dependence study, Figure 3 (b) and Figure 4 (b), we observe a deviation in the normalised response of the X1 cavity in the range 0.5 nA ≤ Beam current ≤ 2.5 nA. This is probably due to amplitude and phase variation of the measurement-offset during measurement. Since the measurement was performed with a spectrum analyser, only the amplitude was measured and assumed as time-invariant. For beam currents higher than 2.5 nA, the BPM response (both amplitude and phase) is sufficiently large to be not affected by such fluctuations in the measurement-offset.

Similarly, in the beam position response study, for smaller product of beam current and position (i.e. beam current × position ≤ 2.5 nA mm), the measurement-offset fluctuation is dominating the amplitude measured by the spectrum analyser. When the product of beam current and position is larger than 2.5 nA mm, the BPM response is not influenced to a greater extent by the measurement-offset.

This is an important observation that will be considered while designing a dedicated measurement chain for the BPM. This dedicated measurement chain will have I/Q demodulation [5] of the BPM signal with respect to the cyclotron RF.

With this dedicated measurement chain having a signal integration time of one-second, a better isolation from RF interference and a stronger amplification, beam position measurement can be performed with this cavity BPM for beam currents in the range (0.1-10) nA.

CONCLUSION AND FUTURE WORK

In this work, we have demonstrated non-interceptive beam position measurement, for beam currents in the range 2.5-10 nA, using a four-quadrant dielectric-filled reentrant cavity monitor, with a spectrum analyser. To our knowledge, this is the first non-interceptive device for beam position measurements at a proton therapy facility.

Following these successful measurements with the BPM prototype, a new cavity BPM has been developed that is expected to deliver at least a factor two better position sensitivity than of the prototype. Initial test-bench measurements are in good agreement with the expectations. Beamline measurements of the new BPM will be performed in the near future.

ISBN: 978-3-95450-222-6 ISSN: 2673-5350 doi:10.18429/JACoW-IBIC2020-WEPP15

ACKNOWLEDGMENT

The authors like to thank the workshop group, vacuum group and the PROSCAN maintenance group for construction and installation of the BPM prototype in the beamline.

REFERENCES

[1] R. Dölling, "Progress of the diagnostics at the PROSCAN beam lines," in *Proc. 8th European Workshop on Beam Diagnostics and Instrumentation for Particle Accelerators (DIPAC'07)*, Venice, Italy, May 2007, pp. 361–363.

[2] S. Srinivasan, P.-A. Duperrex, and J. M. Schippers, "Quadrated dielectric-filled reentrant cavity resonator as a proton beam position siagnostic," in *Proc. 10th Int. Particle Accelerator Conference*, 2019, pp. 2676-2679. doi:10.18429/JACoW-IPAC2019-WEPGW083

[3] J. M. Schippers *et al.*, "The use of protons in cancer therapy at PSI and related instrumentation," *J. Phys. Conf. Ser.*, vol. 41, pp. 61–71, 2006. doi:10.1088/1742-6596/41/1/005

[4] S. Srinivasan, P. Duperrex, and J. M. Schippers, "Reentrant cavity resonator as Beam Current Monitor (BCM) for a medical cyclotron facility," presented at the 9th Int. Beam Instrumentation Conf. (IBIC'20), (virtual conference), Brazil, Sep. 2020, paper WEPP05, this conference.

[5] C. Ziomek and P. Corredoura, "Digital I/Q demodulator," *Proc. IEEE Particle Accelerator Conf.*, Dallas, TX, USA, May 1995, vol. 4, pp. 2663–2665. doi:10.1109/pac.1995.505652

Content from this work may be used under the terms of the CC BY 3.0 licence (© 2020). Any distribution of this work must maintain attribution to the author(s), title of the work, publisher, and DOI

ISBN: 978-3-95450-222-6 ISSN: 2673-5350 doi:10.18429/JACoW-IBIC2020-WEPP16

ADVANCED LIGHT SOURCE HIGH SPEED DIGITIZER*

J. Weber†, J. Bell, M. Chin, E. Norum, G. Portmann
Lawrence Berkeley National Laboratory, Berkeley, CA, USA

Abstract

The Advanced Light Source (ALS) is developing the High Speed Digitizer (HSD), a data acquisition system based on the latest Radio Frequency System-on-Chip (RFSoC) technology. The system includes 8 channels of 4GHz 4Gsps analog input, programmable gain, self-calibration, and flexible data processing in firmware. The initial motivation for the HSD project was to develop a replacement for aging ZTEC oscilloscopes that would be more tightly integrated with the ALS Control System and Timing System than any available commercial oscilloscope. However, a general approach to the design makes the HSD system useful for other applications, including a Bunch Current Monitor, as well as for other facilities beyond ALS.

INTRODUCTION

The ALS currently uses mostly ZTEC digital oscilloscopes and a few in-house designed hardware systems to monitor fast signals around the accelerator, including integrating current transformers (ICTs), wall current monitors, traveling wave electrodes, and fast magnet pulsers. The ZTEC scopes were desirable because they have no local display, so they are compact (up to two 4-channel units per 1U rack slot), and each unit runs an EPICS IOC to integrate with the ALS control system. Over time, some of these scopes have proven unreliable. Recently the ALS has experienced some failures of these units that cannot be repaired, leaving the facility with few or no spares of some of the models in production use.

A few years ago, Xilinx introduced RFSoC technology that integrates high speed data converters (DACs and ADCs) with programmable logic and dedicated CPUs in a single chip [1]. By including the ADCs, this architecture simplifies the rest of the analog/RF front end hardware design for fast analog signals. The high channel density makes the cost per channel of a full system design competitive with an equivalent commercial oscilloscope.

The High Speed Digitizer (HSD) is a new design being developed for ALS based on the Xilinx ZCU111 RFSoC evaluation kit [2]. The kit includes 8 ADCs with 12-bit 4 GSps 4 GHz performance, which are sufficient to meet the ALS fast signal channel density and performance requirements. An SFP interface to a high speed serial transceiver receives the 2.5 Gbps timing event stream into an embedded event receiver (EVR), enabling synchronous sampling with the accelerator RF frequency, and integrated triggering. The Ethernet interface allows integration with the ALS control system. A controlled impedance RFMC expansion connector provides direct access to the RFSoC analog inputs.

At ALS, the existing Bunch Current Monitor (BCM) system is already based on the ZCU111 with a different front end, and will be replaced with an HSD unit so it is on a common hardware platform with other HSD units. APS is also using the existing ALS BCM hardware, and is evaluating the HSD as an upgrade to the BCM and a potential solution for monitoring fast signals as well. Other accelerators have also expressed interest in evaluating this system for similar applications.

ARCHITECTURE

The HSD system architecture is consistent with the network-attached device (NAD) model used for ALS in-house designed instrumentation systems, as shown in Fig. 1. The architecture is flexible in that the number of soft IOCs required to support devices and how they are connected can be adjusted to trade off network bandwidth, CPU performance, and maintenance complexity. In the case of ALS, the small number of HSD units and low average data transfer rate make it suitable for a single soft IOC. Each HSD unit communicates with the EPICS soft IOC via a clean and simple UDP interface, which allows either side to be upgraded independently. Each unit also receives the timing event link from the timing distribution infrastructure.

The HSD design is intended to be general purpose to accommodate multiple applications, including as a Fast Scope and Bunch Current Monitor, and others that fit the specifications. The firmware can be modified to achieve this with the same hardware configuration.

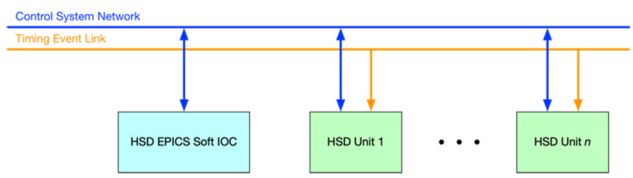

Figure 1: High Speed Digitizer (HSD) units in a network-attached device (NAD) architecture.

HARDWARE

The HSD hardware consists of a ZCU111 board with an analog front end board (HSDAFE) connected to the RFMC mezzanine interface, and a front panel board (HSDFP) containing an LCD display and connectors for front panel pushbuttons. Panel mount SMA patch cables connect the 8 analog input channels from the front panel to the HSDAFE. Different cable lengths compensate for differences in trace lengths on the board, so the input path length matches across all channels. A split ribbon cable harness connects the HSDFP to two PMOD connectors on the

* Work supported by the Director, Office of Science, Office of Basic Energy Sciences, of the U.S. Department of Energy under Contract No. DE-AC02-05CH11231
† jmweber@lbl.gov

Content from this work may be used under the terms of the CC BY 3.0 licence (© 2020). Any distribution of this work must maintain attribution to the author(s), title of the work, publisher, and DOI

ISBN: 978-3-95450-222-6 ISSN: 2673-5350 doi:10.18429/JACoW-IBIC2020-WEPP16

ZCU111. Ethernet, fiber, and USB patch cables connect front panel feedthrough connectors to the ZCU111 for the control system, EVR, and console interfaces, respectively. Figure 2 shows the front panel and hardware inside the HSD chassis.

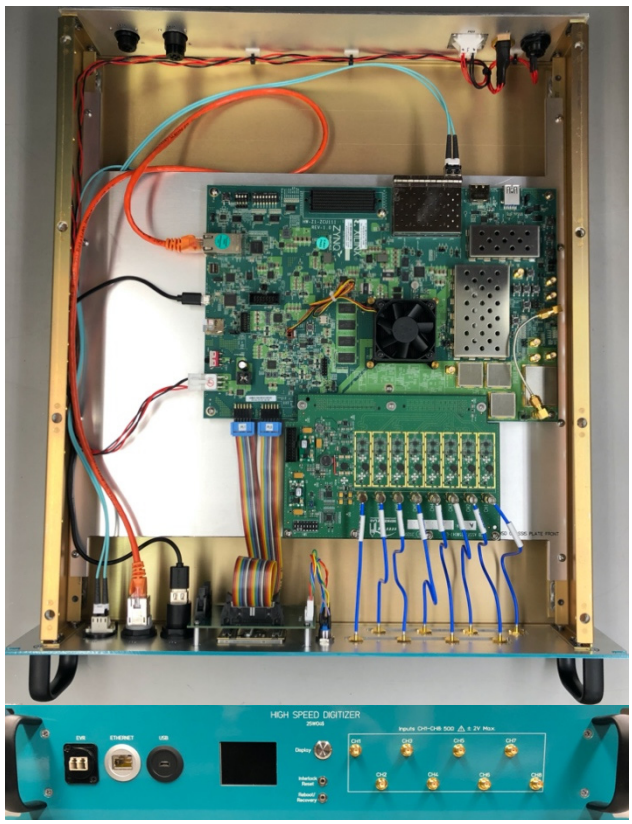

Figure 2: HSD chassis top view (top) and front view (bottom).

The HSDAFE has identical front end circuits for each of the 8 analog inputs, as shown in Fig. 3. The maximum analog input level is ±2 V (+16 dBm) and is protected from overvoltage by a dual Schottky barrier diode. The input signal is then attenuated by 6 dB. An RF MEMS SP4T switch selects between four input paths: DC-coupled, AC-coupled, DC calibration, or ADC training. To simplify the design, calibration and training signals are shared across all channels, so only one channel can be calibrated or trained at a time. The training signal is a digital output from the ZCU111 connected through a passive RC low pass filter into the RF switch.

A 15 dB attenuator scales the maximum signal amplitude to the fixed gain amplifier input range. A programmable gain amplifier is scaled so a full scale input signal at the SMA connector drives the RFSoC ADC full scale at a gain of +6 dB, where the maximum gain is +26 dB, providing 20 dB of usable programmable gain range in 1 dB steps. A simple differential RC low pass filter at 2 GHz provides anti-aliasing at the ADC input. A single capacitor can be replaced with a different value to change the filter bandwidth, or removed to drive the ADC unfiltered.

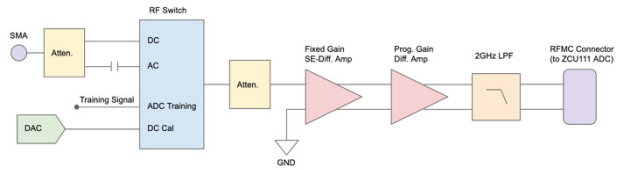

Figure 3: HSDAFE board analog input channel block diagram.

FIRMWARE

The firmware is flexible and can be adapted to various applications by changing the sampling clock generation, signal processing algorithm, and data acquisition and triggering operation. Figure 4 contains a high level block diagram of the HSD firmware. Off-chip peripherals are represented by circles, firmware IP cores are rectangles. The *RF Data Converter* [3] and *ZYNQ* [4] blocks are Xilinx cores, the *EVR* core is an evolution of a design for the ALS accelerator timing system upgrade [5] and the *Acquisition* core is an new LBL design for this system. Currently there are two versions of firmware in development: Fast Scope (FS) and Bunch Current Monitor (BCM).

For the FS application, the ADC sampling clock runs at f_{RF}*8 (~4 GHz). The *Acquisition* core supports flexible triggering from the EVR or self-trigger detection, and stores up to 64 k values for each channel in block RAM. Data can be acquired continuously or in segments of programmable separation and length (i.e., for Booster TWE measurements of the same bunches at different times during the ~0.5 sec ramp). For the BCM application, the ADC sampling clock runs at f_{RF}*80/11 (~3.6 GHz). The *Acquisition* core computes and stores a sum at each point over a 'turn', which is multiple actual turns of the beam, with interleaved sampling similar to a sampling oscilloscope.

For both applications, the rest of the firmware is the same. The *EVR* core decodes the recovered RF EVR clock and timing events from the event link. The EVR clock is sent off-chip to a clock generation and distribution circuit to generate the ADC sampling clocks. The *EVR* core contains trigger selection and control logic, and sends triggers to the *Acquisition* core. Analog inputs from the HSDAFE are connected to the ADCs in the *RF Data Converter* core. ADC parallel data is sent from the *RF Data Converter* to the *Acquisition* core, where it is triggered, processed, and stored as needed for the target application.

The *ZYNQ* core contains the embedded processor that runs the FPGA application. The FPGA firmware, bootstrap loader and executable image are stored in a single file on the micro SD card. This file can be uploaded to, or downloaded from, the card using the TFTP server in the FPGA application. The application runs from DRAM and the console is available on the USB port. The I2C interface is used to control ZCU111 and HSDAFE devices, including the calibration DAC, ID EEPROM, and port expanders that select the RF switch positions. The Ethernet interface is used to communicate with the EPICS soft IOC. The AXI bus connects the ZYNQ processor to the other cores.

Content from this work may be used under the terms of the CC BY 3.0 licence (© 2020). Any distribution of this work must maintain attribution to the author(s), title of the work, publisher, and DOI

ISBN: 978-3-95450-222-6 ISSN: 2673-5350 doi:10.18429/JACoW-IBIC2020-WEPP16

Content from this work may be used under the terms of the CC BY 3.0 licence (© 2020). Any distribution of this work must maintain attribution to the author(s), title of the work, publisher, and DOI

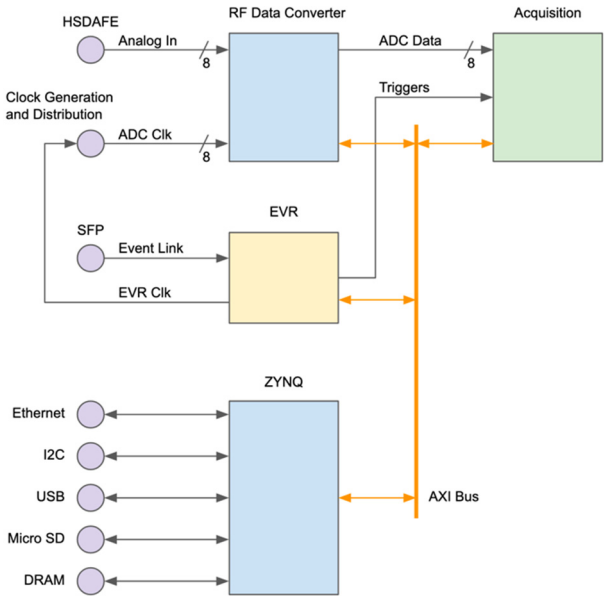

Figure 4: HSD firmware block diagram.

STATUS

For the FS application, an ALS Booster Ring BPM button signal was used to measure a single pass of a typical 4 bunch pattern, with each bunch separated by ~8 ns. First, the button was connected to a 2 GHz bandwidth Tektronix oscilloscope with 50 Ohms DC-coupled input. Then the button was connected to the HSD through a 1.3 GHz low pass filter into a 50 Ohms DC-coupled input. The measurements are shown in Figs. 5 and 6. The data was taken on different injection cycles, so the amplitude differs slightly, but the overall shape demonstrates that the HSD has sufficient bandwidth and resolution to capture a fast signal at the ALS.

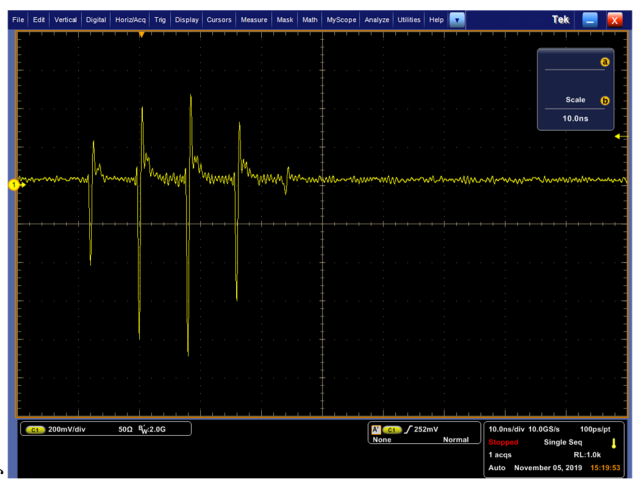

Figure 5: ALS Booster Ring BPM button signals captured on a 2 GHz Tektronix oscilloscope.

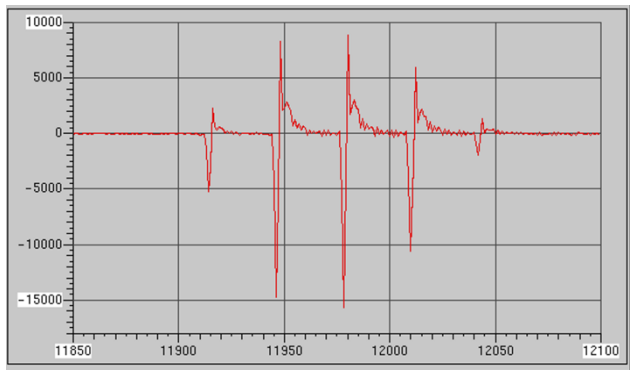

Figure 6: ALS Booster Ring BPM button signals through a 1.3 GHz low pass filter captured on the HSD.

For the BCM application, high level application captures were taken at both ALS and APS using versions of the HSD prototype design. Figure 7 shows a typical ALS storage ring fill pattern with a single cam bucket at higher current. The red bars represent stored beam current, and the blue bars show the most recent injection.

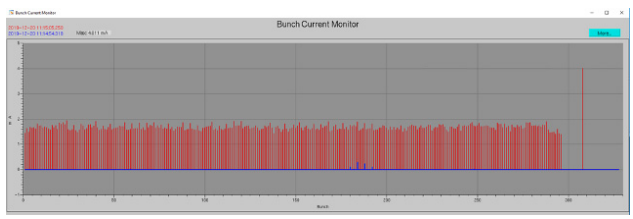

Figure 7: ALS Bunch Current Monitor with a typical storage ring fill pattern.

The High Speed Digitizer production first article has been built and is planned to be installed at ALS in the next few months. The remaining ALS production units are being built, and will be installed later this year. ALS-U production units will be built when the project receives construction phase funding approval.

CONCLUSION

The High Speed Digitizer meets the performance goals for both ALS and ALS-U as both a fast oscilloscope and Bunch Current Monitor, and shows promise for additional applications and accelerators. Features such as 8 channels, tight integration with the timing system for triggering and RF-synchronous sampling, and flexible firmware, along with lower cost per channel are advantages over equivalent commercial oscilloscope products. With low quantities and low average data rates, the network-attached device architecture is a good fit for the EPICS control system at ALS and ALS-U.

ACKNOWLEDGMENTS

The authors would like to thank Steve Shoaf and Hanh Bui for testing multiple versions of the HSD system at APS, and for sharing measurements taken there.

ISBN: 978-3-95450-222-6 ISSN: 2673-5350 doi:10.18429/JACoW-IBIC2020-WEPP16

REFERENCES

[1] Xilinx, https://www.xilinx.com/products/silicon-devices/soc/rfsoc.html

[2] Xilinx, https://www.xilinx.com/products/boards-and-kits/zcu111.html

[3] Xilinx, https://www.xilinx.com/products/intellectual-property/rf-data-converter.html

[4] Xilinx, https://www.xilinx.com/products/intellectual-property/zynq-ultra-ps-e.html

[5] J. Weber *et al.*, "ALS timing system upgrade," in *Proc. IBIC'14*, Monterey, CA, USA, Sep. 2014, paper MOPD18, pp. 187-190.

Content from this work may be used under the terms of the CC BY 3.0 licence (© 2020). Any distribution of this work must maintain attribution to the author(s), title of the work, publisher, and DOI

ISBN: 978-3-95450-222-6 ISSN: 2673-5350 doi:10.18429/JACoW-IBIC2020-WEPP17

UPGRADE AND FIRST COMMISSIONING OF TRANSVERSE FEEDBACK SYSTEM FOR SSRF*

N. Zhang†, B. Gao, L. Lai, R. Yuan, Shanghai Synchrotron Radiation Facility, Shanghai, China

Abstract

To be a part of the transverse feedback system upgrade plan in SSRF PHASE II project, a set of Dimtel feedback processors [1] was installed to replace the previous set. In the commissioning, the ability of supressing the transverse oscillation was tested and evaluated, also, beam diagnostics and control tools of the processors was used for injection transient analysis, tune tracking and bunch cleaning. The results of the commissioning and data analysis will be presented in this paper.

INTRODUCTION

SSRF is a third generation 3.5 GeV synchrotron light source with 720 bucket in the storage ring and a RF frequency of 499.654 MHz. The transverse feedback (TFB) system was started in 2010, and the feedback kicker consists of one vertical electrode and one horizontal electrode, one feedback processor designed by Spring-8 to produce 2 independent channel of feedback signal for both planes. In SSRF PHASE II project, 16 more beam line will be built before 2022, and more IUVs are planned to be installed in the storage ring, which would lead impedance of the whole ring increase from 4M Ohm to 8M Ohm. Another challenge for beam transverse motion control is a newly introduced hybrid operation mode, which consists of about 500 filled buckets of 0.5mA and one high current bucket of 20mA. It is evaluated that the feedback system could suppress the transverse instability even when the product of impedance and beam current increases to 3 times, but the limitation of individual bunch current is 10mA. If only one electrode is used for each plane, the dynamic range for each channel is required to reach 32dB, it would be very difficult for TFB processors and power amplifier configuration. So a 3-electrodes kicker scheme was designed, compared with the 2-electrodes kicker, one more vertical electrode was specialized for controlling the hybrid bunch. 2 TFB processors were also to be added to fit the new kicker plan, one for normal buckets in both planes, the other for the big bunch in vertical plane. Since the 3-electrodes kicker is planned to install one year later, the commissioning only refers to the normal operation mode processor.

FEEDBACK SETUP

A stripline kicker with 3 electrodes talked above is going to operate as a transverse feedback actuator in all modes. Normal operation mode is driving when driving a horizontal electrode and a vertical one, Hybrid mode is driving when driving all the 3 electrodes. The designed kicker is shown in Figure 1.

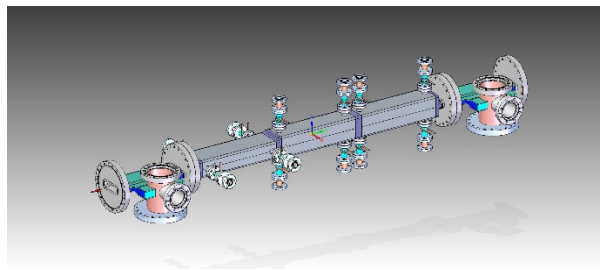

Figure 1: Transverse feedback kicker with 3 electrodes, the first electrode is horizontal electrode, and the 2 and 3 are vertical electrodes.

The feedback electronics includes one hybrid network, one FBE-500LT front-end, and 2 iGp-12 processors. The hybrid signal of differential horizontal and differential vertical (Δx + Δy), and the differential vertical (Δy) of the beam motion are created from BPM signals in the hybrid network (Fig. 2). The 2 channel signals would be processed by FBE-500LT and then fed to iGp-12 separately.

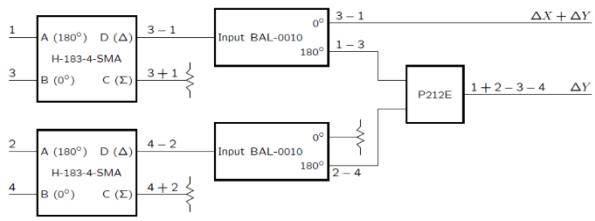

Figure 2: Layout of hybrid network.

Since one iGp-12 only have only one pair of differential input channels, the 16-step FIR filter was specially designed to provide feedback signals in both X and Y plane simultaneously, which is shown in Figure 3. And the differential output is divided into 2 way to fed X and Y kickers.

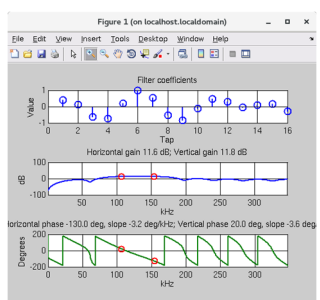

Figure 3: 16 step FIR design of feedback for both X and Y plane.

† zhangning@zjlab.org.cn.

Content from this work may be used under the terms of the CC BY 3.0 licence (© 2020). Any distribution of this work must maintain attribution to the author(s), title of the work, publisher, and DOI

ISBN: 978-3-95450-222-6 ISSN: 2673-5350 doi:10.18429/JACoW-IBIC2020-WEPP17

COMMISSIONING AND TEST

The commissioning of Dimtel feedback system was arranged in a Machine Study after all the hardware had been installed in the rack above power amplifiers, and the old system was left unperturbed. The feedback loop was first closed in single bunch mode, after the parameters of timing, phase and FIR filter were optimized in the mode, the beam current was injected up to 3mA gradually when the instability could be observed and suppressed by the system. In order to check the feedback performance at full current, the multi-bunch mode was switched, and the beam current was increased step by step. Subsequently, the different experiments were also performed:

- Grow-damp measurement at 245mA;
- Injection transients with and without feedback;
- Single bunch tune tracking;
- Bunch cleaning test.

Feedback Performance Evaluation

The previous transverse feedback electronics in SSRF had been running stable and achieving good feedback effect for about 10 years. But recently, it may not worked in the optimal state, as some cables were replaced and reconnected for device maintenance requirement [2].

The Dimtel feedback system provided a set of diagnostics tools, which would help to evaluate the feedback effect. In the experiment, when beam current reached to 120mA, we switched feedback setup to the previous one and then ran it into feedback loop firstly, after capturing some steady-state data and some sets during injection, the Dimtel setup was switched back, and capturing the same data. The distributions of oscillation envelopes and mode evolution in Fig. 4 showed the different feedback effect between 2 setups, and mean mode amplitude in Fig. 5 indicated the main instability mode. The bunch oscillation were well suppressed by Dimtel setup, while there are greater bunch oscillation not fully suppressed by feedback and mode amplitude by old system.

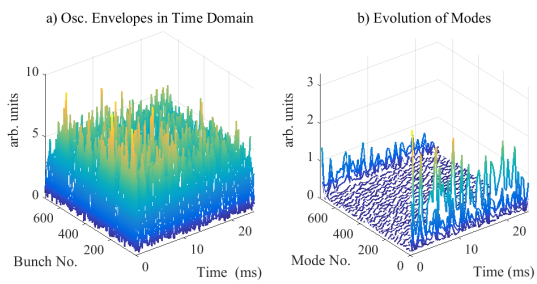

(a)

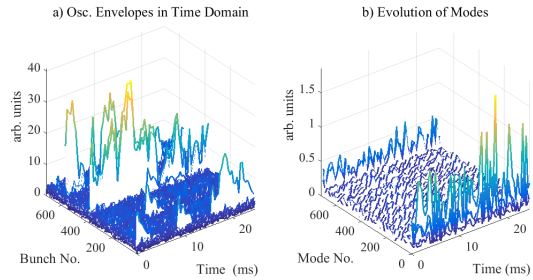

(b)

Figure 4: 3-D Bunch Beatron oscilloation and mode distribution, (a) for iGp setup and (b) for previous setup.

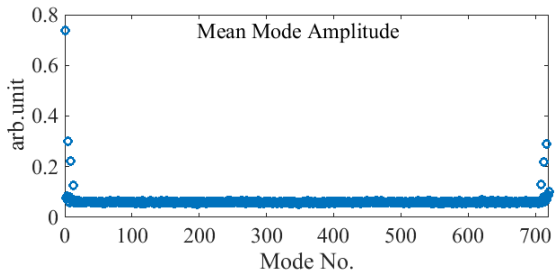

Figure 5: Mean mode amplitude for Dimtel setup, which is the same for previous setup.

By analysis the injection data sets, injection transients also gave the conclusion about the feedback effects between 2 setups. Figure 6 showed the injection transients when Dimtel setup ON / OFF. It is clear that the setup caused faster transient damping and lower peak amplitude with feedback ON. And some individual bunch transient characteristics were demonstrated in Fig. 7, which showed worse feedback effect or even out of control with previous setup.

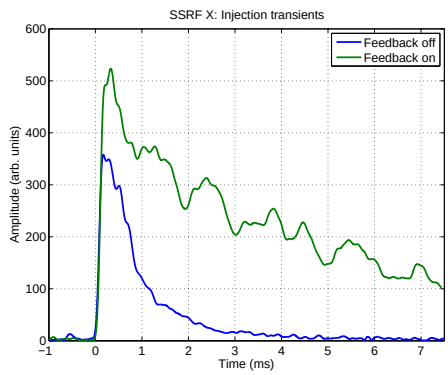

Figure 6: Injection transients comparison with Dimtel setup ON / OFF.

Content from this work may be used under the terms of the CC BY 3.0 licence (© 2020). Any distribution of this work must maintain attribution to the author(s), title of the work, publisher, and DOI

ISBN: 978-3-95450-222-6 ISSN: 2673-5350 doi:10.18429/JACoW-IBIC2020-WEPP17

Content from this work may be used under the terms of the CC BY 3.0 licence (© 2020). Any distribution of this work must maintain attribution to the author(s), title of the work, publisher, and DOI

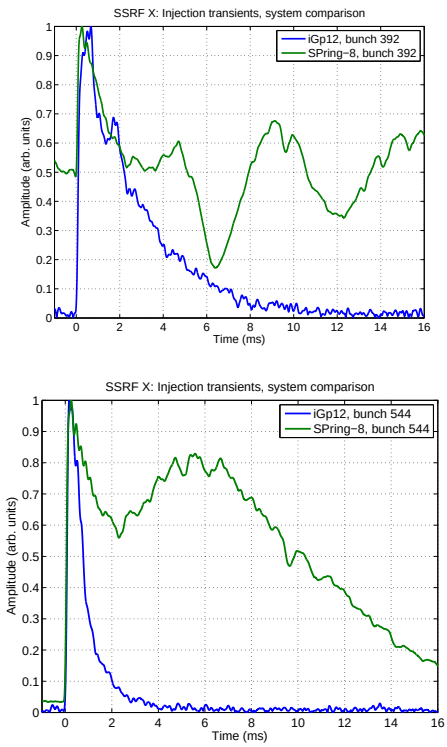

Figure 7: System comparison for bunch #392 and #544 injection transients.

Grow / Damp Measurement

Grow/damp measurement is important to determine the source and strength of coupling impedances. The Dimtel feedback electronics could be turned OFF for a short period of time to allow the instabilities to grow and then turned back ON to damp the motion. This kind of grow/damp measurement is useful to characterize the unstable modes in the storage ring. A grow-damp measurement at 245 mA with mode 719 (-1) being dominant is shown in Figure 8. The mode is considered as resistive wall instability [3].

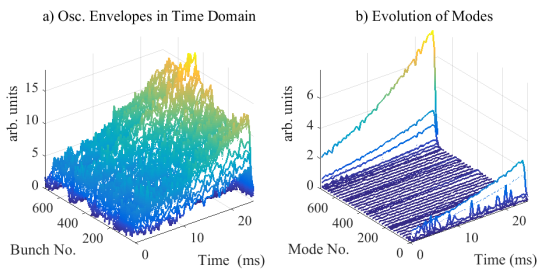

Figure 8: 3-D bunch oscillation envelope and mode evolution in grow-damp measurement.

Grow /damp rate was calculated by fitting grow /damp curve in exponential transients formula of mode 719, which is showed in Figure 9.

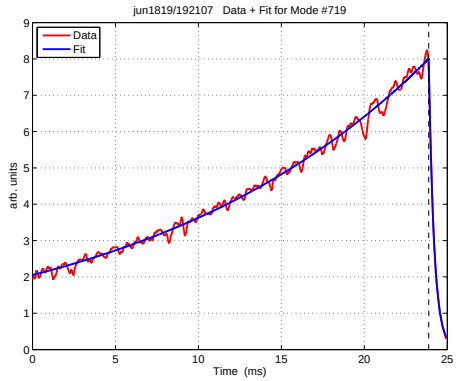

Figure 9: exponential fit of mode 719, Growth rate of 0.057 ms^{-1}, damping rate of -3.0 ms^{-1}.

The current dependency of growth / damping rate study is showed in Figure 10. When current is changed in a very small span (about 0.6mA), it showed clear linear behaviour of growth /damping rate, and very fast damping, scales linearly with gain.

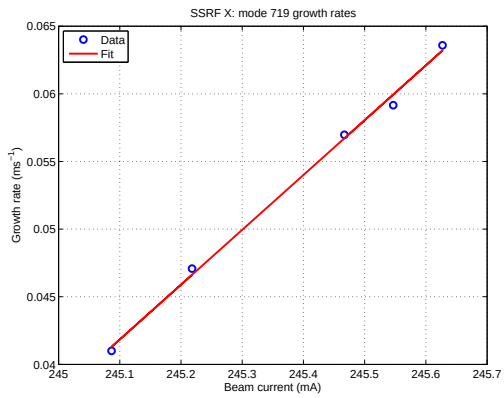

Figure 10: Beam current dependency of growth rates and linear fitting.

Tune Tracking

IGp-12 processor offered a sinusoidal drive generator, which could be employed to sweep sinusoidal excitation for a selected bunch at lower amplitude (20-40 μm). Betatron tune could be measured by the normalized excitation frequency. Response is detected relative to the excitation to determine the phase shift. In closed loop, phase tracker adjusts the excitation frequency to maintain the correct phase shift value; Decimation factor in phase tracker controls tracking bandwidth. Figure 11 showed the fast tune tracking for over 140ms in horizontal plane.

ISBN: 978-3-95450-222-6 ISSN: 2673-5350 doi:10.18429/JACoW-IBIC2020-WEPP17

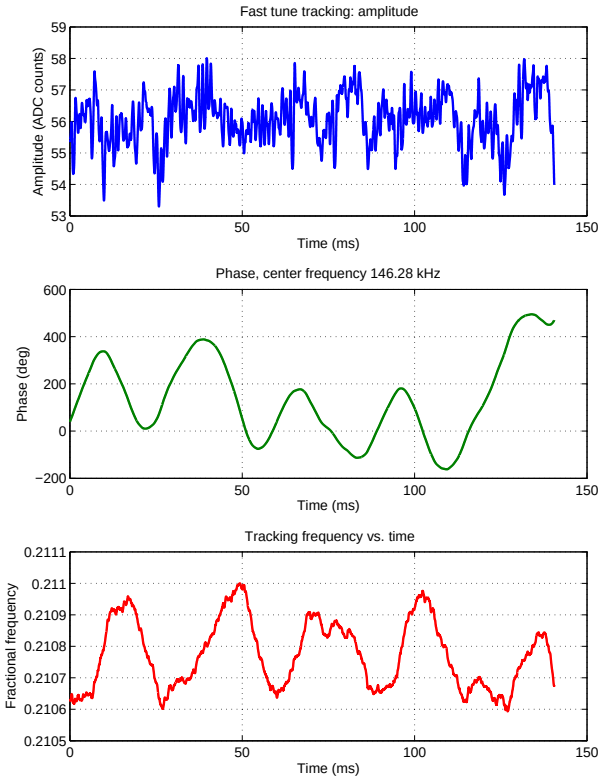

Figure 11: Excition betaron oscillation amplitude (top), phase (middle) and Fast tune tracking (bottom) over 140ms.

Bunch Cleaning

Individual bunches could be kicked out using the integrated bunch driving function. By this mean, highly purified filling-pattern could be demonstrated. The function was tested by driving a selected bunch at the frequency across the vertical betatron tune, the sweeping range and sweeping frequency could be adjusted to knock out the bunch effectively. Figure 12 shows the #600 bunch was successfully kicked out.

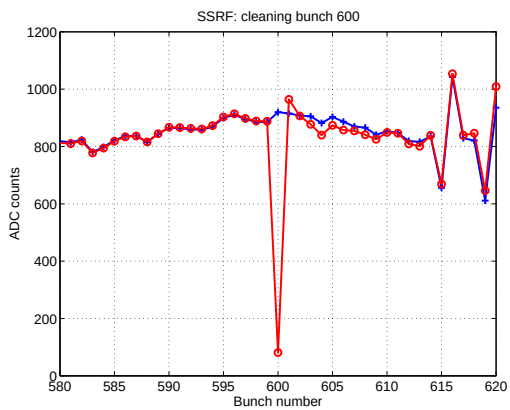

Figure 12: Bunch #600 was kicked out using vertical plane excitation with little effect on nearby bunches.

CONCLUSION

We have constructed and tested a transverse bunch-by-bunch feedback system using the Dimtel electronics in SSRF. The feedback system has shown sufficient performance to suppress the transverse instabilities up to a beam current of 245 mA. We have also performed the grow-damp transient analysis of instabilities, and determined that the mode #719(-1) of the horizontal plane grows most rapidly among all instability modes which is considered as resistive wall instability. It is proved that one set iGp-12 processor could be used for the feedback for both vertical and horizontal planes, only by reasonable FIR design. The setup will be continued to optimized and installed month later.

ACKNOWLEDGEMENTS

The work of staff in Physics, Linac and Operation groups of SSRF is gratefully acknowledged. We also wish to thank D Teytelman (Dimtel Inc.) for hardware and commissioning support which made the feedback demonstration possible.

REFERENCES

[1] K. Tian *et al.*, "Commission of the Transverse Bunch-by-Bunch Feedback at SPEAR3", in *Proc. 10th Int. Particle Accelerator Conf. (IPAC'19)*, Melbourne, Australia, May 2019, pp. 4081-4084. doi:10.18429/JACoW-IPAC2019-THPRB112

[2] W. X. Cheng, B. Bacha, Y. Hu, O. Singh, H. Xu, and D. Teytelman, "Commissioning of Bunch-by-Bunch Feedback System for NSLS2 Storage Ring", in *Proc. 3rd Int. Beam Instrumentation Conf. (IBIC'14)*, Monterey, CA, USA, Sep. 2014, paper WEPD27, pp. 707-711.

[3] Y. M. Zhou, Y. B. Leng, N. Zhang, and H. J. Chen, "Bunch Phase Measurement for Storage Ring", in *Proc. 8th Int. Particle Accelerator Conf. (IPAC'17)*, Copenhagen, Denmark, May 2017, pp. 341-344. doi:10.18429/JACoW-IPAC2017-MOPAB093

Content from this work may be used under the terms of the CC BY 3.0 licence (© 2020). Any distribution of this work must maintain attribution to the author(s), title of the work, publisher, and DOI

ISBN: 978-3-95450-222-6 ISSN: 2673-5350 doi:10.18429/JACoW-IBIC2020-WEPP20

MEASUREMENTS OF ULTRAVIOLET FEL SEED LASER PULSE WIDTH BROADING IN THIN β-BBO CRYSTALS*

Chunlei Li[1], Xingtao Wang, Wenyan Zhang, Lie Feng, Bo Liu†
Shanghai Advanced Research Institute, Chinese Academy of Science, Shanghai, China
[1] also at Shanghai Institute of Applied Physics, Chinese Academy of Science, Shanghai, China

Abstract

Short pulse, high power seed lasers have been implemented to improve the longitudinal coherence and shot-to-shot reproducibility of Free Electron Lasers (FEL). The laser pulse duration is typically 100 - 200 fs with wavelengths in the 260 nm range produced from third harmonic generation of a Ti:sapphire laser. The pulse duration must be measured accurately for seeded FEL operation. The Ultraviolet (UV) pulse width measurement can be carried out with intensity cross-correlation based on the difference frequency generation (DFG) in ultrathin β-Barium Borate (BBO) crystals. The DFG output pulse broadened due to group velocity mismatch between the 266.7 nm and 800 nm components. The broadening effect depends on the BBO crystal thickness so we explored 0.015 mm, 0.055 mm and 0.1 mm thick samples. To the best of our knowledge, this is the first time that β-BBO crystal with thickness of only 0.015 mm has been used to measure the UV seed laser pulse width. Experiment results show the measured pulse width broadens with increased BBO thickness in agreement with a theoretical model.

INTRODUCTION

Particle accelerator and laser technologies are effectively combined in FEL facilities, with the latter being a key factor determining the ultimate performance [1]. Laser technology is used at many strategic points: (1) cathode drive laser (257-267 nm, 5-30 ps) to create the electron bunch, (2) laser heater (400-1030 nm, 15-20 ps) to increase beam energy spread [2], and (3) seed laser (210-280 nm, 90-300 fs) to improve longitudinal coherence and reproducibility of the FEL output [3].

Two-beam cross correlation can be used to characterize the temporal structure of photocathode drive laser pulse [4-7] and the resulting electron bunch length [8]. The drive laser pulse width is in a range of 5-50 ps, so pulse broadening caused by the group velocity mismatch (GVM) in ultrathin (<0.1 mm) BBO crystal is negligible. However, pulse broadening has to be understood when measuring the seed laser pulse in the range of 100-300 fs.

In this paper, pulse broadening was experimentally investigated using β-BBO crystals with three different thicknesses to experimentally determine the effect of GVM on the measurement. Ultrathin crystals with thickness of only 0.015 mm were found to have the least broadening effect.

*This study was sponsored by Shanghai Sailing Program (18YF1428700).
†Corresponding author: liubo@zjlab.org.cn

SEED LASER SYSTEM

Figure 1 shows a schematic for Shanghai soft X-ray free electron laser (SXFEL) seed laser system. The laser consists of 4 main stages: (1) Oscillator, (2) Amplifier, (3) third harmonic generation (THG), and (4) beam transport line. The oscillator (Vitara-T, Coherent Inc.) is pumped by a 4.88 W green CW Verdi laser (Coherent Inc.) to deliver a 0.7 W stream of 79.33 MHz pulses at 800 nm with horizontal polarization to a synchronized regenerative Ti:Sapphire amplifier (Elite Duo, Coherent Inc.). The pre-amplified oscillator pulses have 7nJ energy and are stretched to 200 ps using a grating pair, then amplified by the regen and recompressed (CPA system). The output has 3 mJ in 100 fs (FWHM). The infrared (IR) pulses are then tripled to 266.7 nm with 300 μJ and a bandwidth of 0.8 nm. The UV light is then transported to the main FEL undulator through vacuum beam transport lines.

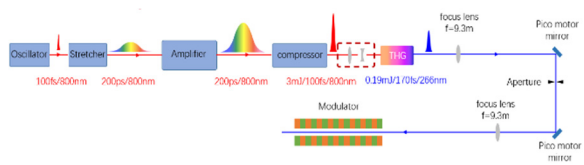

Figure 1: Schematic of SXFEL seed laser system.

The structure of THG optics is shown in Fig. 2. Here the compressed IR pulse is frequency-doubled to 400 nm in a β-BBO crystal (type I, o + o = e, 0.5 mm, θ =29.2°), and subsequently undergoes sum-frequency generation when re-mixed with 800 nm in a second β-BBO crystal (type I, 0.5 mm, θ=44.4°). The conversion efficiency from 800 nm to 266 nm was about 10%. The 266.7 nm UV pulse width was measured by co-linear cross correlation as presented in the following section.

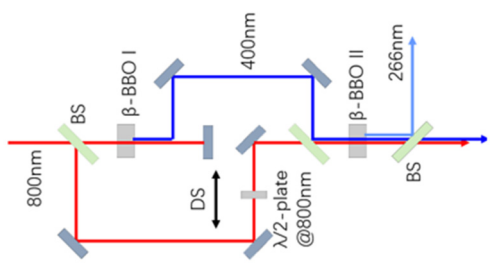

Figure 2: Structure of third harmonic generation (THG) device. BS-beam splitter; DS-delay stage.

Content from this work may be used under the terms of the CC BY 3.0 licence (© 2020). Any distribution of this work must maintain attribution to the author(s), title of the work, publisher, and DOI

ISBN: 978-3-95450-222-6 ISSN: 2673-5350 doi:10.18429/JACoW-IBIC2020-WEPP20

THEORETIC FRAMEWORK FOR THE CROSS CORRELATION MEASUREMENT

For the collinear cross correlation measurement, three light waves travel through the crystal in the same direction. Due to the fact that the β-BBO medium is a negative-uniaxial crystal ($n_e < n_o$), the three waves travel at different phase velocities corresponding to different refractive indices n_{IR}, n_{DFG}, n_{UV}. The frequency and phase matching conditions are expressed in Eqs. (1) and (2) which must be satisfied simultaneously.

$$\omega_{IR} + \omega_{DFG} = \omega_{UV} \tag{1}$$

$$n_{IR}\omega_{IR} + n_{DFG}\omega_{DFG} = n_{UV}\omega_{UV} \tag{2}$$

where n_{IR}, n_{UV}, and n_{DFG} are the refraction indices for 800nm, 266.7nm and 400nm light. ω_{IR}, ω_{UV} and ω_{DFG} are frequencies of the above three wavelengths.

Within the anisotropic β -BBO crystal, the three refractive indexes n_{IR} , n_{DFG} , n_{UV} are dependent on frequency, field polarization and propagation direction relative to the principal axes. This offers a set of free variables that can be manipulated to satisfy the matching conditions. Precise control of the refractive indexes at all three frequencies can be achieved by appropriate selection of field polarization and beam orientation in the BBO crystal.

β-BBO has a uniaxial crystal structure characterized by its optic axis and frequency dependent ordinary and extraordinary refractive indexes $n_o(\omega)$ and $n_e(\omega)$. For an o-wave $n(\omega) = n_o(\omega)$; for an e wave $n(\omega) = n_e(\theta, \omega)$ also depends on the angle θ between the direction of the wave and the optic axis of the crystal, which is shown in Fig.3. and expressed in Eq.(3) [9].

$$\frac{1}{{n_e}^2(\theta,\omega)} = \frac{\cos^2\theta}{{n_o}^2(\omega)} + \frac{\sin^2\theta}{{n_e}^2(\omega)} \tag{3}$$

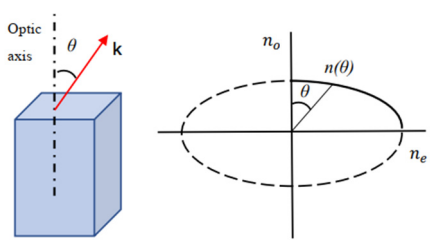

Figure 3: Refractive index $n(\theta)$ of the extraordinary wave. θ is the angle between the optic axis and the direction of propagation. Vector k shows beam propagation direction.

For the cross correlation measurements discussed here with different BBO crystal thicknesses, the output DFG signal intensity is correlated with the temporal delay between the IR and UV pulses. The cross-correlation overlap integral for intensity output can be expressed as Eq. (4) [10]:

$$I(\tau)_{cc} = \alpha \int_{-\infty}^{\infty} I_{uv}(t) I_{IR}(t-\tau) dt \tag{4}$$

where $I_{uv}(t)$ and $I_{IR}(t-\tau)$ are the temporal intensities for the two input beams, τ is the time delay between them, α is an overall conversion efficiency factor and $I(\tau)_{cc}$ is the output signal intensity of the 400 nm DFG output pulse.

By assuming ideal light pulses with Gaussian distribution along with negligible frequency chirp and negligible group velocity mismatch, the full width at half maximum (FWHM) τ_{cc} of the output envelope is:

$$\tau_{cc} = \sqrt{\tau_{IR}^2 + \tau_{UV}^2} \tag{5}$$

Since τ_{IR} can be directly measured by intensity auto correlation, τ_{UV} can be derived from measurement of τ_{cc}.

More generally, if one of the input beam profiles is known and we measure $I(\tau)_{cc}$, then a more accurate result for the unknown beam profile can be derived by numerical deconvolution according to Eq.(6). Specifically, we include the effects of both the group velocity mismatch (GVM) between two input pulses and the thickness of BBO crystal [11, 12] in the integration. The GVM roughly broadens the output pulse by a linear factor $\delta t = L * GVM$, where L is the thickness of BBO crystal for collinear propagation [13]. To estimate the input pulse width in this case, the broadening value δt has to be deduced from the pulse width of the 400 nm output signal. Then the UV input pulse width can be derived by deconvolution according to Eq. (5).

$$I_{cc}(\tau) \approx \int_{-\infty}^{\infty} \left\{ \exp\left[-2ln2 \left(\frac{t}{\tau_{UV}} \right)^2 \right] \right\}^2 \times \left\{ exp\left[-2ln2 \left(\frac{t-\tau}{\tau_{IR}} \right)^2 \right] \otimes sqr\left[\frac{t}{\Delta\left(v_g^{-1}\right)_{cc} l_c} + \frac{1}{2} \right] \right\}^2 dt \tag{6}$$

In Eq. (6)

$$sqr(x) = \begin{cases} 1, & |x| \le 1/2 \\ 0, & otherwise \end{cases},$$

τ_{UV} is the FWHM pulse width of UV beam, and τ_{IR} is the FWHM pulse width of IR beam. $\Delta\left(v_g^{-1}\right)_{cc}$ is the GVM between the UV and IR beams, l_c is the thickness of β-BBO crystal and ⊗ denotes convolution. The expression for group velocity and group velocity mismatch are given by in Eq. (7) and (8), respectively [14]:

Content from this work may be used under the terms of the CC BY 3.0 licence (© 2020). Any distribution of this work must maintain attribution to the author(s), title of the work, publisher, and DOI

ISBN: 978-3-95450-222-6 ISSN: 2673-5350 doi:10.18429/JACoW-IBIC2020-WEPP20

Content from this work may be used under the terms of the CC BY 3.0 licence (© 2020). Any distribution of this work must maintain attribution to the author(s), title of the work, publisher, and DOI

$$v_g = \frac{c}{n}\left(1 + \frac{\lambda}{n}\frac{dn}{d\lambda}\right) \quad (7)$$

$$\Delta\left(v_g^{-1}\right)_{cc} = \mathrm{GVM} = \frac{1}{V_g^{IR_o}} - \frac{1}{V_g^{UV_e}} \quad (8)$$

Here c is the speed of light, λ is wavelength in μm, $V_g^{IR_o}$ is the IR o-ray group velocity, $V_g^{UV_e}$ is the e-ray UV group velocity with a crystal cutting angle θ =44.4 °. n is refractive index of the BBO crystal. The refractive indices for the *o*-ray and *e*-ray in BBO can be calculated according to Eq. (9) and Eq. (10) [15-17]. These parameters were also cross-checked using SNLO software [18].

$\frac{dn_o(\lambda)}{d\lambda}$ and $\frac{dn_e(\lambda)}{d\lambda}$ are expressed in Eq. (11) and Eq. (12).

The refraction indices for a 266.7 nm e-ray propagating through the BBO crystal with a cutting angle $\theta = 44.4°$ were calculated using Eqs. (3), (9) and (10).

$$n_o(\lambda) = \sqrt{2.7405 + \frac{0.0184}{\lambda^2 - 0.0179} - 0.0155\lambda^2} \quad (9)$$

$$n_e(\lambda) = \sqrt{2.3730 + \frac{0.0128}{\lambda^2 - 0.0156} - 0.0044\lambda^2} \quad (10)$$

$$\frac{dn_o(\lambda)}{d\lambda} = \frac{1}{2} * \frac{-\frac{0.0184}{(\lambda^2 - 0.0179)^2} * 2\lambda - 0.0155 * 2\lambda}{\sqrt{2.7405 + \frac{0.0184}{\lambda^2 - 0.0179} - 0.0155\lambda^2}} \quad (11)$$

$$\frac{dn_e(\lambda)}{d\lambda} = \frac{1}{2} * \frac{-\frac{0.0128}{(\lambda^2 - 0.0156)^2} * 2\lambda - 0.0044 * 2\lambda}{\sqrt{2.3730 + \frac{0.0128}{\lambda^2 - 0.0156} - 0.0044\lambda^2}} \quad (12)$$

CROSS-CORRELATION MEASUREMENT

In order to explore pulse broadening for different β-BBO crystal thicknesses, a DFG cross correlator was constructed as shown in Fig. 4.

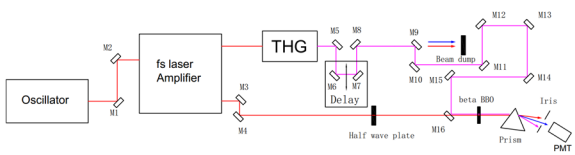

Figure 4: Schematic of the collinear cross-correlation diagnostic system. A prism was used to spatially separate the frequency components at the output stage.

The 800 nm IR pulses from the Vitara oscillator have a bandwidth of 50 nm and pulse energy of about 1 nJ. The UV beam is produced by the THG tripler shown in Fig. 2. The THG beam is filtered by dichroic mirror M9 and the 800 nm and 400 nm components are directed to beam blocks. The UV beam is directed to the β-BBO crystal (CASTECH, type I phase matched at θ = 44.4°, ϕ= 0°) by M10-M16. M16 is dichroic mirror where the UV and IR beams spatially overlap. M6 and M7 were installed on high precision delay stages (M-ILS200CCL, Newport) to adjust the UV beam arrival time for temporal overlap with the IR beam. In order to meet the phase match conditions in the β-BBO crystal, a half wave plate was inserted in the beam path to rotate the IR beam polarization into the vertical plane. Three β-BBO crystals with different thicknesses of 0.1 mm, 0.055 mm and 0.015 mm were tested to study VGM pulse broadening effects.

To separate the three output beams, a fused silica prism was inserted as shown in Fig.4. An iris with diameter ~1mm and a bandpass filter (Semrock, FF01-389/3-25) were installed after the prism to reduce background noise. By adjusting UV pulse arrival time with the adjustable delay stage, the 400 nm pulse intensity cross correlation envelope was measured at a photomultipler tube (PMT) (Hamamatsu, H10711-210). The PMT position was adjusted with a kinematic V-clamp (Thorlab, KM200V/M) and the data was acquired on an integrating oscilloscope (Tektronix, DPO4054). The scan motion of delay stage and DFG signal acquisition were then correlated in a LabVIEW gui interface.

RESULTS AND DISCUSSION

The intensity cross correlation curves for the 400 nm DFG signal using three different β -BBO crystal thicknesses are plotted in Figs. 5 (a-c). The horizontal axis is the temporal delay between two input beams and vertical axis is the normalized signal intensity. The experiment data are plotted in blue dots with error bars. In order to derive the FWHM value of the data curve, nonlinear least-squares fitting was performed with the Levenberg-Marquardt algorithm. The simulated curves calculated by Eq. (6) are also shown in Figs. 5 (a-c) (red curve) and the corresponding FWHM values are plotted in Fig. 6.

Our cross correlation measurements performed with three β-BBO crystals of thickness 0.015 mm, 0.055 mm and 0.1mm. The FWHM pulse widths of the corresponding cross correlation signals were 248 fs, 272 fs and 307 fs, respectively. As the BBO thickness increases, the FWHM of measured cross correlation signal broadens due to the GVM effect. The measured data plotted in Fig.5 (a-c) (blue line) was fitted using Eq. (6) with τ_{IR}=57 fs, τ_{UV}=248 fs yielding $\Delta\left(v_g^{-1}\right)_{cc}$ = 671.5 fs/mm. Furthermore, we believe that we can reliably extract the broadened UV pulse width by deconvolution from the cross correlation data.

ISBN: 978-3-95450-222-6 ISSN: 2673-5350 doi:10.18429/JACoW-IBIC2020-WEPP20

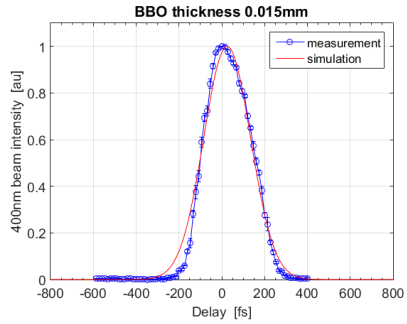

(a)

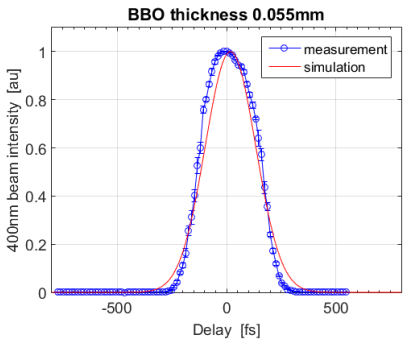

(b)

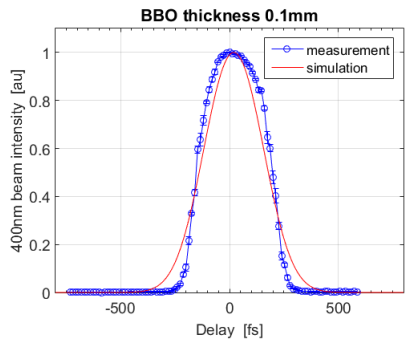

Figure 5: Cross correlation data with error bars (blue line) and numerical fits (red line) using 0.015 mm, 0.055 mm, and 0.1 mm β-BBO crystal for DFG. All curves are fitted by Eq. (6) with τ_{IR}=57 fs, τ_{UV}=248 fs, and $\Delta\left(v_g^{-1}\right)_{cc}$= 671.5 fs/mm.

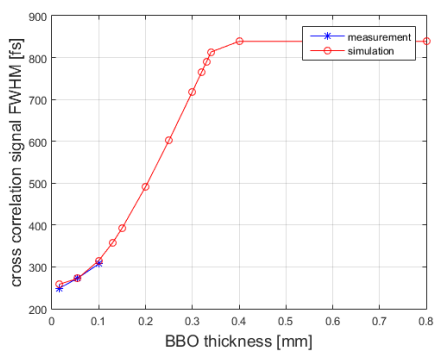

Figure 6: FWHM of cross correlation signal from data in Fig 5. For these data Eq. (6) with τ_{IR}=57 fs, τ_{UV}=248 fs, and $\Delta\left(v_g^{-1}\right)_{cc}$= 671.5 fs/mm.

CONCLUSION

In conclusion, pulse broadening of the 400 nm DFG cross-correlation signal was experimentally investigated in three different β-BBO crystal thicknesses. The data includes the most thin 0.015 mm BBO crystal thickness measurements for the first time to our knowledge. The results show that the 400nm DFG pulse width increases as the BBO thickness increases as predicted. For the case with a 0.055 mm crystal the measured ~272 fs FWHM pulse length is in very good agreement with theory and the two other measurements are within a about 4 percent.

The results agree well with the theoretical model integrating over β-BBO thickness with group velocity modulation as a function of wavelength taken into consideration. In practice, dispersion, spatial chirp and other nonlinear mechanisms also play important roles in pulse broadening. Therefore, further study are underway to explore their influence.

ACKNOWLEDGMENTS

The authors would like to thank Jeff Corbett for his precious comments and the proofreading of the manuscript, M.B. Danailov for constructive discussions, and Guorong Wu and his group in Dalian coherent light source for fruitful discussions converning the PMT device.

This work was sponsored by Shanghai Sailing Program (18YF1428700).

REFERENCES

[1] M.B. Danailov, A. Demidovich, R. Ivanov, I. Nikolov, and P. Sigalotti, "Laser systems for next generation light sources", in *Proc. 23rd Particle Accelerator Conf. (PAC'09)*, Vancouver, BC, Canada, May. 2009, paper MO4GRI03, pp. 122-126.

[2] S. Gilevivch *et al.*, "LCLS-II gun and laser heater systems", LCLS-II-2.2-PR-0085-R1, 2017.

[3] M. B. Danailov *et al.*, "Design and first experience with the fermi seed laser", in *Proc. 33rd Int. Conf. on Free Electron Laser (FEL'11)*, Shanghai, China, Aug. 2011, paper TUOC4, pp. 183-186.

[4] J. Good *et al.*, "Preliminary on–table and photo-electron results from the PIZT quasi-ellipsoidal photocathode laser system", in *Proc. 38th Int. Conf. on Free Electron Laser (FEL'17)*, Santa Fe, NM, USA, Aug. 2017, pp. 418-420. doi:10.18429/JACoW-FEL2017-WEPO06

[5] Dong Wang, Lixin Yan, and Wenhui Huang, "UV pulse shaping with α-BBO crystals for the photocathode RF gun", in *Proc. 7th Int. Particle Accelerator Conf. (IPAC'16)*, Busan, Korea, May 2016, pp. 4079-4081. doi:10.18429/JACoW-IPAC2016-THPOW059

[6] Lixin Yan *et al.*, "Measurements of laser temporal profile and polarization dependent quantum efficiency", in *Proc. 22nd Particle Accelerator Conf. (PAC'07)*, Albuquerque, NM, USA, Jun. 2007, paper TUPMN056, pp. 1052-1054.

[7] T. Rublack *et al.*, "Development of a quasi 3D ellipsoidal photocathode laser system for PIZT", in *Proc. 5th Int. Particle Accelerator Conf. (IPAC'14)*, Dresden, Germany, Jul. 2014, pp. 2069-2071. doi:10.18429/JACoW-IPAC2014-WEPRO055

Content from this work may be used under the terms of the CC BY 3.0 licence (© 2020). Any distribution of this work must maintain attribution to the author(s), title of the work, publisher, and DOI

ISBN: 978-3-95450-222-6 ISSN: 2673-5350 doi:10.18429/JACoW-IBIC2020-WEPP20

Content from this work may be used under the terms of the CC BY 3.0 licence (© 2020). Any distribution of this work must maintain attribution to the author(s), title of the work, publisher, and DOI

[8] T. Miller *et al.*, "Bunch length measurements with laser/SR cross correlation", in *Proc. 1st Int. Particle Accelerator Conf. (PAC'10)*, Kyoto, Japan, May 2010, paper WEOCMH03, pp. 2408-2410.

[9] Bahaa E.A. Saleh and Malvin Carl Teich, "Polarization Optics" in *Fundamentals of Photonics*, Bahaa E.A. Saleh, Ed, Second Edition, Hoboken, New Jersey, USA: Wiley Wiley, 2007, pp. 220-221.

[10] Andrew M. Weiner, "Ultrafast pulse measurement methods" in Ultrafast Optics, Glenn Boreman Ed, Hoboken, New Jersey, USA: Wiley, 2009, pp. 100-110.

[11] Jing Yang *et al.*, "Pulse broadening of deep ultraviolet femtosecond laser from second harmonic generation in $KB_2BO_3F_2$ crystal", *Optics Communications*, vol. 288, pp: 114-117, 2013.

[12] D. C. Edelstein *et al.*, "Femtosecond ultraviolet pulse generation in β-BaB_2O_4", *Appl. Phys. Lett.,* vol. 52, no.26, pp. 2211-2213, 1988.

[13] D. Gutierres Cornoel, "Analysis of auto and cross correlator", Lee Teng Intership Paper, Department of Physics, Illinois Institute of Technology, USA, Aug. 2017.

[14] Eugene Hecht, "The superposition of waves" in Optics, Fifth Edition, Eugene Hecht Ed, Person Education, 2017, pp. 304-306.

[15] John G. Power, and Chunguang Jing, "Temporal laser pulse shaping for RF photocathode guns: the cheap and easy way using UV birefringent crystals", in *Proc. 13th Workshop on Advanced Accelerator Concepts (ACC'08)*, Santa Cruz, CA, USA, Jan. 2009, pp. 689-694.

[16] D. N. Nikogosyan, "Beta barium borate (BBO)", *Appl. Phys. A*, vol. 52, pp. 359–368, 1991.

[17] X. T. Wang *et al.*, "Drive laser temporal shaping techniques for Shanghai soft X ray free electron laser", in *Proc. 39th Conf. on Free Electron Laser (FEL'19)*, Hamburg, Germany, Aug. 2019, pp. 466-468. doi:10.18429/JACoW-FEL2019-WEP058

[18] A. V. Smith, "How to select nonlinear crystals and model their performance using SNLO software", in *Proc. SPIE vol 3928, Nonlinear Materials, Devices, and Applications*, Mar. 2000, San Jose, CA, USA, pp. 1-8.

ISBN: 978-3-95450-222-6 ISSN: 2673-5350 doi:10.18429/JACoW-IBIC2020-WEPP21

EVALUATION OF A NOVEL PICKUP CONCEPT FOR ULTRA-LOW CHARGED SHORT BUNCHES IN X-RAY FREE-ELECTRON LASERS*

B. Scheible†, A. Penirschke, Technische Hochschule Mittelhessen (THM), Friedberg, Germany
M. K. Czwalinna, H. Schlarb, Deutsches Elektronen-Synchrotron (DESY), Hamburg, Germany
W. Ackermann, H. De Gersem, Technische Universität Darmstadt (TUDa), Darmstadt, Germany

Abstract

The all-optical synchronization systems used in various X-ray free-electron lasers (XFEL) such as the European XFEL depend on transient fields of passing electron bunches coupled into one or more pickups in the Bunch Arrival Time Monitors (BAM). The extracted signal is then amplitude modulated on reference laser pulses in a Mach-Zehnder type electro-optical modulator. With the emerging demand of the experimenters for future experiments with ultra-short FEL shots, fs precision is required for the synchronization systems even with 1 pC bunches. Since the sensitivity of the BAM depends in particular on the slope of the bipolar signal at the zero crossing and thus, also on the bunch charge, a redesign with the aim of a significant increase by optimized geometry and bandwidth is inevitable. In this contribution a possible new pickup concept is simulated and its performance is compared to the previous concept. A significant improvement of slope and voltage is found. The improvement is mainly achieved by the reduced distance to the beam and a higher bandwidth.

INTRODUCTION

Free-electron lasers (FEL) became an important light source for experiments in various fields since they provide ultra-short pulses with extreme brilliance in atomic length and time scales [1]. FEL are well suited for applications in pump-probe experiments [1], where the timing jitter is specifically critical [2], as well as for capturing image sequences with atomic resolution on fs-time-scales, even below the FEL repetition rate [1, 3, 4].

For the generation of ultra-short X-ray pulses, FEL with short and ultra-low charge electron bunches (≤1 pC) have been found as a favorable option [5, 6]. Short bunches may shorten the X-ray pulse, reduce timing jitter and lead to single-spike operation, if sufficiently small compared to the cooperation length of the SASE process [2, 5, 6]. The European XFEL (EuXFEL) was upgraded from initially 1 nC electron bunches to cover a range from 0.02 nC to 1 nC [7] with a possible bunch length below 3 fs in the undulator section [8]. Moreover, a decrease to ultra-low charges of 1 pC is targeted.

The application in time-resolved experiments entails tight requirements for the overall machine synchronization in order to reduce the timing jitter [2]. The timing information is also used for post-processing experimental data [1]. The synchronization concerns all critical subsystems, specifically in the injector and if present the seeding and the pump laser [1]. Furthermore, the instrumentation must be suited for a broad spectrum of operation modes with different bunch properties even in a single bunch train [9, 10]. Besides, bunch arrival time monitors (BAM) are installed throughout the whole facility, thus experiencing different bunch properties.

A tremendous improvement in synchronization, exceeding RF techniques, and reduction of arrival time as well as energy jitter was achieved by the implementation of an all-optical synchronization system with two different feedback loops [11]. Though some updates have been introduced [12, 13], the basic scheme in use by the Deutsches Elektronen-Synchrotron (DESY) remained unchanged.

In this contribution the all-optical synchronization system will be briefly introduced with special attention on the state-of-the-art cone-shaped pickups, followed by a analytical discussion of the principal parameters determining the BAM resolution. These are the basis for three designs, which are presented at the end of this paper.

ALL-OPTICAL SYNCHRONIZATION SYSTEM

The all-optical synchronization system, as successfully tested at the free-electron laser in Hamburg (FLASH) by Löhl [11], mainly comprises of a mode-locked reference laser, length stabilized fiber links and different end-stations for synchronization and arrival time measurement [10–15]. The arrival time is non-destructively measured with respect to the reference laser in the BAM, which include high-bandwidth pickup electrodes in the RF unit, a Mach-Zehnder type electro-optical modulator (EOM) and the data acquisition system (DAQ) [10, 15].

Basic Working Principle of BAM

The transient electric fields of passing electron bunches are extracted in the RF unit and, if foreseen, initially processed with analogue components like RF combiners, limiters or attenuators [11, 12]. The received bipolar signal is transmitted over radiation hard silicon dioxide coaxial cables to the EOM [12], there it is probed at its zero-crossing by the reference laser [11]. Any temporal deviation will lead to an additional voltage, which the EOM turns into an amplitude modulation of the laser pulse. Therefore, the laser amplitude holds the timing information, which can be retrieved in the DAQ [11]. The signal slope at its zero crossing strongly influences the BAMs temporal resolution.

* This work is supported by the German Federal Ministry of Education and Research (BMBF) under contract no. 05K19RO1
† bernhard.scheible@iem.thm.de

Content from this work may be used under the terms of the CC BY 3.0 licence (© 2020). Any distribution of this work must maintain attribution to the author(s), title of the work, publisher, and DOI

ISBN: 978-3-95450-222-6 ISSN: 2673-5350 doi:10.18429/JACoW-IBIC2020-WEPP21

Content from this work may be used under the terms of the CC BY 3.0 licence (© 2020). Any distribution of this work must maintain attribution to the author(s), title of the work, publisher, and DOI

The minimum design requirement for the currently installed BAM was ≥ 300 mV ps^{-1} with 20 pC bunches [12].

RF Unit and Pickups

The RF unit so far comprises four identical pickups mounted circularly around the beam line. The combination of opposite pickup signals compensates for the orbit dependency [16]. The original pickups used at FLASH were of button-type and designed for a 10 GHz bandwidth [17]. This pickup struggled with ringing and strong signal reflections at the alumina vacuum feedthrough [17] degrading the signal strength and resolution for charges below 150 pC [18]. Hence, a new design was required [18].

A novel pickup (Fig. 1, left), similar to those designed for the CERN linear collider test facility [19], was proposed as a solution in FEL applications [20]. The cone-shaped design, finalized in [12], with 40 GHz bandwidth became a new standard device used at the EuXFEL and other FEL.

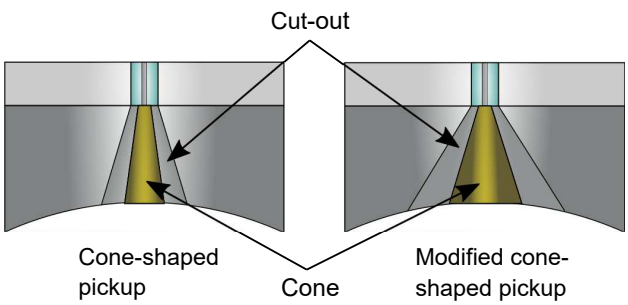

Figure 1: Cross section of the 1st gen. cone-shaped pickup (left) and the modified 2nd gen. cone-shaped pickup for high peak-to-peak voltage (right) adapted from [13].

Due to high losses in the RF path a design update was necessary (Fig. 1, right). The second generation of cone shaped pickups were optimized towards a maximum signal voltage at the cost of its slope by increasing the active surface and letting the cone slightly protrude into the beam pipe [13]. A limit was reached, where a larger surface, e.g., more than a few bunch lengths, further decreases the slope without an increase in peak-to-peak voltage [13]. The protrusion increases the inductance, which unfavorably deforms the signal shape [13]. Nonetheless, a combination of both modifications increased the peak-to-peak voltage sufficiently for 20 pC bunches while maintaining an acceptable slope [13].

Recently the performance of the state-of-the-art system was evaluated at the EuXFEL. The correlation of two adjacent monitors with less than 1 m distance was analyzed. Examining the measured arrival-times for a period of 1 min gave a timing jitter of approximately 6 fs r.m.s. caused by the BAM resolution and critical parts of the reference laser distribution system [21].

RF Signal

The limitations of current pickup structures are evident in the theoretical consideration of the time domain voltage signal. The calculations can be simplified by assuming a Gaussian bunch and a rectangular pickup surface. Depending on the frequency range, the signal looks like a charge source, a current source or intermediate [22]. The image charge on the pickup surface is calculated by

$$Q_{\mathrm{im}} = \int_{-\infty}^{\infty} \frac{\varrho(z - c_0 t) w(z)}{2\pi r_{\mathrm{pickup}}} \mathrm{d}z, \tag{1}$$

with the linear charge density ϱ of the ultra-relativistic bunch, pickup width $w(z)$ and the distance between pickup surface and bunch r_{pickup} [23]. Fringing fields at the gap between flush mounted pickup and beam pipe may be introduced in a constant factor. The maximum voltage is proportional to the bunch charge, Q_{bunch}. This is also true for the signal slope of the cone shaped pickups, as empirically shown at FLASH [16]. Furthermore, the maximum voltage is inversely proportional to r_{pickup} and is depending on the ratio of pickup and bunch lengths as well. The function approaches the maximum value asymptotically and deviates only slightly from the value for a pickup longer than a few bunch lengths [13, 22]. This also effects the signal slope, as the maximum voltage barely changes in this region while both extrema drift apart, leading to a decreasing slope [13].

Additionally, the signal width is limited by the bandwidth. The product of a signal's rise time τ as response to a step function and the frequency bandwidth Δf satisfies[1]

$$\tau \Delta f = 1. \tag{2}$$

This rise time serves as an upper limit and can be expressed by the maximum slope S_{max} and the peak-to-peak voltage U_{PP} with $\tau = U_{\mathrm{PP}} \cdot S_{\mathrm{max}}^{-1}$ giving

$$S_{\mathrm{max}} \leq V_{\mathrm{pp}} \cdot \Delta f. \tag{3}$$

ULTRA-LOW CHARGE MODE

For new experiments in the EuXFEL, with an ultra-low charge mode (≤1 pC), the 2nd generation pickups are incapable of providing the required signal for fs resolution. Therefore, the BAM will be upgraded with a novel pickup structure and new EOM.

Planned Signal Improvement

New layouts are restrained in each facility by design regulations and previous design choices. For the next BAM upgrade in the European XFEL a smaller pipe diameter is now permitted. The possible reduction from 40.5 mm [12] to 10 mm gives a potential fourfold signal increase. When additionally the bandwidth is raised one can expect an improvement by one order of magnitude. Moreover, it is possible to combine multiple signals and to shorten the lossy RF path for further improvement.

The downside of these changes is a shorter dynamical range and a higher damage risk due to increased likeliness of direct beam impacts and high voltages at high charge mode. Special attention must be given to machine protection for all subsequent components.

[1] Denote that the right-hand side of the related uncertainty inequalities by Küpfmüller [24] and Gabor [25] depend on the definitions of bandwidth and duration.

ISBN: 978-3-95450-222-6 ISSN: 2673-5350 doi:10.18429/JACoW-IBIC2020-WEPP21

Aperture Reduction

A straightforward option for improvement is the sole reduction of the beam pipe aperture. A diameter of 10 mm is possible in combination with the smaller first-generation cone-shaped pickup. The second-generation pickups cannot be installed in a four-pickup configuration with this diameter due to its dimensions, as the cut-outs would overlap. A simulation with the wakefield solver of CST PARTICLE STUDIO™ yields a slope of 1746 mV ps^{-1} with 13.7 V peak-to-peak voltage and a dynamical range of 12.4 ps at the nominal 20 pC. The ringing of the signal pictured in Fig. 2 initially is significantly higher but rapidly decreases during the first 0.3 ns.

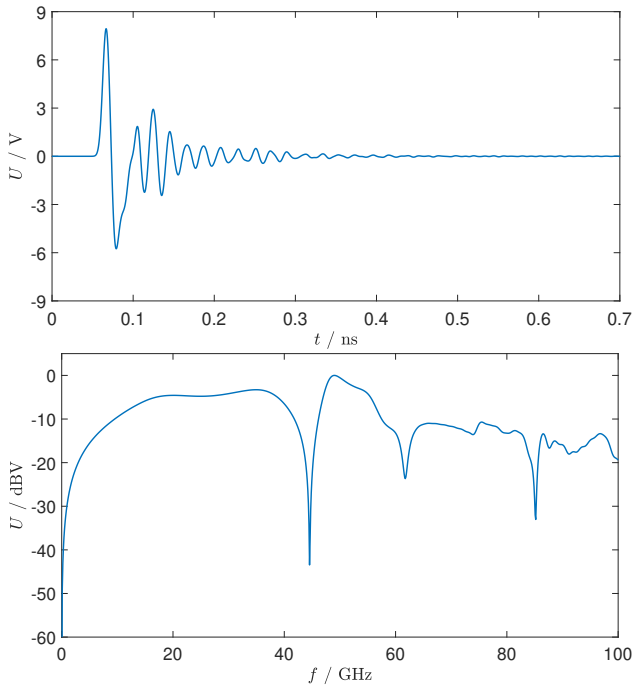

Figure 2: Simulated signal in time domain (top) and its normalized spectrum (bottom) taken at the end of the vacuum feedthrough of a single pickup with 10 mm minimum distance.

90-GHz Cone Shaped Pickup

We proposed a new concept with pickups scaled to support up to 90 GHz 2019 with the dimensions specified in Table 1 [26]. This pickup was simulated afterwards in a BAM like setup, with four identical pickups equally distributed around a pipe section, omitting the proposed signal combination. In addition, the former bunch parameters have been initially used. These are a super relativistic ($v = c_0$) Gaussian bunch with $\sigma = 1$ mm and charge of 20 pC. Therefore, the voltage can be compared to the well-described state-of-the-art pickups according to Angelovski et al. [13, 16].

The bipolar signal pictured in Fig. 3 has a peak-to-peak voltage of 3.52 V and the peaks are separated by 8.01 ps, more than doubling the slope to 722.4 mV ps^{-1}. Though the pipe radius was decreased nearly by a factor of four, the gain is only 2.4. The increased bandwidth leads to a reduced rise time of 7.9 ps but it cannot compensate for the missing protrusion and the smaller active area. Thus, the pickup cannot outperform the 1st generation, but a smaller peak-to-peak voltage gives advantages in machine protection. Reducing the bunch charge to 1 pC accordingly gives a slope of 36.2 mV ps^{-1}, which undershoots the minimum target by about a factor of 4. For a further increase the combination of more than two signals is planned. By the combination of 8 pickups, without any phase shift and 3 dB attenuation at each stage, a factor of 2.8 might be possible. Eight pickups has been determined as the limit, because 400 Ω pickups would be necessary due to the impedance change at a T junction type combiner, to have a 50 Ω connection to the EOM. This is well above the vacuum impedance and requires tiny components. A less radical option is the combination of 4 pickups for a potential improvement of factor 2.

Table 1: Specifications of the 90 GHz-Pickup in [26], the Modified Pickup (Gen. 2) from [16] and the Original (Gen. 1) from [12]

	Draft'19	**Gen. 2**	**Gen. 1**
Cut-out dia.	1.00 mm	1.62 mm	1.62 mm
Tapered cut-out dia.	2.26 mm	13.6 mm	5.60 mm
Cone dia.	0.45 mm	0.70 mm	0.70 mm
Tapered cone dia.	1.02 mm	6 mm	2.42 mm
Cone height		6 mm	6 mm
Protrusion		1 mm	0 mm
Relative permittivity	3.75	4.1	4.1
Line impedance	50 Ω	50 Ω	50 Ω

Compared to both preceding pickup generations, the voltage is approximately proportional to the radius of the circular pickup surface. This may indicate a bunch-pickup ratio where only the pickup width, but not its length is relevant.

Printed Circuit Board BAM

For ultra-short bunches the transition to a short rectangular pickup on a printed circuit board (PCB) with a trace thickness still larger than the bunch length appears possible. This concept possibly allows for a 100 GHz pickup without the drawback of smaller dimensions. Further benefits are the possibility to use well-known components with precise production methods and well-described materials. The transmission lines (TL) and combination network may be realized on the PCB reducing the RF path, which is specifically important to prevent dispersion effects in broadband quasi-TEM TLs. A microstrip is favorable for its width, but entails dispersion and is less shielded. Therefore, it is planned to use a microstrip (MS) for coupling to the field and a stripline (SL) for the combination network. A preliminary simulation, shown in Fig. 4, of a PCB based pickup was done with a 1.55 mm wide and about 15 mm long 50 Ω SL in a $\epsilon_r = 4.03$ substrate disc with 10 mm aperture inside. For a 20 pC bunch the simulation returns a slope of

Content from this work may be used under the terms of the CC BY 3.0 licence (© 2020). Any distribution of this work must maintain attribution to the author(s), title of the work, publisher, and DOI

ISBN: 978-3-95450-222-6 ISSN: 2673-5350 doi:10.18429/JACoW-IBIC2020-WEPP21

Content from this work may be used under the terms of the CC BY 3.0 licence (© 2020). Any distribution of this work must maintain attribution to the author(s), title of the work, publisher, and DOI

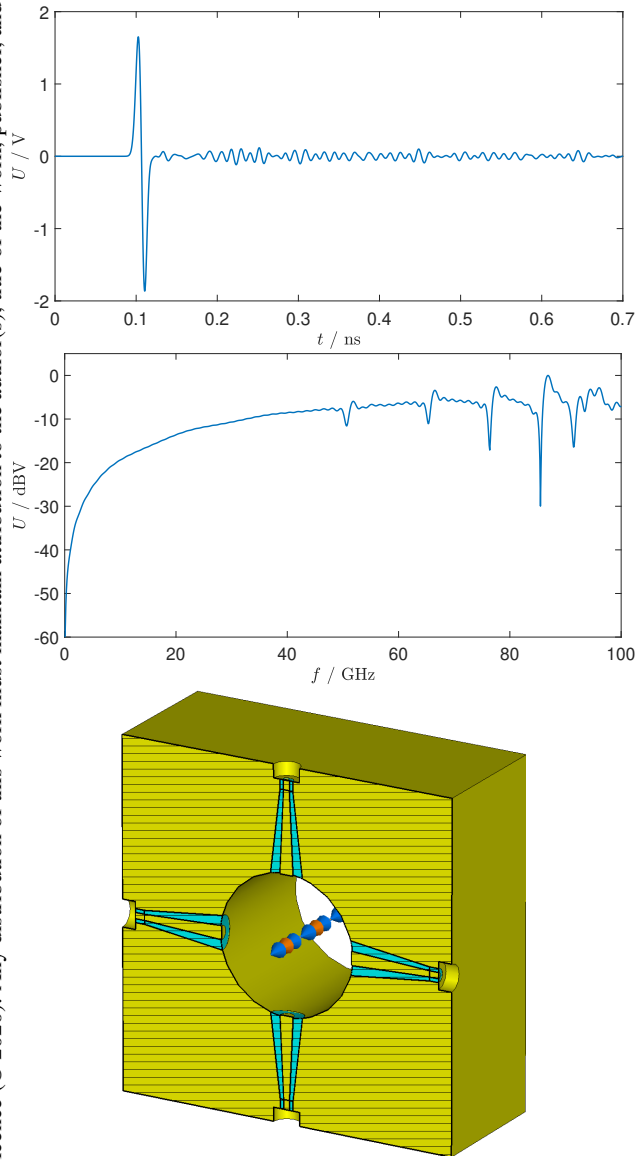

Figure 3: The signal in time domain (top) and its normalized spectrum (center) taken at the end of the vacuum feedthrough of a single pickup as well as the simulation model with 90 GHz cone-shaped pickups (bottom).

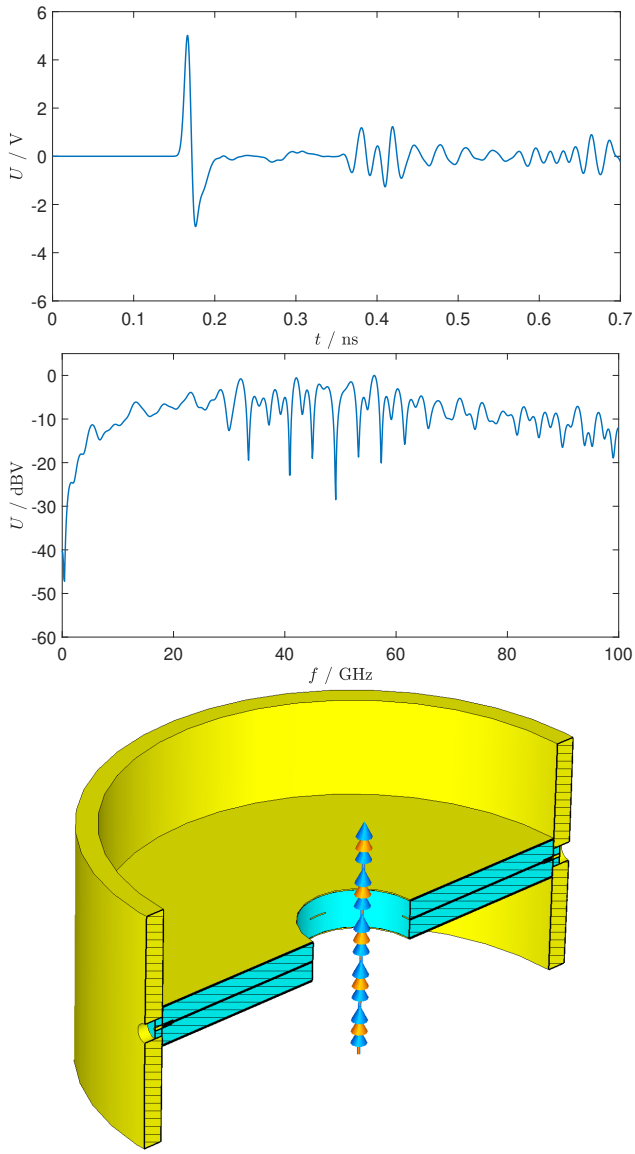

Figure 4: The signal in time domain (top) and its normalized spectrum (center) taken at the end of the vacuum feedthrough of a single pickup as well as the simulation model with 50 Ω stripline pickups (bottom).

about 1270 mV ps^{-1}. The SL pickup is exceeding the current as well as the 90 GHz cone-shaped pickups, but does not achieve the performance of a generation 1 pickup of equal aperture. Furthermore, crosstalk and reflections at the vacuum feedthrough as well as the open pickup end generate delayed but significant ringing.

CONCLUSION

A high bandwidth cone-shaped pickup with 10 mm aperture leads to a significant improvement by reduction of the distance and increase of the bandwidth. If a maximum voltage is of no concern, a configuration of 1st generation pickups in a 10 mm beam pipe is a simple solution estimated sufficient for bunch charges down to 4 pC. In case of ultra-short bunches a PCB-type BAM may be suited to support 100 GHz without the drawback of reduced dimensions. With the current design restrictions, a signal combination is inevitable. Further studies of an integrated combination network are required to reduce signal reflections and losses. Furthermore, it is necessary to investigate the properties of PCB boards regarding vacuum suitability and radiation hardness. Specifically, potential damages caused by beam incident need to be assessed.

REFERENCES

[1] E. J. Jaeschke, S. Khan, J. R. Schneider, and J. B. Hastings, "Synchrotron light sources and free-electron lasers: Accelerator physics, instrumentation and science applications",

ISBN: 978-3-95450-222-6 ISSN: 2673-5350 doi:10.18429/JACoW-IBIC2020-WEPP21

2nd Edition, Cham: Springer International Publishing, 2020. doi:10.1007/978-3-030-23201-6

[2] E. A. Seddon *et al.*, "Short-wavelength free-electron laser sources and science: a review", *Rep. Prog. Phys.* vol. 80, no. 11, Oct. 2017. doi:10.1088/1361-6633/aa7cca

[3] C. M. Günther *et al.*, "Sequential femtosecond X-ray imaging", *Nat. Photon.*, vol. 5, pp. 99-102, Feb. 2011. doi:10.1038/nphoton.2010.287

[4] W. Lu *et al.*, "Development of a hard X-ray split-and-delay line and performance simulations for two-color pump-probe experiments at the European XFEL", *Rev. Sci. Instrum.*, vol. 89, no. 6, Jun. 2018. doi:10.1063/1.5027071

[5] J. B. Rosenzweig *et al.*, "Generation of ultra-short, high brightness electron beams for single-spike SASE FEL operation", *Nucl. Instrum. Methods Phys. Res., Sect. A*, vol. 593, no. 1-2, pp. 39-44, Aug. 2008. doi:10.1016/j.nima.2008.04.083

[6] S. Reiche, P. Musumeci, C. Pellegrini, and J. B. Rosenzweig, "Development of ultra-short pulse, single coherent spike for SASE X-ray FELs", *Nucl. Instrum. Methods Phys. Res., Sect. A*, vol. 593, no. 1-2, pp. 45-48, Aug. 2008. doi:10.1016/j.nima.2008.04.061

[7] W. Decking and T. Limberg, "Technical Note: European XFEL post TDR description", European XFEL GmbH, Hamburg (Germany), XFEL.EU TN-2013-004-01, 2013.

[8] T. Tschentscher, "Technical report: Layout of the X-Ray Systems at the European XFEL", European XFEL Facility GmbH, Hamburg (Germany), XFEL.EU TR-2011-001, 2011.

[9] Y. Kot, T. Limberg, and I. Zagorodnov, "Technical report: Different charges in the same bunch train at the European XFEL", Deutsches Elektronen-Synchrotron (DESY), Hamburg (Germany), DESY-13-215, 2013.

[10] M. Viti *et al.*, "Recent upgrades of the bunch arrival time monitors at FLASH and European XFEL", in *Proc. IPAC'17*, Copenhagen, Denmark, May 2017, pp. 695-698. doi:10.18429/JACoW-IPAC2017-MOPIK072

[11] F. Löhl *et al.*, "Electron bunch timing with femtosecond precision in a superconducting free-electron laser", *Phys. Rev. Lett.*, vol. 104, no. 14, p. 144801, Apr. 2010. doi:10.1103/PhysRevLett.104.144801

[12] A. Angelovski *et al.*, "High bandwidth pickup design for bunch arrival-time monitors for free-electron laser", in *Phys. Rev. Spec. Top. Accel Beams*, vol. 15, no. 11, Nov. 2012. doi:10.1103/PhysRevSTAB.15.112803

[13] A. Angelovski *et al.*, "Pickup signal improvement for high bandwidth BAMs for FLASH and European - XFEL", in *Proc. 2nd Int. Beam Instrumentation Conf. (IBIC'13)*, Oxford, UK, Sep. 2013, paper WEPC40, pp. 778-781.

[14] J. Kim *et al.*, "An integrated femtosecond timing distribution system for XFELs", in *Proc. EPAC'06*, Edinburgh, UK, Jun. 2006, paper THOPA03, pp. 2744-2746.

[15] T. Lamb *et al.*, "Large-scale optical synchronization system of the European XFEL with femtosecond precision", in *Proc. IPAC'19*, Melbourne, Australia, May 2019, pp. 3835-3838. doi:10.18429/JACoW-IPAC2019-THPRB018

[16] A. Angelovski *et al.*, "Evaluation of the cone-shaped pickup performance for low charge sub-10 fs arrival-time measurements at free electron laser facilities", *Phys. Rev. Spec. Top. Accel. Beams*, vol. 18, no. 1, Jan 2015, p. 012801. doi:10.1103/PhysRevSTAB.18.012801

[17] A. Kuhl *et al.*, "Analysis of new pickup designs for the FLASH and XFEL bunch arrival time monitor system", in *Proc. DIPAC'11*, Hamburg, Germany, May 2011, paper MOPD34, pp. 125-127.

[18] M. K. Bock *et al.*, "Benchmarking the performance of the present bunch arrival time monitors at FLASH", in *Proc. DIPAC'11*, Hamburg, Germany, May 2011, paper TUPD28, pp. 365-367.

[19] Y. Yin, E. Schulte, and T. Ekelof, "Recovery of CTF beam signals from a strong wakefield background", in *Proc. 1995 IEEE Particle Accelerator Conference (PAC'95)*, vol. 4, Dallas, TX, USA, 1995, pp. 2622-2624. doi:10.1109/PAC.1995.505638

[20] A. Angelovski *et al.*, "Pickup design for a high resolution bunch arrival time monitor for FLASH and XFEL", in *Proc. DIPAC'11*, Hamburg, Germany, May 2011, paper MOPD33, pp. 122-124.

[21] S. Schulz *et al.*, "Few-femtosecond facility-wide synchronization of the European XFEL", in *Proc. FEL'19*, Hamburg, Germany, Aug. 2019, pp. 318–321. doi:10.18429/JACoW-FEL2019-WEB04

[22] J. Y. Huang, I. H. Yu, W. H. Hwang, M. H. Chun, and S. C. Kim, "Analysis of pickup signals in the time domain and the frequency domain for the beam position monitor at the Pohang Light Source", *J. Korean Phys. Soc.*, vol. 48, no. 94, Apr. 2006, pp. 768-771.

[23] S. R. Smith, "Beam position monitor engineering", in *Proc. 7th Beam Instrumentation Workshop (BIW'96)*, Illinois, USA, May 1996, *AIP Conference Proceedings*, vol. 390, no. 1, pp. 50-65. doi:10.1063/1.52306

[24] K. Küpfmüller, "Der Zusammenhang zwischen den Frequenzcharakteristiken und den Ausgleichsvorgängen.", "Einführung in die theoretische Elektrotechnik", Springer Berlin Heidelberg, 1932, pp. 268-272. ISBN: 978-3-662-35949-5

[25] D. Gabor, "Theory of communication. Part 1: The analysis of information.", *J. Inst. Electr. Eng. 3.*, vol. 93, no. 26, p. 429–441, Nov. 1946. doi:10.1049/ji-3-2.1946.0074

[26] A. Penirschke, M. K. Czwalinna, H. Schlarb, M. Kuntzsch, and W. Ackermann, "Concept of a novel high-bandwidth arrival time monitor for very low charges as a part of the all-optical synchronization system at ELBE", in *Proc. IBIC'19*, Malmö, Sweden, Sep. 2019, pp. 560–563. doi:10.18429/JACoW-IBIC2019-WEPP019

Content from this work may be used under the terms of the CC BY 3.0 licence (© 2020). Any distribution of this work must maintain attribution to the author(s), title of the work, publisher, and DOI

ISBN: 978-3-95450-222-6 ISSN: 2673-5350 doi:10.18429/JACoW-IBIC2020-WEPP22

SUBMICROPULSE ENERGY-TIME CORRELATIONS OF 40-MeV ELECTRON BEAMS AT FAST*

R. Thurman-Keup†, A. H. Lumpkin, Fermi National Accelerator Laboratory, Batavia, IL, USA

Abstract

We have recently extended our ability to explore submicropulse effects in relativistic electron beams to energy-time (E-t) correlations. The Fermilab Accelerator Science and Technology (FAST) facility consists of a photoinjector, two superconducting TESLA-type capture cavities, one superconducting ILC-style cryomodule, and a small ring for studying non-linear, integrable beam optics called IOTA. The linac contains, as part of its instrumentation, an optical transport system that directs optical transition radiation (OTR) from an Al-coated Si surface to an externally located streak camera for bunch length measurements. For the first time, an OTR screen after the spectrometer magnet was used for measurements of submicropulse E-t correlations. The projected, micropulse time profile was fit to a single Gaussian peak with $\sigma = 11.5 \pm 0.5$ ps for 500 pC/micropulse and with a 200-micropulse synchronous sum, in agreement with the upstream bunch-length measurement at a non-energy-dispersive location. The submicropulse E-t images were explored for four rf phases of CC1, and the E vs. t effects will be presented.

INTRODUCTION

The Fermilab Accelerator Science and Technology (FAST) facility was constructed for advanced accelerator research [1]. It consists of a photoinjector-based electron linac followed by an ILC-type cryomodule and a small ring called IOTA (Integrable Optics Test Accelerator) for studying non-linear optics among other things [2]. Presently under construction, is an RFQ-based proton injector to supply protons to the IOTA ring. To support operations in the electron linac, an optical transport system was installed to take light from various sources (synchrotron radiation, transition radiation) and send it to various instruments including a Hamamatsu streak camera located outside the enclosure [3]. In this paper, we present the first measurements from a newly installed optical transport line that takes optical transition radiation (OTR) from an Al-coated Si surface after the spectrometer magnet to the streak camera. The transport is arranged in such a way as to map the energy direction of the OTR screen to the spatial direction in the streak camera, allowing for a measurement of the energy-time (E vs. t) phase space of a micropulse.

FAST FACILITY

The FAST facility (Fig. 1) begins with a 1.3 GHz normal-conducting rf photocathode gun with a Cs_2Te-coated cathode. The photoelectrons are generated by irradiation with a YLF laser at 263 nm that can provide several μJ per pulse [4]. Following the gun are two superconducting 1.3 GHz capture cavities (CC1 and CC2) that accelerate the beam to its design energy of around 50 MeV. After acceleration, there is a section for doing round-to-flat beam transforms, followed by a magnetic bunch compressor and a short section that can accommodate small beam experiments. At the end of the experimental section is a spectrometer dipole which can direct the beam to the low energy dump. If the beam is not sent to the dump, it enters the ILC-type cryomodule where it receives up to 250 MeV of additional energy and is sent to either a high-energy dump or the IOTA ring. Table 1 lists the typical beam parameters.

Table 1: Beam Parameters for FAST

Parameter	Value
Energy	20 – 300 MeV
Micropulse Charge	< 10 fC – 3.2 nC
Micropulse Frequency	0.5 – 9 MHz
Macropulse Duration	≤ 1 ms
Macropulse Frequency	1 – 5 Hz
Transverse Emittance	> 1 μm
Micropulse Length	0.9 – 70 ps

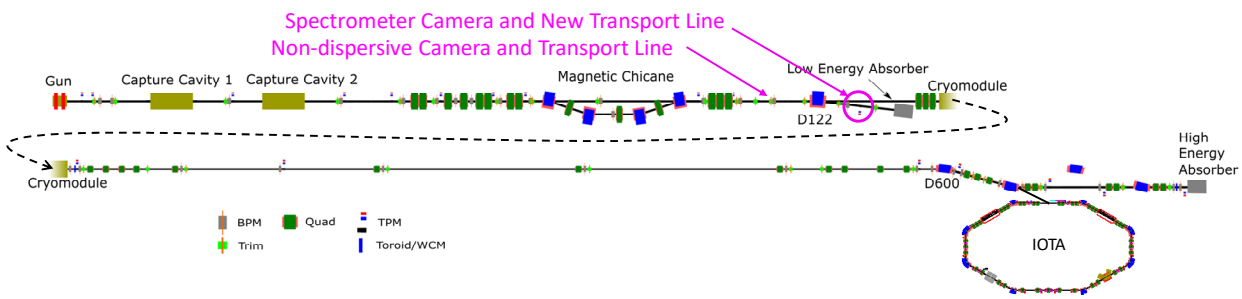

Figure 1: Layout of the FAST facility. D122 is the spectrometer magnet, after which is the OTR source for the new optical transport line.

* This manuscript has been authored by Fermi Research Alliance, LLC under Contract No. DE-AC02-07CH11359 with the U.S. Department of Energy, Office of Science, Office of High Energy Physics.
† keup@fnal.gov

Content from this work may be used under the terms of the CC BY 3.0 licence (© 2020). Any distribution of this work must maintain attribution to the author(s), title of the work, publisher, and DOI

ISBN: 978-3-95450-222-6 ISSN: 2673-5350 doi:10.18429/JACoW-IBIC2020-WEPP22

EXPERIMENTAL SETUP

The experimental setup used for these measurements utilizes a new transport line for the existing Optical and Terahertz Instrumentation System, OTIS [3] (see Fig. 2).

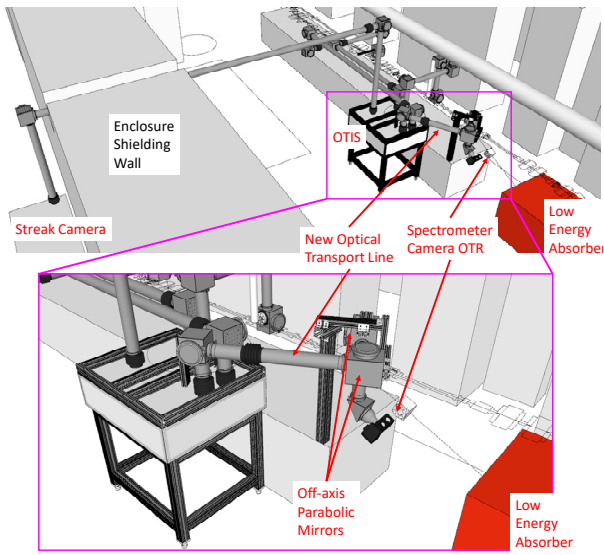

Figure 2: Overview the Optical and Terahertz Instrumentation System (OTIS). The new transport line originates from the spectrometer camera.

The new transport line originates at the optical transport for the spectrometer camera (Fig. 3) where it splits the OTR light coming from the Al-coated Si plate using a Thorlabs BP245B1 pellicle-type beamsplitter and sends half the light through a pair of Edmund Optics 35-564 off-axis paraboloidal mirrors to collimate the light before transport to the Hamamatsu C5680 streak camera. The streak camera is equipped with mirror input optics to reduce optical dispersion, and a M5675 synchroscan unit to

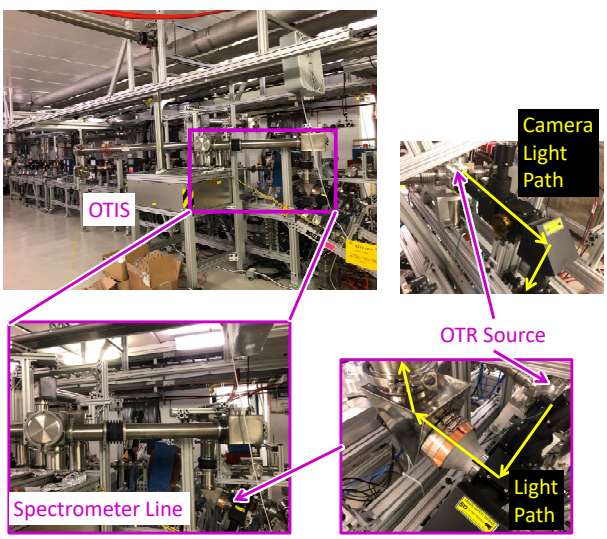

Figure 3: Pictures showing the new optical transport line from the spectrometer camera source point. The yellow arrows show the beginning light path for the new transport line and the spectrometer camera.

enable the accumulation of many micropulses while avoiding significant phase jitter (see [5] for more details). The transport line itself is comprised of stainless steel (SS316) boxes with flat mirrors, and 4-inch-diameter SS316 tubes.

Figure 4 shows the effective optical path for the light originating from the OTR screen. From the OTR source, the light propagates through a focusing section before encountering the beam splitter. At that point, the light to the streak camera traverses two off-axis paraboloidal mirrors to collimate the light which travels ~14 meters to the streak camera.

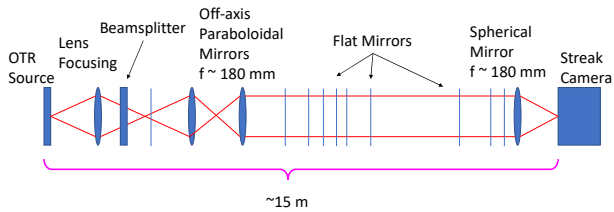

Figure 4: Effective optical path of the new transport line from OTR source, to streak camera (not to scale). There are 10 flat mirrors (indicated by the thin lines) in addition to the labeled optical components.

The alignment of the transport line was accomplished via a laser injected through a viewport on the input side of the spectrometer magnet. It was focused at the location of the OTR screen and allowed to exit by reflection off the screen which allowed us to both align and adjust the collimation of the transport line (Fig. 5). In attempting to align the transport line it was discovered that the OTR screen is not positioned at 45 degrees to the beam. It appears to be off by about 5 degrees which complicated the alignment slightly as the focusing properties of off-axis parabolic mirrors are sensitive to the position and direction of the light. In Fig. 5, the misalignment can be seen at the beamsplitter. This caused the light to follow a zig-zag path inducing distortion from the paraboloidal mirrors.

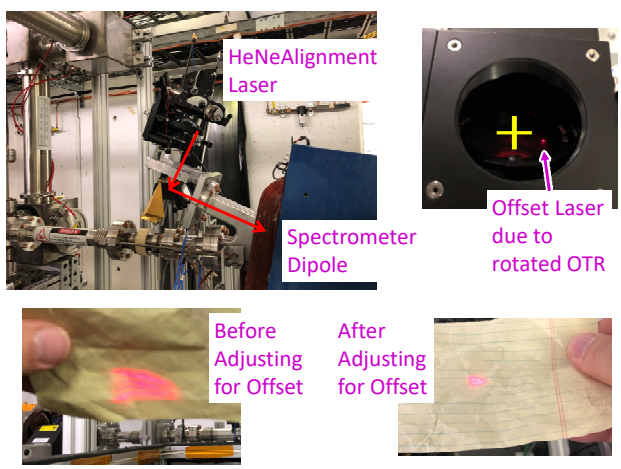

Figure 5: Alignment of the transport line is via a HeNe laser injected through a viewport before the spectrometer magnet. The before and after pictures show the distortion induced by the rotated OTR screen. The yellow cross is the ideal laser position.

Content from this work may be used under the terms of the CC BY 3.0 licence (© 2020). Any distribution of this work must maintain attribution to the author(s), title of the work, publisher, and DOI

ISBN: 978-3-95450-222-6 ISSN: 2673-5350 doi:10.18429/JACoW-IBIC2020-WEPP22

Content from this work may be used under the terms of the CC BY 3.0 licence (© 2020). Any distribution of this work must maintain attribution to the author(s), title of the work, publisher, and DOI

MEASUREMENT

The measurement of the E-t phase space utilizes changes in the rf phase of the first capture cavity, CC1. The beamline was setup with the gun providing ~4.5 MeV, CC1 providing ~23 MeV, CC2 providing ~13 MeV, and 500 pC per micropulse. The beam was directed into the low energy absorber and imaged on a YAG:Ce screen with the camera system in the dispersive spectrometer line. Figure 6 shows this image of the beam focused to minimize the beta function contribution to the energy measurement.

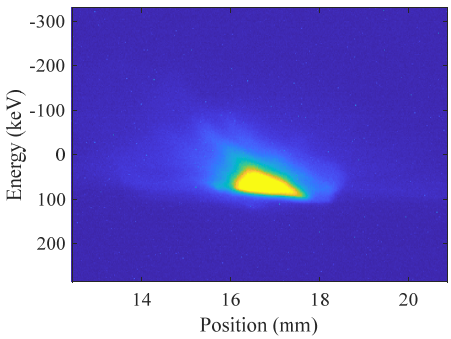

Figure 6: Beam image from the YAG:Ce screen of the spectrometer camera. The image is saturated, but the uncorrelated energy spread can be seen to be <50 KeV.

The YAG:Ce screen was then moved out, the Al-coated Si, was moved in, and the electron beam was steered as necessary to bring the light onto the streak camera. To verify that the streak camera was indeed seeing light from the electron bunches, the images from the spectrometer line were fit for the bunch length and compared to streak camera images taken in the upstream non-dispersive line.

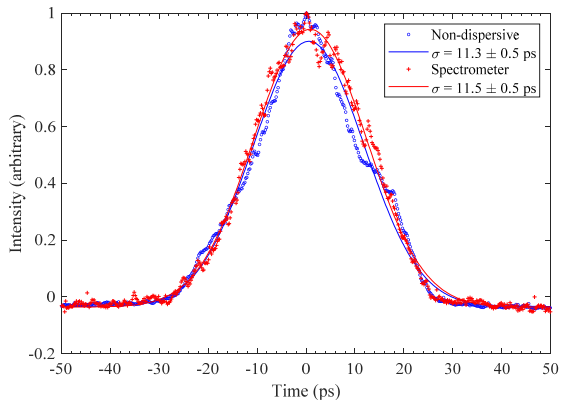

Figure 7: Projections of streak camera images from both the new spectrometer line and the upstream non-dispersive line.

The images from the spectrometer are an accumulation of 10 images, each an accumulation of 200 micropulses. The image from the non-dispersive line is 10 images of 150 micropulses. The projections of these images are fit with a gaussian plus background and shown in Fig. 7 with the fit values which are consistent.

To determine the sensitivity of the setup to changes in the E-t phase space, the phase and amplitude of CC1 were changed to move the beam off the rf crest and induce a slope in the phase space. Again, 10 images of 200 micropulses each were accumulated and summed for each of four phase values, 0, 5, 10, and 15 degrees off crest. Figure 8 shows the images from these four conditions.

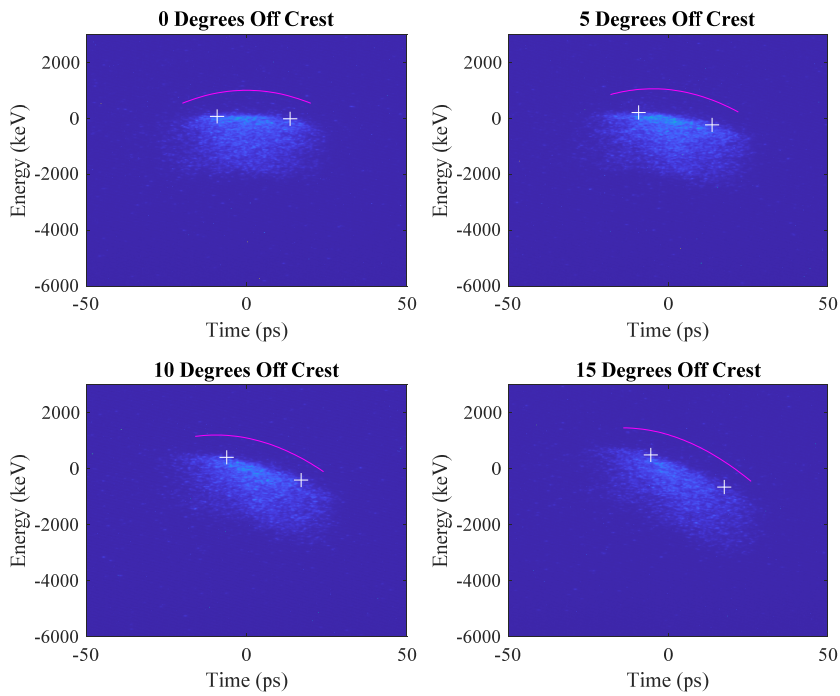

Figure 8: Streak camera images for four phase offsets of the CC1 accelerating gradient. The white crosses are the points used to determine the slope induced by the rf phase offset, and the red curves are the expected energy curve given the calibration from the points. For reference, a micropulse rms length of 11.5 ps corresponds to 6.2 degrees.

ISBN: 978-3-95450-222-6 ISSN: 2673-5350 doi:10.18429/JACoW-IBIC2020-WEPP22

Also shown on the images are the points (crosses) which were used to obtain the slope induced by the rf. Using those points together with the slope of the rf sinusoid we obtain a calibration constant for the 5, 10, and 15 degrees off crest cases of 10.9, 10.7, and 10.9 KeV/pixel respectively. The consistency builds confidence in the technique. Using the calibration constants, we also plot the predicted energy curvature from the sinusoidal shape of the rf from CC1 and CC2 (but not including effects from the gun).

As one can see in the images, the upper side of the image seems to fit well with the expectation, however, the vertical size does not correspond well at all with the expected energy spread, particularly the 0-degree case. From Fig. 6, we would expect something on the order of 50 to 100 KeV, but from the 0-degree image, the spread is more like 2 MeV. One possible explanation for this is poor focusing resulting from the rotated OTR screen.

An additional cross-check of the expected energy spread from the rf phase offset is seen in Fig. 9. This is the spectrometer camera image of the OTR screen for 15 degrees off crest. For a micropulse with rms length of 11.5 ps, the expected rms energy spread from the slope of the rf is ~500 KeV. Accounting for the actual sinusoidal shape of the rf results in a rms energy spread of 580 KeV. The gaussian fit in Fig. 9 has a sigma of 383 KeV. Some of this discrepancy may be due to poor positioning of the beam on the OTR screen since it appears that part of the beam may be off the screen.

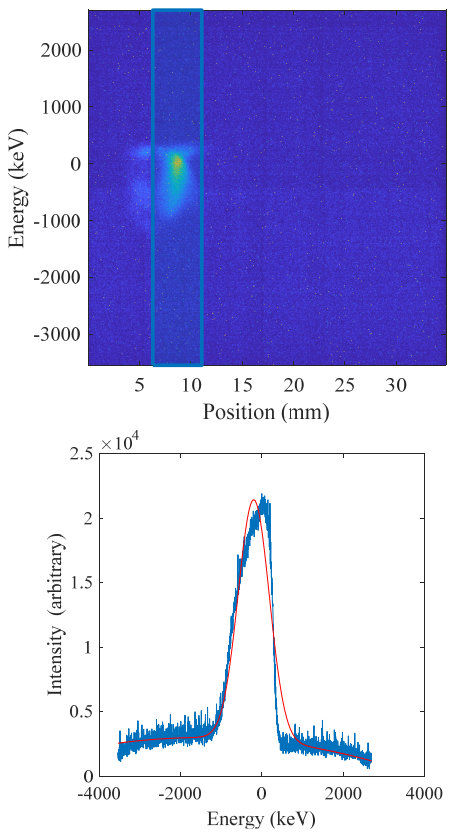

Figure 9: Top) Spectrometer camera image of beam with 15-degree rf phase offset. Bottom) The energy spread projection within the boxed region of interest and a gaussian fit with sigma of 383 KeV.

SUMMARY

At FAST, we have installed a new transport line from the OTR screen in the spectrometer beamline to the streak camera outside the enclosure. This has enabled us to make the first direct measurements of E-t phase space of electron micropulses. Preliminary results indicate that the technique should be reliable provided that the optical transport is well aligned. To that end, further improvements require a realignment of the OTR screen followed by realigning of the remaining transport.

ACKNOWLEDGEMENTS

The authors would like to thank the FAST department staff for their efforts in support of operations at the FAST facility, and C. Drennan for support of these endeavors within the instrumentation department.

REFERENCES

[1] P. Garbincius *et al.*, "Proposal for an accelerator R&D user facility at Fermilab's Advanced Superconducting Test Accelerator (ASTA)", FNAL, Batavia, IL, USA, Rep. Fermilab-TM-2568, Oct. 2013.

[2] S. Antipov *et al.*, "IOTA (Integrable Optics Test Accelerator): facility and experimental beam physics", *J. Instrum.*, vol. 12, p. T03002, 2017. doi:10.1088/1748-0221/12/03/T03002

[3] R. Thurman-Keup, A. H. Lumpkin, and J. Thangaraj, "An optical and terahertz instrumentation system at the FAST linac at Fermilab", in *Proc. IBIC'17*, Grand Rapids, MI, USA, Aug. 2017, pp. 342-346. doi:10.18429/JACoW-IBIC2017-WEPCC04

[4] J. Ruan *et al.*, "Commission of the drive laser system for advanced superconducting test accelerator", in *Proc. IPAC'13*, Shanghai, China, May 2013, pp. 3061-3063, paper WEPME057.

[5] A. H. Lumpkin *et al.*, "Direct observations of submicropulse electron-beam effects from short-range wakefields in Tesla-type superconducting rf cavities", presented at IBIC'20, Santos, Brazil, Sep. 2020, paper TUPP17, this conference.

Content from this work may be used under the terms of the CC BY 3.0 licence (© 2020). Any distribution of this work must maintain attribution to the author(s), title of the work, publisher, and DOI

ISBN: 978-3-95450-222-6 ISSN: 2673-5350 doi:10.18429/JACoW-IBIC2020-WEPP24

Content from this work may be used under the terms of the CC BY 3.0 licence (© 2020). Any distribution of this work must maintain attribution to the author(s), title of the work, publisher, and DOI

PROTOTYPE DESIGN OF BUNCH ARRIVAL TIME MEASUREMENT SYSTEM BASED ON CAVITY MONITOR FOR SHINE*

Y.M. Zhou†, S.S. Cao, J. Chen, Y.B. Leng#

Shanghai Advanced Research Institute, CAS, Shanghai, China

Abstract

The Shanghai high repetition rate XFEL and extreme light facility (SHINE) is planned to be built into one of the most efficient and advanced free-electron laser user facilities over the world to provide a unique tool for kinds of cutting-edge scientific research. The measurement of bunch arrival time is one of the key issues to optimize system performance. This is because the FEL facility relies on the synchronization of electron bunch and seeded lasers. Currently, there are mainly two methods to measure the bunch arrival time: the electro-optical sampling method and the RF cavity-based method. Considering the latter one has a simpler system and lower cost, the method has been adopted by SXFEL. The previous results show that the measurement uncertainty of bunch arrival time has achieved to be 45 fs, which can be further optimized. For SHINE, the bunch arrival time resolution is required to be better than 25 fs@100pC, and 200 fs@10 pC. The RF cavity-based method will also be applied. This paper will present the system prototype design and related simulation results.

INTRODUCTION

To achieve high-intensity and ultra-fast short wavelength radiation, several X-ray FEL facilities have been completed or under construction around the world[1-3]. Shanghai HIgh repetition rate XFEL aNd Extreme light facility (SHINE) is the first hard X-ray FEL light source in China, which constructed began in April of 2018. The total length of the entire device reached 3.1 km. It will build an 8GeV superconducting linear accelerator, 3 undulator lines, 3 beamlines, and 10 experiment stations in phase-I. It can provide the XFEL radiation in the photon energy range of 0.4-25keV. The main parameters are presented in Table 1[4]. The SHINE has many excellent characteristics such as ultra-high brightness (up to 109 times that of the third-generation synchrotron radiation), high repetition frequency (1MHz), femtosecond ultra-fast pulse (pulse width < 100fs), and strong spatial and temporal coherence. Moreover, it also possesses nano-level ultra-high spatial resolution capabilities and femtosecond-level ultrafast time resolution. Therefore, the establishment of the SHINE will provide cutting-edge research methods such as high-resolution imaging, ultra-fast process exploration, and advanced structural analysis for physics, chemistry, life sciences, materials science, energy science, and other disciplines, forming a unique and multidisciplinary interdisciplinary advanced scientific research platform.

High precision bunch arrival time is one of the key technologies because it is the foundation for the synchronization of electron bunches and seeded lasers. At present, two main detection methods, the electro-optical sampling method and the RF cavity-based method, are widely used. Since the system of the latter method is very simple and economical, it has been successfully applied to SXFEL. The measurement uncertainty of bunch arrival time has reached 45fs[5, 6]. However, DESY conducted a theoretical analysis on this and found that the theoretical limit of this method is 1-3fs[7], and the best result obtained by the LCLS experiment is 13fs[8]. Therefore, we consider further optimizing the system to improve the measurement accuracy. It is hoped that the RF cavity-based method can be applied to the SHINE and achieve 25fs@100pC, 200fs@10pC measurement uncertainty of bunch arrival time.

This paper will focus on the prototype design of the bunch arrival time measurement system (BAM) based on the cavity monitor in the SHINE. The system mainly includes four modules: cavity probe, RF front-end, local oscillator, and signal acquisition system. A detailed introduction and experimental simulation results have been presented.

Table 1: Main Parameters of the SHINE

Parameter	Value
Beam energy	8GeV
Energy spread	0.01%
Photon energy	0.4-25keV
Repetition rate	1MHz
Wavelength	0.05-3.0mm
Pulse length	20-50fs
Bunch Charge	10-300pC

SYSTEM FRAMEWORK

A typical framework of the bunch arrival time system is shown in Figure 1. The main method is to perform digital acquisition after down-converting the signal to an intermediate frequency (IF) signal. A cavity probe used to measure the bunch arrival time is installed at a specific position in the accelerator, and the signal of the probe is led out via a long/short cable as the RF input of the RF front-end. The

*Work supported by National Natural Science Foundation of China (2016YFA0401903) and Ten Thousand Talent Program and Chinese Academy of Sciences Key Technology Talent Program
†zhouyimei@zjlab.org.cn
#lengyongbin@sinap.ac.cn

ISBN: 978-3-95450-222-6 ISSN: 2673-5350 doi:10.18429/JACoW-IBIC2020-WEPP24

local oscillation (LO) signal obtained by the main oscillator after multiplier/divider is used as the LO input of the RF front-end. Then, the two signals complete signal shaping, filtering, down-conversion, and amplification in the RF front-end. At last, the IF signal will change from an analog signal to a digital signal in the data acquisition system, and complete offline/online processing at the terminal. Therefore, the entire system consists of four major modules: cavity probe, RF front-end, local oscillator, and signal acquisition system.

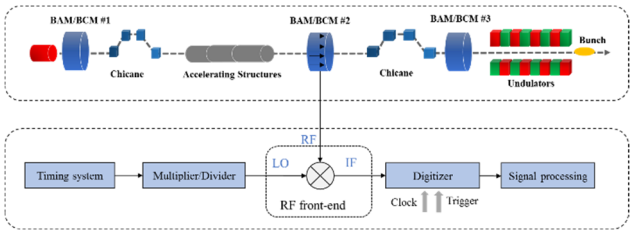

Figure 1: Typical diagram of bunch arrival time system.

Currently, the parameter settings of the BAM prototype refer to the SXFEL. Future beam experiments will also be carried out on this facility. Next, the design and construction of each module will be introduced one by one.

Cavity Probe

When the beam passes through the center of the cavity, the common-mode field is most excited. Therefore, the TM010 mode signal is used as the main mode to extract phase information (bunch arrival time). The electric field center of this mode is symmetrical, and the intensity is almost independent of the transverse position at the paraxial position.

Many parameters need to be considered when designing a phase cavity, such as frequency, damping time, bandwidth, signal amplitude, and load quality factor, etc. For the prototype design, the working frequency of the cavity is temporarily selected at 5771.5MHz. Besides, other parameters of electronic devices need to be considered comprehensively. In short, it is necessary to increase the signal-to-noise ratio of the output signal and reduce the crosstalk of the cavity to the bunch.

The main design of the cavity is done using CST/MAFIA simulation tools, and the structure refers to Spring-8. Considering the high repetition frequency of SHINE, we designed three BAM prototype probes with damping times of 100ns, 200ns, and 300ns, and only one of them will be selected as the final BAM probe after testing. The main technical parameters are shown in Table 2. For detailed design content and test results, please refer to the paper WEPP13 in this conference[9].

Table 2: Main Technical Parameters of Phase Cavity

Parameter	Cavity 1	Cavity 2	Cavity 3
Frequency (MHz)	5771.5	5771.5	5771.5
Damping time (ns)	100	200	300
Bandwidth (MHz)	3.18	1.59	1.06
Q load	1813	3626	5440
Vpeak (V/nC)	11.4	3.9	6.7
Radius (mm)	19.9	19.9	19.9
Length (mm)	3	4	7.5

RF Front-end

The goal of the RF front-end is to achieve signal filtering, amplification, and down-conversion. To reduce the loss of effective signals, it needs to be close to the cavity probe in the tunnel. The design block diagram is shown in Figure 2. Three prototypes with different design techniques have also been delivered to different companies for production. A narrow-band BPF with 5771MHz center frequency and 100MHz bandwidth is used to remove the interference signal and noise of non-primary mode. The system uses cascaded adjustable attenuation and fixed gain amplifiers. The purpose of that is to broaden the dynamic range and reduce the noise figure so that the system can obtain the best performance. Besides, a limiter is added after the attenuator to prevent damage to the amplifier, mixer, and other components in the subsequent circuit. The last-stage analog voltage variable attenuator (VVA) is used to control the attenuation accuracy.

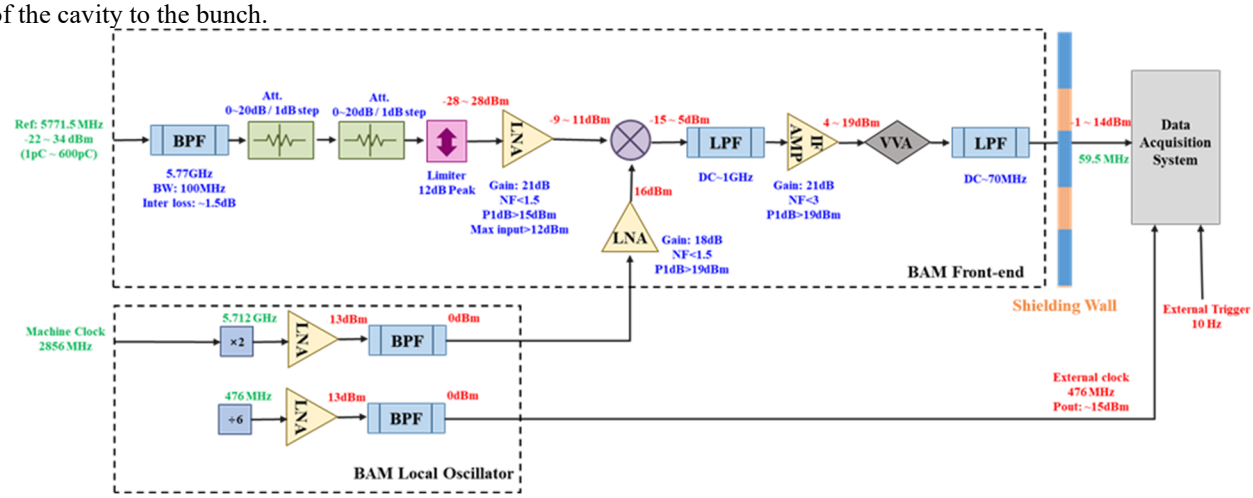

Figure 2: Design block diagram of BAM front-end for SHINE.

Content from this work may be used under the terms of the CC BY 3.0 licence (© 2020). Any distribution of this work must maintain attribution to the author(s), title of the work, publisher, and DOI

ISBN: 978-3-95450-222-6 ISSN: 2673-5350 doi:10.18429/JACoW-IBIC2020-WEPP24

Content from this work may be used under the terms of the CC BY 3.0 licence (© 2020). Any distribution of this work must maintain attribution to the author(s), title of the work, publisher, and DOI

Local Oscillator

The clock frequency of the local oscillator unit mainly refers to 2856MHz of SXFEL. After the multiplier, the LO signal frequency is 5712MHz. Therefore, the IF signal obtained after down-conversion is 59.5MHz. To achieve system integration, the local oscillator module will be combined with the front-end module in the same chassis. The phase jitter of the output local oscillator signal is about 60fs rms @ 10Hz~10MHz when the phase jitter of the 2856MHz input signal is 50fs rms.

The whole system can work in the input power range of -22~34dBm, and the corresponding bunch charge is about 1pC~600pC, which meets the design requirements.

Signal Acquisition System

For signal processing, a dedicated DBPM based on commercial data acquisition boards is under development for SHINE, which is convenient for debugging and application.

At present, the formulation of the plan has been completed, and the modular design of the daughter-mother board structure with the FMC interface will be adopted. FPGA will use the ZYNQ MPSoC system to improve system compactness and stability. The DBPM used for IF signal sampling will select an ADC with 12 bits and 500MHz sampling rate.

SIMULATION RESULTS

To evaluate the influence of different parameters on time resolution, simulations based on CST and MATLAB were carried out.

Assuming that the signal sampling is stable and the initial phase is zero, the main factors that affect the arrival time resolution are signal amplitude, damping time, signal length, and front-end noise. Figure 3 shows the CST simulation results of the cavity probe with a damping time of 100ns. The condition is completed under 100pC bunch charge. After 100MHz BPF filtering, the signal becomes as shown in Figure 4. Some spurious noise and interference signals have been removed. The signal amplitude is about 1.14V (14dBm). Then, the signal is mixed with an ideal LO signal (16dBm) and sampled by a sampling rate of 500MHz. The IF signal result is shown in Figure 5.

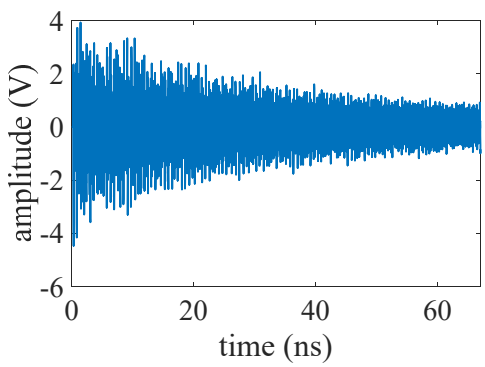

Figure 3: Signal of 100ns damping time by CST.

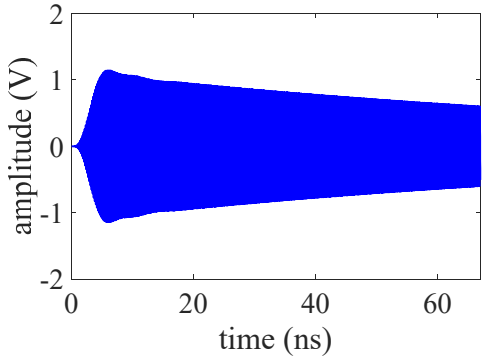

Figure 4: Signal filtered by a 100MHz BPF.

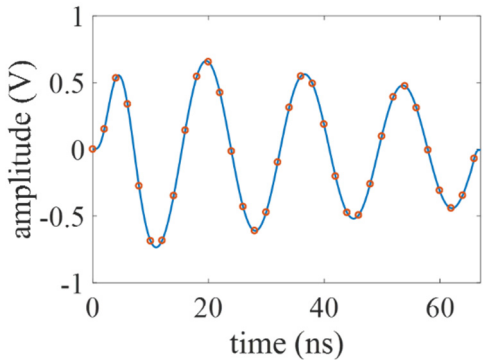

Figure 5: IF signal sampled by 500MHz.

After evaluation, the larger the signal amplitude, the better the phase resolution, as shown in Figure 6. When the signal is not amplified (0.66V), the phase resolution can reach 12fs under 0.1% noise. However, due to the limitation of the ADC acquisition board, when the signal amplitude is close to the ADC full scale (1.1V), the signal needs to be amplified by 1.6 times (4dB). The best phase resolution that this system can achieve is 8fs. This result is only based on an ideal theoretical model.

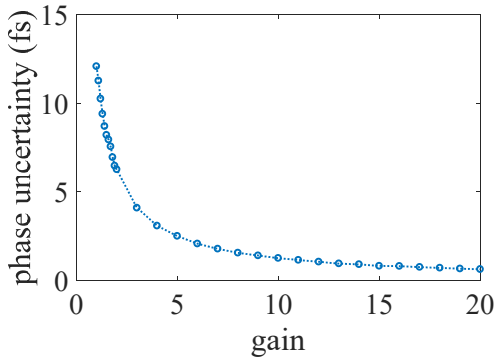

Figure 6: Phase uncertainty of different gain.

CONCLUSIONS

The prototype design of a bunch arrival time measurement system (BAM) based on the cavity monitor was completed. The entire system design and framework were described in detail, including four main modules: cavity probe, RF front-end, local oscillator, and signal acquisition system. The ideal simulation results have been presented.

ISBN: 978-3-95450-222-6 ISSN: 2673-5350 doi:10.18429/JACoW-IBIC2020-WEPP24

When the signal is sampled at full scale, the best phase resolution can reach 8fs, which meets the design requirements.

REFERENCES

[1] W. A. Barletta, et al., "Free electron lasers: Present status and future challenges", *Nucl. Instr. Meth. A*, vol. 618, pp. 69-96, 2010. doi:10.1016/j.nima.2010.02.274

[2] M. Altarelli, et al., "The European x-ray free-electron laser", *Technical Design Report, DESY*. pp. 1–26. 2006.

[3] R. Ganter, "SwissFEL-Conceptual design report", *Technical Design Report, Paul Scherrer Institute (PSI),* 2010.

[4] K. Li and H. Deng, "Systematical design and three-dimensional simulation of X-ray FEL oscillator for Shanghai Coherent Light Facility", *Nucl. Instr. Meth. A*, vol. 895, pp. 40-47, 2018. doi.org/10.1016/j.nima.2018.03.072

[5] S. S. Cao, J. Chen, Y. B. Leng, and R. X. Yuan, "The Application of Beam Arrival Time Measurement at SXFEL", in *Proc. 7th Int. Beam Instrumentation Conf. (IBIC'18)*, Shanghai, China, Sep. 2018, pp. 342-345. doi:10.18429/JACoW-IBIC2018-WEOA04

[6] S.S. Cao, et al., "Optimization of beam arrival and flight time measurement system based on cavity monitors at SXFEL", submitted for published.

[7] M. Hansli *et al.*, "A Beam Arrival Time Cavity for REGAE at DESY", in *Proc. 5th Int. Particle Accelerator Conf. (IPAC'14)*, Dresden, Germany, Jun. 2014, pp. 1820-1822. doi:10.18429/JACoW-IPAC2014-TUPRI104

[8] J. C. Frisch *et al.*, "Femtosecond Operation of the LCLS for User Experiments", in *Proc. 1st Int. Particle Accelerator Conf. (IPAC'10)*, Kyoto, Japan, May 2010, paper TUPE066, pp. 2287-2289.

[9] S. S. Cao, R. Jiang, Y. B. Leng, and R. X. Yuan, "Design and Test of Prototypes of Cavity Beam Position Monitor for SHINE", presented at *the 9th Int. Beam Instrumentation Conf. (IBIC'20)*, Santos, Brazil, Sep. 2020, paper WEPP13, this conference.

Content from this work may be used under the terms of the CC BY 3.0 licence (© 2020). Any distribution of this work must maintain attribution to the author(s), title of the work, publisher, and DOI

ISBN: 978-3-95450-222-6 ISSN: 2673-5350 doi:10.18429/JACoW-IBIC2020-WEPP26

Content from this work may be used under the terms of the CC BY 3.0 licence (© 2020). Any distribution of this work must maintain attribution to the author(s), title of the work, publisher, and DOI

EFFECT OF PHASE MODULATION ON THE TRANSVERSE BEAM SIZE AND EMITTANCE OF THE HLS-II RING*

Yunkun Zhao, Baogen Sun†, Jigang Wang, Fangfang Wu, Sanshuang Jin
National Synchrotron Radiation Laboratory (NSRL),
University of Science and Technology of China (USTC)

Abstract

In this paper, the radio-frequency (RF) phase modulation method is exploited to investigate the variations in the transverse beam size and emittance at Hefei Light Source (HLS-II). Meanwhile, a certain quantitative analysis was performed on the stability and practicability of the beam transverse profile measurement systems. The experiments show that the RF phase modulation method can effectively explore the robustness and stability of beam transverse profile measurement systems over the range of 20.0–22.5 kHz, which is close to the first-harmonic of the synchrotron frequency. It is concluded that when the modulation amplitude of the external phase perturbation is less than 0.04 rad, this optical system can be capable of maintaining reliable and stable working status. This is also useful for analyzing the influence of RF phase noise on the subsequent beam measurement and diagnostics, which including the deterioration of beam quality, emittance blowup, beam jitter, and beam loss.

INTRODUCTION

In the synchrotron radiation (SR) storage ring light sources, it is crucial to real-time high-accuracy monitor the variations of the transverse beam size and emittance. With this in mind, HLS-II is equipped with two transverse beam profile measurement systems as that of the synchrotron light imaging system and interferometric system to precisely measure the beam size, emittance, and energy spread on the basis of the actual measurement requirement [1, 2]. In previous machine experiments, a RF phase modulation method is developed to improve beam lifetime and explore longitudinal beam characteristics in the HLS-II storage ring. However, we found that the transverse beam size and emittance are affected by the parametric resonances resulting from the introduced phase perturbation [3, 4]. Therefore, it is necessary to deeply research and elaborate the variations of beam transverse profile and beam emittance subjected to the external RF phase modulation. It has considerable physical and engineering guiding significance in the operation, commissioning, and beam manipulation of the HLS-II storage ring and our future Hefei Advanced Light Facility (HALF) [5]. Considering that the preliminary machine measurement are carried out in the single-bunch operation mode, we mainly focused on investigating the stability and feasibility of the beam transverse profile measurement systems by use of the changes on the transverse beam size and emittance. Furthermore, the dependence curve of the beam energy spread as a function of the RF phase modulation frequency is further analyzed under different modulation amplitudes.

THE MEASUREMENT PRINCIPLE

As for the HLS-II storage ring, it is noted that the interferometer and imaging system are installed on the dedicated diagnostic beamlines B7 and B8, respectively. Correspondingly, the underlying equations for the transverse beam emittance and energy spread can be separately expressed as

$$\begin{cases} \varepsilon_x = \dfrac{\sigma_{x,\mathrm{B7}}^2\eta_{x,\mathrm{B8}}^2-\sigma_{x,\mathrm{B8}}^2\eta_{x,\mathrm{B7}}^2}{\beta_{x,\mathrm{B7}}\eta_{x,\mathrm{B8}}^2-\beta_{x,\mathrm{B8}}\eta_{x,\mathrm{B7}}^2} \\ \delta = \left(\dfrac{\sigma_{x,\mathrm{B8}}^2\beta_{x,\mathrm{B7}}-\sigma_{x,\mathrm{B7}}^2\beta_{x,\mathrm{B8}}}{\beta_{x,\mathrm{B7}}\eta_{x,\mathrm{B8}}^2-\beta_{x,\mathrm{B8}}\eta_{x,\mathrm{B7}}^2}\right)^{1/2} \end{cases} \tag{1}$$

Where the subscripts B7 and B8 represent the parameters at the light source points respectively, ε_x for the horizontal beam emittance, δ for the beam energy spread, η_x for the dispersion function in the horizontal direction, σ_x for the horizontal beam size, and β_x for the beta function in the horizontal plane, x. Similarly, the vertical beam emittance can be obtained by

$$\varepsilon_y = \sigma_y^2/\beta_y \tag{2}$$

Here, σ_y and β_y indicate the beam size and beta function in the vertical direction y, respectively. To the best of our knowledge, the applied external RF phase modulation will bring about the obvious parametric resonances in the case that the modulation frequency is close to an integral multiple of the synchrotron oscillation frequency. In the case that the modulation frequency of the RF system approaches to a single harmonic of the synchrotron frequency, which corresponding to the standard Hamiltonian equation related to the charged particle motion can be described by [3, 4]

$$\langle H_1 \rangle_t = (\omega_s - \omega_m) J - \frac{\omega_s J^2}{16} - \frac{\omega_s a_m}{2}(2J)^{\frac{1}{2}} \cos\psi - \omega_s \tag{3}$$

In Eq. (3), it is worth pointing out that the systematic Hamiltonian formalism is an invariant. ω_s denotes the synchrotron oscillation angular frequency, which is equal to $\omega_s = 2\pi f_s$, where f_s represents the synchrotron frequency. Whereas ω_m denotes the modulation angular frequency of the external RF noise that is equivalent to $\omega_m = 2\pi f_m$, in which f_m represents the modulation frequency, and a_m represents the phase

* Work supported by the National Natural Science Foundation of China under Grant 11575181, Grant 51627901 and Grant 11705203, the Anhui Provincial Natural Science Foundation under Grant 1808085QA24, and the Fundamental Research Funds for the Central Universities under Grant WK2310000080
† bgsun@ustc.edu.cn

ISBN: 978-3-95450-222-6 ISSN: 2673-5350 doi:10.18429/JACoW-IBIC2020-WEPP26

error modulation amplitude. It is noted that J and ψ denotes the action-angle coordinates. In terms of the aforementioned theoretical Eq. (3) and in combination with the characteristic parameters of the HLS-II storage ring, we simulated the particle motion trajectories at different modulation amplitudes for the case of the RF modulation frequency approaching to the synchrotron frequency, as shown in Fig. 1.

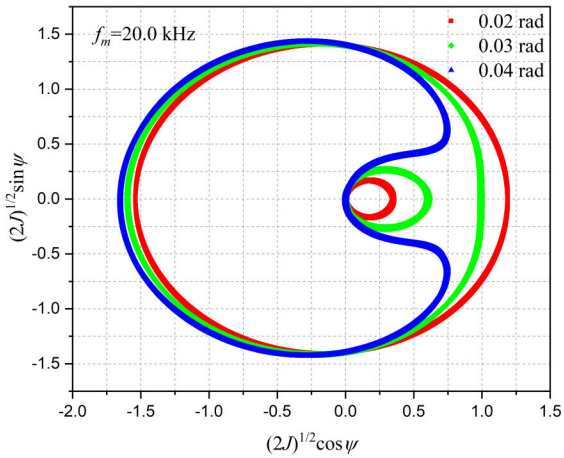

Figure 1: The particle trajectories under different RF phase modulation amplitudes (f_s = 21.3 kHz and f_m = 20.0 kHz).

In Fig. 1, the red square, green diamond, and blue triangle stand for the Hamiltonian tori with the modulation amplitudes of 0.02, 0.03, and 0.04 rad, respectively. For the sake of simplicity and convenience, it is mentioned that the simulated Hamiltonian torus in phase space is chosen to be the modulation frequency of 20.0 kHz. It can be clearly seen that the introduction of the phase noise has a great impact on the charged particle motion trajectory and bunch volume. The main reason is attributed to the parametric resonance effect and the beam dilution theory. It should be emphasized that this method can give rise to the deterioration of beam emittance in the case of improving beam lifetime and suppressing beam instability. As a consequence, we aim to investigate the variations of beam characteristic parameters which including transverse beam size, emittance and energy spread related to phase modulation. There is no doubted that this has outstanding importance on machine research and beam dynamics analysis at the HLS-II storage ring.

EXPERIMENTAL SETUP AND RESULTS

According to the above-mentioned theoretical analysis, in which the experimental arrangement is distinctly depicted in Fig. 2.

As shown in Fig. 2, it can be clearly observed that the experimental measurement system is mainly composed of the RF system, the synchrotron light interferometer system, and the synchrotron light imaging system. Note that the interferometer and the imaging system are installed on the source points B7 and B8, respectively. The interferometer system is divided into horizontal and vertical interferometer, which are employed for measuring the horizontal and

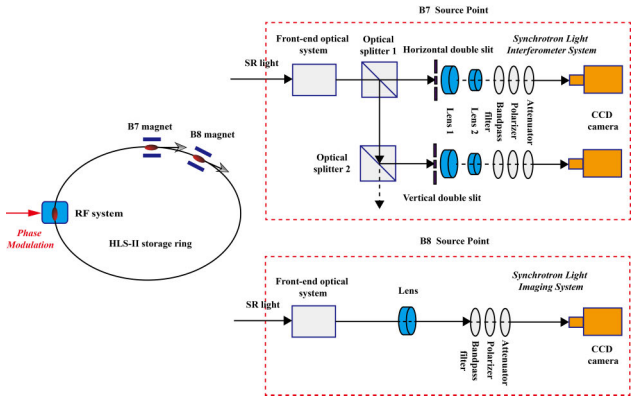

Figure 2: Schematic diagram of the experimental measurement system.

vertical beam size, respectively. In comparison, the imaging system is relatively simple and compact, which is the most direct universal beam profile measurement method. It should be pointed out that the optical attenuator is being taken to modulate the light intensity to avoid the damage to CCD camera. With regard to the polarizer, whose role is to extract the polarization component of the SR light. In addition, it is emphasized that the band-pass filter is utilized for selecting the spectrum of the SR light and reducing the influence of chromatic aberration. To do that we can real-time monitor the beam size and emittance using the two beam transverse profile measurement systems.

In Fig. 2, it is especially mentioned that the RF phase modulation method is developed for investigating and analyzing the changes of beam size and emittance. It is well-known that the introduction of phase noise into RF system can obviously affect the beam performance in the HLS-II storage ring. Consequently, we are devoted to explore the stability, measurement accuracy and applicability of the beam transverse profile measurement system in view of the external RF phase disturbance. The measured results are shown in Figs. 3 and 4, respectively.

As plotted in Fig. 3, (a) and (b) indicate the dependence curves of the horizontal beam size and emittance with modulation frequency, respectively. Nevertheless, Fig. 4, (a) and (b) separately reveal the variations of beam size and emittance in vertical direction as increasing the modulation frequency. Here, the blue square, green circle, and magenta triangle signify the changes of the transverse beam size and emittance with the increase of the RF phase modulation frequency at the modulation amplitudes of 0.02, 0.03 and 0.04 rad. It is apparent that the measured values have obvious discrepancy when increasing the modulation amplitude in vicinity of the synchrotron frequency 20.0–22.5 kHz. This is mainly originated from the parametric resonance effect caused by the external RF phase noise, of which can manipulate bunch electron density and simultaneously bring perturbation to the beam. It is directly observed that when the modulation amplitude is increased to 0.04 rad, which results in the beam transverse profile measurement systems

Content from this work may be used under the terms of the CC BY 3.0 licence (© 2020). Any distribution of this work must maintain attribution to the author(s), title of the work, publisher, and DOI

ISBN: 978-3-95450-222-6 ISSN: 2673-5350 doi:10.18429/JACoW-IBIC2020-WEPP26

Content from this work may be used under the terms of the CC BY 3.0 licence (© 2020). Any distribution of this work must maintain attribution to the author(s), title of the work, publisher, and DOI

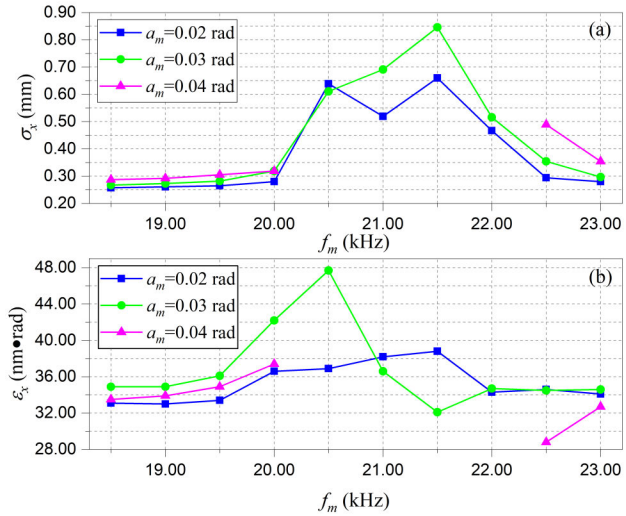

Figure 3: The change cure of the horizontal beam size and emittance versus the modulation frequency.

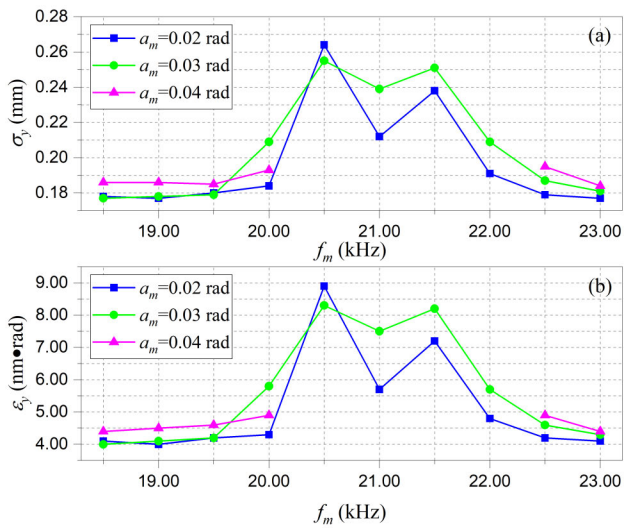

Figure 4: The change cure of the vertical beam size and emittance with respect to the modulation frequency.

can no longer accurately measure the beam size and emittance as a result of the violent bunch jitter and oscillation. Additionally, it will bring about these systems to fail to maintain the stable operation state. Therefore, in order to ensure the measurement reliability and feasibility of the beam transverse profile measurement systems, the tolerance level of the experimental system associated with the external RF phase noise should be avoided no more than 0.04 rad.

It is noted that the resolution of the beam transverse profile measurement systems are also affected by the depth of field effect and the curvature error. Besides, the installation error of the optical system and environmental disturbances also give rise to the measurement error. However, the error caused by these external factors to the optical measurement system is approximately several micrometers, which is much lower than the sudden variation in the beam size being attributed to RF phase noise. In summary, the simple and flexible RF phase modulation method in the sense that is capable of roughly and intuitively providing the useful guidance for accelerator operation and commissioning.

In addition, we also further measured the change in beam energy spread under the case of the external RF phase modulation in the experiment accordingly, as shown in Fig. 5.

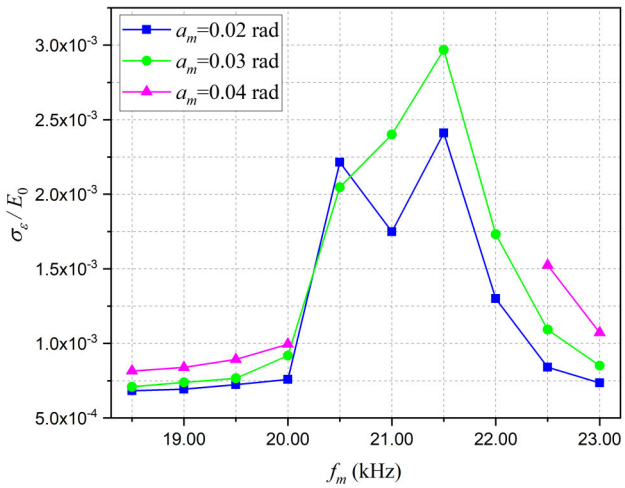

Figure 5: The beam energy spread variation curve via the modulation frequency at different modulation amplitudes.

From Fig. 5, it is evident that there is a severe variation on beam energy spread under the condition of the phase modulation ranging from 20.0 to 22.5 kHz. This means that this RF phase modulation approach has a great impact on beam performance. In the future research work, we will attempt to further expand the application scenarios based on this phase modulation method, of which including improving beam performance, analyzing RF noise, and studying the beam instability of the HLS-II storage ring.

CONCLUSION

In general, it is desirable to explore and discuss the stability, feasibility and practicability of the beam transverse profile measurement systems on the HLS-II storage ring by means of the RF phase modulation method. It has demonstrated that these beam transverse profile measurement systems can be effective of maintaining measurement reliability in the case of the modulation amplitude of the external phase noise is less than 0.04 rad within the range of 20.0–22.5 kHz. At the same time, this phase modulation approach is of great significance to the operation, machine research and beam diagnosis of the HLS-II storage ring. Furthermore, it can provide feasible suggestions and ideas for researching the physical phenomena such as emittance dilution, beam jitter, and beam loss in the synchrotron storage ring light sources.

ACKNOWLEDGEMENTS

This work was supported in part by the National Natural Science Foundation of China under Grant 11575181, Grant 51627901 and Grant 11705203, the Anhui Provincial Natural

ISBN: 978-3-95450-222-6 ISSN: 2673-5350 doi:10.18429/JACoW-IBIC2020-WEPP26

Science Foundation under Grant 1808085QA24, and the Fundamental Research Funds for the Central Universities under Grant WK2310000080.

REFERENCES

[1] K. Tang *et al.*, "Transverse beam size measurement system using visible synchrotron radiation at HLS II", *Chinese Phys. C*, vol. 40, no. 9, p. 097002, 2016. doi:10.1088/1674-1137/40/9/097002

[2] C. Cheng *et al.*, "Beam size and position measurement based on logarithm processing algorithm in HLS II", *Chinese Phys. C*, vol. 40, no. 4, p. 047004, 2016. doi:10.1088/1674-1137/40/4/047004

[3] H. Huang *et al.*, "Experimental determination of the Hamiltonian for synchrotron motion with rf phase modulation", *Phys. Rev. E*, vol. 48, no. 6, pp. 4678–4688, 1993. doi:10.1103/PhysRevE.48.4678

[4] N. P. Abreu *et al.*, "Longitudinal dynamics with rf phase modulation in the Brazilian electron storage ring", *Phys. Rev. ST Accel. Beams*, vol. 9, no. 12, pp. 124401, 2006. doi:10.1103/PhysRevSTAB.9.124401

[5] P. Yang *et al.*, "Design of a hybrid ten-bend-achromat lattice for a diffraction-limited storage ring light source", *Nucl. Instrum. Meth. A*, vol. 943, p. 162506, 2019. doi:10.1016/j.nima.2019.162506

Content from this work may be used under the terms of the CC BY 3.0 licence (© 2020). Any distribution of this work must maintain attribution to the author(s), title of the work, publisher, and DOI

ISBN: 978-3-95450-222-6 ISSN: 2673-5350 doi:10.18429/JACoW-IBIC2020-WEPP27

AN ALTERNATIVE PROCESSING ALGORITHM FOR THE TUNE MEASUREMENT SYSTEM IN THE LHC

L. Grech*, G. Valentino
Department of Communications and Computer Engineering, University of Malta, Msida, Malta
D. Alves, M. Gasior, S. Jackson, R. Jones, T. Levens, J. Wenninger
Beams Department, CERN, Geneva, Switzerland

Abstract

The betatron tune in the Large Hadron Collider (LHC) is measured using a Base-Band-Tune (BBQ) system. Processing of these BBQ signals is often perturbed by 50 Hz noise harmonics present in the beam. This causes the tune measurement algorithm, currently based on peak detection, to provide tune estimates during the acceleration cycle with values that clearly oscillate between neighbouring harmonics. The LHC tune feedback cannot be used to its full extent in these conditions as it relies on stable and reliable tune estimates. In this work we present two alternative tune measurement algorithms, designed to mitigate this problem by ignoring small frequency bands around the 50 Hz harmonics and estimating the tune from spectra with gaps. One is based on Gaussian Processes and the other is based on a weighted moving average. We compare the tune estimates of the new and present algorithms and put forward a proposal that can be implemented during the renovation of the BBQ system for the next physics run of the LHC.

INTRODUCTION

The tune (Q) of a circular accelerator is defined as the number of betatron oscillations per turn [1]. This is a critical parameter in the Large Hadron Collider (LHC) which has to be monitored and corrected in order to ensure stable operations [2] and adequate beam lifetime. The Base-Band Q (BBQ) system in the LHC is used to measure the tune. It essentially consists of an electromagnetic pickup followed by a diode-based detection and acquisition system [3]. The diode detectors pick-up a small modulation caused by betatron motion on the large beam intensity pulses and converts it to baseband, which for the LHC is in the audible frequency range. The BBQ system in the LHC is sensitive enough to not require that the beam is externally excited in order to measure the tune, picking-up the residual beam oscillations. This normally results in a frequency spectrum where the tune is the dominant peak [3, 4].

Since the start of the LHC, spectral components at harmonics of the 50 Hz mains frequency have been observed with several different diagnostic systems [5]. Studies have shown that these modulations are on the beam itself, although their source is unclear. These harmonics are clearly visible in the BBQ system, resulting in a frequency spectrum polluted with periodic lines every 50 Hz (Fig. 1). Since these harmonics are also present around the betatron tune, they are a potential source of error for the tune estimation algorithm. The current tune estimation algorithm applies a series of filters and averaging techniques which have been developed in order to mitigate the impact of the 50 Hz harmonics on the final measured value. However, it is not uncommon to have the estimated tunes oscillate between neighbouring 50 Hz harmonics. The fact that the tune estimate locks-in to a particular ~50 Hz harmonic is clearly not desirable. On top of that, having the tune jump from one line to another affects the tune feedback system, causing it to switch off as a protective measure against unstable behaviour.

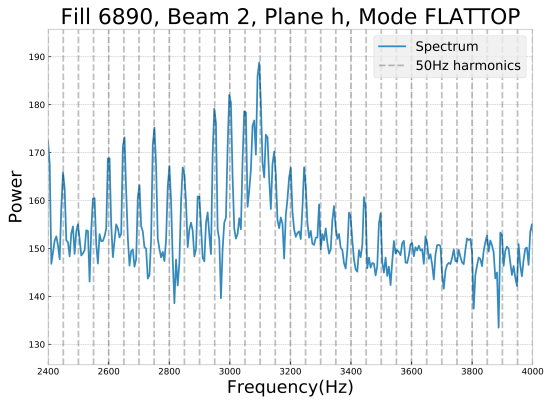

Figure 1: Example of 50 Hz harmonics present in the BBQ spectrum.

In this paper, we present a study on alternative approaches for the tune estimation algorithm. The common underlying idea is to mask-out the 50 Hz harmonics from the frequency spectrum of the BBQ signal. Following this, a polynomial fit, a weighted moving average and Gaussian Processes have been selected for comparison in terms of tune estimation performance.

We begin by describing the presently implemented tune estimation algorithm and then proceed to describe the proposed alternatives. We then perform a thorough comparison of all methods by simulating numerous plausible BBQ spectra for different tune values and widths. Finally we show two examples with comparisons between all three methods applied to recorded BBQ data and finish with concluding remarks.

* leander.grech@um.edu.mt

Content from this work may be used under the terms of the CC BY 3.0 licence (© 2020). Any distribution of this work must maintain attribution to the author(s), title of the work, publisher, and DOI

ISBN: 978-3-95450-222-6 ISSN: 2673-5350 doi:10.18429/JACoW-IBIC2020-WEPP27

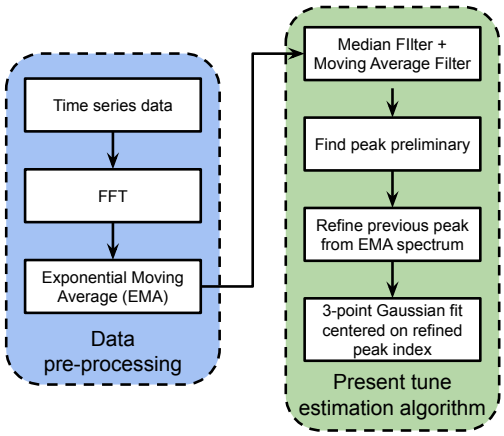

Figure 2: Present algorithm diagram.

PRESENT TUNE ESTIMATION ALGORITHM

The present tune measurement system is normally configured to provide a spectrum of 1024 frequency bins at a rate of 6.25 Hz. Since the original signal is sampled at the LHC revolution frequency of approximately 11 kHz, the spectral resolution is approximately 5.5 Hz. The set of sequential processing blocks which form the present tune estimation algorithm is depicted in Fig. 2. First, each calculated spectrum update is passed through a bank of independent exponential moving average filters, each of them working on a single frequency bin. This pre-processing stage is essentially used to reduce spectral noise. Median and average filters are subsequently applied to the spectrum to increase its smoothness and mitigate the effect of the 50 Hz harmonics. At this stage the frequency corresponding to the maximum value of the processed spectrum is taken. This frequency is subsequently refined by going back to the output of the bank of exponential moving averages and performing a Gaussian fit of the spectral region in its immediate vicinity.

ALTERNATIVE ALGORITHMS

With a spectral resolution of 5.5 Hz, changes of the mains frequency at the percent level hardly impact the centre and width of the spectral regions containing the 50 Hz harmonics. Therefore, the periodic regions with the observed 50 Hz harmonics remain fairly unchanged. These regions have a finite width mainly due to the effect of the jitter on the 50 Hz mains frequency coupled with the smoothing introduced by the spectral filter bank.

With this in mind, we have added an extra pre-processing stage immediately after the exponential moving average filter bank which removes the spectral points lying inside the affected regions. The reasoning behind this stage is that the information contained in this region is completely dominated by the presence of the 50 Hz harmonics peaks and can often mask the true tune peak. Furthermore, even if the tune itself happens to be on top of a 50 Hz dominated region, and since the overall number of disregarded points will be less than a fourth of the total number of points, the spectral baseline can still be recovered. This leaves us with an overall smoothed-out spectrum which contains periodic gaps every 50 Hz.

The approach we propose is to employ algorithms capable of handling non-uniformly sampled signals (in this case, spectra with frequency gaps) for interpolation prior to retrieving the maximum of the spectral baseline, corresponding to the true tune value.

The first naive approach was to fit a polynomial over the spectrum with gaps, however it was observed that a 10^{th} order or higher polynomial is needed to obtain a close fit. This approach did not prove to be very reliable, especially at the extremities of the spectrum, where the quality of the fit is worst, resulting in poor estimates of the tune frequency.

We will now describe two more promising algorithms considered in this study.

Weighted Moving Average

The second algorithm which was attempted was a Weighted Moving Average (WMA). Here we consider a sliding window of size $2L + 1$, where the weight of each component within the window depends on its distance from the center of the window. Therefore:

$$\hat{y}_i(L) = \frac{\sum_{j=-L}^{L} w(j, L) \times y_{i+j}}{\sum_{j=-L}^{L} w(j, L)}$$

where:

$$w(k, L) = \begin{cases} L - |k| & , \text{if } \exists\, y_{i+j} \\ 0 & , \text{if } \nexists\, y_{i+j} \end{cases} \quad (1)$$

Here the second case of Eq. (1) occurs at the edges of the spectrum and where a frequency bin has been removed to form a gap. When setting up the algorithm, one has to take care to make the sliding window greater than the size of the largest gap in the array to avoid that the averaging is performed within the gap.

Gaussian Processes

The third algorithm uses a Bayesian modelling approach with Gaussian Processes where, by using the available data points, a statistical model is built which includes all the uncertainty introduced in the data when the 50 Hz harmonics are removed from the dataset. Gaussian Processes can be thought of as a distribution of functions where, by drawing a sample from the distribution, one of the infinitely possible functions described by the Gaussian Process is obtained [6]. Such a sample function is drawn from a multi-variate normal distribution:

$$f(X) \sim \mathcal{N}(\mu = m(x), \Sigma = k(X, X)) \quad (2)$$

where $m(x)$ is usually assumed to be a zero vector and $k(X, X)$ is a positive definite covariance function. The aim would ultimately be to predict the output, y_2, of some input dataset, X_2. Given some previously observed data, (X_1, Y_1),

Content from this work may be used under the terms of the CC BY 3.0 licence (© 2020). Any distribution of this work must maintain attribution to the author(s), title of the work, publisher, and DOI

ISBN: 978-3-95450-222-6 ISSN: 2673-5350 doi:10.18429/JACoW-IBIC2020-WEPP27

Content from this work may be used under the terms of the CC BY 3.0 licence (© 2020). Any distribution of this work must maintain attribution to the author(s), title of the work, publisher, and DOI

a covariance matrix, Σ, can be built. Σ models the joint variability of the input variables via a prior function, also known as a kernel. One such kernel is the exponentiated quadratic kernel, or Radial Basis Function (RBF) kernel, which uses the squared Euclidean distance between points x_a and x_b as a measure of correlation between the points:

$$k(x_a, x_b) = e^{-\frac{1}{2\sigma^2}\|x_a - x_b\|^2} \quad (3)$$

Here σ is a free parameter controlling the smoothness of the resulting distribution. Under these conditions a new distribution can be derived, which takes in the observations from (X_1, Y_1) to make predictions over a new input dataset, X_2:

$$P(y_2 \mid y_1, X_1, X2) \sim \mathcal{N}(\mu_{2|1}, \Sigma_{2|1}) \quad (4)$$

where:

$$\mu_{2|1} = \left(\Sigma_{11}^{-1}\Sigma_{12}\right)^\top y_1$$
$$\Sigma_{2|1} = \Sigma_{22} - \left(\Sigma_{11}^{-1}\Sigma_{12}\right)^\top \Sigma_{12}$$
$$\Sigma_{ab} = k(X_a, X_b)$$

BENCHMARKING

When it comes to real experimental data, it is not possible to know the precise value of the tune. As a consequence, we decided to do the performance evaluation of these algorithms via multiple spectral simulations of second-order systems where we know the true value of the tune. The spectrum of a second-order system is given by:

$$G(\omega) = \frac{\omega_{\text{res}}^2}{\sqrt{(2\omega\omega_{\text{res}}\zeta)^2 + (\omega_{\text{res}}^2 - \omega^2)^2}} + \mathcal{N}(0, \sigma), \quad (5)$$

where the resonant frequency, i.e. the true tune value, is given by:

$$\omega_{\text{res}}^{\text{true}} = \sqrt{1 - 2\zeta^2}\omega_{\text{res}}. \quad (6)$$

Here ζ is a damping factor that controls the width of the resonance, and $\mathcal{N}(0, \sigma)$ an additive spectral noise term. Since the motion of a particle in a circular accelerator can be described by a Hill's equation we can assume that the frequency spectrum of the beam as seen by the BBQ system is approximated by that of second-order system.

A Monte Carlo approach was used to sample the resonant frequencies and the damping factors which were used to simulate the frequency spectrum of the beam. Moreover Gaussian noise, as well as 50 Hz harmonics were artificially introduced into the simulated spectrum. By using this approach, the reliability of these algorithms could be impartially assessed.

The resonant frequencies were sampled from a normal distribution with a mean of 3 kHz and a standard deviation of 200 Hz, while the damping factors were sampled from a uniform, logarithmic distribution of base 10 within the range $[10^{-4}, 10^{-1}]$ corresponding to different tune resonance widths. These ranges were chosen to mimic real experimental observations. Figure 3 shows an example of a simulated spectrum having a resonant frequency of 3 kHz and ζ of 0.01. The simulated spectrum also has 50 Hz harmonics and Gaussian noise superimposed. On the same figure, the orange plot shows the resulting spectrum with gaps, after dropping all the data within a 10 Hz window around each harmonic.

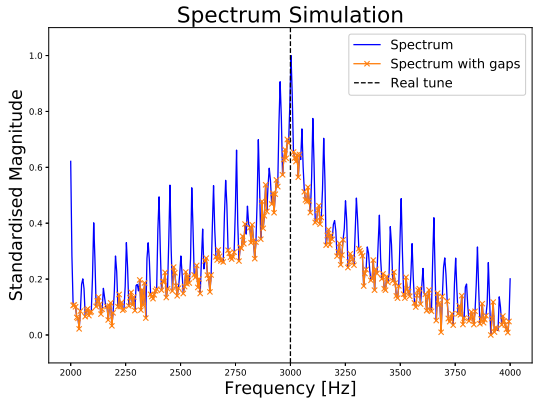

Figure 3: Example of a simulated spectrum with f_{rev} = 3 kHz and $\zeta = 0.01$.

For each simulated spectrum, all four algorithms were used to estimate the tune, and the statistics of the estimation error assessed in order to benchmark the different approaches. The Weighted Moving Average (WMA) was performed using three different window sizes (10, 30, 60), while the Gaussian Process (GP) was performed using three different length scales (25, 70, 130), where the length scale is associated with the σ free parameter as seen in Eq. (3). The polynomial fit was of degree 15 and the original algorithm (BQ) as presently implemented in the online system was faithfully re-implemented in order to be compared against the new algorithms.

RESULTS

Monte Carlo Simulation Results

An overview of the statistics of the tune estimation errors obtained from the Monte Carlo simulation can be seen in Fig. 4 and in Table 1. The first observation one can make is that there seems to be a similar systematic error in the BQ, WMA60 and GP130 algorithms. There is also a smaller systematic error in GP70 and WMA30. GP25 and WMA10 show a higher accuracy, in the sense that the mean of the errors is centred almost perfectly around 0, however they seem to lack the precision of BQ, GP70, GP130, WMA30 and WMA60. POLY15 shows a small systematic error, but a poor precision when compared to all the other methods.

Another important aspect that is shown in Table 1 is the worst case estimation error, directly related to the tails of the distribution. Overall, it seems that algorithms set up to achieve high accuracy have a poorer precision. This suggests that there is a trade-off of between precision and accuracy that can be controlled by the parameters of each algorithm.

ISBN: 978-3-95450-222-6 ISSN: 2673-5350 doi:10.18429/JACoW-IBIC2020-WEPP27

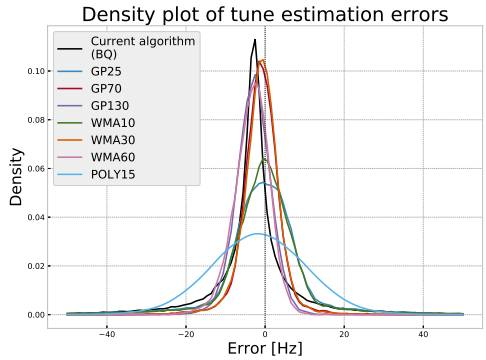

Figure 4: Density plot of the errors from the Monte Carlo simulation. In the legend, WMA30 refers to WMA with a window of size 30, GP130 refers to GP with a length scale of 130, and so on.

Table 1: Tune Estimation Error Statistics

Algorithm	μ[Hz]	σ[Hz]	Max abs err[Hz]
BQ	-3.0	12.8	114.7
GP25	-0.2	12.4	119.1
GP70	-1.1	5.2	43.8
GP130	-3.0	4.4	22.3
WMA10	-0.2	11.6	119.0
WMA30	-1.0	4.9	98.4
WMA60	-3.4	4.6	144.1
POLY15	-2.5	82.8	1371.8

Performance with Real Data

Figures 5 and 6 show two examples of reasonably performing configurations of both WMA and GP when applied to real spectra from the BBQ system. From Fig. 5 one can see that the general tune estimates of the three algorithms are comparable in terms of accuracy. However, zooming-in (Fig. 6) we can see how the BQ algorithm is affected by the presence of the 50 Hz harmonics with large downward spikes which do not completely reach the harmonic frequency due to the Gaussian fit. It can also be seen from this figure that the WMA10 estimates seem to be more stable than those from both the BQ and GP algorithms.

CONCLUSION

A new approach based on the rejection of spectral points affected by 50 Hz harmonics is proposed to improve tune measurements at the LHC. In line with this approach, three methods were benchmarked against the presently implemented tune estimation algorithm which is known to underperform in the presence of these polluting harmonic components.

A Monte-Carlo simulation of second-order system frequency spectra was performed in order to generate spectra which mimic real beam spectra but for which the tune value is exactly known. The results obtained indicate that when properly configured both the WMA and GP algorithms can

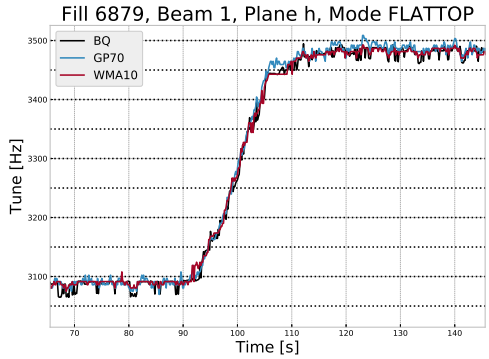

Figure 5: Tune trace plot with real data during the tune change when reaching FLATTOP.

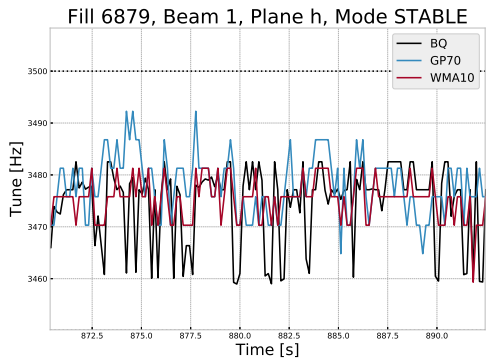

Figure 6: Tune trace plot with real data from STABLE beams.

achieve a better performance than the current algorithm in terms of accuracy and precision. Examples using real experimental spectra confirm this observation, with the WMA algorithm performing best.

This study will now be extended to more algorithms with the aim of selecting the most robust, accurate and precise one for real-time implementation on the LHC.

REFERENCES

[1] S. Baird, "Accelerators for pedestrians", CERN, Geneva, Switzerland, Rep. AB-Note-2007-014, Feb. 2007.

[2] R. J. Steinhagenm, "LHC Beam Stability and Feedback Control-Orbit and Energy", Ph.D. thesis, RWTH Aachen U., Aachen, Germany, 2007.

[3] M. Gasior and O. R. Jones, "High Sensitivity Tune Measurement by Direct Diode Detection", in *Proc. DIPAC'05*, Lyon, France, Jun. 2005, paper CTWA01, pp. 312–314.

[4] M. Gasior, "Tuning the LHC", *BE Newsletter*, no. 4, pp. 5–6, May 2012. Rep. CERN-BE-Note-2017-004.

[5] S. Kostoglou, G. Arduini, L. Intelisano, Y. Papaphilippou, and G. Sterbini, "Impact of the 50 Hz harmonics on the beam evolution of the Large Hadron Collider". arXiv:2003.00140

[6] C. E. Rasmussen and C. K. I. Williams, *Gaussian Processes for Machine Learning*, The MIT Press, 2006.

Content from this work may be used under the terms of the CC BY 3.0 licence (© 2020). Any distribution of this work must maintain attribution to the author(s), title of the work, publisher, and DOI

ISBN: 978-3-95450-222-6 ISSN: 2673-5350 doi:10.18429/JACoW-IBIC2020-WEPP28

Content from this work may be used under the terms of the CC BY 3.0 licence (© 2020). Any distribution of this work must maintain attribution to the author(s), title of the work, publisher, and DOI

HIGH-ACCURACY DIAGNOSTIC TOOL FOR BEAM POSITION MONITOR TROUBLESHOOTING IN SSRF BASED ON CLUSTERING ANALYSIS *

R. T. Jiang†[1], Y. B. Leng†[1], C. Jian[1]

[1] Shanghai Advanced Research Institute, Chinese Academy of Sciences, Shanghai, 201204, China

Abstract

Beam position monitors (BPMs) are important to monitor the beam moving steadily. In spite of some data is viewed and analysed, a large fraction of data has never been effectively analysed in accelerator operation. It lead to some useful information not coming to the surface during the beam position monitor troubleshooting processing.

We will describe in this paper our efforts to use clustering analysis techniques to pull out new information from existing beam data. Our focus has been to look at malfunction of BPM, associating basic running data that is β oscillation of X and Y directions, energy oscillation and doing predictive analysis. Clustering analysis results showed that 140 BPMs could be classified into normal group and fault group and abnormal BPM could be separated. Based on the results, the algorithm could locate fault BPM and it could be an effective supplement for data analysis in accelerator physics.

INTRODUCTION

The storage ring in SSRF is equipped with 140 BPMs located at 20 cells of the storage ring to monitor the beam dynamics[1] . Each one can give a specific signal that can indicate some properties of the beams at its position individually. Usually, these BPMs are used to inform the accelerator physicists and operators the local status of the beams, such as the beam position and (relative) beam current or lifetime. Meanwhile, the BPM also serve as the orbit feedback system to ensure stability of the beam dynamics[2]. Comparing the measured and computed values of the beam dynamics at each position, one can tell how well the state of runtime accelerator. It could literally see that the BPMs are the eyes and ears for the SSRF. However, a typical BPM system consists of the probe (button-type or stripline-type), electronics (Libra Electronics/ Brilliance in SSRF) and transferring component (cables and such), and complex composition parts easily lead lots of failure. Ever since the SSRF commissioning in 2009, the BPM have occurred all kinds of malfunction. They were permanently damage of individual probe or corresponding cable, misaligned (position/angle) probes, high-frequency vibrations, electronics noise, and others. These faults mean useless of the signals from the BPM and seriously affect the light source supply time. Hence, it is essential to find an effective tool to detect the faulty BPM for operation of the storage ring.

In our study, we put much effort into real-time processing of data, in order to present to operators results that allow them to either diagnose the health of the system or have a signal on which to perform some optimization process. With development in machine learning methods, a series of powerful analysis approaches make it possible for detecting beam position monitor's stability. Cluster analysis is one of machine learning methods. It is aimed at classifying elements into categories on the basis of their similarity[3]. Its applications range from astronomy to bioinformatics, bibliometric, and pattern recognition. Clustering by fast search and find of density peaks is a new approach based on the idea that cluster centres are characterized by a higher density than their neighbours and by a relatively large distance from points with higher densities[4]. This idea forms the basis of a clustering procedure in which the number of clusters arises intuitively, outliers are automatically spotted and excluded from the analysis. It is able to detect non-spherical clusters and automatically find the correct number of clusters. Based on the advantage of clustering by fast search and find of density peaks, this study establish a multi-dimensional clustering analysis model and monitor the running status of accelerator malfunction.

EXPERIMENTAL DATA AND ANALYSIS METHOD

In this study, the experimental data were collected from the BPM turn-by-turn (TBT) data under the different beam intensity, respectively, are 69 mA 73 mA 78 mA 88 mA 90 mA 96 mA 100mA 104mA 108 mA 111 mA 115 mA 120 mA 124 mA 130 mA 134 mA 140 mA 144 mA 157 mA. By analysing the raw data, we extracted the data of transverse oscillation of X and Y direction, energy oscillation data to judge the faulty BPM. A multi-dimensional clustering analysis model was established and the three characteristic factors were the iuput variables to locate the BPM malfunctions at different beam intensity. The model has a assumptions that cluster centres are surrounded by neighbours with lower local density and that they are at a relatively large distance from any points with a higher local density. For each data point i, it will compute two quantities: its local density ρi and its distance δi from points of higher density. Both these quantities depend only on the distances dij between data points, which are assumed to satisfy the triangular inequality. The local density ρi of data point i is defined as

* Work supported by Chinese Academy of Sciences Key Technology Talent Program
† jiangruitao@sinap.ac.cn
† lengyongbin@sinap.ac.cn

ISBN: 978-3-95450-222-6 ISSN: 2673-5350 doi:10.18429/JACoW-IBIC2020-WEPP28

$$\rho_i = \sum_j \chi(d_{ij} - d_c) \qquad (1)$$

where χ (x) =1 if x < 0 and χ (x)=0 otherwise, and dc is a cutoff distance. Basically, ρi is equal to the number of points that are closer than dc to point i. The algorithm is sensitive only to the relative magnitude of ρi in different points, implying that, for large data sets, the results of the analysis are robust with respect to the choice of dc. In this paper, the dc is 0.02. On the other hand, δi is measured by computing the minimum distance between the point i and any other point with higher density:

$$\delta_i = \min_{j:\rho_j > \rho_i} (d_{ij}) \qquad (2)$$

For the point with highest density, we conventionally take $\delta_i = \max_j (d_{ij})$. Note that δi is much larger than the typical nearest neighbour distance only for points that are local or global maxima in the density. Thus, cluster centres are recognized as points for which the value of δi is anomalously large. Generally, the value of δi and ρi represent whether the point is cluster centre, the typical characteristic of cluster centre is the value of δi and ρi are larger. Decision graph could depict the value of δi and ρi and show which points are cluster centre.

RESULTS AND DISCUSSION

In the data processing, the BPM signals are the average of 140 ID* 2048 turns at different beam intensity. Figure 1 showed that the analysis result under the 157 mA beam intensity. Theoretically, the farther away the reference value 1, the more easily faulty of BPMs. 75# and 68# BPMs could be the malfunction of BPMs, because they are far away the reference value 1.

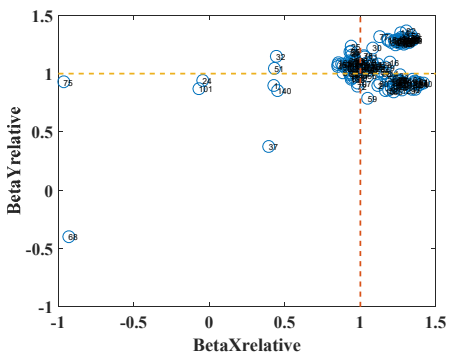

Figure 1: Scatter diagram of cluster analysis based on transverse oscillation of X and Y direction.

Meanwhile, it could see that the all BPMs could be classified three categories from the scatter diagram. In order to verify the observation results, we calculate the decision graph is showed in Figure 2. Theoretically, faulty BPMs corresponds to the smaller ρ and the larger δ , cluster cores mean the larger ρ and the larger δ[5]. So it could be drawed a conclusion that 75# and 68# are faulty BPMs and the 127#,105# and 47# BPMs represents three cluster cores. In order to find out which BPM belongs to one of the three categories, the model give answer and Fig.3 shows the clustering results of all BPMs.

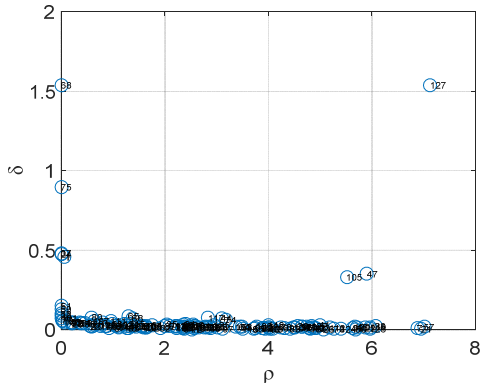

Figure 2: Decision graph.

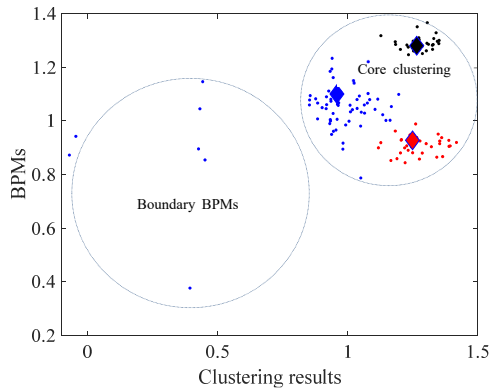

Figure 3: Clustering results for all BPMs.

The clustering results with respect to all BPM are shown in Figure 3. From the clustering results, 140 BPMs can be classified into three normal group and boundary BPMs. And that, the abnormal BPMs are filtered out in Figure 3. According to the absence number, we can find the abnormal BPMs are 68# and 75#.

To ensure the accuracy of clustering results, the input variables increase to three for the multi-dimensional clustering analysis model. They are, respectively, transverse oscillation of X and Y direction and energy oscillation. The result is shown in Figure 4.

Content from this work may be used under the terms of the CC BY 3.0 licence (© 2020). Any distribution of this work must maintain attribution to the author(s), title of the work, publisher, and DOI

ISBN: 978-3-95450-222-6 ISSN: 2673-5350 doi:10.18429/JACoW-IBIC2020-WEPP28

Content from this work may be used under the terms of the CC BY 3.0 licence (© 2020). Any distribution of this work must maintain attribution to the author(s), title of the work, publisher, and DOI

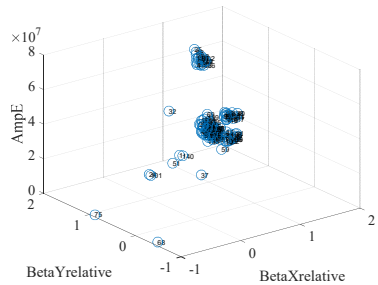

Figure 4: Scatter diagram based on transverse oscillation of X , Y direction and energy oscillation.

Based on the multi-dimensional clustering analysis model, the research results showed that no matter the input variables are two or three, the faulty BPMs are both 68# and 75#. It illustrated that the faulty BPMs are not sensitive to the beam characteristic, so we can be sure that they are faulty. The analysis results are shown in the Table 1.

Table 1: The Analysis Results of Cluster Analysis

BI/mA	Faulty BPMs		Cluster Cores		
157mA	68#	75#	47#	105#	127#
144 mA	68#	75#	108#	118#	119#
140 mA	68#	75#	42#	38#	105#
134 mA	68#	75#	70#	91#	47#
130 mA	68#	75#	76#	78#	110#
124 mA	68#	75#	40#	77#	97#
120 mA	68#	75#	47#	49#	70#
115 mA	68#	75#	53#	110#	126#
111 mA	68#	75#	5#	6#	133#
108 mA	68#	75#	6#	47#	57#
104 mA	68#	75#	5#	8#	71#
100 mA	68#	75#	29#	73#	83#
96 mA	68#	75#	29#	31#	106#
90 mA	68#	75#	26#	126#	
88 mA	68#	75#	26#	29#	118#
78 mA	68#	75#	8#	53#	89#
73 mA	68#	75#	35#	38#	126#
69 mA	68#	75#	57#	106#	122#

The result demonstrates the faulty BPMs can be detected and the multi-dimensional clustering analysis model could classify beam data into different clusters on the basis of their similarity. But each BPM belonging to the clusters is different that depends on the beam intensity. The cluster distribution result of 1# BPM is shown in Figure 5. Which cluster core it belonging to depends on the experiment data, no matter which category it is, it's normal BPM. The cluster distribution result of all BPM is shown in Fig. 6 (not include 68# and 75# BPM).

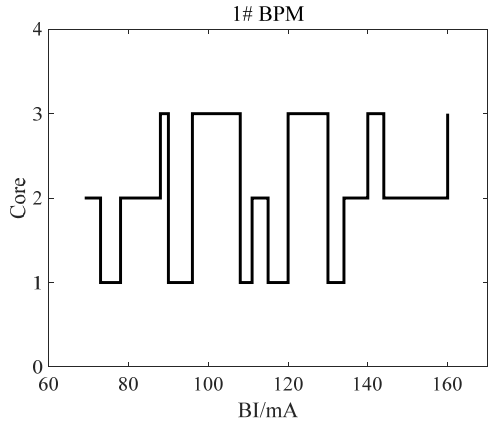

Figure 5: Cluster distribution of 1# BPM.

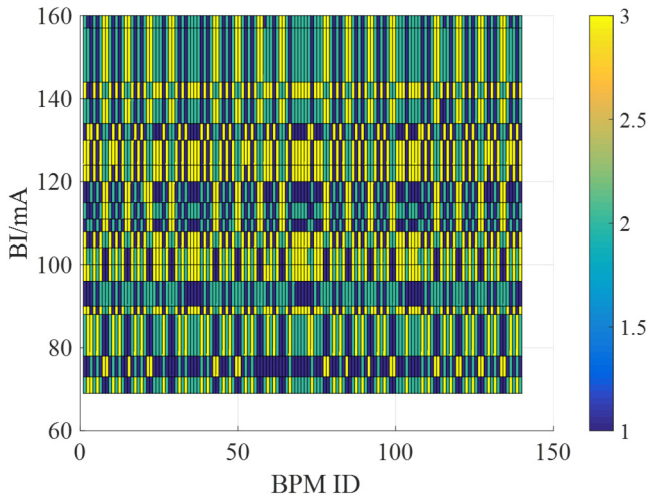

Figure 6: Cluster distribution of each BPM.

CONCLUSION

As the key beam diagnostics tool, BPM systems are widely equipped in all kinds of accelerators and are being used in daily operation and machine study. To better ensure the operation of the light source, a proper method detecting faulty beam position monitor or monitoring their stability is essential. This study proposed a multi-dimensional clustering analysis model to search faulty BPMs.

The experimental results demonstrate that 68# and 75# BPM are faulty, the other BPMs could be classified three categories. Whether the three categories belong to one big category, it needs to further study. In short, the proposed method could capture the faulty BPMs and would be meaningful in the field of beam diagnosis.

REFERENCES

[1] Leng Y B, *et al.*, "Beam position monitor system for SSRF storage ring", *Nucl Sci Tech*, vol.33, no.6, pp.401–404, 2010

[2] Cheng Z C, *et al.*, "Performance evaluation of BPM system in SSRF using PCA method", *CPC*, vol.38, no.6, pp. 112-116, 2014.

ISBN: 978-3-95450-222-6 ISSN: 2673-5350 doi:10.18429/JACoW-IBIC2020-WEPP28

[3] P O Brown, *et al.*, Cluster analysis and display of geneome-wide expression patterns. Qual Quant. vol.14, no.1, pp. 75-100, 1980.

[4] Rodriguez, *et al.*, Clustering by fast search and find of density peaks. Science, vol.344, no.6191, pp.1492, 2014.

[5] R. Jiang, F. Z. Chen, Z. C. Chen, and Y. B. Leng, "Identification of Faulty Beam Position Monitor Based Clustering by Fast Search and Find of Density Peaks", in *Proc. 7th Int. Beam Instrumentation Conf. (IBIC'18)*, Shanghai, China, Sep. 2018, pp. 114-117. doi:10.18429/JACoW-IBIC2018-MOPC02

Content from this work may be used under the terms of the CC BY 3.0 licence (© 2020). Any distribution of this work must maintain attribution to the author(s), title of the work, publisher, and DOI

ISBN: 978-3-95450-222-6 ISSN: 2673-5350 doi:10.18429/JACoW-IBIC2020-WEPP29

Content from this work may be used under the terms of the CC BY 3.0 licence (© 2020). Any distribution of this work must maintain attribution to the author(s), title of the work, publisher, and DOI

ENERGY GAIN MEASUREMENT FOR ELECTRONS ACCELERATED IN A SINGLE-CYCLE THz STRUCTURE*

Sergey Kuzikov†, Sergey Antipov, Pavel Avrakhov, Euclid Techlabs LLC, Bolingbrook, IL, USA
Sergey Bodrov, Alexey Fedotov, Andrey Stepanov, Alexander Vikharev
Institute of Applied Physics of Russian Academy of Sciences, Nizhny Novgorod, Russia

Abstract

Gradients on the order of 1 GV/m have been obtained via single cycle (~1 ps) THz pulses produced by the conversion of a high peak power laser radiation in nonlinear crystals (~1 mJ, 1 ps, up to 3% conversion efficiency). For electron beam acceleration with such broadband (0.1-5 THz) pulses, we propose arrays of parabolic focusing micro-mirrors with common central. To measure energy gain of electrons in the THz structure we propose applying a voltage (up to 400 kV) to the structure respecting the cathode and anode. Electrons become preliminary accelerated at the entrance that makes design of the structure simpler, because velocity of particles is near to be constant and almost equals the speed of light. On the other hand, the anode can be reached only by the electrons accelerated in the THz field so that one can directly measure the resulting energy gain at the anode.

SINGLE-CYCLE THz STRUCTURES

High-field single cycle THz pulses are now produced by means of laser light rectification in a nonlinear crystal [1-2]. Such pulses can potentially provide ~1 GV/m acceleration of sub-picosecond bunches. In [3-8], a new accelerating structure design was proposed, which introduces a set of waveguides with different adjusted lengths.

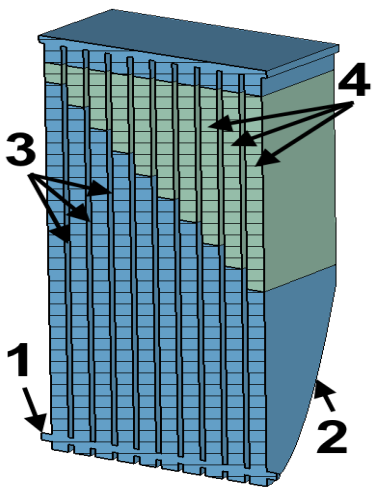

Figure 1: Sketch of broad band THz structure based on dielectric delay waveguides: 1 – beam channel, 2 – mirrors of the parabolic shape, 3 – oversized vacuum waveguides, 4 – delay waveguides filled with dielectrics.

Accelerating structure design is based on waveguide array with different adjusted delays, in which the synchronism of accelerated particles with transversely propagating picosecond THz pulse is to be sustained (Figure 1). Inserted dielectric slabs of the different lengths provide the synchronism of the accelerated particles with transversely propagating single-cycle THz pulse (Figure 2). In the transverse direction, the accelerating structure introduces focusing parabolic mirrors. These mirrors enhance the accelerating field seen by electrons by several times. Such design allows for an overall reduction of losses and mitigation of the negative action of frequency dispersion in the waveguide, because most pathway of THz pulse propagation lies in a wide oversized waveguide. The THz pulse is focused in at the very end of the structure.

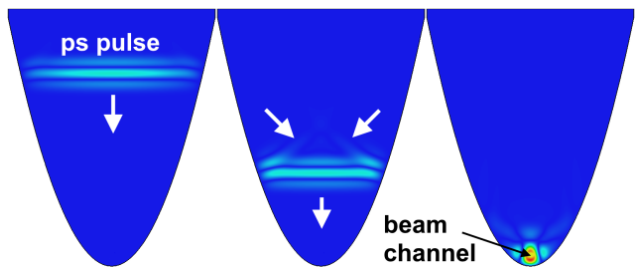

Figure 2: E-field distributions at the parabolic mirror while focusing the short THz pulse, for the time correspondent to beginning of focusing at t=3.6 ps (left), for time when focusing is close to maximum at t=7.6 ps (center), and in maximum of focusing (right) at t=11.6 ps.

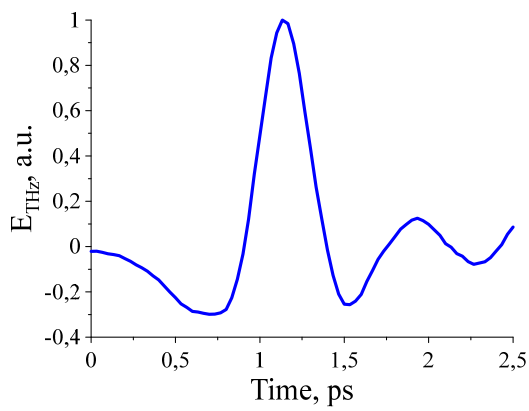

Figure 3: Experimental oscillogram of the single cycle THz pulse shape.

The structure in Figure 2 consists of the identical parabolic mirrors described above. The structure is fed by a single-cycle THz pulse propagating in parallel to metallic blades where the E-field is perpendicular to these blades.

* This work was supported by the Russian Science Foundation under Grant 19-42-04133.
† s.kuzikov@euclidtechlabs.com

ISBN: 978-3-95450-222-6 ISSN: 2673-5350 doi:10.18429/JACoW-IBIC2020-WEPP29

The experimental oscillogram of the single cycle THz pulse obtained in Institute of Applied Physics is shown in Figure 3.

Leading into the parabolic mirrors there are dielectric plate delay lines that provide necessary synchronism of a short electron bunch flying through the structure. That is why, neighboring dielectric plates have incrementally decreasing lengths counting from the left side to the right side. The mentioned increment is given by:

$$\Delta = \frac{P}{\sqrt{\varepsilon}-1}. \quad (1)$$

Where ε - is dielectric permittivity, P – is a period of the structure.

Fields and a bunch in the accelerating structure are shown in Figure 4 for sequent time points. Here the bunch flies from left to right, and time proceeds from left to right as well. Beam pipe diameter was chosen as much less than cell length, in order to not perturb the THz pulse focusing and to prevent a considerable power leakage along the whole structure.

Figure 6 shows the incident pulse field distribution before parabolic mirrors and the fields in the 1st, 5th, and 10th cells, correspondingly. Note that the maximum accelerating electric fields in the cells are almost 3.5 times higher than the incident pulse field. The magnetic field in each cell is closer to zero than the corresponding electric fields maxima so that deflection forces at structure's axis are remarkably low.

Beam Dynamics Simulations

Beam dynamics were simulated using CST Microwave Studio. For simulations, we used the structure parameters shown in the Table 1, and the bunch parameters: 0.01 pC charge, initial energy 50 keV, bunch length 0.25 ps, bunch diameter 10 μm (at cathode). The structure design was performed so that all cells have equal lengths. The mentioned dielectric delays compensated grows of particle velocity from cell to cell.

In this simulation, for the full THz pulse energy about 2 μJ the maximum of the electric field in each cell was as high as 220 kV/cm. As one can see in the Figure 5, the electron bunch was accelerated up to energy more than 55.7 keV, in accordance with our expectations.

Fabrication

The accelerating structure will be fabricated from the copper foil of 50 μm thickness with 20 μm partitions by means of laser ablation technique. Dielectric delay inserts will be produced from Teflon. The parts will be assembled all together being tightened between flanges and lined up with stainless steel pins.

The described THz structure could also be produced by a femtosecond laser ablation system developed at Euclid Techlabs. This technology has already been tested for production of a 270 GHz Photonic Band Gap (PBG) structure made of high resistivity silicon. The prototype structure of 2.5 mm length was produced using this fs laser ablation technology [8].

Table 1: Parameters of THz Accelerating Structure Fed by 1 ps THz Pulses

Parameters	Value
Number of cells	10
Dielectric permittivity	2.1
Cell length	0.05 mm
Beam pipe diameter	0.1 mm
Focal length	0.13 mm
Iris thickness	0.05 mm
Width	3.0 mm
Length	1.0 mm

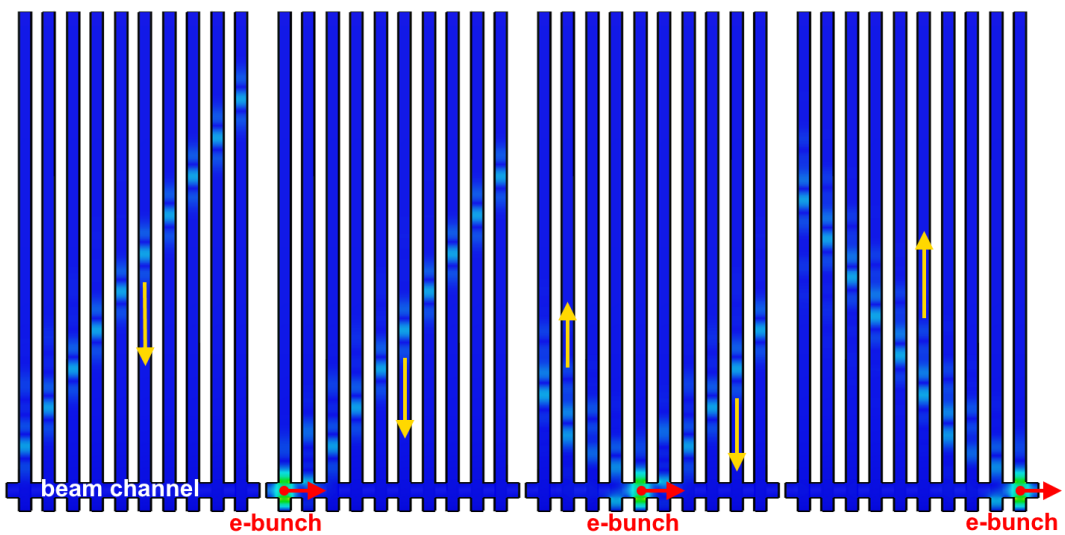

Figure 4: Front view of dielectric delay line THz accelerating structure (time proceeds from left to right).

Content from this work may be used under the terms of the CC BY 3.0 licence (© 2020). Any distribution of this work must maintain attribution to the author(s), title of the work, publisher, and DOI

ISBN: 978-3-95450-222-6 ISSN: 2673-5350 doi:10.18429/JACoW-IBIC2020-WEPP29

Content from this work may be used under the terms of the CC BY 3.0 licence (© 2020). Any distribution of this work must maintain attribution to the author(s), title of the work, publisher, and DOI

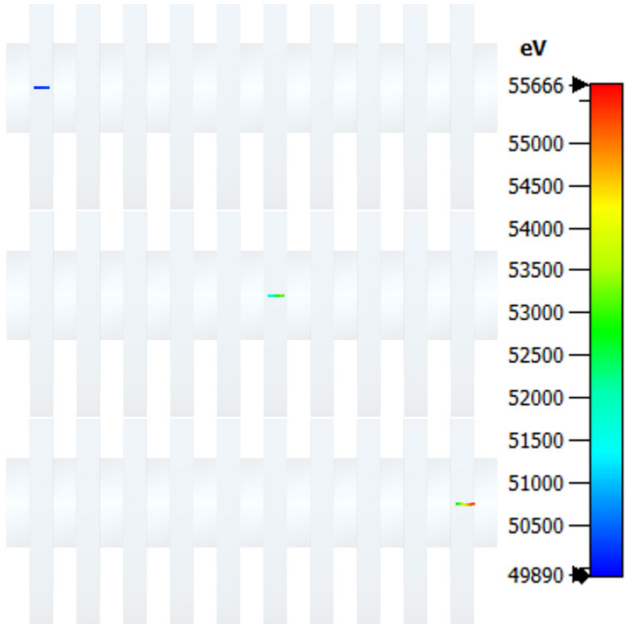

Figure 5: Bunch acceleration for three sequent time frames: top – bunch enters the first cell (t=11.6 ps), center – bunch crosses middle line (t=15.6 ps), bottom – bunch arrives the end (t=18.8 ps).

EXPERIMENTAL SETUP

Experiments with THz Pulse Generation in $LiNbO_3$ Crystal

In preliminary experiments we converted laser pulses into THz radiation using ~100 fs, 7 mJ laser with 10 Hz repetition rate [9]. Laser pulses with tilted front of the intensity were formed with a diffraction grating (1700 lines per mm). We investigated how conversion efficiency depends on optical beam size and duration (Figure 6).

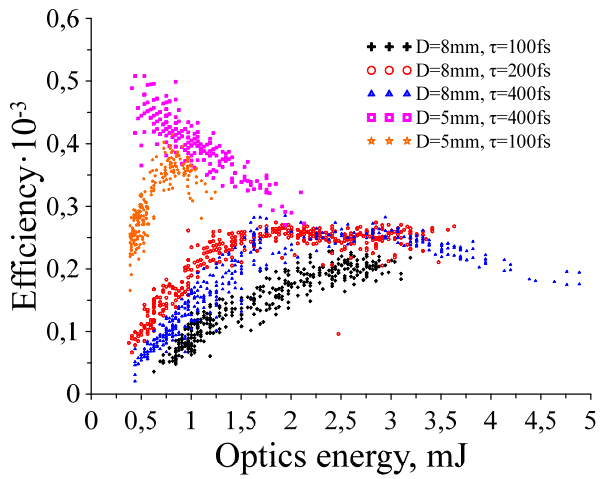

Figure 6: Efficiency of optical to THz radiation conversion in $LiNbO_3$ vs optical pulse energy for different pulse lengths and laser beam sizes.

It was found out that the efficiency for 100 fs laser pulses of 8 mm diameter linearly grows up with laser energy until 2 mJ and saturates at 3 mJ. For longer laser pulses (200-400 fs) the efficiency saturates at as low energy as 1.5 mJ and becomes 20 % more than in case of the short pulses. It was also shown that decreasing of laser beam diameter by 1,5 times enhanced the efficiency at low beam energies. However, the saturations came faster in comparison with wider beams, at 0.5-1 mJ. Maximum of the efficiency, 0.05%, was observed at 0.7 mJ and 400 fs pulse duration.

Electron Gun

We plan to study acceleration of electrons to be accelerated up to 50 keV prior the THz structure. For that purpose, we elaborated an electron gun based on a needle cathode irradiated by 800 nm TiSa laser (Figure 7). The use of the same laser for electron emission and THz generation allows to simplify synchronization issues substantially. Preliminary experiments with a needle (~1 μm) cathode showed that the emission current grows up with energy of laser pulse and then saturates. Maximum emitted charge in our experiments was as high as 10 pC.

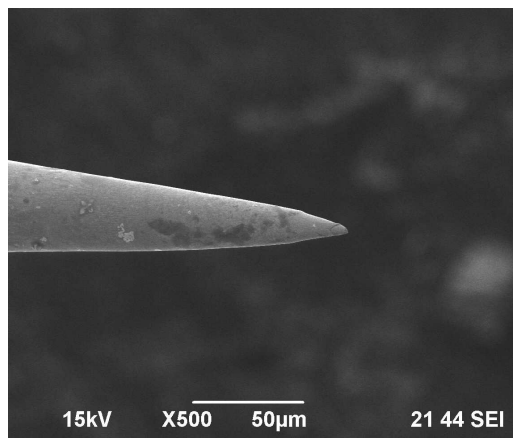

Figure 7: Tungsten cathode needle as shown in electronic microscope.

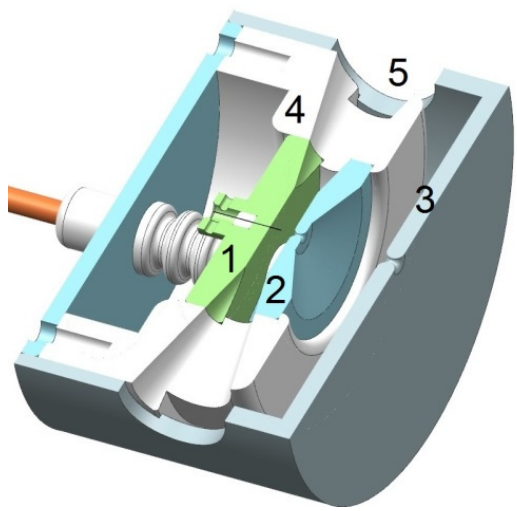

Figure 8: Electron DC acceleration gun: 1 – needle cathode, 2 – intermediate anode, 3 – main anode, 4 – insulator, 5 – gate for laser beam.

ISBN: 978-3-95450-222-6 ISSN: 2673-5350 doi:10.18429/JACoW-IBIC2020-WEPP29

In the proposed electron gun the needle cathode will be set under 100 V negative potential with respect to the first intermediate anode (Figure 8). The intermediate cathode is aimed to collect electrons with high transverse velocities. A section between anodes will be designed as a quasi-Pierce gun to provide beam focusing. We anticipate getting at the gun exit about 1 mm diameter bunches with 50 keV energy of the electrons. Before the THz structure we are going to put 70 μm iris to mitigate velocity and position spreads.

Energy Gain Measurement

We consider two experimental methods to measure energy gain. The first method is a classical measurement method by means of spectrometer based on DC deflecting magnet (Figure 9).

The second method exploits another idea. To measure energy gain of electrons we propose applying a voltage (50-100 kV) to the structure respecting the cathode and anode. Electrons arrive to the structure being accelerated up to 50 keV. Behind the THz structure electrons lose their energy being experienced the deceleration equals to the prior DC acceleration so that only energy accumulated in the THz structure would be remained. The anode can be reached only by the electrons accelerated in the THz field so that one can directly measure the resulting energy gain by means of the YAG screen.

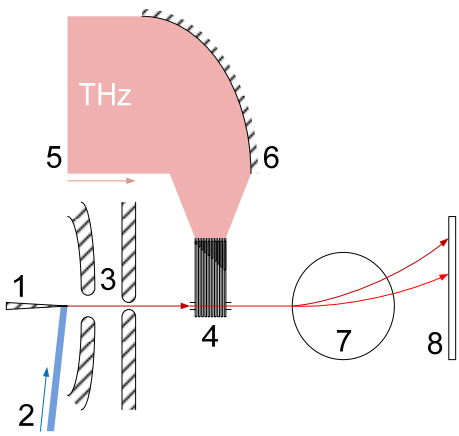

Figure 9: Sketch of experimental setup based on spectrometer measurements: 1 – needle cathode, 2 – laser beam, 3 – accelerating DC gun, 4 – THz accelerating structure, 5 – THz beam, 6 – parabolic focusing mirror, 7 – spectrometer, 8 – YAG screen.

CONCLUSION

Acceleration gradients at level GV/m could be reached in a multi-cell structure using picosecond single-cycle THz pulses produced by the conversion of laser radiation in nonlinear crystals. Energy gain measurements include needle cathode irradiated by femtosecond laser, DC acceleration section, multi-cell THz structure, and spectrometer or DC deceleration section before YAG screen.

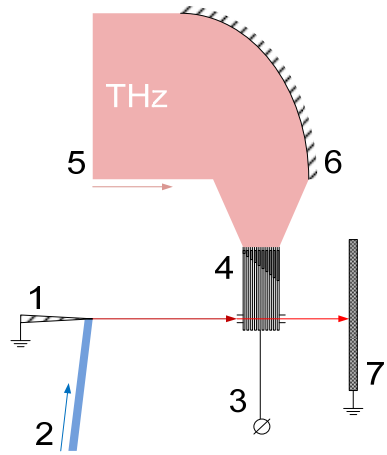

Figure 10: Sketch of experimental setup based on deceleration section measurements: 1 – needle cathode, 2 – laser beam, 3 –accelerating section, 4 – THz accelerating structure, 5 – THz beam, 6 – parabolic focusing mirror, 7 – deceleration section, 8 – YAG screen.

REFERENCES

[1] C. Vicario, A. V. Ovchinnikov, S. I. Ashitkov, M. B. Agranat, V. E. Fortov, and C. P. Hauri, "Generation of 0.9-mJ THz pulses in DSTMS pumped by a Cr:Mg_2SiO_4 laser" *Opt. Lett.*, vol. 39, no. 23, pp. 6632–6635, 2014. dio:10.1364/OL.39.006632

[2] D. Zhang *et al.*, "Femtosecond phase control in high-field terahertz-driven ultrafast electron sources", *Optica*, vol. 6, no. 7, pp. 872-877, 2019. dio:10.1364/OPTICA.6.000872

[3] S. V. Kuzikov, A. E. Fedotov, N. Yu. Peskov, A. N. Stepanov, and A. A. Vikharev, "Millimeter and submillimeter-wave, high-gradient accelerating structures", *AIP Conf. Proc.*, vol. 1812, p. 060002, 2017. dio:10.1063/1.4975869

[4] S. V. Kuzikov, S. Shchelkunov, and A. A. Vikharev, "Concepts for a Short Wavelength rf Gun", *AIP Conf. Proc.*, vol. 1812, p. 080005, 2017. dio:10.1063/1.4975891

[5] Yu. A. Sergeev *et al.*, "Strong terahertz fields: interaction with condensed matter and electron acceleration", *EPJ Web Conf.*, vol. 149, p. 05009, 2017. doi:10.1051/epjconf/201714905009

[6] S. V. Kuzikov, S. P. Antipov, O. A. Ivanov, A. A. Vikharev, and A. L. Vikharev, "Novel Concepts of a High-Brightness Photoinjector RF Gun", in *Proc. 38th Int. Free Electron Laser Conf. (FEL'17)*, Santa Fe, NM, USA, Aug. 2017, pp. 397-400. doi:10.18429/JACoW-FEL2017-WEA04

[7] S. V. Kuzikov, A. A. Vikharev, S. P. Antipov, and E. Gomez, "Single Cycle THz Acceleration Structures", in *Proc. North American Particle Accelerator Conf. (NAPAC'19)*, Lansing, MI, USA, Sep. 2019. dio:10.18429/JACoW-NAPAC2019-WEPLO11

[8] S.V. Kuzikov *et al.*, "Quasi-Optical THz Accelerating Structures", *AAC2018 Workshop*, 12-17 August 2018, Breckenridge, Colorado.

[9] S. B. Bodrov. A. N. Stepanov, and M. I. Bakunov, "Generalized analysis of terahertz generation by tilted-pulse-front excitation in a $LiNbO_3$ prism", *Opt. Express,* vol. 27, pp. 2396-2410, 2019. doi:10.1364/OE.27.002396

Content from this work may be used under the terms of the CC BY 3.0 licence (© 2020). Any distribution of this work must maintain attribution to the author(s), title of the work, publisher, and DOI

ISBN: 978-3-95450-222-6 ISSN: 2673-5350 doi:10.18429/JACoW-IBIC2020-WEPP31

Content from this work may be used under the terms of the CC BY 3.0 licence (© 2020). Any distribution of this work must maintain attribution to the author(s), title of the work, publisher, and DOI

DESIGN OF THE BEAM DIAGNOSTIC SYSTEM FOR THE NEW 3 GeV LIGHT SOURCE IN JAPAN

H. Maesaka†, T. Fukui, RIKEN SPring-8 Center, Kouto, Sayo, Hyogo, Japan
H. Dewa, T. Fujita[1], M. Masaki[1], S. Takano[1, 2], JASRI, Kouto, Sayo, Hyogo, Japan
K. Ueshima, QST Harima District, Kouto, Sayo, Hyogo, Japan
[1]also at QST Harima District, Kouto, Sayo, Hyogo, Japan
[2]also at RIKEN SPring-8 Center, Kouto, Sayo, Hyogo, Japan

Abstract

We designed and developed the beam diagnostic system for the new 3 GeV light source project in Japan. To achieve the performance goals of the light source, we need to precisely measure various beam parameters of the storage ring, such as beam position, stored current, beam size, betatron tune, etc. We developed a button-type beam position monitor (BPM) with a single-pass resolution of less than 0.1 mm for a 0.1 nC injected bunch and with sub-μm closed-orbit distortion resolution for more than 100 mA stored current. The BPM stability was evaluated to be 5 μm for more than one month. The stored current is monitored by two DC current-transformers, which are attached to a vacuum chamber designed to have small beam impedance and small temperature rise. The beam size is measured by an X-ray pinhole camera with a 10 μm resolution. We will install a 3-pole wiggler as a radiator for the X-ray pinhole camera and diagnostics with visible light. Since the resistive wall impedance is expected to be high in the storage ring, we developed a bunch-by-bunch feedback (BBF) system to suppress the beam instability. We tested FPGA-based high-speed electronics for BBF and confirmed sufficient damping performance. A realtime betatron-tune monitor is also implemented in the BBF system. Thus, the beam diagnostic system is ready for the construction of the new light source.

INTRODUCTION

A new 3 GeV light source is now being constructed in Sendai, Japan [1], and will be completed in 2023. It will generate highly brilliant X-rays more than 10^{21} photons/s/mm^2/mrad^2/0.1%BW around 1 keV photon energy. These X-rays are emitted from a brilliant electron beam having a small natural emittance of 1.1 nm rad and a high beam current of 400 mA. This electron beam performance will be realized with a double double-bend achromat lattice on a 16-cell storage ring with a circumference of 349 m.

To provide the brilliant and stable X-rays to users, the electron beam needs to be stored stably with the design performance. Therefore, the various beam parameters, such as the beam orbit, current, size, etc. have to be monitored precisely and stably. Since a low-emittance storage ring has a narrow dynamic and physical aperture, the electron beam should be precisely steered within the aperture in the commissioning stage by using beam monitors and by tuning various magnets. Consequently, we have designed a precise and stable beam diagnostic system based on the development results of the beam monitors for the SPring-8 upgrade project [2]. In the following sections, we describe the design and test results of the beam monitors for the new 3 GeV light source.

OVERVIEW OF THE BEAM DIAGNOSTIC SYSTEM

In the commissioning of the storage ring of the new light source, the trajectories of a 0.1 nC bunch from the injector linac need to be measured with a resolution of 0.1 mm std. by the single-pass (SP) mode BPM. To adjust and keep the beam orbit to the ideal one in the user operation, a sub-μm resolution is necessary for the closed-orbit distortion (COD) mode BPM for a stored beam of more than 100 mA. The BPM should also be stable within 5 μm in one operation cycle (~1 month). The total stored beam current and each bunch current must be precisely monitored to keep the stored current and the bunch filling pattern constantly in the top-up injection mode. The bunch phase should also be monitored to inject a beam at an appropriate timing in the RF bucket. A precise realtime betatron-tune monitor is necessary to correct the tune shift caused by the gap changes of the insertion devices. Since the storage ring is equipped with narrow aperture vacuum chambers, the beam impedance will excite the beam instability. Therefore, a bunch-by-bunch feedback control system is also required to cure the beam instability.

Based on the above requirements, we designed a beam diagnostic system for the 3 GeV storage ring, as listed in Table 1. We use button-type BPMs for the beam orbit measurement. Seven BPMs are distributed in a unit cell and 112 BPMs are used in total. The stored beam current is measured by two DC current transformers (DCCTs), which are installed into a short straight section (SSS) for beam monitors (SSS-MON1). A 3-pole wiggler is also installed in SSS-MON1 for an X-ray pinhole camera to monitor the beam size. Visible light from the wiggler is also extracted

Table 1: List of Beam Monitors

Diagnostic instruments	Number of units
Beam position monitor (BPM)	112 (7 per cell)
Beam current monitor (DCCT)	2
Stripline BPM	2
Beam size monitor	1
Betatron tune monitor	1 (in BBF)
Beam instability control (BBF)	1

† maesaka@spring8.or.jp

ISBN: 978-3-95450-222-6 ISSN: 2673-5350 doi:10.18429/JACoW-IBIC2020-WEPP31

for other measurements, such as a streak camera for the bunch length, an optical interferometer for the beam size, etc. Two stripline BPM pickups and a stripline kicker are integrated into another SSS (SSS-MON2) for a bunch current and phase monitor, betatron-tune measurement, beam instability feedback control, etc.

DESIGN AND PERFORMANCE OF EACH BEAM MONITOR

Beam Position Monitor

We employ button-type BPM pickups originally developed for the SPring-8 upgrade project [3, 4]. A schematic drawing of the BPM pickup is shown in Fig. 1. The vacuum chamber is the combination of an octagonal beam duct and an antechamber made of stainless steel. Four button-electrodes are attached to the top and bottom planes of the beam duct. The electrode is made of Molybdenum and the diameter is 7 mm. The horizontal spacing of the electrodes is 12 mm and the vertical aperture is 16 mm. The hole diameter for the button electrode is 8 mm and, therefore, the gap of the electrode is 0.5 mm. The beam position sensitivity factor was estimated to be approximately 7 mm for both horizontal and vertical directions. These dimensions were carefully designed to suppress the beam impedance and heat generation [3]. A water-cooling channel is also equipped to the BPM chamber to reduce the temperature rise. The BPM signal is extracted from a reverse-polarity SMA connector since the normal SMA jack connector has a spring part, the force of which can be lost by a high-temperature brazing process of the electrode.

BPM signals are transferred to the readout electronics through coaxial cables. Since cables near the BPM chamber are exposed to a large dose of radiation, radiation-resistive coaxial cables are necessary. We tested several candidates in the SPring-8 storage ring. The cables are placed on an X-ray absorber, where the dose rate is more than 10 kGy per day. As a result, semirigid cables with dielectric materials of SiO_2 and PEEK were confirmed to have sufficient radiation resistivity. Therefore, we use one of these semirigid cables to extract the BPM signal from the BPM head. Since the radiation-resistive semirigid cable is expensive, lossy, and hard to make a long cable, we use a corrugated coaxial cable to transfer the signal from the accelerator tunnel to the outside. We confirmed that a corrugated coaxial cable is not damaged by radiation if it is more than 1 m apart from the electron beam.

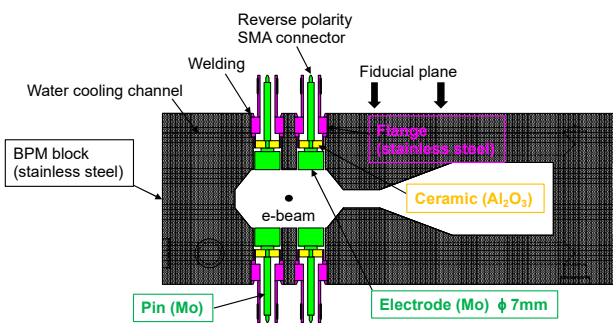

Figure 1: Cross-section of the BPM vacuum chamber with button electrodes.

As described in the previous section, the BPM readout electronics are required to have both the SP and COD detection functions with sufficient precision, accuracy, and stability. For the COD measurement, several data rates are needed: slow data with 10 Hz, fast data with 10 kHz, and turn-by-turn data with 859 kHz. The slow data is used for COD monitor and correction. The fast data is for abnormal orbit alarm to protect beamline components, etc. The turn-by-turn data is for the analysis of fast phenomena. To implement these functions, we employed the MTCA.4 platform [5] for the readout electronics [6]. The BPM signal is fed into a BPM rear transition module (RTM) of the MTCA.4 standard and a 509 MHz signal synchronized to the acceleration frequency is extracted. The signal is transmitted to a digitizer advanced mezzanine card (AMC), which has 10 channels of ADCs with a sampling frequency of 370 MHz and a vertical resolution of 16 bits. The beam position is calculated by an FPGA on the digitizer AMC. Since the MTCA.4 has a high-speed backplane, large BPM data from the digitizer AMC can be easily transferred to a CPU module.

The basic performance of the BPM system was evaluated in SPring-8 [4, 6]. The prototype BPM chamber having four sets of BPMs was installed in one of the straight sections. Two BPMs from the four were processed by the MTCA.4 electronics. The BPM resolution was estimated by comparing the position data from the two BPMs [6]. The SP resolution was obtained to be 0.02 mm for a bunch charge of 0.13 nC. The COD resolution of the 10 kHz fast data was 0.4 μm for a stored beam current of 30 mA. Long-term stability was also evaluated, as shown in Fig. 2. The vertical axis of this trend graph is balance error, which is defined as the maximum difference among the four values from the three-electrode BPM calculation process [7]. The balance error is constant and independent of the beam position if the gains of all the four electrodes are stable. Variations of the balance error indicate some drifts of BPM hardware. The trend graph shows that the balance error variation was about 5 μm for more than one month, even if the filling pattern was changed several times. Thus, the BPM system has sufficient position resolution and stability.

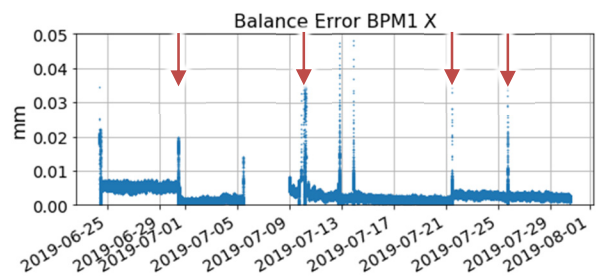

Figure 2: Trend graphs of balance error data (horizontal). Filling patterns were changed several times, which are indicated by arrows.

Content from this work may be used under the terms of the CC BY 3.0 licence (© 2020). Any distribution of this work must maintain attribution to the author(s), title of the work, publisher, and DOI

ISBN: 978-3-95450-222-6 ISSN: 2673-5350 doi:10.18429/JACoW-IBIC2020-WEPP31

Content from this work may be used under the terms of the CC BY 3.0 licence (© 2020). Any distribution of this work must maintain attribution to the author(s), title of the work, publisher, and DOI

Stored Beam Current Monitor

The stored beam current monitor will be installed in one of the short straight sections (SSS-MON1). A schematic view of the beam current monitor is illustrated in Fig. 3. The current monitor consists of two DCCTs for redundancy. We employed Bergoz NPCT [8] as a sensor head. It has 1 $\mu A/\sqrt{Hz}$ noise level at the full range of ± 1 A and the full bandwidth of 10 kHz. The RF wakefield from the electron beam is absorbed by SiC around the ceramics gap and the nonlinear response of the DCCT due to the RF wakefield is suppressed. The heat generated in SiC is taken by a copper block with a water-cooling channel. The temperature rise of the DCCT coming from a 400 mA stored beam is estimated to be less than 1 K by using a three-dimensional thermal analysis code, as shown in Fig. 3 (right). Although NPCT has a finite thermal coefficient of 5 $\mu A/K$, the thermal drift is expected to be sufficiently small. Thus, the stored beam current monitor can measure the beam current with the order of 1 μA precision, corresponding to ~1 pC of the stored beam charge. Since the beam charge from the injector linac is the order of 100 pC, the injection efficiency can be evaluated with 1% precision, which is enough for the regulation of radiation safety.

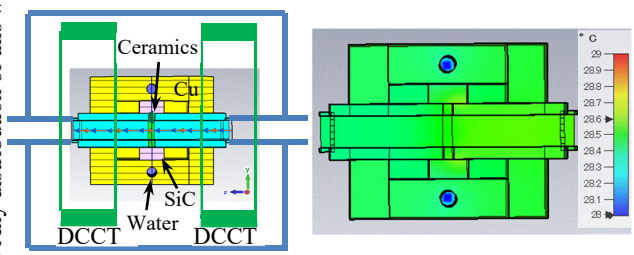

Figure 3: Schematic view of the stored beam current monitor (left) and the thermal analysis result (right).

Beam Size Monitor

To estimate the beam emittance and the x-y coupling ratio from the beam size, we will use an X-ray pinhole camera, as shown in Fig. 4. A 3-pole wiggler is installed in SSS-MON1 together with the DCCTs as an X-ray radiator. The design of the X-ray pinhole camera is based on that of SPring-8 [9]. The distance from the light source to the pinhole is ~5 m and that from the pinhole to the camera is ~10 m. The optimum pinhole size is estimated to be approximately 13×13 μm^2 when ~50 keV photons are used, and the optical resolution is expected to be approximately 4 µm. The beam radius at the SSS is 80 (H) × 6 (V) μm^2 std. and the design value of the x-y coupling ratio is 1%. Therefore, the beam size monitor has a sufficient resolution for both axes. Since the beam emittance can be estimated from the horizontal size, the beam size monitor is precise enough for the emittance measurement. To measure the x-y coupling ratio precisely less than 1%, we need a more precise method to achieve a sufficient resolution, such as X-ray interferometry [10].

Visible radiation from the 3-pole wiggler is also extracted to measure various beam parameters. The beam size can be monitored by an interferometer and the bunch length can be measured by using a streak camera. Therefore, we extract the visible light to the outside of the accelerator tunnel and guide to a dark room for visible light diagnostics. The detailed setup of the visible light diagnostics is still under consideration.

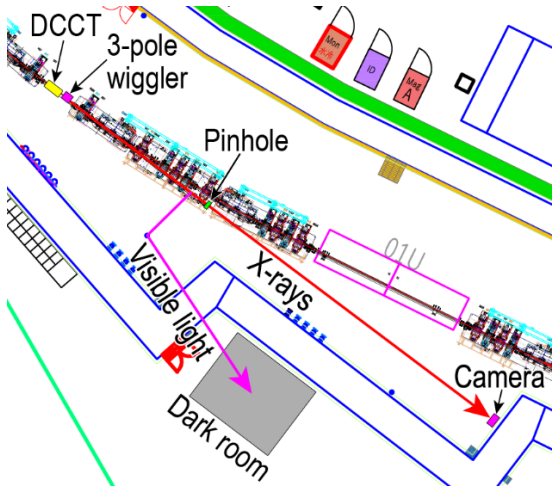

Figure 4: Setup of the beam size monitor and the visible light extraction line.

Bunch Current and Phase Monitor

The bunch current and phase data are necessary to monitor the filling pattern and the injection timing for top-up operation. Electrons should be filled to the bunch that has the largest current deficit. Since the synchronous phase of each bunch is slightly different from each other, the injection timing should be adjusted bunch-by-bunch.

We will use a stripline BPM at an SSS (SSS-MON2) for the bunch current and phase measurement. One of the candidates for data acquisition is an MTCA.4 high-speed digitizer with a sampling rate of around 5 GSPS. The bunch current is obtained from the peak value of the pulse signal from each bunch and the bunch phase is from the rising edge timing. We have another plan to use a high-speed oscilloscope for backup. This method was already applied to the SPring-8 storage ring, and hence no development is needed. However, a commercial oscilloscope does not have high-speed data transfer to our control system. We will decide the data acquisition method in the near future.

Beam Instability Control and Tune Monitor

The suppression of beam instability is necessary to store a high-current electron beam stably since the threshold current for the transverse instability is estimated to be less than 100 mA due to narrow vacuum chambers of the storage ring. Although the instability can be suppressed by a larger chromaticity value, the top-up injection efficiency can be degraded by the chromaticity. Therefore, we use a bunch-by-bunch feedback (BBF) system to suppress the beam instability. The required damping time is estimated to be 0.01 ms for a bunch current of 1 mA.

The beam signal is picked up by a stripline BPM and the counter kick signal is calculated by a fast signal processor bunch-by-bunch. The kick signal is amplified by a wideband power amplifier and fed into a 4-electrode stripline

ISBN: 978-3-95450-222-6 ISSN: 2673-5350 doi:10.18429/JACoW-IBIC2020-WEPP31

kicker. The length of the kicker electrode is 0.3 m to kick each bunch with a time interval of 2 ns. The stripline BPM and the stripline kicker will be installed to SSS-MON2. We employ Dimtel iGp12 [11] as a signal processor, which has 509 MSPS ADCs and DACs, high-speed FPGA, and bunch-by-bunch feedback control firmware. The required kicker signal power is estimated to be 250 W for each kicker electrode to achieve the demanded damping time.

A betatron-tune monitor is necessary for the evaluation of the beam optics, automatic tune stabilization, etc. In general, the betatron tune is measured from a frequency response of the transverse oscillation. Since the BBF system has a BPM and a kicker to measure the transverse frequency response, some betatron-tune measurement functions are already implemented to iGp12. The tune can be measured by three methods: (1) A bunch is shaken by a swept sine signal and the tune is calculated from the Fourier transform of the BPM signal. (2) The sinusoidal kick phase is locked to the resonance of the betatron oscillation. (3) The tune value is calculated from a spectral notch under the BBF on. For the methods (1) and (2), the BBF for one of the bunches is turned off and the bunch is shaken by a signal for the tune measurement. Therefore, the tune can be monitored in realtime with sufficiently small perturbation.

We evaluated the BBF and tune monitor performances of iGp12 at SPring-8. The present BPM, kicker, and power amplifiers for the SPring-8 BBF system [12] were used. The grow-damp test result is shown in Fig. 5. A transverse orbit fluctuation was excited by a forced oscillation and the orbit was stabilized by turning on the feedback. The damping time was obtained to be 0.6 ms for a bunch current of 0.5 mA. If we convert this result to the 3 GeV light source by beam energy, beta function, circumference, physical aperture, etc., the damping time is approximately 0.01 ms for a 1 mA bunch, which satisfies the requirement.

The realtime tune monitor was also tested with the same setup. The tune was appropriately obtained with the accuracy of 2×10^{-4} for the swept sine method. The tune measurement precision of the phase lock method was 1×10^{-5} at the acquisition rate of 5 Hz. Since the required tune stability is 10^{-3} level, the tune monitor has enough resolution for the tune stabilization.

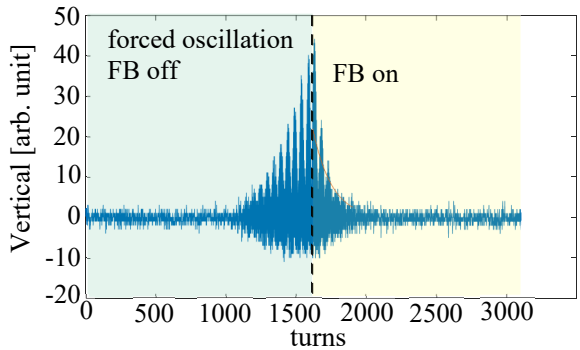

Figure 5: Grow-damp test result of the BBF system.

SUMMARY

The beam diagnostic system for the new 3 GeV light source in Japan has been developed based on the beam diagnostic system design of the SPring-8 upgrade project. The performance of the button BPM was examined in SPring-8. The SP resolution was confirmed to be 0.02 mm for a 0.13 nC single bunch and the COD resolution was 0.4 µm for 10 kHz fast data with the stored beam current of 30 mA. The stability of the BPM was also evaluated to be approximately 5 µm for more than one month. The stored current will be monitored by two DCCTs with 1 µA precision. The beam size will be measured by an X-ray pinhole camera with a 4 µm resolution. Although the detailed designs of the DCCT and the pinhole camera are different from SPring-8, the concepts themselves were already confirmed in SPring-8. The beam instability will be suppressed by the FPGA-based BBF system. This system was also tested in SPring-8 and the sufficient damping performance was confirmed. The realtime betatron-tune monitor is implemented in the BBF system and the resolution was evaluated to be 2×10^{-4} for the swept sine method and 1×10^{-5} for the phase lock method. Thus, the performance of the beam diagnostic system was confirmed to be sufficient for the new light source.

REFERENCES

[1] N. Nishimori, T. Watanabe, and H. Tanaka, "A Highly Brilliant Compact 3 GeV Light Source Project in Japan", in *Proc. 10th Int. Particle Accelerator Conf. (IPAC'19)*, Melbourne, Australia, May 2019, pp. 1478–1481. doi:10.18429/JACoW-IPAC2019-TUPGW035

[2] H. Maesaka *et al.*, "Development of Beam Diagnostic System for the SPring-8 Upgrade", in *Proc. 7th Int. Particle Accelerator Conf. (IPAC'16)*, Busan, Korea, May 2019, pp. 149–151. doi:10.18429/JACoW-IPAC2016-MOPMB028

[3] M. Masaki *et al.*, "Design Optimization of Button-type BPM Electrode for the SPring-8 Upgrade", in *Proc. 5th Int. Beam Instrum. Conf. (IBIC'16)*, Barcelona, Spain, Sep. 2016, pp. 360–363. doi:10.18429/JACoW-IBIC2016-TUPG18

[4] H. Maesaka *et al.*, "Development of Beam Position Monitor for the SPring-8 Upgrade", in *Proc. 7th Int. Beam Instrum. Conf. (IBIC'18)*, Shanghai, China, Sep. 2018, pp. 204–207. doi:10.18429/JACoW-IBIC2018-TUOC04

[5] PICMG MicroTCA open standard. https://www.picmg.org/openstandards/microtca/

[6] H. Maesaka *et al.*, "Development of MTCA.4-based BPM Electronics for SPring-8 Upgrade", in *Proc. 8th Int. Beam Instrum. Conf. (IBIC'19)*, Malmö, Sweden, Sep. 2019, pp. 471–474. doi:10.18429/JACoW-IBIC2019-WEBO03

[7] T. Fujita *et al.*, "Long-term Stability of the Beam Position Monitors at SPring-8", In *Proc. 5th Int. Beam Instrum. Conf. (IBIC'15)*, Melbourne, Australia, Sep. 2015, pp. 359–363. doi:10.18429/JACoW-IBIC2015-TUPB020

[8] Bergoz Instrumentation, https://bergoz.com/

[9] S. Takano, *et al.*, "Recent Progress in X-ray Emittance Diagnostics at SPring-8", In *Proc. 5th Int. Beam Instrum.*

Content from this work may be used under the terms of the CC BY 3.0 licence (© 2020). Any distribution of this work must maintain attribution to the author(s), title of the work, publisher, and DOI

ISBN: 978-3-95450-222-6 ISSN: 2673-5350 doi:10.18429/JACoW-IBIC2020-WEPP31

Conf. (IBIC'15), Melbourne, Australia, Sep. 2015, pp. 283–287. doi:10.18429/JACoW-IBIC2015-TUCLA02

[10] M Masaki, *et al.*, "X-ray Fresnel diffractometry for ultralow emittance diagnostics of next generation synchrotron light sources", *Phys. Rev. Accel. Beams*, vol. 18, p. 042802, 2015. doi:10.1103/PhysRevSTAB.18.042802

[11] Dimtel, Inc., https://www.dimtel.com/

[12] T. Nakamura and K. Kobayashi, "FPGA-based Bunch-by-Bunch Feedback Signal Processor", in *Proc. 10th Int. Conf. on Accelerator and Large Experimental Physics Control Systems (ICALEPCS'05)*, Geneva, Switzerland, Oct. 2005, PO2.022-2.

Content from this work may be used under the terms of the CC BY 3.0 licence (© 2020). Any distribution of this work must maintain attribution to the author(s), title of the work, publisher, and DOI

ISBN: 978-3-95450-222-6 ISSN: 2673-5350 doi:10.18429/JACoW-IBIC2020-WEPP33

PROGRESS OF PROFILE MEASUREMENT REFURBISHMENT ACTIVITIES AT HIPA

R. Dölling†, E. Johansen, M. Roggli, M. Rohrer
Paul Scherrer Institut, 5232 Villigen PSI, Switzerland

Abstract

At PSI's High Intensity Proton Accelerator (HIPA) facility some 180 profile monitors and 10 radial probes are in use to measure transverse beam profiles in beam lines and cyclotrons at energies of 0.87 to 590 MeV. Mechanical malfunctions and increased noise in some devices, a lack of spare parts and the obsolescence of most of the driver and read-out electronics as well as extended requirements to the measurement, necessitate the development of improved versions of the electronics and of several monitors. We give an update on the status of three projects in this regard: A long radial probe in the Ring Cyclotron, a profile monitor and BPM at 590 MeV in high radiation environment and new loss monitor electronics, which should also serve as a basis for the profile monitor readout.

INTRODUCTION

Operation of HIPA started more than 40 years ago [1]. Meanwhile, a majority of HIPA beam diagnostics has reached an age of 20 to 35 years. Some twenty years ago, the focus of development resources shifted to PSI's newer accelerator facilities SLS, Proscan and SwissFEL. With the aging hardware, we have over the years, gravitated towards an increasingly critical situation. Many diagnostics need to be renewed or refurbished in the next decade.

Since HIPA is a user facility, accelerator development today proceeds at a much slower pace than in the initial years. Nevertheless, the approach based on Joho's N^{-3} scaling law [2, 3] is followed, where increased acceleration voltages in the RF cavities of the cyclotrons result in decreased beam losses and allow higher beam currents. A complementary approach [4, 5], based on a more detailed knowledge of beam and beam loss in the machine, would profit from profile measurements with high dynamic range or more than one dimension, as reported, e.g., in [6].

The replacement of components is a rare opportunity to adapt, improve or extend the functionality of diagnostics, which can support operation and development of the accelerator facility. At IBIC'19 and Cyclotrons'19 we reported on the start of the above mentioned three projects in this regard. For all three, we choose a design which allows later changes and improvements and already implements a number of concrete improvements. These projects will also generate expertise for the production of spares or the replacement of other similar monitors, respectively will serve as a basis for the replacement of the CAMAC profile monitor electronics. In the following, we give an update on the status and further steps of these projects.

† rudolf.doelling@psi.ch

RADIAL PROBE IN RING CYCLOTRON

We detailed the design of the basic version of the probe proposed in [7]. The downstream probe head will carry a vertical and two diagonal wires to determine the radial projected profiles of all turns and, to a certain degree [8], of most of the vertical profiles. Shielding electrodes at both sides along the probe carrier [7], which can be biased, will, hopefully, help to prevent disturbances by plasma clouds.

Realization of the hardware has progressed. The long service vacuum chamber including support, turbo pump and vacuum valves, as well as the mechanism to move the probe carrier into the cyclotron (Fig. 1) are ready. Fabrication of the rail guiding the carrier inside the cyclotron and of the 3-wire probe head (Fig. 2) is underway. The design of electrical feedthroughs and details of wiring nears completion. Wiring and lab testing of the complete assembly is still pending. We hope to be able to install the probe in the Ring Cyclotron in the coming, exceptionally short shutdown in February to replace the defect probe and to gain experience with the new design.

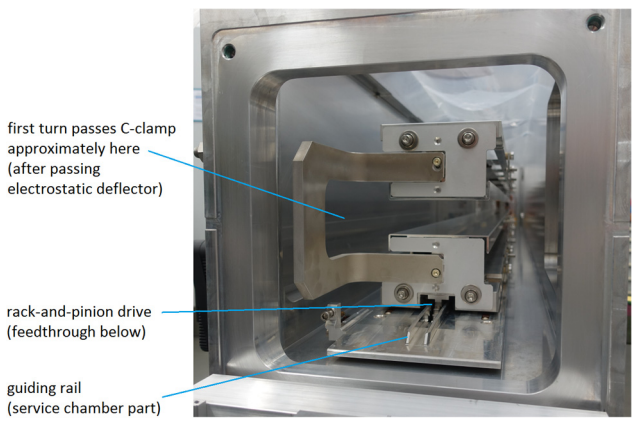

Figure 1: Probe carrier in parking position in the service chamber (in the lab, seen from cyclotron centre).

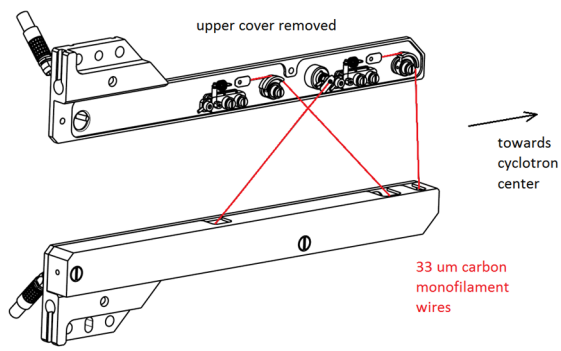

Figure 2: 3-wire probe head (seen from cyclotron side).

Content from this work may be used under the terms of the CC BY 3.0 licence (© 2020). Any distribution of this work must maintain attribution to the author(s), title of the work, publisher, and DOI

ISBN: 978-3-95450-222-6 ISSN: 2673-5350 doi:10.18429/JACoW-IBIC2020-WEPP33

Content from this work may be used under the terms of the CC BY 3.0 licence (© 2020). Any distribution of this work must maintain attribution to the author(s), title of the work, publisher, and DOI

PROFILE MONITOR AND BPM IN SINQ BEAM LINE

We developed a detailed design for the monitor plug proposed in [9], which preserves the strict modularity (Figs. 3-6). To transfer the movement of the external drive to the profile monitor mechanism, we now intend to use a magnetic linear feedthrough from UHV Design Ltd. [10] (Fig. 5). NdFe magnets are used in the feedthrough and motor in order to achieve a lower activation than that with CoSm magnets. Alternatively, a conventional feedthrough with bellow can be used, requiring a much stronger motor. Force sensors measure the transferred force. This should allow an online diagnosis of the health of the mechanism at the highly activated lower end of the plug.

Procurement of components just starts. If production and assembly run smoothly, we may be able to install the plug, still without BPM, in the beam line in the coming shutdown to replace the defect monitor.

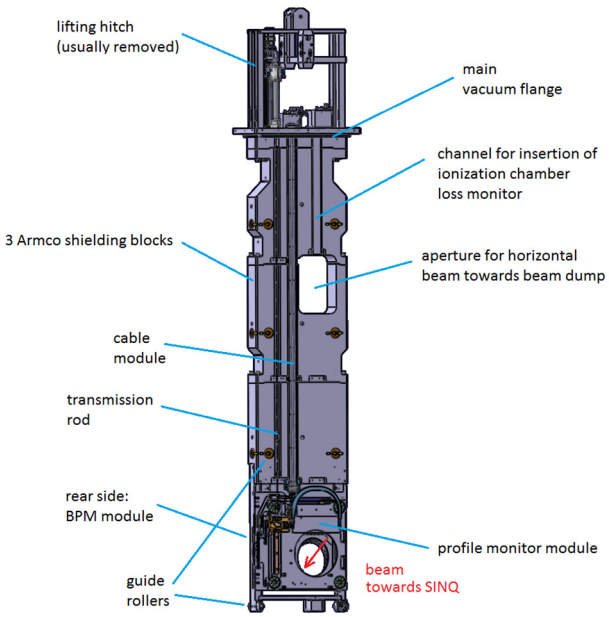

Figure 3: Monitor plug MHP45/46.

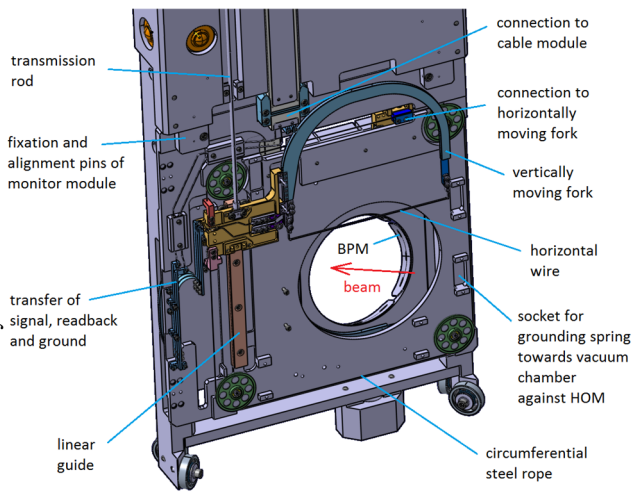

Figure 4: Profile monitor module.

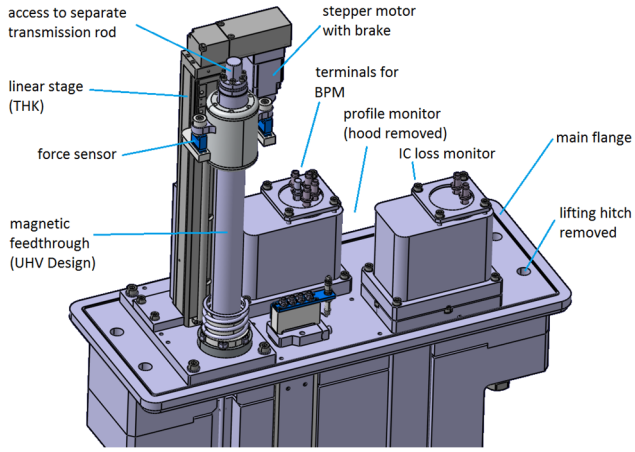

Figure 5: Upper part of monitor plug.

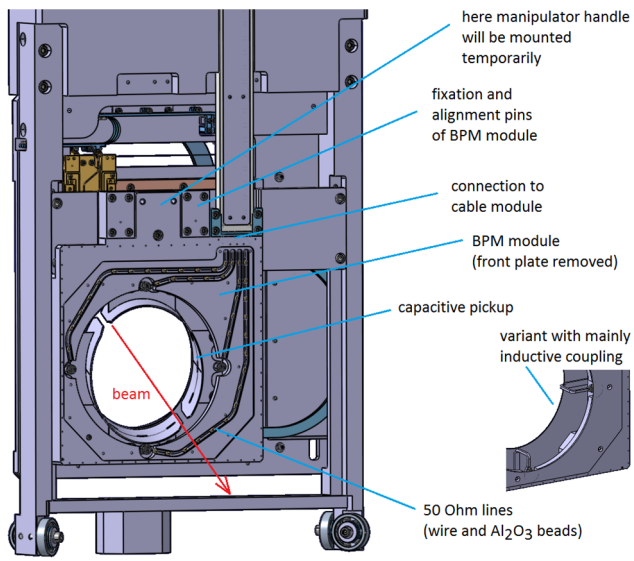

Figure 6: BPM module.

We plan to install, at the same time, a short version of this plug, without the three shielding blocks, together with a correspondingly shorter test chamber in the horizontal beam line towards UCN. There, radiation levels are much lower, and individual parts can be exchanged with hands-on access after testing. In particular, the BPM (Fig. 6), in a variant for horizontal beam, will be tested in order to evaluate the strength of higher order modes (HOM) and measures for their limitation. The situation should be comparable due to grounding springs between modules and towards the vacuum chamber located close to the BPM. Foregoing simulations are pending. Hence, manufacturing and installation of the BPM module will take place later.

The same design can be used at four plug locations, with only small variations to shielding blocks and BPM (horizontal/tilted/rectangular) or a double profile monitor unit for observation of both beam lines towards beam dump and SINQ. Dimensional changes are needed to accommodate the other six locations.

ISBN: 978-3-95450-222-6 ISSN: 2673-5350 doi:10.18429/JACoW-IBIC2020-WEPP33

LOSS MONITOR ELECTRONICS

We improved the design of the electronics module discussed in [11] and studied the performed of the first prototype.

Log-Amplifier and Internal Shielding

The logarithmic transimpedance amplifier converts the measured current into a voltage. This circuit is very sensitive to noise and the circuit is under a metallic shielding. An ADL5304 from Analog Devices defines the core of the log-amplifier circuit. The bandwidth of the log-amplifier decreases at low input currents (Fig. 7).

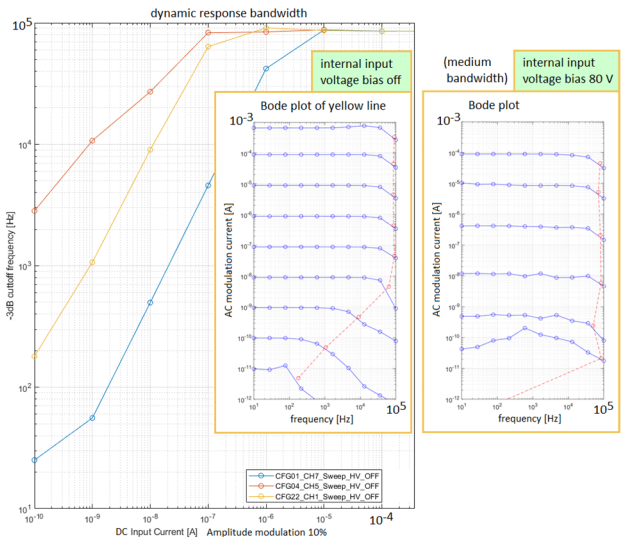

Figure 7: Bandwidth as function of input current for three circuit configurations. Without input voltage bias, the average of DC current is correctly represented within the bandwidth. With the bias on, this is the case only above a DC current of ~30 µA.

At higher currents above 10 nA the bandwidth is limited by the ADC anti-aliasing filter that is set to 50 kHz. With lower currents, the amplification in the log-amplifier is increased and the sensitivity to noise increases. A plot of a 10% current modulation is showing strong noise at a DC current of 1 nA (Fig. 8).

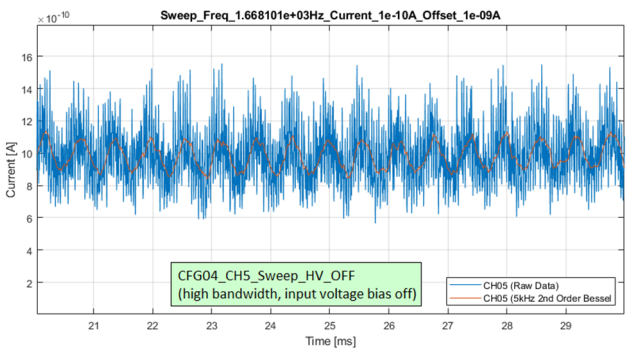

Figure 8: Measured current with 10% 1668 Hz modulation.

To find out where the noise comes from the amplitude spectrum was analysed (Fig. 9). Beside 50 Hz noise, there are several high-frequency spurs. To isolate the power supply of the log-amplifier, a Recom R1D-1205-R DC/DC converter is used in the prototype. This circuit is switching typically at 60 kHz. The spectrum is showing that most noise stems from this DC/DC converter, as there is major peak in the spectrum at 60 kHz.

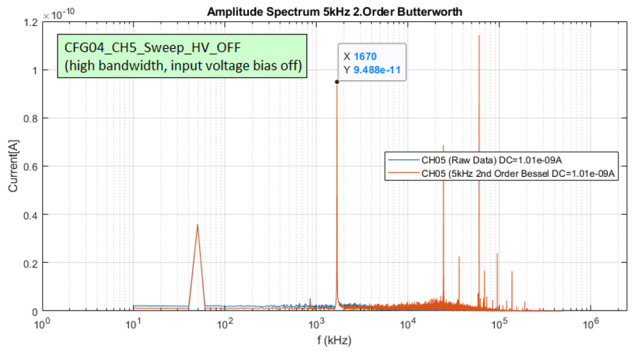

Figure 9: Amplitude spectrum from Fig. 8.

The actual layout provides no shielding between the DC/DC circuit and the log-amplifier because both are under the same shielding cover (Fig. 10). Switching noise from the DC/DC circuit couples strongly into the log-amplifier circuit.

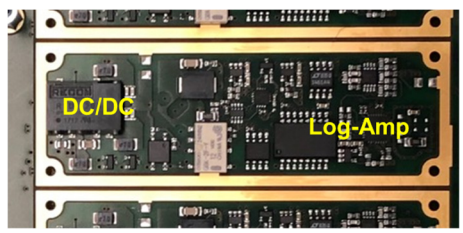

Figure 10: Layout of log-amplifier and DC/DC circuit.

The production circuit needs improvements to reduce the noise from the DC/DC converter. The following improvements are proposed: the DC/DC circuit is placed outside the log-amplifier shielding. The switching frequency of the DC/DC is increased.

The most important measure is to add shielding for the DC/DC converter noise. The shielding itself is more efficient at a higher frequency. Increasing the switching frequency also shifts the noise above the cut-off frequency of the anti-aliasing filter. This will contribute to less noisy signals seen by the ADC circuit.

In the prototype, the shielding material is aluminum, which has a low relative permeability and is not efficient for shielding low frequencies. It might therefore be a better choice to use standard shielding covers made out of cold rolled steel – CRS (Fig. 11). These shields have a resistivity of 4.6e-7 Ωm and relative permeability of ~2000. At a frequency of 60 kHz the skin depth in CRS is around 31 um. This makes a 200 um CRS shielding cover damping the field -56 dB at 60 kHz and -118 dB at 270 kHz – a higher switching frequency where commercial DC/DC converters are available.

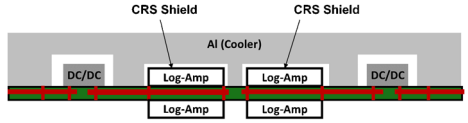

Figure 11: Improved shielding concept.

Content from this work may be used under the terms of the CC BY 3.0 licence (© 2020). Any distribution of this work must maintain attribution to the author(s), title of the work, publisher, and DOI

ISBN: 978-3-95450-222-6 ISSN: 2673-5350 doi:10.18429/JACoW-IBIC2020-WEPP33

Content from this work may be used under the terms of the CC BY 3.0 licence (© 2020). Any distribution of this work must maintain attribution to the author(s), title of the work, publisher, and DOI

EMC

Electromagnetic compatibility is important to test and required to guarantee that the log-amplifier not goes into latch-up due to unexpected noise. Strong noise signals may occur due to lightning or switching of high-power equipment.

Fast transient bursts up to 500 V were applied to the signal cable utilizing a capacitive coupling clamp (Fig. 12). Higher levels were not tested at this time, because only two prototypes are available and there is potential risk of destroying the electronics at higher levels. The test criterion is IEC61000-4-4 type B: Measurement distorted, but the channel must recover to normal operation after the burst.

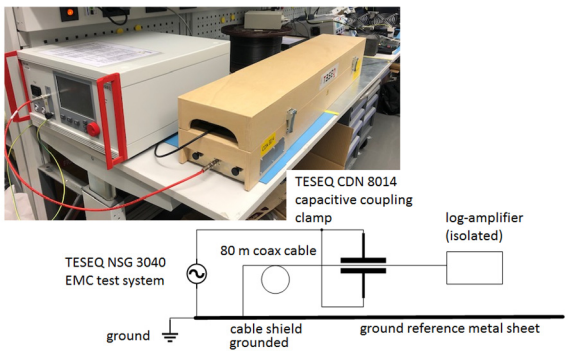

Figure 12: EMC burst test with capacitive coupling clamp.

Measurements of the output signal from the ADC is showing how the bursts influences the measured current strongly (Fig. 13). There is no latch-up and the circuit recovers after the bursts.

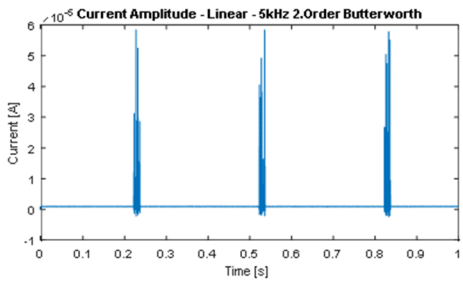

Figure 13: 1.0 µA input current, -200V burst.

Moderate noise signals from external sources, as motor electronics or switching power supplies, coupled via cabling and ground, should not lead to a shift of the average signal level. Lab tests are foreseen to verify this.

Cooling

In the first prototype of the device, the focus was on circuit design. In the second prototype, the cooling design and manufacturability will take precedence. The first prototype showed that some components were not well cooled in the initial design. All components were operating inside the allowed temperature range, but for some components the temperature was quite high.

To improve the cooling and at the same time reduce the number of mechanical parts, a massive milled aluminium cooler replaces the cover plate of the device (Fig. 14). All components with high power losses connect thermally directly to this cooler.

One component type with improved cooling are the SFP+ modules. These circuits are using improved cages with integrated thermal pad, called Thermal Bridge Technology [12]. The improved cooling lowers the temperature and increases expected lifetime for the electro-optical components.

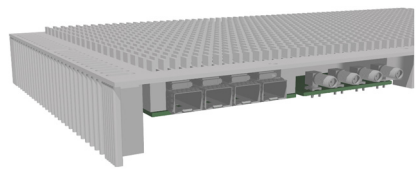

Figure 14: Improved cooling concept.

In addition, other components with high power consumption, like the System-on-Module and the 24 V DC/DC converter, connect with thermal pads directly to the cooler.

ACKNOWLEDGEMENTS

We like to thank Roger Senn for assembling the radial probe and contributing to its design. We thank Pedro Baumann, Gregor Gamma, Daniel Laube, Christian Nyfeler, Thomas Rauber, Roger Senn for providing information on the existing hardware, beam line environment and handling procedures, equipment and needs and for contributing to the mechanical design of the monitor plugs. We thank Roland Heyder for producing the CAD models and drawings for the monitor plugs. We thank Waldemar Koprek and Daniel Llorente for continued firmware support and Damir Anicic for Linux support.

AUTHOR CONTRIBUTIONS

MRog and EJ advanced the electronics. MRog performed the depicted measurements. RD advanced the monitor plug. MRoh advanced the long probe. EJ wrote the electronics chapter and RD the remaining parts of the paper.

REFERENCES

[1] U. Schryber *et al.*, “Status report on the new injector at SIN”, in *Proc. Cyclotrons’81*, Caen, France, Sep. 1981, paper ABI-05, pp. 43-53.

[2] W. Joho, “High intensity problems in cyclotrons”, in *Proc. Cyclotrons'81*, Caen, France, Sep. 1981, pp. 337-347.

[3] C. Baumgarten, “Factors influencing the vortex effect in high-intensity cyclotrons”, in *Proc. Cyclotrons'19*, Cape Town, South Africa, Sep. 2019, pp. 270-274. doi:10.18429/JACoW-Cyclotrons2019-WEB03

[4] A. Adelmann, R. Dölling, and M. Seidel, “Precise simulations of high-intensity cyclotrons”, PSI Scientific Report 2010, Villigen, Switzerland, pp. 54-55.

[5] M. Frey, J. Snuverink, C. Baumgarten, and A. Adelmann, “Matching of turn pattern measurements for cyclotrons using multiobjective optimization”, *Phys. Rev. Accel. Beams*, vol. 22, no. 6, p. 064602, 2019. doi:10.1103/PhysRevAccelBeams

ISBN: 978-3-95450-222-6 ISSN: 2673-5350 doi:10.18429/JACoW-IBIC2020-WEPP33

[6] R. Dölling, "Bunch-shape measurements at PSI's high-power cyclotrons and proton beam lines", in *Proc. Cyclotrons'13*, Vancouver, Canada, Sep. 2013, paper TU3PB01, pp. 257-261.

[7] R. Dölling, G.G. Gamma, V. Ovinnikov, M. Rohrer, P. Rüttimann, and R. Senn, "Development of a replacement for the long radial probe in the Ring Cyclotron", in *Proc. Cyclotrons'19*, Cape Town, South Africa, Sep. 2019, pp. 86-89. doi:10.18429/JACoW-Cyclotrons2019-MOP024

[8] L. Rezzonico *et al.*, "Diagnostics for high intensity beams", in *Proc. BIW'94,* Vancouver, Canada, Oct. 1994, *AIP Conf. Proc.,* vol. 333, pp. 398-494, 1995.

[9] R. Dölling *et al.*, "Development of modular spare parts for the profile and position monitors of the 590 MeV beam line at HIPA", in *Proc. IBIC'19*, Malmö, Sweden, Sep. 2019, paper TUPP035, pp. 402. doi:10.18429/JACoW-IBIC2019-TUPP035

[10] UHV Design Ltd, http://www.uhvdesign.com

[11] R.Dölling, E. Johansen, W. Koprek, D. Llorente Sancho, and M. Roggli, "Development of new loss monitor electronics for the HIPA facility", in *Proc. IBIC'19*, Malmö, Sweden, Sep. 2019, paper MOPP024, pp. 141. doi:10.18429/JACoW--MOPP024

[12] TE connectivity, https://www.te.com

Content from this work may be used under the terms of the CC BY 3.0 licence (© 2020). Any distribution of this work must maintain attribution to the author(s), title of the work, publisher, and DOI

ISBN: 978-3-95450-222-6 ISSN: 2673-5350 doi:10.18429/JACoW-IBIC2020-WEPP34

Content from this work may be used under the terms of the CC BY 3.0 licence (© 2020). Any distribution of this work must maintain attribution to the author(s), title of the work, publisher, and DOI

FIRST BEAM PROFILE MEASUREMENTS BY BEAM INDUCED FLUORESCENCE AT THE J-PARC NEUTRINO EXTRACTION BEAMLINE

S. Cao, M. Friend*, K. Nakayoshi, K. Sakashita
High Energy Accelerator Research Organization (KEK), Tsukuba, Japan
M. Hartz, Kavli IPMU (WPI), University of Tokyo, Tokyo, Japan and TRIUMF, Vancouver, Canada
Y. Koshio, A. Nakamura, Okayama University, Okayama, Japan

Abstract

A Beam Induced Fluorescence (BIF) profile monitor is under development at the J-PARC neutrino extraction beamline, where neutrinos are produced using 30 GeV protons from the J-PARC MR accelerator. Towards the goal of continuously and non-destructively measuring the 1.3 MW proton beam profile spill-by-spill using fluorescence from proton interactions with injected gas, a full working prototype monitor was installed in the beamline in 2019. The prototype includes a scheme for pulsed injection of N_2 gas into the ultra-high vacuum beampipe and two optical readout arms, a conventional one using an Image Intensifier coupled to a CID camera, along with an array of optical fibers coupled to a Multi-Pixel Photon Counter array. Initial beam tests of the system were carried out in early 2020, and BIF light was successfully observed in both optical systems. Details of the prototype monitor, along with first proton beam profile measurement results, will be shown. Improvement plans towards continuous operation of the new profile monitor will also be discussed.

J-PARC AND THE NEUTRINO EXTRACTION BEAMLINE

The J-PARC Main Ring (MR) accelerator currently provides a 515 kW 30 GeV beam to the J-PARC neutrino extraction beamline for the T2K experiment [1]. The beam structure consists of eight ~13 ns (1σ) bunches with a bunch spacing of 581 ns. Currently, $\sim 2.65 \times 10^{14}$ protons per spill are supplied with a spill repetition rate of 2.48 s, while upgrades are planned to increase the number of protons per spill to 3.2×10^{14} and decrease the repetition rate to 1.16 s.

The position and profile of the proton beam extracted into and propagated through the neutrino extraction beamline must be continuously monitored to prevent any damage to equipment due to mis-steered beam, as well as to understand the proton beam properties as inputs into physics analyses.

Currently, the beam profile is measured by a suite of 19 Segmented Secondary Emission Monitors (SSEMs), 18 of which can only be used periodically or during beam tuning. This is because each SSEM causes 0.005% beam loss, which is enough to cause radio-activation of and possibly even damage to beamline equipment. Of course, this loss is proportional to the beam power, and the total induced loss will increase as the number or protons per pulse and beam spill repetition rate are increased.

Development towards a continuous, non-destructive beam profile monitor is therefore underway. Due to the large number of protons per bunch, and therefore the relatively high beam-induced space-charge field in the J-PARC neutrino extraction beamline, a Beam Induced Fluorescence (BIF) monitor [2] was chosen as a suitable profile monitor candidate. The BIF monitor detects light induced by de-excitation of gas which has been excited or ionized by interactions with incident protons. The longitudinal and transverse pattern of the induced fluorescence should match that of the original proton beam, allowing for an indirect measurement of the proton beam position and profile.

J-PARC NEUTRINO BEAMLINE BEAM INDUCED FLUORESCENCE MONITOR

Development of the J-PARC neutrino extraction beamline BIF monitor has been underway since 2015, with a full working prototype installed in the beamline in 2019 [3]. A a photograph of the installed prototype is shown in Fig. 1.

The monitor includes of a series of valves for gas injection into the beam pipe, as well as transparent fused quartz windows mounted on the bottom and side of the beam pipe to allow fluorescence light to escape. The inner surface of the beampipe near the interaction region is coated with a 1-μm-thick coating of Diamond Like Carbon in order to minimize reflections within the beampipe. As shown in Fig. 2, two separate optical focusing and transport systems are used – one mounted on the side of the beam pipe to make a measurement of the vertical transverse beam position and profile, and one mounted on the bottom of the beam pipe to make a measurement of the horizontal beam properties.

The vertical beam measurement arm consists of a series of lenses and mirrors to focus the light downwards onto an array of silica core optical fibers. These optical fibers are used to transport the fluorescence light away from the high-radiation area near the beamline and into a lower-radiation environment inside a subtunnel ~30 meters away, where an array of Multi-Pixel Photon Counters (MPPCs) is used to detect the light.

The horizontal beam measurement arm consists of a more conventional light detection system – two lenses focus the induced fluorescence light onto a gated Micro-Channel Plate (MCP) based Image Intensifier, which is coupled to a

* mfriend@post.kek.jp

ISBN: 978-3-95450-222-6 ISSN: 2673-5350 doi:10.18429/JACoW-IBIC2020-WEPP34

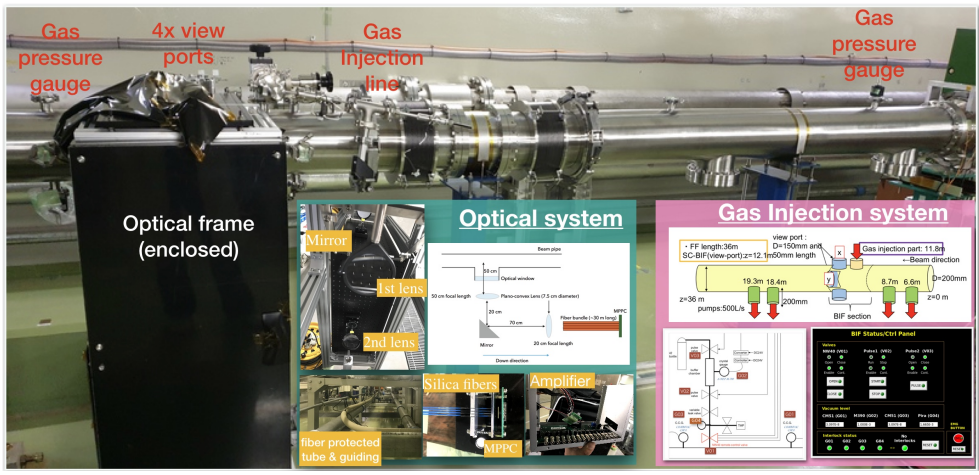

Figure 1: Photograph of the installed prototype BIF monitor.

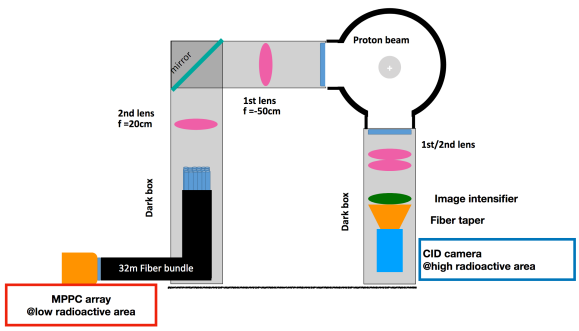

Figure 2: Schematic diagram of the BIF monitor optical systems.

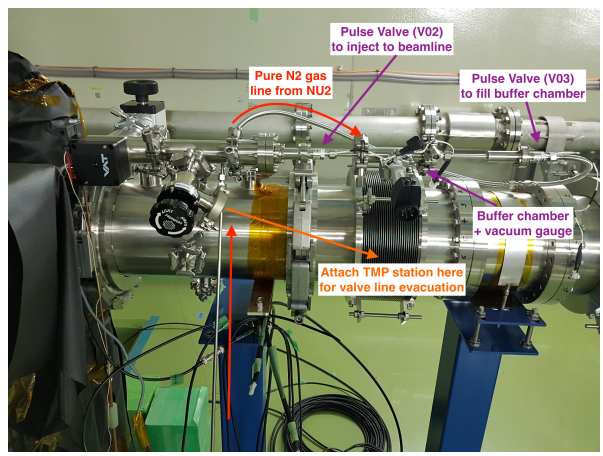

Figure 3: Photograph of the gas injection system for the installed prototype BIF monitor.

radiation-hard Charge Injection Device (CID) camera by a fiber taper. Gating of the Image Intensifier allows for integration of all BIF light over each 5 µs beam spill.

MPPCs have a ns-level response time and single-photon sensitivity. They are therefore very useful for detecting photons at low light levels, as well as for understanding any time-dependence of the beam induced fluorescence light. Measurement of the time-dependence is essential at the J-PARC neutrino beamline, since the measured beam profile could be distorted if ionized gas moves in the relatively high beam-induced space charge field before BIF light is produced.

The Image Intensifier and CID camera arm, on the other hand, has the advantage that it is high-resolution, as well as being relatively radiation hard. This means that the system can be mounted directly to the beampipe, without the additional complication of transport to a lower radiation environment.

First in-situ beam tests using the full working system were carried out in early 2020.

GAS INJECTION SYSTEM

The gas injection system is designed to provide a localized pressure bump of $\sim 1\times10^{-2}$ Pa when the beam passes, while allowing the pressure to fall back to the standard level of 1×10^{-5} Pa between spills. This is achieved using a pulsed gas injection system with sub-ms-long gas pulses injected directly before each beam spill. N_2 gas is used currently, although upgrades to different gas types may be possible.

A buffer chamber upstream of the pulsed gas injection valve, filled periodically by another pulse valve, helps to prevent continuous injection of gas in case of valve failure. A remotely-controlled pneumatic valve is also installed downstream of the gas injection system, where an interlock system closes this valve in case any pressure along the beamline or within the BIF valve injection line becomes higher than a set threshold.

A photograph of the gas injection system is shown in Fig. 3.

Pumping is done by 500 L/s ion pumps installed at various locations along the beamline. New pumps specifically for the BIF monitor were installed 1.7 and 2.8 m upstream of the gas injection point.

Injection of gas followed by a full pumpdown of the beamline for each beam spill with a 2.48 or 1.16 s repetition rate

Content from this work may be used under the terms of the CC BY 3.0 licence (© 2020). Any distribution of this work must maintain attribution to the author(s), title of the work, publisher, and DOI

ISBN: 978-3-95450-222-6 ISSN: 2673-5350 doi:10.18429/JACoW-IBIC2020-WEPP34

Content from this work may be used under the terms of the CC BY 3.0 licence (© 2020). Any distribution of this work must maintain attribution to the author(s), title of the work, publisher, and DOI

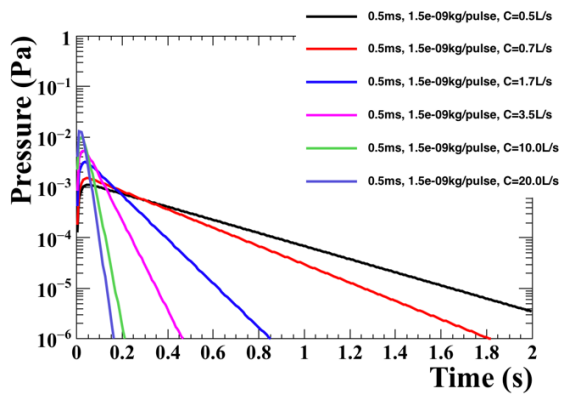

Figure 4: Estimation of the expected pressure bump when a 500 µs-long gas pulse of 1.5×10^{-9} kg is injected assuming different values for the valve conductance.

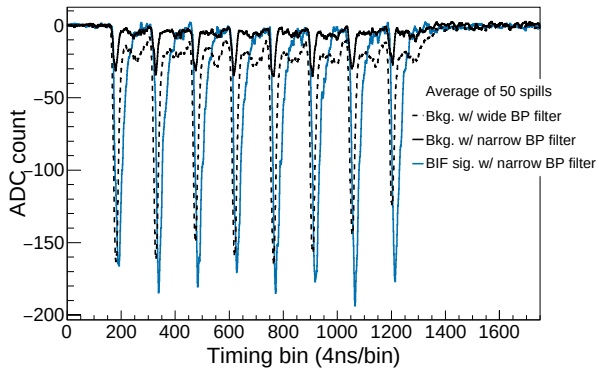

Figure 5: Observed beam-induced background on an optical fiber before and after background mitigation (with optical filtering of 400±200 nm and 400±40 nm respectively). The observed BIF signal light after mitigation is also shown.

requires fast injection and fast pumpdown. This is achieved by reducing the conductance of the gas injection valve line as much as possible. Estimates of the conductance of the currently installed gas line based on data taken so far show that a conductance of only ~1 L/s has been achieved, while conductance of around 10 L/s is desired, as shown in Fig. 4.

MITIGATING BACKGROUNDS

Beam induced background on both optical systems must be mitigated in order to maximize the BIF signal to background ratio.

The Image Intensifier was found to produce a constant beam-induced background of ~2.5×10^6 photons/spill over the full surface area, most likely due to incident beam loss on the MCP. This was reduced by a factor of ~0.6 by installing a concrete hut around the optical system placed under the beamline. Improvements in shielding could further reduce this background, although increasing the Image Intensifier gain could increase it.

Cherenkov light produced by beam loss particles incident on the optical fiber array near the beamline also constitute a considerable background. This background was reduced by aggressive optical filtering, where wavelengths outside of 400±40 nm were cut, while the expected wavelength of the BIF light is 390 nm [4]. An optical baffle was also installed to select light outgoing from the fibers at angles <12°. The observed background and BIF light from the optical fibers before and after background mitigation is shown in Fig. 5. Various studies were also performed to extract the wavelengths of the induced background light and the BIF light, and results will be released in a future publication.

FIRST PROFILE MEASUREMENTS

A series of in-situ beam tests were carried out, with different quantities of gas injected into the beamline at different times relative to the beam spill. A clear BIF signal was observed with injected gas down to ~1×10^{-8} kg/pulse. The intensity of the observed light was clearly correlated with the amount of injected gas and was correlated between the two optical systems. The shape of the injected gas pulse could be clearly mapped out by adjusting the relative timing between the beam spill and gas injection.

The measured and extracted vertical beam profile from the optical fiber and MPPC array is shown in Fig. 6. Analysis of the MPPC data is ongoing to extract information about the time-dependent distortion of the profile due to space charge effects.

The measured horizontal and longitudinal beam profile from the Image Intensifier and CID camera system is shown in Fig. 7. A 1D projection of the extracted horizontal profile is also shown.

The measured horizontal and vertical beam widths are relatively consistent with the expected beam width at the BIF monitor location based on an optics fit to neighboring profile monitors. The measured vertical beam position is also consistent with neighboring monitors, while additional alignment and calibration of the camera system is necessary to confirm that the horizontal beam position is also consistent.

A precise calculation of the number of produced photons as a function of the quantity of injected gas or the expected gas pressure is underway.

IMPROVEMENTS TOWARDS A WORKING MONITOR

Various upgrades to the BIF monitor working prototype are necessary before continuous use is possible.

Further alignment and calibration of the optical systems is necessary and is underway. Especially, mis-alignment of the fiber taper relative to the Image Intensifier or CID camera may be distorting the collected beam image shown in Fig. 7.

Currently, the required amount of gas injected for a clear beam profile measurement is ~1×10^{-8} kg/pulse, while the original design calls for injecting only 5×10^{-10} kg/pulse to maintain ion pump lifetime. Improvements in the valve line

ISBN: 978-3-95450-222-6 ISSN: 2673-5350 doi:10.18429/JACoW-IBIC2020-WEPP34

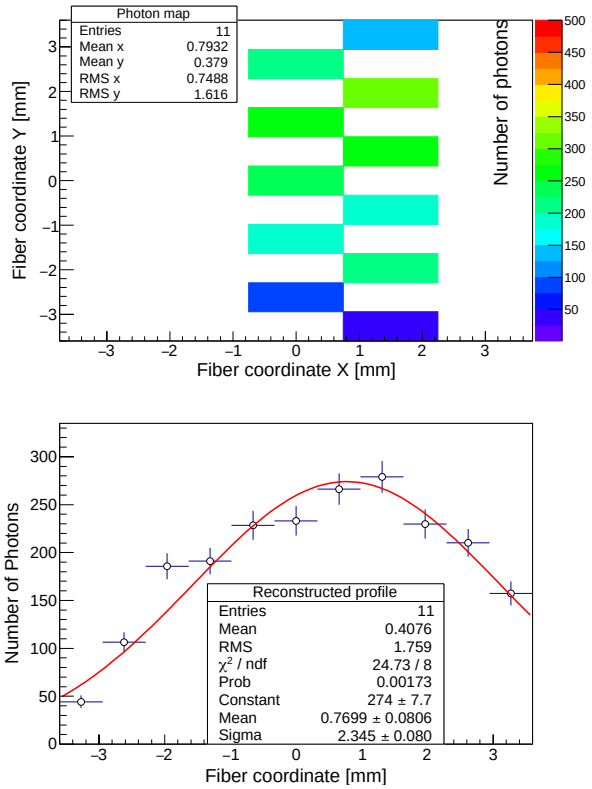

Figure 6: 2D (top) and 1D (bottom) measurements of the vertical proton beam profile (in optical system coordinates) by the optical fiber and MPPC array.

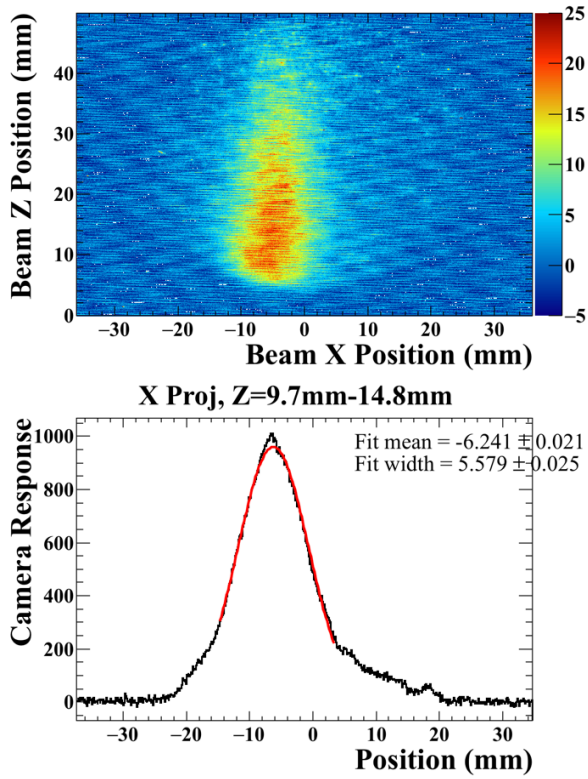

Figure 7: 2D (top) and 1D (bottom) measurements of the horizontal proton beam profile (in beam coordinates) by the Image Intensifier and CID camera.

conductance are planned, which should allow for the necessary pressure bump of $\sim 1 \times 10^{-2}$ Pa with $\sim 5 \times 10^{-10}$ kg/pulse injected, as shown in Fig. 4.

Additional optical fibers would help increase the amount of collected light. Shorter optical fibers leading to a radiation-hard photon detection system could reduce beam-induced backgrounds as well as loss of photons due to attenuation in the optical fibers. Such upgrades would also improve the signal to noise ratio and are under consideration now.

A higher gain Image Intensifier is also under consideration for the horizontal readout arm.

CONCLUSION

A working prototype BIF monitor has been installed in the J-PARC neutrino extraction beamline. First beam tests are promising and show that a clear beam profile can be reconstructed by two different optical detection systems. Upgrades are underway in order to increase the pressure bump at the BIF interaction region, as well as to increase the photon collection efficiency.

ACKNOWLEDGMENT

The authors would like to thank the members of the neutrino beam group at J-PARC, as well as the T2K OTR group from Imperial College London for their valuable help and support. This work was supported by Japanese KAKENHI Grant-in-Aids (16H06288, 16H00875, 26105504).

REFERENCES

[1] K. Abe *et al.*, "The T2K Experiment", *Nucl. Instr. and Meth. A*, vol. 659, pp. 106-135, 2011. doi:10.1016/j.nima.2011.06.067

[2] F. Becker *et al.*, "Beam induced fluorescence (BIF) monitor for transverse profile determination of 5 to 750 MeV/u heavy ion beams", in *Proc. DIPAC'07*, Venice, Italy, paper MOO3A02, pp. 33-35.

[3] S. Cao *et al.*, "Development of a Beam Induced Fluorescence Monitor for Non-Destructively Profiling MW Proton Beam at the J-PARC Neutrino Beamline", in *Proc. IBIC'19*, Malmö, Sweden, Sep. 2019, pp. 358–362. doi:10.18429/JACoW-IBIC2019-TUPP024

[4] M.A. Plum *et al.*, "N_2 and Xe gas scintillation cross-section, spectrum, and lifetime measurements from 50 MeV to 25 GeV at the CERN PS and Booster", *Nucl. Instr. and Meth. A*, vol. 492, pp. 74–90, 2002. doi:10.1016/S0168-9002(02)01287-1

Content from this work may be used under the terms of the CC BY 3.0 licence (© 2020). Any distribution of this work must maintain attribution to the author(s), title of the work, publisher, and DOI

ISBN: 978-3-95450-222-6 ISSN: 2673-5350 doi:10.18429/JACoW-IBIC2020-WEPP36

Content from this work may be used under the terms of the CC BY 3.0 licence (© 2020). Any distribution of this work must maintain attribution to the author(s), title of the work, publisher, and DOI

RECENT PROGRESS ON THE COMMISSIONING OF A GAS CURTAIN BEAM PROFILE MONITOR USING BEAM INDUCED FLUORESCENCE FOR HIGH LUMINOSITY LHC

M. Ady, O. R. Jones, S. Mazzoni†, I. Papazoglou, C. Pasquino, A. Rossi,
S. Sadovich, G. Schneider, R. Veness, CERN, Geneva, Switzerland
P. Forck, S. Udrea, GSI, Darmstadt, Germany
N. Kumar, A. Salehilashkajani, C. P. Welsch, H. D. Zhang
University of Liverpool and Cockcroft Institute, Warrington, UK

Abstract

For the high-luminosity upgrade of the Large Hadron Collider ("HL-LHC"), active control of proton beam halo will be essential for safe and reliable operation. Hollow Electron Lenses can provide such active control by enhancing the depletion of halo particles, and are now an integral part of the high luminosity LHC collimation system. The centring of the proton beam within the hollow electron beam will be monitored through imaging the fluorescence from a curtain of supersonic gas. In this contribution we report on the recent progress with this monitor and its subsystems, including the development of an LHC compatible gas-jet injection system, the fluorescence imaging setup and preliminary test measurement in the LHC.

INTRODUCTION

The high-luminosity upgrade of the Large Hadron Collider ("HL-LHC") is a major upgrade of LHC that aims at extending its operability by a decade by increasing its instantaneous luminosity by a factor five beyond its present design value [1]. At the core of the HL-LHC is the upgrade of the focusing triplets to allow for a smaller β* in the interaction region, combined with compact superconducting radio frequency crab cavities for bunch rotation. These are advanced technical solutions that require a substantial modification of a number of LHC subsystems. The collimation system for HL-LHC, for instance, will require an improved cleaning performance to cope with the increased stored beam energy. To achieve this, is it envisaged to control the diffusion of halo particles by means of a Hollow Electron Lens (HEL) [2]. This will enclose the circulating proton beam with a low energy electron beam, deflecting any halo protons that drift into the electron beam, while leaving the proton beam core unaffected. Key to a correct operation of the HEL is the centring of the circulating proton beam within the hollow electron beam to guarantee that the core will propagate in a region of negligible electromagnetic field. To monitor the HEL alignment, a beam gas curtain (BGC) profile monitor using fluorescence is under development in the framework of the HL-LHC project through a collaborative effort between CERN, GSI and the Cockcroft Institute / University of Liverpool. In this contribution we report on recent progress with the development of the BGC and its subsystems and on the installation of a prototype that will be operated during the next LHC physics run.

BGC PRELIMINARY STUDIES

Beam Gas Curtain Models and Simulations

Gas curtain generation in the BGC consists of several stages between the gas injection point and the beam interaction chamber. These stages are separated by skimmers, selecting only the central, co-linear part of the gas jet while rejecting the rest. The resulting pressure drop is approximately 2 orders of magnitude per stage. The Monte Carlo code Molflow+ was used to simulate the pressure distribution after the final skimmer, assuming a free molecular flow regime after the first skimmer. Skimmer sizes were therefore calculated so that the expanding gas curtain achieves a width of 20 mm at the interaction point, which is sufficiently wide to cover the hollow electron beam and allow a margin for beam position changes.

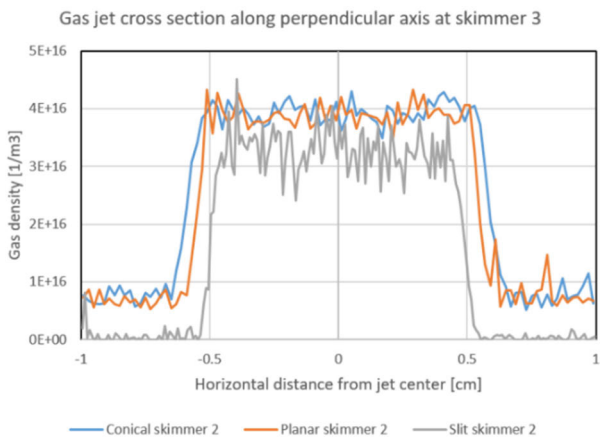

Figure 1: Density profiles for different second skimmer shapes before the interaction point.

Given the skimmer positions (determined by mechanical constraints) and the required sizes, a series of simulations were carried out to verify the gas density in the system to optimize the density within the jet and low contaminations outside of the stream. Figure 1 shows the density profiles at skimmer 3 for different second skimmer shapes before the interaction point. The planar con-

ISBN: 978-3-95450-222-6 ISSN: 2673-5350 doi:10.18429/JACoW-IBIC2020-WEPP36

figuration is seen to perform the best and is the one chosen for the LHC prototype instrument.

One of the factors which may limit the spatial resolution of the BGC beam diagnostics set-up is the thickness of the gas curtain. To estimate its influence, a simplified 2D model was developed, with the assumption that the curtain is considered to have a lateral extension much larger than the beam under investigation and the same gas density throughout the width of the curtain. Since the gas density is very low, the refractive index of the curtain can be considered equal to that of vacuum (i.e. $n_C = 1$). The charged particle beam has radial symmetry, which in 2D means that its flux depends only on the distance from the beam axis. Background gas density is neglected, since it is homogeneously distributed and therefore has no contribution to the shape of the profile. Finally, ideal optics with a practically infinite depth of field is assumed and the detector has just one dimension. Under these conditions the detected intensity profile can be calculated (see [3] and references therein).

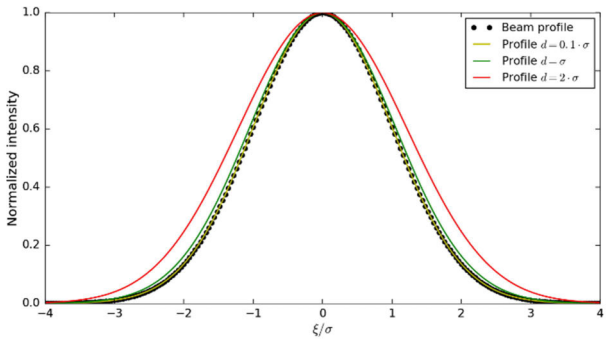

Figure 2: Recorded profiles estimated based on the present 2D model as a function of the curtain thickness d.

When considering a charged particle beam with a Gaussian transverse profile of RMS width σ, and a curtain with parabolic density distribution, the observed profiles are presented in Fig. 2 for curtain thicknesses $d = 0.1\cdot\sigma$, σ, and $2\cdot\sigma$. At $d = 2\cdot\sigma$ the increase of the profile width in the image is clearly visible, with the observed RMS width $\approx 1.2\cdot\sigma$. According to this model, the profile is expected to be reproduced with relatively good accuracy if d is kept below $2\cdot\sigma$. However, if increasing the signal strength is of a higher priority one has to consider that signal amplitude saturation occurs due to the recorded profile's FWHM increasing with the curtain's thickness. The model shows that curtain thicknesses beyond $d \approx 5\cdot\sigma$ bring no benefit in terms of signal strength.

Electron Beam Measurements with the BGC Lab Model

A laboratory model of the BGC is installed at the Cockcroft Institute, UK, and is shown in Fig. 3. The instrument can generate a gas curtain with a density around $\sim 10^{16}$ molecules/m^3 within a size of 8×1.5 mm^2. Because of the differential pumping, the pressure in the interaction chamber maintained at $\sim 10^{-9}$ mbar even with a highly outgassing electron gun nearby. The profile of a 5 keV electron beam was recently measured using Nitrogen (N_2), Neon (Ne) and Argon (Ar) gas where the wavelengths of the fluorescence photons are centred at 391.4 nm, 585.4 nm and 476.5 nm respectively. A photon-counting method was used to create the image from the fluorescence generated from the gas-beam interaction.

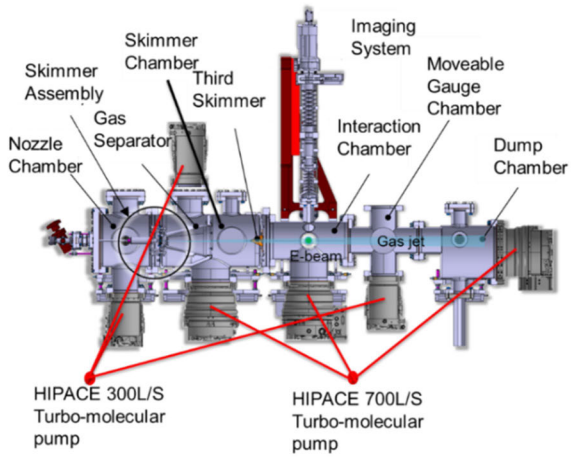

Figure 3: Schematic view of the prototype BGC monitor at the Cockcroft Institute.

Unlike N_2, the wavelength of the fluorescent photons emitted from both Ne and Ar are in the same range of the spectrum as the electron gun filament emissions. This leads to an increase in background noise for these gases which is hard to remove even by using a narrow bandpass filter around the wavelength of interest. A small, blackened aluminium foil with an opening diameter of 3 mm was therefore placed between the electron gun and the interaction region in the vacuum to reduce the filament light. A set of background measurements was also taken with no gas-curtain present to allow this background to be subtracted from the data. The normalised intensity plots of nitrogen, neon and argon are displayed in Fig. 4, showing a good agreement between the three profiles.

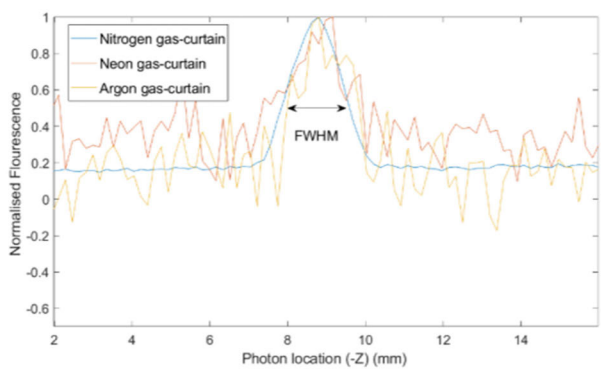

Figure 4: Normalised intensity plots of nitrogen (400 s integration time), neon and argon (4000 s integration time).

The photon detection rate is approximately 10 time lower for Ar and Ne when compared to N_2 under similar conditions. This is due to their smaller cross-sections and,

Content from this work may be used under the terms of the CC BY 3.0 licence (© 2020). Any distribution of this work must maintain attribution to the author(s), title of the work, publisher, and DOI

ISBN: 978-3-95450-222-6 ISSN: 2673-5350 doi:10.18429/JACoW-IBIC2020-WEPP36

Content from this work may be used under the terms of the CC BY 3.0 licence (© 2020). Any distribution of this work must maintain attribution to the author(s), title of the work, publisher, and DOI

for Ne, also lower photo-cathode efficiency, which is compensated somewhat by a higher gas curtain density. The number of photons detected can be estimated [4] for each gas to the correct order of magnitude based on gas curtain density, cross section, e-beam current and optical properties. A comparison between the theoretical estimations and the measured photon number shows a reasonable agreement, as shown in Table 1. For both the HEL expected photons and lab conditions the gas-curtain density is assumed to be 2.5×10^{-16} m^{-3}. The e-beam used in lab conditions has a current of 0.65 mA and 5 KeV energy. The lower measured photon with respct to the estimated one can be explained by a lower than expected gas-curtain density, especially in the case of Nitrogen, overestimation of the solid angle or optics transmission or photon losses in the intensifier. Scaling this to the properties of the future device foreseen for the electron lens, the expected photon rate will be at least 4 orders of magnitude higher, reducing the required integration time to obtain correct image to below the second.

Table 1: Comparison of the Fluorescence Photon Rate (in Counts/s) for Different Working Gases for the Prototype BGC Monitor and the Final Electron Lens BGC Monitor

Emitter	HEL expected	Lab conditions	Measured
N_2	3.4×10^{6}	8.8×10^{2}	1.7×10^{1}
Ne	2.5×10^{4}	6.5	1.6
Ar	2.3×10^{4}	6.0	1.3

LHC Fluorescence Tests

Beam profile measurements based on fluorescence in the CERN PS and SPS accelerators are reported in literature [5,6] for various gases including Ar and N_2.

While these tests show promising results for beam profile reconstruction, their extrapolation to the case of the LHC is not trivial due to the significantly different beam energy. In order to quantify the S/N to be expected in the LHC, a Beam Induced Fluorescence (BIF) test instrument was installed in the course of 2018. The optical instrument is composed of two 50 mm diameter, 300 mm focal length doublets that project the image of the center plane of the beampipe onto a single micro channel plate (MCP) intensified camera with a Multialkali photocathode.

A remote controlled filter wheel allows a neutral density (ND1 – ND2) or a bandbass (340 ± 40 nm, 585 ± 40 nm) filter to be inserted in the light path. The entire optical instrument is enclosed in a light tight container. A gas injection system allows Neon gas to be introduced inside the beam pipe up to a pressure of approximately 5×10^{-8} mbar. Measurements were performed in the second half of 2018 with both protons and Pb ions, at energies from 450 Z GeV to 6.5 Z TeV. The case of Pb ions at 450 Z GeV is the one that yielded the best signal to noise, with the lowest amount of optical background. Figure 5 (a) shows the fluorescence image of Pb ions at 450 Z GeV with a very long (1286 s) exposure time. Optical background and showers generated by beam loss have been subtracted from the image. The fluorescence signal appears as a streak at the very top of the image. The off-centre position of the beam with respect to the centre of the viewport is believed to be caused by a misalignment of the vacuum chamber, whose precise position with respect to the beam pipe centre was not measured before installation. Figure 5 (b) shows a Gaussian fit of the vertical profile of the fluorescence image averaged over 10 mm. The resulting width (σ = 2.2 mm) could not be directly cross-checked with another instrument as no other profile measurement device can currently measure a nominal Pb ion beam at injection energy. It is possible however to deduce that the average transverse beam size could not have been greater than 2.1 mm. This is derived from the measurement of the beam size at high energy as performed by the Beam Synchrotron Radiation Telescope (BSRT) and rescaled to an energy of 450 Z GeV assuming no emittance growth during the energy ramp. The fluorescence measurement is therefore consistent with such a value. However, further studies are clearly needed to better characterize the accuracy, as the measurement of the LHC beam profile was not the main goal of the test.

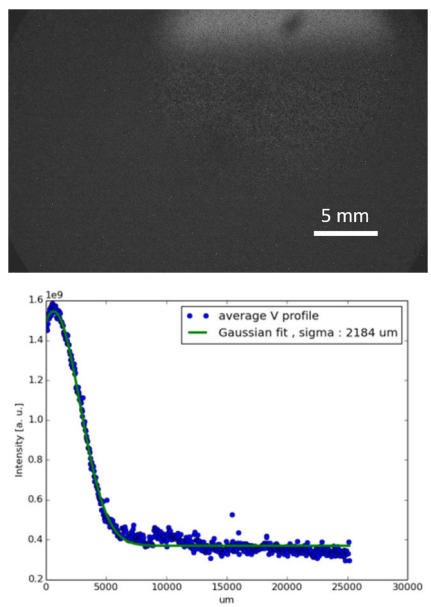

Figure 5: Top: Fluorescence image of Pb ions at 450 Z GeV with an integration time of 1286 s and the optical background subtracted. The black mark is due to a defect of the photocathode. Bottom: Fit of the vertical profile averaged longitudinally over 10 mm.

When reducing integration time, the BIF setup allows us to measure the evolution of the beam profile as a function of time, as shown in Fig. 6 where integration time was set to 40 seconds. The measurement was performed during the filling of the LHC, with a circulating charge ranging from 2×10^{12} C to 1.2×10^{13} C. Data points before 18:40:00 (hh:mm:ss) are to be discarded as the stored beam current was too low for the selected exposure time.

Measurements with Pb ions at high energy and with protons at both injection and high energy are inconclusive

ISBN: 978-3-95450-222-6 ISSN: 2673-5350 doi:10.18429/JACoW-IBIC2020-WEPP36

due to an insufficient signal to noise ratio. For the particular case of protons at high energy (the relevant case for HEL alignment), the main source of noise is suspected to be synchrotron radiation reflected from the copper beam pipe surface opposite to the viewport. This resuls in a background 10^4 times higher than the one measured for the Pb ions at injection. This test therefore highlighted the importance of a reducing any parasitic reflection from entering the imaging optics by means of proper coating for absorption.

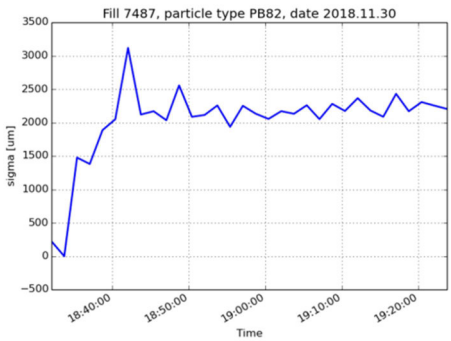

Figure 6: Beam size (σ) as a function of time for Pb ions beam. Integration time is 40 s.

INSTALLATION OF BGC PROTOTYPE IN THE LHC

A BGC prototype has been designed and is currently being built. The installation of the demonstrator instrument will happen in two phases. The first phase, now installed, includes the main gas curtain interaction chamber, a simple gas injection system and the optical instrument used for previous fluorescence measurements. In order to minimise optical background the entire vacuum chamber is blackened with amorphous carbon coating (see Fig. 7), with a reflectivity of about 10-15% [7], while in front of the camera, a specially designed plate is inserted with a vacuum compatible, multilayer coating to give a reflectivity of 0.2-0.5% at the wavelength of interest (585.4 nm). By applying these coatings, the optical background reaching the camera should be sufficiently reduced to allow imaging at high energy with protons. In phase 2 the full BGC instrument will be installed, including the supersonic gas curtain generation and the final optical system (see Fig. 8). The selected working gas is injected at a pressure of 10 bar through a 30 mm nozzle. The jet is then shaped with a series of 3 skimmers, resulting in a final equivalent pressure in the 10^{-7} mbar range (corresponding to a density of 2.47×10^9 cm^{-3}) while the background pressure is expected to be in the 10^{-9} mbar range. A gas dump system is placed on the opposite side of the gas injection system in order to collect the gas curtain after the beam interaction to maintain as low as possible a background pressure in the interaction chamber. A slit aperture matching the gas curtain dimensions is placed at the entrance to the dump chamber, which allows the gas jet to enter but prevents the majority of any reflected gas from re-entering the interaction volume.

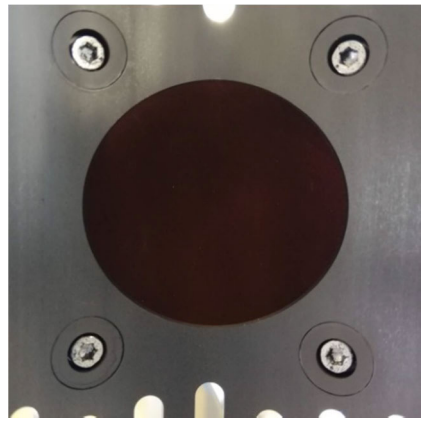

Figure 7: Amorphous carbon coating together with the multilayer coated plate.

This gas is then extracted using a high conductance pump. The gas injection system and gas dump are scheduled for testing at the Cockcroft Institute in 2020, with a subsequent test on the HEL test stand at CERN foreseen in 2021, before installation in the LHC.

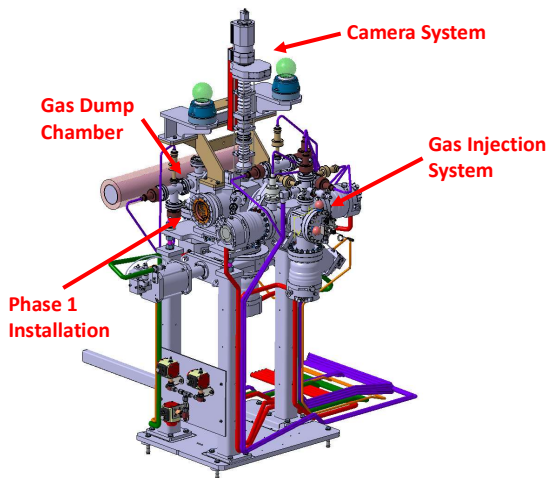

Figure 8: Phase 2 of the final BGC demonstrator.

SUMMARY

We have presented the recent progress of the BGC development, including simulation and analysis of the gas curtain shaping, fluorescence measurements of 5 keV electrons in the laboratory and of Pb ions in the LHC. A BGC demonstrator has been installed in the LHC with blackened vacuum chamber surfaces for improved optical background reduction. The BGC demonstrator will be operated during the next LHC physics run scheduled to start in 2022.

REFERENCES

[1] G. Apollinari *et al.*, "High-Luminosity Large Hadron Collider (HL-LHC) Technical Design Report V. 0.1", CERN, Geneva, Switzerland, Rep. CERN-2017-007-M, 2017.

[2] G. Stancari, A. Valishev, G. Annala, G. Kuznetsov, V. Shiltsev, D. A. Still, and L. G. Vorobiev, "Collimation with Hollow Electron Beams", *Phys. Rev. Lett.*, vol. 107, p. 084802, 2011. doi: 10.1103/PhysRevLett.107.084802

Content from this work may be used under the terms of the CC BY 3.0 licence (© 2020). Any distribution of this work must maintain attribution to the author(s), title of the work, publisher, and DOI

ISBN: 978-3-95450-222-6 ISSN: 2673-5350 doi:10.18429/JACoW-IBIC2020-WEPP36

[3] S. Udrea and P. Forck, "CERN e-lens Milestone 1.6 report v2", Rep. CERN EDMS 2333413, Sept. 2018.

[4] R. Veness *et al.*, "Development of a Beam-Gas Curtain Profile Monitor for the High Luminosity Upgrade of the LHC", in *Proc. IBIC'18*, Shanghai, China, Sep. 2018, pp. 472-476. doi:10.18429/JACoW-IBIC2018-WEPB16

[5] M. A. Plum, E. Bravin, J. Bosser, and R. Maccaferri, "N2 and Xe gas scintillation cross-section, spectrum, and lifetime measurements from 50 MeV to 25 GeV at the CERN PS and Booster", *Nucl. Instrum. Methods in Phys. Res. A*, vol. 492, pp. 74–80, 2002. doi: 10.1016/S0168-9002(02)01287-1

[6] A. Variola, R. Jung, and G. Ferioli, "Characterization of a nondestructive beam profile monitor using luminescent emission", *Phys. Rev. ST Accel. Beams,* vol. 10, p. 122801, 2007. doi: 10.1103/PhysRevSTAB.10.122801

[7] J. Glutting, "Blackening Investigation for the BGC Interaction Chamber", Rep. CERN EDMS 2052543, Dec. 2018.

Content from this work may be used under the terms of the CC BY 3.0 licence (© 2020). Any distribution of this work must maintain attribution to the author(s), title of the work, publisher, and DOI

ISBN: 978-3-95450-222-6 ISSN: 2673-5350 doi:10.18429/JACoW-IBIC2020-WEPP37

TRANSVERSE PHASE PORTRAIT TOMOGRAPHY OF PROTON BEAMS AT INR RAS LINAC

A. I. Titov[1†], S. A. Gavrilov[1]
Institute for Nuclear Research of the Russian Academy of Sciences, Moscow, Russia
[1]also at Moscow Institute of Physics and Technology (State University), Moscow, Russia

Abstract

Measuring of the parameters of the transverse phase portraits is crucial for beam dynamics. A method of tomographic reconstruction is implemented at INR RAS linac as an alternative to already existing quadrupole variation method. In this work new feature of disturbing online measurements of phase portrait parameters and important experimental results are discussed. Comparison of tomographic method with quadrupole variation method is presented.

INTRODUCTION

Measuring of the parameters of the transverse phase space is crucial for beam dynamics. For low-energy beams these measurements can be made with slit-grid or pepper pot devices. However, for high-energy beams another method is applied – a quadrupole variation method (QVM). A typical layout of components, required for QVM measurements, is presented on Fig. 1.

Another way of measuring beam transverse phase portrait parameters, which can be attributed to QVM, is a tomographic reconstruction. It can be implemented with the same layout as QVM and differs only in processing of obtained information. Feasibility of tomographic reconstruction method is based on Radon transform and was firstly implemented in 70s [1].

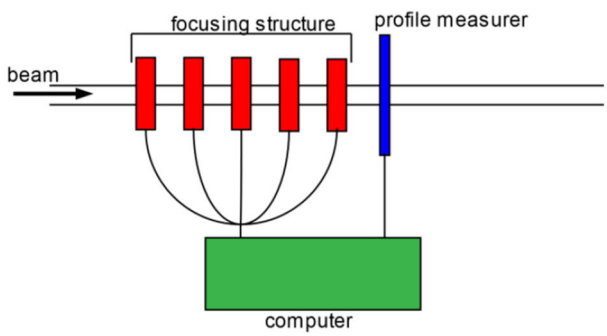

Figure 1: Typical layout of components required for quadrupole variation method measurements.

At INR RAS linac automatic procedure of emittance measurements was developed and implemented at the exit of accelerator on the base of ionization Beam Cross Section Monitor (BCSM) [2]. This procedure provides disturbing online emittance measurements during routine accelerator operation. Also a program for offline measurements was implemented.

† aleksandr.titov@phystech.edu

DESIGN FEATURES

As it was previously mentioned tomography is based on BCSM, which schematic configuration is presented on Fig. 2. Image from its phosphor screen is transferred via catadioptric system and acquired with Basler acA780-75gm camera, which is installed under concrete shielding of accelerator. Camera is connected with computer in the control room via optic fibre.

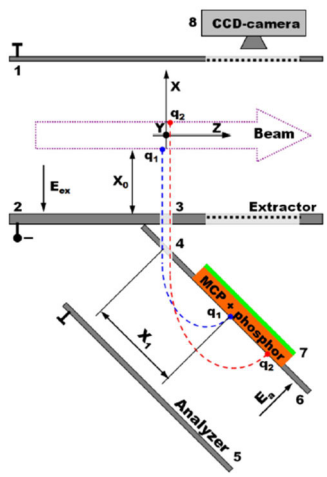

Figure 2: BCSM schematic configuration.

Phase portrait rotation is performed by eight quadrupole doublets, located before BCSM. They are powered by two independent current sources. Transfer matrix method is used for description of focusing structure of accelerator.

SOFTWARE FEATURES

Tomography software at INR is written mostly in LabVIEW [3], tomography kernel is written in Python. Image acquisition and calibration is based on luminescent diagnostics software for INR RAS Proton Irradiation Facility (PIF) and has been described in detail in [4].

Online tomography consists of several steps, which include preplanning of measurements, the measurements of beam profiles and tomographic reconstruction. Preplanning step includes input of currents, which will be set on lenses current sources. After preplanning step user starts up the measurements for tomography.

During the measurement step program changes currents in the sources according to the plan, then the program measures profiles. After making all planned measurements, the program returns initial currents in the sources

Content from this work may be used under the terms of the CC BY 3.0 licence (© 2020). Any distribution of this work must maintain attribution to the author(s), title of the work, publisher, and DOI

ISBN: 978-3-95450-222-6 ISSN: 2673-5350 doi:10.18429/JACoW-IBIC2020-WEPP37

Content from this work may be used under the terms of the CC BY 3.0 licence (© 2020). Any distribution of this work must maintain attribution to the author(s), title of the work, publisher, and DOI

and starts tomographic reconstruction based on acquired profiles.

Reconstruction step starts with making transfer matrixes for each measured profile. Obtained profiles are transformed with use of the transfer matrixes and converted into a sinogram. The rotation angles in phase space are also obtained from transfer matrixes. The sinogram and rotation angles are then transmitted to tomography kernel.

The tomography kernel is based on Simultaneous Algebraic Reconstruction Technique (SART) algorithm [5]. It is considered as a fast converging algorithm, which needs fewer projections for same level of RMS error in comparison with most of other algorithms. Figure 3 shows level of error depending on number of iterations for different amount of projections. SART algorithm is taken from open-source code package called “scikit-image” [6].

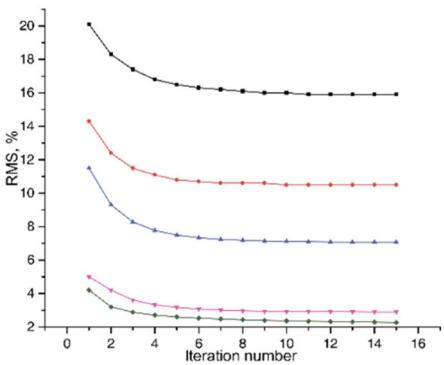

Figure 3: RMS error depending on number of iterations for different amount of projections. Black line (2 projections), red (10 projections), blue (20 projections), pink (100 projections), green (200 projections).

For most of measurement cases at INR RAS linac there are nearly ten projections taken for reconstruction. As it can be seen from Fig. 3, for 10 projections SART converges at 5th iteration, so that amount of iterations is used.

Reconstruction results, obtained by tomography kernel, are then post-processed. Each phase portrait is split into 20 sub portraits so that summarized intensity in each of them varies by 5 % of the total intensity of the original phase portrait. An envelope is calculated for every sub portrait, and this envelope is approximated by a phase ellipse (Fig. 4). Twiss parameters, emittance and center of each phase ellipse are calculated. All that data is displayed for user. One of tabs of the program with tomography settings and data is presented on Fig. 5.

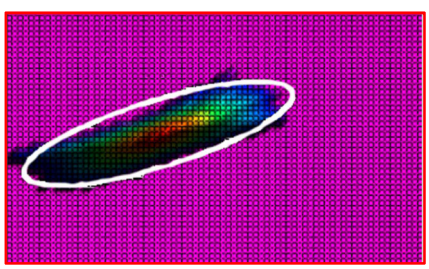

Figure 4: An approximation of phase portrait by a phase ellipse.

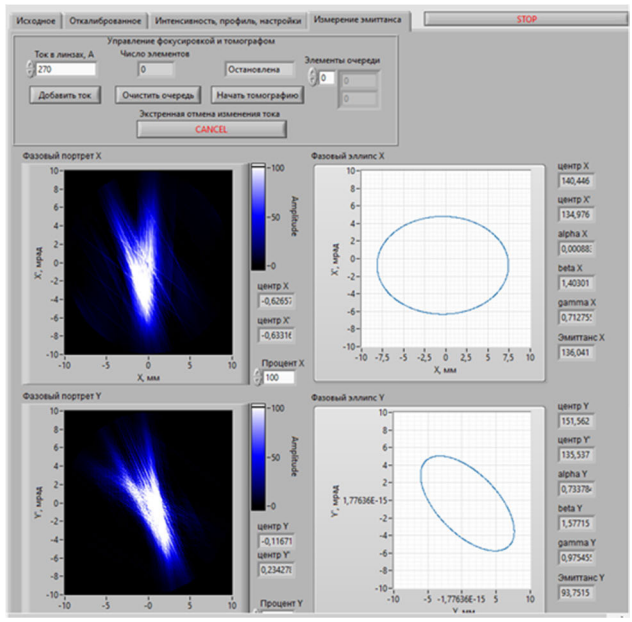

Figure 5: Main program tab with tomography data and settings.

Components and algorithms being used for tomographic reconstruction make restraints on errors of measurements. RMS errors of measurement of phase ellipse center were determined as 0.7 mm and 0.7 mrad. RMS relative errors of Twiss parameters and emittance measurement are 21%.

The program for offline tomography uses the same kernel as online version. As an input offline program needs an array of profiles, which were previously measured, and an array of transfer matrixes for every profile. This program can process data not only from BCSM but also from other profile measurers at INR linac. However, this feature has only been theoretically proved as feasible and has not been yet properly tested.

EXPERIMENTAL RESULTS

For now tomography at INR linac is going through various tests. Tests of online tomography system are mainly aimed at working out the sequence of actions during measurements. Tests of tomography itself are mainly carried out using offline tomography program with data from previous accelerator runs.

Figure 6 (a) shows results of tomography based on previously collected data from BCSM. It is seen that various “tail” artefacts exist. These artefacts are admissible inaccuracies of SART, which can be cut off. Method of splitting phased portrait to sub portraits, described in previous chapter, allows choosing sub portrait without artefacts.

A minimum of a specially constructed weight function was chosen as a selection criterion. This function uses a similarity of measured and reconstructed profiles. Figure 6 (b) shows phase portrait without artefacts. From now that phase portrait is considered as a result of tomography.

ISBN: 978-3-95450-222-6 ISSN: 2673-5350 doi:10.18429/JACoW-IBIC2020-WEPP37

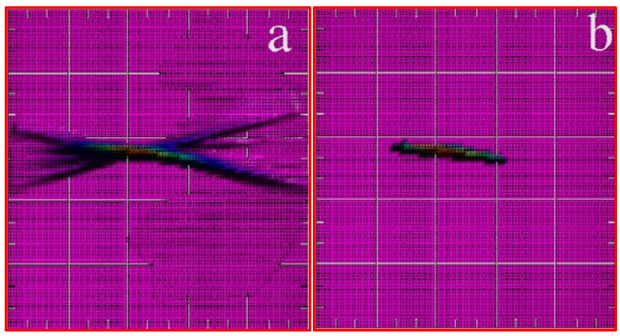

Figure 6: (a) is a raw result of reconstruction; (b) is a result without artefacts.

Tomographic reconstruction was implemented as an alternative to a method of transverse profiles [7], which is a main method for measuring transverse phase space parameters of the beam at INR linac. A comparison between two methods was made, using previously obtained data. Phase ellipses for both methods and axes are presented on Figs. 7 (a) and 7 (b). Centres of ellipses were artificially combined, because transverse profiles method calculates phase ellipse centre apart from reconstruction of the phase ellipse itself.

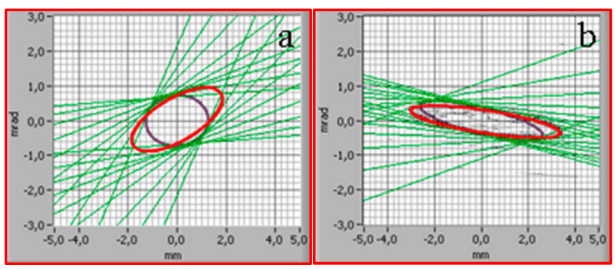

Figure 7: (a) results of tomographic reconstruction (red) and transverse profiles method (brown) for X-axis, (b) results of tomographic reconstruction (red) and transverse profiles method (brown) for Y-axis.

As it can be seen from Fig. 7, results of reconstruction are different, especially for X-axis. A simulation of beam transfer through elements, which were used for measurements, has been done for both methods. Figure 8 shows dynamics of beam position and size in the final part of the transfer line for both methods.

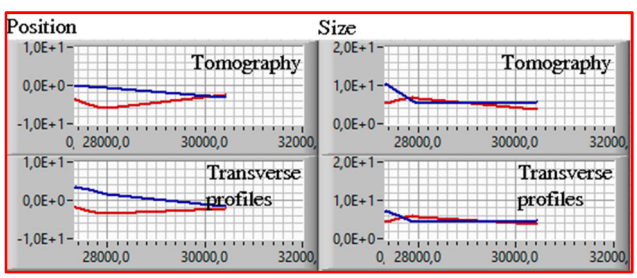

Figure 8: Dynamics of beam position and size in the final part of modelled transfer line. Blue lines are for X-axis, red are for Y-axis.

Results of simulation were compared with real measured beam position and size. Difference between real and reconstructed values, measured in standard deviations of tomographic reconstruction method, are presented in Table 1.

Table 1: Difference Between Measured and Reconstructed Beam Parameters Measured in Standard Deviations

Parameter	Tomography	Transverse profiles
x	0.9	2.8
y	0.6	1.2
σ_x	0.5	0.1
σ_y	0.5	0.1

It is seen that tomographic method is better at reconstructing beam centre than transverse profiles method, while transverse profiles method is better at reconstructing beam size, however difference between measured beam size and reconstructed from tomographic reconstruction data is less than 1 standard deviation. This proves that the tomographic method is a working alternative for transverse profiles method.

Differences in reconstruction results of two methods based on the same data can be explained by how methods treat obtained data. Tomographic reconstruction uses all information given by profile measurer and does not make any constrains on phase portrait parameters. Transverse profiles method only uses information about position and size of the beam. Moreover, transverse profiles method makes severe constrains on phase portrait parameters, based on beam size.

CONCLUSIONS

Transverse phase portrait tomography is a new method implemented at INR RAS linac. With a new method a first disturbing online emittance measurements during routine accelerator operation has been done at INR RAS. Based on previously collected data, a comparison of tomographic method and transverse profiles method has been done. This comparison showed efficiency of the implemented method.

REFERENCES

[1] J. S. Fraser, "Beam Analysis Tomography," *IEEE Transactions on Nuclear Science*, vol. 26, pp. 1641-1645, 1979. doi: 10.1109/TNS.1979.4330456

[2] S.Gavrilov *et al.*, "Two-dimensional non-destructive diagnostics for accelerators by Beam Cross Section Monitor", *JINST,* vol. 9, p. P01011, 2014. doi:10.1088/1748-0221/9/01/P01011

[3] LabVIEW, http://www.ni.com/ru-ru/shop/labview.html

[4] A. I. Titov and S. A. Gavrilov, "Luminescent Diagnostics for Low Intensity Proton Beams at INR RAS Linac", in *Proc. 26th Russian Particle Accelerator Conf. (RuPAC'18)*, Protvino, Russia, Oct. 2018, pp. 489-491. doi:10.18429/JACoW-RUPAC2018-THPSC39

Content from this work may be used under the terms of the CC BY 3.0 licence (© 2020). Any distribution of this work must maintain attribution to the author(s), title of the work, publisher, and DOI

ISBN: 978-3-95450-222-6 ISSN: 2673-5350 doi:10.18429/JACoW-IBIC2020-WEPP37

[5] A. H. Andersen and A. C. Kak, "Simultaneous algebraic reconstruction technique (SART): a superior implementation of the ART algorithm", *Ultrasonic Imaging,* vol. 6, pp. 81-94, 1984. doi: 10.1016/0161-7346(84)90008-7

[6] Stéfan van der Walt *et al.*, "scikit-image: Image processing in Python", *PeerJ*, vol. 2, p. e453, 2014. doi:10.7717/peerj.453

[7] P. I. Reinhardt-Nickoulin *et al.*, "Emittance Measurements at the Exit of INR Linac", in *Proc. 23rd Russian Particle Accelerator Conf. (RuPAC'12)*, Saint Petersburg, Russia, Sep. 2012, paper WEPPD055, pp. 668-670.

Content from this work may be used under the terms of the CC BY 3.0 licence (© 2020). Any distribution of this work must maintain attribution to the author(s), title of the work, publisher, and DOI

ISBN: 978-3-95450-222-6 ISSN: 2673-5350 doi:10.18429/JACoW-IBIC2020-WEPP38

DIAMOND BEAM HALO MONITOR*

S. V. Kuzikov†, S. P. Antipov, P. V. Avrakhov, E. W. Knight, Y. Zhao,
Euclid Techlabs LLC, Bolingbrook, IL, USA
J. G. Power, ANL, Lemont, Illinois, USA

Abstract

Beam halo measurement is important, because novel x-ray free electron lasers like LCLS-II have very high repetition rates, and the average power in the halo can become destructive to a beamline. Diamond quad detectors were previously used for electron beam halo measurements at KEK. Diamond is the radiation hard material which can be used to measure the flux of passing particles based on a particle-induced conductivity effect. However, the quad detectors have metallic contacts for charge collection. Their performance degrades over time due to the deterioration of the contacts under electron impact. We recently demonstrated a diamond electrodeless x-ray flux monitor based on a microwave measurement of the change in the resonator coupling and eigen frequency. We propose similar measurements with a diamond put in a resonator that intercepts the halo. Without electrodes, such a device is more radiation resistant. By measuring the change in RF properties of the resonator, one can infer the beam halo parameters. In a similar manner to traditional beam halo monitors, the diamond plate can be scanned across the beam to map its transverse distribution.

DIAMOND BLADE CONCEPT

Beam halo has a relatively low charge density. However, for high intensity beams, the actual number of particles in the halo is typically quite large. For this reason, the halo is associated with an uncontrolled beam loss, and must be monitored and mitigated [1]. It is difficult to use typical fluorescent screens to monitor beam halo, since the core of the beam will produce a high signal that can leave the halo signal too small to differentiate. The wire scanners allow beam profile characterization its transverse distribution [2]. Even though refractory metals such as tungsten are used for the wires, they must be replaced from time to time due to beam damage. We consider the use of diamond for a sensing material, because of its extraordinary mechanical, electrical, and thermal properties. Large bandgap, radiation hardness, high saturated carrier velocities, and low atomic number make diamond an attractive candidate for the detection of ionizing radiation and charged particles [3]. Diamond quadrant detectors have been successfully used to measure beam halo at KEK [4]. We propose an electrodeless measurement of the charged particle-induced conductivity of the diamond by means of a microwave resonator reflection measurement [5]. A diamond blade will be used to intercept electrons. The blade will be inside a critically coupled resonator, i.e., when fed microwaves at the resonant frequency, there will be no reflection from the resonator. Due to electron interactions with the diamond, the diamond will become weakly conductive. Because of that, the microwave properties of the resonator will change, and it will start to reflect power at the resonant frequency, a signal whose amplitude will be correlated to the intercepted charge from the halo. We propose a reflection-based measurement to detect beam halo (Fig. 1). A diamond blade/wire scans across the beam. The signal recorded is resonator coupling change due to particle-induced conductivity in diamond. The role of charged particles is to promote bound electrons into the conduction band across the band gap.

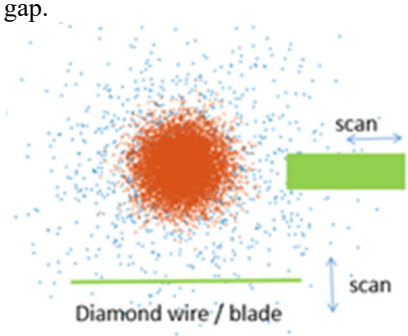

Figure 1: Diamond blade beam halo scanning.

Simulations for Scanning Diamond Blade Scrapper Monitor

To simulate the response of the device to different current densities in the beam halo, we utilized a simple model of a diamond blade positioned between a 100% reflector and a variable reflector (Fig. 2).

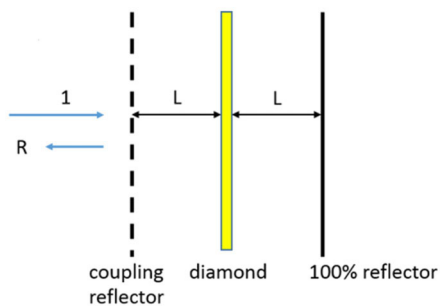

Figure 2: Simulation of resonator S_{11} for beam and no beam for the initial near to critical coupling.

We can adjust the reflectivity of the second reflector to provide critical coupling to this simple resonator. When the coupling is tuned to critical, we can demonstrate a sharp resonance (see Fig. 3). If we change the concentra-

* This work was supported by DoE SBIR grant # DE-SC0019642.
† s.kuzikov@euclidtechlabs.com

Content from this work may be used under the terms of the CC BY 3.0 licence (© 2020). Any distribution of this work must maintain attribution to the author(s), title of the work, publisher, and DOI

ISBN: 978-3-95450-222-6 ISSN: 2673-5350 doi:10.18429/JACoW-IBIC2020-WEPP38

Content from this work may be used under the terms of the CC BY 3.0 licence (© 2020). Any distribution of this work must maintain attribution to the author(s), title of the work, publisher, and DOI

tion of electrons in the conduction band from 0 to 10^{12} cm^{-3}, the coupling is significantly reduced, i.e., there is a strong reflection from the device. This reflection can be used to measure of the charge passing through the diamond blade. Following results from [3], we assume that there is no dependence on electron beam energy (between MeV and GeV) on how many electrons are promoted into conduction band when electrons pass through diamond.

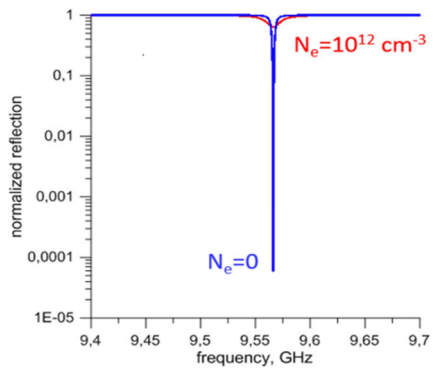

Figure 3: Simulation of resonator S_{11} for beam and no beam for the initial near to critical coupling.

If we scan the effective concentration of carriers in the conduction band of the diamond, N_e, and plot the reflection signal as a function of time (see Fig. 4), we observe generally nonlinear response of the resonator. To measure such high concentrations with the test resonator, we first note that the quality factor of this resonator is completely dominated by the conductivity losses in the diamond blade. Therefore, the decay time of a transient measurement (Fig. 4) is fully governed by the relaxation time of the diamond's conductivity.

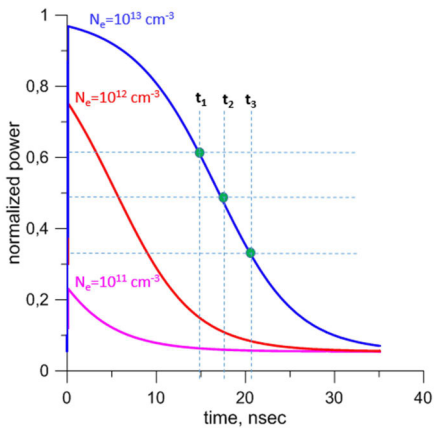

Figure 4: Time response of resonator for different carrier concentrations.

We take a 5-ns relaxation time as a representative time for diamond. The concentration (N_e) evolves as $N_0 \times exp(-t/\tau)$, where τ is the relaxation time. Therefore, during relaxation, N_e decreases and enters a linear region. That is why one can take several test resonator signal points, where the response is linear, for several subsequent times t_1, t_2, t_3. This would allow one to determine τ as well as N_e at $t=0$.

BEAM TEST OF DIAMOND SAMPLES

X-band Test Resonators

To test diamond as sensitive elements we purchased several diamond samples for resonators to be installed in VBS (Fig. 5). The first sample (10 mm × 14 mm × 0.3 mm) was produced by Applied Diamonds Inc. (Fig. 5a). The second purchased sample (circular disk ∅8 mm, 0.5 mm thickness) was made by II-VI company and qualified as a detector grade. The third one is a square single crystal sample (4.5 mm × 4.5 mm × 0.5 mm) produced by Element6. In order to compare diamonds, we decided to carry out experiments with simplified resonators where diamonds are located in the center and catch most part of the electron beam. In all resonators samples are irradiated by particles being perpendicular to the beam. Because all the purchased diamonds have different sizes and different shapes, we produced resonators individually for each sample (Fig. 6).

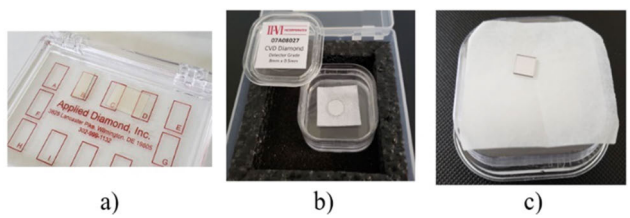

Figure 5: Diamond samples: a – CVD electronic grade sample from Applied Diamonds Inc., b – detector grade CVD diamond from II-VI, detector grade single crystal diamond from ElementSix.

For the smallest our diamond produced by Element6 we designed a "fork" support to hold the sample securely (Fig. 6b). We tuned each resonator to provide critical coupling (β≈1) at 6.5-7.5 GHz. The resonators had unloaded Q-factors ~1000, the loaded Q-factors varied from 30 (II-VI) to 200 (Applied Diamond). Figure 6 shows S11 parameter for the tuned resonator with Element6 sample (Q=100).

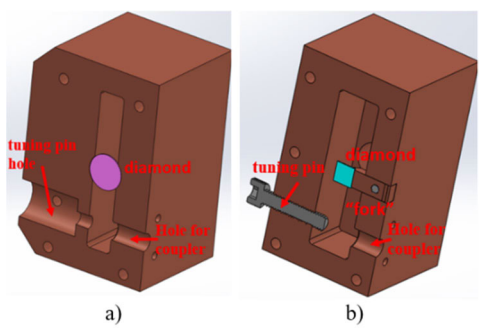

Figure 6: Test resonators: a – copper resonator to accommodate circular diamond sample of II-VI, b – copper resonator to accommodate square samples of Applied Diamond and Element6.

ISBN: 978-3-95450-222-6 ISSN: 2673-5350 doi:10.18429/JACoW-IBIC2020-WEPP38

Figure 7 shows low-power measurement setup (Fig. 7a) and S11 parameter for the resonator with built-in Element6 diamond sample (Fig. 7b).

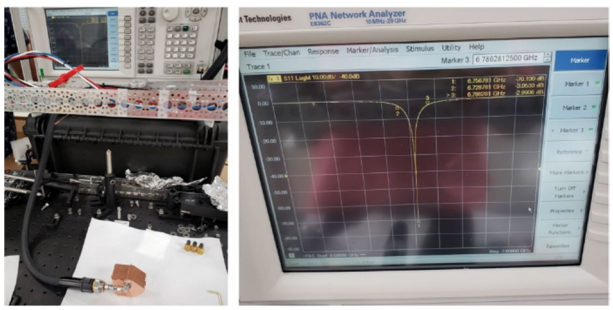

a) b)

Figure 7: Tuning of copper resonator with built-in diamond sample (Element6) before installation at VBS: a – network measurement setup, b – final curve for the tuned resonator.

Tests with DC Gun

For high-power tests we decided to use Vertical Beam Test Stand (VBS) at EuclidTechlabs. The VBS is a DC gun of an electronic microscope delivering 20-200 keV electron beam with current up to 0-50 μA. In VBS the electron beam is accelerated toward the floor, with the compressed air lines for the pneumatic gate valve, focusing solenoid, and finally lead-enclosed experimental beamline following the electron gun. A solenoid provided the ability to focus the electron beam. The data acquisition system was controlled by a PC running LabVIEW. Figure 8 shows the experimental setup (Fig. 8a), the installed tube included a resonator with a sample to be tested (Fig. 8b), and the removable YAG screen upstream the test resonator (Fig. 8c). The YAG screen was mounted on a pneumatic actuator at a 45-degree angle with respect to the beam. In experiments with diamond resonators we could steer the electron beam with frequency 5 Hz so that a half of time electrons fly at axis and irradiate diamond, the rest 50% of time electron beam is strongly deflected not irradiating diamond at all. We tuned beam focus with the condenser lens to get maximum current at YAG screen. Then YAG screen was led out of the tube to measure resonator response by the steered beam.

Figure 9 shows typical oscillogram of the resonator signal with inserted Element6 diamond when the current was as low as 7 μA and beam energy was about higher limit of 200 keV. One can see that RF signal is modulated by the incoming electron beam with the frequency 5 Hz. Even with this small current the measured signal was pretty recordable. No beam signal was as low as -38 dB. The higher beam current generated the stronger response signal. The highest recorded signal for 7 μA current and 200 keV voltage was as high as -13 dB.

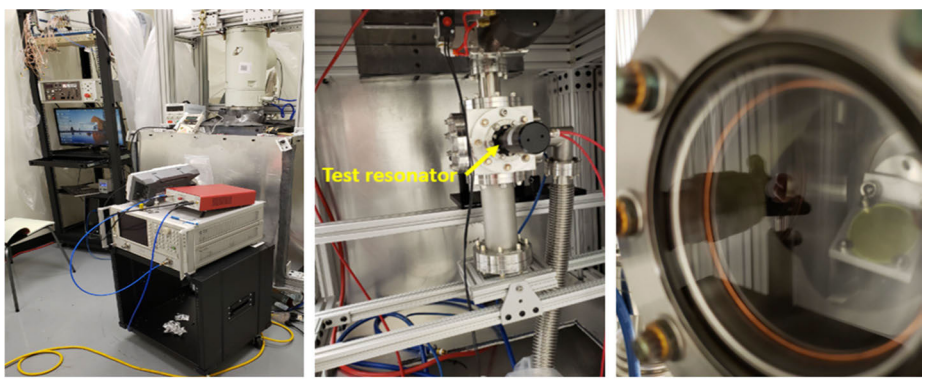

a) b) c)

Figure 8: VBS test stand with installed test resonator: a – overall view, b – test resonator in vacuum chamber installed in the bottom, c – view through quartz window to YAG-screen.

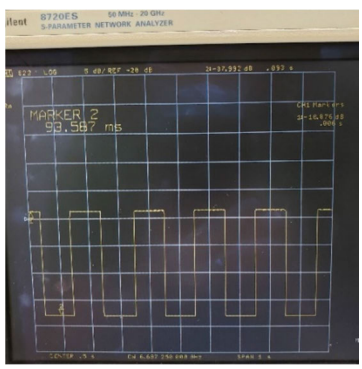

Figure 9: Monitor time response for 5 Hz steered beam.

Because the resonator with Applied Diamond sample showed less signal in comparison with Element6 diamond resonator we kept going to measure the resonator with Element6 diamond. We plotted dependence of test resonator signal on current for different beam energies (Fig. 10). The signal grows up with current from minimum at -38 dB to maximum, because number of free carriers increases. At 7 μA all curves tend to the saturation, The higher beam energy the higher test resonator signal. That might be caused by increase of electron penetration depth in a diamond. This effect is limited by diamond thickness. That can explain why near 200 keV beam energy test resonator signal stops to increase, the curves for 175 keV and 200 keV are almost coincident.

Content from this work may be used under the terms of the CC BY 3.0 licence (© 2020). Any distribution of this work must maintain attribution to the author(s), title of the work, publisher, and DOI

ISBN: 978-3-95450-222-6 ISSN: 2673-5350 doi:10.18429/JACoW-IBIC2020-WEPP38

Content from this work may be used under the terms of the CC BY 3.0 licence (© 2020). Any distribution of this work must maintain attribution to the author(s), title of the work, publisher, and DOI

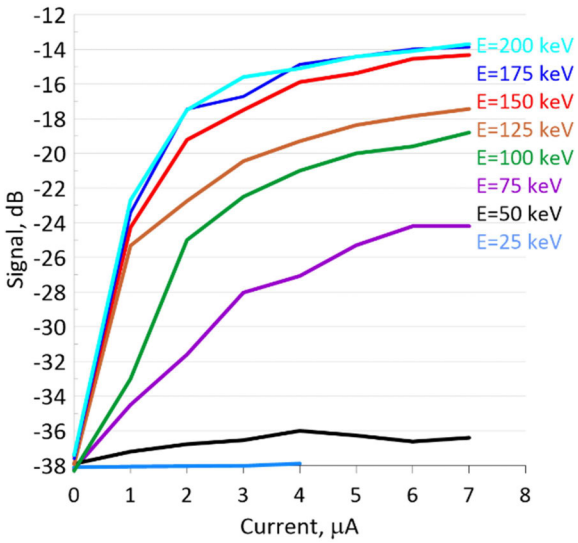

Figure 10: Experimental plot of beam monitor response amplitude vs beam current for several beam energies.

DESIGN OF HALO MONITOR FOR TEST IN AWA

We have been designing the scanning diamond blade scrapper halo monitor to be tested at Argonne Wakefield Accelerator (AWA) with multi-MeV electron beam (Fig. 11). The main idea behind this design is to create an ultra-high vacuum compatible device which would allow to investigate all physical properties and to proceed to the final beam halo monitor fabrication. Figure 12 shows the current design for the monitor resonator. In Fig. 13 one can see S_{11} parameter for the designed monitor. The device utilizes the 4.5" bellow to allow 1D scanning range ±15 mm. The bellow is controllable by a precise motor with a controller. The blade scrapper is mounted in vacuum side at the end of WR112 waveguide. The waveguide is connected to a ceramic RF window which separates ultra-high vacuum part from air.

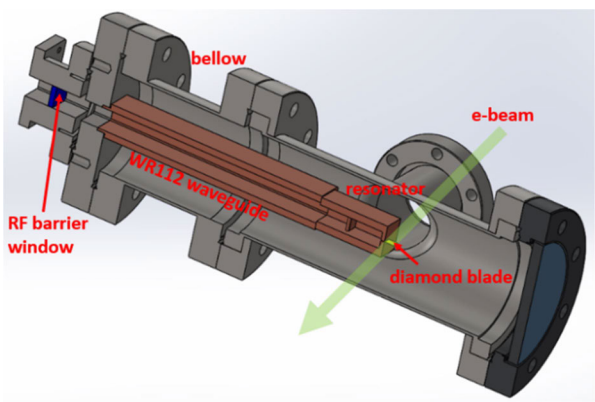

Figure 11: Engineering design of scanning diamond blade scraper halo monitor based on motorized bellow for tests at AWA.

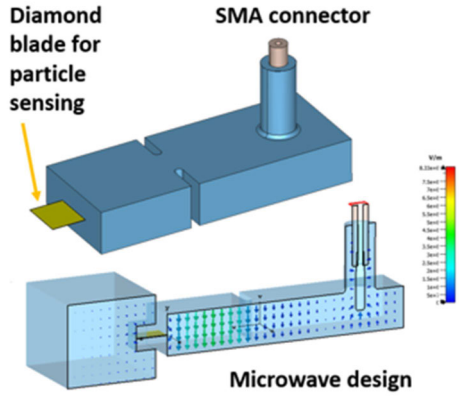

Figure 12: RF design of a diamond blade halo detector resonator with RF connector.

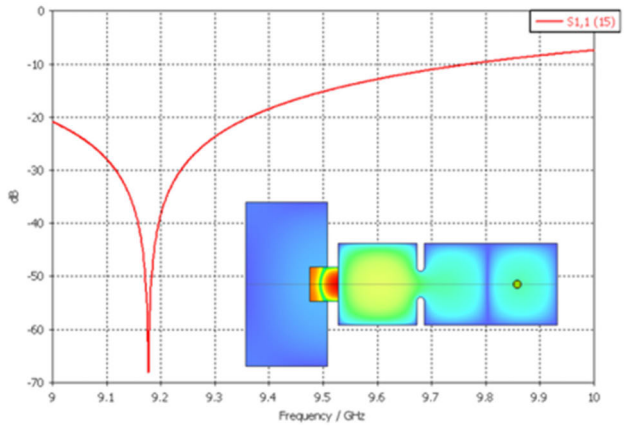

Figure 13: Reflection simulation and field distribution in the resonator.

CONCLUSION

We proposed diamond blade concept and developed engineering design for halo scanning measurements. The carried out VBS tests allowed to select the best diamond sample for beam halo tests with multi-MeV beam at AWA. We plan to complete design of the remotely steering monitor prototype and fabricate it by November. The AWA tests are planned by end of this year.

REFERENCES

[1] M. R. Hadmack and E. B. Szarmes, "Scanning Wire Beam Position Monitor for Alignment of a High Brightness Inverse-Compton X-ray Source", in *Proc. 2nd Int. Beam Instrumentation Conf. (IBIC'13)*, Oxford, UK, Sep. 2013, paper WEPF21, pp. 856-859.

[2] E. Gaubas *et al.*, "Profiling of Current Transients in Capacitor Type Diamond Sensors", *Sensors*, vol. 15, pp. 13424-13458, 2015. doi:10.3390/s150613424

[3] Shan Liu, "Development of Diamond Sensors for Beam Halo and Compton Spectrum Diagnostics after the Interaction Point of ATF2", Ph.D. thesis, Université Paris Sud - Paris XI, 2015.

[4] S. Liu *et al.*, "In Vacuum Diamond Sensor Scanner for Beam Halo Measurements in the Beamline at the KEK Accelerator Test Facility", *Nuclear Instruments and Methods in*

ISBN: 978-3-95450-222-6 ISSN: 2673-5350 doi:10.18429/JACoW-IBIC2020-WEPP38

Physics Research A, vol. 832, p. 231–242, 2016. doi: 10.1016/j.nima.2016.06.122

[5] S. P. Antipov, S. V. Kuzikov, S. Stoupin, and A. A. Vikharev, "Detection of X-Rays and Charged Particles via Detuning of the Microwave Resonator", in *Proc. 9th Int. Particle Accelerator Conf. (IPAC'18)*, Vancouver, Canada, Apr.-May 2018, pp. 1958-1960. doi:10.18429/JACoW-IPAC2018-WEPAF058

Content from this work may be used under the terms of the CC BY 3.0 licence (© 2020). Any distribution of this work must maintain attribution to the author(s), title of the work, publisher, and DOI

ISBN: 978-3-95450-222-6 ISSN: 2673-5350 doi:10.18429/JACoW-IBIC2020-THAO04

Content from this work may be used under the terms of the CC BY 3.0 licence (© 2020). Any distribution of this work must maintain attribution to the author(s), title of the work, publisher, and DOI

BEAM COUPLING IMPEDANCE ANALYZE USING BUNCH-BY-BUNCH MEASUREMENT*

X. Y. Xu[1], Shanghai Institute of Applied Physics, CAS, Shanghai, China
Y. B. Leng†, Shanghai Advanced Research Institute, CAS, Shanghai, China
[1]also at University of Chinese Academy of Sciences, Beijing, China

Abstract

Beam coupling impedance is very important parameters for advanced synchrotron radiation facilities. Till now there is no online method to measure beam impedance directly. But some beam parameters such as betatron tune amplitude and frequency, synchrotron phase, bunch lifetime and so on, can be modulated by beam impedance effects. So wake field and beam impedance information could be retrieved by measuring bunch-by-bunch beam 3D positions and analyzing bunch index dependency of above beam parameters. A bunch-by-bunch 3D positions and charge measurement system had been built at SSRF for this purpose and the performance is not good enough for beam impedance analyze due to cross talk between bunches. We upgraded the measurement system to minimize cross talk and improve resolution this year. New beam experiment results and corresponding analyze will be introduced in this paper.

INTRODUCTION

The advanced synchrotron radiation light sources have the following basic characteristics: ultralow beam emittance (few nmrad or even tens of pmrad), ultra-high beam stability (orbital feedback control accuracy is mostly micron or submicron level), high average beam current (above 300mA), small-aperture beam vacuum pipe (below 30mm in diameter), a large number of vacuum inserts in , top-up operation mode, small dynamics aperture, with high time resolution experiment ability (time resolution ps order) and so on. The use of small-aperture vacuum pipes and a large number of inserts makes the problem of beam instability caused by the wakefield particularly prominent. Under this condition, the problem of strong beam wakefield (large beam impedance) will become a key issue that limits the further improvement of light facility performance [1]. Correspondingly, how to optimize the beam impedance in the design stage and how to accurately target the source of beam impedance during the commissioning and operation stage to give optimization opinions is the key technical issues that must be resolved when development of the next generation of advanced synchrotron radiation facility.

Under ideal conditions, the particles move steadily in the storage ring. Due to the action of the strong focusing principle and the principle of automatic phase stabilization, the particles make β oscillations around the closed orbit in the transverse. The synchronous particles in the longitudinal direction make synchronous oscillations. When the oscillation amplitude is small, the transverse oscillation can be considered as simple harmonic vibration. The bunches running in the pipeline will excite the wakefield. If the wakefield decays slowly, it will have an effect on the subsequent bunches. The oscillation amplitude of the bunches under the effect of the wakefield may increase, causing instability. Because its effect is that many bunches are coupled together through the wakefield, it is called coupling instability. The wakefield that can produce coupling instability must not be attenuated before the next bunch arrives. The impedance corresponding to such a wakefield is an impedance with a higher quality factor Q value, or narrow-band impedance. These narrow-band impedances correspond to the higher-order modes of the cavity-like.

At present, the research methods of beam wakefield and impedance mainly include four methods: analytical method, simulation calculation method, emulation test, and beam machine research.

The above methods have their own advantages and limitations in application. The analytical method has the most complete theory, but it can only calculate simple and regular structures, which is not suitable for a new generation of high-performance light sources with many IVU. The simulation calculation method has great application value in the pre-research stage of the accelerator storage ring, but as the structure of the storage ring becomes more and more complex, the device structure cannot be perfectly reconstructed in the software, which has a great influence on the accuracy of the simulation results. In addition, the complicated storage ring structure also brings about the problems that the algorithm cannot converge normally, the calculation time is long, and the resources are occupied. The emulation test method can measure the impedance of some devices in the laboratory. Its disadvantage is that on the one hand, the cold test result in the experiment cannot be completely equal to the result after installation. On the other hand, it is inevitable that the connector will be tightened during the electrical signal input process. The transition section excites a lot of noise signals and causes measurement errors. In order to tighten and straighten the center wire, it is impossible to make it very thin, and there is a certain systematic error. The beam machine research method can directly measure the accelerator beam wakefield, but most of the existing methods require specially designed machine research experiments to measure the wakefield in a special bunch filling mode. The storage ring structure will be adjusted during operation (for example,

* Work supported by National Natural Science Foundation of China (No.11575282) and Ten Thousand Talent Program and Chinese Academy of Sciences Key Technology Talent Program
† lengyongbin@sinap.ac.cn

ISBN: 978-3-95450-222-6 ISSN: 2673-5350 doi:10.18429/JACoW-IBIC2020-THAO04

the magnetic gap of the insert in the vacuum will change at any time according to user needs), which will affect the wakefield function in real time, relying on special machine research to traverse all states to determine the corresponding beam wakefield, will inevitably take up a lot of equipment running time, reducing equipment operating efficiency.

WAKEFIELD ANALYSIS BY BUNCH-BY-BUNCH POSITION

If the basic parameters (charge amount, three-dimensional position, etc.) of all bunches in storage ring can be independently measured, and the measurement accuracy is high enough, then we can use all the bunches in the storage ring as sources and witnesses. When the wakefield effect is strong enough, the required wakefield information can be obtained by analyzing the changes of the bunch parameters. In the normal operation of synchrotron radiation light source, if we can find a suitable physical process in which the wakefield effect is sufficiently obvious, then we can achieve real-time in-situ beam wakefield measurement without changing the beam conditions and without affecting the user's experiment [2–4].

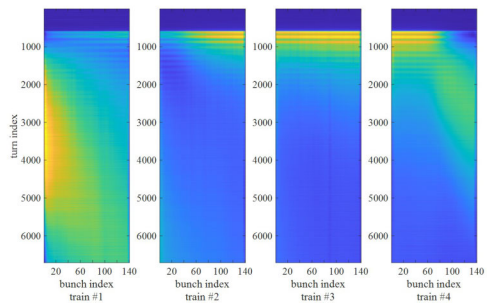

Figure 1: Transverse position during injection transient at x-axis.

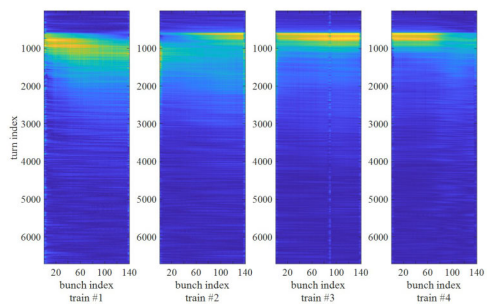

Figure 2: Transverse position during injection transient at y-axis.

For the transverse wakefield, only when the excitation bunch has a relatively large transverse position offset, it is possible to excite a sufficiently large field strength to generate a physical quantity to be measured that can meet the measurement accuracy requirements. During the normal operation of the synchrotron radiation source, such beam conditions are not available most of the time. However, in the transient process of injection, due to the existence of the kicker field, almost all the bunches will deviate greatly from the equilibrium orbit (on the order of millimeters) at the moment of injection, and then perform a transversely damped simple harmonic oscillation (coherent Beta oscillation) to excite The stronger transverse wakefield becomes the excitation bunch (shown in Fig. 1 and Fig. 2). At the same time, all bunches will be affected by this transverse wakefield to produce incoherent Beta oscillations, and at the same time become the witness bunches. Therefore, as long as we can capture the transient process of injection, accurately determine the change in the transverse position of each bunch during this process, and separate the coherent Beta oscillation and incoherent Beta oscillation of each bunch, we can use fitting Incoherent Beta oscillation waveform to obtain the information of the transverse wake field. The capture of injection process data can be achieved by using the amplitude jump of the BPM signal at the injection time as a trigger condition. The separation of coherent Beta oscillation and incoherent Beta oscillation data can be realized by analyzing the multi-bunch multi-turn data matrix by using the principal component analysis method (PCA). We hope to find a wakefield function that can satisfy the transverse oscillation evolution of each bunches. If under the effect of the wakefield potential, the transverse oscillation evolution process predicted by the model is consistent with the measured data, then this wakefield function is worthy of trust.

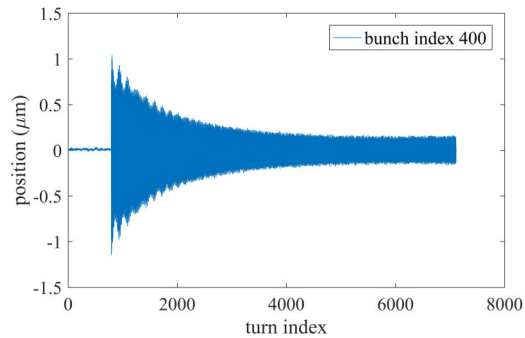

Figure 3: Transverse position of bunch 400 at y-axis.

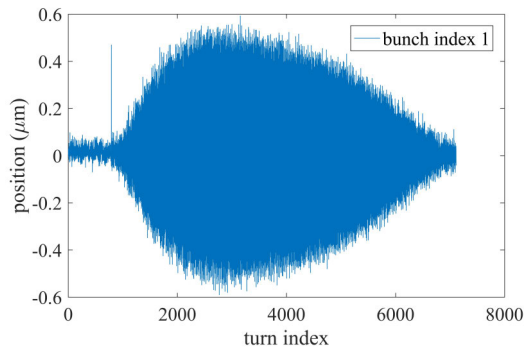

Figure 4: Transverse position of bunch 1 at y-axis.

Content from this work may be used under the terms of the CC BY 3.0 licence (© 2020). Any distribution of this work must maintain attribution to the author(s), title of the work, publisher, and DOI

ISBN: 978-3-95450-222-6 ISSN: 2673-5350 doi:10.18429/JACoW-IBIC2020-THAO04

Content from this work may be used under the terms of the CC BY 3.0 licence (© 2020). Any distribution of this work must maintain attribution to the author(s), title of the work, publisher, and DOI

Some bunches that were originally stable in transverse position increased rapidly after injection (shown in Fig. 3). The envelope is an exponential decay, so it could be considered as a betatron damping oscillation invoked exclusively by the kickers mainly. The spatial vector indicated that the kickers fields influencing the bunches were not constant. In bunch index 1, this effect of kickers is very small. Therefore, the change of the transverse oscillation amplitude of 1st bunch is mainly affected by the wakefield (shown in Fig. 4). The wake oscillation of a bunch is determined by the betatron oscillations of all bunches. The propagation coefficient of the wakefield is considered a constant once the drive bunch and the witness bunch are decided, so the amplitude of second mode of a bunch is a linear combination of the amplitudes of the first modes of all bunches (including itself). Due to the special filling mode, there are more than 40 empty buckets in front of bunch 1st. Therefore, the length of the global wakefield of the storage ring is much longer than dozens of bunches.

$$W_x(j-i) = \frac{\Delta x_i}{q_i q_j} \cdot x_j \tag{1}$$

According to the definition of wakefield, we define the global equivalent wakefield with Eq. (1). Where $W_x(j-i)$ is the influence on the oscillation amplitude in y-axis after $j-i$ buckets. x_i and x_j is transverse oscillation amplitudes of bunches. q_i and q_j are charges of bunches. Taking the oscillation amplitude of each bunch in the current turn as known data, calculate the transverse position of the follow thousands of turns according to the equivalent global wakefield and damping coefficient as parameters, and compare it with the measured value. Taking the minimum residual error between the predicted position value and the measured position value as the optimization goal, we found a rough equivalent wakefield function shown in Fig. 5.

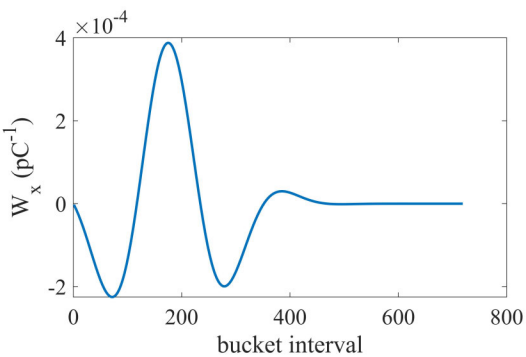

Figure 5: A specific solution of equivalent wakefield function in x-axis shows the coupling relationship between the bunches.

There are more than 500 bunches in the storage ring under normal operation in SSRF. The coupling relationship between bunches is very complicated, so there is more than one solution of the equivalent wakefield function that can satisfy the evolution trend of each bunches transverse amplitudes. In the future, it is necessary to eliminate the error solution of the equivalent global wakefield by different filling modes data. In addition, considering the effect of the driving force of the transverse movement of the bunches, the wakefield force influence on the transverse oscillation of the bunch is related to the oscillation phase, so the model needs to be further optimized.

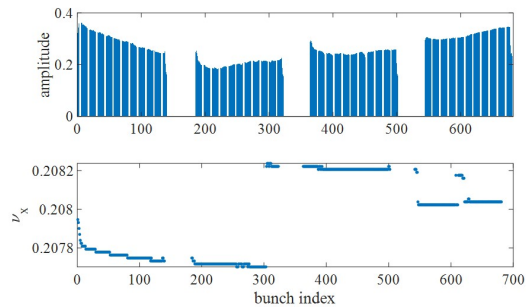

Figure 6: The frequency shift of betatron oscillation at x-axis.

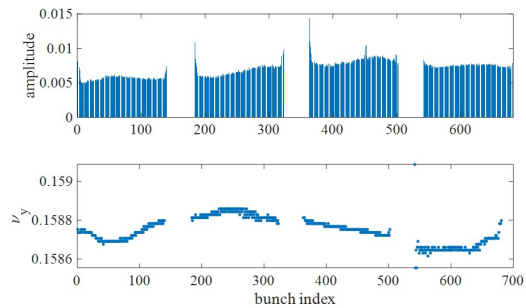

Figure 7: The frequency shift of betatron oscillation at y-axis.

The frequency shift of betatron oscillation has been observed (shown in Fig. 6 and Fig. 7). Due to transverse quadrupolar wakefield, the frequency of betatron oscillation is dependent on bunch index. This means that transverse quadrupolar wakefield are expected to be extracted from the bunch-by-bunch position data. However, the impact of the transverse quadrupolar wakefield into tune is very small, which places high requirements on the measurement accuracy. In the next step, more experiments need to be done to determine whether the difference in operating points is always present, rather than caused by measurement errors.

In order to further study this phenomenon, a special beam experiment was done. In this experiment, we turned off the transverse feedback system and turned off the insert vacuum undulators (IVU) in turn. Due to the closing of the feedback system, the transverse oscillation of the bunch will be maintained at a relatively large magnitude for a long time. The relationship between the average tune of bunches and the state of IVU is shown in Fig. 8. It can be seen that the average tune becomes larger with the opening of IVU.

ISBN: 978-3-95450-222-6 ISSN: 2673-5350 doi:10.18429/JACoW-IBIC2020-THAO04

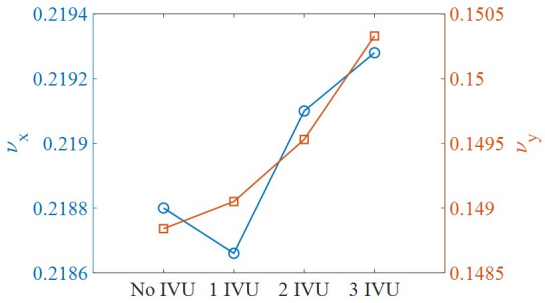

Figure 8: The frequency shift of betatron oscillation with different IVU status.

CONCLUSION

The analysis of coupling impedance and wakefield is of great significance for optimizing the structure of the IVU and finding the source of beam instability. This paper proposes some methods for in-situ analysis of the wakefield in the normal operation model of the storage ring. These methods are based on the bunch-by-bunch three-dimensional position measurement and charge measurement technology. In the storage ring, hundreds of bunches are both the source and the witness. By monitoring the position of each bunch, the evolution process of the bunch position under the action of the coupled wakefield is clearly seen. Using the PCA method, the wakefield oscillation mode can be separated.

In theory, if a sufficiently complete mathematical model is established, the value of the wakefield function between the bunches can be solved. With the existing computing resources, a relatively simple model was established to describe the evolution of the transverse oscillation amplitude of each bunch over time under the combined action of the wakefield and the damping term. We use this model to predict the evolution trend of the transverse oscillation amplitude of these bunches in the follow thousands of turns through the transverse oscillation amplitudes of all bunches in the current turn. The model works well in some data sets, but it is not universal, and the wakefield solution applicable to a set of data is not unique. Therefore, more data is needed to screen the solutions of the wakefield. The data with different IVU states are analyzed. When the insert is very close to the beam, the beam is affected by a large short-range impedance wall and shows obvious instability in the string. In addition, the difference in the transverse oscillation frequency of the bunch can be observed, which is the basis for analyzing the quadrupole wakefield.

The analysis of the coupled wakefield has just begun. The current simplified model can only roughly agree with the transverse oscillation evolution process of bunches in some cases. Since the predicted value is used to calculate the future position, the cumulative error is quickly amplified after thousands of turns. The equivalent coupled wakefield function found by the current model needs to be further verified. In the future, our model needs to be further improved. For example, the influence of the transverse oscillation phase difference of the bunches will be accepted into the model. For the longitudinal wakefield, we plan to start from the longitudinal balance phase of each bunch, and calculate the longitudinal wakefield function through the difference of the acceleration phase.

REFERENCES

[1] H. Tanaka, "Trends and Challenges in the Future Storage Ring Light Sources", presented at the 60th ICFA Advanced Beam Dynamics Workshop (FLS'18), Shanghai, China, Mar. 2018, paper MOA2PL01, unpublished.

[2] Adolphsen, C. and Bane, K. and Higo, T. and Kubo, K. and Miller, R. and Ruth, R. and Thompson, K. and Wang, J, "Measurement of Wake-Field Suppression in a Detuned *X*-Band Accelerator Structure," *Phy. Rev. Lett.*, vol. 74, no. 13, p. 2475-2478, Mar. 1995. doi:10.1103/PhysRevLett.74.2475

[3] Chen, Zhichu and Yang, Yong and Leng, Yongbin and Yuan, Renxian, "Wakefield measurement using principal component analysis on bunch-by-bunch information during transient state of injection in a storage ring," *Phys. Rev. ST Accel. Beams*, vol. 17, p. 112803, Nov. 2014. doi:10.1103/PhysRevSTAB.17.112803

[4] X. Y. Xu, Y. B. Leng, and Y. M. Zhou, "Machine Learning Application in Bunch Longitudinal Phase Measurement", in *Proc. 10th Int. Particle Accelerator Conf. (IPAC'19)*, Melbourne, Australia, May 2019, pp. 2625–2628. doi:10.18429/JACoW-IPAC2019-WEPGW064

Content from this work may be used under the terms of the CC BY 3.0 licence (© 2020). Any distribution of this work must maintain attribution to the author(s), title of the work, publisher, and DOI

ISBN: 978-3-95450-222-6 ISSN: 2673-5350 doi:10.18429/JACoW-IBIC2020-THA005

Content from this work may be used under the terms of the CC BY 3.0 licence (© 2020). Any distribution of this work must maintain attribution to the author(s), title of the work, publisher, and DOI

ADVANCED LASER-DRIVEN PLASMA ACCELERATOR ELECTRON-BEAM DIAGNOSTICS WITH COTR-BASED TECHNIQUES*

A. H. Lumpkin†, Fermi National Accelerator Laboratory, Batavia, IL, USA
M. LaBerge, M. Downer, University of Texas at Austin, Austin, TX, USA
D. W. Rule, Silver Spring, MD, USA
A. Irman, Helmholtz-Zentrum Dresden-Rossendorf, Dresden, Germany

Abstract

A significant advance in laser-driven plasma accelerator (LPA) electron-beam diagnostics has recently been demonstrated based on coherent optical transition radiation (COTR) imaging. We find COTR signal strengths from a microbunched subset of beam exiting the LPA to be several orders of magnitude higher than that of incoherent optical transition radiation (OTR). The transverse sizes are only a few microns as deduced from the point-spread-function-related lobe structure. In addition, the far-field COTR interferometric images obtained on the same shot provide beam-size limits plus divergence and pointing information at the sub-mrad level when compared to a modified analytical model. The integrated image intensities can be used to estimate the microbunching fraction and relatable to the LPA process. Initial results in a collaborative LPA experiment will be reported for electron beam energies of about 215 MeV. A revised configuration is proposed to record energy and energy spread via COTR on the same shot with the interferometer.

INTRODUCTION

The periodic longitudinal density modulation of relativistic electrons at the resonant wavelength (microbunching) is a well-known, fundamental aspect of free-electron lasers (FELs) [1]. In one classic case, microbunching fractions reached 20% at saturation of a self-amplified spontaneous emission (SASE) FEL resulting in gains of 10^6 at 530 nm [2]. In that experiment the concomitant z-dependent gain of coherent optical transition radiation (COTR) was also measured at the $>10^5$ level. Microbunching at visible wavelengths in laser-driven plasma accelerators (LPAs) had been reported previously [3,4], but it has only recently been measured in near-field and far-field images on a single shot for the first time with significant COTR enhancements involved [5-7].

We reintroduce a modified analytical model for COTR interferometry (COTRI) first developed for the SASE-FEL-induced microbunching case [8] to evaluate now the LPA case [7]. The coherence function was treated in this analytical model that addresses both cases and the expected fringe patterns. In the modified model, we consider the increase in the effective beam size in the drift between the foils due to the divergence term [9]. This term has negligible effects for low divergences of the microbunched electrons.

In the FEL, one identified microbunched transverse cores of 25-100 microns in extent while in the LPA the recently reported transverse sizes at the exit of the LPA were a few microns [5-8]. In the latter case, signal enhancements $>10^5$ and extensive fringes out to 30 mrad in angle space were recorded.

EXPERIMENTAL ASPECTS

The LPA at HZDR

The LPA is based on the DRACO laser with a peak power of 150 TW at a central wavelength 800 nm interacting with a He gas jet (with 3% Nitrogen) at the Helmholtz-Zentrum Dresden-Rossendorf (HZDR) facility [10]. The LPA was operated with a plasma electron density n_e ~3 x 10^{18} cm^{-3} in the self-truncated ionization-injection mode. Beam energies of ~215 MeV in a quasi-monoenergetic peak were observed in a downstream spectrometer. After the LPA, a 75-μm thin Al foil blocked the laser pulse and was followed by an Al-coated Kapton foil as shown in Fig. 1. The latter's back surface provided the source point of the near field (NF) COTR imaging, and a polished 200-μm thick Si mirror at 45° to the beam direction redirected this light to the microscope objective. The configuration provided a magnification factor of 42 at the camera and a calibration factor of 0.09 μm/pixel. This mirror was located 18.5 mm downstream of the Al-coated Kapton and also generated backward COTR that combined with the first source to provide COTRI in the far-field (FF) imaging camera. The significantly enhanced signal allowed the splitting of the signal into two NF cameras as well as a FF camera with a 633±5 nm bandpass filter (BPF) as shown schematically in Fig. 2.

We propose an extension of the single-shot diagnostics coverage to electron beam energy, energy spread, and optical spectroscopy on the same shot by replacing the thick Si mirror at 45 degrees with a few-μm thin Al/Ti mirror/foil. This is so thin that the energy loss in transit for 215 MeV would be in the 10-4 range so energy spread info is also preserved. Since the scattering is much less than 1/γ we expect the microbunching fraction to be preserved also. An Al foil at the spectrometer focal plane and narrowband filter in front of the camera would allow the imaging of the COTR for the microbunched electrons.

* This manuscript has been authored by Fermi Research Alliance, LLC under Contract No. DE-AC02-07CH11359 with the U.S. Department of Energy, Office of Science, Office of High Energy Physics.
† lumpkin@fnal.gov

ISBN: 978-3-95450-222-6 ISSN: 2673-5350 doi:10.18429/JACoW-IBIC2020-THAO05

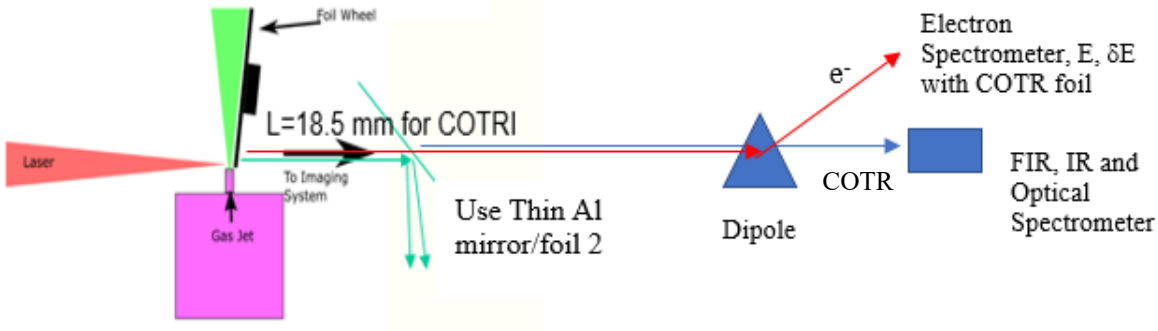

Figure 1: Schematic of an LPA showing the laser, gas jet, and foil geometry with a foil separation L= 18.5 mm for COTRI [5,6]. The proposed *thin* second foil of the interferometer would enable the preservation of energy and microbunching aspects in the electrons for the downstream measurements on the same shot as the interferometer and generate the forward COTR for the optical spectroscopy measurements.

Possible energy dispersion effects on the microbunching fraction need to be assessed. The electron beam continues to the Lanex screen for potential ensemble electron energy measurements and charge measurements.

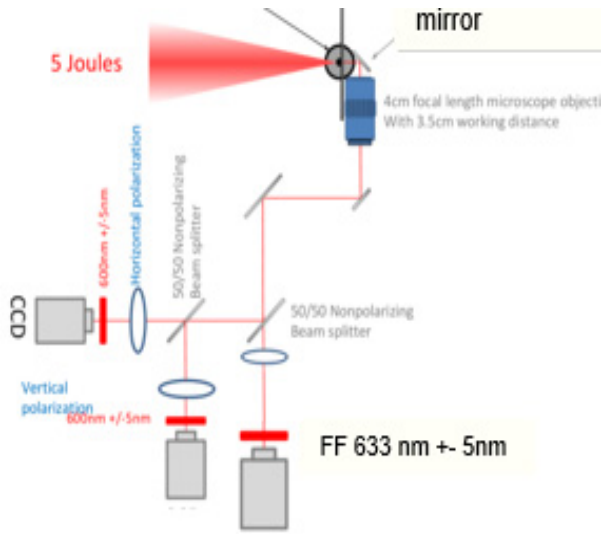

Figure 2: Schematic of the LPA and an early version of the NF and FF imaging setup using the beam splitters to redirect the optical signals to the different cameras [5,6]. The NF imaging could be used on the spectrometer screen.

MODIFIED ANALYTICAL MODEL

Currents induced when a charged particle beam enters and exits a foil generate backward and forward OTR in cones of half-angle $1/\gamma$ around the specular reflection and beam direction, respectively [11]. Thus, the configuration in Fig. 1 generates OTR at 90° to the beam direction, enabling minimally invasive OTR characterization. Upon exiting a foil, a single electron generates W_1 photons per unit frequency ω per unit solid angle Ω, as given by

$$\frac{d^2W_1}{d\omega d\Omega} = \frac{e^2}{\hbar c}\frac{1}{\pi^2\omega}\frac{\left(\theta_x^2 + \theta_y^2\right)}{\left(\gamma^{-2} + \theta_x^2 + \theta_y^2\right)^2} \quad (1)$$

where $\hbar$ is Planck's constant/2π, e is electron charge, c is the speed of light, and θ_x and θ_y are radiation angles [11].

When N_B of the N particles are microbunched, a coherence function $\boldsymbol{J(k)}$ becomes involved, and for two foils an interference function $\boldsymbol{I(k)}$. The spectral angular distribution function then becomes

$$\frac{d^2W}{d\omega d\Omega} = \left|r_{\parallel,\perp}\right|^2 \frac{d^2W_1}{d\omega d\Omega}\left[N\boldsymbol{I(k)} + N_b\left(N_b - 1\right)\boldsymbol{J(k)}\right] \quad (2)$$

where $|r_{\parallel,\perp}|^2$ is reflectance of the second (Si) foil for parallel, perpendicular polarization components, respectively. The reflectance reduces intensity of OTR from the first foil (via reflection from Si) and OTR generated at the Si wafer (via Eq. 2) equivalently. In the modified experimental configuration, this would be an Al foil, however with higher reflectance. $\boldsymbol{I(k)}$ is [11]

$$\boldsymbol{I(k)} = 4\sin^2\left[\frac{kL}{4}\left(\gamma^{-2} + \theta_x^2 + \theta_y^2\right)\right] \quad (3)$$

where $k = |\boldsymbol{k}| = 2\pi/\lambda$, using a small-angle approximation. Choosing L = 18.5 mm provided good fringe contrast, while enabling near-field optics to focus on the first foil. The coherence function can be defined as

$$\boldsymbol{J(k)} = \left(H_1(\boldsymbol{k}) - H_2(\boldsymbol{k})\right)^2 + H_1(\boldsymbol{k})H_2(\boldsymbol{k})\boldsymbol{I(k)} \quad (4)$$

where $H_j(\boldsymbol{k}) = \rho_j(\boldsymbol{k})/Q = g_j(k_x)g_j(k_y)F(k_z)$ for a microbunch of charge distribution $\rho_j(\boldsymbol{x})$ and total charge Q, with j = 1, 2. Here we have introduced two microbunch form factors, H_1 and H_2, to account for the increase in bunch radius from the first to the second interferometer foil due to beam divergence. Details of the Fourier transforms are in reference [7]. If $\boldsymbol{J(k)} << 1$ or in Eq. (2). $N_B \to 0$, only the incoherent OTR term (~N) remains.

ANALYTICAL MODEL RESULTS

215-MeV COTRI Results

Relevant former model results are shown in Fig. 3 illustrating the divergence effect on fringe visibility (negative angles) and the beam size effect on the enhancement of

Content from this work may be used under the terms of the CC BY 3.0 licence (© 2020). Any distribution of this work must maintain attribution to the author(s), title of the work, publisher, and DOI

ISBN: 978-3-95450-222-6 ISSN: 2673-5350 doi:10.18429/JACoW-IBIC2020-THAO05

Content from this work may be used under the terms of the CC BY 3.0 licence (© 2020). Any distribution of this work must maintain attribution to the author(s), title of the work, publisher, and DOI

fringes (positive angles) at 215 MeV. One can see the fringe visibility is reduced for the 1.0-mrad case vs the 0.5-mrad case at the left. On the right, the coherence function is shown to be dramatically reduced at larger angles for the larger beam sizes. This means the FEL case only had a few visible fringes while the LPA fringe data extend out to 30 mrad. The foil separation was 18.5 mm and λ= 633±5 nm.

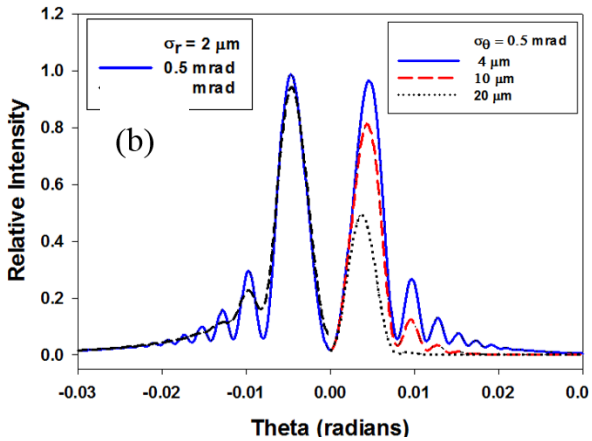

Figure 3: COTRI calculations for the effects of beam divergence (θ<0) for a fixed beam size of 2 μm and the effects of microbunched beam size on fringe intensity for a fixed beam divergence of 0.5 mrad (θ>0).

1.0-GeV COTRI Results

The next case considered was for 1-GeV electrons with a foil spacing, L= 50.8 mm, BPF of 633 ± 5 nm, and initial beam sizes of 10 and 30 μm. Three polarization components are considered: the parallel component in the observation plane, Ipar; the perpendicular component to this plane, Iperp; and the sum of these two components, Itot, which is observed if no linear polarizer is used. With the low divergence of 0.1 mrad, the beam size changes in the drift of 50.8 mm are minimal in the Ipar plot of Fig. 4a and are similar to Fig. 7a of reference [6] with a constant-beam-size model. However, with the larger divergence value of 0.7 mrad, the fringe visibility is greatly reduced in Fig. 4b, and the beam size changes from 10 to 36.9 μm in the drift. This also reduces the fringe peak intensities.

Interestingly, the interference terms result in the first lobes being at ± 2.8 mrad instead of at ± 0.5 mrad, the 1/γ value. This enables divergence sensitivity in the 0.1 to 0.5 mrad range in the central valley which normally would not be as accessible with the single-foil angular distribution pattern with the smaller 1/γ opening angle. This is true even for the 30-μm initial beam size with Itot COTRI cases as shown in Fig. 5. We trade outer fringe visibility effects in the 10-μm case for the central minimum visibility effects with the larger 30-μm beam size.

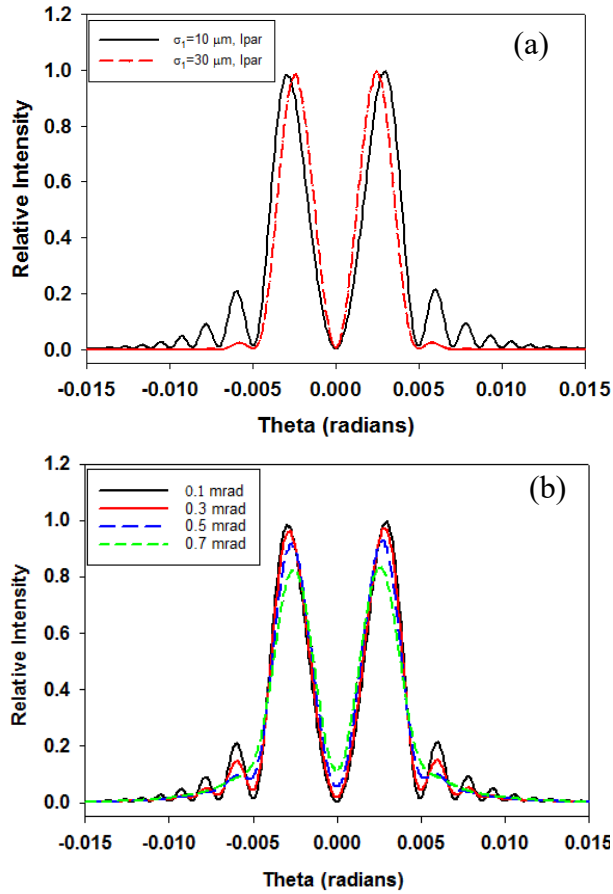

Figure 4: Plots of Ipar COTRI patterns at 1.0 GeV for (a) two initial beam sizes σr1 of 10 and 30 μm showing the coherence gain factor effects on the observed fringes for the parameters in text. Peaks at angles beyond ±5 mrad have lower gain factors in the σr1 = 30-μm case. and (b) four divergence values for σr1 = 10 μm showing the effect on the central minimum and peaks 2,3 with reduced visibility at the 700-μrad case with σr2 = 36.9 μm at foil 2.

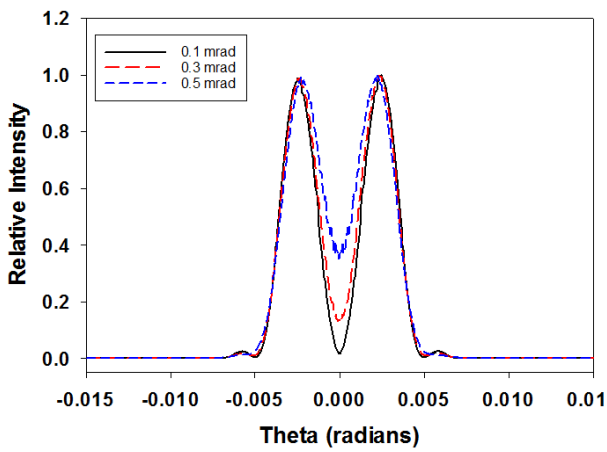

Figure 5: Plots of Itot COTRI patterns at 1 GeV for an initial beam size σ_{r1} of 30 μm and divergences of 0.1, 0.3, and 0.5 mrad. The divergence sensitivity is in the central valley in these cases.

ISBN: 978-3-95450-222-6 ISSN: 2673-5350 doi:10.18429/JACoW-IBIC2020-THAO005

EXAMPLE EXPERIMENTAL RESULTS

Examples of the NF and FF images from the same LPA shot at 215 MeV from a previous experiment [6] are shown in Figs. 6 and 7, respectively. In Fig. 6a we see the vertically polarized COTR point spread function (PSF) lobes for two beamlets separated on the x axis (laser polarization axis) by about 6 μm. This is consistent with the earlier VORPAL simulations that exhibited a bimodal spatial distribution on the laser polarization axis, but not on the orthogonal axis [12]. A sample of the analysis technique which used the measured PSF lobe separation of 5.0 μm in y to determine the vertical beam size of about σ = 2.0 μm is shown in Fig. 6b. In Fig. 7a, the FF COTRI pattern is shown whose fringe number and visibility are compared to Fig. 3 earlier model [8] results as well as the revised model [7] results to obtain a sub-mrad divergence of 0.4 ± 0.2 mrad and a beam size less than 4 μm. In addition, the analysis of the intensity of the FF image referenced to a calibrated laser source at 633 nm led to an estimated COTR gain $>10^5$ [7]. This is surprisingly similar to the SASE FEL COTR result at saturation [2], although the number of microbunched electrons in the LPA case is 30-50 times smaller, as is the beam distribution.

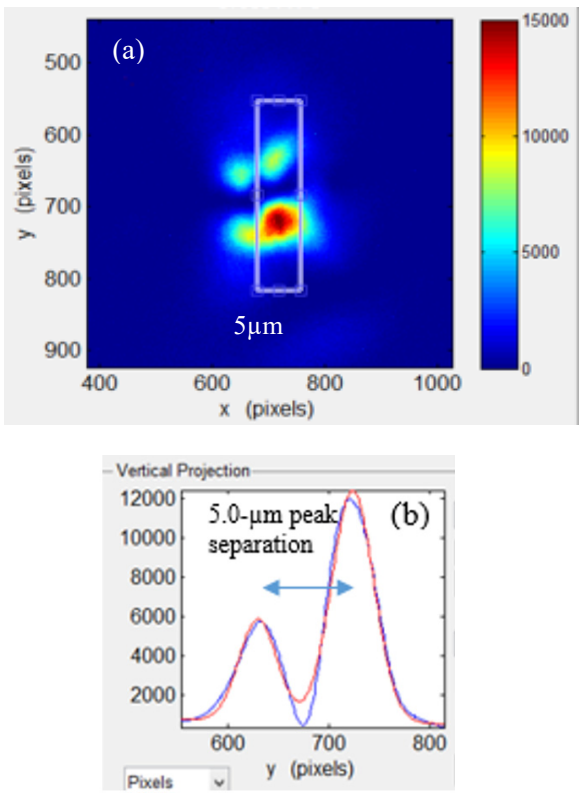

Figure 6: a) Vertically polarized NF image showing two pairs of coherent PSF lobes for two beamlets separated by about 6 μm. b) vertical profile of right hand beamlet with a 5-μm lobe separation which is mapped to 4.6 μm (FWHM) or 2.0 μm (σ).

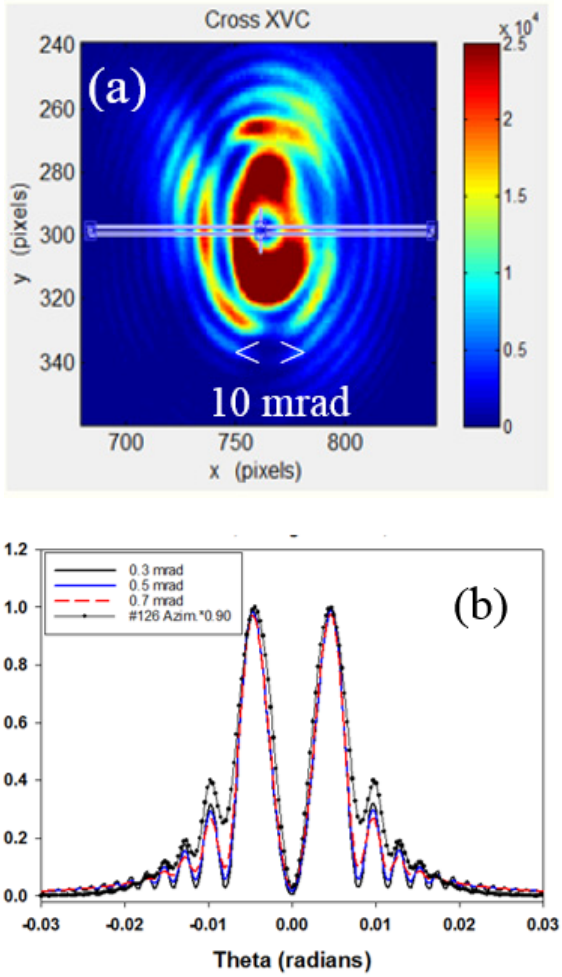

Figure 7: (a) Example of a FF COTRI image at 633±5 nm from the same shot as Fig. 6. (b) Comparison of the azimuthally averaged over a quadrant data and the COTRI model for 0.3-, 0.5-, and 0.7-mrad divergence. The fringe peak positions are well matched, but the relative intensities of some outer fringes are higher in the data. The best match is 0.5 mrad.

SUMMARY

In summary, we have recalled a classic SASE FEL case where the electron microbunching was tracked as a function of z, and a COTRI model was applied [2]. We have compared that observed COTR gain seen at saturation to a recent LPA experiment that obtained single shot NF and FF images to determine beam size and divergence. We have noted the similar COTR gain >105 in the two experiments, although there is a marked difference in the transverse size of the microbunched portion. In the case of the LPA, this microbunching appears to be a fundamental aspect of the LPA process and merits further investigation. We also suggest that the LPA microbunching at the 1% level in a narrow band might be used to seed a visible light SASE FEL experiment by adding an undulator(s) downstream of the LPA.

Content from this work may be used under the terms of the CC BY 3.0 licence (© 2020). Any distribution of this work must maintain attribution to the author(s), title of the work, publisher, and DOI

ISBN: 978-3-95450-222-6 ISSN: 2673-5350 doi:10.18429/JACoW-IBIC2020-THAO05

Content from this work may be used under the terms of the CC BY 3.0 licence (© 2020). Any distribution of this work must maintain attribution to the author(s), title of the work, publisher, and DOI

ACKNOWLEDGEMENTS

The first author acknowledges the support of C. Drennan and M. Lindgren of the Accelerator Division at Fermilab. The University of Texas authors acknowledge support from DoE grant DE-SC0011617, and M.C.D. from the Alexander von Humboldt Foundation. The Helmholtz-Zentrum Dresden-Rossendorf author acknowledges support from the Helmholtz Association under program Matter and Technology, topic Accelerator R&D.

REFERENCES

[1] K.-J. Kim, Z. Huang, and R. Lindberg, *Synchrotron Radiation and Free-Electron Lasers: Principles of Coherent X-ray Generation*. Cambridge, United Kingdom: Cambridge University Press, 2017. doi:10.1017/9781316677377

[2] A. H. Lumpkin *et al.*, "Evidence for Microbunching "Sidebands" in a Saturated Free-Electron Laser Using Coherent Optical Transition Radiation", *Phys. Rev. Lett.*, vol. 88, p. 234801, 2002. doi:10.1103/PhysRevLett.88.234801

[3] Y. Glinec, *J.* Faure, *A.* Norlin, *A.* Pukhov, and *V.* Malka, "Observation of Fine Structures in Laser-Driven Electron Beams Using Coherent Transition Radiation", *Phys. Rev. Lett.*, vol. 98, p. 194801, 2007. doi:10.1103/PhysRevLett.98.194801

[4] C. Lin *et al.*, "Long-Range Persistence of Femtosecond Modulations on Laser-Plasma-Accelerated Electron Beams", *Phys. Rev. Lett.*, vol. 108, p. 094801, 2012. doi:10.1103/PhysRevLett.108.094801

[5] M. LaBerge *et al.*, "Observation of annular point spread function of optical transition radiation from low-emittance e-beams emerging from a laser-plasma accelerator", presented at the 3rd European Advanced Accelerator Concepts Workshop. (EAAC'17), Elba, Italy, Sep. 2017, unpublished.

[6] A. Lumpkin *et al.*, "Observations of Coherent Optical Transition Radiation Interference Fringes Generated by Laser Plasma Accelerator Electron Beamlets", in *2018 IEEE Advanced Accelerator Concepts Workshop (AAC)*, Breckenridge, CO, United States, Aug. 2018, pp. 1-5. doi:10.1109/AAC.2018.8659381

[7] A. H. Lumpkin *et al.*, "Coherent Optical Signatures of Electron Microbunching in Laser-Driven Plasma Accelerators", *Phys. Rev. Lett.*, vol. 125, p. 014801, 2020. doi:10.1103/PhysRevLett.125.014801

[8] D. W. Rule and A. H. Lumpkin, "Analysis of Coherent Optical Transition Radiation Interference Patterns Produced by SASE-Induced Microbunches", in *Proc. 19th Particle Accelerator Conf. (PAC'01)*, Chicago, IL, USA, Jun. 2001, paper TPAH029, pp.1288-1290. doi:10.1109/PAC.2001.986656

[9] M. Migliorati *et al.*, "Intrinsic normalized emittance growth in laser-driven electron accelerators", *Phys. Rev. ST Accel. Beams*, vol. 16, p. 011302, 2013. doi:10.1103/PhysRevSTAB.16.011302

[10] U. Schramm *et al.*, "First results with the novel petawatt laser acceleration facility in Dresden", *J. Phys.: Conf. Ser.*, vol. 874, p. 012028, 2017. doi:10.1088/1742-6596/874/1/012028

[11] L. Wartski, S. Roland, J. Lasalle, M. Bolore, and G. Filippi, "Interference phenomenon in optical transition radiation and its application to particle beam diagnostics and multiple-scattering measurements", *J. Appl. Phys.*, vol. 46, pp. 3644-3653, 1975. doi:10.1063/1.322092

[12] A. H. Lumpkin, R. A. Crowell, Y. Li, and K. Nemeth, "A Compact Electron Spectrometer for an LWFA", in *Proc. 29th Int. Free Electron Laser Conf. (FEL'07)*, Novosibirsk, Russia, Aug. 2007, paper WEAAU05, pp. 294-297.

ISBN: 978-3-95450-222-6 ISSN: 2673-5350 doi:10.18429/JACoW-IBIC2020-THAO06

FEATURES OF THE METAL MICROSTRIP DETECTORS FOR BEAM PROFILE MONITORING

V. M. Pugatch, D. M. Ramazanov, O. S. Kovalchuk
Institute for Nuclear Research NAN, Kyiv, Ukraine

Abstract

Features of Metal Microstrip Detectors (MMD) are presented for application in beam profile monitoring of charged particles and synchrotron radiation beams. Through an innovative plasmachemistry etching production process, thin metal micro-strips only 1–2 μm thick are aligned. Because of the very thin nature of the strips, the MMD is nearly transparent, and can be used in situ for measuring, tuning and imaging the beam online. Metal structure of sensors guaranties high radiation tolerance (about 100 MGy) providing their stable response to the beam particles (by the secondary electron emission) independent upon the accumulated fluence. The spatial resolution of the MMD is determined by the strips pitch constituting from 5 to 100 μm in currently manufactured samples. The data obtains with MMDs read out by the low noise X-DAS system providing integration time from 1 to 500 ms, and the ability to process signals in real time. The scope of MMD & X-DAS is scientific and applied research using beams: in control systems of accelerators and synchrotron radiation sources. New possibilities are discussed for equipment requiring high spatial resolution and radiation hardness.

INTRODUCTION

Beam diagnostics is an important component of any accelerator. In modern experiments in high-energy physics, particle fluxes reach extremely large values. The increase in intensities and energy leads to an increase in radiation loads on the detector systems. It is known that silicon, scintillation and other detector systems used in most experiments have limited radiation resistance, and at too high radiation fluxes lose their performance. In addition, the main requirement for conducting physical experiments is that the measuring device must not distort the measured value. To date, most detector systems do not meet this statement. In this case, the requirements for detector systems for precision measurements are only increasing. Medical accelerators play a special role in this task, because the life and health of patients depend on the precision of the accuracy and intensity of the beam. A detector system that would independently control the position, size and intensity of the ionizing radiation beam would significantly increase the reliability and safety of irradiation.

This paper describes a detector system that can be used to monitor a beam for various types of radiation therapy, and for accelerators used in high-energy physics experiments. The direction of research is the development of detectors based on the phenomenon of secondary electron emission. Features of secondary electron emission allow to create structurally simple reliable detector systems for monitoring the flow of charged particles and X-rays. This type of detectors includes metal microstrip detectors presented in this article [1–4].

METAL MICROSTRIP DETECTOR

A distinctive feature of MMD from micro-detectors based on semiconductor or insulating materials, which either completely absorb the investigated beam or significantly deform it, metal sensor is almost ideal operation as a measuring and monitoring device without distorting the characteristics of the investigated particle beam or synchrotron radiation. The MMD sensor is made entirely of metal, making this detector one of the most radiation-resistant.

Principle of Operation

Figure 1 shows the operation principle of an MMD second emission monitor grid with ultra-thin wires/strips. One end of each strip is connected to a charge integrator or other measuring system and the other to a stable current source. Incident x-rays on the strips initiate secondary electron emission as they pass through the nearly transparent medium. When this happens, a positive charge appears at the integrator end and is measured.

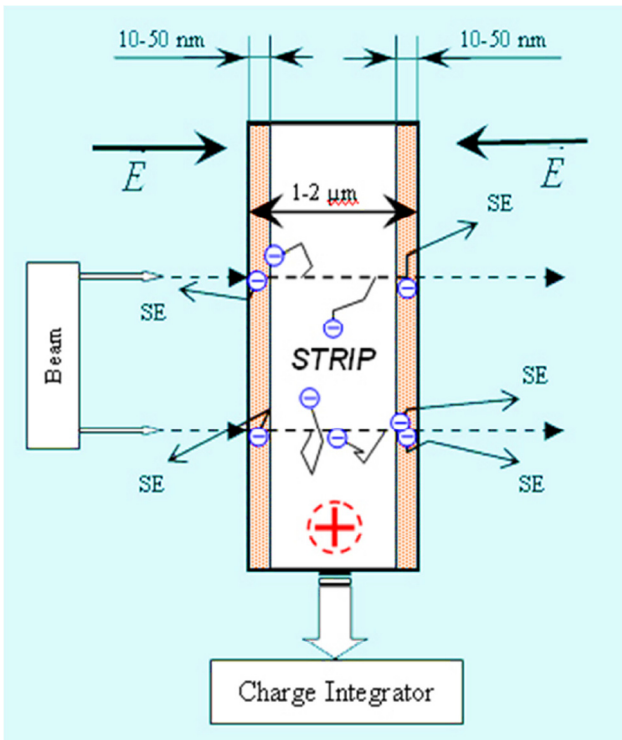

Figure 1: Operation principle of MMD.

Content from this work may be used under the terms of the CC BY 3.0 licence (© 2020). Any distribution of this work must maintain attribution to the author(s), title of the work, publisher, and DOI

ISBN: 978-3-95450-222-6 ISSN: 2673-5350 doi:10.18429/JACoW-IBIC2020-THA006

Content from this work may be used under the terms of the CC BY 3.0 licence (© 2020). Any distribution of this work must maintain attribution to the author(s), title of the work, publisher, and DOI

To improve the extraction of secondary electrons, an accelerating electric field is applied around the strip. This technology works with x-rays, proton and ion beams. Additionally, the strips are 99.9% transmitting to x-rays, significantly reducing radiation degradation that is experienced by absorbing detectors.

MMD PRODUCTION TECHNOLOGY

The design, technology and structure of MMD are determined by the principle of operation and application requirements. The main feature of MMD, which determines the complexity of the production process, is the micrometric size of the bands that serve as sensors. Figures 2 to 4 show MMDs for different purposes.

Figure 2: MMD 1024, 1024 strips with a pitch of 60 µm for heavy ions registration in mass spectrometry.

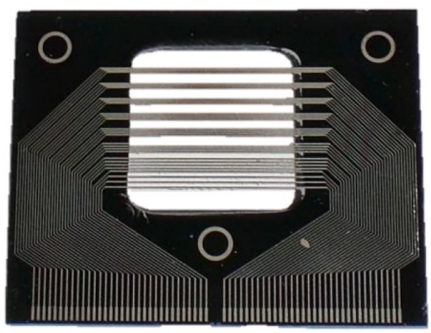

Figure 3: MMD32v, 32 strips with variable pitch (2 to 300 µm) for micro-beams focusing.

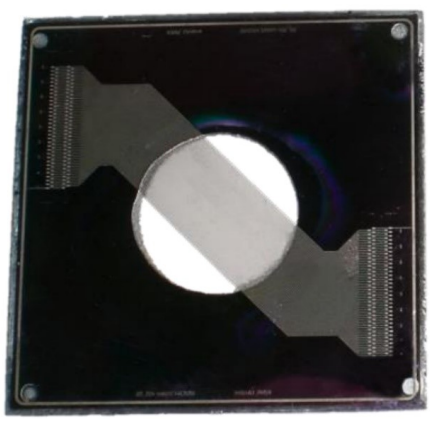

Figure 4: MMD64, 64 strips with a step of 100 µm – for XY-positioning and profiling of mini- and micro-beams of charged particles and X-ray radiation.

MMD production technology includes micro photolithography, plasma chemical etching and assembly. These steps are briefly described below. The sensor layer of the prototype MMD may include from 1 to 1000 strips with a maximum length of 15 mm (at greater length, they begin to tear) with a width of 5 to 100 µm. The strips are placed on a silicon wafer with a thickness of 500 µm or 300 µm. Each band is connected to an individual input channel of the reading electronics.

Photolithography

Two dielectric layers are created on the silicon wafer to insulate future nickel bands from the semiconductor. Initially, silicon oxide (SiO_2, 0.1-0.3 µm thick) is grown and subsequently coated with silicon nitride 0.2 µm thick (Si_3N_4). To improve adhesion, the dielectric layer is covered with a thin titanium film (about 50 nm). Finally, a nickel film 1–2 µm thick is applied. This multilayer structure is created on both sides of the silicon wafer. Strips with connecting plates are formed on the front side by photolithography methods, while on the back side of the Si-plate a nickel mask for future plasma chemical etching is stored.

Plasma Chemical Etching

To remove silicon from the working zone of MMD (due to which the metal strips hang freely there), a plasma chemical reactor is used in KINR with variable ion energy. First, with the help of an additional mask made of metal foil on the front side of the plate, a thin surface layer (20–80 µm) of silicon is removed. Then, through a rectangular window on the back, plasma chemical etching is performed. The initial etching rate is in the range of 2–5 µm per minute at an ion energy of 80 eV and a current of 10 A. When the thickness of the silicon wafer approaches 50–100 µm in the working area of the sensor, the etching rate slows to 0–3 µm per minute, the current decreases up to 4 A, and the energy of ions up to 20 eV. Thus, it is possible to make MMD with completely remove silicon from the working area and leave only nickel strips. In the same way the accelerating layers are made. The only difference is the number of bands: the accelerating layers have two bands located at a distance that is slightly wider than between the outer bands of the sensor layer. In the same way the accelerating layers are made. The only difference is the number of lanes, the accelerating layers have much fewer sprays.

Assembling

The sensor and high voltage are glued to special ceramic plates. Ceramics connected to the PCB base also with glue. Each strip is connected by supersonic welding with metallization on an adapter, which can be in the form of a flexible polyamide multichannel cable or in the form of prepared PCB. The entire structure is locked in a protective metal frame to avoid mechanical damage and electromagnetic interference. The X-DAS connection to detector is provided by Samtec LSHM connectors. The reading system is connected directly to the computer, and the corresponding software presents the data online on the computer display.

ISBN: 978-3-95450-222-6 ISSN: 2673-5350 doi:10.18429/JACoW-IBIC2020-THAO06

DATA ACQUISITION SYSTEM

The MMD requires special reading equipment. The sensor reading system have to be highly sensitive, radiation resistible and has other characteristics to satisfy capabilities of the MMD.

Sens Tech X-DAS System

The XDAS reading system, which is a modular system for a wide range of applications, best meets the requirements of MMD. XDAS is a very flexible system. It allows you to create large detector arrays that are read simultaneously in an accessible digital format. The XDAS system has a modular architecture, which allows you to operate freely by placing detector modules in space. The system consists of Detector Head Boards (XDAS-DH) with analogue output and Signal Processing Boards (XDAS-SP) with 16-bit digital output. Each detector module has 128 channels. With a USB2 adapter, the output is transferred to a PC. The number of read strips in the system reaches 21.504 (128x24DHx7SP). The system has low electronic noise, dynamic range on the maximum charge at the input from 3 pC to 60 pC. The minimum signal integration time is 60 µs with simultaneous data accumulation and reading. The dynamic range of the output signals is 16 bits.

The inputs of the reading system are connected to the microstrip sensors by means of specially designed and manufactured adapters. Connect to a control computer via a USB 2.0 or Ethernet port. The number of samples in each of the 128 registration channels (maximum 65536 samples) corresponds to the intensity of the quanta registered in a particular channel. Gamma quant energy – from 10 keV.

CHARACTERISATION OF THE MMD+X-DAS SYSTEM

To characterize the bundle of microstrip metal detector and X-DAS reading system, studies were carried out on a Pu-239 alpha particle source and on a tandem generator with protons. The measurements were carried out with different detector models, in vacuum and atmosphere.

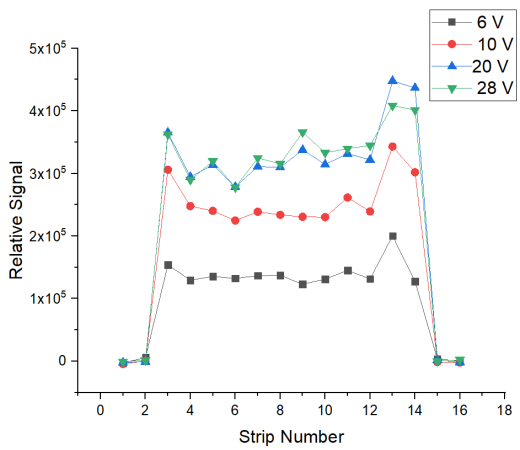

Figure 5: Dependency of the detector response on the voltage at the accelerating electrodes.

MMD Studies on Alpha Source Pu-239

Measurements of a 16-channel microstrip detector with a X-DAS reading system on alpha particles with an energy of 5.24 MeV from the Pu-239 isotope were performed. Figure 5 shows the dependence of the detector response on the voltage at the accelerating electrodes.

Research on the Tandem Generator KINR NASU (Kiev)

Characteristic studies of MMD operation on a proton beam were performed on a tandem generator of the Kyiv Institute for Nuclear Research of the NAS Ukraine in a vacuum chamber on the central ion pipe of the proton hall. For these studies, a detector with two microstrip metal sensors MMD64, specially designed for two-dimensional measurement of the beam profile of charged particles (see Fig. 6), was prepared [5].

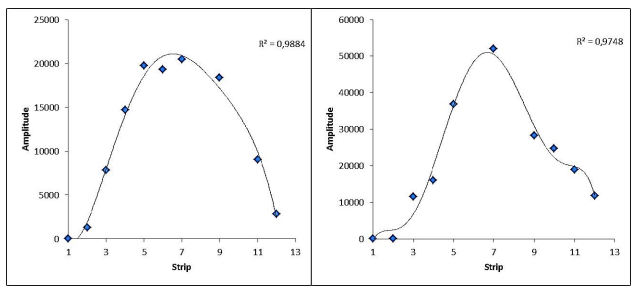

Figure 6: Spatial (horizontal and vertical) Proton beam profiles.

The detectors were mounted in an aluminium frame with a 25-pin D-Sub connector. 12 strips were connected from each sensor. This number of strips was chosen due to the limited number of electrical connectors on the vacuum chamber (see Fig. 7).

Figure 7: Photo of MMD installed in an accelerator vacuum chamber.

Figure 8 shows a photo of the studied sensor (nickel strips thickness: 2 µm, step: 100 µm, width: 40 µm). Two sensors are mounted on top of each other forming an angle of 90 degrees between the strips, to obtain a two-dimensional intensity distribution of the studied beam.

Content from this work may be used under the terms of the CC BY 3.0 licence (© 2020). Any distribution of this work must maintain attribution to the author(s), title of the work, publisher, and DOI

ISBN: 978-3-95450-222-6 ISSN: 2673-5350 doi:10.18429/JACoW-IBIC2020-THAO06

Content from this work may be used under the terms of the CC BY 3.0 licence (© 2020). Any distribution of this work must maintain attribution to the author(s), title of the work, publisher, and DOI

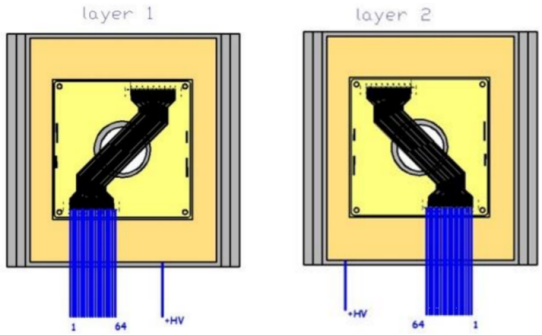

Figure 8: Layout of sensors in the MMD-64 detector.

CONCLUSION

Micro-strip metal detectors of various shapes and types for measuring the profile and position of charged particle beams in the atmosphere and in vacuum have been developed and manufactured.

MMDs of various configurations, made in the Institute of Nuclear Research of the National Academy of Sciences of Ukraine according to the original technology of plasma-chemical etching. The thickness of the sensors is 1–2 µm, the step is from 2 µm, the number of strips is up to 1024. The possibility of using mmd with a commercially available multi-channel X-DAS reading system has been tested.

REFERENCES

[1] N. M. Tkatch and V. A. Kiva, *Scientific Papers of the Institute for Nuclear Research*, No. 2(4), p. 72, 2001.

[2] E. J. Sternglass, "Theory of Secondary Electron Emission by High-Speed Ions", *Phys. Rev.*, vol. 108, pp. 1–12, 1957. doi:10.1103/PhysRev.108.1

[3] H. Rothard *et al.*, *Springer Tracts in Modern Physics*, Springer, Berlin, 1992, p. 97.

[4] O. Fedorovich *et al.*, "Plasma technologies for manufacturing of metal micro-strip detectors of ionizing radiation", *11th International Conference on Plasma Physics and Controlled Nuclear Fusion*, 11–16 September 2006, Abstracts, Alushta 2006, p. 172.

[5] V. Pugatch *et al.*, "Micro-strip metal foil detectors for the beam profile monitoring", in *Proc. DIPAC'05*, Lyon, France, 2005, pp. 18-20, paper CTMM02.

ISBN: 978-3-95450-222-6 ISSN: 2673-5350 doi:10.18429/JACoW-IBIC2020-THPP04

TESTBED DEVELOPMENT FOR THE CHARACTERISATION OF AN ASIC FOR BEAM LOSS MEASUREMENT SYSTEMS

F. Martina[1], C. Zamantzas, L. Giangrande, J. Kaplon, P. V. Leitao, CERN, Geneva, Switzerland
[1]also at Dept. of Electrical Engineering and Electronics, University of Liverpool, Liverpool, UK

Abstract

A high-performance, radiation-hardened, application-specific integrated circuit (ASIC) is under development at CERN for digitising signals from beam losses monitoring systems in harsh radiation environments. To fully characterise and validate both the analogue and digital parts of these ASICs, an automated testbed has been developed. Here we report on the components used to build this set-up, its capabilities as well as the methodology of the data analysis. Focus is given to the data collection, the automation and the efficient computation methods developed to extract the merit factors of two different ASIC designs from prototype manufacturing runs.

INTRODUCTION

In view of the HL-LHC upgrade [1], a new version of the Beam Loss Monitoring (BLM) front-end electronics is under development. The BLM system is one of the critical systems for the protection of the particle accelerator against damage (or quenches [2] in the case of the LHC) caused by the energy deposition from lost beam particles and their secondary particle cascades [3].

The new key component of this BLM front-end, as compared to the old system [4-6], is a custom-designed Application Specific Integrated Circuit (ASIC), hereafter referred to as the BLMASIC. The aim of the design is to guarantee high resolution measurements in harsh radiation areas, where off-the-shelf components (COTS) cannot be used. To achieve this, two different BLMASIC architectures have been investigated and designed: one based on current-to-frequency conversion (BLMASIC-CFC, the same concept as the currently operational system); and one implementing a delta-sigma converter (BLMASIC-ΔΣ).

The aim of the present research is to measure the ASIC performance and have a first validation of their conformity to the specified requirements for the system. This includes looking at their linearity, their measurement resolution, their temperature stability, their robustness to electrostatic discharge (ESD) at the input, their tolerance to radiation and faults, and their compatibility with the other components required for the BLM system upgrade.

Even though the estimated performance of the device has been simulated using sophisticated tools, tests on the real component are essential to qualify its behaviour after the manufacturing process. There are physical effects not included in the simulations that depend on the fabrication run, and others that are intrinsically too complex to be taken into account. The versatile testbed built should also allow a direct comparison of the two architectures and provide the necessary information to take the decision on which one to select for the final production.

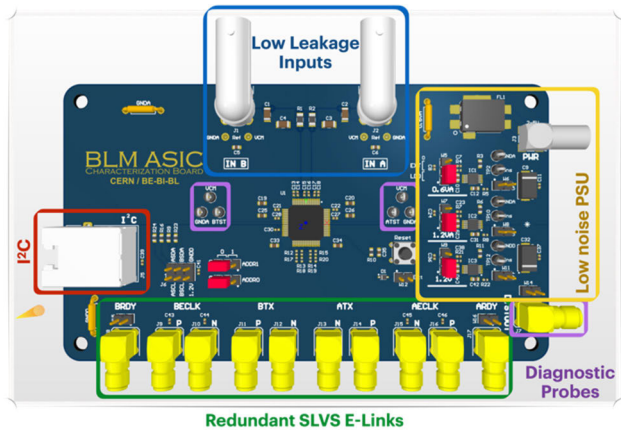

Figure 1: Characterisation Board.

This work focuses on the architecture and assembly of a testbed to perform this testing. It includes the design of a characterisation board, the selection of suitable laboratory instrumentation, the development of the acquisition and configuration firmware, as well as the software for future batch data analysis. An example of noise performance characterisation using this testbed is reported.

TESTBED ARCHITECTURE

In order to validate the performance of the BLMASICs, a multi-layer characterisation PCB has been designed, which provides direct access to the device interfaces, including all the debug features available (Fig. 1). The board is equipped with low leakage BNC inputs for injecting test currents into the device; redundant SLVS lanes to provide the clock and output the digital data stream; an I^2C bus to read and configure all the internal registers; three diagnostic probes, which are connected to a programmable multiplexer switching among several internal analogue and digital signals. The final module can either be powered from external power supplies or using the low noise supplies provided by the characterization board. When this last option is chosen, shunt resistors can be used to monitor the current consumption on the power bus.

Content from this work may be used under the terms of the CC BY 3.0 licence (© 2020). Any distribution of this work must maintain attribution to the author(s), title of the work, publisher, and DOI

ISBN: 978-3-95450-222-6 ISSN: 2673-5350 doi:10.18429/JACoW-IBIC2020-THPP04

Content from this work may be used under the terms of the CC BY 3.0 licence (© 2020). Any distribution of this work must maintain attribution to the author(s), title of the work, publisher, and DOI

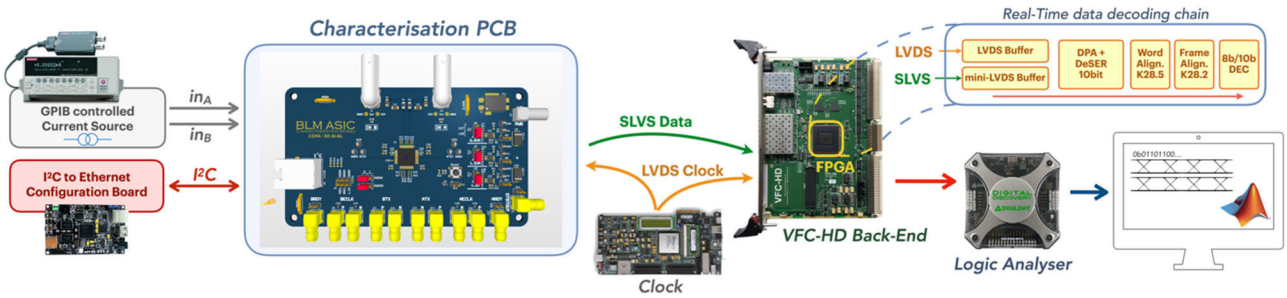

Figure 2: Testbed Assembly.

The requirements for high accuracy and robustness for the final product were also been taken into account during the selection of components and the PCB manufacturing technology. In addition, as radiation testing will be necessary for the final validation stage, the board has been designed in such a way as to be easily modifiable for use in such an environment.

Both the board schematics and the layout have been studied to minimise the effect of parasitic signals on the test measurements. The architecture of the complete testbed used for the measurements is shown in Fig. 2.

The standard CERN Beam Instrumentation VME64x Carrier Board (VFC-HD) FPGA [7] runs the firmware to acquire the real-time data stream. This is also the same back-end hardware planned to be used for the final installation system. In the testbed, the VFC-HD performs the 8b/10b data stream decoding and collects the measurement values from the relevant memory addresses. An external logic analyser, driven by a MATLAB script, is connected to the carrier board and saves long histories of acquired data to computer file. The same script is able to program the internal registers of the BLMASIC under test via a custom designed Ethernet to I^2C interface, and to configure the current source generating the test signal through a commercial Ethernet to GPIB adapter. Finally, an external FPGA board is employed to deliver the required clock to the acquisition system.

In order to verify the performance of a BLMASIC under particular conditions, additional firmware modules have been developed. For example modules that are able to single out spikes in the measurement data or indicate a faulty response. During validation of the BLMASIC-CFC, we exploited the ASIC signal probes to acquire data coming directly from the integrated analogue circuit of the ASIC, bypassing the digital processing stages. This helped to identify and correct rare erroneous conditions in the logic network of the device. With this setup it was therefore possible to properly characterise the analogue performance of the circuit, without having to wait for delivery of the next ASIC version with the correction included.

Each of the testbed instruments is directly connected to the CERN internal network. This architecture makes it possible to run automated measurement sessions and to control the overall system remotely, even when the operators are teleworking. This feature has been extensively used during the recent periods with COVID-19 restrictions.

DATA ANALYSIS

The criticality of the BLM system implies a stringent verification of all requirements before proceeding with the installation of new components. The testbed is therefore being exploited fully to carry on an accurate study of the behaviour of both BLMASICs. This starts with testing basic device operation, checking the power consumption, the initialisation and the digital interface functionalities. The next step is to check the analogue-to-digital conversion performance, which is the core functionality of the circuit. This was performed by the injection of current sweeps at the input while simultaneous reading the internal measurement registers. This comparison between the set current and the acquired data led to a preliminary characterisation of the device linearity and the behavioural mismatch of the input channels. To verify the conversion error and resolution, and to measure the electronic noise, various levels of fixed currents were set within the overall measurement range, with the standard deviation computed on specified time windows. This often required the acquisition of hundreds of seconds of data in order to obtain the required measurement resolution on the averages and standard deviations. The subsequent processing time could therefore also become highly time-consuming. To optimise this time a multi-threaded, C++, batch data analysis was implemented, allowing operations to be performed on multi-core computers. This reduced the required time from many hours to less than ten minutes. The analysis flow includes the following steps:

- A large number of raw current measurement samples are loaded from file into computer memory;
- The samples are clustered in groups of a specified size, representing a certain time window;
- The averaging is performed within each of the groups;
- The standard deviation is computed amongst all averages;
- The procedure is repeated for all the time windows under consideration.

This method gives relevant information about the ASIC electronic noise limits and, at the same time, helps to evaluate the suitable averaging time needed to achieve a given precision.

Figure 3 shows an example of current measurement noise as a function of the time window used for averaging

ISBN: 978-3-95450-222-6 ISSN: 2673-5350 doi:10.18429/JACoW-IBIC2020-THPP04

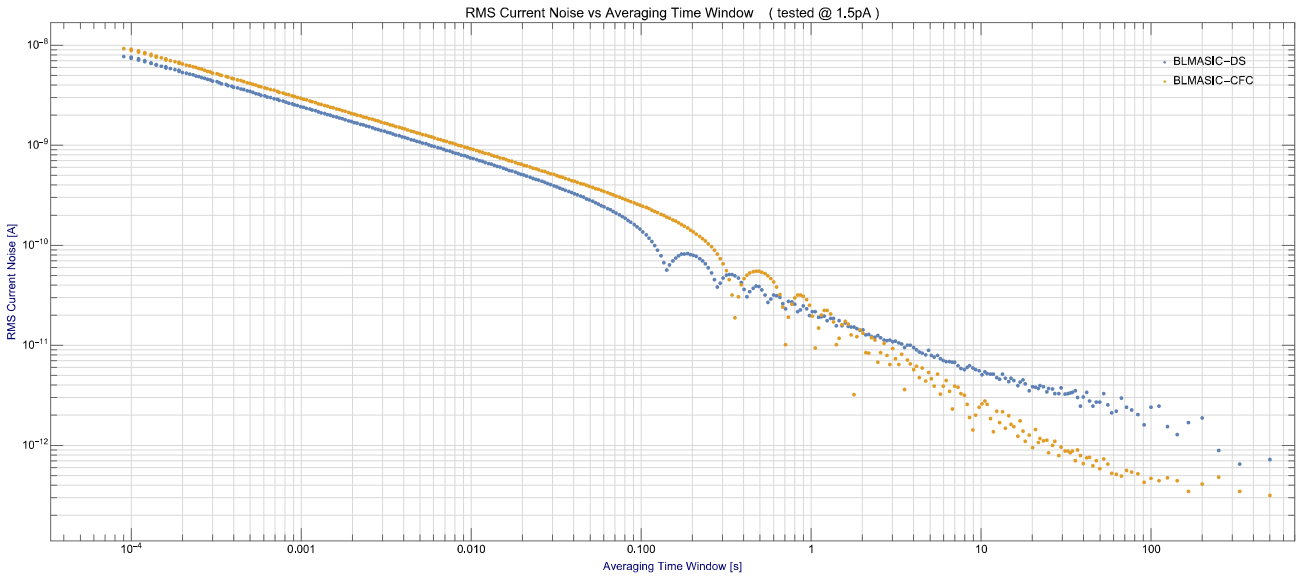

Figure 3: Example of noise characterisation with current measurement noise plotted against the time window used for averaging. BLMASIC-ΔΣ in blue, BLMASIC-CFC in orange.

For times larger than 10 seconds, because of the reduced number of clusters, the rms_{noise} suffers from some casual fluctuations, which can be smoothed acquiring data for a longer period. At a long enough integration time we would expect the measurement rms_{noise} to reach the limit given by the digitisation stage. The BLMASIC specifications require to measure current signals down to 1 pA. From our measurements we see that such a precision it is not limited by the analogue electronic noise in both the device architectures since, for long averaging windows, the rms_{noise} reached a plateau below this value. Furthermore, in concrete measurements we can achieve the pA precision for averaging time greater than 200s.

CONCLUSIONS

A versatile testbed for characterisation of BLMASICs has been reported. The first tests using this infrastructure were carried during the first half of 2020 and have already produced valuable results.

As well as characterising the two ASIC architectures, the testbed had allowed us to investigate and correct erroneous behaviour in these devices, which has led to modifications in the design before submission of a second version, which will be again be validated using the same testbed in the future.

The plan for the next version of the testbed is to integrate other components involved in the final BLM upgrade, in particular a high-speed optical transceiver for data transmission.

REFERENCES

[1] G. Apollinari, I. Béjar Alonso, O. Brüning, M. Lamont, and L. Rossi, "High-Luminosity Large Hadron Collider (HL-LHC): Preliminary Design Report", CERN, Geneva, Switzerland, Rep. CERN-2015-005, 2015. doi: 10.5170/CERN-2015-005

[2] C. Kurfuerst, B. Dehning, E. Holzer, A. Nordt, M. Sapinski, and C. Fabjan, "Quench Prevention of the LHC Quadrupole Magnets", Diploma thesis, Vienna U. Technology, Vienna, Austria, 2010. Rep. CERN-THESIS-2010-070.

[3] B. Dehning et al., "The LHC Beam Loss Measurement System", in *Proc. 22nd Particle Accelerator Conf. (PAC'07)*, Albuquerque, NM, USA, Jun. 2007, paper FRPMN071, pp. 4192-4194. doi: 10.1109/PAC.2007.4439980

[4] W. Viganò, M. Alsdorf, B. Dehning, M. Kwiatkowski, G. Venturini, and C. Zamantzas, "10 Orders of Magnitude Current Measurement Digitisers for the CERN Beam Loss Systems", *JINST*, vol. 9, p. C02011, 2013. doi: 10.1088/1748-0221/9/02/C02011

[5] C. Zamantzas, M. Alsdorf, B. Dehning, S. Jackson, M. Kwiatkowski, and W. Vigano, "System Architecture for Measuring and Monitoring Beam Losses in the Injector Complex at CERN", in *Proc. 1st Int. Beam Instrumentation Conf. (IBIC'12)*, Tsukuba, Japan, Oct. 2012, paper TUPA09, pp. 347-350.

[6] E. Effinger, B. Dehning, J. E. Emery, G. Ferioli, and C. Zamantzas, "Single gain radiation tolerant LHC beam loss acquisition card", in *Proc. 8th European Workshop on Beam Diagnostics and Instrumentation for Particle Accelerators (DIPAC'07)*, Venice, Italy, May 2007, paper WEPC06, pp. 319-321

[7] A. Boccardi, M. Barros Marin, T. E. Levens, B. Szuk, W. Vigano, and C. Zamantzas, "A Modular Approach to Acquisition Systems for Future CERN Beam Instrumentation Developments", in *Proc. 15th Int. Conf. on Accelerator and Large Experimental Physics Control Systems (ICALEPCS'15)*, Melbourne, Australia, Oct. 2015, pp. 1103-1106. doi:10.18429/JACoW-ICALEPCS2015-THHB2O02

Content from this work may be used under the terms of the CC BY 3.0 licence (© 2020). Any distribution of this work must maintain attribution to the author(s), title of the work, publisher, and DOI

ISBN: 978-3-95450-222-6 ISSN: 2673-5350 doi:10.18429/JACoW-IBIC2020-THPP05

Content from this work may be used under the terms of the CC BY 3.0 licence (© 2020). Any distribution of this work must maintain attribution to the author(s), title of the work, publisher, and DOI

PROPERTIES OF CHERENKOV DIFFRACTION RADIATION AS PREDICTED BY THE POLARISATION CURRENTS APPROACH FOR BEAM INSTRUMENTATION

D. M. Harryman*, K. V. Fedorov, P. Karataev
JAI, Royal Holloway, University of London, Egham, Surrey, UK
L. Bobb, Diamond Light Source, Oxfordshire, UK
M. Bergamaschi, R. Kieffer, K. Lasocha, T. Lefevre, S. Mazzoni, A. Schloegelhofer
CERN, Geneva, Switzerland
A. P. Potylitsyn, Tomsk Polytechnic University, Tomsk, Russia

Abstract

Cherenkov-Diffraction Radiation (ChDR) appears when a charged particle moves in the vicinity of a dielectric medium with velocity higher than the phase velocity of light inside the medium. As the charged particle does not contact the medium, the emission of ChDR is a phenomenon that can be exploited for a range of non-invasive beam diagnostics. Experimental tests are underway on the Booster To Storage-ring (BTS) test-stand at Diamond Light Source to explore the use of dielectric radiators as Beam Position Monitor (BPM) pickups by measuring the incoherent ChDR emission. In order to compliment the experiments on the BTS test-stand, ChDR simulations have been performed using the Polarisation Currents Approach (PCA) model. This paper explores the PCA simulations for the BTS test-stand, and the application for future diagnostics.

CHERENKOV DIFFRACTION RADIATION

Cherenkov Diffraction Radiation (ChDR) appears when a charged particle moves in the vicinity of a dielectric medium with velocity higher than the phase velocity of light inside the medium [1]. Detecting ChDR in accelerators is being explored in the development of non-invasive beam diagnostics [2]. ChDR appears at the same distinctive angle as Cherenkov radiation that is given by

$$\cos(\theta_{\mathrm{Ch}}) = \frac{1}{\beta n}, \tag{1}$$

where θ_{Ch} is angle of ChDR emission, β is ratio of the particles velocity compared to the vacuum velocity of light, and n is the refractive index of the radiator [3,4]. The emission angle of ChDR allows for a detection system to be designed that can discriminate against noise such as synchrotron radiation. A theoretical model to predict the emission of ChDR has been developed in [5–7], the model developed is called the Polarisation Currents Approach (PCA).

RADIATOR GEOMETRIES

The PCA model can be applied to different radiator geometries where the geometry selected will effect the ChDR emission [5,7]. Figure 1 shows a prismatic ChDR radiator where the notation used is as follows; γ is the Lorentz factor β is ratio of the particles velocity compared to the vacuum velocity of light, λ is the wavelength of the radiation, $\varepsilon(\lambda)$ is the wavelength dependant permittivity of the prism, θ_{Ch} is the Cherenkov angle, a is the length of the surface parallel with the electron trajectory, φ is the vertex angle of the prism, δ is $(90° - \varphi)$, b is the impact parameter, h is the angled impact parameter (where $b = h\cos(\delta)$), and ϕ, θ are respectively the azimuthal and polar angles of the emitted radiation [7].

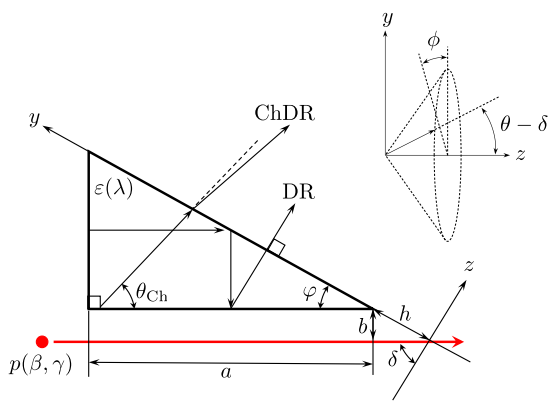

Figure 1: Prismatic Radiator Geometry.

Using a prismatic radiator, the ChDR is generated at the Cherenkov angle which is distinctively different to that of the particle trajectory, once the ChDR reaches the emission surface of the prism it will be emitted at a refracted angle using Snells law [8]. Knowing the index of refraction for the prism, the outside interface, and the Cherenkov angle for that radiator, the vertex angle of the prism is selected for a desired extraction angle. As the ChDR is generated along the entire target length it will be emitted along the majority of the extraction surface.

Extensive work has been done in [7] to obtain the ChDR angular distribution emitted from a prismatic radiator when a charge particle moves parallel to one side (see in Fig. 1). Each polarisation component is then given by Eqs. (2), (3) and (4), where $\hbar$ denotes the reduced Plank constant, α is the fine structure constant, c is the vacuum speed of light, and the notation from Fig. 1 has been used [7].

* daniel.harryman.2018@live.rhul.ac.uk

ISBN: 978-3-95450-222-6 ISSN: 2673-5350 doi:10.18429/JACoW-IBIC2020-THPP05

$$\frac{\mathrm{d}^2W_1}{\mathrm{d}\lambda\mathrm{d}\Omega} = \frac{\alpha\hbar c\beta^2\cos^2(\theta-\delta)}{2\pi^2\lambda^2K^2|P|^2}\left|\frac{\varepsilon(\lambda)-1}{\varepsilon(\lambda)}\right|^2\times\Bigg|1-\exp\Big[-ia\frac{2\pi}{\beta\lambda}(P+\Sigma\cdot\cot(\varphi))\sin(\varphi)\Big]$$
$$-\frac{P\exp\Big[i\frac{2\pi}{\beta\lambda}\Sigma\cdot a\cdot\cos(\varphi)\Big]}{P+\Sigma\cdot\cot(\varphi)}+\frac{P^2+\Sigma^2\cdot\cot^2(\varphi)}{P^2-\Sigma^2\cdot\cot^2(\varphi)}\exp\Big[-ia\frac{2\pi}{\beta\lambda}P\cdot\sin(\varphi)\Big]$$
$$-\frac{\Sigma\cdot\cot(\varphi)\exp\Big[-i\frac{2\pi}{\beta\lambda}\Sigma\cdot a\cdot\cos(\varphi)\Big]}{P-\Sigma\cdot\cot(\varphi)}\Bigg|^2\times \tag{2}$$
$$\frac{\exp\Big[-\frac{4\pi}{\gamma\beta\lambda}(h+a\cdot\cos(\varphi))K\cos(\delta)\Big]}{1-\beta^2\cos^2(\theta-\delta)+\beta^2\sin^2(\delta)(1-\sin^2(\theta-\delta)\sin^2(\phi))+2\beta\sin(\delta)\sin(\theta-\delta)\cos(\phi)}$$
$$\times\left|\frac{\varepsilon(\lambda)}{\varepsilon(\lambda)\cos(\theta-\delta)+U}\right|^2|\cos(\delta)(\gamma^{-1}\sin(\theta-\delta)-iKU\cos(\phi))+$$
$$\sin(\delta)(iK\sin(\theta-\delta)+\gamma^{-1}U\cos(\phi))-\gamma\beta U\sin(\theta-\delta)\sin^2(\phi)|^2,$$

$$\frac{\mathrm{d}^2W_2}{\mathrm{d}\lambda\mathrm{d}\Omega} = \frac{\alpha\hbar c\beta^2\cos^2(\theta-\delta)}{2\pi^2\lambda^2K^2|P|^2}\left|\frac{\varepsilon(\lambda)-1}{\varepsilon(\lambda)}\right|^2\gamma^2\sin^2(\phi)\left|\frac{\sqrt{\varepsilon(\lambda)}}{\cos(\theta-\delta)+U}\right|^2(\sin^2(\theta-\delta)+|U|^2)$$
$$\times\Bigg|1-\exp\Big[-ia\frac{2\pi}{\beta\lambda}(P+\Sigma\cdot\cot(\varphi))\sin(\varphi)\Big]-\frac{P\exp\Big[i\frac{2\pi}{\beta\lambda}\Sigma\cdot a\cdot\cos(\varphi)\Big]}{P+\Sigma\cdot\cot(\varphi)}+$$
$$\frac{P^2+\Sigma^2\cdot\cot^2(\varphi)}{P^2-\Sigma^2\cdot\cot^2(\varphi)}\exp\Big[-ia\frac{2\pi}{\beta\lambda}P\cdot\sin(\varphi)\Big]-\frac{\Sigma\cdot\cot(\varphi)\exp\Big[-i\frac{2\pi}{\beta\lambda}\Sigma\cdot a\cdot\cos(\varphi)\Big]}{P-\Sigma\cdot\cot(\varphi)}\Bigg|^2\times \tag{3}$$
$$\frac{\exp\Big[-\frac{4\pi}{\gamma\beta\lambda}(h+a\cdot\cos(\varphi))K\cos(\delta)\Big]}{1-\beta^2\cos^2(\theta-\delta)+\beta^2\sin^2(\delta)(1-\sin^2(\theta-\delta)\sin^2(\phi))+2\beta\sin(\delta)\sin(\theta-\delta)\cos(\phi)}$$
$$\times[1-\beta^2\cos^2(\theta-\delta)+2\beta\gamma^{-2}\sin(\theta-\delta)\cos(\phi)-\gamma^{-2}\sin^2(\delta)(K^2-\gamma^{-2})],$$

$$U=\sqrt{\varepsilon(\lambda)-\sin^2(\theta-\delta)},$$
$$P=\cos(\delta)-\beta U+i\gamma^{-1}K\sin(\delta),$$
$$\Sigma=\sin(\delta)+\beta\sin(\theta-\delta)\cos(\phi)-i\gamma^{-1}K\cos(\delta), \tag{4}$$
$$K=\sqrt{1+(\gamma\beta\sin(\theta-\delta)\sin(\phi))^2},$$

An approximation made in Eqs. (2), (3), and (4) is that the prism is infinite in length in the plane orthogonal to the particle trajectory.

Another type of ChDR radiator is the Accumulator shown in Fig. 2. The benefit of the accumulator ChDR radiator is that the ChDR is accumulated along the length of the radiator. The ChDR is kept inside the target via total internal reflection until it reaches the reflective surface at the end where it is extracted [2,9]. Similar to a prismatic radiator the vertex angle, φ is selected to specify the ChDR extraction angle for an accumulator radiator.

DIAMOND LIGHT SOURCE BEAM TEST-STAND

Diamond Light Source is a 3rd generation synchrotron light source in the U.K. The Diamond accelerator chain consists of three accelerators; a linac, a booster synchrotron, and a storage ring. On the Booster to Storage-ring (BTS) transfer line is a beam test-stand available for testing accelerator components and novel diagnostic instrumentation. In recent years a ChDR experimental setup has been installed onto the Diamond beam test-stand in order to examine the properties of incoherent ChDR and its application as a Beam Position Monitor (BPM) pickup [9].

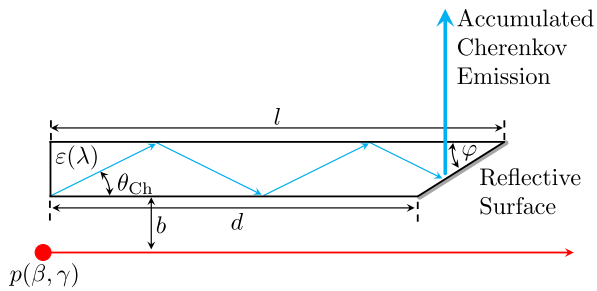

Figure 2: Accumulator Radiator Geometry.

The booster synchrotron can extract through the BTS in two modes, Multi-Bunch extraction or Single-Bunch extraction. Table 1 shows the nominal Single-Bunch extraction beam parameters of the BTS.

The BTS ChDR experiment is fitted with a CVD Diamond accumulator target with a length, of 15 mm and a vertex an-

Content from this work may be used under the terms of the CC BY 3.0 licence (© 2020). Any distribution of this work must maintain attribution to the author(s), title of the work, publisher, and DOI

ISBN: 978-3-95450-222-6 ISSN: 2673-5350 doi:10.18429/JACoW-IBIC2020-THPP05

Content from this work may be used under the terms of the CC BY 3.0 licence (© 2020). Any distribution of this work must maintain attribution to the author(s), title of the work, publisher, and DOI

Table 1: Single-Bunch Extraction Parameters on the Diamond BTS [10]

Standard BTS Parameter	Value
Beam Energy	3 GeV
Horizontal Beam Size σ_x	1.27 – 1.42 mm
Vertical Beam Size σ_y	0.57 – 0.6 mm
Extraction Rate	5 Hz
Max Bunch Charge (SBE)	0.2 nC
Bunch Length	$\simeq$ 2.5 mm

gle, of 12.5°. It is assumed that the angular distributions simulated from a prismatic radiator will have similar angular distributions to those measured from the accumulator radiator as long as the length, vertex angle, and properties of the medium are kept the same.

The ChDR emission is coupled out of the radiator through a viewport into an optical system. The optical system features a polariser and a filter wheel fitted with 0.4 and 0.55 µm bandpass filters [9].

SIMULATIONS

Single Particle Simulations

Multiple radiators can be configured in classical BPM configurations, where only a single intensity measurement is needed from each radiator. To obtain an intensity measurement from a ChDR radiator a detector would be placed at the ChDR emission angle of the radiator. The intensity read by the detector would then be proportional to the energy of the emitted radiation. The energy of emitted radiation, ΔW in the fixed angular and wavelength intervals, $\Delta\Omega$ and $\Delta\lambda$ can be simulated using

$$\Delta W = \int_{\Delta\Omega} \mathrm{d}\Omega, \int_{\Delta\lambda} \frac{\mathrm{d}^2 W}{\mathrm{d}\lambda \mathrm{d}\Omega} \mathrm{d}\lambda, \tag{5}$$

where $\mathrm{d}W$ is the energy emitted per unit of wavelength, $\mathrm{d}\lambda$, per unit of solid angle, $\mathrm{d}\Omega$ [7]. The solid angle component is given by

$$\mathrm{d}\Omega = \sin(\theta)\mathrm{d}\theta\mathrm{d}\phi, \tag{6}$$

where θ is the polar angle of the angular distribution, and ϕ the azimuthal. By producing a series of angular distributions with Eqs. (2), (3), and (4) then integrating each one, parameter dependencies of the emitted ChDR can be calculated.

Figure 3 shows the spectrum of ChDR emitted for a single 3 GeV electron from the ChDR radiator used on the BTS test-stand at Diamond for range of impact parameters.

The spectrum for the 1 and 100 µm impact parameters in Fig. 3 follow the Cherenkov dependence of $1/\lambda$. As the impact parameter is increased the ChDR intensity drops, across all wavelengths but dramatically more at shorter wavelengths resulting in a peak appearing when

$$b \simeq \frac{\gamma\lambda}{2\pi}, \tag{7}$$

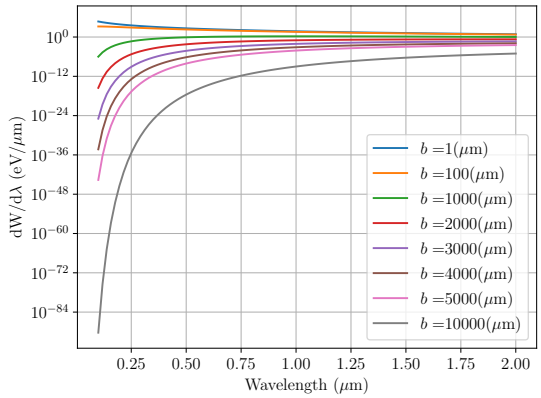

Figure 3: Single particle ChDR spectral emission at a range of impact parameters, b, from the ChDR radiator installed on the BTS test-stand.

as this is the edge of the pre-wave zone [11]. Figure 4 shows the impact parameter dependence for a single particle and the setup on BTS test-stand at fixed wavelengths. At impact parameters of < 500 µm the short wavelength of 0.4 µm dominates, beyond this limit the longer wavelength of 0.55 µm does. This effect continues for all wavelengths, for a ChDR BPM with a working impact parameter region of at least several millimetres an optical system in the infrared region would be better suited. Using the same theory a ChDR beam halo monitor would require an optical detection system sensitive to shorter wavelengths to dampen the signal from the core of the beam.

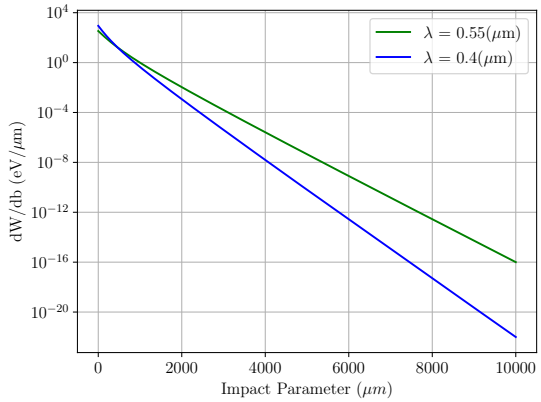

Figure 4: ChDR impact parameter dependence at fixed wavelengths from the ChDR radiator installed on the BTS test-stand from a single 3 GeV electron.

Beam Distribution Simulations

In order to simulate angular distributions for a beam profile the single particle angular distributions are calculated using Eqs. (2), (3) and (4) at each impact parameter then scaled by the bunch charge at that impact parameter. The

ISBN: 978-3-95450-222-6 ISSN: 2673-5350 doi:10.18429/JACoW-IBIC2020-THPP05

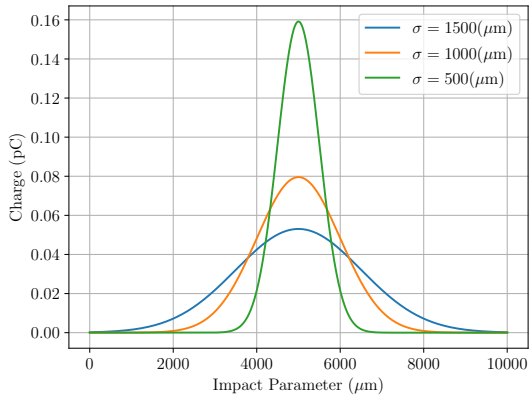

Figure 5: Horizontal transverse beam distributions centred at an impact parameter of 5 mm with a charge of ≃ 0.2 nC each.

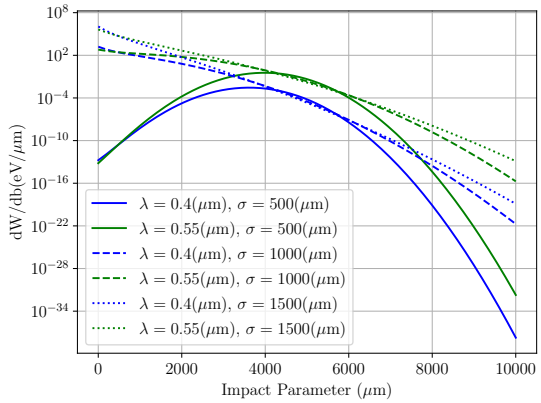

Figure 6: Signal contribution at each impact parameter emitted from the BTS ChDR radiator from the beam distributions in Fig. 5.

simulations in this paper only consider a horizontal beam profile due to the infinite length assumed in Eqs. (2), (3) and (4).

Initial testing on the BTS has shown that the horizontal beam size can be changed between ≃ 0.5 to 1.5 mm. Figure 5 shows three different horizontal beam profiles centred at an impact parameter of 5 mm each profile considers a bunch charge of 0.2 nC.

In order to verify the PCA model when extended to a multi-electron beam the predicted angular distributions and dependency scans must be compared to experimental data. Particles that directly collide with the radiator will generate Cherenkov radiation that will be measured by the optical system introducing noise into the measurements. The PCA model shows the spectral dependence of Cherenkov radiation and ChDR are different so long as the impact parameter is sufficiently large (see Fig. 3). To confirm the PCA model it is beneficial to work in a regime where the ChDR spectral response does not follow that of Cherenkov radiation.

By performing an element wise multiplication between transverse beam distributions and impact parameter dependencies shown in Fig. 5 and 4 respectively the intensity contribution at each impact parameter from the respective beam distribution is produced (see Fig. 6).

Figure 6 shows the horizontal beam size of 1000 and 1500 µm result in a signal that is dominated by the edge of the beam profile located at low impact parameters. This is of concern as particles at impact parameters close to the radiator produce a spectrum that appears as the Cherenkov spectrum (see Fig. 3).

Figure 7 shows the effect of horizontal beam size on ChDR emission intensity for a beam centred at an impact parameter of 5000 µm. The smaller the horizontal beam size the more the signal becomes dominated by the core of the beam resulting in an emission dominated by longer wavelengths. Conversely as the beam size gets larger the signal becomes

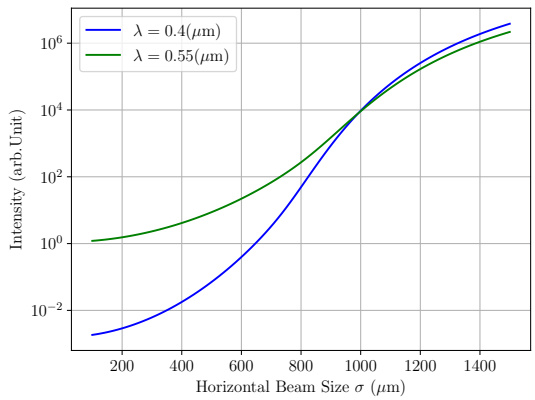

Figure 7: Effect of horizontal beam size from a beam at centred at an impact parameter of 5000 µm on ChDR intensity yield from the radiator on the BTS test-stand.

dominated by the edge of the distribution near the radiator favouring the signal from the shorter wavelengths.

CONCLUSION

This paper presents simulations of ChDR emission for the BTS test-stand at Diamond Light Source using the PCA model. It has been found that ChDR emission at longer wavelengths is most sensitive to the core of the beam, whereas shorter wavelengths are dominated by the particles in the beam tails. For BPM applications, an infrared system is most suitable whereas a beam halo monitor could be developed using the ChDR emission in the visible range.

Future steps for this research will compare the angular distributions measured from the optical system on the BTS test-stand with those simulated. Differences are expected between the simulations and measurements due to the different radiator geometries used in each. More in-depth and useful experiments would compare the spectral emission and impact parameter dependences.

Content from this work may be used under the terms of the CC BY 3.0 licence (© 2020). Any distribution of this work must maintain attribution to the author(s), title of the work, publisher, and DOI

ISBN: 978-3-95450-222-6 ISSN: 2673-5350 doi:10.18429/JACoW-IBIC2020-THPP05

Content from this work may be used under the terms of the CC BY 3.0 licence (© 2020). Any distribution of this work must maintain attribution to the author(s), title of the work, publisher, and DOI

REFERENCES

[1] R. Kieffer, *et al.* "Direct observation of incoherent Cherenkov diffraction radiation in the visible range", *Phys. Rev. Lett.*, vol. 121, p. 054802, Aug 2018. doi:10.1103/PhysRevLett.121.054802

[2] T. Lefèvre *et al.*, "Cherenkov Diffraction Radiation as a tool for beam diagnostics", in *Proc. IBIC'19*, Malmö, Sweden, Sep. 2019, pp. 660–664. doi:10.18429/JACoW-IBIC2019-THA001

[3] P.A. Cerenkov, "Visible radiation produced by electrons moving in a medium with velocities exceeding that of light", *Phys. Rev.*, vol. 52, pp. 378–379, Aug 1937. doi:10.1103/PhysRev.52.378

[4] I. Tamm, "Radiation emitted by uniformly moving electrons", *Journal of Physics (USSR)* vol. 1, pp. 439–454, 1937.

[5] M. V. Shevelev and A. S. Konkov, "Peculiarities of the generation of Vavilov-Cherenkov radiation induced by a charged particle moving past a dielectric target", *Journal of Experimental and Theoretical Physics*, vol. 118, no. 4, pp. 501–511, Apr. 2014. doi:10.1134/S1063776114030182

[6] D. V. Karlovets and A. P. Potylitsyn, "Universal description for different types of polarization radiation", Aug. 2009. arXiv:0908.2336

[7] A. S. Konkov, J. S. Markova, A. P. Potylitsyn, V. V. Bleko, V.V. Soboleva, and P. V. Karataev, "Theoretical model for incoherent Cherenkov diffraction radiation Report II", Tomsk Polytechnic University Internal Report, Apr. 2018.

[8] E. Hecht, "Optics, Global Edition", Pearson Education Limited, 2016, pp. 109, 170–173.

[9] D. M. Harryman *et al.*, "First Measurements of Cherenkov-Diffraction Radiation at Diamond Light Source", in *Proc. IBIC'19*, Malmö, Sweden, Sep. 2019, pp. 624–628. doi:10.18429/JACoW-IBIC2019-WEPP037

[10] L. Bobb, "Parameters for Experimental Proposals in Booster-to-Storage Ring (BTS) test-stand at Diamond Light Source", Diamond Light Source, May 2017, unpublished.

[11] P. V. Karataev, "Pre-wave zone effect in transition and diffraction radiation: Problems and solutions", *Physics Letters A*, vol. 345, no. 4, pp. 428–438, 2005. doi:10.1016/j.physleta.2005.07.027

ISBN: 978-3-95450-222-6 ISSN: 2673-5350 doi:10.18429/JACoW-IBIC2020-THPP08

DEVELOPMENT OF BEAM ABNORMAL STATE MONITORING PROCESSOR ON SSRF STORAGE RING*

L. W. Lai†, Y. B. Yan, Y. B. Leng
SSRF, Shanghai Advanced Research Institute, Chinese Academy of Sciences, Shanghai, China

Abstract

An abnormal beam state monitoring processor has been developed on SSRF, which is based on the hardware of self-developed digital BPM processor. By applying digital signal processing algorithms in the on-board FPGA, the processor keeps monitoring the beam running state. Once abnormal event is detected, the processor will record the abnormal event type and store the turn-by-turn beam position data before and after the event for later analyzing. The abnormal events including beam loss and beam position jump.

INTRODUCTION

SSRF starts operation since 2009, some unexplained beam loss events occurred on the storage ring during the operation. And the number is rising in this year. BPM data analyzing is one of the effective means to find the possible reason. Libera Electron and Brilliance are deployed on SSRF for BPM signal processing. Libera has a Post mortem input interface. “Post mortem input signal is linked typically with machine protection system. The input signal is usually connected with critical events, such as beam loss.There is a dedicated memory buffer reserved for post mortem data. After Postmortem trigger arrival, the history before the trigger arrival is stored in this buffer. User can access this buffer from the control system. Postmortem buffer contains turn-by-turn data [1]. However, This function relies on the input “Post mortem” signal from interlock system. Sometimes partial beam loss and orbit deviation may not trigger the interlock function, then Libera can’t buffer the BPM turn-by-turn data for analyzing.

An in-situ DBPM has been developed in SSRF. Based on the platform, a serial of processors been developed successfully for variety applications over the past few years, including stripline BPM, cavity BPM, BAM, booster BPM, storage ring BPM. The DBPM has been deployed in DCLS, SXFEL, SSRF and Sirus linac in a large scale [2, 3]. Table 1 lists the DBPM specifications and Figure 1 shows the DBPM hardware structure and picture. It consists of an ADC daughter board and a FPGA+ARM mother board.

Compared to the commercial products, DBPM is much more flexible to develop functions for special user applications on the FPGA and ARM. This paper will introduce the development and application of a beam state monitoring processor based on the DBPM. The processor buffers the BPM data when abnormal events are detected by itself. Abnormal events including user specified beam loss and beam orbit out of range.

Table 1: DBPM Specifications

Parameter	Value
Channels	4
Central Frequency	500MHz
Bandwidth	~20MHz
Dynamic range	31dB
ADC bits	16
Max ADC rate	125MSPS
FPGA	Xilinx xc5vsx50t
CPU	Arm
Clock	Ext./Int.
Trigger	Ext./Self/Period
Software	Arm-Linux/EPICS

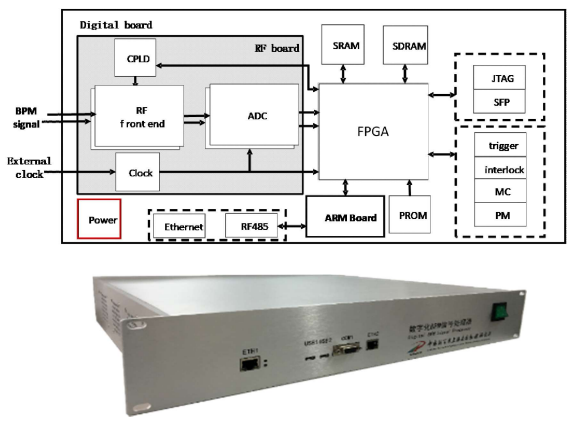

Figure 1: DBPM Processor.

PROCESSOR OVERVIEW

The DBPM in SSRF provides various rate beam position data, including turn-by-turn, 50kHz FA, 10kHz FA and SA. Figure 2 shows the function diagram of the processor.

The processed BPM turn-by-turn data, FA 50kHz data, FA 10kHz data are fed into the function. One of the data is switched by user as the abnormal event detection source, and also fed into a 16384 FIFO. External trigger signal is input to avoid injection events. Then the position data X,Y and sum data S are fed into two different processing channels. The X/Y data are compared to the user configured high limit and low limit respectively. The

*Work supported by Youth Innovation Promotion Association, CAS (Grant No. 2019290); The National Key Research and Development Program of China (Grant No. 2016YFA0401903).
† lailongwei@zjlab.org.cn

Content from this work may be used under the terms of the CC BY 3.0 licence (© 2020). Any distribution of this work must maintain attribution to the author(s), title of the work, publisher, and DOI

ISBN: 978-3-95450-222-6 ISSN: 2673-5350 doi:10.18429/JACoW-IBIC2020-THPP08

Content from this work may be used under the terms of the CC BY 3.0 licence (© 2020). Any distribution of this work must maintain attribution to the author(s), title of the work, publisher, and DOI

processor will generate interlock signal when orbit is over-range. The S data is used for the calculation of relative beam loss value. An interlock signal will also be generated when the relative beam loss value is greater than the user configured limit. Then the interlock type is recorded and the interlock signal is used as a write enable signal to buffer the X/Y data from FIFO for analyzing. The FIFO stores 16384 points beam position data before events detected. The data are stored on the processor and copied to local computer automatically.

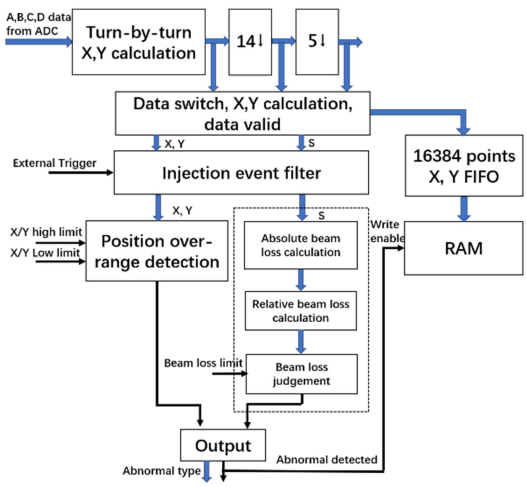

Figure 2: Function block diagram.

An EPICS IOC was developed based on the IOC of SSRF storage ring DBPM. An added EDM control panel in Figure 3 was designed to configure the function. Configuration parameters including the X/Y upper limit values, the X/Y lower limit values and the relative beam loss threshold value.

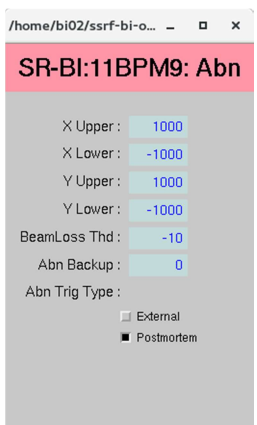

Figure 3: Function block diagram.

OPERATION ON SSRF

The processor was deployed on SSRF storage ring from April 10th, 2020 to May 3rd ,2020. Some abnormal events and were recorded during this time. The first 16384 points of the data is the X/Y orbit data before the detected trigger, the remaining is after the trigger. Turn-by-turn data is selected at this time.

Figure 4 is the data captured at April 10th 23:43, on which obvious orbit drift appeared at about 6000 turns, then the beam lost totally after about 10,000 turns. Checking with operation log, an orbit interlock event was recorded at that time. The buffered data reveals the possible reason of the beam loss is the magnet failure.

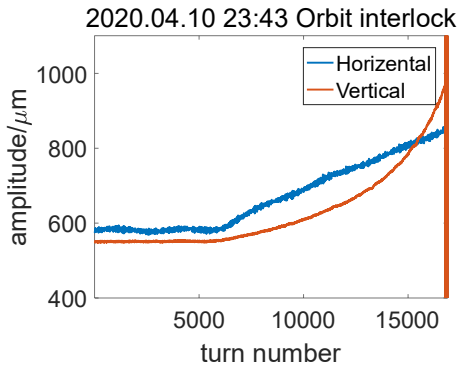

Figure 4: Data of orbit interlock event.

Figure 5 is the data captured at April 4th 23:23. The orbit seems quite normal before the beam lost. Operation log recorded a temperature alarm interlock at that time. It is likely that the temperature interlock system has failed.

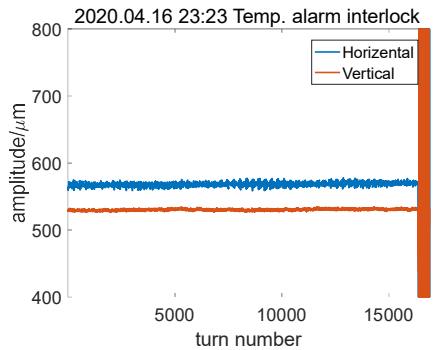

Figure 5: Data of temperature alarm interlock event.

Figure 6 is the data captured at April 22nd 11:35. There was no beam lost, but periodic orbit oscillation can be seen. Checking with the operation log, bunch defocusing was recorded at that time. The beam behavior is consistent with the data.

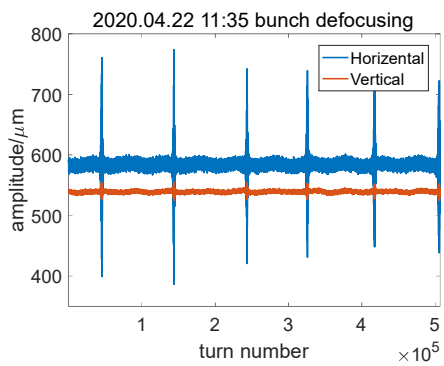

Figure 6: Orbit interlock.

ISBN: 978-3-95450-222-6 ISSN: 2673-5350 doi:10.18429/JACoW-IBIC2020-THPP08

SUMMARY

The in-situ developed DBPM is a ideal platform to develop extended applications because of the high-speed real-time signal processing chip FPGA and the embedded controller Arm. This paper introduced the design and application of a beam abnormal state monitoring processor based on the DBPM. Some abnormal events have been recorded during SSRF operation. It could be a helpful instrument for the analyzing of unknown failure in SSRF and improve the operation efficiency.

REFERENCES

[1] Libera Brilliance Specification. http://www.i-tech.si

[2] L. W. Lai et al., "The Development and Applications of the Digital BPM Signal Processor at SINAP", in Proc. 60th ICFA Advanced Beam Dynamics Workshop on Future Light Sources (FLS'18), Shanghai, China, Mar. 2018, pp. 43-45. doi:10.18429/JACoW-FLS2018-TUP1WD03

[3] L.W. Lai, Y.B. Leng, Y.B. Yan, et,al. "The Development and Applications of the Digital BPM Signal Processor at SINAP", in Proc. 60th ICFA Advanced Beam Dynamics Workshop on Future Light Sources(FLS2018), Shanghai, China, March 2018, pp.43-45. doi:10.18429/JACoW-FLS2018-TUP1WD03

Content from this work may be used under the terms of the CC BY 3.0 licence (© 2020). Any distribution of this work must maintain attribution to the author(s), title of the work, publisher, and DOI

ISBN: 978-3-95450-222-6 ISSN: 2673-5350 doi:10.18429/JACoW-IBIC2020-THPP10

INFLUENCE OF A BELLOW TO A CAVITY BPM FOR SINBAD

D. Lipka*, DESY, Hamburg, Germany

Abstract

A cavity beam position monitor acts for the detection of the beam location within a pipe with high precision and best resolution. Some of them are used as a fixed point to refer the other parts of the beamline. To be able to fix the monitor against the other vacuum components bellows need to be adapted next to the monitor to relax the other part of the vacuum chamber. The bellow itself can create a resonance which would influence the resonator of the cavity beam position monitor. In this study the influence of the bellow to a cavity beam position monitor is investigated with simulations for a SINBAD project. The result is that the influence to the dipole resonator is below 0.1 %.

INTRODUCTION

SINBAD is a dedicated accelerator R&D facility currently under commissioning at DESY, Hamburg, and will host the ARES linac (Accelerator Research Experiment at SINBAD). It consists of a normal conducting photo-injector and a 100 MeV S-band linear accelerator with beam repetition rates between 10 and 50 Hz for the production of low charge beams (0.5–30 pC) with (sub-) fs duration and excellent arrival time stability [1–4]. For dedicated user experiments bunch charges up to 1000 pC are foreseen. At a bunch compressor a tube diameter of 40.5 mm is requested with high demand on the monitoring of the beam position. Therefore a cavity beam position monitor (CBPM) with best resolution is foreseen as the monitor, the design of the European XFEL will be used [5]. Bellows will be installed before and after the CBPM to relax the vacuum chamber. Such a bellow consists of blades which have a larger diameter of the vacuum tube and will create resonances which could influence the signalof the CBPM. Therefore the influence has to be investigated and if necessary be minimized.

SETUP

Bunch compressors are essential for the generation of short bunches with applications in e.g. colliders, free electron lasers and advanced accelerator concepts. The up-and-coming ARES accelerator located at SINBAD, DESY will support the formation of 100 MeV, pC, sub-fs electron bunches for Laser Wake Field Acceleration research and development [6]. The bunch compressor consists of four dipoles and two collimators. To monitor the beam properties a screen station and a CBPM will be installed. Since the compressor needs to be variable in the beam deflection a relative large beam pipe is requested. One version of the CBPMs of the European XFEL has a beam tube diameter of 40.5 mm which will be used for this bunch compressor at SINBAD too [5].

* Dirk.Lipka@desy.de

The CBPM consists of a reference and dipole resonator and is adapted from a design of SACLA [7]. The working resonance frequency of the monopole mode of the reference resonator and the dipole mode of the dipole resonator are tuned to the same value of 3.3 GHz. The first resonator is necessary to measure the amplitude from the monopole mode as a function of charge to normalize the signal from the second resonator and define the beam direction. The second resonator provides a signal generated by the dipole mode proportional to the beam offset; for this the dominant monopole mode of the dipole resonator needs to be reduced. This is done by waveguides or slots [8]. The setup is shown in Fig. 1. Here only the dipole resonator on the left side

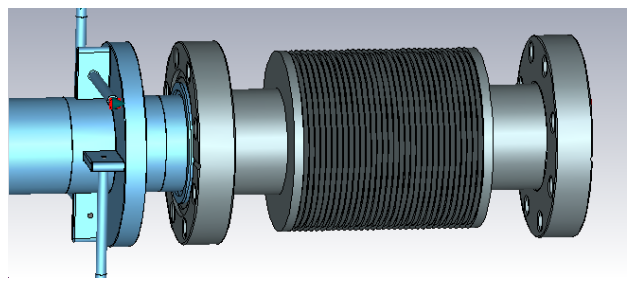

Figure 1: 3-dimensional simulation view of the vacuum part of the dipole resonator on the left in blue with the bellow on the right.

is shown and simulated with the simulation tool CST [9] because the reference resonator provides much higher amplitudes such that an influence from the bellow can be ignored. In Fig. 1 can be seen the dipole resonator vacuum view with slots and feedthroughs for the horizontal and vertical plane; a reversed reality view. The bellow is shown in normal view such that one can see the flanges and blades. Each blade forms a resonator which can induce resonances near the CBPM working frequency due to similar diameters and their amplitude can be enhanced because of the repetitive design. The field of the bellow resonances can be transmitted to the dipole resonator due to the relative large beam tube diameter but will be attenuated due to the distance between resonator and first blade of 73.7 mm.

SIMULATION OF THE INFLUENCE OF THE BELLOW

The tool CST provides beam simulations including wakefield generation which is capable to monitor the fields along the beamline. Resonances due to the beam propagation will be induced into the setup and can be visualized. Here voltage monitors are defined at the end of the feedthroughs from the slots to measure the responds of the beam at the exit of the CBPM. The simulation time of the beam propagation is defined until 18 ns which corresponds to the processing

Content from this work may be used under the terms of the CC BY 3.0 licence (© 2020). Any distribution of this work must maintain attribution to the author(s), title of the work, publisher, and DOI

ISBN: 978-3-95450-222-6 ISSN: 2673-5350 doi:10.18429/JACoW-IBIC2020-THPP10

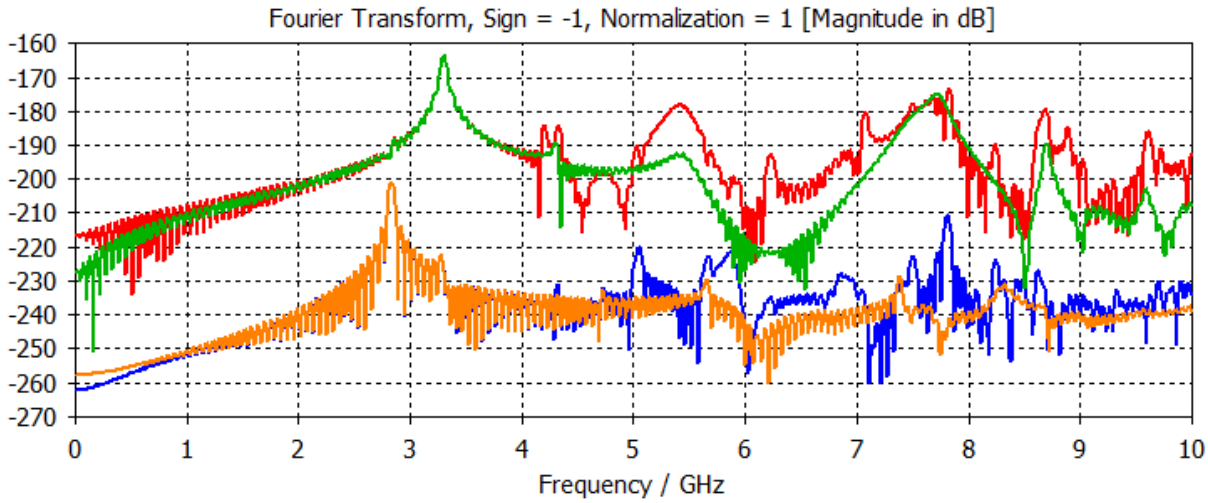

Figure 2: Signal spectrum measured at the exit of the CBPM dipole resonator with (red) and without (green) bellow at 1 mm beam offset. Similar spectrum is shown for the vertical plane without offset with (blue) and without (brown) bellow.

time of the used electronics: within this time window the peak of the down-converted signal in frequency domain will be measured in reality. The voltage monitors provides the voltages as a function of time and include all resonances in time domain which would enter the beginning of the cables, this will be visualized in frequency domain by a Fourier transformation. Settings of the simulations are: 1 nC beam charge, horizontal offset of 1 mm (to generate dipole and quadrupole modes) and centered in vertical direction; the wakefield solver is used with hexahedral mesh. A high number of mesh cells are used to reach a low resolution of the simulation results.

In Fig. 2 the Fourier transformed signals on the horizontal and vertical CBPM exits with and without bellow are shown. The green line provides the signal without bellow and 1 mm offset; this one shows the dominant dipole resonance at 3.3 GHz. Similar amplitude for the case with bellow is shown with the red line. At lower frequencies the uncertainty of the case with bellow is larger due to the larger amplitude variations but is still within the trend. At 2.8 GHz a small resonance is visible for the horizontal plane; this corresponds to the transmission of the monopole mode of the dipole resonator which is already negligible compared to the dipole mode and is reduced by the slot. This is a prove that the slots reduce the monopole mode, compare with [8].

For the horizontal case the red line with bellow shows higher amplitudes for several higher frequencies, for example 4.2 GHz, 4.3 GHz, 5.4 GHz, 6.2 GHz and so on. These resonances are generated in the bellow and transmitted until the feedthrough exit of the dipole resonator. Other frequencies can be generated too but will not be monitored due to the position of the voltage monitor. But these other not visible resonances are of no concern since they will not be transmitted to the electronics.

The voltage amplitudes in the vertical plane are shown in Fig. 2 too: with (blue) and without (brown) bellow. At the dipole resonance frequency of 3.3 GHz the vertical plane shows a reduction of the amplitude by lower than -60 dB which corresponds to the orthogonal de-coupling of the resonator [10]. The resonance of 2.8 GHz is the monopole mode of the dipole resonator, the amplitude is below the case with offset. For higher frequencies additional resonances compared with the horizontal plane are visible which are generated and transmitted to the vertical feedthrough at 5 GHz, 5.7 GHz, 5.9 GHz and so on.

Important for the influence of the signals are the amplitude change due to the bellow with offset. In this case the horizontal plane is used because in the vertical plane with centered beam shows no amplitude at the working frequency. The amplitudes are compared at the dipole resonance of 3.3 GHz with and without bellow within the bandwidth of the electronics of about 50 MHz. In this case the amplitude in frequency domain increases by 0.06 % with bellow which is negligible small. Therefore this influence for the CBPM signal processing can be ignored.

Higher order modes are visible and transmitted to the exit of the CBPM into the cables. These indicate that modes are generated and transmitted, other not transmitted modes which are not visible from these voltage monitor positions can be generated too but are of no importance for the CBPM functionality. Therefore this method is useful to prove the influence of the bellow to the CBPM. But higher modes are existing and could transmit to other components and their influence have to be proven as well.

SUMMARY

A CBPM will be installed in the bunch compressor of SINBAD. To relax the mechanics of the vacuum tube bellows will be attached on each side. The influence of additional induced fields due to the beam in the system CBPM and bellow are simulated and found to be negligible because at the working frequency of the electronics the change of amplitude is small. Higher order modes are visible too but

Content from this work may be used under the terms of the CC BY 3.0 licence (© 2020). Any distribution of this work must maintain attribution to the author(s), title of the work, publisher, and DOI

ISBN: 978-3-95450-222-6 ISSN: 2673-5350 doi:10.18429/JACoW-IBIC2020-THPP10

Content from this work may be used under the terms of the CC BY 3.0 licence (© 2020). Any distribution of this work must maintain attribution to the author(s), title of the work, publisher, and DOI

are outside of the working frequency of the used electronics. This is proven with beam simulations without monitoring all resonances separately by using the wakefield solver. This provides a general method to prove the influence.

REFERENCES

[1] U. Dorda *et al.*, "Status and Objectives of the Dedicated Accelerator R&D Facility (SINBAD) at DESY", in *Proc. 3rd European Advanced Accelerator Concepts Workshop (EAAC'17)*, Elba, Italy, Sept. 2017. arXiv:1801.02825.

[2] U. Dorda *et al.*, "The Dedicated Accelerator R&D Facility Sinbad at DESY", in *Proc. 8th Int. Particle Accelerator Conf. (IPAC'17)*, Copenhagen, Denmark, May 2017, pp. 869–872, doi:10.18429/JACOW-IPAC2017-MOPVA012.

[3] B. Marchetti *et al.*, "Status update of the Sinbad-Ares linac under construction at DESY", in *Proc. 8th Int. Particle Accelerator Conf. (IPAC'17)*, Copenhagen, Denmark, May 2017, pp. 1412–1414, doi:10.18429/JACOW-IPAC2017-TUPAB040.

[4] E. Panofski *et al.*, "Status Report of the SINBAD-ARES RF Photoinjector and LINAC Commissioning", in *Proc. 10th Int. Particle Accelerator Conf. (IPAC'19)*, Melbourne, Australia, May 2019, pp. 906–909. doi:10.18429/JACoW-IPAC2019-MOPTS026

[5] D. Lipka, D. Nölle, M. Siemens and S. Vilcins, "Development of Cavity BPM for the European XFEL", in *Proc. 25th Linear Accelerator Conf. (LINAC'10)*, Tsukuba, Japan, Sep. 2010, paper TUP094, pp. 629–631.

[6] F. Lemery *et al.*, "Overview of the ARES Bunch Compressor at SINBAD", in *Proc. 10th Int. Particle Accelerator Conf. (IPAC'19)*, Melbourne, Australia, May 2019, pp. 902–905. doi:10.18429/JACoW-IPAC2019-MOPTS025

[7] H. Maesaka *et al.*, "Development of the RF Cavity BPM of XFEL/SPring-8", in *Proc. 9th European Workshop on Beam Diagnostics and Instrumentation for Particle Accelerators (DIPAC'09)*, Basel, Switzerland, May 2009, paper MOPD07, pp. 56–58.

[8] Balakin, Vladimir; Bazhan, Anatoli; Lunev, Pavel; Solyak, Nikolay; Vogel, Vladimir; Zhogelev, Pavel; Lisitsyn, A.; Yakimenko, Vitaly, "Experimental Results from a Microwave Cavity Beam Position Monitor", in *Proc. 18th Particle Accelerator Conf. (PAC'99)*, New York, NY, USA, Mar. 1999, paper THAR2, pp. 461–463.

[9] Computer Simuation Technology, http://www.cst.com.

[10] D. Lipka *et al.*, "Orthogonal Coupling in Cavity BPM with Slots", in *Proc. 9th European Workshop on Beam Diagnostics and Instrumentation for Particle Accelerators (DIPAC'09)*, Basel, Switzerland, May 2009, paper MOPD02, pp. 44–46.

ISBN: 978-3-95450-222-6 ISSN: 2673-5350 doi:10.18429/JACoW-IBIC2020-THPP11

STUDY OF MULTI-BLADED PHOTON BPM DESIGNS

Y.-R. E. Tan*, AS - ANSTO, Clayton, Australia

Abstract

New beamlines will be installed in at the AS in the next few years and photon BPMs will be part of the front end design. A theoretical study of the potential benefits of a multi-bladed photon BPM design has been simulated using beam profiles from SPECTRA. The results show that it is possible to remove the gap/field dependence of the photon BPM by a least squares fit of the distribution, in this test case a Gaussian distribution, to the beam profile sampled by the multiple blades.

INTRODUCTION

The majority of photon BPMs (XBPMs) that are located in the front-end of beamlines at light sources use metallic blades as the detector. As synchrotron radiation illuminate the surface of the metallic blades, photo-electrons are ejected (PE effect) and the current is proportional to the photon flux and energy. The drain current at the blade is measured using a picoammeter or equivalent. The strength of such a design is its fairly straight forward design, ability to reach µm resolutions and robustness. The most typical configuration is a pair of blades on either side of the photon beam to measure the vertical displacement. This is typical for dipole and wiggler sources. If transverse directions are required then four blades are used, either arranged in the cardinal directions or rotated by 45°. This is commonly used for undulator sources. There are two well known issues, upstream contamination from other radiation sources and a gain (calibration factor) that depends on the photon distribution, which in turn depends on the insertion device parameter, K_u. This is particularly problematic for APPLEII type insertion devices that have many more degrees of freedom and potential photon distributions. To overcome some of the deficiencies issue other approaches to photon beam detection is being developed such as photoconduction based designs using diamond or SiC based detectors [1], fluorescence based [2] or residual gas [3].

The first issue of upstream photon contamination is difficult to address and is only an issue if the photon flux from the ID at the blade is comparable to the flux from other sources (blades are too far away or K < 1) [4]. This report investigates the potential benefits of fitting a Gaussian distribution to the photon distribution sampled at four or more locations. This approach is investigated numerically and compared to traditional methods to show that it has the potential to be more robust against changes to K_u.

* eugene.tan@ansto.gov.au

PHOTON DISTRIBUTION AND BLADE CONFIGURATION

The source radiation will be modelled on a 22 mm period IVU with a K_u between 1.03 and 1.85. Some design parameters include an assumed beamline acceptance of 1.11 mrad by 0.40 mrad and XBPM's located 6.9 m from the source. Assuming the extent of the blade is located at +0.3 mrad and maximum beam offsets of ± 1 mm, the minimum observation angle of the blade is approximately 0.2 mrad. In Fig. 1 the energy spectrum at two extreme K_u values has been calculated using SPECTRA [5] showing that above 3 keV the flux peaks have decreased by an order of magnitude. For this study we have limited simulation to an integration of photon distributions calculated at 100 intervals between 100 eV and 3.5 keV. A plot of such a distribution is shown in Fig. 2 for $K_u = 1.03$ along with the blade configuration. A simple blade geometry has been adopted, with a set of 2 mm long vertical blades with a range of horizontal gaps between the blades, $S_x = [0.5, 1.0, 1.5, 2.0, 2.5]$ (mm).

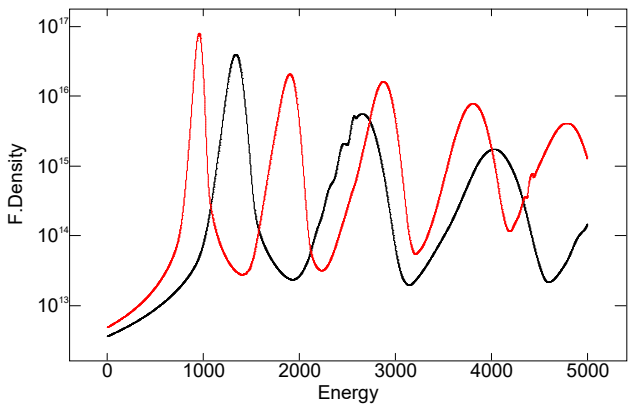

Figure 1: Flux density at an observation angle $\theta_y = 0.2$ mrad for a $K_u = 1.03$ (black) and 1.85 (red).

CENTROID CALCULATIONS

Four methods will be evaluated. The first two are the difference over sum (DS) method given by

$$x^{DS} = K_x^{DS} \frac{[(b_4 + b_9) - (b_2 + b_7)]}{b_2 + b_4 + b_7 + b_9}$$

$$y^{DS} = K_y^{DS} \frac{[(b_2 + b_4) - (b_9 + b_7)]}{b_2 + b_4 + b_7 + b_9}$$

the center of mass (CM) method,

$$x^{CM} = K_x^{CM} \frac{\Sigma_{n=1}^{5} w_n b_n}{\Sigma_{n=1}^{5} b_n}$$

$$y^{CM} = K_y^{CM} \frac{\Sigma_{n=12,9,4,11} w_n b_n}{\Sigma_{n=12,9,4,11} b_n}$$

Content from this work may be used under the terms of the CC BY 3.0 licence (© 2020). Any distribution of this work must maintain attribution to the author(s), title of the work, publisher, and DOI

ISBN: 978-3-95450-222-6 ISSN: 2673-5350 doi:10.18429/JACoW-IBIC2020-THPP11

Content from this work may be used under the terms of the CC BY 3.0 licence (© 2020). Any distribution of this work must maintain attribution to the author(s), title of the work, publisher, and DOI

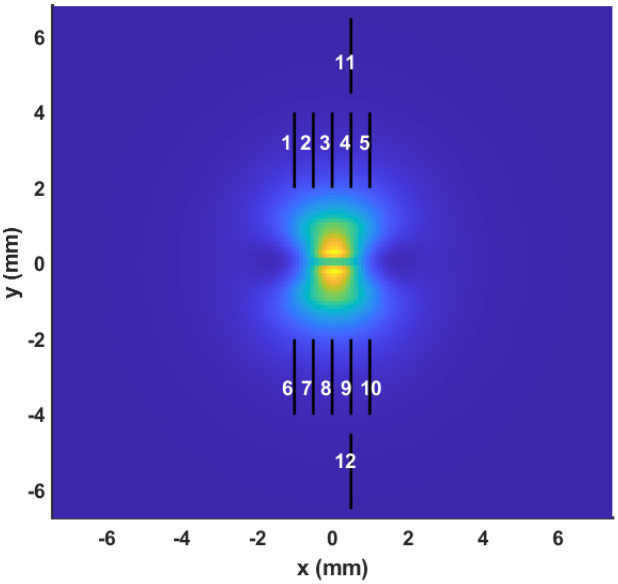

Figure 2: Photon distribution for $K_u = 1.03$. In this plot the vertical blade arrangement has a horizontal gap between the blades of $S_x = 0.5$ mm. In the simulations, five different configuration of $S_x = [0.5, 1.0, 1.5, 2.0, 2.5]$ will be compared. Blades, b_3 and b_8 remain in the same location while all the others are shifted.

where $K_{x,y}$ are the scaling/calibration factors and b_n are signals from the individual blades shown in Fig. 2. The final two are Gaussian fitting algorithms: Caruana's algorithm and Guo's improved iterative version found in Reference [6]. Guo's algorithm improves on Caruana's by applying a weighted least squares technique, making it more immune to the effects of noise in the data.

SIMULATION

The photon distribution is shifted horizontally and vertically over a range of ±1 mm and the signals from the blade is the integration of the photon flux along the length of the blade[1]. The peak of the photon distribution is normalised to unity and noise with a sigma of 0.005 was introduced to each of the blades to test the response of the methods in the presence of noise. For each offset, 100 data sets with noise was generated. The values of $K_{x,y}$ is given by the gradient a line over the small range $x/y = [-0.2\text{ mm}, +0.2\text{ mm}]$.

K_u Dependence

With the effective values of $K_{x,y}$ for the different blade separations and undulator parameters, it is possible to get a sense of how the four methods compare. Figure 3 shows just one example of the relative change in the gain, $\delta K_{x,y}$, as a function of K_u for $S_x = 1$ mm. In this particular configuration the Gaussian methods are decidedly less affected

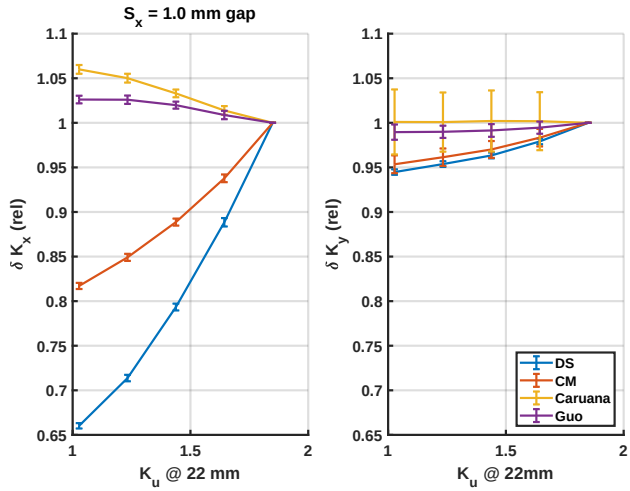

Figure 3: Relative change in $K_{x,y}$ as a function of K_u

Table 1: Table of $G_{x,y} = \Delta\delta K_{x,y}/\Delta K_u$. The Group of Values at the Top Represent G_x and the Bottom Group G_y. The Coloured Boxes Represent the Configurations Where the Noise in the Position Resolution is Less Than 15 µm as Shown in Table 2

S_x	DS	CM	Caruana	Guo
0.5 mm	0.469	0.408	0.001	-0.003
1.0 mm	0.416	0.221	-0.076	-0.034
1.5 mm	0.320	0.086	-0.108	-0.002
2.0 mm	0.222	0.017	-0.075	-0.148
2.5 mm	0.140	-0.068	-0.056	-0.238
3.0 mm	0.055			
4.0 mm	-0.001			
5.0 mm	-0.009			
0.5mm	0.127	0.104	0.000	0.029
1.0mm	0.066	0.056	0.001	0.011
1.5mm	-0.024	-0.010	-0.002	-0.016
2.0mm	-0.105	-0.066	-0.001	-0.038
2.5mm	-0.159	-0.098	0.005	-0.045
3.0mm	-0.177			
4.0mm	-0.151			
5.0mm	-0.099			

by the change in K_u. To see how this changes for different values of S_x, the gradient of the the relative change given by $G_{x,y} = \Delta\delta K_{x,y}/\Delta K_u$ has been calculated and tabulated in Table 1.

In the case of DS, for a given vertical gap (required stay clear for the beam line acceptance) and this particular geometry, it is not possible to simultaneously minimise G_x ($S_x = 4.0$ mm) and G_y ($S_x = 1.4$ mm). The same is true for the CM method and shows very similar trends to the DS method. This is to be expected as both methods perform linear extrapolation and would only be accurate if the photon distribution resembled a triangle, or where the gradients,

[1] The photoemission properties of the material of the blade are not considered as this study is a comparison of algorithms

ISBN: 978-3-95450-222-6 ISSN: 2673-5350 doi:10.18429/JACoW-IBIC2020-THPP11

Table 2: Minimum and Maximum Linearity Range (in mm) and the Minimum and Maximum Position Resolution, $\sigma_{x,y}$ (in µm), for the Range of $K_u = [1.03, 1.85]$. The Highlighted Boxes Indicate Where $\sigma_{x,y} < 15$ µm

S_x	DS (mm / µm)	CM (mm / µm)	Caruana (mm / µm)	Guo (mm / µm)
0.5mm	0.63-0.80 / 12.6-19.3	0.53-0.80 / 09.1-13.2	0.50-0.80 / 15.6-21.7	0.51-0.80 / 15.0-21.5
1.0mm	0.47-0.61 / 07.5-10.5	0.60-0.67 / 08.7-09.5	0.48-0.59 / 09.9-10.7	0.61-0.74 / 08.4-10.1
1.5mm	0.46-0.52 / 07.3-08.5	0.76-0.80 / 11.3-12.1	0.57-0.62 / 13.0-15.6	0.80-0.80 / 09.1-09.8
2.0mm	0.48-0.50 / 08.5-08.7	0.80-0.80 / 15.5-17.8	0.70-0.78 / 22.8-29.6	0.50-0.80 / 11.0-11.6
2.5mm	0.49-0.51 / 09.9-11.5	0.80-0.80 / 21.6-26.2	0.80-0.80 / 41.9-55.2	0.55-0.60 / 13.3-15.5
3.0mm	0.51-0.57 / 12.6-16.2			
4.0mm	0.66-0.72 / 23.6-33.0			
5.0mm	0.79-0.80 / 45.8-63.1			
0.5mm	0.41-0.42 / 05.8-06.2	0.46-0.48 / 16.2-17.7	0.80-0.80 / 56.4-74.4	0.39-0.40 / 11.4-13.8
1.0mm	0.42-0.44 / 06.6-08.1	0.48-0.51 / 18.4-22.9	0.80-0.80 / 60.3-82.7	0.40-0.41 / 12.7-16.3
1.5mm	0.44-0.48 / 08.5-12.4	0.53-0.60 / 23.1-33.4	0.80-0.80 / 67.9-99.2	0.41-0.44 / 15.2-22.0
2.0mm	0.50-0.55 / 12.1-20.0	0.60-0.72 / 31.8-51.5	0.80-0.80 / 81.7-123	0.44-0.49 / 20.2-32.4
2.5mm	0.50-0.65 / 18.2-33.1	0.70-0.80 / 46.4-78.4	0.80-0.80 / 102-156	0.48-0.60 / 28.5-49.7
3.0mm	0.63-0.80 / 29.3-55.2			
4.0mm	0.80-0.80 / 74.6-140			
5.0mm	0.80-0.80 / 179-317			

$\Delta b_n / \Delta x$, are similar at the blades and the distribution is symmetric.

As the photon distribution is closer to a Gaussian distribution, using fitting algorithms to extract the sigma, amplitude and offset should be more robust. This is reflected in the results where both Gaussian methods have the smallest values of $G_{x,y}$. The smallest values are achieved when the distribution is sufficiently sampled with closely spaced blades. $G_{x,y}$ increases with increasing values of S_x.

Linearity and Resolution

In addition to minimising the dependence on K_u it is also important to determine the extent of the linear region and the position resolution for a given amount of noise introduced into the system [2]. The linearity range is given as the horizontal or vertical region where the residual error is less than the position resolution. An example of such an analysis of the linearity and resolution is show in Fig. 4 and results of the four methods has been tabulated in Table 2.

In terms of position resolution, the DS method is the best followed by Guo's algorithm. It was surprising to see how sensitive to noise Caruana's algorithm turns out to be. Guo's algorithm was far more robust and showed similar linearity and slightly worse resolution compared to the DS method.

Taking both tables into consideration the CM and Caruana methods would be discarded in favour of the DS and Guo's methods. One issue with the DS method is that to get good linearity and small values for $G_{x,y}$ the blades have to be far apart. This results in smaller signals and therefore poorer position resolution overall. Guo's method on the other hand performs better with blades closer to the centroid, larger

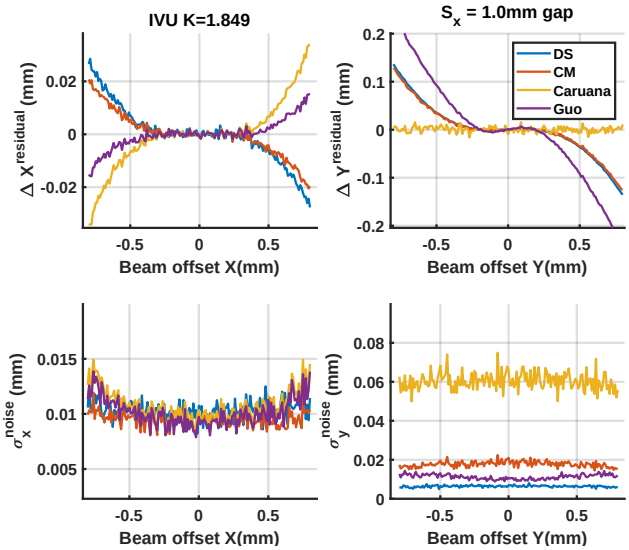

Figure 4: Plot of the residual error (top row) and the spread of the position calculations due to noise on the blades, position resolution (bottom row).

signals and good position resolution overall. In the two cases, optimised configuration and parameters would be:

- DS method: S_x = 1.4 mm, G_x = +0.30, G_y = -0.01, $\sigma_{x,y} \approx 10$ µm, Linear range > ±0.44 mm
- Guo's method: S_x = 1.0 mm, G_x = -0.03, G_y = +0.01, $\sigma_{x,y} \approx 16$ µm, Linear range > ±0.40 mm

This shows that using more blades and a Gaussian fitting algorithm can be a viable option that minimise both G_x and G_y the dependence on K_u. What has not been considered here are mechanical considerations such as shadowing of

[2] The resolution calculation is used here as a measure of robustness of the four methods to noise

Content from this work may be used under the terms of the CC BY 3.0 licence (© 2020). Any distribution of this work must maintain attribution to the author(s), title of the work, publisher, and DOI

ISBN: 978-3-95450-222-6 ISSN: 2673-5350 doi:10.18429/JACoW-IBIC2020-THPP11

Content from this work may be used under the terms of the CC BY 3.0 licence (© 2020). Any distribution of this work must maintain attribution to the author(s), title of the work, publisher, and DOI

up and downstream XBPMs, material response and thermal considerations (larger signals → higher heat-loads).

CONCLUSION

When using multiple blades and a Gaussian distribution as an approximation of the photon distribution, it is possible to improve XBPMs robustness to changes in K_u while maintaining linearity and resolution. An extension of this would be to adapt Guo's algorithm to fit a 2D Gaussian function and potentially requiring fewer number of blades.

REFERENCES

[1] S. Nida *et al*, "Silicon carbide X-ray beam position monitors for synchrotron applications", *J. Synchrotron Rad.*, vol. 26, pp. 28–35, 2019. doi:10.1107/S1600577518014248

[2] B. X. Yang *et al.*, "Design and Development for the Next Generation X-ray Beam Position Monitor System at the APS", in *Proc. IPAC'15*, Richmond, VA, USA, May 2015, pp. 1175–1177. doi:10.18429/JACoW-IPAC2015-MOPWI014

[3] P. Ilinski, U. Hahn, H. Schulte-Schrepping, and M. Degenhardt, "Residual Gas X-ray Beam Position Monitor Development for PETRA III", *AIP Conference Proceedings*, vol. 879, pp. 782–785, 2007. 10.1063/1.2436177

[4] G. Decker and O. Singh, "Method for reducing x-ray background signals from insertion device x-ray beam position monitors", *Phys. Rev. ST Accel. Beams*, vol. 2, p. 112801, 1999. doi:10.1103/PhysRevSTAB.2.112801

[5] T. Tanaka and H. Kitamura, "SPECTRA: a synchrotron radiation calculation code", *J. Synchrotron Rad.*, vol. 8, pp. 1221–1228, 2001. doi:10.1107/S090904950101425X

[6] H. Guo, "A Simple Algorithm for Fitting a Gaussian Function [DSP Tips and Tricks]", *IEEE Signal Processing Magazine*, vol. 28, pp. 134–137, 2011, doi:10.1109/MSP.2011.941846

ISBN: 978-3-95450-222-6 ISSN: 2673-5350 doi:10.18429/JACoW-IBIC2020-THPP12

CHARACTERIZATION STUDY OF A BUTTON BPM WITH AN APPROACH TO AUTOMATED MEASUREMENTS

Yogesh Verma*, Indian Institute of Science Education and Research (IISER), Mohali, Punjab, India
Madhuri Aggarwal, Vipul Joshi, Ashish Sharma
Inter University Accelerator Centre (IUAC), New Delhi, India

Abstract

Beam position monitors (BPMs) are one of the very important diagnostic components of any accelerator system giving information about beam position. It is a class of non-intercepting devices which use the coupling of the EM field around a charged particle bunch to some sort of conductor electrodes to recover beam position information from the beam-induced signals. In this paper, a characterization study of an in-house developed Button BPM including sensitivity measurement and transfer impedance studies is presented. Sensitivity measurement was done using the stretched wire method by passing current pulses through the wire of different diameters like 0.5 mm and 1 mm, thus mimicking the behavior of the actual beam. Sensitivity information was then used to reciprocate the 2-D position map of the device. Owning to the time taken for such huge measurements, an automated BPM test bench approach of the whole setup is developed by remote interfacing over LAN. A substantial decrease in measurement time was observed along with a reduction in measurement error.

INTRODUCTION

In particle accelerators, a beam position monitor (BPM) provides crucial information about the beam. A typical button BPM consists of four button-type electrodes mounted inside the surface of cylindrical pipe in vacuum. The main idea is to measure the charges induced by the time varying electric field of the beam particles on an insulated metal plate [1]. By measuring the electrode signal of various electrodes,the relative gains of the electrodes can be calculated. Studies have been performed in calculating the optimal dimension of BPM for maximum gain [2]. Button BPM have been used extensively and deployed at various accelerator systems [3, 4] ranging from ring systems [5] to developing test bench for proton LINAC [6] and with an approach to automation [7].

This paper presents a characterization study of a button BPM with transfer impedance studies and position sensitivity measurements with a development of an automated BPM test bench. Stretched wire method [8] with wire of different diameters 0.5 mm and 1 mm is implemented for sensitivity and mapping measurements to mimic the actual beam. Automated test bench for BPM have been considered an alternative to manual measurements (position mapping, sensitivity etc.) due to consumption of huge amount of time resource. In comparison to a Libera DAQ based automated test bench [7], the approach presented in this paper is cost effective due to usage of generally available lab equipment's. A comparison of manual measurements vs automated measurements is also been performed to evaluate the performance of automated measurements.

The paper is divided in various sections, first section provides a description of the test setup and device under test. The second section provides the transfer impedance study for both the wires and the third section presents the position sensitivity measurements. Paper is concluded with 2-D position mapping with development and implementation of automated test bench.

TEST BENCH SETUP

Figure 1 shows the automated BPM test bench setup which consists of a function generator, 2 sets of X-Y scanner motor assembly, motion controller, a DSO, Device Under Test (DUT) (BPM) and stretched wire with weights.

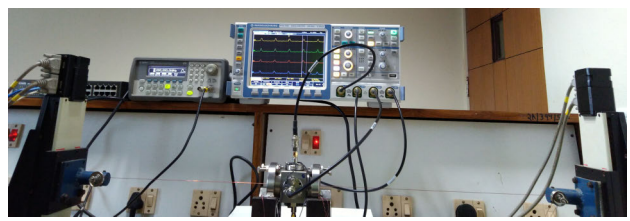

Figure 1: Automated Test bench Setup with Device Under Test (BPM).

Device Under Test

DUT in present case is a cylindrical SS pipe of length 88 mm with DN 63 flange having outer diameter of 63 mm and inner diameter of 35 mm with 4 electrodes (buttons) mounted using vacuum compatible 50 Ω SMA feed-through. Electrodes are of 6mm radius and made of Aluminium.

TRANSFER IMPEDANCE

Transfer impedance relates BPM output signal with the beam current. For measuring the Transfer Impedance of the Button BPM, the modified co-axial cable method [9] is used. In this method the total output voltage for the DUT is given as an infinite summation of the reflected and the transmitted signal converging to a definite value. Schematic setup is shown in Fig. 2. The port-1 node is fixed with the Vector Network Analyzer (VNA) and the port-2 node is varied to all the 4 electrodes to obtain respective transmission coefficients.

* yverma132@gmail.com

Content from this work may be used under the terms of the CC BY 3.0 licence (© 2020). Any distribution of this work must maintain attribution to the author(s), title of the work, publisher, and DOI

ISBN: 978-3-95450-222-6 ISSN: 2673-5350 doi:10.18429/JACoW-IBIC2020-THPP12

Content from this work may be used under the terms of the CC BY 3.0 licence (© 2020). Any distribution of this work must maintain attribution to the author(s), title of the work, publisher, and DOI

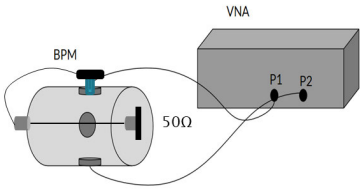

Figure 2: Setup for Transfer Impedance Measurement.

The variation of transfer impedance with frequency is shown in Fig. 3. The difference between electrodes impedance for a specific wire could be due to misalignment of geometric axis with sag in the wire. Another reason is the bad coupling between the input part and the button electrodes.

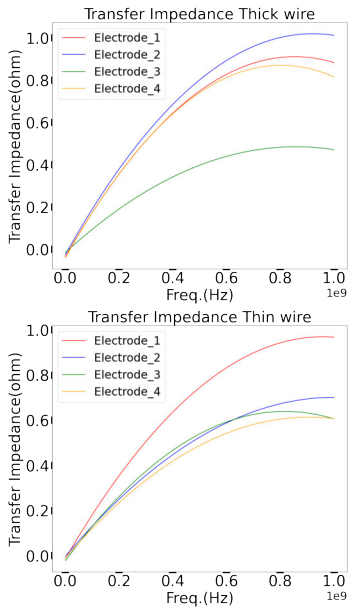

Figure 3: Transfer Impedance vs Freq. (Hz).

POSITION SENSITIVITY

Position Sensitivity is measured using stretched wire method [8] by passing current pulses through the copper wire of different diameters (0.5 mm and 1 mm). Best possible pulse characteristics out of function generator with 5 V pulses of 5 MHz rate with 20 ns pulse width are employed to the wire terminated in 50 Ω to mimick electron beam pulses. This is rough approximation of IUAC-FEL [10]. S_x and S_y can be calculated as slopes to normalized difference (Eqs. (1) and (2)) vs distance (mm) curves. The span of our distance (mm) in present case is from -8 mm to +8 mm for thin wire where as -4 mm to +4 mm for thick wire to consider only linear region as at large displacements, non-linearity arises due to the fact that position sensitivity is no longer a constant but start depending on position.

$$(\delta V/\sum V)_x = (V_R - VL)/(V_R + VL) \quad (1)$$

$$(\delta V/\sum V)_y = (V_U - VD)/(V_U + VD) \quad (2)$$

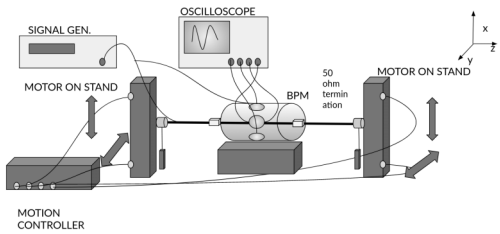

Figure 4: Setup for Position Sensitivity Measurement.

Signal is fed by signal generator and acquisition is done by DSO. The wire is moved using Motion controller which controls the stepper motor mounted on stands. The setup for position sensitivity measurement is shown in Fig. 4 and curves along X and Y axis for both wires are shown in Fig. 5. The normalized difference is not zero at the center indicating

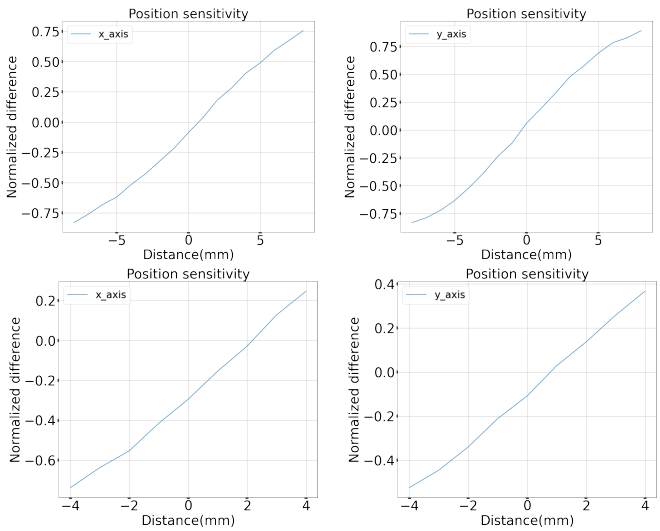

Figure 5: Sensitivity curves for X and Y axis for button BPM for thin wire (up) and thick wire (bottom).

there is a misalignment of buttons. The calculated values of S_x and S_y by calculating slope by fitting sensitivity curves with straight line are listed in Table 1.

Table 1: S_x and S_y Values (mm^{-1})

Wire	S_x	S_y
Thin	0.1176	0.1219
Thick	0.1211	0.1124

POSITION MAPPING

Position mapping is implemented using the same stretched wire method, by moving the wire in the span of -8 mm to +8 mm with various step size. Position Sensitivity values are used reciprocate the 2-D position map for the whole BPM by Eqs. (3) and (4) where S_x and S_y are sensitivity values calculated in previous section. But before making a position map, the wire is aligned to the geometrical center of the

ISBN: 978-3-95450-222-6 ISSN: 2673-5350 doi:10.18429/JACoW-IBIC2020-THPP12

BPM. This is done using the cross-wire method.

$$x = (1/S_x)(\delta V/\sum V)_x \quad (3)$$

$$y = (1/S_y)(\delta V/\sum V)_y \quad (4)$$

Measurements time increases with reduction in resolution or step-size. For step size = 1mm, the total readings counted to be 289 which amount to 5hr to measurement time.

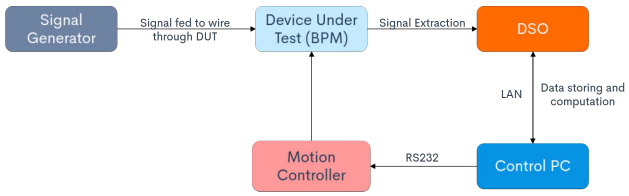

Figure 6: Block Diagram of Automated Test Setup.

Therefore, an approach to automated measurements is taken by developing a automated BPM test bench for 2-D position mapping. The setup of measurement is similar to Fig.4.

Remote Interfacing was done over RS232 towards the NSC-G series motion controller by Newmark for controlling the motion of wire and over LAN for DSO for the acquisition of signal from electrodes. The motion controller is equipped with stepper motors having a resolution of 3.10559×10^{-5} mm per encoder count (1 mm = 32200 encoder counts) that move in x,y directions. Open source Gclib python library is used to control the motion controller and vxi11 is used to interface with DSO for signal extraction and storage. A block diagram of how the automation of system is carried out is given in Fig. 6 . Comparison between automated and manual measurement is shown in Fig. 7 and error comparison in Table 2. By comparison of the error, it can be observed that reduction in human error is done by following automated measurements using test bench. Due to less error using automation all further mapping is performed using automation.

Table 2: Absolute Average Measurement Error (mm) Calculated For Automated and Manual Measurements

Error	X (mm)	Y (mm)
Manual	0.81	0.64
Automated	0.73	0.43

2-D position maps for both wires with various step-size is shown in Figs. 8 and 9. The measured position corresponds accurately with the real position for small distances but at large distances deviation becomes large. This is due to the effect of non-linearity in S_x and S_y, which was assumed to be a constant and independent of the position. Moreover, due to the curvature of the BPM a curved map is obtained and misalignment of button, offset in wire along axis can also be the reason for distortion. Error for various step size and both the wires has been calculated and shown in Table 3.

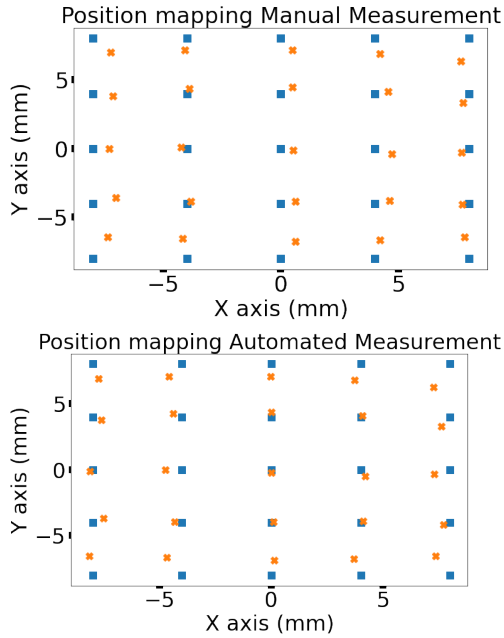

Figure 7: 2-D position mapping of manual (top) and automated (bottom) measurement with 4 mm step size where cross (orange) represents measured position and square (blue) is actual position.

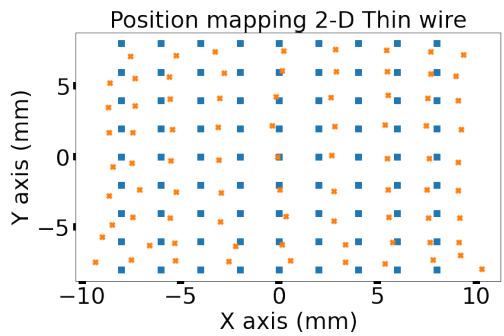

Figure 8: 2-D position map for Thin wire with step-size of 2 mm where cross(orange) represents measured position and square(blue) is actual position.

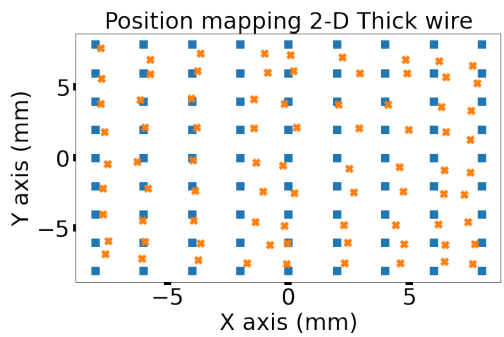

Figure 9: 2-D position map for Thick wire with step-size of 2 mm where cross (orange) represents measured position and square (blue) is actual position.

Content from this work may be used under the terms of the CC BY 3.0 licence (© 2020). Any distribution of this work must maintain attribution to the author(s), title of the work, publisher, and DOI

ISBN: 978-3-95450-222-6 ISSN: 2673-5350 doi:10.18429/JACoW-IBIC2020-THPP12

Content from this work may be used under the terms of the CC BY 3.0 licence (© 2020). Any distribution of this work must maintain attribution to the author(s), title of the work, publisher, and DOI

Table 3: Absolute Average Measurement Error (mm) Calculated for 2-D Position Mapping of Thin and Thick Wires

Error	Thick (x,y)	Thin (x,y)
2mm	(0.45,0.62)	(0.38,0.69)

CONCLUSION

The aim of the paper is to present a characterization study of a button BPM, with the measurement of transfer impedance, position sensitivity and development of a cost-effective automated BPM test bench. Misalignment of button is observed in position sensitivity curves due to non-zero normalized difference at origin. Development and testing of automated test bench results in significant reduction in measurement error which led to adoption of test bench for further 2-D position mapping. Open source libraries and software is implemented to control the stepper motors and DSO. After an easy process of setting the measurement range, the developed BPM test bench carries out the necessary steps itself, provides and stores the results directly after processing them. Exemplary measurements of 2-D mapping of thick and thin wire with various step size have been performed with error measurements. Through automation, the results are obtained quickly and precisely. Further developments will focus on enhancing the user experience even more with building interactive GUI and more precise pulses for realistic beams.

REFERENCES

[1] R. E. Shafer, "Beam position monitoring", *AIP Conf. Proc.*, vol. 249, pp. 601–636, 1992. doi:10.1063/1.41980

[2] A. R. Molaee, M. Sh. Shafiee, M. Mohammadzadeh, and M. Samadfam, "General Consideration for Button-BPM Design", in *Proc. IPAC'14*, Dresden, Germany, Jun. 2014, pp. 3537–3540. doi:10.18429/JACoW-IPAC2014-THPME126

[3] M. T. Gundogan, O. Yavas, A. A. Aydin, E. Kasap, and C. Kaya, "Design, Production and Tests of Button Type BPM for TAC-TARLA IR FEL Facility", in *Proc. IBIC'16*, Barcelona, Spain, Sep. 2016, pp. 27–30. doi:10.18429/JACoW-IBIC2016-MOPG01

[4] D. Lipka, B. Lorbeer, D. Noelle, M. Siemens, and S. Vilcins, "Button BPM Development for the European XFEL", in *Proc. DIPAC'11*, Hamburg, Germany, May 2011, paper MOPD19, pp. 83–85.

[5] N. Eddy *et al.*, "Beam Instrumentation at the Fermilab IOTA Ring", in *Proc. IBIC'19*, Malmö, Sweden, Sep. 2019, pp. 22–28. doi:10.18429/JACoW-IBIC2019-MOBO02

[6] S. Udrea, P. Forck, C. M. Kleffner, K. Knie, and T. Sieber, "The Beam Diagnostics Test Bench for the Commissioning of the Proton Linac at FAIR", in *Proc. IBIC'19*, Malmö, Sweden, Sep. 2019, pp. 196–199. doi:10.18429/JACoW-IBIC2019-MOPP038

[7] M. Schwarz *et al.*, "Development of an Automated BPM Test Bench", in *Proc. IBIC'19*, Malmö, Sweden, Sep. 2019, pp. 651–654. doi:10.18429/JACoW-IBIC2019-WEPP045

[8] S. Zorzetti, N. Galindo Munoz, M. Wendt, and L. Fanucci, "Stretched-Wire Techniques and Measurements for the Alignment of a 15GHz RF-BPM for CLIC", in *Proc. IBIC'15*, Melbourne, Australia, Sep. 2015, pp. 487–491. doi:10.18429/JACoW-IBIC2015-TUPB063

[9] M. Kumar, L. K. Babbar, R. K. Deo, T. A. Puntambekar, and V. K. Senecha, "Modified coaxial wire method for measurement of transfer impedance of beam position monitors", *Phys. Rev. Accel. Beams*, vol. 21, no. 5, p. 052801, 2018. doi:10.1103/PhysRevAccelBeams.21.052801

[10] S. Ghosh *et al*, "Status of the development of Delhi Light Source (DLS) at IUAC", *Nucl. Instrum. Meth. B*, vol. 402, pp. 358–363, 2017. doi:10.1016/j.nimb.2017.03.108

ISBN: 978-3-95450-222-6 ISSN: 2673-5350 doi:10.18429/JACoW-IBIC2020-THPP16

SEPTUM ORBIT FEEDFORWARD CORRECTION AT THE AS

C. Lehmann*, University of Queensland, Brisbane, Australia
Y.-R. E. Tan, M. Atkinson, AS - ANSTO, Clayton, Australia

Abstract

The leakage fields generated by the septum in the injection straight perturbs the beam by as much as 130 µm horizontally and 80 µm vertically during injection. Passive shielding with copper collars and Mu metal sheets has reduced the perturbation but not removed them. The remainder of the perturbation will be corrected using an active feedforward system. This report will discuss the design of the system and the effectiveness of the prototype.

INTRODUCTION

The injection scheme in the storage ring is composed of four injection kicker magnets to create a local bump and two horizontal septa (SEP and SEI) to guide the electrons from the injector system into the storage ring. The arrangement of the septa is shown in Fig. 1 and ideally have no influence on the stored beam. As is commonly found, this is not the case due to stray fields and in 2016 we embarked on a project to improve the beam stability by reducing the effect of the two septa on the stored beam. This report will outline the steps taken, both passive and active measures to remove the disturbance.

Passive Shielding

To shield the stored beam from stray fields from SEI, 5 layers of 0.25 mm mu-metal are rolled around the vacuum chamber covering 1100 mm of the storage ring vacuum chamber. The mu-metal was rolled tight to maximise the inter-layer magnetic coupling with kapton tape wrapped around the vacuum chamber to insulate it from the mu-metal. A single layer of omega shaped mu-metal around 90% of the vacuum chamber circumference and loosely coupled to the septa shield plate was installed in one hard to reach section. SEI was run and inspected for arcs and unusual noises, none were found and the mu-metal foil did not appear to vibrate. Two copper boxes were then installed to shield the septa themselves as some parts of the vacuum chamber did not lend themselves to shielding, in particular near the septa ends which appear to have large fringing fields. The copper shield reduced the peak field measured 100 mm from the septa surface by an order of magnitude, it was not possible to measure the shielding effect of the mu metal. Figure 2 shows that these measures reduced the beam disturbance by only 44%. This result indicates that the majority of the disturbance is not due to the stray septum field hence not easily mitigated by shielding. Induced currents up to 30A were observed in the beam pipe and ground circuits, these may have contributed to the disturbance.

To use active compensation to remove the remaining disturbance would require a dipole kick of 10 µrad and 6.5 µrad in the horizontal and vertical planes, with a bandwidth of 2 kHz. This is outside the bandwidth of the Fast Orbit Feedback System [1] at 450 Hz. Therefore a separate feedforward system is required to compensate for this disturbance.

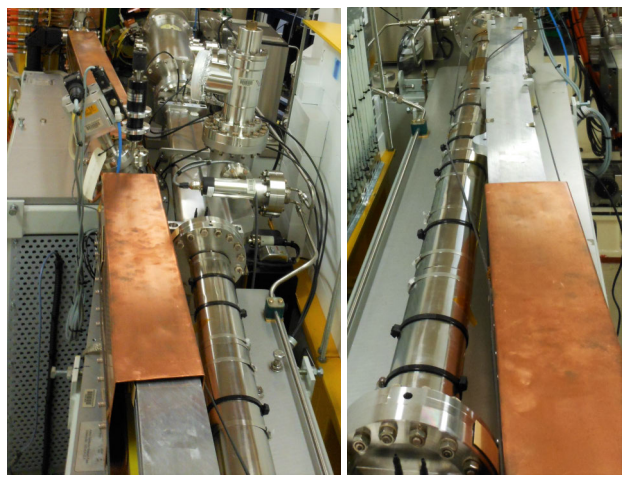

Figure 1: Location of SEP (top of left photo) and SEI (bottom of left photo). Passive shielding using copper sheets around the septa and mu metal sheets around the closest beam chambers (right photo).

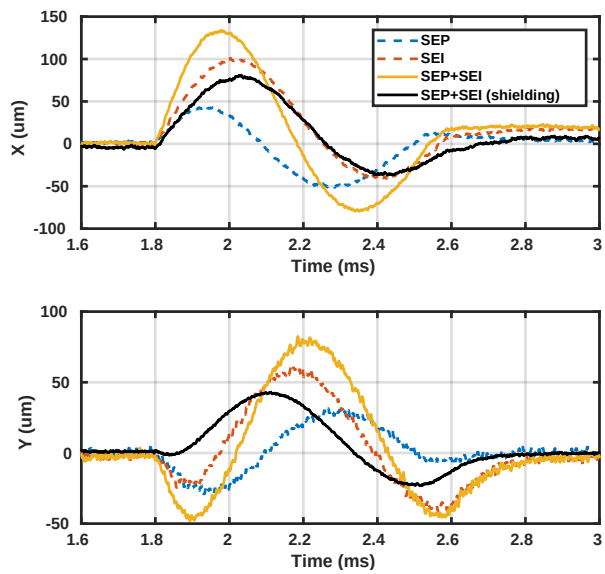

Figure 2: Perturbation from the two septa from turn-by-turn data (1.4 MS/s) and showing the effect of passive shielding that has been installed. Maximum amplitudes reduced from 134.1 µm and 80.5 µm to 80.2 µm and 42.7 µm.

* c.lehmann@uqconnect.edu.au

Content from this work may be used under the terms of the CC BY 3.0 licence (© 2020). Any distribution of this work must maintain attribution to the author(s), title of the work, publisher, and DOI

ISBN: 978-3-95450-222-6 ISSN: 2673-5350 doi:10.18429/JACoW-IBIC2020-THPP16

Content from this work may be used under the terms of the CC BY 3.0 licence (© 2020). Any distribution of this work must maintain attribution to the author(s), title of the work, publisher, and DOI

PERTURBATION MODELLING

The effects of the stray fields from the septum on the beam position throughout the storage ring can be modelled using closed orbit perturbation theory. When modelling the disturbance of a single dipole around the ring, it becomes useful to apply a Floquet transformation to change from the standard (s,x,y) closed orbit coordinates to (ψ, η_x, η_y), as outlined in Reference [2]. In these new coordinates a single dipole kick will cause a sinusoidal perturbation in (η, ψ) space, as described by

$$\eta = \eta_0 \cos(Q\psi + \lambda). \quad (1)$$

However, Eq. 1 is only valid in the domain $[\psi_k, 2\pi]$ where ψ_k is the phase position of the dipole kick. [2] does not correct for this. Once the domain is corrected to $[0, 2\pi]$, η_0 is substituted in, a phase offset λ is calculated to provide closed orbit continuity and the Floquet transform is reversed, the final expression used to describe a single dipole perturbation along an axis of the storage ring is given by,

$$x(s) = \left(\frac{\sqrt{\beta_x(s)\beta_{kx}}}{2|\sin \pi Q_x|} \frac{\delta(Bl)}{B\rho} \right) \cos(Q_x|\psi(s) - \psi_k| - (Q_x - \lfloor Q_x \rfloor)\pi) \quad (2)$$

where x(s) is the deviation along a closed orbit axis as a function of position, β_x is the beta function as a function of position, β_{kx} is the value of the beta function at the dipole location, Q_x is the tune, $\delta(Bl)$ is the dipole kick amplitude, $B\rho$ is the beam rigidity, $\psi(s)$ is the phase as a function of position and ψ_k is the phase at the dipole location.

By using the beta functions, tunes and phases taken from models of the storage ring, Eq. 2 can be used to predict the perturbation around the stored beam due to a dipole kick. The perturbation from the septa was found to be well modelled as a dipole kick, and fits the shape described by Eq. 2.

Dipole Location Modelling

Equation 2 was used to model the optimal location of the dipole corrector by using iterative methods to minimise and measure the net disturbance over the duration of the perturbation. It was also used to find the optimal current waveform for each correction dipole location.

By simulating the effectiveness of a range of locations around the storage ring in MATLAB, the optimal location was found to be immediately adjacent to the septum 2 meters upstream of the injection. Since it also proved convenient to access, this location was chosen for the prototype.

COIL OPTIMISATION

An initial prototype correction dipole was constructed, consisting of 4 pre-wound coils of 1.0 mm copper wire with approximately 200 turns of 30 mm diameter, mounted on the bellows with 1 coil on each side. The coils along each axis were connected in series and driven by a 50V/2A Kepco power supply in current mode. Initial testing of this prototype was partially successful in cancelling the perturbation. With this prototype, kicks of 1.2 µrad were achieved on both x and y axes using the maximum current of 2 A and approaching the 50 V capability of the power supply. This fell short of the 10 µrad and 6.5 µrad kick strengths required to fully cancel the perturbation on the x and y axes respectively. Since using larger power supplies was impractical the required kick amplitude had to be achieved by optimising the coil design and mounting arrangement.

There were two options for the mounting location: on the vacuum tube or bellows. The vacuum tube has a 2 mm thick stainless steel outer layer, and as such will cause significant attenuation and give a noticeable low-pass filter effect to any magnetic field waveform transmitted through it. The bellows have only very thin stainless steel layers and as such will not have significant frequency effects. However, the bellows mounting requires the coils to be mounted further from the beam reducing the effective field. These options will be compared to determine which produces the larger kick amplitude.

Geometry Optimisation

To optimise the coils and increase the kick amplitude, the constraints of the system were evaluated. The total kick strength from a single dipole can be modelled as the compound of the magnetic field produced by a solenoid and the length over which it effects the beam, given by the expression $Bl = \mu NIl/h$. Since the current is already maximised at 2 A, the value of Bl can be most easily increased by increasing the number of turns, increasing the length of the field, and decreasing the height of the magnet (increasing the coil density). For a power supply providing 2 A at 1 kHz with a voltage limit of 50 V, the maximum inductance per coil is calculated to be 2 mH. Since the inductance of a coil is given by the expression $L = \mu N^2 lw/h$, the kick strength can be increased within this inductance constraint by reducing the number of turns, increasing the length and reducing the coil thickness/height.

FEMM Analysis

To investigate these phenomenon further, Finite Element Method Magnetics (FEMM) was used to optimise the coil geometry and compare the two mounting options (bellows or directly on the vacuum chamber). The vacuum chamber cross-section was measured and placed in the simulation, while the bellows were modelled as air. The simulations showed the 1 kHz magnetic field at the beam produced by a vacuum chamber mounting is a factor of 2 better than a bellows mounting, despite the associated frequency effects. As such, to maximise the kick amplitude a vacuum tube mounting was the better option.

The results of this FEMM analysis were later experimentally verified using a frequency sweep with both bellows and vacuum tube mountings. At 1 kHz, the vacuum tube mounting showed a significantly higher kick amplitude.

ISBN: 978-3-95450-222-6 ISSN: 2673-5350 doi:10.18429/JACoW-IBIC2020-THPP16

SETUP

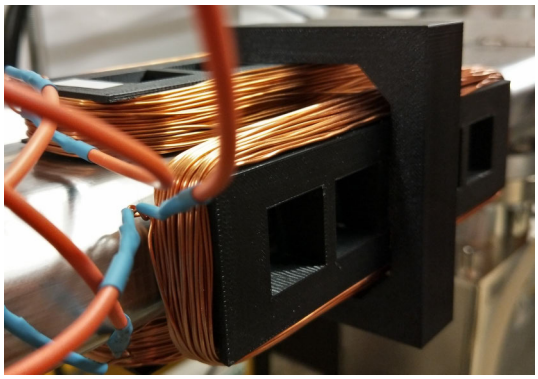

Figure 3: Final coil design with a 3D printed holder to clamp the coils around the vacuum chamber.

The final prototype seen in Fig. 3 consists primarily of a 3D printed mounting and 3 hand-wound air coils of dimension (150 × 40 × 15) mm. The top and bottom coils are connected in series, and each set of cables are fed out of the tunnel to two 50V/2A Kepco power supplies (horizontal and vertical corrector coils). Each power supply is set to Current mode, and provided a voltage waveform by a RedPitaya [3, 4]. The power supplies have been modified such that the +1 to -1 Volt signal from the RF Output channel of the RedPitaya produces a corresponding output current of +2 to -2 Amps from the power supply. Custom voltage waveforms are uploaded to the RedPitaya for each axis as retrieved from the perturbation modelling optimisation. The RedPitaya is triggered by the timing system [5] to generate one waveform synchronised to the storage ring injection. The EPICS interface was used to calibrate the prototype such that the amplitude and timing of its perturbation opposes the perturbation from the septum.

RESULTS

The implementation of active feedforward correction was successful in removing the perturbation from the septum. Figure 4 displays the perturbation cancellation across all BPMs at the moment of maximum perturbation for each axis. Figure 5 indicates this result remains consistent through the entire 1ms duration.

Figure 5 was created by taking the RMS closed orbit deviation across all BPMs for each time sample. The Passive+Active method shows the maximum RMS perturbation was able to be reduced further than by the Passive method alone, from 19.9 µm to 4.5 µm horizontally and from 14.1 to 3.4 µm vertically, a further reduction of over 75% on each axis.

The noise floor may be seen to vary from 1–2 µm. On the Y axis perturbations have been cancelled to the level of the noise floor, but the X axis still shows some minor perturbations. Figure 4 also shows some minor perturbation across some BPMs on the x axis. These remaining perturbations are likely caused by a number of factors. Some error is expected from the calibration process in both the trigger

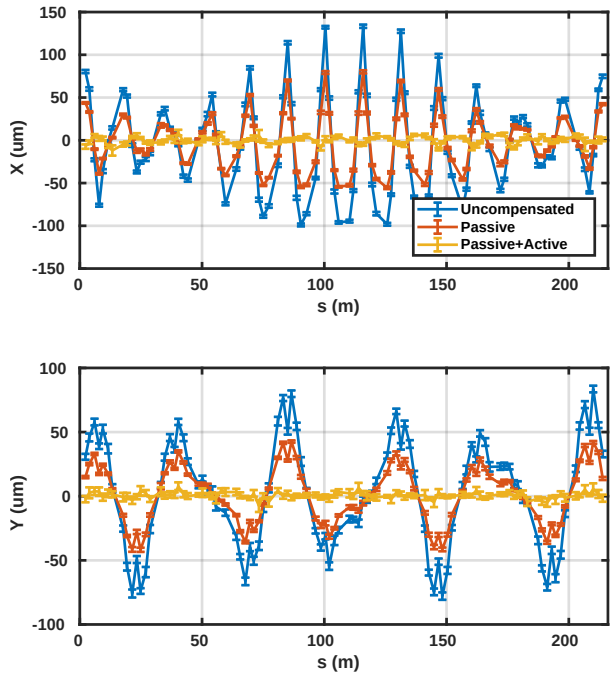

Figure 4: Maximum orbit perturbation at the 2 ms (X) and 2.2 ms (Y) before any compensation, with passive and with combined measures.

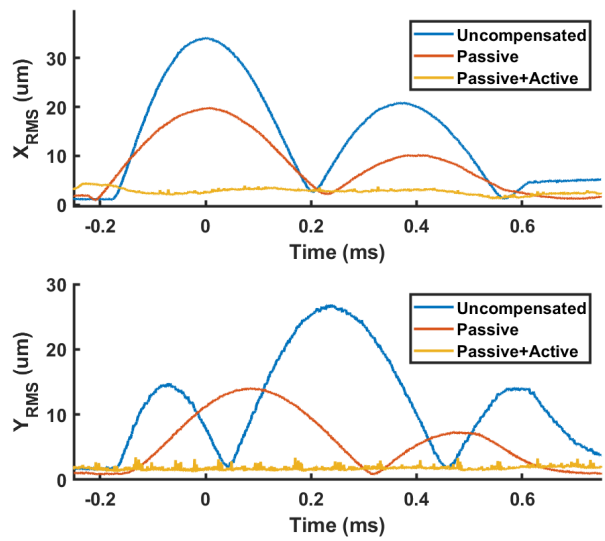

Figure 5: RMS orbit perturbation across all BPMs over full duration before any compensation, with passive and with combined measures.

timing, shape and amplitude of the compensation waveform, but this can be reduced in a later design through iterative optimisation. There is expected to be further error from the distortion of the dipole's magnetic field due to the frequency effects of the vacuum tube. Finally, the perturbation modelling optimisation indicated some minor perturbations would remain due to the co-positioning of the x and y axis correction dipoles, a sacrifice made for convenience.

Content from this work may be used under the terms of the CC BY 3.0 licence (© 2020). Any distribution of this work must maintain attribution to the author(s), title of the work, publisher, and DOI

ISBN: 978-3-95450-222-6 ISSN: 2673-5350 doi:10.18429/JACoW-IBIC2020-THPP16

Content from this work may be used under the terms of the CC BY 3.0 licence (© 2020). Any distribution of this work must maintain attribution to the author(s), title of the work, publisher, and DOI

CONCLUSION

The design and testing of an active feedforward perturbation compensation prototype demonstrates a method for reducing perturbations from the septum with far greater effectiveness than passive shielding alone. By adding active compensation, the net perturbation was able to be further reduced by 75% on each axis such that remaining perturbations approach the noise floor. A more permanent version of this prototype still remains to be constructed.

ACKNOWLEDGEMENTS

Would like to thank the help from Andraz Pozar from the Controls group to help with setting up the EPICS driver for the RedPitaya.

REFERENCES

[1] Y. E. Tan *et al.*, "Commissioning of the Fast Orbit Feedback System at the Australian Synchrotron", in *Proc. IPAC'17*, Copenhagen, Denmark, May 2017, pp. 1770–1773. doi:10.18429/JACoW-IPAC2017-TUPIK040

[2] E. J. N. Wilson, "Imperfections and multipoles", *An Introduction to Particle Accelerators*, Oxford, UK, Oxford University Press, 2001, pp. 77–79. doi:10.1093/acprof:oso/9780198508298.001.0001

[3] Red Pitaya, https://www.redpitaya.com/.

[4] Red Pitaya - EPICS driver (Australian Synchrotron), https://github.com/AustralianSynchrotron/redpitaya-epics

[5] E. D. van Garderen, G. LeBlanc, A. C. Starritt, K. Zingre, and M. L. M. ten Have, "Upgrade of the Timing System at the Australian Synchrotron", in *Proc. DIPAC'09*, Basel, Switzerland, May 2009, paper TUPD27, pp. 357–359.

ISBN: 978-3-95450-222-6 ISSN: 2673-5350 doi:10.18429/JACoW-IBIC2020-THPP20

VIRTUAL SLIT FOR IMPROVED RESOLUTION IN LONGITUDINAL EMITTANCE MEASUREMENT *

K. Ruisard†, A. Aleksandrov, A. Shishlo
Oak Ridge National Laboratory, Oak Ridge, TN, USA

Abstract

A technique to reduce point-spread originating from physical slit width in emittance measurements is described. This technique is developed to improve phase resolution in a longitudinal emittance apparatus consisting of a dipole magnet, energy-selecting slit and bunch shape monitor. In this apparatus, the energy and phase resolutions are directly proportional to the width of the slit. The virtual slit method allows sub-slit resolution, with penalty in measurement time and dynamic range. The bunch phase profile is measured at two points in the energy distribution with a separation less than the physical slit width. The difference of these two profiles is used to reconstruct the profile from a virtual slit of width equal to that separation.

INTRODUCTION

Accurate measurement of beam phase space distributions is crucial for verifying correct operation and understanding accelerator dynamics. Phase space measurement can both be the source for simulation bunches and the basis for benchmarks of accelerator models. Longitudinal parameters in particular reflect dynamics within accelerating structures. Work at the Beam Test Facility (BTF) at the Spallation Neutron Source (SNS) has focused on detailed characterization of the beam distribution, including high-dimensional measurements [1] and development of high-dynamic range diagnostics capable of halo measurement [2]. The goal of this work is to obtain loss-level accuracy with particle-in-cell simulation, where the simulation results can be verified down to the halo level.

The phase space measurements use a slit-scan technique, where each dimension is isolated by masking the beam with a thin slits. While the bunch shape monitor (BSM) has sufficient resolution to image the bunch phase distribution, finite slit widths upstream of the BSM cause significant point spread in the BSM. A virtual slit technique is developed to reduce the point spread effect in the phase measurement, significantly improving the resolution of the phase measurement without modifying the existing hardware.

This paper first describes the apparatus for measurement of the longitudinal phase space at the BTF. The virtual slit technique is introduced for a wide-aperture slit, with an example measurement provided by PIC simulation of the setup. The case of a narrow slit aperture, with reduced but still significant point spread error, is also discussed. The use of a narrow slit complicates the virtual slit approach, but a solution is described. Finally, the data from virtual slit measurements is used to estimate the width of the physical slit aperture.

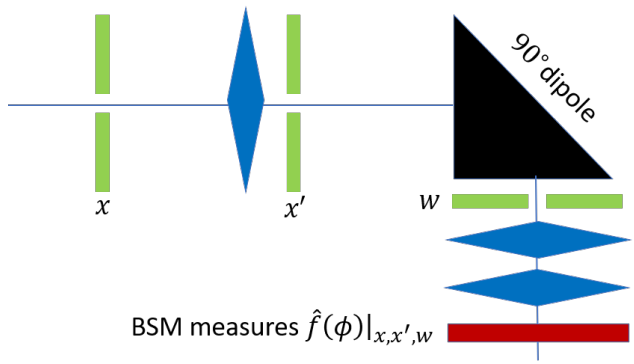

Figure 1: Diagram of longitudinal emittance apparatus. The notation $\hat{f}(\phi)|_{x,x',w}$ is used to indicate that the BSM measures the phase profile for the fraction of the beam that passes through the upstream x, x' and w slits.

APPARATUS

The BTF is a test-stand experiment designed as a clone of the SNS front-end, including H^- ion source, LEBT, RFQ and four MEBT quadrupoles, as well as a MEBT extension enabling extensive phase space diagnostics and transport studies. A detailed description of the facility can be found in [3].

The apparatus for measurement of the longitudinal phase space is situated in the 2.5 MeV MEBT. The device consists of a 90° dipole and energy-selecting slit followed by the BSM. The BSM measures the phase profile for the selected energy. The longitudinal phase space $f(\phi, w)$ is measured by scanning the energy selection. Figure 1 shows the geometry of the emittance measurement. Two vertical slits upstream of the dipole are used to create a beam with small horizontal spread at the dipole entrance. In total there are three vertical slits, indicated by green rectangles. Additionally, three quadrupoles (indicated by blue diamonds) are used to control beam size on the energy slit and at the BSM.

At the energy slit location, two different widths are available: 200 µm and 1 mm. In this document, they will be

* This manuscript has been authored by UT-Battelle, LLC, under Contract No. DE-AC05-00OR22725 with the U.S. Department of Energy. The United States Government retains, and the publisher, by accepting the article for publication, acknowledges that the United States Government retains a non-exclusive, paid-up, irrevocable, world-wide license to publish or reproduce the published form of this manuscript, or allow others to do so, for United States Government purposes. The Department of Energy will provide public access to these results of federally sponsored research in accordance with the DOE Public Access Plan.
† ruisardkj@ornl.gov

Content from this work may be used under the terms of the CC BY 3.0 licence (© 2020). Any distribution of this work must maintain attribution to the author(s), title of the work, publisher, and DOI

ISBN: 978-3-95450-222-6 ISSN: 2673-5350 doi:10.18429/JACoW-IBIC2020-THPP20

Content from this work may be used under the terms of the CC BY 3.0 licence (© 2020). Any distribution of this work must maintain attribution to the author(s), title of the work, publisher, and DOI

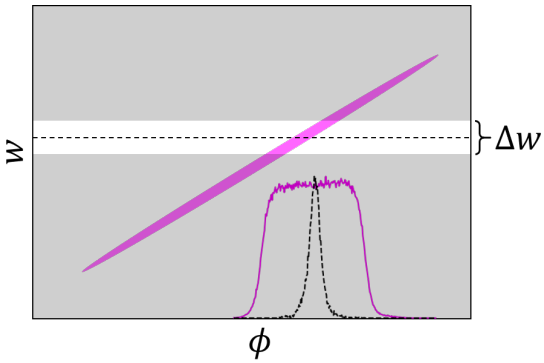

Figure 2: Illustration of longitudinal phase space at the BSM location. The unshaded window represents the portion of beam that passes through a 1 mm energy slit. Due to the high correlation, the projected rms phase width of that beamlet (solid magenta curve) is significantly wider than that of an infinitely thin slice (dashed black).

colloquially referred to as the "narrow" and "wide" slits. After manufacturing, a Phosphor coating is deposited on the slit to enable dual-use as a profile monitor. This deposition is not well-controlled and acts to reduce the width of the slit from the design value. While this is a relatively small error for the wide slit, it measurably affects the width of the narrow slit.

The largest source of error in the emittance apparatus is point spread in the phase measurement, which originates as a result of the width of energy slit and the large linear correlation between phase and energy. The BSM is 4.2 meters downstream of the RFQ exit. Between the RFQ and the BSM, the bunch expands longitudinally and the longitudinal phase space becomes highly correlated as illustrated in Fig. 2. The energy slit makes a selection that is much narrower than the total energy spread in the beam. For the narrow 200 µm slit, $\Delta w \sim 2$ keV compared to rms width 24 keV [4]. Therefore, the point-spread effect on the energy profile is relatively small.

However, the spread in energy is correlated with a spread of arrival phase at the BSM. As depicted in Fig. 2, the projected phase profile of the energy slice Δw is wider than the true phase profile of an infinitely thin slice. The size of this error is much larger relative to the beam width. The rms point spread estimated in [4] is 3.3° compared the expected phase width of 6°. In other words, the phase width of the beam is very near the resolution limits of the emittance apparatus.

For the wide 1 mm slit, $\Delta w \sim 10$ keV. Therefore, the point-spread effect from the slit width is very large in both the phase and energy dimensions.

VIRTUAL SLIT TECHNIQUE

The virtual slit technique reduces the effect of point spread by effectively reducing the slit width without the need for physically modifying the slit. A virtual slit is generated by combining two phase profile measurements that are separated by a small step in energy, where the energy step is smaller than the range that passes through the slit. It is easiest to consider moving the energy slit by a small step δx, where $\delta x < \Delta x$ where Δx is the physical slit width. The two waveforms are subtracted and, as shown, their difference has two peaks: one positive and one negative. Each peak is the phase profile corresponding to the narrow energy band δw of the edge region, where the effective width of the virtual slit is δx. This process is illustrated in Fig. 3 using parameters for the wide slit.

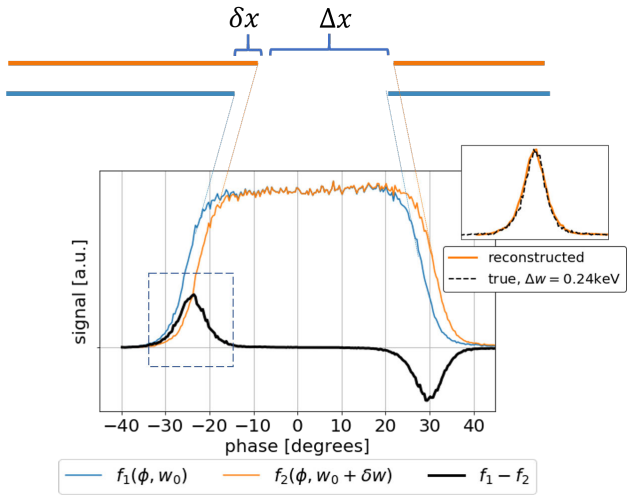

Figure 3: Illustration of virtual slit concept using wide (1 mm) slit. The orange and blue profiles are the phase profile measured with the BSM for two differentially-separated energies, illustrated here as a offset in slit location δx. The black curve is the difference profile, and the region in the dashed outline is the reconstructed phase profile.

This technique is analogous to the measurement of beam profiles using scrapers. In this system, a transverse profile can be measured by scanning a scraper across the beam in $\hat{x}$ and recording the transmitted current. The measured curve is the cumulative function $I(x) = \int_{-\infty}^{x} f(\hat{x})d\hat{x}$ that is differentiated to reconstruct the profile $f(x)$. The change δI for step size δx is proportional to the current that would be measured by a slit of width δx. In the case of the virtual slit, the change of the measured phase profile with incremental energy step, $\delta f(\phi)$, is the profile for a slice of phase space with width equal to the energy step δw.

The profiles shown in Fig. 3 were obtained via simulation of the emittance apparatus. The PIC code PyORBIT is used [5]. A bunch created by self-consistent simulation of the BTF RFQ is propagated to the plane of the energy slit. Slit apertures are applied at the location of the three vertical slits, with width equal to the slit design width (either 200 µm or 1 mm). Multiple simulations are run for various positions of the third (energy) slit, and for each the macroparticle coordinates are saved at the BSM location. For the plot shown, a virtual slit width of $\delta x = 0.05$ mm is used.

Simulation enables comparison between the "true" phase width (the width of a very thin energy slice) with the profile

ISBN: 978-3-95450-222-6 ISSN: 2673-5350 doi:10.18429/JACoW-IBIC2020-THPP20

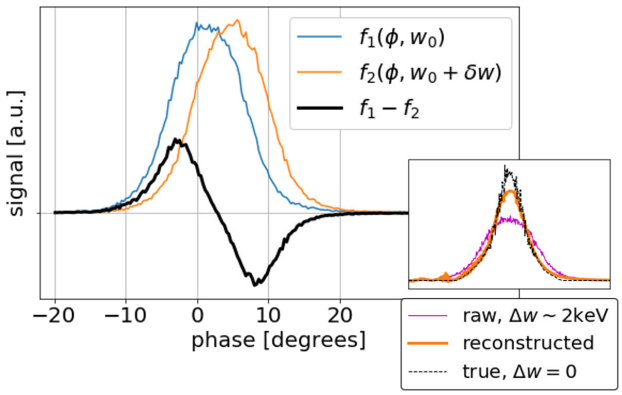

Figure 4: Illustration of virtual slit concept using narrow (0.2 mm) slit. The orange and blue profiles are the phase profile for a small step δw, the black curve is the difference profile. The inset plot compares the raw "measured" phase profile, which includes energy spread from finite slit size, to the reconstructed and true phase profiles.

obtained through the virtual slit technique. The inset plot in Fig. 3 shows this comparison: the true and reconstructed profiles are nearly identical. In this simulation case, the rms width with a 1% threshold is 3.9° for both the virtual slit profile and the thin slice.

Reconstruction of Narrow Slit Profiles

The point spread effect of the narrow slit is a much smaller effect for the narrow, 200 µm slit. However, the point spread error is still the dominant effect in emittance measurements, as discussed in [4]. In the simulation case, for a thin energy slice $\Delta w = 0.2$ keV the 100% rms phase width is 4.2°. However, the phase measured with realistic slit apertures was 5.2°. Even with the narrow slit, the point spread effect leads to ~ 20% overestimation of the measured phase width.

The virtual slit reconstruction can be applied to narrow slit profiles, but there is an extra complication, as illustrated in Fig. 4. Unlike the case with the wide slit, the two difference profiles are not well-separated. It is possible to untangle the profiles if it can be assumed that they are identical except for translation.

Let the true phase profile be $G(\phi)$ and let the black curve in Fig. 4 be called $g(\phi)$. $g(\phi)$ can be expressed as

$$g(\phi) = G(\phi) - G(\phi + \Phi) \tag{1}$$

where Φ is the translation along $\hat{\phi}$. The virtual slit subtraction should deliver two profiles whose centers are separated by a distance proportional to the width of the physical slit. Therefore, $\Phi \propto \Delta x$ for slit width Δx. For a measured difference profile, the separation between peaks can be used to calculated the physical slit width, which is discussed below.

$G(\phi)$ can be reconstructed from the measured $g(\phi)$ by

$$G(\phi) = \sum_{k=0}^{\infty} g(\phi + k\Phi). \tag{2}$$

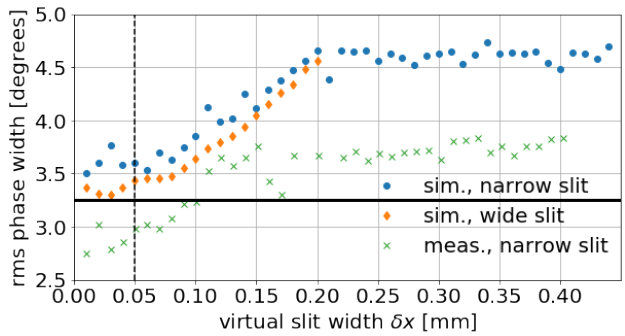

Figure 5: Dependence of reconstructed phase width on size of virtual slit. A 5% threshold is applied.

The assumption that the phase profiles are identical except for translation is valid. In general, the phase profile varies slowly with energy and for a small step $\delta w \sim 0.5$ keV ($\delta x \sim 0.05$ mm) they should be nearly identical. Any inconsistencies are expected to be artifact from particle noise or response of viewscreen in the BSM.

The result of applying the reconstruction in Eq. (2) can be seen in the inset in Fig. 4. It is apparent that the reconstructed profile (solid orange curve) is significantly narrower than the raw curve (solid magenta), which is the uncorrected phase profile, but still wider than the "true" phase width (dashed black). For a threshold of 5%, the raw rms phase width is 4.7° and the reconstructed width is 3.6°. This is still slightly larger than the true width of 3.2°, but the point spread error is reduced.

This extra step in the reconstruction can introduce additional artifact due to imperfect cancellation of the peak and anti-peak waveforms. This can be mitigated by applying the summation in both directions and combining the two reconstructed profiles, or by applying a higher threshold.

Optimal Width of Virtual Slit

The virtual slit should be significantly narrower than the physical slit in order to reduce point spread error. In practice the limit arises due to decreasing signal-noise ratio, which applies to both virtual and physical slits. In simulation this noise originates from granularity of the macroparticle distribution.

In both simulation and measurement, a virtual slit width ≤ 0.05 mm was optimal. The dependence of the reconstructed profile width is shown in Fig. 5. For virtual slit widths larger than the physical slit, the rms width flattens and is equal to the width of the "raw" profile without reconstruction. In both simulation and measurement, as the virtual width is reduced the reconstructed profile saturates at or below 0.05 mm. While the wide slit case reaches the "true" profile width (horizontal line) in simulation, the narrow slit reconstruction is less effective and there is still residual error. This limitation is likely related to the extra step in reconstruction (Eq. (2)).

Content from this work may be used under the terms of the CC BY 3.0 licence (© 2020). Any distribution of this work must maintain attribution to the author(s), title of the work, publisher, and DOI

ISBN: 978-3-95450-222-6 ISSN: 2673-5350 doi:10.18429/JACoW-IBIC2020-THPP20

Content from this work may be used under the terms of the CC BY 3.0 licence (© 2020). Any distribution of this work must maintain attribution to the author(s), title of the work, publisher, and DOI

Measurement of Narrow Slit Width

As mentioned, the virtual slit technique can also be applied to measure the physical width of a slit. This is most useful for the narrow slit, where the contribution of the Phosphor layer depth is relatively large. This complements previous efforts to measure slit width, which include direct optical examination of a spare determined to have a width of 0.17 ± 0.01 mm. Measurement of the installed slit is preferred, which requires an in-situ technique. Two methods were previously applied: (1) 0.27 ± 0.09 from imaging of the slit illuminated by beam and (2) 0.17 ± .01 by measuring the ratio of current transmitted by the wide and narrow slits.

As a third method, the slit width can be determined by looking at the distance between peak and anti-peak in the differential waveform $f_1 - f_2$. This distance, measured in BSM phase, can be transformed to transverse position at the slit with knowledge of the dispersion and linear $\phi - w$ correlation. When the spacing between the two slit positions (δx) is wider than the physical slit (Δx), the phase separation between peaks is linear in δx. However, when $\delta x < \Delta x$, the distance between peaks becomes fixed and is proportional to the slit width Δx. This can be expressed as:

$$\Delta\phi = \begin{cases} \Delta x \frac{d\phi}{dx} & \text{if } \delta x < \Delta x \\ \delta x \frac{d\phi}{dx} & \text{if } \delta x \geq \Delta x \end{cases} \quad (3)$$

Both the slit width Δx and the tranformation $d\phi/dx$ can be determined by fitting Eq. (3) to measurements at different virtual slit spacings. This is illustrated in simulation in Fig. 6, where the slit width is known and is exactly 0.2 mm. A least-squares fit gives $\Delta x = 0.205 \pm 0.002$ mm and $d\phi/dx = 54.0 \pm 0.2$ degrees/mm. Errorbars are derived from fit uncertainty.

A fit to measured data is shown in Fig. 7. In this case, the fitted parameters are $\Delta x = 0.155 \pm 0.002$ mm and $d\phi/dx = 57.2 \pm 0.4$ degrees/mm, errorbars again are due only to fit uncertainty. The $d\phi/dx$ parameter can be independently calculated from calibration data: $d\phi/dx = 58.6 \pm 1.0$ degrees/mm. Based on the agreement of the $d\phi/dx$ parameter, we judge the measured width Δx to be reliable. However, this is noticeably narrower than previous measurements which requires further investigation.

SUMMARY

This paper discussed implementation of a virtual slit technique to improve phase resolution in a longitudinal emittance device. The technique is more broadly applicable to slit-based imaging devices where sub-slit resolution is desired. As demonstrated via simulation, the virtual slit technique can be deployed to enable appropriate phase resolution even in the case of a very wide slit. In the case of a narrow slit, the point spread error on the rms phase can be reduced although not completely eliminated. The virtual slit correction to the narrow slit data is less straightforward than in the wide slit case, requiring an extra step to separate two overlapping phase profiles.

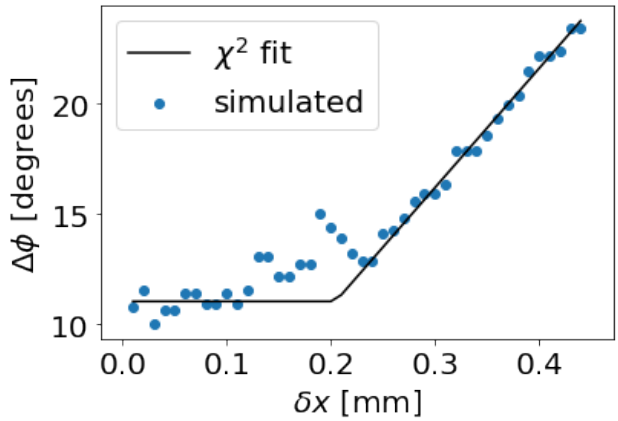

Figure 6: Least squares fit to determine narrow slit width using profiles from simulation with known slit width 0.2 mm.

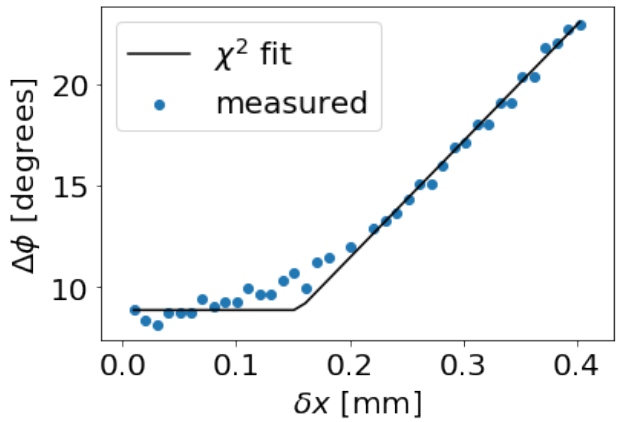

Figure 7: Least squares fit for measured profiles from virtual slit method with narrow slit.

This technique was implemented as an alternative to deconvolution of the point spread function. Deconvolution of measured and simulated signals was attempted, but the method was too sensitive to noise to provide useful results. The virtual slit was less sensitive to noise, although there was a penalty on signal-to-noise ratio similar to the penalty for using a physically narrower slit.

Despite the costs, the virtual slit is a convenient method for improving measurement resolution without modification of hardware, or vacuum breaks. Compared to a physical slit, a continuum of virtual slit sizes is available. This flexibility allows measurement of the physical slit width.

ACKNOWLEDGEMENTS

This research used resources at the Spallation Neutron Source, a DOE Office of Science User Facility operated by the Oak Ridge National Laboratory.

REFERENCES

[1] B. Cathey, S. Cousineau, A. Aleksandrov and A. Zhukov, "First Six Dimensional Phase Space Measurement of an Accelerator

ISBN: 978-3-95450-222-6 ISSN: 2673-5350 doi:10.18429/JACoW-IBIC2020-THPP20

Beam", *Phys. Rev. Lett.*, vol. 121, no. 6, p. 064804, 2018. doi:10.1103/PhysRevLett.121.064804

[2] A. Aleksandrov, in preparation.

[3] Z. Zhang, S. Cousineau, A. Aleksandrov, A. Menshov, and A. Zhukov, "Design and commissioning of the Beam Test Facility at the Spallation Neutron Source", *Nuclear Instruments and Methods in Physics Research A*, vol. 949, p. 162826, 2020. doi:10.1016/j.nima.2019.162826

[4] K. Ruisard, A. Aleksandrov, S. Cousineau, A. Shishlo, V. Tzoganis and A. Zhukov, "High dimensional characterization of the longitudinal phase space formed in a radio frequency quadrupole". arXiv:2008.06565

[5] A. Shishlo, S. Cousineau, J. Holmes, and T. Gorlov, "The Particle Accelerator Simulation Code PyORBIT", *Procedia Computer Science*, vol. 51, pp. 1272–1281, 2015. doi:10.1016/j.procs.2015.05.312

Content from this work may be used under the terms of the CC BY 3.0 licence (© 2020). Any distribution of this work must maintain attribution to the author(s), title of the work, publisher, and DOI

ISBN: 978-3-95450-222-6 ISSN: 2673-5350 doi:10.18429/JACoW-IBIC2020-THPP21

Content from this work may be used under the terms of the CC BY 3.0 licence (© 2020). Any distribution of this work must maintain attribution to the author(s), title of the work, publisher, and DOI

DESIGN AND DEVELOPMENT OF A NOVEL STRIPLINE FAST FARADAY CUP TO MEASURE ION BEAM PROFILE

A. Sharma[1†], R. K. Gangwar, Indian Institute of Technology (ISM), Dhanbad, India
B. K. Sahu, Inter-University Accelerator Centre, New Delhi, India
[1]also at Inter-University Accelerator Centre, New Delhi, India

Abstract

Present day heavy ion accelerators use bunched ion beams of sub-nanosecond time scale for beam acceleration. In order to monitor the longitudinal beam bunch profile, Fast Faraday Cups (FFC) are employed. Owing to the advent of microstrip technology and its fabrication process, planar structures have become easier to fabricate. A novel planar design using the same is developed with a special provision for mounting edge launch connectors through a microstripline feed, followed by a microstrip to stripline transition to again a microstrip structure in the beam interaction hole. The entire structure is symmetrical and bidirectional with 50 Ω transmission lines. An experimental study on via placement around central stripline has also been conducted to not only ensure the field containment around the strip but also for bandwidth enhancement. To measure ion beam currents from 10-100 nA and a bunch width of < 1ns, device has a beam interaction hole of around 10mm. 3 dB bandwidth is measured > 6 GHz resulting in a pulse rise time of ~60 ps or less. The proposed device is also provided with a bias ring on the topmost layer of the 3 layer architecture for electron suppression. In this paper, design, fabrication and RF testing of stripline fast faraday cup is presented.

INTRODUCTION

The 15 UD Pelletron and the upcoming High Current Injector produces pulsed ion beam to be further energized by the Superconducting LINAC of IUAC. The bunch length acceptance of the superbuncher cavity of LINAC is ~1-2 ns which further reduce it to 200-500 ps. In order to determine the time and energy structure of the beam bunches, it is essential to measure the longitudinal profile and Time of Flight of the beam. By employing Fast Faraday Cups, longitudinal profile of a beam can be measured. Stripline FFCs are interceptive devices made up of a printed circuit transmission line of 50Ω or any given impedance [1] which can produce picosecond pickup pulse response when ion beam bunches strike on it. Figure 1 shows typical application of FFC device at IUAC where response times of the order of 50-60 ps or > 6 GHz bandwidth are well suited. Aim of this paper is to design such a novel stripline FFC as per IUAC requirement.

The most notable works on stripline FFC design are found in [2-3] which have used multilayer structure with stitching vias to maintain signal integrity, and bandwidth enhancement. While these devices have a small beam interaction hole and used for very high current, high energy beam species, the proposed design is provided with larger beam interaction hole to cater even for low beam currents produced at IUAC which are of the order to 10-100 nA. Extensive studies on via fencing suggested [4-7] for suppression of spurious modes in stripline geometry using ground-to-ground stitching via filled with copper / metalized rods has been extended for the present case as well.

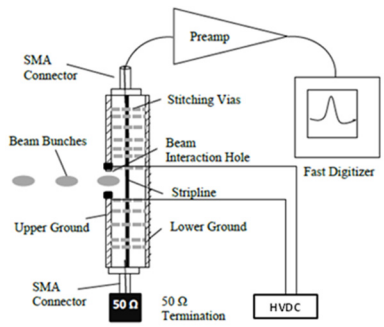

Figure 1: Beamline Test Setup.

Various sections of this paper deals with design equations and novelty implied therein. Emphasis has been given on stitching via placement and its mode suppression-cum-bandwidth extension effects. Paper is concluded by comparison of results of EM simulations done in Ansoft's HFSS with measured results obtained on VNA.

DESIGN DETAILS

The proposed configuration of stripline device is shown in Fig. 2. It is realized as a 3 layer, stacked-up structure of two planar substrates. Upper one has two rectangular notches at both edges so as to connect two SMA edge launch connectors. A beam interaction hole of the order of 10 mm diameter has been made at the center of the device for the beam sizes of the order 3-4 mm in diameter. Lower substrate has a grounded transmission line structure.

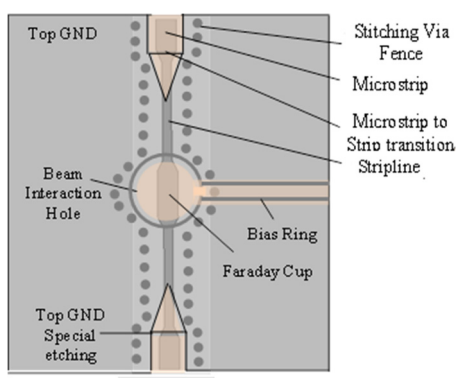

Figure 2: Proposed Stripline FFC Design.

† ashishdelhi.17kt000246@ece.iitism.ac.in

ISBN: 978-3-95450-222-6 ISSN: 2673-5350 doi:10.18429/JACoW-IBIC2020-THPP21

After the removal of notches and central cylinder, the geometry essentially becomes a microstrip based at these locations. So, we use the 50Ω microstripline design formula to calculate the width at these three locations while rest of the central trace is composed of 50Ω stripline. In order to transform the fields from microstrip-to-strip line and vice-versa, tapered transition is employed [8]. Additionally, along the tapered line, the copper pour on the upper substrate is etched in the same tapered fashion so that impedance of the line is still maintained to 50Ω.

The stitching via fence is placed on both side of central trace, shorting the top and bottom ground planes to supress leakage of unwanted modes. In order to further reduce reflections at the transition from microstrip-to-stripline, via fences are placed around the SMA connector closer than other points along the trace [3]. The part of the central trace at the beam interaction hole is called as Faraday Cup. In order to suppress the secondary electron emission, a bias ring can also be provided around the central beam interaction hole to which a negative voltage supply can be connected. To accommodate this ring on the top ground layer, a portion of copper pour is etched and bias trace is insulated from ground plane.

The substrate used is of Teflon class which is preferred for high to ultra-high vacuum conditions. All the microstrip line components are 50Ω, $\lambda_d/4$ line lengths. This is done to ensure that the phase shift experienced by the signal while traversing through the line is between -180 deg. to +180 deg.

Design Formulae

Impedance of planar stripline structure is computed using Eq. (1), (2) [1]:

$$Z_o = \frac{30\pi}{\sqrt{\varepsilon_r}} \frac{b}{W_e + 0.441b}. \tag{1}$$

$$\frac{W_e}{b} = \frac{W}{b} - \begin{cases} 0 & for \frac{W}{b} > 0.35 \\ (0.35 - W/b)^2 & for \frac{W}{b} < 0.35 \end{cases} \tag{2}$$

Where 'W$_e$' is the effective width of central conductor, 'W' is the physical width of central conductor and 'b' is the total height of the substrate. Similarly, impedance based geometry calculations are done for microstrip structure per Eq. (3)-(6).

If (W/H) > 1

$$\varepsilon_{eff} = \frac{\varepsilon_R + 1}{2} + \frac{\varepsilon_R - 1}{2} \left[\frac{1}{\sqrt{1 + 12\left(\frac{H}{W}\right)}} + 0.04\left(1 - \left(\frac{W}{H}\right)\right)^2 \right] \tag{3}$$

$$Z_o = \frac{60}{\sqrt{\varepsilon_{eff}}} lnH\left(8\left(\frac{H}{W}\right) + 0.25\left(\frac{W}{H}\right)\right) \tag{4}$$

If (W/H) > 1

$$\varepsilon_{eff} = \frac{\varepsilon_R + 1}{2} + \left[\frac{\varepsilon_R - 1}{2\sqrt{1 + 12\left(\frac{H}{W}\right)}} \right] \tag{5}$$

$$Z_o = \frac{120\pi}{\sqrt{\varepsilon_{eff}} \left[\frac{W}{H} + 1.393 + \frac{2}{3} ln\left(\frac{W}{H} + 1.444\right) \right]} \tag{6}$$

Figure 3 shows the basic stripline geometry while via-fences. Following considerations are taken into account while designing vias [2-6]:

- Via pitch *'p'* should be randomly varied and is kept less than λ_d $(= c/(\sqrt{\varepsilon_r} f_d))$ to prevent effective RF boundary. Typically less than $\lambda_d/8$, so as to prevent a potential difference between the ground planes leading to a parallel plate mode.
- The via fence-to-fence separation '*s*', should be a minimum 3 to 5 times the strip width.
- If via fence-to-fence separation is too great, a pseudo rectangular waveguide mode can be excited.

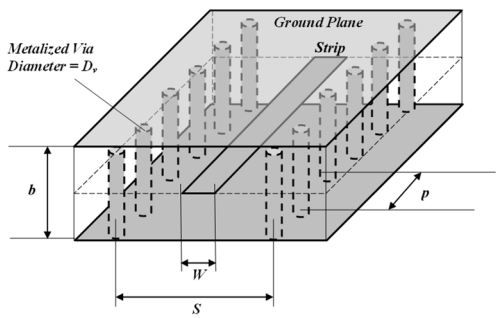

Figure 3: Stripline Structure with Via-Fence.

Mode Suppression

The study in [7] has been extended to the stripline geometry considering that both the ground planes are getting excited by the fringe fields of the central transmission line like a rectangular patch. This rectangular patch now behaves like a parallel plate type of resonant cavity with higher order modes in the absence of via-short. The higher order modes follow the Eq. (7) for determination of cut-off frequency of resulting structure:

$$f_{rmnq} = \frac{c}{2\sqrt{\varepsilon_r}} \sqrt{\left(\frac{m}{L}\right)^2 + \left(\frac{n}{W_g}\right)^2 + \left(\frac{q}{b}\right)^2} \tag{7}$$

Where L, W$_g$, and b represents the length, width and height of the substrate respectively. Eq. (7) can be simplified further due to b << λ_d and can be re-written as:

Content from this work may be used under the terms of the CC BY 3.0 licence (© 2020). Any distribution of this work must maintain attribution to the author(s), title of the work, publisher, and DOI

ISBN: 978-3-95450-222-6 ISSN: 2673-5350 doi:10.18429/JACoW-IBIC2020-THPP21

Content from this work may be used under the terms of the CC BY 3.0 licence (© 2020). Any distribution of this work must maintain attribution to the author(s), title of the work, publisher, and DOI

$$f_{rmn0} = \frac{c}{2\sqrt{\varepsilon_r}}\sqrt{\left(\frac{m}{L}\right)^2 + \left(\frac{n}{W_g}\right)^2} \quad (8)$$

In the Eq. (8), different values of 'm' and 'n' decide the spurious mode that may propagate inside the geometry. Upon the HFSS simulation study for the cases shown in Fig. 4, it is seen that in the absence of via, 3 dB bandwidth is highly restricted to a very low value. However, with the introduction of stitching vias and subsequent variation in the via-fence spacing, the spurious low frequency resonant modes are progressively shifted to higher frequencies thereby increasing the usable 3 dB bandwidth of the resulting device.

Figure 5 (top) shows the plot of Transmission Coefficient (S21) with frequency with and without via whereas in Fig. 5 (bottom), S21 is plotted against frequency for different values of via-fence spacing 's' displaying the bandwidth enhancement with reducing value of 's'.

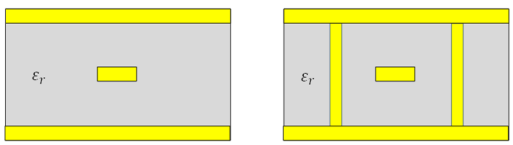

Figure 4: HFSS Design Model for Striplines.

HFSS simulation parameters for the above study are as follows: L = 60.8 mm, W_g = 45 mm, b = 1.6 mm and ε_r = 3.55.

Table 1 shows the list of frequencies as per respective mode for different values of m and n which are obtained from Eq. (8) and the HFSS simulation.

Table 1: Cavity Mode Resonant Frequencies For Stripline Structure Without Via

Mode	Eq. (8)	HFSS results
f_{r110}	2.2 GHz	2.66 GHz
f_{r210}	3.16 GHz	3.55 GHz
f_{r120}	3.73 GHz	3.75 GHz
f_{r310}	4.3 GHz	4.02 GHz
f_{r130}	5.29 GHz	5.365 GHz

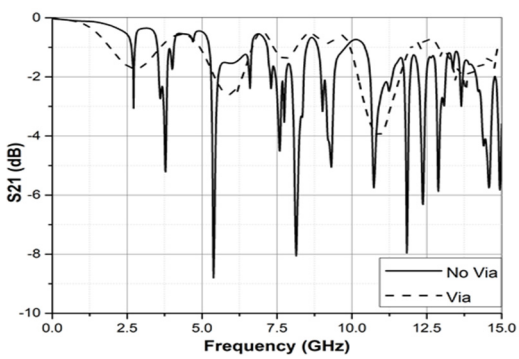

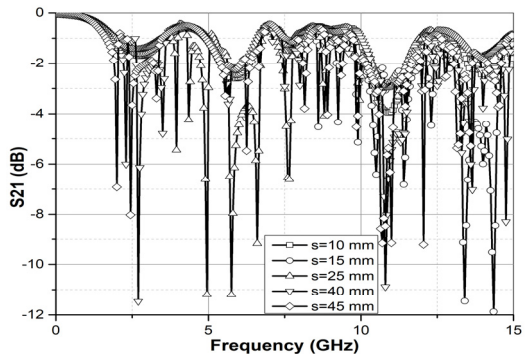

Figure 5: S21 vs Freq. with and without via-fence (top), parametric study with variable via-fence spacing (bottom).

EXPERIMENTAL RESULTS

Design parameters for the proposed design are summarized in Table 2. These are decided after optimized simulation in HFSS. Roger's RO4003C substrate has been used and simulation is performed in driven terminal mode with lumped port and λ_d /4 sized radiation box. The solution frequency of ~10 GHz is used and via pitch is restricted to be $\leq \lambda_d/8$. Figure 6 shows the two types of devices were simulated, i.e. one with bias ring and another without bias ring. Based on the simulations, fabrication is done. Since device is to be made vacuum compatible, two stitched substrates are further sealed by providing a copper sealant at the edges to avoid any air-gap.

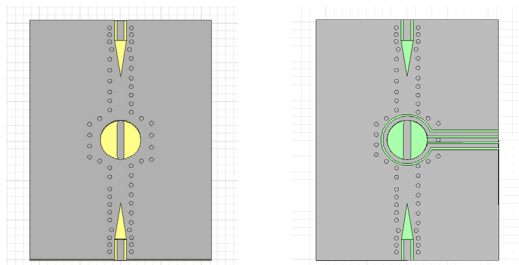

Figure 6: Proposed Stripline FFC design in HFSS.

Table 2: Stripline FFC EM Design Parameters

Parameter	Value
Substrate	RO4003C
Substrate 1 Dimension *(w × l × h)*	45 mm × 60.8 mm × 0.8 mm
Substrate 2 Dimension *(w × l × h)*	45 mm × 60.8 mm × 0.8 mm
Dielectric constant ε_r	3.55
Strip Width	0.7753 mm [50Ω]
Microstrip width	1.804 mm [50Ω]
Via Size (dia.)	1 mm
Via Pitch	≤ 1 mm
Via fence spacing	5.3 mm
Beam Interaction Hole (dia.)	10 mm (upper substrate)

Further, Fig. 7 (top) shows the finished device which is tested on a 6 GHz VNA which is a ZVL series device from Rohde & Schwarz. Figure 7 (bottom) shows the

ISBN: 978-3-95450-222-6 ISSN: 2673-5350 doi:10.18429/JACoW-IBIC2020-THPP21

device under test and Fig. 8 shows the comparison of simulation and measured results.

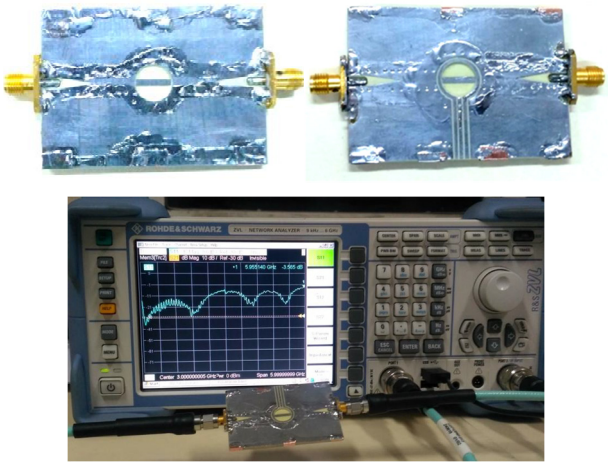

Figure 7: Fabricated Stripline FFC without and with bias ring (top), Measurement Setup (bottom).

The fabricated stripline devices are observed to be useful for a bandwidth of ~ 6 GHz (due to VNA bandwidth limitation) as shown in Fig. 8 where it maintains |S21| < ~3 dB thereby making the device useful to handle beam bunches with a rise time of <~60 ps. However, simulations have shown the bandwidth > 10 GHz.

Some abrupt discontinuities are observed due to co-placement of bias ring which is absent in design without bias.

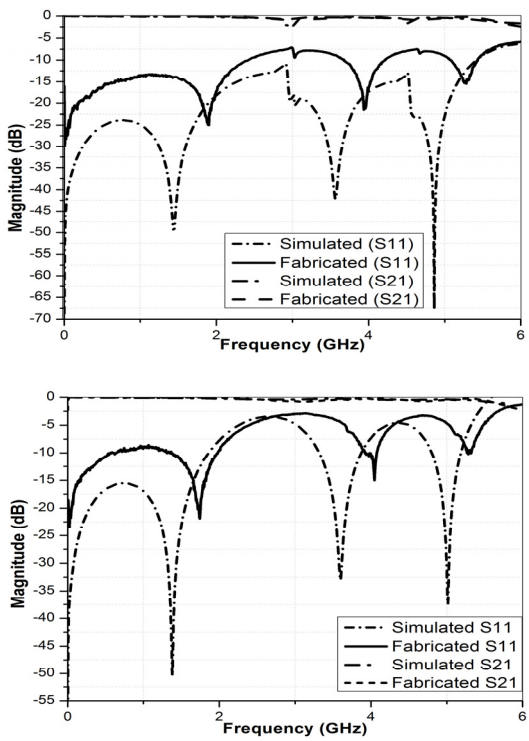

Figure 8: Comparison of Simulated and Measured results FFC with bias ring (top), FFC without bias ring (bottom).

CONCLUSION

Proposed devices are found suitable to measure the ion beam bunch widths of the order of 200 ps to 1 ns out of the IUAC Pelletron, HCI and Linear accelerator. The devices are ready to be mounted on the beam line to perform the measurement.

ACKNOWLEDGEMENTS

Authors would like to acknowledge Dr. S. Ghosh, Prof. A.C. Pandey, and Prof. R. Shekhar to allow them to undertake the study jointly along with usage of resources at IUAC and IIT (ISM).

REFERENCES

[1] *A Designer's Guide to Stripline Circuits*, Microwaves, January 1978, pp. 90–96.
http://www.ece.ualberta.ca/~rambabu/EE470/class_25s.pdf

[2] C. E. Deibele, "Fast Faraday Cup with High Bandwidth", US Patent no. 7012419B2, March 26, 2004.

[3] G. Zhu *et al.*, "Development of bunch shape monitor for high-intensity beam on the China ADS proton LINAC Injector II", *Review of Scientific Instruments*, vol. 89, p. 053303, 2018.

[4] E. Holzman, *Essentials of RF and Microwave Grounding*, Artech House.

[5] J. Gipprich and D. Stevens, "A New Via Fence Structure for Crosstalk Reduction in High Density Stripline Packages", *IEEE MTT-S IMS Digest*, vol. 3, pp 1719-1722, 2001.

[6] G.E. Ponchak, D. Chen, J-G Yook, L.P.B. Katehi, "Characterization of Plated Via Hole Fences for Isolation Between Stripline Circuits in LTCC Packages", *IEEE MTT-S IMS Digest*, vol. 3, 1998.

[7] A. Sain, K.L. Melde, "Impact of Ground via Placement in Grounded Coplanar Waveguide Interconnects", *IEEE Tran. On Components, Packaging And Manufacturing Technology*, vol. 6, no. 1, pp. 136-144, January 2016.

[8] T. Maleszka, G. Jaworski, "Broadband stripline to microstripline transition with constant impedance field matching section for applications in multilayer planar technologies," *18th Int. Conf. on Microwaves, Radar and Wireless Comm.*, Vilinius, 2010, pp 1-4.

Content from this work may be used under the terms of the CC BY 3.0 licence (© 2020). Any distribution of this work must maintain attribution to the author(s), title of the work, publisher, and DOI

ISBN: 978-3-95450-222-6 ISSN: 2673-5350 doi:10.18429/JACoW-IBIC2020-THPP22

Content from this work may be used under the terms of the CC BY 3.0 licence (© 2020). Any distribution of this work must maintain attribution to the author(s), title of the work, publisher, and DOI

A THz-DRIVEN SPLIT RING RESONATOR FOR TEMPORAL CHARACTERIZATION OF FEMTOSECOND MeV ELECTRON BEAM*

Y. Song†, K. Fan, Huazhong University of Science and Technology, Wuhan, China

Abstract

The use of THz-driven split ring resonator (SRR) as a streak camera for sub-ps bunch length measurement has been proposed for a few years. Since then, the feasibility of such a method has been experimentally demonstrated for both keV and MeV electron beam. The structural dimensions of SRR has a substantial impact on the resonance frequency, the field enhancement factor and the interaction region of the streaking field, eventually determining the temporal resolution of the bunch length measurement. Here we discuss the quantitative dependence of the streaking field on the structural dimensions of SRR. Combining with an analytical streaking model, we propose a method to optimize the structural dimensions of SRR such that the finest temporal resolution is achieved with given THz pulse.

INTRODUCTION

In the past decade, the femtosecond-level electron beam and its applications have become one of the main interests in the accelerator field. Such an electron beam is essential in many applications, such as ultrafast electron diffraction (UED) [1,2], self-amplified spontaneous emission free-electron laser (FEL) [3] and laser-plasma wakefield accelerators [4].

By using few MeV electron beam and RF compressor, electron bunch with sub-10 fs duration has been achieved [5], which pushes the requirement for the resolution of temporal characterization towards a single fs level. To data, such temporal resolution can be realized via RF deflector [5, 6]. However, the timing jitter between the RF source and laser system is at a few tens fs level which mean the uncertainty between the streak field and arrival time of the electron beam is about few tens fs. This limits the accuracy for time-of-arrival (TOA) characterization, which is very important for experiments like UED.

To provide a sub-10 fs temporal resolution for bunch length measurement and TOA characterization accuracy, a streak camera based on THz-driven split-ring resonator (SRR) is proposed a few years ago [7].

SRR is a sub-wavelength structure that focuses the incident THz radiation into the gap region, and the enhanced streaking field thus emerges in the gap. The streaking field provided by SRR is potentially up to GV/m level [8] and the frequency is about two orders higher than the RF deflector. Moreover, since the THz radiation is originated from the laser system, the streaking field is tightly synchronized to the laser system. Successful temporal characterization experiments have been demonstrated for both keV [9] and MeV [10-12] electron beam. The experiment results indicate that SRR can provide sub-10 fs temporal resolution for bunch length measurement and sub-fs accuracy for TOA determination.

In this paper, we discuss the optimization of the geometric dimension of a square SRR. The goal of optimization is to obtain the highest streak velocity, and thus the finest temporal resolution. We first present the definition of the temporal resolution and its dependence on the parameters of SRR. Then, we use CST Microwave Studio to calculate the relevant parameters to determine the temporal resolution and therefore perform the optimization.

TEMPORAL RESOLUTION

We first define the passing time $T_p=h/\beta c$ where h is the length of the SRR gap in z-direction (see Fig. 1). β is the normalized velocity, which is about 1 for a few MeV electron beam. ΔT denotes the full-width bunch length of electron beam. The period of the streaking field is defined as T. The resonance frequency of SRR is generally below 1 THz and the electron bunch length we measure is in the fs-level. We can assume that $\Delta T \ll T$.

Consider an electron with longitudinal position ζ where ζ=0 corresponds to the bunch center and ζ=±ΔT/2 the bunch head and tail. The transverse kick of such electron after passing through the SRR gap is

$$\begin{aligned}\Delta P_y(\zeta) &= -e\int_{\zeta-T_p/2}^{\zeta+T_p/2}\bar{E}_y\sin(\omega t+\varphi_0)\,dt \\ &= \frac{-2e\bar{E}_y}{\omega}\sin\left(\frac{\omega}{2}T_p\right)\sin(\omega\zeta+\varphi_0) \\ &\approx -2e\bar{E}_y\sin\left(\frac{\omega}{2}T_p\right)\left[\frac{1}{\omega}\sin\varphi_0-\cos\varphi_0\zeta\right],\end{aligned} \tag{1}$$

where φ_0 is the phase between the electron beam and the streaking field and $\omega=2\pi f_0$ is the angular resonance frequency. Note that we use the assumption $\Delta T \ll T$. $\bar{E}_y$ is the equivalent streak field whose expression is

$$\bar{E}_y = \frac{\omega}{2}\frac{\int_{-\infty}^{+\infty}A(\beta ct)\cos(\omega t)\,dt}{\sin(\omega T_p/2)}E_{\max}, \tag{2}$$

where $A(\beta ct)$ is the normalized profile of the on-axis streaking field (see Fig. 2 for an example) and $E_{\max}$ is the amplitude of the peak streaking field.

The trajectory angle of an electron after the SRR is $\Delta P_y/P$ and thus we define the streaking velocity ω_s is

$$\omega_s = \frac{\left|\Delta P_y(\Delta T/2)-\Delta P_y(-\Delta T/2)\right|}{P\Delta T} = \frac{2e\bar{E}_y}{P}\sin\left(\frac{\omega}{2}T_p\right).$$

Therefore, the temporal resolution of the SRR is

$$\tau_s = \frac{\sigma_{y'0}}{\omega_s} = \frac{\sigma_{y'0}P}{2e\bar{E}_y\sin(\omega T_p/2)}, \tag{3}$$

* Work supported by the National Natural Science Foundation of China (NSFC) 11728508
† kjfan@hust.edu.cn

ISBN: 978-3-95450-222-6 ISSN: 2673-5350 doi:10.18429/JACoW-IBIC2020-THPP22

where $\sigma_{y'0}$ is the unstreaked rms divergence. Combining Eq. (2) and Eq. (3), we have

$$\tau_s \propto \frac{1}{\omega E_{\max}\int_{-\infty}^{\infty} A(\beta ct)\cos(\omega t)\,dt}. \quad (4)$$

Equation (4) indicates that the temporal resolution of SRR is determined by the resonance frequency f_0, the peak streaking field E_{max} and the length of the interaction region. For a given material, the resonance frequency is the function of the dimensions of SRR. The peak streaking field can be expressed as $E_{max}=C_{enh}E_{THz}$ where E_{THz} is the driving field strength and C_{enh} is the field enhancement factor (see Fig. 3). For a given laser system, the upper limit for E_{THz} is fixed while the dimensions of SRR determine the field enhancement factor. Note the integral term in Eq. (4) has a unit of time. The physical meaning of this term is the equivalent interaction time of the streaking process which will be referred as T_e (see Eq. (5)).

$$T_e = \int_{-\infty}^{\infty} A(\beta ct)\cos(2\pi f_0 t)\,dt \quad (5)$$

We denote a parameter F as a product of the resonance frequency, the field enhancement factor and the equivalent interaction time, as shown in Eq. (6). The parameter F can be regarded as an alternative measure for ω_s and the temporal resolution. F has a unit of 1, which means it can be used as an absolute measure for the streaking performance.

$$F = f_0 C_{enh} T_e \quad (6)$$

STRUCTURAL OPTIMIZATION

Square SRR Model

The square SRR model we use for structural optimization is shown in Fig. 1. Here we use four dimensions (l, h, g, w) to describe a square SRR. The material of this SRR is copper.

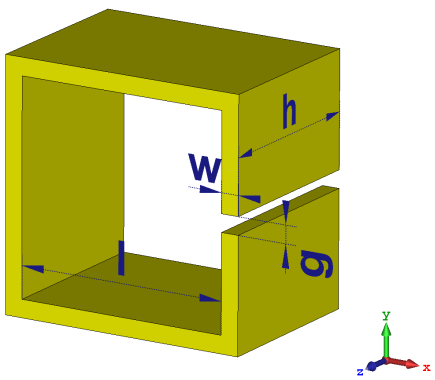

Figure 1: The dimensions of a square SRR.

The parameter l has the most impact on the resonance frequency that scales inversely with l. Moreover, the field enhancement factor is positively correlated to the ratio l/g, which increases with l. The parameter h determines the interaction region of SRR, and thus, $A(z)$. Figure 2 shows the field profile A(z) of an SRR with h=100 μm for example.

The parameter g and w also affect the streaking performance of SRR. A smaller g and w will increase the field enhancement factor significantly. However, there is a practical consideration for the acceptance of an electron beam. In this work, we set g=w=10 μm to allow fC level bunch charge to pass.

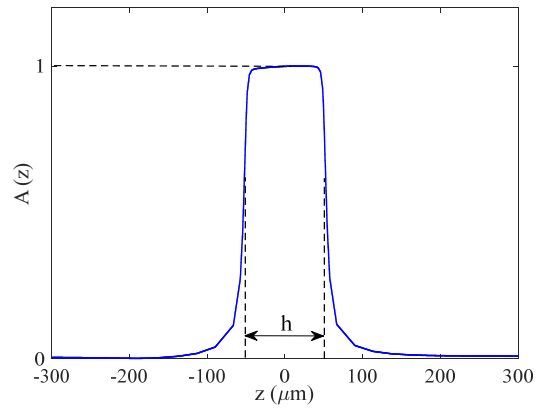

Figure 2: The normalized profile of the streaking field. The dimensions of the square SRR for are l=100 μm, h=100 μm, g=10 μm and w=10 μm.

To obtain the field enhancement factor C_{enh}, the THz driving field is set to 1 V/m. As we can see from Fig. 3, the field enhancement factor of this SRR is 12.455. Note that the magnetic field in the gap region is negligible compared to the electric field. Therefore, the contribution of the magnetic field will be neglected in this work.

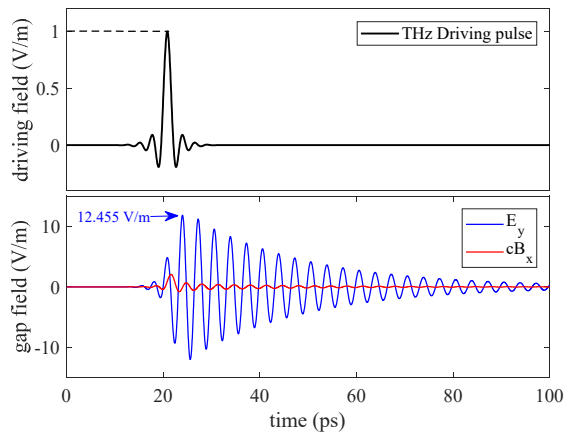

Figure 3: The THz driving field and induced gap field as functions of time. The dimensions for this SRR model are l=100 μm, h=100 μm, g=10 μm and w=10 μm.

Simulation Results

We first scan the parameter l while other dimensions are fixed at h=100 μm, g=10 μm and w=10 μm. Figure 4 shows the quantitative dependence of resonance frequency on l. The resonance frequency drops as we enlarge the SRR. The dependence of the field enhancement factor on l is more complicated as can be seen from Fig. 5. The streak field in the gap region has both the oscillating behavior and decaying behavior (see Fig. 3). Figure 5 shows thata the field enhancement factor increases with l in general. However, due to the combination of the oscillating and decaying behavior, the dependence of field enhancement factor on l is not a smooth curve.

Content from this work may be used under the terms of the CC BY 3.0 licence (© 2020). Any distribution of this work must maintain attribution to the author(s), title of the work, publisher, and DOI

ISBN: 978-3-95450-222-6 ISSN: 2673-5350 doi:10.18429/JACoW-IBIC2020-THPP22

Content from this work may be used under the terms of the CC BY 3.0 licence (© 2020). Any distribution of this work must maintain attribution to the author(s), title of the work, publisher, and DOI

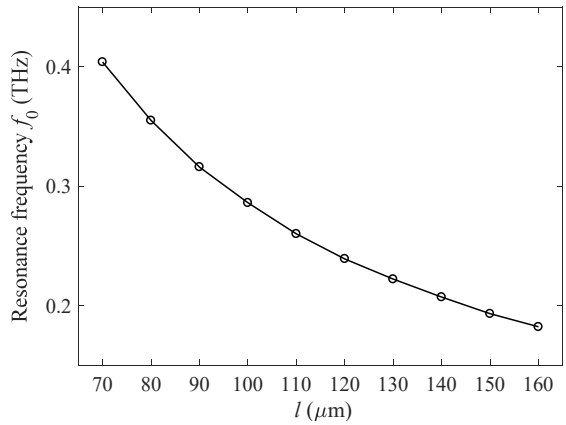

Figure 4: The resonance frequency as a function of *l*.

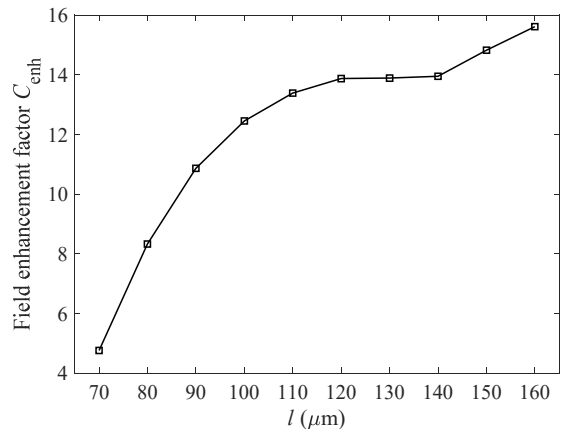

Figure 5: The field enhancement factor as a function of *l*.

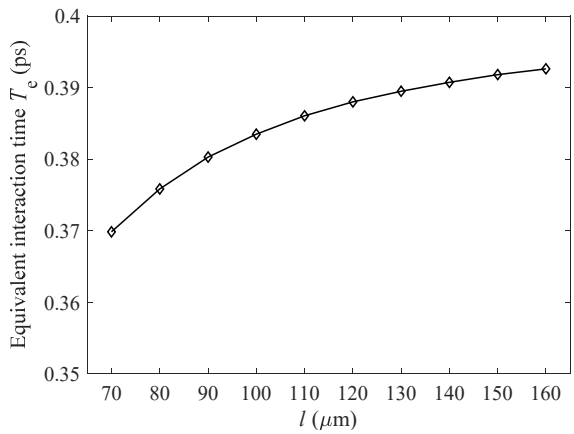

Figure 6: The equivalent interaction time as a function of *l*.

Figure 6 shows the *l* has little impact on the equivalent interaction time. This is expected since *l* only affects the resonance frequency and has no influence on the length of the interaction region. In Fig. 7, we show the production of all three parameters. As we can see, the highest *F* is obtained at *l*=100 μm which corresponds to the highest streak velocity and thus the smallest temporal resolution.

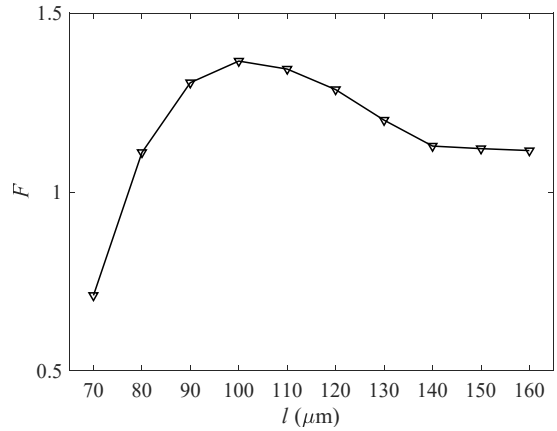

Figure 7: The parameter *F* as a function of *l*.

Next, we scan the parameter *h*. Other dimensions of the SRR are fixed at *l*=100 μm, *g*=10 μm, and *w*=10 μm. In Fig. 8-10, we show the dependence of resonance frequency, field enhancement factor, and equivalent interaction time on *h*. As we can see, a larger *h* results in a longer the equivalent interaction time since it expands the interaction region. However, both the resonance frequency and field enhancement factor drop as we increase *h*. Such character of the square SRR indicates an optimal *h* may exists. The dependence of *F h* is shown in Fig. 11. As we can see, the optimal *h* is about 300 μm which increases the streak velocity about two times comparing to *h*=100 μm.

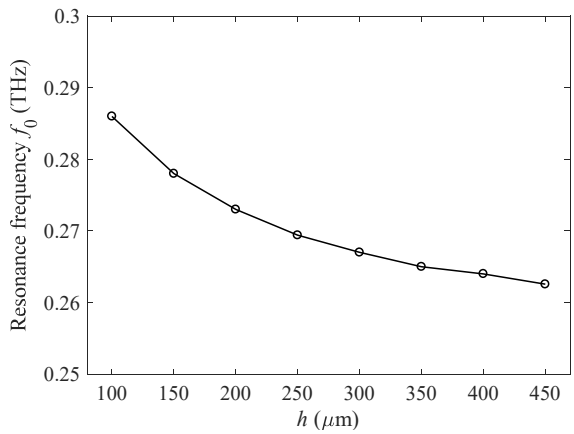

Figure 8: The resonance frequency as a function of *h*.

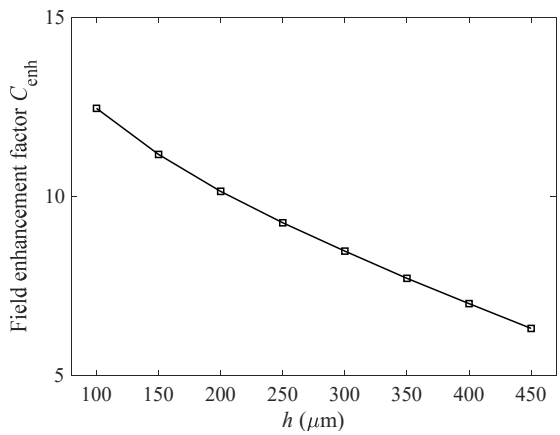

Figure 9: The field enhancement factor as a function of *h*.

ISBN: 978-3-95450-222-6 ISSN: 2673-5350 doi:10.18429/JACoW-IBIC2020-THPP22

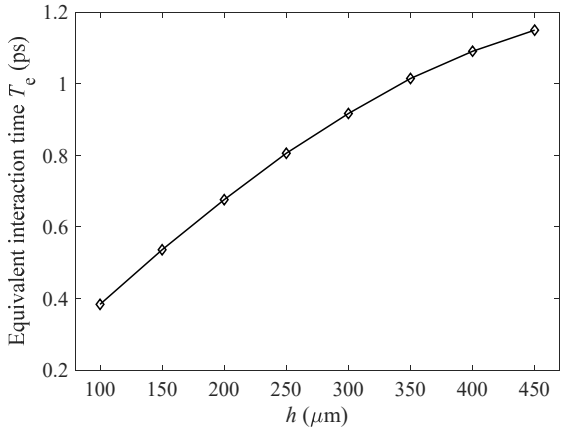

Figure 10: The equivalent interaction time as a function of h.

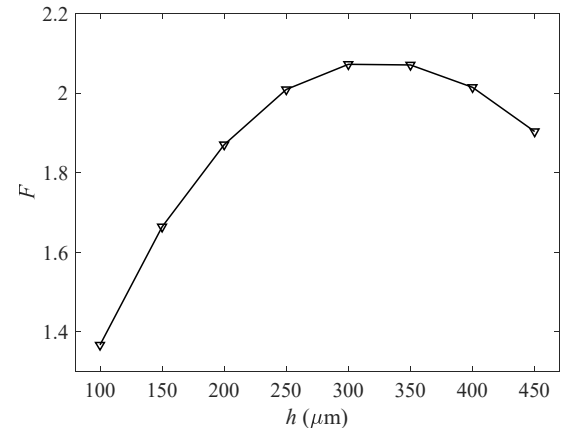

Figure 11: The parameter F as a function of h.

Eventually, we decide the final dimensions for the square SRR is l=100 μm, h=100 μm, g=10 μm and w=10 μm. Here we assume the peak streaking field is 50 MV/m and the unstreaked rms divergence is 50 μrad, which are both practical according to recent experiment [10-12]. In this case, the temporal resolution calculated by Eq. (3) is about 6.15 fs. With improved efficiency in THz generation [13] and higher laser power, it is possible to increase the peak streak field to 500 MV/m level and reach a sub-fs temporal resolution.

SUMMARY AND CONCLUSION

In this paper we study the dependence of streaking performance of a square SRR on its dimensions. By analytically deriving the expression for temporal resolution, we demonstrate that the temporal resolution of SRR is inversely proportional to three parameters which are the resonance frequency, field enhancement factor and the equivalent interaction time. The quantitative dependence of these three parameters on SRR dimensions is studied via CST simulation.

We focus on the l and h dimension of SRR. They decide the transverse and longitudinal size of the SRR. We find that SRR with larger l has a larger field enhancement factor while the resonance frequency is smaller. This property indicates that an optimal l exists that produces the smallest temporal resolution. Meanwhile, if we increase h, the equivalent interaction time increases as well, but the resonance frequency and field enhancement factor both drop. Again, an optimal h is found to obtain the smallest temporal resolution. With the optimized dimension, the square SRR can provide sub-10 fs temporal resolution with 50 MV/m peak streak field.

Note that the optimization algorithm is preliminary which is used to reveal the dependence of streak performance on the SRR dimensions. A multi-dimensional single-objective optimization algorithm is required to realize a full and accurate optimization.

REFERENCES

[1] R. J. D. Miller, "Femtosecond crystallography with ultrabright electrons and x-rays: Capturing chemistry in action", *Science*, vol. 343, p. 1108-1116, 2014.

[2] G. Sciaini and R. Miller, "Femtosecond Electron Diffraction: Heralding the Era of Atomically Resolved Dynamics", *Rep. Prog. Phys*., vol. 74, p. 96101-96136, 2011.

[3] I. Grgura *et al*., "Ultrafast X-ray pulse characterization at free-electron lasers", *Nature Photonics*, vol. 6, p. 852-857, 2012.

[4] J. Faure, et al., "Controlled injection and acceleration of electrons in plasma wakefields by colliding laser pulses". *Nature* vol. 444, p. 737-739, 2006.

[5] J. Maxson, *et al*., "Direct Measurement of Sub-10 fs Relativistic Electron Beams with Ultralow Emittance". *Phys. Rev. Lett.*, vol. 118, p. 154802, 2017.

[6] S. Park, *et al*., "Measurement of low-energy and low-charge ultrashort bunches using an S-band RF deflector", *Nuclear instruments and methods in physics research*, vol. 927, p. 194-201, 2019.

[7] J. Fabiańska, *et al*., "Split ring resonator based THz-driven electron streak camera featuring femtosecond resolution", *Scientific Reports*, vol. 4, p. 5645, 2014.

[8] H. Merbold, *et al*., "Near field enhancement for THz switching and THz nonlinear spectroscopy applications", *CHIMIA International Journal for Chemistry*, vol. 65, p. 316-319, 2011.

[9] C. Kealhofer, *et al*., "All-optical control and metrology of electron pulses". *Science*, vol. 352, p. 429, 2016.

[10] L. Zhao, et al., "Terahertz streaking of few-femtosecond relativistic electron beams", *Physical Review X*, vol. 8, p. 021061, 2018.

[11] R. Li, *et al*., "Terahertz-based subfemtosecond metrology of relativistic electron beams", *Physical Review Accelerators and Beams*, vol. 22, 2019

[12] X. L. Shen, *et al*., "A THz driven split-ring resonator based ultrafast relativistic electron streak camera", *AIP advances*, vol. 9, p. 085209, 2019.

[13] J. A. Fülöp, *et al*., "Efficient generation of THz pulses with 0.4 mJ energy". *Optics Express*, vol. 22, p. 020155, 2014.

Content from this work may be used under the terms of the CC BY 3.0 licence (© 2020). Any distribution of this work must maintain attribution to the author(s), title of the work, publisher, and DOI

ISBN: 978-3-95450-222-6 ISSN: 2673-5350 doi:10.18429/JACoW-IBIC2020-THPP23

TRACKING FREQUENCY REFERENCE PHASE CHANGES AT POINT OF USE BASED ON BPM MEASUREMENTS

A. Tipper*, M. G. Abbott, G. Rehm†, Diamond Light Source, Oxfordshire, UK

Abstract

Multibunch Feedback systems in Diamond use the RF reference signal to homodyne downconvert the 3rd harmonic of BPM signals and sample the detected output. Uncertain reference phase variations due to upstream adjustments to the RF system previously necessitated regular manual realignment of the reference phase. Implementation of a local carrier recovery and symbol synchronizer at the BPM output by locking the local reference phase to the measured beam phase has been shown to significantly improve the stability and robustness of the system and remove the dependence on absolute RF phase. The system has been successfully deployed on the storage ring at Diamond and has been operating live since October 2019.

INTRODUCTION

The Diamond Multibunch Feedback (MBF) system [1] uses the Libera Bunch by Bunch Front End to provide a 1.5 GHz local oscillator for homodyne detection of the Beam Position Monitor (BPM) signal and a 500 MHz sampling clock as shown in Fig. 1. An IQ mixer is constructed using phase shifters and balanced mixers within the front end to enable measurement of the relative phase of BPM and reference. During operation the adjustment of the RF subsystems cause significant deviations in the measured phase requiring regular manual realignment of the phases within the front end. The variation over 9 months operation is shown in Fig. 2 which shows multiple step changes in the reference phase due to machine adjustments and the subsequent manual realignments. The data indicates a mean time between rephasing of 20 days. To improve this situation a project to investigate beam locked carrier recovery loops at Diamond, internally known as "Doris", was initiated based on Fig. 3 to lock the phase of the MBF clock to the beam.

In order to phase align the 500 MHz reference clock to the clock component in a BPM output a number of possible architectures were examined including

1. Phase locked loop
2. Analogue Delay locked loop
3. Digital IQ Beam locked loop (BLL)

Option (1) adds unwanted phase noise and suffers from nonlinear phase detection issues due to the use of balanced mixers as high frequency phase detectors. Full 360° phase tracking may be difficult to guarantee. Option (2) cannot guarantee continuous phase tracking due to the finite delay achievable whereas option (3) has full 360° linear phase detection and tracking with low additive phase noise. The use of IQ modulators and demodulators for phase detection

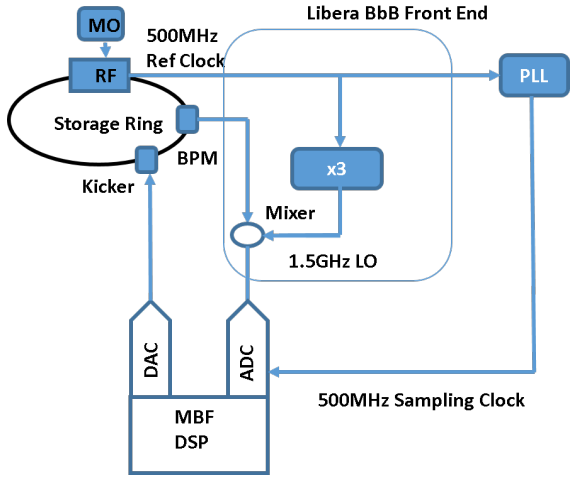

Figure 1: Original architecture.

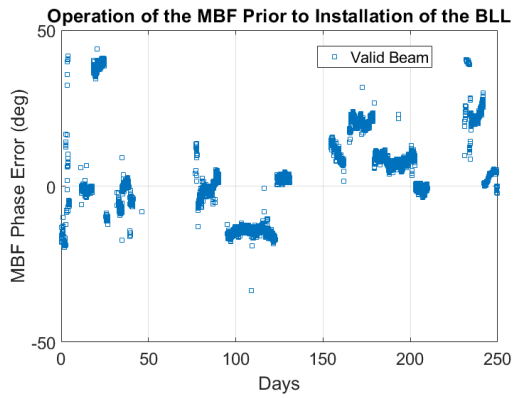

Figure 2: Measured phase variation over 9 months.

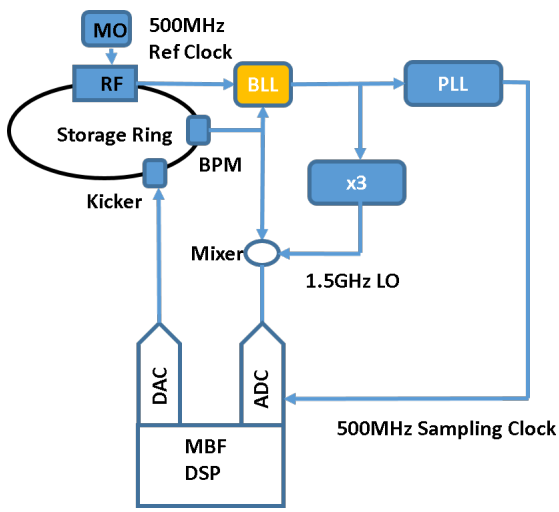

Figure 3: Improved architecture.

* alan.tipper@diamond.ac.uk
† Now at HZB, Berlin, Germany

Content from this work may be used under the terms of the CC BY 3.0 licence (© 2020). Any distribution of this work must maintain attribution to the author(s), title of the work, publisher, and DOI

ISBN: 978-3-95450-222-6 ISSN: 2673-5350 doi:10.18429/JACoW-IBIC2020-THPP23

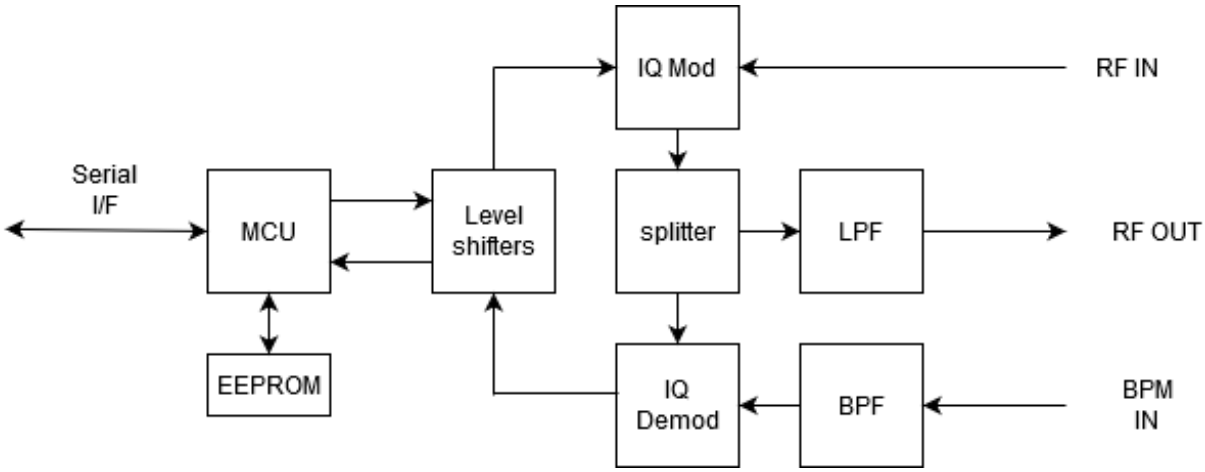

Figure 4: Block diagram of the beam locked loop.

and phase shifting is well established [2]. Option (3) was chosen and the block diagram of the Beam Locked loop is shown in Fig. 4.

DESCRIPTION

The RF reference input is connected to an IQ modulator operated as a voltage controlled phase shifter. By applying a constant modulus dc input to the I and Q inputs from a pair of Digital to Analogue Converters (DACs) any phase shift can be achieved. The modulator is realised as a polyphase shifter followed by two analogue multipliers and a summing network. The output of the modulator is split between a feedback path and an output. The output is further filtered by a low pass filter (LPF) to suppress harmonic distortion from the modulator. The BPM input is buffered by a broadband low noise amplifier and a LPF + Automatic gain Control (AGC) amplifier to generate a constant amplitude signal and to provide a good RF input match up to at least 3 GHz. The signal is then band pass filtered using a Surface Acoustic Wave (SAW) filter to extract the reference clock component and passed through a high gain limiting amplifier to provide the local oscillator drive to an IQ demodulator.

For the feedback path the IQ demodulator splits the filtered BPM signal into in phase and quadrature components again using a polyphase splitter and the resulting signals are multiplied by the modulator output to yield an I and Q output. In this configuration the IQ demodulator functions as a full 360° range phase detector. The demodulator I and Q differential outputs are converted to single ended and low pass filtered before being sampled by a pair of Analogue to Digital Converters (ADCs). Multiple samples are taken and averaged yielding an IQ digital signal updated every 10 ms.

The IQ data is processed in an ARM Cortex M4 microcontroller (MCU) to generate a phase feedback signal using a floating point arctan function which is subtracted from the set point value to yield a phase error. The phase error is passed to a discrete time PID controller to drive the phase error to zero. If no BPM signal is present the PID is maintained at its previous value and the modulator is held in a phase holdover mode.

The output of the PID element drives a polar to rectangular converter (floating point sin and cos functions) to yield I and Q values to set the DACs. PID parameters, ADC averaging, phase set point and open/closed loop operation can be managed via a serial RS232 management interface to the EPICS system.

The control firmware was written in bare metal (no operating system) C and a simple cooperative scheduler based on a superloop was implemented to provide basic multitasking for real time control, serial management and general housekeeping. All of the hardware was mounted in a self contained 1U shelf for integration with the multibunch feedback system.

CLOSED LOOP DYNAMICS

The feedback loop implemented a PID structure in floating point software. The full closed loop path is shown in Fig. 5. The Output phase θ_{out} is related to the filtered beam phase θ_f and the RF reference input phase θ_{in} as detailed below.

$$\theta_{out} = \frac{\theta_{in}}{1 + \mathrm{tf}} + (\theta_f + setpoint)\frac{\mathrm{tf}}{1 + \mathrm{tf}} \quad (1)$$

where

$$\mathrm{tf} = \frac{(k_i + k_p + k_d) - (k_p + 2k_d)z^{-1} + k_d z^{-2}}{1 - z^{-1}} \cdot H(z) \quad (2)$$

$$H(z) = Z\left[\frac{1}{s}\frac{\theta}{\theta_{dac}}\right] \cdot (1 - z^{-1}) \quad (3)$$

$Z[u]$ is the z transform of $u(s)$ and tf is the open loop transfer function. The setpoint, k_p,k_i and k_d parameters are user programmable tuning values.

$H(z)$ models the effects of analogue filtering and zero order hold in the DAC. For this application these effects are small as we are targeting low bandwidths in the 1–10 Hz region whilst sampling at 100 Hz and with a filtering cut off

Content from this work may be used under the terms of the CC BY 3.0 licence (© 2020). Any distribution of this work must maintain attribution to the author(s), title of the work, publisher, and DOI

ISBN: 978-3-95450-222-6 ISSN: 2673-5350 doi:10.18429/JACoW-IBIC2020-THPP23

Content from this work may be used under the terms of the CC BY 3.0 licence (© 2020). Any distribution of this work must maintain attribution to the author(s), title of the work, publisher, and DOI

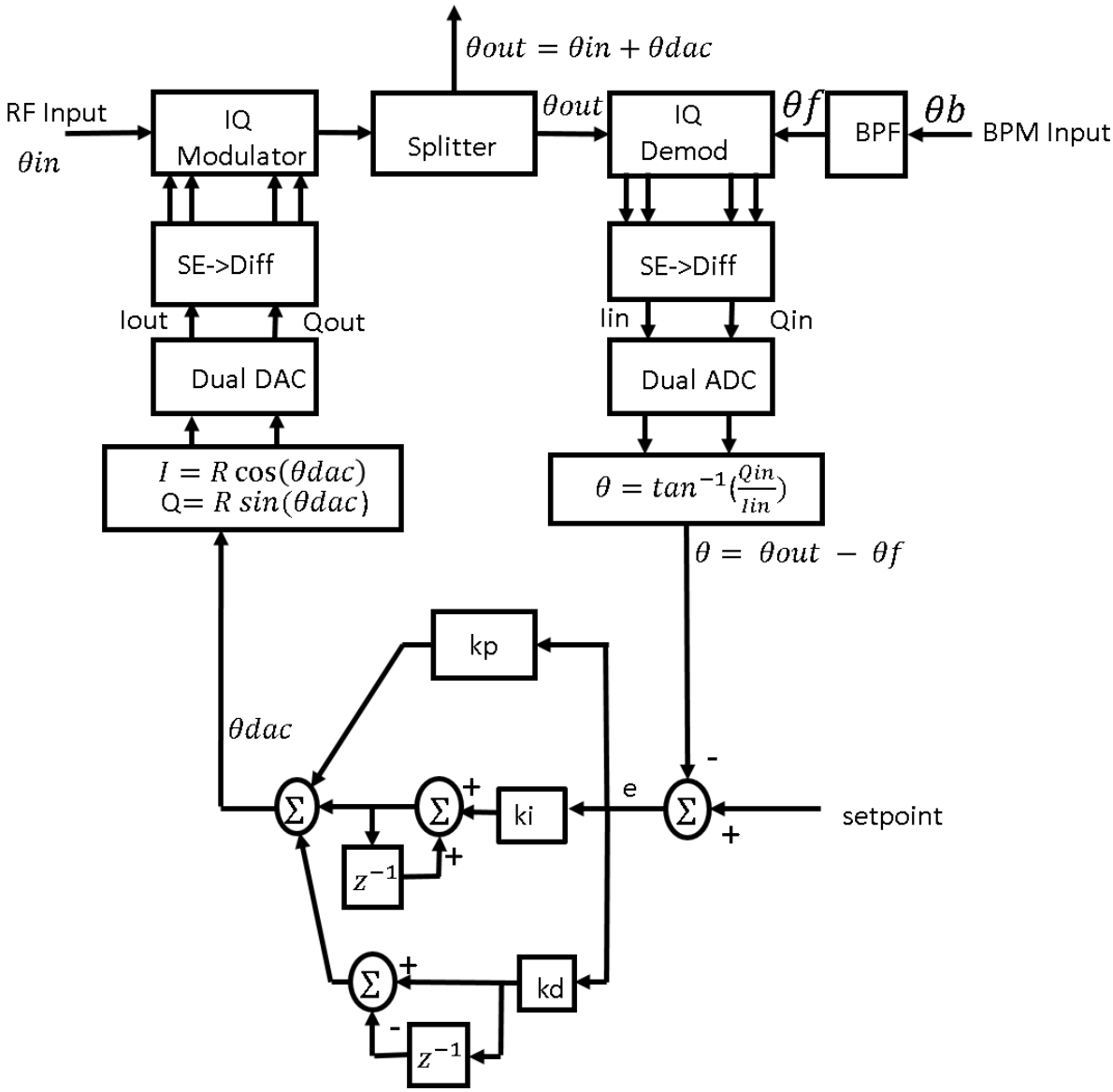

Figure 5: Feedback control loop.

at 300 Hz. Furthermore with no dominant analogue pole the dynamics can be controlled with a simple 1st order integrator i.e $k_p = k_d = 0.0$ in this case equation 3 reduces to:

$$\mathrm{tf} = \frac{k_i}{1 - z^{-1}} \tag{4}$$

which for $k_i = 0.5$ corresponds to a −3 dB closed loop bandwidth of 8 Hz and a 99% settling time of 100 ms.With these settings the loop provides a low pass response to the BPM phase and a high pass response to the RF input phase, both cutting off at 8 Hz.

OPERATION

The prototype hardware has been operating in the Diamond storage ring since October 2019. Closed loop phase error data measured at the ADC inputs was collected over EPICS using the serial interface every 30 seconds for 29 hours and shows a 0.21 ps rms output jitter as shown in Fig. 6. The variation of phase error with beam current is shown in Fig. 7 showing less than 5° error at low beam current and effective locking at all currents above 1 mA. The variation of phase with beam current is due to residual amplitude to phase conversion in the AGC amplifier prior to the SAW filter.

The plot of long term closed loop phase alignment, measured using an independent IQ phase detector, over 12 months is shown in Fig. 8. Prior to Oct 2019 the reference phase was subject to large shifts during operational adjustments of the RF system periodically corrected by manual phase realignment.After this date the beam locked hardware was fully operational and the measured phase has remained stable since that time. The vertical transients in the figure are beam loss events.

ISBN: 978-3-95450-222-6 ISSN: 2673-5350 doi:10.18429/JACoW-IBIC2020-THPP23

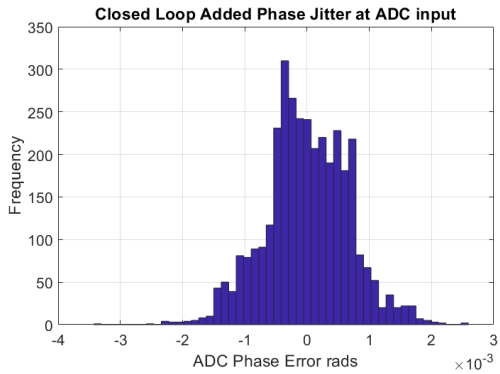

Figure 6: Measured added jitter at 300 mA beam current.

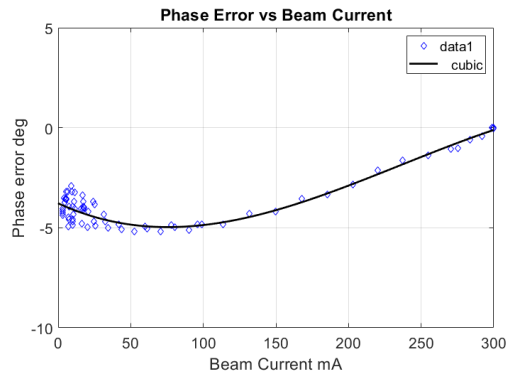

Figure 7: Measured phase error variation with beam current.

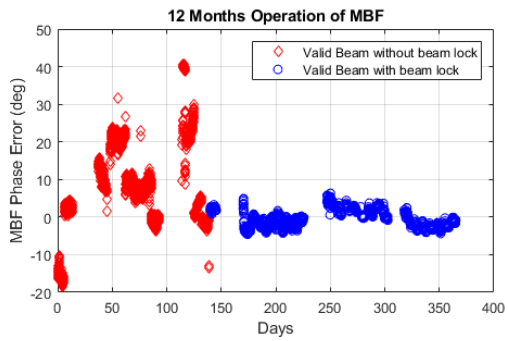

Figure 8: Measured phase alignment over 12 months storage ring operation.

CONCLUSIONS

A carrier recovery and clock synchronisation system phase locking the 500 MHz reference frequency to a local BPM signal with operating beam current range of 1 to 300 mA has been designed and trialled on the Diamond Synchrotron. With a closed loop bandwidth of 8 Hz the design fully tracks slow phase movements in the BPM phase with low additive phase noise. Whereas previously the phase alignment would be necessary every 20 days the system now runs without intervention and has so far operated for over 220 days without significant phase shifts. Several prototypes have been built and evaluated. One unit has been installed in the storage ring to provide the timing clock to the TMBF system. The serial management interface has been demonstrated with the EPICS control system to allow complete remote management of the installed hardware.

ACKNOWLEDGEMENTS

The authors would like to thank Eric Plouviez for sharing the concept of an analogue beam locked loop in use at the ESRF.

REFERENCES

[1] M. G. Abbott, G. Rehm, and I. S. Uzun, "A new transverse and longitudinal bunch by bunch feedback processor" in *Proc. 16th Int. Conf. on Accelerator and Large Experimental Control Systems (ICALEPCS'17)*, Barcelona, Spain, Oct. 2017, pp. 1649–1654. doi:10.18429/JACoW-ICALEPCS2017-THPHA115

[2] M. Gaspar, C. Gough, and M. Mailand, "Phase shifter and IQ demodulator" presented at the 7th European Synchrotron Light Source RF Meeting, Oct. 2003, CELLS-ALBA, Barcelona, Spain.

Content from this work may be used under the terms of the CC BY 3.0 licence (© 2020). Any distribution of this work must maintain attribution to the author(s), title of the work, publisher, and DOI

ISBN: 978-3-95450-222-6 ISSN: 2673-5350 doi:10.18429/JACoW-IBIC2020-THPP25

Content from this work may be used under the terms of the CC BY 3.0 licence (© 2020). Any distribution of this work must maintain attribution to the author(s), title of the work, publisher, and DOI

MEASUREMENTS OF ION INSTABILITY AND EMITTANCE GROWTH FOR THE APS-UPGRADE*

J. Calvey, M. Borland, T. Clute, J. Dooling, L. Emery, J. Gagliano, J. Hoyt,
S. Kallakuri, L. Morrison, U. Wienands, Argonne National Laboratory, Lemont, USA

Abstract

Ions are produced in an accelerator when the beam ionizes residual gas inside the vacuum chamber. If the beam is negatively charged, ions can become trapped in the beam's potential, and their density will increase over time. Trapped ions can cause a variety of undesirable effects, including instability and emittance growth. Because of the challenging emittance and stability requirements of the APS-Upgrade storage ring, ion trapping is a serious concern.

To study this effect at the present APS, a gas injection system was installed. A controlled pressure bump of Nitrogen gas was created over a 6 m straight section, and the resulting ion instability was studied using several different detectors. Measurements were taken using a pinhole camera, spectrum analyzer, bunch-by-bunch feedback system, and a gas bremsstrahlung detector. Studies were done under a wide variety of beam conditions, and at different pressure bump amplitudes. In this paper we report on the results of some of these measurements, and discuss the implications for present and future electron storage rings.

INTRODUCTION

The APS-Upgrade is a 4th-generation light source currently under development at Argonne National Laboratory [1], with a design emittance of 42 pm at 6 GeV. In order to make use of this ultra-low emittance, potential instabilities must be anticipated and mitigated.

One particular source of concern is ion instability. Trapped ions can lead to quickly growing transverse (usually vertical) instability, due to coupled motion between the beam and the ions. The strength of the instability is generally proportional to the average beam current, and inversely proportional to the beam size [2]. Thus ions are particularly dangerous for the APS-U, which will have high current and low emittance. Simulations predict a strong coherent instability for 324 bunch mode, which we plan to mitigate with a compensated gap scheme [3]. But even if the coherent instability is damped, incoherent effects such as emittance growth may still be an issue.

To better understand the ion instability and anticipate issues in the APS-U storage ring, we installed a gas injection system in an empty insertion device (ID) straight section of the present APS storage ring. This enabled us to create a controlled and localized pressure bump, and study the resulting instability. This paper will explain the setup and operation of the gas injection system, describe the instruments used to study the instability, and show the results of some studies we performed.

SYSTEM SETUP

The gas injection system was installed in a spare insertion device straight section in Sector 25 of the APS. Nitrogen gas was chosen for the experiment, for two reasons. First, it was readily available and well understood by vacuum technicians. Second, it is readily pumped by both ion pumps and NEG coating, making the pressure bump easy to localize.

As shown in Fig. 1, the gas injection mechanism was connected to a port on the flange upstream of the spool piece (where the ID would normally be located). The system is operated from the mezzanine above the mechanism. To create a controlled pressure bump, the gas system is first pressurized with ~10 psi of N_2. The leak rate is controlled by two gate valves, operated manually from the mezzanine. Below each gate valve is a pre-set manual leak. Opening valve 5 in Fig. 1 gives a ~100 nTorr bump, while valve 6 gives a ~900 nTorr bump. Using pre-set leaks helps ensure that the amplitude of the pressure bump does not reach the μTorr scale.

A picture of the gas injection system inside the tunnel is shown in Fig. 2. The trident on the upstream end of the spool piece contains both of the pre-set manual leaks, as well as a cold cathode gauge to monitor the pressure inside the system.

The ion pump located next to the gas injection location is disabled for the study. A cold cathode gauge (`SR25:CC1`) was installed on the downstream end of the spool piece, to measure the pressure near the peak of the bump. In order to localize the bump, the other ion pumps indicated in the figure are kept on. The activated NEG coating in the chambers upstream and downstream of the gate valves provide additional pumping.

For the 900 nTorr leak, the ion pump downstream of the system (`25:2IP1`) reads ~200 nTorr, and the next pump downstream (`26:3IP1`) reads ~40 nTorr. Downstream of this, the ion pump `26:2IP2` reads below 10 nTorr. The same result is seen in the upstream direction: ion pump `25:2IP5` reads a little above 100 nTorr, and `25:2IP4` peaks at ~20 nTorr. Thus the pressure pump is essentially contained in the ~6 m between 25:2IP4 and 26:2IP1.

DIAGNOSTICS

Several diagnostics were employed to study the ion instability- a pinhole camera, spectrum analyzer, feedback system, and gas bremsstrahlung detector. Unless stated oth-

* Work supported by the U.S. Department of Energy, Office of Science, Office of Basic Energy Sciences, under Contract No. DE-AC02-06CH11357.

ISBN: 978-3-95450-222-6 ISSN: 2673-5350 doi:10.18429/JACoW-IBIC2020-THPP25

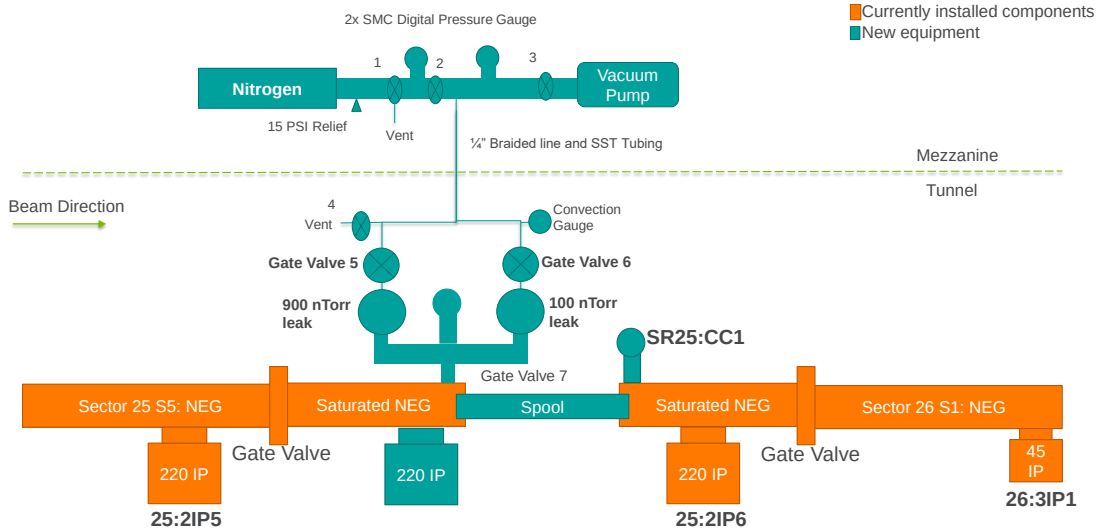

Figure 1: Layout of gas injection system.

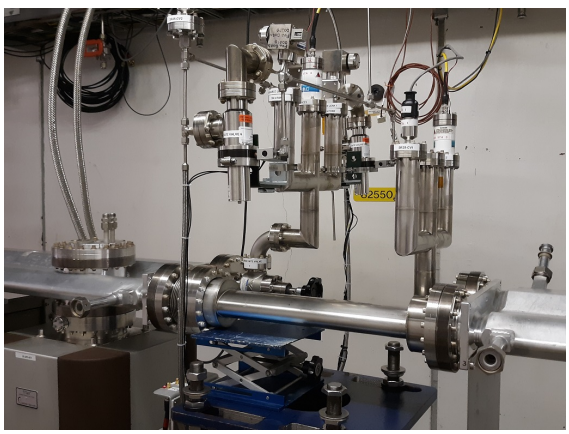

Figure 2: Picture of the gas injection system inside the tunnel.

erwise, the measurements presented here were done with 324 bunches, ~100 mA beam current, at 6 GeV.

Pinhole Camera

The horizontal and vertical beam size at the APS is measured by a pinhole camera located in a bending magnet beamline, and the emittances are calculated from the measured beam size using the beta function and dispersion derived from a calibrated model.

Figure 3 shows two example images from the pinhole camera. The left plot shows a beam image that is blown up vertically due to ions. The right image shows a case where the ion instability has been mitigated using train gaps (see below).

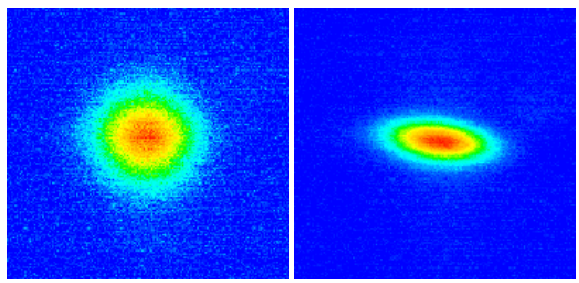

Figure 3: Pinhole camera images. Left: one train with no gaps; the beam is blown up vertically due to ion instability. Right: 4 trains with gaps; the instability is suppressed.

Spectrum Analyzer

The clearest signature of ion instability is peaks in the lower vertical betatron sidebands of the revolution harmonics, near a characteristic ion frequency given by Eq. (1). Here N_e is the bunch population, $r_p \approx 1.54 \times 10^{-18}$ m is the classical proton radius, S_b is the bunch spacing, σ_x and σ_y are the horizontal and vertical beam sizes, and A_{ion} is the atomic mass of the ion.

$$\omega_{i,0} \approx c \left(\frac{4 N_e r_p}{3 A_{ion} S_b (\sigma_x + \sigma_y) \sigma_y} \right)^{1/2} \quad (1)$$

Measurements of the vertical beam spectrum were taken using a Keysight N9020B MXA in spectrum analyzer mode. The spectrum was taken using ten consecutive sweeps, in order to get good frequency resolution (150 Hz) over the whole range (88 MHz for 324 bunches). The spectrum data is postprocessed to find peaks, and filtered to pick out peaks at the lower vertical betatron sidebands, where ion instability is observed. This process is illustrated in Fig. 4. Here we observe a clear ion frequency peak at ~7 MHz.

Content from this work may be used under the terms of the CC BY 3.0 licence (© 2020). Any distribution of this work must maintain attribution to the author(s), title of the work, publisher, and DOI

ISBN: 978-3-95450-222-6 ISSN: 2673-5350 doi:10.18429/JACoW-IBIC2020-THPP25

Content from this work may be used under the terms of the CC BY 3.0 licence (© 2020). Any distribution of this work must maintain attribution to the author(s), title of the work, publisher, and DOI

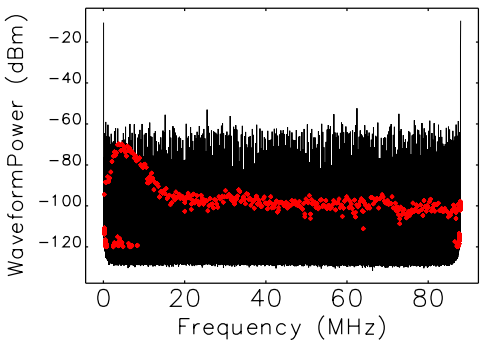

Figure 4: Example spectrum analyzer measurement for 324 bunches. The full measurement is shown by the black lines and is dominated by revolution harmonics; peaks at the lower vertical betatron sidebands are shown as red diamonds.

Feedback System

A Dimtel iGp12-1296F feedback processor [4] is used to directly measure bunch-by-bunch beam motion. Vertical displacement output from a BPM processor is connected to the Dimtel front-end. There are three independent data acquisition engines available: two multi-bunch and one single-bunch. For the present measurements we have used the multi-bunch unit with SRAM memory. It can capture up to 34 ms of beam motion every 500 ms. Two types of data are measured with the Dimtel system:

- Multi-turn data: Y-plane motion of all 324 bunches over several thousand turns is measured. The strength of the modes as a function of time is computed from frequency spectrum of this data.
- Modal amplitudes from iGp12: The processor computes modal amplitudes instantaneously for the selected side band frequency (the vertical tune in our case).

Figure 5 shows an example of multi-turn data taken with the Dimtel feedback system. It shows the strength of the 324 modes over ~9,000 turns. The upper half of these (i.e. modes 161 – 323) have a direct correspondence with the lower vertical betatron sidebands, as shown in Fig. 4. It is interesting to note that the mode amplitudes are not constant in time. Rather, the instability seems to shift between different modes.

Gas Bremsstrahlung Detector

Gas bremsstrahlung (GB) radiation is generated when high-energy electrons circulating in the storage ring interact with residual background gas molecules in the vacuum chamber. The interaction leads to the generation of high-energy photons. For our experiment, a detector was set up to measure GB photons generated inside the pressure bump. If properly calibrated, such a detector can provide a direct measurement of the gas pressure at the beam location.

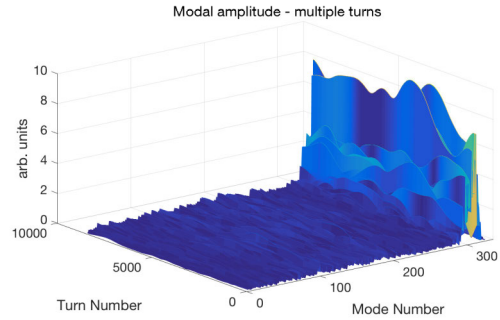

Figure 5: Measurement from the Dimtel feedback system, showing unstable modes over ~9,000 turns.

GB photons enter the upstream end of a Pb:Glass detector. Low-energy photons are blocked by a disk of tungsten located just upstream of the detector. A high-energy photon will enter the Pb:Glass and create an electromagnetic shower consisting primarily of electrons, positrons, and photons. The shower constituents are high enough energy to generate visible Cerenkov radiation. The Cerenkov pulse is detected by the a photo-multiplier tube (PMT), which in turn generates a negative output electrical signal. The height of the pulse recorded by the calorimeter PMT corresponds to photon energy. There are four channels with different set thresholds; pulses exceeding the threshold are counted. Thus the detector also provides a rough measurement of the photon energy spectrum.

Figure 6 shows an example measurement taken with the GB detector. The three channels shown have different thresholds, but all the signals are roughly proportional to the beam current. Quantitative analysis of these data is underway.

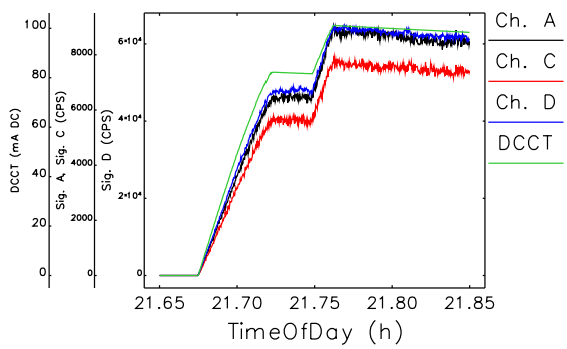

Figure 6: Gas bremsstrahlung detector measurement. Each channel corresponds to a different photon energy threshold.

RESULTS

Measurements have been taken with the instruments described above as a function of pressure bump amplitude, coupling, chromaticity, and bunch pattern. Here we describe one interesting experiment, in which data was taken as a

ISBN: 978-3-95450-222-6 ISSN: 2673-5350 doi:10.18429/JACoW-IBIC2020-THPP25

function of the number of bunch trains. All of these data were taken at 100 mA, 6 GeV, and with the 900 nTorr bump.

It is well known [5] that using gaps between bunch trains can clear out the ions and prevent instability. For this experiment, we divided the standard 324 bunch train into 2, 4, and 9 trains, with a 12 bunch gap in between them. This gap length was chosen to be large enough to clear out most of the N_2^+ ions. In each case, the individual bunch charge was adjusted to give approximately 100 mA total current.

Table 1 lists the horizontal and vertical emittance measured by the pinhole camera, for each of the bunch patterns listed above. The nominal emittances are $\epsilon_x = 1.83$ nm and $\epsilon_y = 0.024$ nm. For a single train with no gaps, both emittances are significantly blown up due to the ions. With 2 trains with a gap between them, both emittances are reduced, though still much larger than their nominal values. There are two possible explanations for this. First, for a sufficiently high ion density, the instability can grow to a significant amplitude over a single bunch train (the "fast-ion" instability [6]). In addition, the blown up beam sizes will change the trapping criteria [7], and a 12 bunch gap may no longer be sufficient.

Increasing the number of trains to 4 eliminated the horizontal blowup, but did not have much effect on the vertical. This suggests that (at least some of) the horizontal blowup was due to resistive wall instability. This motion in the horizontal plane can potentially shake out some of the ions, reducing the ion instability in the vertical plane. Thus the benefit of additional ion clearing with four trains is mostly canceled out. Finally, the 9 train case shows very little blowup in the vertical plane. The combination of shorter trains and more ion clearing gaps is enough to nearly eliminate the instability.

Table 1: Emittances Measured by the Pinhole Camera, with Different Numbers of Train Gaps

Gaps	ϵ_x (nm)	ϵ_y (nm)
0	4.0	0.056
2	2.94	0.044
4	1.78	0.043
9	1.85	0.025

These conclusions are supported by measurements of the vertical beam spectrum (Fig. 7). Based on calculations (Eq. (1)), the expected ion frequency for N_2 at the gas injection location is about 10 MHz. With no gaps, the measured frequency is actually ~4 MHz, due to the beam size blowup in both planes. As the number of gaps is increased, the ion frequency moves to a higher and higher frequency, as the beam size gets smaller. With 9 gaps, the peak ion frequency is back at the expected 10 MHz. The overall amplitude of the spectrum also decreases with more gaps.

The same trend is seen in the Dimtel data. Figure 8 plots the modal amplitudes for each of these cases. Because these modes are above the Nyquist frequency, their frequency is actually $(323 - n_{mode}) \times f_{rev}$, where the revolution frequency $f_{rev} = 271$ kHz. So this plot is consistent with Fig. 7: as the number of trains is increased, the modal amplitudes are reduced and shift to higher frequency.

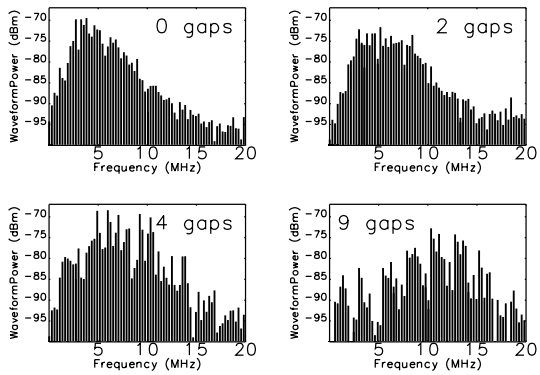

Figure 7: Vertical beam spectrum for different numbers of trains.

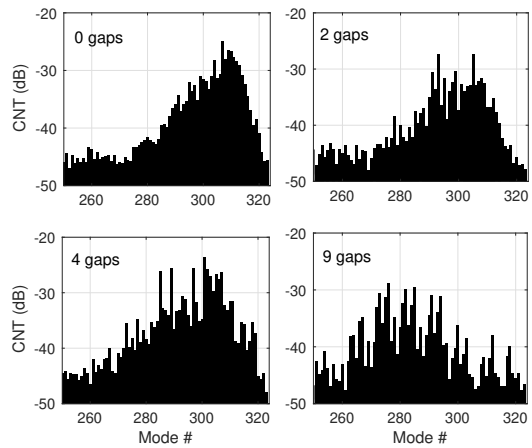

Figure 8: Modal amplitudes for different numbers of trains.

CONCLUSIONS

A gas injection system has been designed and installed in the APS storage ring, for the purpose of studying ion instability. The system works as designed, and allows for two localized pressure bump amplitudes. Measurements have been taken with a pinhole camera, spectrum analyzer, feedback system, and gas bremsstrahlung detector, in a wide variety of beam conditions. Measurements taken with a single train with no gaps show a significantly blown up beam size in both planes, and a corresponding reduction in the ion frequency. These effects persist (at a lower level) when ion clearing gaps are introduced, suggesting that the ion-induced beam size blowup reduces the effectiveness of the gaps. Using more gaps helped mitigate the instability further, with 9 gaps mostly eliminating the effect.

Content from this work may be used under the terms of the CC BY 3.0 licence (© 2020). Any distribution of this work must maintain attribution to the author(s), title of the work, publisher, and DOI

ISBN: 978-3-95450-222-6 ISSN: 2673-5350 doi:10.18429/JACoW-IBIC2020-THPP25

Content from this work may be used under the terms of the CC BY 3.0 licence (© 2020). Any distribution of this work must maintain attribution to the author(s), title of the work, publisher, and DOI

REFERENCES

[1] T. E. Fornek, "Advanced Photon Source Upgrade Project preliminary design report", APS, Argonne, IL, USA, Rep. APSU-2.01-RPT-002, Sep. 2017. doi:10.2172/1423830

[2] H. Hereward, "Coherent instability due to electrons in a coasting proton beam", CERN, Geneva, Switzerland, Rep. CERN-71-15, Jul. 1971. doi:10.5170/CERN-1971-015

[3] J. Calvey and M. Borland, "Modeling ion effects for the Argonne Advanced Photon Source upgrade", *Phys. Rev. Accel. Beams*, vol. 22, no. 11, p. 114403, 2019. doi:10.1103/PhysRevAccelBeams.22.114403

[4] iGp12, https://www.dimtel.com/products/igp12

[5] D. Villevald and S. Heifets, "Ion Trapping in the SLAC B-factory High Energy Ring", SLAC, Stanford, USA, Rep. SLAC-TN-06-032, May 1993.

[6] T. O. Raubenheimer and F. Zimmermann, "A Fast beam - ion instability in linear accelerators and storage rings", *Phys. Rev. E*, vol. 52, pp. 5487–5497, 1995. doi:10.1103/PhysRevE.52.5487

[7] Y. Baconnier and G. Brianti, "The Stability of Ions in Bunched Beam Machines", CERN, Geneva, Switzerland, Rep. CERN/SPS/80-2, Mar. 1980.

ISBN: 978-3-95450-222-6 ISSN: 2673-5350 doi:10.18429/JACoW-IBIC2020-THPP26

TRANSVERSE BROAD-BAND IMPEDANCE STUDIES OF THE NEW IN-VACUUM CRYOGENIC UNDULATOR AT BESSY II STORAGE RING

M. Huck*, J. Bahrdt, H. Huck, A. Meseck, M. Ries
Helmholtz-Zentrum Berlin für Materialien und Energie (HZB), Berlin, Germany

Abstract

The first radiation from the cryogenic permanent magnet undulator (CPMU17) has been observed in December 2018 at BESSY II storage ring at HZB, and since then this device has served as a light source for beamline commissioning. It is the first in-vacuum undulator installed at BESSY II, and a new in-vacuum APPLE undulator (IVUE32) is planned to be installed in near future. Thus, a detailed study of the interactions between such an in-vacuum device and the electron beam is required. Beam-based measurements using orbit-bump and tune-shift methods have been applied to estimate the vertical impedance of CPMU17. For CPMU17 the first results of broad-band impedance studies are presented.

INTRODUCTION

The constantly growing requests of various research fields for synchrotron radiation with higher photon energies demands designing undulators with smaller magnetic periods and gaps. After succeeding in constructing and optimizing small gap in-vacuum undulators (IVUs) in the last two decades, the challenging impacts of such small gaps on beam dynamics can nowadays be estimated and mitigated using modern experimental techniques and high-power numerical calculations. These studies are specially required for complex structures, short bunches and variable polarization IVUs such as CPMU17 and IVUE32. One of the most important related issues is the wake fields effect. Wake fields arise when the relativistic electrons travel inside chambers with nonuniform geometrical cross-section or a resistive wall.

IMPEDANCE BY VARIABLE BEAM OFFSET AND CURRENT

A particle beam that travels off-axis through a vacuum chamber section with a nonzero broad-band transverse impedance will be deflected due to the electromagnetic forces of the wake fields generated by the particle beam itself. In frequency domain and in case of transverse impedance, such a beam-impedance interaction can be represented by a quantity called *transverse kick factor* defined by [1]

$$k_\perp = \frac{1}{2\pi}\int_{-\infty}^{\infty} Z_\perp(\omega)h(\omega)\mathrm{d}\omega, \qquad (1)$$

where $Z_\perp(\omega)$ is the frequency-dependent *transverse impedance* and $h(\omega) = \lambda(\omega)\lambda^*(\omega)$ is the bunch power spectrum, with $\lambda(\omega)$ the Fourier transform of beam linear density $\lambda(t)$. The kick factors can be calculated for both horizontal and vertical directions. However, in our studies the focus is on the kick in the vertical direction, because a small gap in-vacuum undulator comprise a flat geometry (two parallel plates), i.e. the width of the structure (46 mm in our case) is larger than its height (half gap of 3 mm-11 mm). And the interaction of the electrons with surrounding structure in the vertical direction is stronger than in the horizontal one. This interaction will cause a linear kick of the beam vertical momentum as follows

$$\Delta y' = eqk_\perp y_0/E, \qquad (2)$$

where q is the beam charge, y_0 is the beam vertical offset, E is the beam energy, and e is the electron charge. Based on Eq. (2), a method called *orbit bump method* has been developed in 1999 at Budker Institute, Novosibirsk [2] to estimate the transverse kick factor of an individual section. The closed orbit distortion (COD) due to an impedance at a section can be expressed by [1]:

$$\Delta y(s) = \frac{\Delta q}{E/e}k_\perp y_0 \frac{\sqrt{\beta(s)\beta(s_0)}}{2sin\pi Q_y} cos(|\mu(s)-\mu(s_0)|-\pi Q_y), \qquad (3)$$

where Q_y is the vertical betatron tune, $\beta(s), \mu(s)$ and $\beta(s_0), \mu(s_0)$ are respectively the betatron function and phase through the whole ring and at the location of the impedance. y_0 can be varied by introducing a closed-orbit-bump using correction coils. The orbit distortions $\Delta y(s)$ can be measured using beam position monitors (BPMs) at a high and a low beam current with a charge variation of Δq. By measuring and subtracting $\Delta y(s)$ in 4 states i.e. combination of *high-, low-current* and *with-, no-bump*: $\Delta y(s) = (\Delta y_{wbh} - \Delta y_{nbh}) - (\Delta y_{wbl} - \Delta y_{nbl})$, a COD equal to $\Delta y(s)$ is obtained which is directly proportional to $k_\perp$.

Contributions of dipole and quadrupole components in a wake field expansion have different effects on beam dynamics and can be distinguished by different measurements and models. Due to crossing terms in field expansion in a non-symmetric structure such as an IVU, $k_\perp(\omega)$ in Eq. (3) is determined with both dipole and quadrupole terms [1]. However, the quadrupole impedance manifests itself only in multi-bunch interactions [3]. The orbit bump technique is based on the *single-bunch* effect, yielding the contributions from geometric and resistive-wall broad-band dipole impedance. This technique or a variation of it has been implemented at several other institutes such as APS [4], ELLETRA [5], Diamond light source [1], Photon Factory at KEK [6], and ALBA [7].

IN-VACUUM CRYOGENIC UNDULATOR

The new in-vacuum cryogenic permanent magnetic undulator CPMU17 has been installed in summer 2018 at BESSY

* maryam.huck@helmholtz-berlin.de

Content from this work may be used under the terms of the CC BY 3.0 licence (© 2020). Any distribution of this work must maintain attribution to the author(s), title of the work, publisher, and DOI

ISBN: 978-3-95450-222-6 ISSN: 2673-5350 doi:10.18429/JACoW-IBIC2020-THPP26

Content from this work may be used under the terms of the CC BY 3.0 licence (© 2020). Any distribution of this work must maintain attribution to the author(s), title of the work, publisher, and DOI

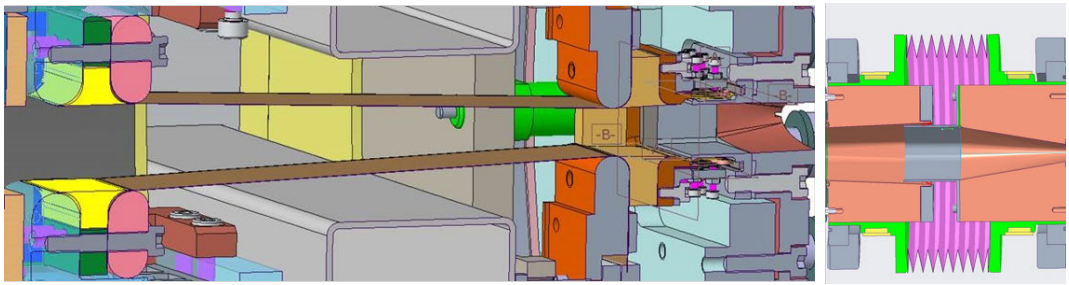

Figure 1: Schematics of the vacuum components inside the CPMU17 undulator chamber, including the tapered part and the taper section (left), and a bellow with an extra tapered octagon-ellipse transition part at ID down- and upstream (right).

II, and in fall 2018 the first undulator radiation from this device was detected. The characterization and implementation of this device has been presented in [8]. In order to reduce the geometrical discontinuities, the magnets are covered with a two layer RF-shielding foils made of Copper and Nickel. The 50 µm Copper is coated on a 50 µm thick Nickel foil. The Nickel side is attracted by magnetic forces whereas the Copper side faces the electron beam. The choice of Copper is to reduce the resistive impedance of the device. Furthermore, due to the small skin depth of Copper especially at high frequencies, electromagnetic radiation does not penetrate deeply into the Copper and will be damped in the first 0.6 µm of its surface at 10 GHz and 6 µm at 100 MHz. Another foil made of a Copper-Beryllium alloy connects the magnet part to the taper section (Fig. 1). The special construction of the taper section (Fig. 2) enables a variable taper which at one end has a fixed height of 11 mm and at the other end has a height equal to the variable magnetic gap. Down- and upstream the ID, there are bellows with cooled Copper tubes with variable cross section inside, both for the purpose of heat transport and for RF shielding the bellow discontinuities. Along the bellow, the wall cross-section is tapered from elliptical shape to an octagonal one, and there are two such transitions at either sides of the CPMU17 and two more at either sides of the UE48 (another ID downstream the CPMU17).

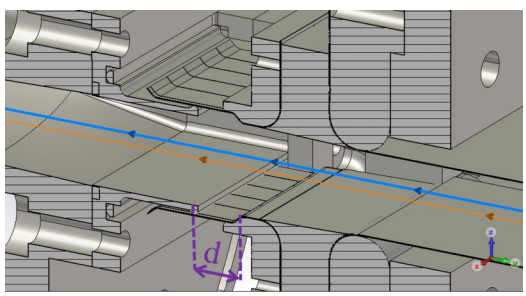

Figure 2: CAD model of the taper section used for the CST simulations.

CST Simulation

The taper section enables a variable tapering system to reduce the geometrical impedance, but it also introduces small discontinuous regions which might cause RF resonances inside the structure. The effects of this issue on wake fields has been estimated [9] using the wake field solver of the CST studio-suite simulation tool [10], and been taken into account during the design of the ID. Simulation showed, that the electromagnetic power deposited by the beam on the structure increases at larger distances of d shown in Fig. 2 [9], as do the kick factors. In operational cooled state $d \approx 2.35$ mm at 6 mm gap, and $d \approx 3.35$ mm at 22 mm. Preliminary simulation results for the taper section, tapered part and magnet part with resistive Cu foils at gap of 6 mm suggests a total kick factor of $k_y \approx 2 \times 10^{14}$ V/C/m. The contribution of the 4 bellows, 3 BPMs, and the other vacuum components and resistive walls should be added to this value. For this simulation, a rms bunch-length of $\sigma = 8.4$ mm and a beam charge of 8×10^{-9} C is used and the simulation follows the approach described in [11, 12] and used in [13].

BEAM BASED MEASUREMENTS

Two different beam-based methods are used to study the short-range wake fields of the CPMU17. One measurement used the orbit bump method and the other one vertical betatron tune-shift with bunch current change, both with a single bunch electron beam.

Orbit Bump Measurement

For this measurement the storage ring current was switched to low current already 3 hours prior to measuring CODs, reducing obit drift due to the temperature changes

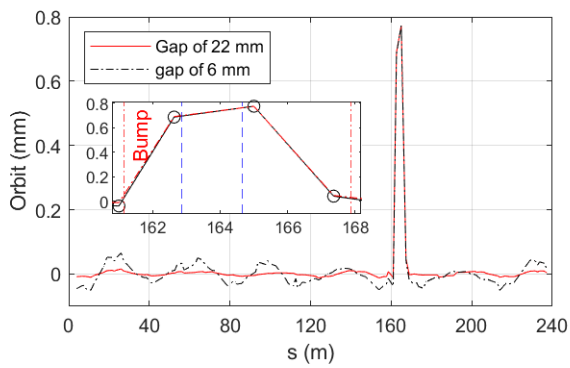

Figure 3: Vertical orbit bump at gap of 22 mm and 6 mm. The inset figure shows the bump shape closer; vertical blue lines show the place of the CPMU17 and the circle datapoints shows the position of the 3 BPMs within the bump.

ISBN: 978-3-95450-222-6 ISSN: 2673-5350 doi:10.18429/JACoW-IBIC2020-THPP26

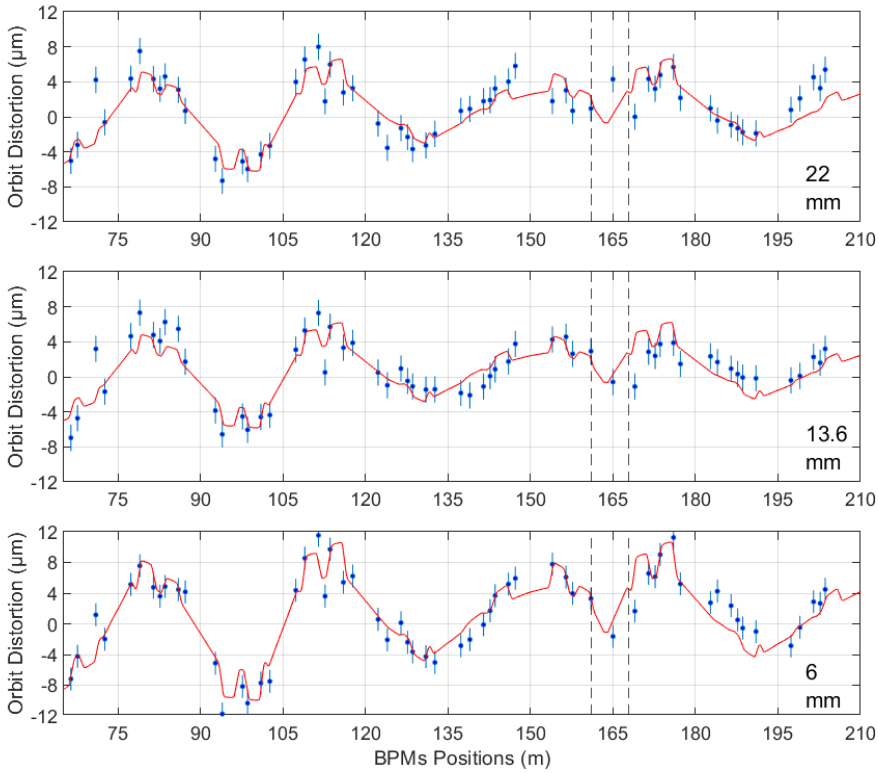

Figure 4: Three examples of closed orbit distortion $\Delta y(s)$ at gap of 22 mm, 13.6 mm and 6 mm, respectively from top to bottom. The longitudinal positions of the bump in ring is marked with vertical dashed black lines at 161.1 (downstream) and 167.9 m (upstream). The ID in ring is located between 162.87 m and 164.67 m.

of the machine. The orbit- and tune-feedback systems were turned off, but the tune feed-forward was still applied. A bump was generated using 4 steerers covering a section over a total length of about 6.4 m. The height of the bump was restricted by the machine protection system to about 0.8 mm. Two example bumps at gap of 22 mm and 6 mm are shown in Fig. 3. The bump was optimized at the gap of 22 mm with almost no disturbance outside the bump, but at the other gaps, a distortion of up to 50 μm has been observed. The amplitude of this distortion increases by decreasing the gap. This behavior was expected due to strong focusing effects while the steerers remain constant. The beam used for the measurement was a single bunch with a beam current of 4 mA and 16 mA, (low- and high-current states); corresponding to a charge difference of $\Delta q = 9.6 \times 10^{-9}$ C and an average charge of 8.0×10^{-9} C.

Three example CODs at gaps of 22 mm, 13.6 mm and 6 mm are shown in Fig. 4. In these graphs, the blue dots show average values of 18 measurements taken for 36 seconds. The standard deviation of the BPM signals over this period of time was very close to zero, the accuracy is about 1.5 μm. The red solid line is the orbit deviation calculated using the Eq. (3). It can be seen, that the amplitude of the COD at gap of 13.6 mm has the smallest value among the three, and it increases with increasing or decreasing the gap. This is a reasonable trend, because the height of the following section is 11 mm. Hence, the tapered part is flat at a gap with a height closer to this value and the impedance is the smallest. Determining the exact kick-factor minimum needs more detailed studies at gaps around 11 mm.

A fit of the measured data with the theoretical formula in Eq. (3) yields kick factors of $(6.8 \pm 0.4) \times 10^{14}$ V/C/m, $(4.0 \pm 0.3) \times 10^{14}$ V/C/m, and $(4.2 \pm 0.4) \times 10^{14}$ V/C/m, respectively at the gaps of 6 mm, 13.6 mm, and 22 mm. They are calculated excluding BPMs at longitudinal position from zero (70 m downstream the bump) to 64 m; At this area, there are obvious phase discrepancies between the measured data and the theory at gaps larger than 6 mm. Possible source for this discrepancies could be the ID focusing-effects on betatron function and phase, and linear optics-distortion due to the gap variation, not taken in to account in these analyses. Used parameters are a vertical betatron tune of $Q_y = 6.726$, a beam energy of 1.7 GeV, an average bump height of 0.73 mm measured with respect to the mechanical aperture of the U17, and an over the bump length averaged betatron phase and function of $\mu(s_0) = 28.7$ rad and $\beta(s_0) = 1.65$ m at the location of CPMU17. Because inside the undulator the beta function has a very small variation (Fig. 5), a constant value for $\beta(s_0)$ in Eq. (2) has been used. The vertical betatron function at the straight section of CPMU17 was (already before the installation) adjusted to low values with a local lattice modification to exclude a fatal beam scraping at the magnetic structure [14]. Installing an IVU in such a mini-beta section implies the advantage that the beam orbit will have less distortion due to the wake fields according to Eq. (3). The phase advance along the ID was 1.21 rad, less than 1π;

Content from this work may be used under the terms of the CC BY 3.0 licence (© 2020). Any distribution of this work must maintain attribution to the author(s), title of the work, publisher, and DOI

ISBN: 978-3-95450-222-6 ISSN: 2673-5350 doi:10.18429/JACoW-IBIC2020-THPP26

Content from this work may be used under the terms of the CC BY 3.0 licence (© 2020). Any distribution of this work must maintain attribution to the author(s), title of the work, publisher, and DOI

this condition is required for using the orbit bump method, so that the sections with the same impedance and with a phase difference of π do not lead to zero orbit deviations outside the bump [1, 2].

A length of 1.8 m inside the bump region is already covered by the undulator itself, and in the rest of the region there is not any significant geometrical discontinuities which could contribute to the measured impedance. The major sources of the geometrical and resistive wakes in this region lies within the undulator itself, mainly at the taper section, the tapered part and also four tapered transition parts shown in Fig. 1, and 3 BPMs within the bump.

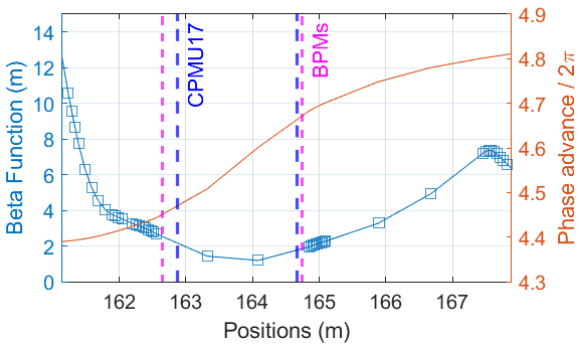

Figure 5: Vertical betatron function and phase advance within the bump. Dashed lines display the location of CPMU17 and its surronding BPMs.

Tune Shift Measurement

In our second studies, the variation of the vertical betatron tune was measured vs. single bunch current change. The slope of this variation is an indication of the *vertical dipolar kick factor* $k_\perp$ according to the following equation [5, 13, 15, 16]:

$$\frac{dQ_{yF}}{dI_b} = -\frac{<\beta> k_\perp}{4\pi\nu_{rev}(E/e)}, \qquad (4)$$

where I_b is the bunch current, $\nu_{rev} = 1.249\,\text{MHz}$ is the revolution frequency, Q_{yF} is the coherent *fractional vertical tune* [15], and E is the beam energy. Both dipole and quadrupole wakes contribute to the coherent tune shift, but theoretically the quadrupole term is smaller than the dipole one, and it can be detected by introducing quadrupole field oscillations [15].

We used conventional strip-line kickers to induce vertical dipolar oscillations, and the vertical fractional tune-shift was measured using the beam diagnostics system for two cases with ID open and closed. The tune feedback system was off, while the tune feed-forward table, for compensating the undulator focusing effect, was still applied. This table corrects the gap-dependent vertical tune-shift of about $\Delta\nu_y = 2.8\,\text{kHz}$ (moving from gap of 22 mm to 6 mm) with an accuracy of about $d\nu_y = \pm 0.7\,\text{kHz}$. The resolution of the betatron frequency measurement was $d\nu_y = 140\,\text{Hz}$ (rms of the statistical errors). At each current, the betatron frequency was measured for several times and averaged (Fig. 6). The slopes of the linear fits are

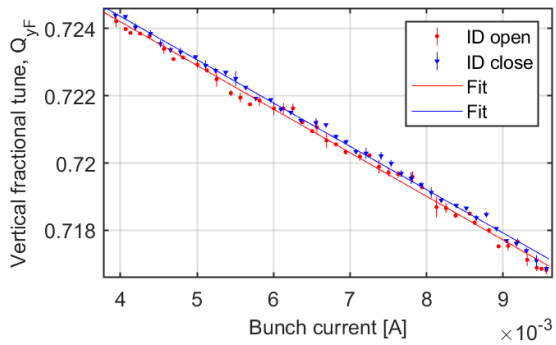

Figure 6: Tune shift by current change. Dots are the measured data with statistical errors, solid lines are linear fits.

$(-1.2864 \pm 0.076)\,\text{A}^{-1}$ and $(-1.2954 \pm 0.011)\,\text{A}^{-1}$, respectively at closed and open gaps, resulting in a slope difference of $(9.1 \pm 13.6) \times 10^{-3}\,\text{A}^{-1}$ between the two cases. By substituting this value in Eq. 4, we get a kick value of $(1.5 \pm 2.2) \times 10^{14}$ V/C/m. The large error shows, that the contribution of the CPMU17 to the total dipole vertical kick-factor of BESSY II is too small, to be resolved by this measurements accuracy. Applying the difference of kick factors at open and closed ID derived by the OBM method above, $\Delta k_y = (2.6 \pm 0.5) \times 10^{14}$ V/C/m to Eq. (4), slope difference of $(16 \pm 3) \times 10^{-3}\,\text{A}^{-1}$ is deduced which corresponds to a tune change of $dQ_{yF} = (1.5 \pm 0.6) \times 10^{-5}$ (when the bunch current sweeps by 1 mA). Hence, a betatron frequency change of $d\nu_y = (20 \pm 4)$ Hz is expected, for which a measurement accuracy in the same order is required.

CONCLUSION

The major impedance contributors of the first cryogenic permanent undulator at BESSY II have been identified, and the impact of the taper section, magnets-shielding and tapered foils on the impedance have been separately approximated using CST simulations. The vertical kick factors have been experimentally evaluated using orbit-bump and tune-shift techniques. The two measurement methods and preliminary simulation results agree to a good extent. Further studies with more accurate measurements, data analyses, simulations and theoretical models are being carried out, to determine and compare the contributions of all ID parts to the impedance. Furthermore, a modification of the vacuum chamber is under development to investigate possible resonances by installing RF antennas in ID vacuum chamber. In addition, studies of coupled bunch instabilities, in particular growth-damp measurements are planned. The impedance evaluation will be also conducted with few-bunch and multi-bunch fill patterns.

ACKNOWLEDGMENTS

The author would like to acknowledge with much appreciation O. Tanaka (KEK), V. Smaluk (BNL), B. Salvant (CERN), V. Dürr, D. Wolk, S. Grimmer, T. Schroeter, T. Flisgen, W. Frendtrup, M. Scheer, S. Liangliang, and H.W. Glock (HZB) for their help and support.

ISBN: 978-3-95450-222-6 ISSN: 2673-5350 doi:10.18429/JACoW-IBIC2020-THPP26

REFERENCES

[1] V. Smaluk, R. Fielder, A. Blednykh, G. Rehm, and R. Bartolini, "Coupling impedance of an in-vacuum undulator: Measurement, simulation, and analytical estimation", *Phys. Rev. ST Accel. Beams*, vol. 17, p. 074402, 2014. doi:10.1103/PhysRevSTAB.17.074402

[2] V. Kiselev and V. Smaluk Budker Institute of Nuclear Physics, "A method for measurement of transverse impedance distribution along storage ring", in *Proc. DIPAC'99*, Chester, UK, May 1999, paper PT19, pp.202–204.

[3] A. Blednykh, G. Bassi, Y. Hidaka, and V. Smaluk, "Low-frequency quadrupole impedance of undulators and wigglers", *Phys. Rev. Accel. Beams*, vol. 19, p. 104401, 2016. doi:10.1103/PhysRevAccelBeams.19.104401

[4] L. Emery, G. Decker, and J. Galayda, "Local Bump Method for Measurement of Transverse Impedance of Narrow-Gap ID Chambers in Storage Rings", in *Proc. 19th Particle Accelerator Conf. (PAC'01)*, Chicago, IL, USA, Jun. 2001, paper TPPH070, pp.1823-1825.

[5] E. Karantzoulis, V. Smaluk, and L. Tosi, "Broad band impedance measurements on the electron storage ring ELETTRA", *Phys. Rev. ST Accel. Beams*, vol. 6, p. 030703, 2003. doi:10.1103/PhysRevSTAB.6.030703

[6] O. A. Tanaka *et al.*, "Evaluation of the Transverse Impedanse of Pf in-Vacuum Undulator Using Local Orbit Bump Method", in *Proc. 7th Int. Beam Instrumentation Conf. (IBIC'18)*, Shanghai, China, Sep. 2018, pp. 89–92. doi:10.18429/JACoW-IBIC2018-MOPB08

[7] Z. Martí, G. Benedetti, T. F. G. Günzel, and U. Iriso, "Local Impedance Measurements Using the Orbit Bump Method at ALBA", in *Proc. IPAC'19*, Melbourne, Australia, May 2019, pp. 240–242. doi:10.18429/JACoW-IPAC2019-MOPGW066

[8] J. Bahrdt *et al.*, "Characterization and Implementation of the Cryogenic Permanent Magnet Undulator CPMU17 at Bessy Ii", in *Proc. IPAC'19*, Melbourne, Australia, May 2019, pp. 1415–1418. doi:10.18429/JACoW-IPAC2019-TUPGW014

[9] Thomas Flisgen, "Internal report on CPMU17 impedance studies", HZB, Berlin, Germany, 2018, unpublished.

[10] Computer Simulation Technology (CST), CST Studio Suite, particle dynamics, accelerator components, cavities, wake fields, https://www.3ds.com/products-services/simulia/products/cst-studio-suite/solvers/

[11] Benoit Salvant, "Transverse single-bunch instabilities in the CERN SPS and LHC", presented at Beam physics for FAIR Workshop, Bastenhaus, Germany, Jul. 2010.

[12] C. Zannini, "Electromagnetic simulation of CERN accelerator components and experimental applications", Ph.D. Thesis, Phys. Dept., Ecole Polytechnique Federale de Lausanne, Lausanne, Switzerland.

[13] O. A. Tanaka *et al.*, "Impedance evaluation of in-vacuum undulator at KEK Photon Factory", *J. Phys.: Conf. Ser.*, vol. 1067, p. 062008, 2018. doi:10.18429/JACoW-IPAC2018-THPAK001

[14] J. Bahrdt *et al.*, "Measurements of the Lattice Modifications for the Cryogenic Undulator CPMU17", in *Proc. IPAC'16*, Busan, Korea, May 2016, pp. 4031–4034. doi:10.18429/JACoW-IPAC2016-THPOW039

[15] S. Sakanaka, T. Mitsuhashi, and T. Obina, "Observation of transverse quadrupolar tune shifts in the Photon Factory storage ring", *Phys. Rev. ST Accel. Beams*, vol. 8, p. 042801, 2005. doi:10.1103/PhysRevSTAB.8.042801

[16] T. F. Günzel, "Coherent and Incoherent Tune Shifts Deduced from Impedance Modelling in the ESRF-Ring", in *Proc. EPAC'04*, Lucerne, Switzerland, Jul. 2004, paper WEPLT083, pp. 2047–2049.

Content from this work may be used under the terms of the CC BY 3.0 licence (© 2020). Any distribution of this work must maintain attribution to the author(s), title of the work, publisher, and DOI

ISBN: 978-3-95450-222-6 ISSN: 2673-5350 doi:10.18429/JACoW-IBIC2020-THPP29

Content from this work may be used under the terms of the CC BY 3.0 licence (© 2020). Any distribution of this work must maintain attribution to the author(s), title of the work, publisher, and DOI

APPLICATION OF WAVELET ALGORITHM IN TUNE MEASUREMENT*

X. Yang[1,2], L. W. Lai†, F. Z. Chen,
SSRF, Shanghai Advanced Research Institute, Chinese Academy of Sciences, Shanghai, China
[1]also at University of Chinese Academy of Sciences, Beijing, China
[2]also at Shanghai Institute of Applied Physics, Chinese Academy of Sciences, Shanghai, China

Abstract

Tune is a very important parameter for storage ring of advanced synchrotron radiation facilities. At present, fast Fourier transform (FFT) is the core algorithm of the beam spectrum analysis used in tune measurement. Taking into account the nonlinear effect in the accelerator, tune changes during the process of storage ring injection and booster energy upgrading. However, the Fourier method is used to analyse the global sampling point, and the ability to distinguish the local variation of the tune in the sampling time is poor. This paper leads wavelet analysis method as the core algorithm into beam spectrum analysis method, further analyses the change of the tune with beam amplitude in sampling time, and compares this new algorithm with the traditional Fourier method. New experimental results and corresponding analysis for the data from SSRF will be introduced in this paper.

INTRODUCTION

Tune measurement is very important for a storage ring. Some key accelerator parameters are calculated by measuring the tune value, including beta function, chromaticity, impedance, etc [1]. SSRF starts top-up operation since 2012. Injection introduced beam oscillation can be used to measure real-time tune value on storage ring during user operation [2, 3]. Fast Fourier transform (FFT) is the most commonly used algorithm in the tune calculation, which frequency resolution is determined by the number of sampling points N, that is 1/N. The tune accuracy and tune drift measurement in the injection process is limited by the short oscillation damping time (about 10,000 turns).

As for the booster ring, the tune drift during ramping reflects the real-time operating status of the booster. The short-time Fourier transform (STFT) is used to calculate the tune drift [4]. However, the short ramping time (about 20,000 turns) during booster top-up injection makes the accurate tune drift measurement with STFT difficult.

Wavelet transform is a commonly used time-varying frequency analysis algorithm. There already have some related researches on beam analysing using Wavelet. The signal is analysed by selecting an appropriate base function with limited energy on the time axis. The continuous wavelet transform is defined as following quotation.

$$WT(a,\tau) = \frac{1}{\sqrt{a}}\int_{-\infty}^{\infty} f(t) * \psi\left(\frac{t-\tau}{a}\right) dt$$

where ψ is the mother wavelet, τ is the delay coefficient, and α is the scale coefficient which can be converted to corresponding frequency. The final result is a two-dimensional array of coefficients (a, τ) [5, 6].

This article uses Morlet wavelet as the mother wavelet to analyse the turn-by-turn data from storage ring and booster of SSRF during injection. Morlet wavelet is a complex wavelet whose envelope is the Gauss function. Its analytical formula is:

$$m(t) = e^{j\omega_0 t} e^{-t^2/2}$$

The real part image of the function is shown in the Figure 1.

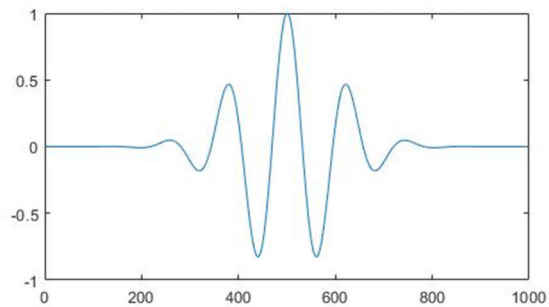

Figure 1: Morlet Wavelet.

ALGORITHM EVALUATION

Before use this new algorithm, we must test this wavelet method with Monte Carlo method. We established some test signals to simulate the real sampling.

It can be seen that FFT is restricted by the number of sampling points, and the frequency resolution is always in a relatively poor range in the Fig. 2. It cannot capture the subtle changes of tune. However, the morlet wavelet method has a relatively high value when the number of points is relatively small. The resolution is concentrated in the vicinity of the true frequency, and there is a lot of jitter when the SNR is low. As the number of sampling points increases, the stability of the morlet wavelet method is greatly improved, but the resolution of the FFT does not change significantly.

There is a special parameter in morlet wavelet analysis called analysis length, which affects the degree of time-frequency emphasis of wavelet analysis. The larger the analysis length, the higher the frequency resolution and the lower the time resolution, and vice versa. Use the simulation signal to analyse, get Fig. 3.

*Work supported by Youth Innovation Promotion Association, CAS (Grant No. 2019290);
† lailongwei@zjlab.org.cn

ISBN: 978-3-95450-222-6 ISSN: 2673-5350 doi:10.18429/JACoW-IBIC2020-THPP29

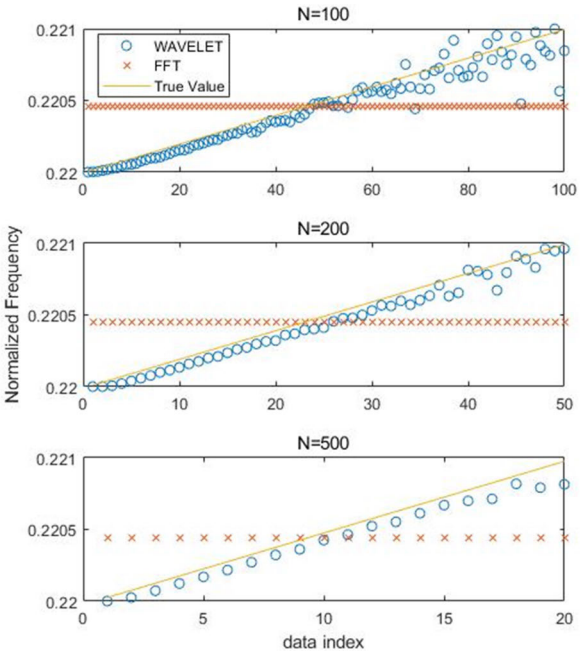

Figure 2: The relationship between test results and the number of sampling points.

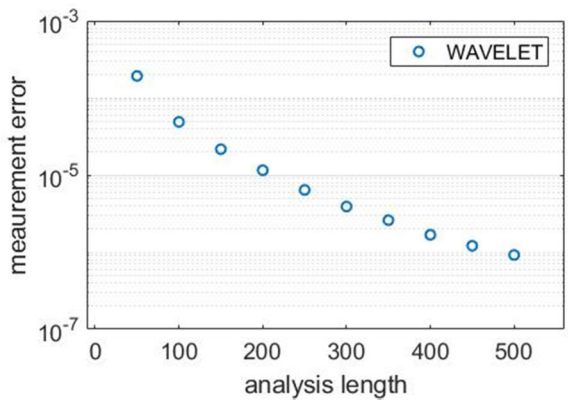

Figure 3: The relationship between test results and analysis length.

In Fig. 3, it can be seen that as the analysis length increases, the frequency resolution increases significantly. Considering the time resolution requirement, a minimum analysis length should be selected after a certain frequency resolution requirement is met.

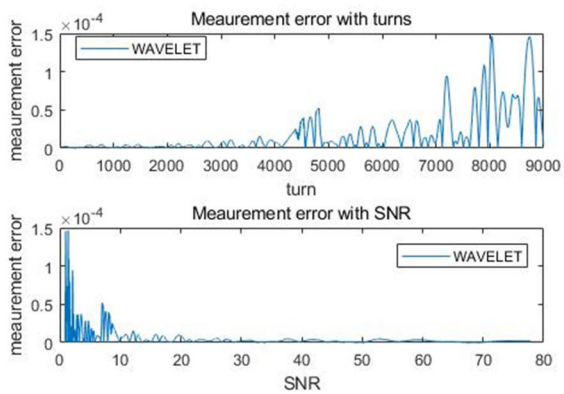

Figure 4: The relationship between test results and SNR.

Figure 4 shows the variation of measurement uncertainty with the number of turns. As the number of turns increases, the SNR decreases, and the frequency uncertainty increases significantly. The horizontal axis is replaced by the SNR in the figure below, which is easy to get. When it is greater than 10, the algorithm is available and has a higher frequency resolution. Combining the measurement error of the instrument and the collected value, a meaningful number of analysis points can be obtained.

Fortunately, such data will be deliberately avoided when designing the tune, so the systematic error can be small.

Figure 5 simply shows the variation of frequency uncertainty with test frequency.

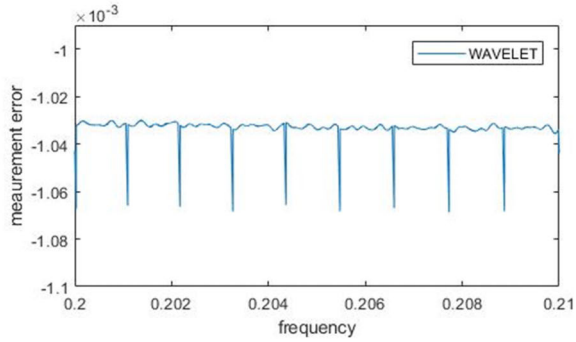

Figure 5: Test results and frequency dependence.

APPLICATION IN STORAGE RING

The test results show that the application of morlet wavelet algorithm in the extraction of storage ring tune is feasible.

The sampling result of the beam position during the injection of SSRF storage ring is shown in Fig. 6.

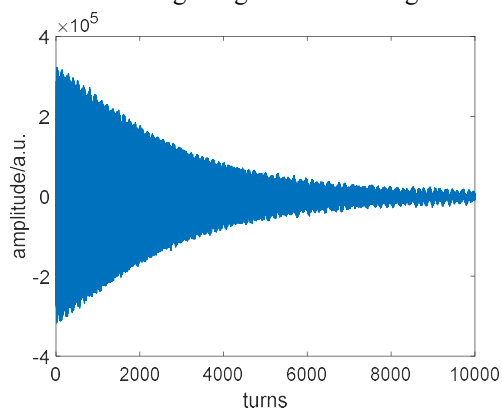

Figure 6: Injection horizontal turn-by-turn beam position data from SSRF storage ring.

The measurement resolution of turn-by-turn position is 2.1 μm, and the corresponding random noise peak-to-peak value is 7.6 μm. Before the SNR dropped to 10. We get about 9000 sampling points. Calculations within this range can be considered effective.

Here, the wavelet analysis algorithm is used to analyse the circle-by-lap horizontal position data of SSRF storage ring injection.

Content from this work may be used under the terms of the CC BY 3.0 licence (© 2020). Any distribution of this work must maintain attribution to the author(s), title of the work, publisher, and DOI

ISBN: 978-3-95450-222-6 ISSN: 2673-5350 doi:10.18429/JACoW-IBIC2020-THPP29

Content from this work may be used under the terms of the CC BY 3.0 licence (© 2020). Any distribution of this work must maintain attribution to the author(s), title of the work, publisher, and DOI

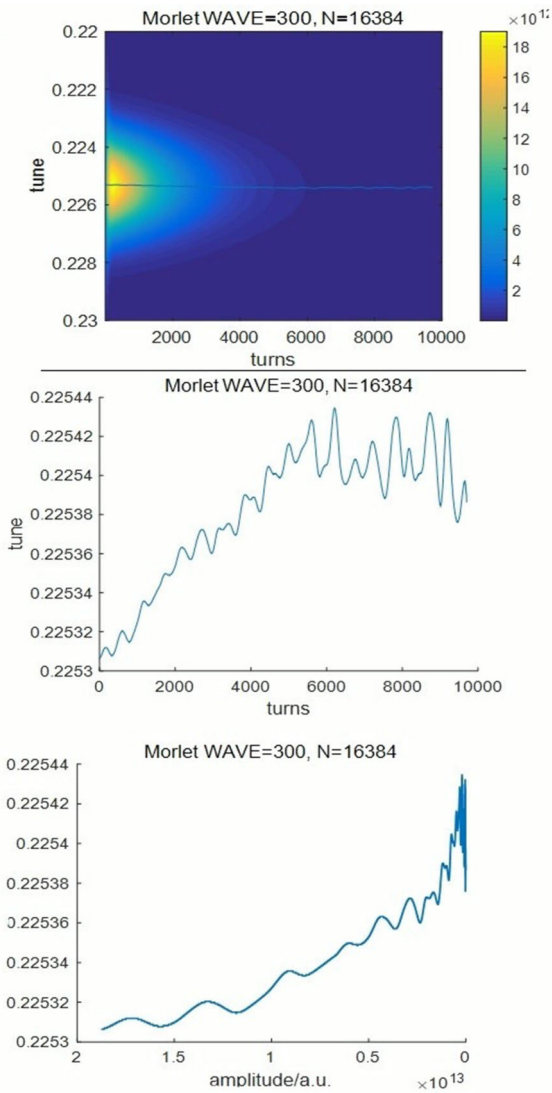

Figure 7: Wavelet analysis of horizontal tune drift during SSRF storage ring injection.

Figure 7 shows tune during the injection increased from 0.22530 to 0.22543. Before applying this algorithm to tune measurement, we think that the average value of the whole process is the actual tune seen by the bunch, but after considering the nonlinearity, this is not accurate. After replaced the horizontal axis with the bunch amplitude, it can be seen that as the amplitude decreases, tune increases approximately linearly. When the amplitude is 0, tune is corrected to 0.22542. Compared with the original correction of 0.0001, this is very meaningful.

APPLICATION IN SSRF BOOSTER

Transverse oscillations are also introduced during the injection process of the booster. Figure 8 shows the horizontal and vertical turn-by-turn position data of the SSRF booster during the injection and boosting period. Compared with the storage ring, the transverse oscillation caused by the injection on the booster is not so obvious.

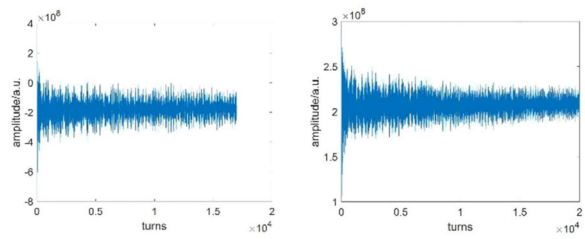

Figure 8: Injection horizontal (left) and vertical (right) turn-by-turn beam position data from SSRF booster.

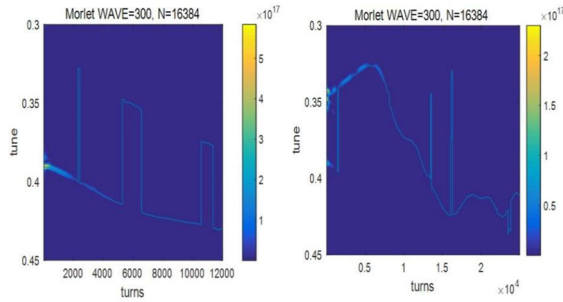

Figure 9: Morlet Wavelet analysis of horizontal (up) and vertical (bottom) tune drift measurement during SSRF storage ring injection.

Figure 9 is the use of wavelet analysis algorithm to extract the horizontal and vertical tune changes during the energy-up period of the booster. It can be seen that except for some of the weak oscillation amplitudes Part of the calculation results are unreliable, the changing trajectories of tune in the horizontal and vertical directions are gradually clear. Among them, the transverse tune increases unidirectionally, and the vertical tune decreases first and then increases. Due to the weak amplitude of the transverse oscillation, it is difficult to calculate the tune with some data, and obvious noise can be seen.

CONCLUSION

The simulation proves that the morlet wavelet algorithm can measure the time-varying tune. When the data analysis window is selected as 100 cycles, tune change as small as 0.00001 can be detected.

During the period of storage ring injection and booster's energy upgrade, tune has obvious change. By applying the morlet wavelet algorithm, the complete trajectory of the tune drift during the booster's energy upgrade process can be tracked.

Therefore, this new algorithm can be used to perform undisturbed tune measurement during the top-up injection period for SSRF, which provides an effective tool for the beam instability research and performance optimization of the accelerator.

REFERENCES

[1] A. Hofmann, “Beam Diagnostics and Applications”, in *AIP Conference Proceedings*, vol. 451, pp. 3-22, 1998. doi:10.1063/1.57022

[2] Leng Yongbin, Yan Yingbing, Yuan Renxian, and Zhou Weimin, “Betatron tune measurement system for Shanghai Synchrotron Radiation Facility storage ring”, *High Power*

ISBN: 978-3-95450-222-6 ISSN: 2673-5350 doi:10.18429/JACoW-IBIC2020-THPP29

Laser and Partcle Beams, vol. 22, pp. 2412-2416. doi: 10.3788/HPLPB20102210.2412

[3] Duan Qing-ming, Yang Yong-liang, Wu Fang-fang, "The Design of Tune Measurement System for HLS Ⅱ Storage Ring", *Nuclear Electronics and Detection Technology*, vol. 1, pp. 20-28, 2007.

[4] Leng Yongbin, "SSRF booster tune measurement data acquisition system", *Nuclear Techniques*, vol. 32, pp. 645-648, 2009.

[5] M. Feldman. "Non-linear Free Vibration Identification via the Hilbert Transform", Journal of Sound and Vibration, vol. 208, pp. 475-489, 1997. doi: 10.1006/jsvi.1997.1182

[6] I. Daubechies, "The wavelet transform, Time-frequency localization and signal analysis", IEEE Transactions on Information Theory, vol. 36, pp. 961-1005, 1990. doi: 10.1109/18.57199

Content from this work may be used under the terms of the CC BY 3.0 licence (© 2020). Any distribution of this work must maintain attribution to the author(s), title of the work, publisher, and DOI

ISBN: 978-3-95450-222-6 ISSN: 2673-5350 doi:10.18429/JACoW-IBIC2020-THPP33

Content from this work may be used under the terms of the CC BY 3.0 licence (© 2020). Any distribution of this work must maintain attribution to the author(s), title of the work, publisher, and DOI

SIMULATION METHODS FOR TRANSVERSE BEAM SIZE MEASUREMENTS USING THE HETERODYNE NEAR FIELD SPECKLES OF HARD X-RAYS

A. Goetz*, D. Butti, S. Mazzoni, G. Trad, CERN, Geneva, Switzerland
U. Iriso, A. A. Nosych, L. Torino, ALBA-CELLS, Cerdanyola Del Vallés, Spain
B. Paroli, M. A. C. Potenza, M. Siano, L. Teruzzi, Università degli Studi di Milan, Milano, Italy

Abstract

Heterodyne Near Field Speckles (HNFS) is a special type of interferometry technique where radiation is scattered by nanoparticles suspended in a medium. The weak scattered waves and the intense transmitted beam form an interference pattern, which is modulated by the spatial coherence of the radiation and by the scattering properties of the nanoparticles. The random superposition of many such interference patterns results in a speckle field from which the spatial coherence of the radiation, thus the transverse beam profile, can be determined. In this contribution we present approaches for simulating the HNFS patterns from hard X-ray radiation and compare then with data from experiments at the ALBA synchrotron.

INTRODUCTION

With photon beam energies of up to 100 keV in combination with an unprecedented brightness and manifold focusing possibilities, third-generation light sources have become an indispensable tool for modern nanoscale science [1]. Precise knowledge about the coherence properties of the synchrotron radiation offers a wide range of technical applications. It is at the basis of many coherence-based techniques [2], and can also give insights into the transverse particle beam distribution. As such, coherence measurements are currently studied in the context of a non-invasive transverse beam profile monitor for the Future Circular Collider, FCC-ee [3].

In this framework, the Heterodyne Near Field Speckle method is particularly appealing since it allows to access the 2D transverse coherence properties of an X-ray beam without the need of any dedicated X-ray optics. Originally introduced in the optical domain as a particle-sizing technique by Giglio et al. [4], it has been recently extended by Alaimo et al. in 2009 to the characterization of the spatial coherence properties of undulator X-ray beams [5]. An extensive study on the application of the HNFS method to spatial and temporal coherence measurements of visible synchrotron radiation has been reported in 2016 by Siano et al. [6].

In spite of its experimental success, the method still lacks robust simulations that take into account the peculiar features of undulator radiation and the optical properties of the scattering particles. In this contribution we aim to compare two different approaches of simulating X-ray Heterodyne Near Field Speckles.

* alexander.goetz@cern.ch

THEORY OF THE HNFS

As far as transverse coherence is concerned, the radiation emitted by a single electron moving through an undulator is fully coherent. A statistical ensemble of electrons, with a Gaussian shaped profile with horizontal size σ_x and vertical size σ_y, gives rise to coherence areas of size $\sigma_{vcz,x/y}$ at a distance z from the undulator center. These coherence areas follow the Van Cittert and Zernike theorem [7, 8]:

$$\sigma_{vcz,x/y} = \frac{\lambda z}{2\pi\sigma_{x/y}} \tag{1}$$

where $\sigma_{\mathrm{vcz,x/y}}$ is the transverse coherence length along the *x/y* direction, λ is the radiation wavelength, z is the distance from the center of the undulator and $\sigma_{x/y}$ is the rms size of the electron beam along the corresponding direction. When such a partially coherent wavefront impinges onto a suspension of particles with diameter d (a colloidal suspension), the synchrotron radiation is scattered. The weakly scattered spherical waves interfere with the intense trans-illuminating beam to generate Heterodyne Near Field Speckles [6]. The near field conditions, which are eponymous to this technique, require to measure the resulting interference pattern at distances z_2 downstream the scattering plane fulfilling

$$z_2 < \frac{\sigma^2_{vcz,x/y}}{\lambda} \tag{2}$$

Let us write the field of the synchrotron radiation produced by a given electron with index l as $E_l(\mathbf{x})$, the positions of the colloids with index j as $\mathbf{x}_j$ and their scattering amplitude function as $S(\mathbf{x})$. The interference image is then given by

$$I(\mathbf{x}) = \sum_l \left| \sum_j E_l(\mathbf{x}) + E_l(\mathbf{x}_j) \cdot S(\mathbf{x} - \mathbf{x}_j) \right|^2 \tag{3}$$

The individual electrons are assumed to be uncorrelated, which is why they are summed outside of the absolute square. The intensity captured by a sensor is then Fourier transformed and the corresponding power spectrum $I(\mathbf{q})$ is computed with a spatial frequency variable $\mathbf{q}$. The power spectrum shows fringes that decay due to the scattering amplitude function (the particle form factor) $S(\mathbf{q})$, the spatial coherence of the radiation $C(\mathbf{q})$ and the optical transfer function $H(\mathbf{q})$. It is additionally shaped by the Talbot oscillations $T(\mathbf{q})$ and exhibits a noise pedestal $P(\mathbf{q})$ [6]:

$$I(\mathbf{q}) = S(\mathbf{q}) \cdot T(\mathbf{q}) \cdot C(\mathbf{q}) \cdot H(\mathbf{q}) + P(\mathbf{q}) \tag{4}$$

ISBN: 978-3-95450-222-6 ISSN: 2673-5350 doi:10.18429/JACoW-IBIC2020-THPP33

Notice how the first four terms would appear in the form of a convolution in direct space, whereas they are represented by a multiplication in the reciprocal space, which makes it easy to examine individual terms. In particular, the envelope of the Talbot oscillations gives access to the 2D transverse coherence properties of the incoming undulator radiation. The 2D transverse profile of the electron beam is then retrieved by recalling the Van Cittert and Zernike theorem.

SIMULATION A: USING SRW AS A MAXWELL EQUATION SOLVER

First published in 1997 at the ESRF [9], Synchrotron Radiation Workshop (SRW) is an algorithm for the numerical evaluation of synchrotron radiation from an arbitrary magnet including undulators in synchrotrons. It is well established in the accelerator community and it is widely used for studies on synchrotron radiation. Beside calculations of the electric field, it also allows this field to be propagated through drift spaces, lenses, apertures or arbitrary 2D phase shifting and attenuating elements [9].

In our simulations, as a first step a set of electrons at positions $\mathbf{x}_l$ is chosen, representing the transverse beam profile. Using this profile the SRW code is used to create a synchrotron radiation wavefront given the specification of the NCD-SWEET undulator beamline at ALBA reported in Table 1.

Table 1: ALBA-CELLS NCD-SWEET Undulator Parameter

parameter	value
beam size σ_x	130 µm
beam size σ_y	6.5 µm
beam divergence σ'_x	47.6 µrad
beam divergence σ'_y	11.9 µrad
beam energy	2.96 GeV
undulator number of periods	92
undulator period length	21.6 mm
monochromator energy	12.4 keV
monochromaticity of radiation $\Delta E/E$	1e-4
distance from undulator to sample z	33 m

At a radiation energy of 12.4 keV, the silica colloids have a refractive index of $n-1 = \delta+\beta i = 3.59e{-}6{+}1.98e{-}8i$ [10]. While the real part causes a phase shift and is thus responsible for refraction, the imaginary part leads to absorption. The latter has been neglected in our simulations since $\beta \ll \delta$. For the simulation it is assumed that each colloid in the suspension imposes a phase shift on the wavefront. This phase shift is scaled according to the effective path length through the spherical structure of the colloids, yielding a phase shift profile for all the colloid positions $\mathbf{x}_j$. A Heaviside function is used to suppress negative values in the square root:

$$\Delta\phi(\mathbf{x}) = \sum_j \sqrt{1-\left(\frac{|\mathbf{x}-\mathbf{x}_j|}{R}\right)^2}\cdot\frac{2R\delta\omega}{c}\cdot H(R-|\mathbf{x}-\mathbf{x}_j|) \tag{5}$$

This phase shift mask is applied to the wavefront by multiplying it with $e^{i\Delta\phi}$ and propagated with SRW until the plane z_2 where the image is formed. The intensity distribution at this plane is then computed as the squared modulus of the electric field. This process is repeated for each radiating electron. In a final step all the images are summed to produce the final speckle pattern. The power spectrum of the resulting speckle image is shown in Fig. 1.

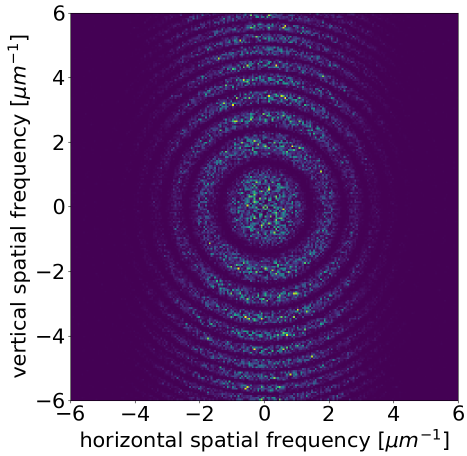

Figure 1: 2D power spectrum of the simulated speckle pattern at distance $z_2 = 10$ cm after the colloids. With reference to Eq. (1), the plot reveals the wide beam size in the horizontal and the narrow beam size in the vertical plane.

In order to extract the coherence properties of the incoming X-ray beam along the horizontal and vertical direction, crosscuts are taken through the center of the 2D power spectrum along the horizontal and vertical axis, respectively. The accuracy of these crosscuts can be further increased by calculating the angular average over double-cone sectors for each plane.

The computational effort is usually quite high for this type of simulation. For about 1000 macro-electrons, with which a good reproduction of the transverse beam profile can be achieved, about 300 CPUH and a diskspace of about 1 TB is necessary.

SIMULATION B: USING FOURIER OPTICS IN HETERODYNE CONDITIONS

Let $e_t(\mathbf{x},z)$ and $e_s(\mathbf{x},z)$ denote the intense transmitted field and the total faint scattered radiation, respectively. The latter can be expressed as $e_s = \sum_{j=1}^{N} e_{s,j}$, where $e_{s,j}$ is the spherical wave scattered by the j-th particle with position $\mathbf{x}_j$ and N is the total number of scattering centers. Both e_t and $e_{s,j}$ can be related to the incident beam e_0:

$$\begin{aligned} e_t(\mathbf{x},z) &= e_0(\mathbf{x})\exp(ikz) \\ e_{s,j}(\mathbf{x},z) &= e_0(\mathbf{x}_j)\frac{S(\theta_j)}{ikz}\exp(ikz)\exp\left(\frac{k|\Delta\mathbf{x}_j|^2}{2z}\right), \end{aligned} \tag{6}$$

Content from this work may be used under the terms of the CC BY 3.0 licence (© 2020). Any distribution of this work must maintain attribution to the author(s), title of the work, publisher, and DOI

ISBN: 978-3-95450-222-6 ISSN: 2673-5350 doi:10.18429/JACoW-IBIC2020-THPP33

Content from this work may be used under the terms of the CC BY 3.0 licence (© 2020). Any distribution of this work must maintain attribution to the author(s), title of the work, publisher, and DOI

where $k = 2\pi/\lambda$, $\Delta\mathbf{x}_j = \mathbf{x} - \mathbf{x}_j$ and $S(\theta_j)$ is the particle form factor as a function of the scattering angle $\theta_j = \arctan(|\Delta\mathbf{x}_j|/z)$. Under heterodyne conditions $|e_s| \ll |e_t|$ [6], the self-beating (homodyne) term $|e_s|^2$ of the scattered field can be neglected and the speckle intensity distribution I in Eq. (3) is given by the sum of many independent single-particle contributions s_j [6]:

$$I(\mathbf{x}, z) = |\langle e_0(\mathbf{x})\rangle|^2 + \sum_{j=1}^{N} s_j(\mathbf{x}, z)\,, \tag{7}$$

where angular brackets denote ensemble averages over many iterations of the incident field [8] and s_j describes the interference between the scattered spherical wave and the transmitted partially coherent beam:

$$s_j(\mathbf{x}, z) = \frac{2}{kz}|J(\Delta\mathbf{x}_j)| \cdot |S(\theta_j)| \cdot \cos\left[\frac{k}{2z}|\Delta\mathbf{x}_j|\right]. \tag{8}$$

In Eq. (8), $J(\Delta\mathbf{x}) = \langle e_0(\mathbf{x}+\Delta\mathbf{x})e_0^*(\mathbf{x})\rangle$ is the Mutual Coherence Function (MIF) [8] describing the transverse coherence of the incoming X-ray beam. We emphasize how Eq. (7) and Eq. (8) provide the exact, rigorous solution to the sum over many independent electrons in Eq. (3). By this we mean that computations based on Eq. (3) give the same results as Eq. (8) for a single scattering particle.

In Eq. (8), it is only required to accurately characterize J and S. The former is related to the Fourier transform of the source intensity distribution (Van Cittert and Zernike theorem) [8] and it is therefore easily computed for a Gaussian electron beam. The latter can be calculated by means of the exact Mie theory of light scattering for spherical particles [11]. Furthermore, for small scatterers with $d = 500$ nm or smaller, $S(\theta_j) \sim S(0)$ to a good approximation, which greatly simplifies the task.

The method is sketched in Fig. 2. Remarkably, the computation time is independent of N and it is only limited by the size of the simulation mesh. Furthermore, the required storage space is reduced to a minimum, since the output of the simulation is typically a single raw file of $\sim 10^6$ double values.

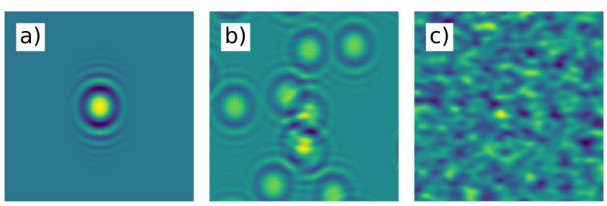

Figure 2: A sketch of simulation method B. (a) Single-particle interference image as in Eq. (8). (b) Few-particle case. (c) Many-particle (speckle) case.

The simulated speckle fields are then convoluted with the Point Spread Function (PSF) of the optical system (related to the Fourier transform of the term $H(q)$ in Eq. (4)) to account for resolution losses. We can also benefit from the linearity of Eq. (7) with respect to the single-particle contribution to perform such a convolution operation directly on Eq. (8), thus preventing aliasing artifacts in the simulated images.

The only free parameter is the mean intensity value $|\langle e_0\rangle|^2$ of the incoming beam. We typically assume $|\langle e_0\rangle|^2 = 1$ throughout the simulation, and then scale the mean value of the overall intensity distribution to match experimental data. This also provides an efficient way to account for the quantum efficiency of the detector and the read-out gain.

COMPARISON WITH EXPERIMENTAL DATA

One of the biggest challenges of the experiment is to measure the transfer function $H(q)$. It is mainly influenced by the scintillator and the microscope objective setup, which converts the X-rays into visible light and projects it onto the sensor. Additionally to this calibration curve, a water sample is imaged in order to find the pedestal, on top of which the signal is expected to appear. Both curves have been experimentally determined and properly accounted for in the imaging process of the simulated speckle patterns.

A comparison between the simulated horizontal profile of the heterodyne speckle power spectrum and actual data is reported in Fig. 3.

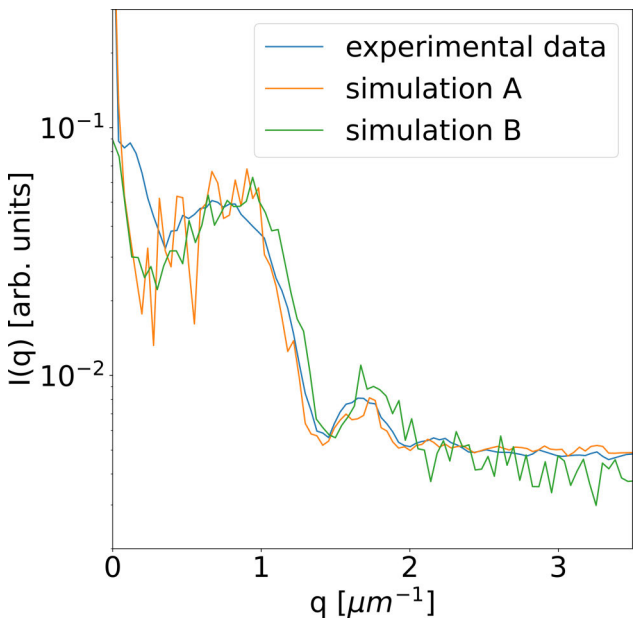

Figure 3: The power spectrum of the experimental data is compared with simulations A and B for the ALBA-CELLS NCD-SWEET in a distance $z_2 = 0.2$ m, at a radiation wavelength of $\lambda = 0.1$ nm, for the horizontal plane.

Agreement is found between simulations and the measured curve. Remarkably, simulation A and simulation B yield the same results, in spite of the fundamentally different approaches adopted. The raw speckle pattern are presented in Fig. 4 for completeness.

ISBN: 978-3-95450-222-6 ISSN: 2673-5350 doi:10.18429/JACoW-IBIC2020-THPP33

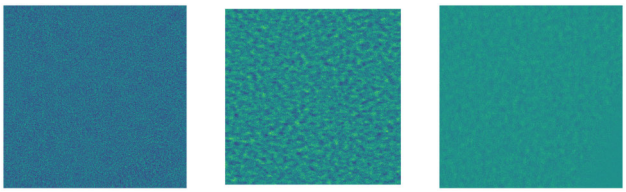

Figure 4: From left to right, the raw speckles pattern of simulation A, simulation B and the experimental data are shown.

CONCLUSION

The main advantage of simulation A is the precise calculation of the synchrotron radiation of an arbitrarily parameterized undulator, while simulation B is based on the assumption that the Van Cittert and Zernike theorem holds true for a given magnetic structure. Simulation B neglects the homodyne terms of the scattered waves, while simulation A takes them into account. Notice how this is not actually necessary, thanks to the heterodyne conditions of the technique. As for the scattering sample, simulation A relies on the approximation of two dimensional phase shifting obstacles, while simulation B applies the exact Mie formulas for spherical particles. Concerning the computational efficiency, simulation A scales linearly with the number of radiation electrons, while simulation B overcomes this issue by computing the radiation MIF through the Van Cittert and Zernike theorem. Finally, the computational complexity does not depend on the number of colloids for both simulation techniques.

We have tested the two simulation methods against real data from an undulator X-ray beam at the NCD-SWEET beamline at ALBA. Simulations compare well with actual measurements, especially regarding the horizontal profiles of the heterodyne speckle power spectrum. This proves the validity of the Van Cittert and Zernike theorem in describing the coherence properties of the incoming X-ray wavefronts. Additional investigations, both numerically and experimentally, are ongoing for the vertical transverse coherence length.

REFERENCES

[1] D. Mills, *Third Generation Hard X-ray Synchrotron Radiation Sources*. New York, USA: John Wiley and Sons, 2002.

[2] K.A. Nugent, "Coherent methods in the X-ray sciences", *Advances in Physics*, vol. 59, pp. 1–99, 2010. doi:10.1080/00018730903270926

[3] M. Benedikt *et al.*, "FCC-ee: The Lepton Collider", *Eur. Phys. J. Spec. Top.*, vol. 288, pp. 425–426, 2019. doi:10.1140/epjst/e2019-900045-4

[4] D. Brogioli, A. Vailati, M. Giglio, "Heterodyne near-field scattering", *Appl. Phys. Lett.*, vol. 81, p. 4109, 2002. doi:10.1063/1.1524702

[5] M. D. Alaimo, M. A. C. Potenza, M. Manfredda, G. Geloni, M. Sztucki, T. Narayanan, and M. Giglio, "Probing the Transverse Coherence of an Undulator X-Ray Beam Using Brownian Particles", *Phys. Rev. Lett.*, vol. 103, p. 194805, 2009. doi:10.1103/physrevlett.103.194805

[6] M. Siano *et al.*, "Transverse Beam Size Diagnostics using Brownian Nanoparticles at ALBA", in *Proc. IBIC'16*, Barcelona, Spain, Sep. 2016, pp. 248–252. doi:10.18429/JACoW-IBIC2016-MOPG73

[7] M. Born and E. Wolf, *Principles of Optics*. Cambridge, England: Cambridge University Press, 1999.

[8] J. W. Goodman, *Statistical Optics*. New York, USA: Wiley-Interscience, 2000.

[9] O. Chubar and P. Elleaume, "Accurate and Efficient Computation of Synchrotron Radiation in the Near Field Region", in *Proc. EPAC'98*, Stockholm, Sweden, Jun. 1998, paper THP01G, pp. 1177–1179.

[10] S. Kuznetsov, "X-Ray Optics Calculator", IMT RAS, Chernogolovka, Russia, http://purple.ipmt-hpm.ac.ru/xcalc/xcalc_mysql/ref_index.php

[11] H.C. Hulst, *Light Scattering by Small Particles*. New York, USA: John Wiley and Sons, 1957.

Content from this work may be used under the terms of the CC BY 3.0 licence (© 2020). Any distribution of this work must maintain attribution to the author(s), title of the work, publisher, and DOI

ISBN: 978-3-95450-222-6 ISSN: 2673-5350 doi:10.18429/JACoW-IBIC2020-THPP34

Content from this work may be used under the terms of the CC BY 3.0 licence (© 2020). Any distribution of this work must maintain attribution to the author(s), title of the work, publisher, and DOI

CALIBRATION AND IMAGE RESTORATION FOR THE BEAM PROFILE MEASUREMENT SYSTEM*

L. X. Hu[1], Y. T. Song†, K. Z. Ding,
Institute of Plasma Physics, Chinese Academy of Sciences, Hefei, China
Y. C. Wu, Hefei CAS Ion Medical and Technical Devices Co., Ltd, Hefei, China
[1]also at University of Science and Technology of China, Hefei, China

Abstract

The transverse beam profile parameters are closely related to the beam tuning and optimization of the cyclotron. In order to improve the precision and efficiency of beam profile measurement system, A calibration method has been implemented for the calibration of the imaging system. Moreover, a new image noise reduction algorithm has been developed to improve the image quality, and then to improve the measurement accuracy of the beam profile parameters. In addition, two image restoration algorithms have also been adopted to eliminate the effects of defocusing blur. The experiment results show that the calibration of the imaging system enable the system to provide quantitative information for beam diagnosis. The image noise reduction and restoration algorithm greatly improve the measurement accuracy of beam profile parameters.

INTRODUCTION

The beam profile parameters are one of the important parameters, which represent the beam quality [1]. The performance of the accelerator and the safe and stable operation are closely related to the transverse beam distribution [2]. The measurement of beam profile parameters can provide an important basis for the debugging and commissioning of the accelerator and the improvement of beam quality [3]. The most commonly used beam profile measurement instruments include: Scintillator detector [4], OTR target [5], synchronized light imaging [6] and wire scanning [7].

Due to the limitation of the imaging system and the influence of the imaging and signal transmission environment, there will inevitably be distortion and deviation between the observed image and the actual image, which is called image degradation [8]. The main factors leading to the image degradation of the scintillator detector include：

- The image distortion caused by the aberration and nonlinear distortion of the imaging system;
- Various noises introduced by the imaging system and image transmission process;
- Defocus blur caused by inaccurate focus of the camera.

The phenomenon of image degradation has a significant impact on the image measurement and analysis.

* Work supported by grants 1604b0602005 and 1503062029.
† email address: hulx@ipp.ac.cn

IMAGING SYSTEM CALIBRATION

Basis of Coordinate Transformation

The conversion relationship between the pixel coordinate system and the world coordinate system is given by

$$z_c \cdot \begin{bmatrix} u \\ v \\ 1 \end{bmatrix} = \begin{bmatrix} f_x & 0 & u_0 & 0 \\ 0 & f_y & v_0 & 0 \\ 0 & 0 & 1 & 0 \end{bmatrix} \cdot \begin{bmatrix} \boldsymbol{R}_{3\times3} & \boldsymbol{T}_{3\times1} \\ \boldsymbol{0} & 1 \end{bmatrix} \cdot \begin{bmatrix} x_w \\ y_w \\ z_w \\ 1 \end{bmatrix} = \boldsymbol{M_1 M_2 X_w} \quad (1)$$

where $[u \quad v]$ is the coordinates in the pixel coordinate system, u_0 and v_0 denote the translation amount of the image coordinate system relative to the pixel coordinate system, f is the focal length of the camera, $\boldsymbol{R}_{3\times3}$ represents the rotation matrix, $\boldsymbol{T}_{3\times1}$ represents the translation matrix, $[x_w \quad y_w \quad z_w]$ is the coordinates in the world coordinate system. $\boldsymbol{M_1}$ is called the internal parameter matrix. $\boldsymbol{M_2}$ is called the external parameter matrix.

Camera Distortion

The image distortion of the visual system occurs in the process of imaging. The radial and tangential distortion have great influences on the image. Radial distortion occurs when light rays bend more near the edges of a lens than they do at its optical center. Tangential distortion occurs when the lens and the image plane are not parallel.

The radial distortion is corrected by the Taylor series expansion shown in Eq. (2) and (3):

$$x_c = x(1 + k_1 r^2 + k_2 r^4 + k_3 r^6), \quad (2)$$

$$y_c = y(1 + k_1 r^2 + k_2 r^4 + k_3 r^6), \quad (3)$$

where k_1, k_2 and k_3 are radial distortion coefficients, r represents the distance from the imaging center, (x, y) and (x_c, y_c) are the undistorted and the distorted points.

The tangential distortion is corrected by the following formulas:

$$x_c' = x + [2p_1 y + p_2(r^2 + 2x^2)], \quad (4)$$

$$y_c' = y + [2p_2 x + p_1(r^2 + 2y^2)], \quad (5)$$

where p_1 and p_2 are tangential distortion coefficients of the lens.

Camera Calibration

For stereo applications, these distortions need to be corrected first. To find the internal and external parameters and camera distortion parameters, what we have to do is to provide some sample images of a well-defined pattern (e.g. chess board). Important input data needed for camera

ISBN: 978-3-95450-222-6 ISSN: 2673-5350 doi:10.18429/JACoW-IBIC2020-THPP34

calibration is a set of 3D real world points and its corresponding 2D image points. With these data, some mathematical problem is solved in background to get the distortion coefficients. That is the summary of the whole story. For better results, we need at least 10 test patterns [9].

Through the calibration, the internal parameter matrix of the camera and the distortion coefficients can be calculated. Furthermore, each image can be re-projected to obtain new projection points.

IMAGE DEGRADATION MODEL

Image Noise

Theoretically, noise is generally regarded as unpredictable random errors, which can only be recognized by statistical methods, and can be described by random processes. The digital characteristics of mean, variance, and correlation function are usually used to describe the characteristics of the image noise.

Impulse noise is a common multiplicative noise caused by the external interference to image sensors and transmission channels. Gaussian noise is an additive noise, which is generally generated by photosensitive elements.

Defocus Blur

For the scintillator detector, the ideal imaging formula is shown in Eq. (6):

$$\frac{1}{f} = \frac{1}{u} + \frac{1}{v} \tag{6}$$

where f is the focal length of the camera, u and v are the object distance and image distance, respectively.

However, if the focal length, object distance and image distance in the imaging system do not satisfy the imaging formula, a point on the original image will become a uniformly distributed disk instead of a point.

Therefore, the point spread function (PSF) of the degraded image caused by defocus is shown in Eq. (7):

$$h(x,y) = \begin{cases} \frac{1}{\pi R^2} & x^2 + y^2 \le R^2 \\ 0, & otherwise \end{cases}. \tag{7}$$

where R is the blur radius.

Modelling

For the degradation of the scintillator detector imaging system, the impulse response and noise pollution are considered. Generally speaking, the imaging system is considered as a linear space-invariant system, that is, the degradation result of each pixel in the image only depends on the gray value of the point, rather than the coordinates of the pixel.

Assuming that the original image is $f(x,y)$, the observed image $g(x,y)$ is obtained under the combined action of the PSF $h(x,y)$ and the additive noise $n(x,y)$.The degradation process can be expressed as:

$$g(x,y) = \int_{-\infty}^{+\infty}\int_{-\infty}^{+\infty} f(\alpha,\beta)h(x-\alpha,y-\beta)d\alpha d\beta + n(x,y). \tag{8}$$

Equation (8) can be expressed as:

$$g(x,y) = f(x,y) \otimes h(x,y) + n(x,y). \tag{9}$$

where $\otimes$ represents the spatial convolution. Therefore, it is very important to study the PSF for the establishment and analysis of degradation model.

NOISE REDUCTION

Description of the Algorithm

An impulse noise filter based on image segmentation and region growing (ISRGF) has been proposed for removing high level of impulse noises. The proposed algorithm is composed of two stages. The aim of the first stage is to detect possible image edges according to predefined image edge patterns, and to remove impulse noise temporarily. In the second stage, image edge detection and image edge tacking algorithms have been applied to divide the preliminary denoised image into irregular regions. For each corrupted pixel, an eight-neighbor region-growing algorithm has been designed to generate a computational domain. The weighted mean of the pixels in the computational domain is calculated to replace the current corrupted pixel.

Image Edge Detection

To preserve the edge details of the image, the image edges need to be detected as accurately as possible. However, the image edges are seriously damaged for highly corrupted images. Based on that, a variety of image edge patterns were defined for accurate image edge detection.

Figure 1 shows two typical image edge patterns. The noise-free pixels within the window are divided into two sets by the image edge, which are denoted by $A_{i,j}$ and $B_{i,j}$ respectively. In Fig. 1, the orange filled squares represent pixels at the image edge, the $A_{i,j}$ and $B_{i,j}$ are denoted by blue filled and green filled squares respectively.

The center pixel $p_{i,j}$ is considered to be located on the image edge if Eqs. (10) and (11) are both satisfied:

$$min[min(A_{i,j}) - max(B_{i,j}), min(B_{i,j}) - max(A_{i,j})] \ge th_1, \tag{10}$$

$$max(E_{i,j}) - min(E_{i,j}) \le th_2, \tag{11}$$

where, $max(A_{i,j})$ and $min(A_{i,j})$ represent the maximum and the minimum value in set $A_{i,j}$ respectively, $E_{i,j}$ denotes the set of noise-free pixels at the potential image edge, th_1 and th_2 denote the given thresholds.

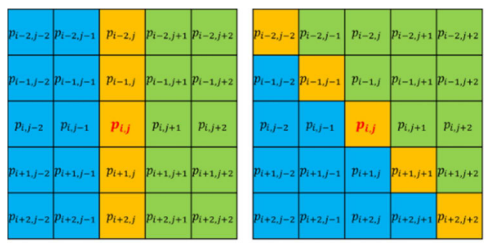

Figure 1: Two typical image edge patterns.

Content from this work may be used under the terms of the CC BY 3.0 licence (© 2020). Any distribution of this work must maintain attribution to the author(s), title of the work, publisher, and DOI

ISBN: 978-3-95450-222-6 ISSN: 2673-5350 doi:10.18429/JACoW-IBIC2020-THPP34

Content from this work may be used under the terms of the CC BY 3.0 licence (© 2020). Any distribution of this work must maintain attribution to the author(s), title of the work, publisher, and DOI

The corrupted pixels are replaced temporarily according to the results of image edge detection. If the corrupted pixel is located on the image edge, it is replaced by the median value of set $E_{i,j}$. Otherwise, it is replaced by the median value of set $A_{i,j}$ or $B_{i,j}$.

Image Segmentation

To achieve the purpose of image segmentation, the Canny edge detector has been adopted to perform edge detection on the preliminary denoised image firstly. Then an edge tracking algorithm has been designed to link the discrete pixels at the adjacent image edge which with similar grey values. Hence, the image edges linked by the edge tracking algorithm are marked with the same number, while discontinuous image edges are marked with different numbers.

The detailed steps of the edge tracking algorithm are described as follows.

1. Scan the image output from the Canny edge detector, and for pixels at image edges, mark the first unmarked pixel (x_0, y_0) with a new number.
2. Check whether the pixel (x, y) in the eight-neighbor of (x_0, y_0) is located on image edges which with similar gray value. If yes, mark it with the same number with (x_0, y_0), and push it into a stack.
3. Extract a pixel from the stack, and take it as (x_0, y_0), then return to step 2).
4. Return to step 1) when the stack is empty.
5. Terminate the procedure until all pixels at image edges are marked.

Figures 2 (a) and (b) show the original image and the result of image edge linking. As can be seen in Fig. 2 (b), the adjacent pixels at image edges which with similar grey values share the same colour, while different image edges are assigned different colours. So that the original image is segmented into many irregular regions by image edges.

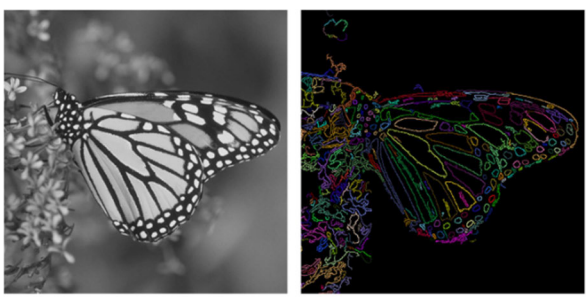

(a) (b)

Figure 2: Image segmentation and image edge linking.

Region Growing

It is obvious that pixels in the same region have similar gray values. Therefore, the corrupted pixel is replaced by the average value of the irregular region which contained the corrupted pixel, instead of the median-type value of the fixed or adaptive windows.

For each corrupted pixel, the eight-neighbour region-growing algorithm has been applied to add adjacent noise-free pixels in the same region into the corresponding computational domain. The computational domain will stop growing when the size of the computational domain or the recursive steps reach the corresponding set value.

Figure 3 shows the results of the region growth in two cases. Different regions are represented by squares filled with different colors. The orange and yellow filled squares denote pixels at image edges. The red filled squares represent the corrupted pixels, and the region surrounded by the red closed dotted line denotes its computational domain.

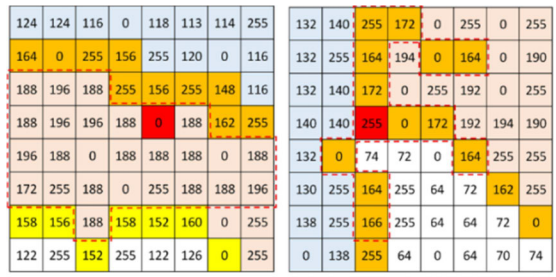

(a) (b)

Figure 3: The results of region growing for (a) corrupted pixel in the texture, (b) corrupted pixel at the image edge.

Weighted Mean Filter

For pixels within the computational domain that are closer to the current corrupted pixel, the higher correlation is considered. Thus, the corrupted pixel is replaced by the weighted mean which defined in Eq. (12).

$$p_{i,j}^{corrupted} = \frac{\sum_{p_{x,y} \in M_{i,j}} w_{x,y} p_{x,y}}{\sum_{p_{x,y} \in M_{i,j}} w_{x,y}} \tag{12}$$

where $M_{i,j}$ is the computational domain of the corrupted pixel $p_{i,j}$, $w_{x,y}$ is the weight of $p_{x,y}$, $d_{x,y}$ is the chessboard distance between $p_{x,y}$ and $p_{i,j}$, and n is a constant.

For isolated corrupted pixel which is surrounded by the image edge, its corresponding computational domain is an empty set. Therefore, the corrupted pixel is replaced by the mean of noise-free pixels in its eight-neighbor.

Quantitative Results Comparison

Several typical images have been tested to assess the quantitative performance of the ISRGF in terms of PSNR (Peak-Signal-to-Noise Ratio) and SSIM (Structural Similarity Index Measure). The grayscale image, namely 'Lena' with size of 512×512 was taken as an example to compare with other representative filters. Different densities of impulse noises varied from 10% to 90% have been added into the test image artificially.

Figure 4 shows the restoration results in terms of PSNR of different filters. It is obvious that the ISRGF has achieved better performance at both low and high noise densities.

ISBN: 978-3-95450-222-6 ISSN: 2673-5350 doi:10.18429/JACoW-IBIC2020-THPP34

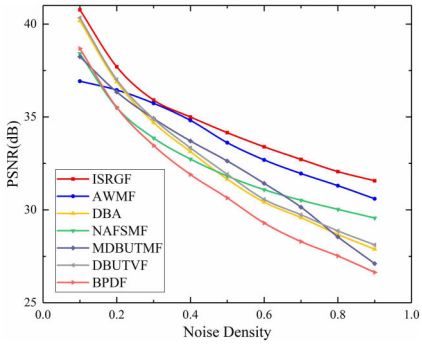

Figure 4: Comparisons of restoration results in PSNR of different algorithms.

IMAGE DEBLURRING

Estimates of the PSF

For the PSF of the defocus blur, the model is uniquely characterized by the defocus radius R. Current estimation methods for defocus radius include: Bessel function analytical method [10], error-parameter analysis method [11] and Laplace operator-based estimation method [12]. According to the advantages and disadvantages of these methods, the estimation method based on Laplace operator is selected to estimate the defocus radius.

Without considering the image noise, second-order differentiation was performed on the blurred image firstly:

$$\nabla^2 g(x,y) = f(x,y) \otimes \nabla^2 h(x,y). \quad (13)$$

Then a fast Fourier transform was performed on the differentiated image to get the self-correlation S of the image:

$$S = \nabla^2 g(x,y) \bowtie \nabla^2 g(x,y)$$

$$S = (f(x,y) \bowtie f(x,y)) * (\nabla^2 h(x,y) \bowtie \nabla^2 h(x,y)) \quad (14)$$

where $\bowtie$ denotes two-dimensional correlation, $S_f = f(x,y) \bowtie f(x,y)$ represents the self-correlation of the original image, $S_h = (\nabla^2 h(x,y) \bowtie \nabla^2 h(x,y))$ represents the self-correlation of the differential PSF function.

From the curved surface image of self-correlation S, it can be seen that there is a sharp peak in the image, which is surrounded by an annular groove [13]. The theoretical value of the radius of the annular groove is the defocus radius. Therefore, the defocus radius can be estimated by identifying the radius of the annular groove, and then the PSF of the defocus model can be determined.

Lucy-Richardson algorithm

Lucy-Richardson algorithm [14] is derived from Bayesian statistics. The basic idea of Lucy-Richardson algorithm is to approximate the maximum likelihood estimation of the original image through iterative calculation. The iterative equation is given by

$$f(x,y)^{n+1} = f(x,y)^n \left[\left(\frac{g(x,y)}{h(x,y) \otimes f(x,y)^n}\right) \bowtie h(x,y)\right] \quad (15)$$

where n is the number of iterations.

Wiener Filter

The principle of Wiener filter is to find an optimal restored image to minimize the mean square error with the original image. Wiener filtering can be expressed as:

$$F(u,v) = \left[\frac{1}{H(u,v)} \cdot \frac{|H(u,v)|^2}{|H(u,v)|^2 + \left[\frac{S_{nn}(u,v)}{S_{ff}(u,v)}\right]}\right] G(u,v) \quad (16)$$

where $K = \frac{S_{ff}(u,v)}{S_{nn}(u,v)}$ is the signal-to-noise ratio. Therefore, when the PSF is obtained, the inverse Fourier transform of the above formula can be performed to obtain the restored image under the specified signal-to-noise ratio.

Wiener filter requires a small amount of calculation, and more importantly, it still has a good restoration effect even for highly corrupted images. However, when the signal-to-noise ratio of the image is small, the restoration effect of Wiener filter will deteriorate.

Results and Analysis

The performance of the Wiener and Lucy-Richardson algorithm was compared in Fig. 5. The blur radius of the blurred image is 10 pixels. It can be seen from Fig. 5 that the performance of the Wiener filter is slightly better than the Lucy-Richardson algorithm. However, the restored image of Wiener filter produces more obvious ringing effect.

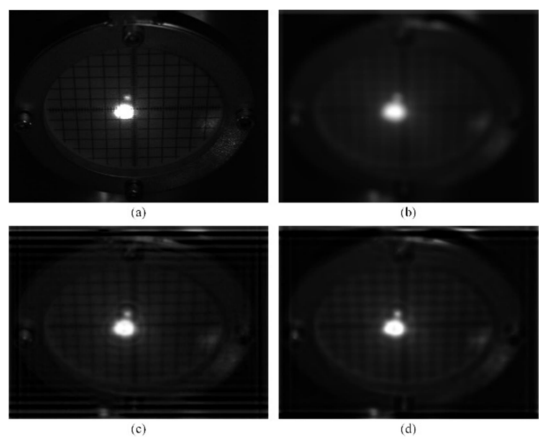

Figure 5: The comparison of the performance of the Wiener filter and Lucy-Richardson algorithm.

CONCLUSION

To improve the precision and efficiency of beam profile measurement system, a calibration method has been conducted for the calibration of the imaging system. Moreover, a new image noise reduction algorithm and two image restoration algorithms have been developed to restore images. The experiment results show that the calibration procedure and image restoration algorithms greatly improve the measurement accuracy of beam profile parameters, which enable the system to provide quantitative information for beam diagnosis.

Content from this work may be used under the terms of the CC BY 3.0 licence (© 2020). Any distribution of this work must maintain attribution to the author(s), title of the work, publisher, and DOI

ISBN: 978-3-95450-222-6 ISSN: 2673-5350 doi:10.18429/JACoW-IBIC2020-THPP34

Content from this work may be used under the terms of the CC BY 3.0 licence (© 2020). Any distribution of this work must maintain attribution to the author(s), title of the work, publisher, and DOI

REFERENCES

[1] J. liu, "Design of the beam profile monitors for compacting THz-FEL source", Master's thesis, University of Science and Technology of China, China, 2016.

[2] B. Walasek-Hohne, C. Andre, P. Forck, *et al.*, "Scintillating screen applications in accelerator beam diagnostics", *IEEE T. Nucl. Sci.*, vol. 59, no. 5, p. 2307-2312, 2012. doi: 10.1109/TNS.2012.2200696

[3] P. Zheng, B. Sun, and P. Lu, "Imaging acquirement system applied to beam profile and emittance measurement for HLS", *Measurement & Control Technology*, vol. 24, no. 5, p. 24-26, 2005. doi: 10.3969/j.issn.1000-8829.2005.05.007

[4] [4] Y. B. Leng et al., "Beam based calibration of X-ray pinhole camera in SSRF", *Chinese Phys. C*, vol. 36, pp. 80-83, 2011. doi:10.1088/1674-1137/36/1/014

[5] P. Forck, "Lecture notes on beam instrumentation and diagnostics", in *Proc. Joint University Accelerator School (JUAS)*, Archamps, France, Mar. 2011.

[6] L. Tang, "Development and Study of Beam Profile Measurement System for HLS II", Ph.D. thesis, University of Science and Technology of China, China, 2012.

[7] M. R. Hadmack and E. B. Szarmes, "Scanning Wire Beam Position Monitor for Alignment of a High Brightness Inverse-Compton X-ray Source", in *Proc. IBIC'13*, Oxford, UK, Sep. 2013, paper WEPF21, pp. 856-859.

[8] H. C. Andrews and B. R. Hunt, "Digital Image Restoration", Englewood Cliffs, New Jersey, USA: Prentice-Hall, 1977. doi:10.1016/0031-3203(79)90032-3

[9] Z. Zhang, "A flexible new technique for camera calibration", *IEEE T. Pattern Anal.*, vol. 22, no. 11, p. 1330-1334, 2000. doi:10.1109/34.888718

[10] S. Treitel, "The complex Wiener filter", *Geophysics*, vol. 39, no. 2, p. 169-173, 1974. doi:10.1190/1.1440419

[11] R. L., Lagendijk, A. M. Tekalp, and J. Biemond, "Maximum likelihood image and blur identification: a unifying approach", *Opt. Eng.*, vol. 29, no. 5, p. 422-436, 1990. doi:10.1117/12.55611

[12] Q. R. Chen, Q. S. Lu, L. Z. Cheng, *et al.*, "Identification of the point spread function from the defocus image using the Laplacian operators", *Computer Engineering & Science*, vol. 27, no. 9, p. 40-43, 2005.

[13] S. Jutamulia, "Joint transform correlators and their applications", in *Proc. SPIE 1812, Optical Computing and Neural Networks*, 1992. doi:10.1117/12.131218

[14] W. H. Richardson, "Bayesian-based iterative method of image restoration", *JoSA*, vol. 62, no. 1, p. 55-59, 1972. doi:10.1364/JOSA.62.000055

ISBN: 978-3-95450-222-6 ISSN: 2673-5350 doi:10.18429/JACoW-IBIC2020-THPP35

LENS CALIBRATION FOR BEAM SIZE MONITORS AT ThomX

S. D. Williams, G. N. Taylor, The University of Melbourne, Melbourne, Australia
I. Chaikovska, N. Delerue, V. Kubytskyi, H. Monard,
A. Moutardier, A. Gonnin, Université Paris-Saclay, Orsay, France

Abstract

ThomX is a novel compact X-ray light source, utilising a laser and 50 MeV electron storage ring to produce X-ray photons via Compton scattering. Screens, observed by zoom lenses and optical cameras, can be used to monitor the transverse beam profile at various points.

An issue with the implementation of this system is that after adjusting the zoom one needs to recalibrate the the optical system, measuring the resolution of the optical system and deducing the transformation from pixel space observed on the camera to geometrical space in the laboratory.

To calibrate and measure the resolution limit of the cameras a USAF 1951 resolution chart that can be moved into or out of the screen position is used.

We will report on and demonstrate the use of open source computer vision libraries to compute this calibration, and the affine transformation between the camera image plane and the screens can be deduced. We will also comment on how consumer available Canon EF mount lenses may be used as a remote controllable optical system.

INTRODUCTION

Beam size measurement is one of the important diagnostic measurements performed at the ThomX light source, and is measured at three stations of the injection line and at two stations just before the two beam dumps.

At each diagnostic station along the beamline a YAG screen, USAF1951 microscope resolution target, and blank screen are mounted on rails driven by a stepper motor. These can be moved in or out of position, in or out of the trajectory of the beam, and are observed by the optical system mounted underneath. The optical system consists of a Tamron B028 18–400mm F/3.5–6.3 telephoto lens and digital camera which is mounted underneath the station. To focus the optical system the internal motors of the lens are used, and to control the zoom level an external belt and motor system is being developed, with the aim that once position at the monitoring station the optical system can be completely controlled from the control room.

We note that the camera and lens image plane is not parallel to the plane of the screens or microscope target, but at roughly forty-five degrees. More information, including descriptions and images of the diagnostic stations, can be find in the ThomX TDR [1].

The work discussed in this publication deals with the calibration of the camera and optical systems used to observe the YAG screens, and the repurposing of Tamron EF lenses for effective remote focus control.

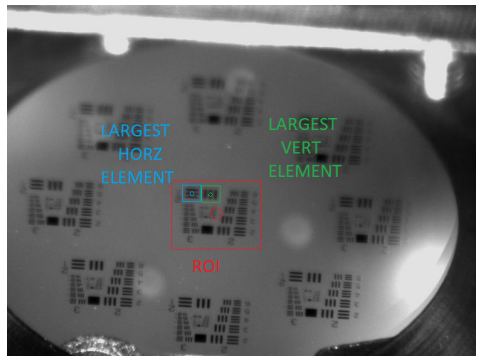

Figure 1: Highlighting a detected region of interest, and the largest horizontal and vertical elements detected.

NOMENCLATURE AND DEFINITIONS

We shall define the following terms now to simplify the reading of this document. Firstly, the entire glass slide is referred to as a USAF1951 test chart. There are nine targets on each USAF1951 test chart, as seen in Fig. 1. Each target is made up of differently but precisely proportioned bar patterns, and we refer to a set of three bars in the same orientation as an element, a set of three elements as a group.

The USAF1951 test chart is a somewhat common calibration chart, and more detail is easily found via an internet search.

OPERATION OF OPTICAL SYSTEM

During the commissioning and later operation of ThomX, the ideal operator workflow is that the operator should be able to adjust the camera zoom to be able to view the entire YAG screen, then zoom in as appropriate to clearly view the beam spot. This means imaging an area of roughly 23 mm by 23 mm to 4 mm by 4 mm at either extreme, and recalibrating the cameras each time the cameras are moved. Recalibrating the cameras, and checking the transverse beam size is expected to occur at least daily, if not more often, and if this were to require manual experienced operator supervision or take too long to run operational run times could be affected. Thus, the process should be nearly entirely automatic, and finished in a reasonable length of time.

The objective of the system calibration is to ascertain the resolution of the system and the appropriate coordinate transform from image pixels to laboratory distances. In this context the resolution refers to the resolving power of the entire optical and camera system, in terms of the size of the smallest details that can be reasonably distinguished.

Content from this work may be used under the terms of the CC BY 3.0 licence (© 2020). Any distribution of this work must maintain attribution to the author(s), title of the work, publisher, and DOI

ISBN: 978-3-95450-222-6 ISSN: 2673-5350 doi:10.18429/JACoW-IBIC2020-THPP35

Content from this work may be used under the terms of the CC BY 3.0 licence (© 2020). Any distribution of this work must maintain attribution to the author(s), title of the work, publisher, and DOI

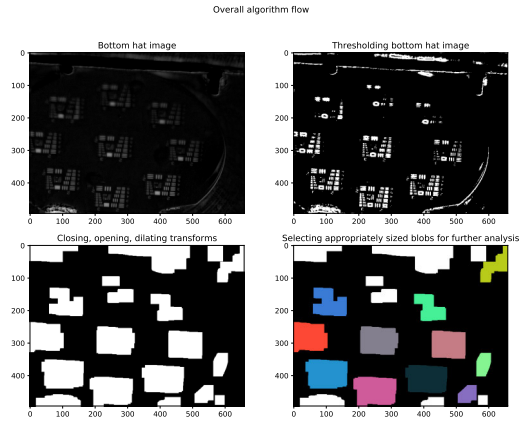

Figure 2: Pictorial representation of ROI detection.

SOFTWARE METHODS

We note that our software relies heavily on the OpenCV library [2]. Images used in this preliminary analysis were from the in situ ThomX cameras, and had a pixel resolution of 659 pixels by 494 pixels. Higher resolution cameras may be introduced later.

Region of Interest Detection

We use a method similar to and influenced by [3], which uses morphological transformations to hight regions made repeated closely spaced structures. Our method is based around using the black/bottom hat to highlight structures less than the size of the structuring element, and then joining and smoothing off these structures with repeated closing, opening, and dilating transforms. This is represented pictorially in Fig. 2, and the original image is similar to those in Fig. 1. We note that future images may be have less depth of field effects, or higher pixel counts, but this is a good example of minimum expected image quality.

The process is as follows:

1. Use the black hat transform to highlight dark structures smaller than the size of the structuring element.
2. We then threshold the image using the combination of an Otsu threshold and a distance map threshold.
3. Perform closing then opening transforms to remove small edge holes or whiskers, and then dilate to ensure we get all of the ROI plus a small border.
4. We then search for complete blobs using a connected components algorith. We then filter based on area, dimensional ratio, and other criteria.

Each ROI found is then expected to contain one complete target, and is analysed further on that basis.

Figure 3: Binarised image, and image showing filtered connected components.

Analysis of Regions of Interest

Figures 1, 3, and 4 add context to the following description of ROI analysis.

First, the blurriness of the ROI is quantified using the ratio of high frequency Fourier elements to the rest of the spectrum, and the high pass filter method from [4].

Then the image is binarised and optionally Fourier filtered.

After that we estimate orientation angle of the entire image by constructing the (dx, dy) gradient field using Sobel operators, filter on gradient magnitude, and then estimate gradient angle per pixel according to $\tan\theta = \frac{dx}{dy}$. As the USAF1951 microscope chart is made mostly of regular straight objects at 90° to each other there will be a peak in angular distribution representing the orientation of the chart.

Individual shapes in the image are found by a connected components algorithm, and then filtered based on area, similarity to a rectangle, dimensional ratio, and whether the shape orientation angle is perpendicular or parallel to the ROI orientation angle. See Fig. 3.

The group number and element number of the smallest element is found by counting the number of horizontal or vertical bar patterns detected and subtracting from the largest group and element numbers, as inputted by during software setup. The resolution of the ROI in each direction is then calculated using the standard USAF1951 chart resolution equation.

The six bars of the largest horizontal and vertical elements in the ROI are then measured, and vectors constructed from their largest dimension. Those dimensional vectors are then used to calculate the linear transformation T from pixel coordinates to real world laboratory coordinates, according to the expression

$$T = X_{\text{geo.}} \cdot U_{\text{img.}}^{T} \cdot \left(U_{\text{img.}} \cdot U_{\text{img.}}^{T} \right)^{-1}$$

$U_{\text{img.}}$ is a matrix formed by stacking horizontally (concatenating) the column vectors found from measuring the elements in the ROI, and $X_{\text{geo.}}$ is a similar matrix formed from similarly horizontally stacking the known geometric dimensions of the bars. As this expression was found in a similar manner to the derivation of ordinary least squares, issues regarding the invertibility of $U_{\text{img.}} \cdot U_{\text{img.}}^{T}$ are similar to those of $A^{T}A$ in the ordinary least squares estimation of A in $y = Ax$. The results of the analysis are then saved to disk.

ISBN: 978-3-95450-222-6 ISSN: 2673-5350 doi:10.18429/JACoW-IBIC2020-THPP35

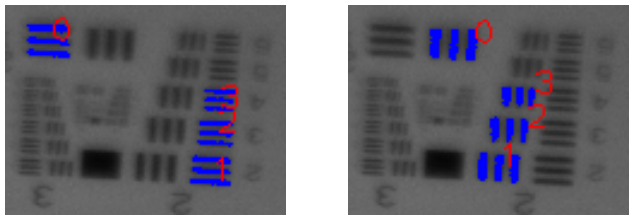

Figure 4: After clustering similarly sized and located horizontally or vertically oriented elements.

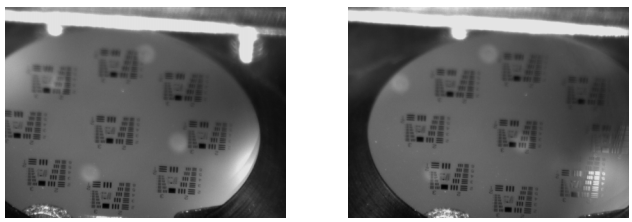

Figure 5: Example images from beginning and end of movement.

Cross Referencing of Results

As each of the ROIs are analysed independently, we are then able to cross reference the results to improve accuracy and check for obvious discrepancies. Group averages of detected bar lengths, focus scores, transformation matrices, etc are also taken. A short report is saved as a JSON or YAML file for use by the immediate operator or other software, and could also be used for tracking performance over time.

Software Performance

Prelimary testing of the software in situ was done by moving the USAF1951 chart from left to right in constant increments of 250 µm and running the analysis software. As the microscope chart is moved using a set of precise linear stages, this allows us to test the stability and accuracy of the software. Images taken from the beginning and end of these movements are shown in Fig. 5.

In Fig. 6 we show a plot of the position of every ROI centre for every image taken, all on the one plot. This summarises how the ROI centres move in fairly straight lines as we increment the USAF1951 microscope chart.

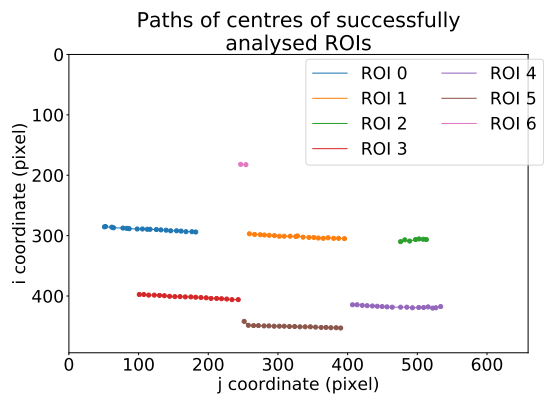

Figure 6: Scatterplot of successfully analysed ROI centres as the chart is moved from left to right.

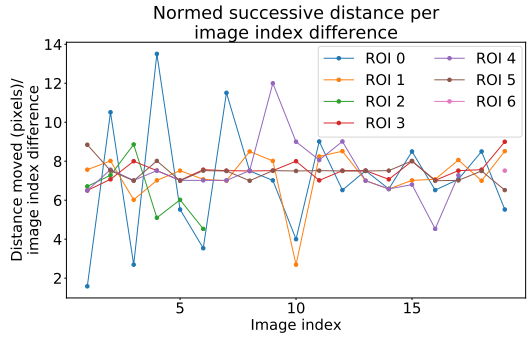

Figure 7: The normed distance between successive ROI centres, divided by picture number difference.

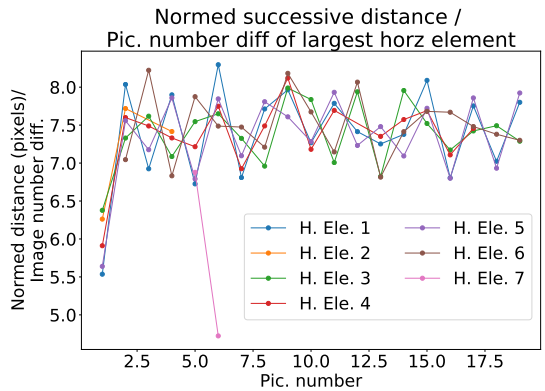

Figure 8: The normed distance between successive largest horizontally oriented element, divided by picture number difference.

In Fig. 7 we have found the displacement vector between ROIs from successive images, and then taken its norm and divided by the difference in image index, which gives an estimate of pixel movement per stage movement. This shows a somewhat steady movement of approximately 7.5 pixels per 250 µm, there there is some visible variation. Although some significant variation can occur at points, we decided this was acceptable, as the goal of the ROI detection was not the precisely locate the ROI in the image, but to indicate an area where only one target should be found.

In Figs. 8 and 9 similar plots have been created, except in this instance the position of the largest elements in each ROI has been used. As these elements will be used later in the ROI analysis for calibration they should be as precisely measured and located as possible. We find that in this case, each time the USAF1951 chart is moved 250 µm on the linear stage the software detects a movement approximately 7.5 pixels, with a variation of generally less than one pixel. The exact reason why there is a sudden jump at the start is unclear however, but note that it is of the order of one pixel and thus very small.

Content from this work may be used under the terms of the CC BY 3.0 licence (© 2020). Any distribution of this work must maintain attribution to the author(s), title of the work, publisher, and DOI

ISBN: 978-3-95450-222-6 ISSN: 2673-5350 doi:10.18429/JACoW-IBIC2020-THPP35

Content from this work may be used under the terms of the CC BY 3.0 licence (© 2020). Any distribution of this work must maintain attribution to the author(s), title of the work, publisher, and DOI

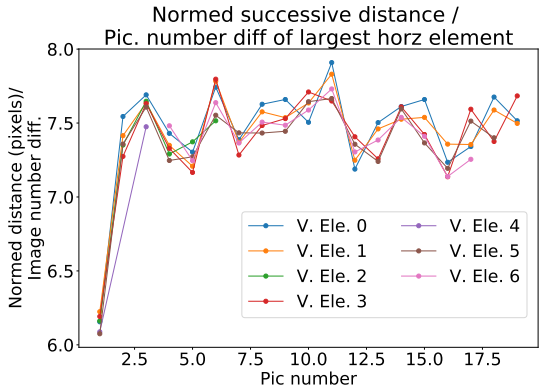

Figure 9: The normed distance between successive largest vertically oriented element, divided by picture number difference.

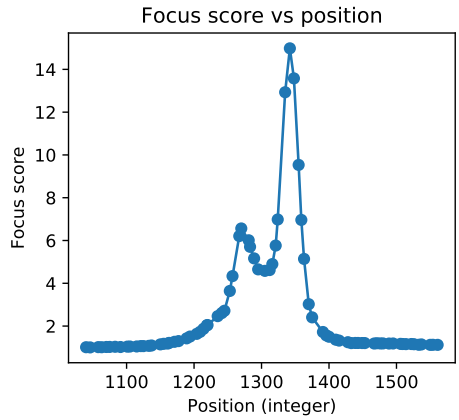

Figure 10: Focus score of image taken at varying positions, positions are arbitrary internal lens coordinates.

HARDWARE

In this section we will discuss work done to repurpose a Tamron Canon EF mount telephoto lens as a novel method to provide an powerful but economical remotely actuated optical system. We note that throughout this section descriptions of the diagnostic stations are outlined in [1], and that further details on reverse engineering lens communication protocols can be found through an internet search.

To investigate how similar the communication protocol is between different lenses we investigated three lens from two manufacturers, Canon and Tamron. We found that all used a similar communication protocol, similar to the common SPI, but with the important difference that the slave device can attempt to push or pull the clock pin to indicate readiness. For our work, we will control the lens using an Arduino Uno, an easily programmed and consumer available microcontroller. Results and plots to follow were based on work done with a Tamron 18–400mm F/3.5–6.3 Di II VC HLD telephoto lens, the model which will be used on the ThomX diagnostic stations, but we expect similar results with other lenses.

Two interfaces to the Arduino/lens were created, one where where the Arduino was sent commands over the USB connection from a host computer that could run a Flask [5] web interface and another where we used an Ethernet shield and developed a simple HTTP server on the Arduino. Upon investigation it was found the interface using the Arduino shield was most practical when in place at ThomX, while the Flask was useful during earlier debugging. All interfaces implemented similar lens operations, including moving the focus and adjusting the aperture.

To focus the lens onto the USAF1951 microscope chart, we move the focus position of a range, taking images, and computing the focus score with the method from [4]. We present the results from carrying this out in Fig. 10, where the clear peak in the focus score corresponded to a well focused image. The second peak upon investigation corresponded to the when the edges of the viewing port were being focused on. Appropriate masking is being discussed as an improvement to the method.

CONCLUSION

To conclude, we have presented a method for the automatic detection of features of a USAF1951 microscope chart, and use that to calibrate an optical system for beam size measurements. Although measurements of a beam were unable to be taken at this stage, we have demonstrated that the software is able to reliably identify and measure features in the image, by slowly and precisely moving the target. We look forward to feature measurements and testing with the beam during the commissioning of ThomX.

ACKNOWLEDGEMENTS

We would to acknowledge and thank the support of many people and programs, but not limited to IJCLab, Nicolas Baudin program, Stephen Gregory, Evan Pyle, and others.

The ThomX project is funded by the French National Research Agency under the Equipex convention ANR-10-EQPX-0051.

REFERENCES

[1] A. Variola *et al.*, “ThomX Technical Design Report”, Rep. LAL RT 14/21, Rep. SOLEIL/SOU-RA-3629, Apr. 2014.

[2] G. Bradski, “The OpenCV Library”, *Dr. Dobb’s Journal of Software Tools*, Nov. 2000.

[3] M. Katona and L. G. Nyúl, “A Novel Method for Accurate and Efficient Barcode Detection with Morphological Operations”, in *Proc. 2012 Eighth International Conference on Signal Image Technology and Internet Based Systems*, Naples, Italy, Nov. 2012, pp. 307–314. doi:10.1109/SITIS.2012.53

[4] F. Shen, L. Hodgson, and K. Hahn, “Digital autofocus methods for automated microscopy”, *Methods in enzymology*, vol. 414, pp. 620–632, 2006. doi:10.1016/S0076-6879(06)14032-X

[5] A. Ronacher, “Flask 1.1”. https://flask.palletsprojects.com/en/1.1.x/.

ISBN: 978-3-95450-222-6 ISSN: 2673-5350 doi:10.18429/JACoW-IBIC2020-THPP36

PROTOTYPE DESIGN OF WIRE SCANNER FOR SHINE*

J.Wan, Shanghai Institute of Applied Physics, Chinese Academy of Science, 202009 Shanghai, China also at University of the Chinese Academy of Science, 100049 Beijing, China
Y.B. Leng†, K.R. Ye, W.M. Zhou, L.Y. Yu, Jie. Chen, B. Gao, F.Z. Chen
Shanghai Advanced Research Institute, CAS, Shanghai, China

Abstract

SHINE is a high repetition rate XFEL facility, based on an 8 GeV CW SCRF linac, under development in Shanghai. In order to meet the requirements of measuring the beam profile of shine in real time and without obstruction, a new diagnostic instrument, wire scanner has been designed. This paper mainly describes the design of wire scanner in shine, and some simulation results are also shown and discussed.

INTRODUCTION

SHINE [1] has 3 undulator lines that consist of FEL-I, FEL-Il and FEL-Ill and 10 experimental stations in phase-I, it can provide the XFEL radiation in the photon energy range of 0.4 -25 keV. In SHINE, wire scanners will be used to monitor the transverse profile of a 10-300 pC eletron beam with a final energy of 8GeV and repetition of 0-1MHz. Providing a high resolution measurement of electron beam profile averaged over many shots is the primary purpose of the wire scanner (WSC). Profile measurements can also be used to determine transverse beam emittance and twiss parameters without changing the magnet settings [2]. Compared to view screens, WSC offer a non-destructive monitoring of the beam transverse profile, and avoiding secondary particle damage to superconducting cavity. At present, the preliminary design scheme WSC in SHINE has been completed. The specific equipment parameters, such as the material, diameter, scanning speed, scanning mode need to be determined according to simulation and performance. Now simulation based on MATLAB has obtained some results.

OVERVIEW

At SHINE, design of WSC includes wire scanner detector, PMT detector, data acquisition electronics, data processing module, and remote monitoring. General block diagram of the WSC is shown in Fig. 1.

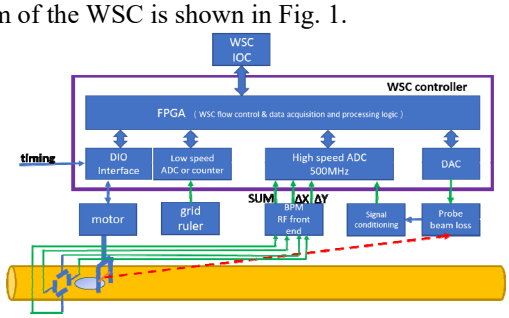

Figure 1: General block diagram of the system.

Wires in wire scanner detector driven by linac motor interacting with electron beam generates γ rays which are received by the PMT detector. Data acquisition electronics is to collect the PMT beam loss signal, wire position backreading and BPM output. Data processing module is responsible for information extraction and Gaussian fitting, and remote monitor implements user interface and terminal control of WSC.

For reason of high repetition rate, slow scanning mode with step by step is more likely to cause damage to wire than fast mode. Therefore SHINE's WSC will apply fast scanning mode, in which wires will be swept fastly and smoothly through the beam pipe at one time to prevent large vibrations.

At present, WSC of SHINE is still in simulation of actual parameters and development of key technologies, and the hardware parts have not been assembled and coordinated to realize functions. Unsolved problems include heating damage of tungsten wire under high repetition rate beam [3], vibration of tungsten wire in fast scanning mode [4] which Influences system resolution, selection of PMT probe position which influences beam loss signal quality, unknown SNR of PMT beam loss signal which also influences system resolution, and optimization of data processing algorithm which influences on system precision and speed. In future, according to the theoretical analysis and simulation results, wire scanner device parameter will be configured which includes wire diameter, scanning speed, PMT requirements, ADC requirements, etc, and beam experiments will be carried out to observe its working state to evaluate the performance of wire scanner.

Wire Scanner Detector

The wire scanner detector will be installed along the beam line. When it needs to be used, commands generated by upper software is sent to control the motor to drive the wires to sweep through the beam. After the measurement, the wires will be moved out of the beam channel to avoid blocking the beam. Wire scanner detector is driven by linear motor, and encoder is used to feedback position. The motion of the wire scanner detector has high reliability, and there is no movement stuck fault, and repetition accuracy of the motion is better than 20 μm. The wire scanner detector mainly includes a vacuum chamber with flange, flexure, linear motor and magnetic grid ruler, 45 degree mounting seat, and independent adjustable supporting base as shown in Fig. 2. We use 10 μm and 20 μm tungsten wires for test recently.

[1] *Work supported by The National Key Research and Development Program of China (Grant No. 2016YFA0401903, 2016YFA0401900)
†lengyongbin@sinap.ac.cn

Content from this work may be used under the terms of the CC BY 3.0 licence (© 2020). Any distribution of this work must maintain attribution to the author(s), title of the work, publisher, and DOI

ISBN: 978-3-95450-222-6 ISSN: 2673-5350 doi:10.18429/JACoW-IBIC2020-THPP36

Content from this work may be used under the terms of the CC BY 3.0 licence (© 2020). Any distribution of this work must maintain attribution to the author(s), title of the work, publisher, and DOI

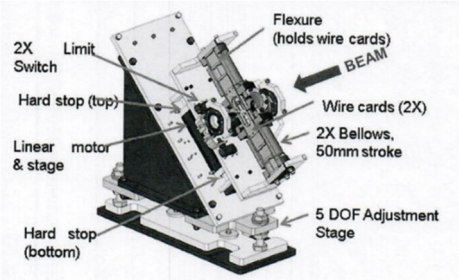

Figure 2: Structure of wire scanner detector.

We use LinMot motor as Mechanical actuator. The Control Panel of LinMot helps the user to access directly to the control and status word of the MC Software. The drive can be commanded from the PC through RS232 cable. A test for controlling motor has finished in which we use python to send control word nor MC software. This enables automatic reading of motor positions. Motor motion curve without loading is shown in Fig. 3.

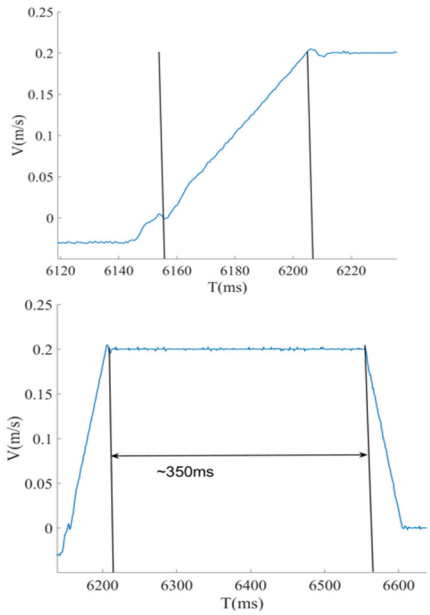

Figure 3: Test of LinMot motor.

However, reading position has two steps. First is that PC sends words to ask LinMot current position of motor, secondly LinMot receives and encodes its response and sends it back to PC, resulting in great uncertainty of response time up to milliseconds. If this scheme is used to measure position of wire at speed of 0.1 m/s, the position resolution will bad than 100μm and this is not acceptable. In this situation, grating ruler as a third party measuring device as shown in Fig. 4 may be helpful. Grating ruler is installed outside of the vacuum chamber. Its slider is connected to the Wire Card, so that slider can move along with motor and grating keep fixed. Considering that grating ruler is easy to be damaged under radiation environment, lead shielding device will be installed to protect grating ruler. When the grating ruler moves, we receive the square wave signal as shown in Fig. This signal can be used as a clock for a counter in FPGA, so that counter value can represent the relative position, and we can record the counter value when trigger from timing system arrive, the response time jitter is lower than 10 μs, equivalent to position jitter lower than 1μm at speed of 0.1 m/s, and the resolution of the grating ruler is 1μm, this is acceptable.

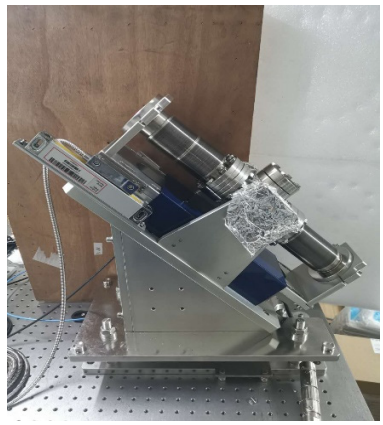

Figure 4: Installation of grating ruler.

PMT Detector

The duty of detecting gamma photons is accomplished by H10720-110. H10720-110 series are photosensor modules containing a metal package PMT as shown in Fig. 5 and a high-voltage power supply circuit.

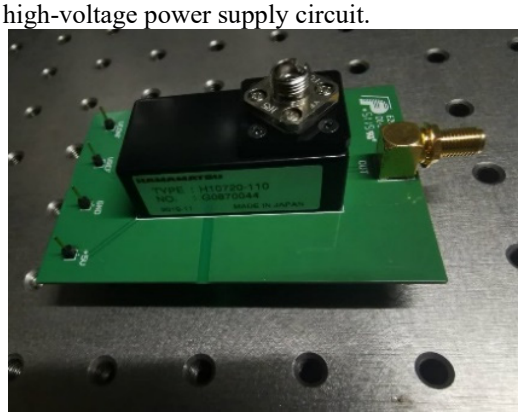

Figure 5: PMT detector.

The scintillator will be placed downstream of the wire target and outside the beam tube. The light generated by γ photon interaction with the scintillator is passed into the PMT through the optical fiber. The typical signal diagram of PMT is shown in Fig. 6 which signal length is around 100ns.

Figure 6: Typical signal diagram of PMT.

ISBN: 978-3-95450-222-6 ISSN: 2673-5350 doi:10.18429/JACoW-IBIC2020-THPP36

Data Acquisition Electronics

Beam loss signal from PMT detector is sampled by the QT7135 data acquisition board. Test shows sampling rate of the ADC sub-board support range in 400Msps-1000Msps and effective number of bits is 11 and the bandwidth is at 500MHz. QT7135 can be connected to ZCU102 evaluation board developed by xilinx through FMC HPC. Data sampled by ADC will be saved to DDR4 on the PL side of the evaluation board through internal bus AXI. The 4 GB, 16-bit wide DDR4 memory system is comprised of one 256 Mb x 16 SDRAM and its part number is MT40A256M16GE-075E. When measurement start the beam diagnostic personnel sends out the command to start scanning on OPI. The command is input into arm in zynq which located in zcu102 through epics control network. Then the arm changes the FPGA pin level to make FPGA start recording data when the motor moves to default position. When the trigger comes, FPGA will record a group of PMT beam loss signal sampling values and record the wire position values, record signal from BPM to calculate the central position bunch by bunch. When sampling the PMT beam loss signal, the selection of specific sampling rate will depend on PMT signal length and DDR frequency. When collecting BPM signals, for beam repetition is 1MHz, sampling rate is no need to be very high and the bandwidth is at least 500MHz. For those reasons, we decide set sampling rate as 500MHz. Position signal generated by a grating ruler is a kind of square wave, we can use it as the clock for the counter generated within FPGA so that wire position can be read with low clock jitter. Final version of data acquisition electronics has not been established, we use these commercial board as test prototype to test the feasibility of the scheme.

Data Processing Modules

Arm on zcu102 board will install Linus OS and be used as EPICS IOC. When the scanning is completed, ARM will retrieve the sampling value of beam loss signal from DDR, extract the beam loss value corresponding to each collision between wire and beam, and call the value of the wire position corresponding to the beam loss signal which will be modified by bunch by bunch central position extracted from BPM data. Finally, position data will do Gaussian fitting with beam loss value and variance of this gaussian could be a measure of beam size.

Remote Monitoring

All the data in the embedded IOC are available as EPICS PVs and display on a Linux host.

SIMULATION RESULTS

When the wire interacts with the beam, the electron density at the location of the wire cannot be accurately represented by the measured beam loss due to the presence of the wire diameter. The wire diameter will cause the gaussian fitting function to be wider, which will lead to beam size measured value being larger. Eq.(1) is concluded by simulation in which beam size of σ measured by wire with diameter D is σ_t:

$$\left(1+\frac{e^{1.43}\left(\frac{\sigma}{D}\right)^{-1.998}}{100}\right)\bullet\sigma=\sigma_t \qquad (1)$$

Simulation based on MATLAB in which 10,000 different beam currents were measured by wire scanner, and the measured results were modified by Eq.(1). The result is shown in Fig. 7.

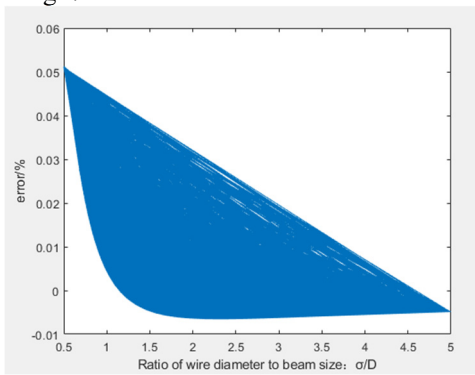

Figure 7: Test of correction formula.

Through another simulation based on MATLAB we also found that with the increase of white noise or wire diameter, the standard deviation of measurement error will increase. This indicates that the greater the noise or wire diameter is, the worse the measurement resolution will be.

CONCLUSION

We have described the system configuration, the content of subsequent test and optimization, present status of WSC in SHINE. This system will be extensively installed on SHINE for beam profile measurements with a resolution target of 10 μm.

REFERENCES

[1] Z. Zhu, Z. T. Zhao, D. Wang, Z. H. Yang, and L. Yin, "SCLF: An 8-GeV CW SCRF Linac-Based X-Ray FEL Facility in Shanghai", in *Proc. 38th Int. Free Electron Laser Conf. (FEL'17)*, Santa Fe, NM, USA, Aug. 2017, pp. 182-184. doi:10.18429/JACoW-FEL2017-MOP055

[2] W. Qiao, Z. Duan, H. Geng, W. B. Liu, and Y. F. Sui, "Wire Scanner Emittance Measurement and Software Design at BEPCII", in *Proc. 4th Int. Particle Accelerator Conf. (IPAC'13)*, Shanghai, China, May 2013, paper MOPME033, pp. 544-546.

[3] Sui Yanfeng, Ma Huizhou, Cao Jianshe, & Ma Li "Design and simulation of the wire scanner for the injector linac of BEPCII", *Chinese Physics C, High Energy Physics and Nuclear Physics,* 32(5), 397-399, (2008).

[4] N.IIda, T.Suwada, Y.Funakoshi, T.Kawamoto, M.Kikuchi, "A Method for Measuring Vibrations in Wire Scanner Beam Profile Monitors", in *Proc. 1st Asian Particle Accelerator Conf. (APAC'98)*, Tsukuba, Japan, Mar. 1998, paper 5D061, pp. 546–549.

Content from this work may be used under the terms of the CC BY 3.0 licence (© 2020). Any distribution of this work must maintain attribution to the author(s), title of the work, publisher, and DOI

ISBN: 978-3-95450-222-6 ISSN: 2673-5350 doi:10.18429/JACoW-IBIC2020-FRAO02

DIRECT DIGITIZATION AND ADC PARAMETER TRADE-OFF FOR BUNCH-BY-BUNCH SIGNAL PROCESSING*

I. Degl'Innocenti†[1], A. Boccardi, M. Wendt, CERN, Geneva, Switzerland
L. Fanucci, Department of Information Engineering, Università di Pisa, Pisa, Italy
[1]also at Department of Information Engineering, Università di Pisa, Pisa, Italy

Abstract

With the technology improvements of analog-to-digital converters in terms of sampling rate and achievable resolution, direct digitization of beam signals is of growing interest in the field of beam diagnostics. The selection of a state-of-the-art analog-to-digital converter for such a task imposes a trade-off between sampling frequency and resolution. Understanding the dependency of the system performance on these features is fundamental. This paper presents an analysis and design methodology for such architectures. Analytical tools are used to guide the designer and to estimate the system performance as a function of the analog-to-digital converter performance. These estimations are then validated by Monte-Carlo simulations. As an example of this methodology an analysis for the next-generation electronics of the Large Hadron Collider beam position monitoring system is presented. The analytical model and the results obtained are discussed, along with comparisons to beam measurements obtained at the Large Hadron Collider.

INTRODUCTION

Beam instrumentation and diagnostics are fundamental in the operation and control of particle accelerators. An instrument for beam diagnostics purposes must process the signal generated by the sensor interacting with the beam, to provide measured values about the beam parameter under consideration, and deliver the information in a digital format with the required performance, typically accuracy, resolution and processing time or bandwidth. The read-out electronics extracts this information from the beam sensor by utilizing a combination of analogue signal conditioning and digital signal processing techniques, with a digitization stage in between.

We define *direct digitization* to mean that the digitization is performed at an early stage in the processing chain, using minimal analog signal conditioning hardware.

Direct digitization has several advantages and limits the total number of hardware components required for the processing electronics. Fewer electronics components typically means less spread in board to board parameters, fewer drift effects and less uncontrolled parasitics, thus improving the general system performance and robustness with respect to environmental changes. In addition, such systems profit from the advantages to process the data in the digital domain. For example, the system can rely on the flexibility of re-programmable algorithms and the possibility to implement complex digital filters that are impossible to build in the analog domain.

On the other hand, a direct digitization based architecture usually imposes higher requirements on the digitization stage, in terms of sampling rate and resolution. Analog-to-digital converters (ADC) with sufficiently high sampling rate and analog bandwidth are needed to digitize bunched beam pulsed signals without loss of information, and to acquire single-shot signal events. ADCs with sufficiently high effective quantization resolution are necessary to obtain high precision measurements covering a large dynamic range. In practice however, the technology imposes a trade-off between the ADC's maximum sampling rate and its effective resolution.

The ADC Performance Trade-off

In characterizing and comparing ADCs a widely used figure of merit is the *performance* P, which is defined as product between the effective number of logical levels (effective number of bits, ENOB) and the maximum sampling rate:

$$P = 2^{ENOB} \cdot f_s \tag{1}$$

In his paper [1] *Walden* produced an overview of ADC performance trends up to 1997, concluding that P has remained relatively steady. Already in 2005 *Bin Le et al.* [2] had observed that technology advancement brought a general improvement in measurement performance, even though not uniformly achieved over a wide range of sampling rates and resolutions. Nevertheless, it is undeniable that higher sampling rates come at the cost of resolution and the parameter P helps to describe the performance boundary of converters with similar characteristics and technology (see Fig. 1).

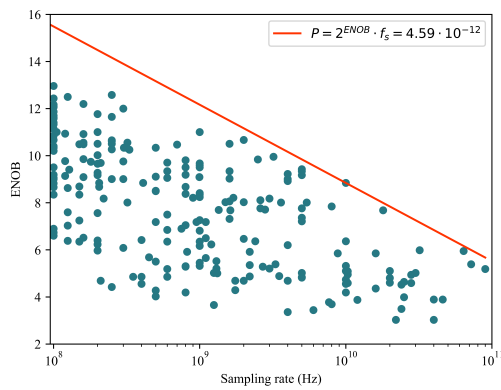

Figure 1: Performance distribution of ADC components in the years 1997 to 2020, showing the resolution in *effective number of bits* versus the maximum sampling rate. The red line represents the performance P boundary, as set by the best ADCs in terms of P. The data are taken from the online database [3].

* Work supported by CERN, Beams Department, Beam Instrumentation Group
† irene.degl'innocenti@cern.ch

Content from this work may be used under the terms of the CC BY 3.0 licence (© 2020). Any distribution of this work must maintain attribution to the author(s), title of the work, publisher, and DOI

ISBN: 978-3-95450-222-6 ISSN: 2673-5350 doi:10.18429/JACoW-IBIC2020-FRAO02

If the resolution is an important feature of a system, then the choice of the ADC must privilege slower ADCs. It is then interesting to understand how slow the sampling rate can be, without incurring an excessive sampling distortion.

The Effects of Undersampling

The *Nyquist-Shannon* theorem [4] states that any band limited, deterministic, analog signal can be perfectly reconstructed by taking equidistant samples with a noiseless converter of infinite resolution at a minimum sampling rate, called the *Nyquist rate*, equal to twice the bandwidth limit of the signal under consideration. In this case the sampling operation does not introduce any distortion to the signal and no information is lost. Of course, practical ADCs have a finite resolution, and may not be able to sample at the required rate. Sampling at, or beyond the *Nyquist* rate with sufficient resolution can therefore be impossible.

For the case of random processes several studies have analyzed and quantified the effects of undersampling [5–8]. In particular [8] took the effect of undersampling combined with limited resolution into account, considering a limited output bitrate. It was demonstrated that in such cases the optimum sampling rate to reconstruct the signal usually lies below the *Nyquist* rate.

For most beam instrumentation applications the emphasis does not lie on full waveform reconstruction, but on the extraction of a single parameter per signal pulse. For example, in the case of beam intensity or beam position monitors it is usually sufficient to measure the amplitude of the pulsed signal. A previous work, [9], examines the specific case of an energy measurement of direct digitally acquired pulsed signals. The same methodology is applied here to two examples of processing Beam Position Monitor (BPM) signals, with the signal-to-noise ratio (SNR) used to evaluate the measurement resolution. In the first example the measurement and simulation results obtained with direct-digitization of a comb band-pass filter output are analyzed and compared. Such a system is foreseen to be deployed for the Large Hadron Collider (LHC) extraction interlock BPMs. In the second example the expected performance for a low-pass filtered read-out architecture is studied, as being considered for a next generation read-out electronics for the LHC orbit system BPMs.

DIRECT DIGITIZATION OF BUNCHED BEAM PULSED SIGNALS

The response of a transducer to the passage of a charged particle bunch is typically a broadband pulsed signal, which depends on the beam velocity, the longitudinal distribution of the particles in the bunch, and the transfer function of the transducer. The characteristics of broadband button or stripline pick-ups, often used for beam position monitors, are discussed in [10]. For bunched hadron beams with near relativistic velocity the pulse duration is typically in the order of a few nanoseconds (see Fig. 2). Both the beam position and the beam intensity are contained within the information

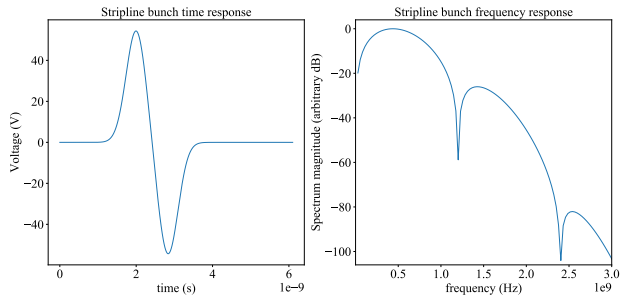

Figure 2: Numerical analysis of the single bunch response of a stripline beam position monitor in time and frequency domain (magnitude only). The electrode length is 125 mm, the width is 6 mm, the beam pipe radius is 44.5 mm, the rms bunch length is 1 ns with an intensity of 1e11 protons and a Gaussian distribution.

in the amplitude of the pulsed signals supplied by the BPM electrodes, and can be extracted by combining electrode signals. For either application, in a direct digitization based system the amplitude is calculated in the digital domain from the samples of the digitized pulse. Some minimum analogue signal conditioning is usually applied to optimize the signal for the sampling procedure.

The preferred method to measure the amplitude of each pulse is based on the calculation of the root mean square (RMS) of its samples, which is the square root of an estimation of the averaged power of the pulse [9]. This algorithm allows us to use all samples of the waveform, weighting them with respect to their amplitude, and should, ideally, be independent of the sampling time (or phase) between the signals of sampling clock and analog beam pulse.

The single bunch, single pass beam position can be calculated from the RMS amplitude supplied by two opposing pickup electrodes as the ratio of their difference and their sum [10].

[9] defines the averaged power P_T of a pulsed signal $x(t)$ within a time window T as:

$$P_T = \frac{1}{T}\int_0^T |x(t)|^2 dt \tag{2}$$

and an estimator $\hat{P}_T$:

$$\hat{P}_T = \frac{1}{N}\sum_{n=0}^{N-1} \hat{x}_n^2 \tag{3}$$

for the calculated power from the sampled sequence $\hat{x}_n$, taking a limited sampling rate and a limited resolution into account. The amplitude of the pick-up signal is then calculated as square root of Eq. (3). The SNR of the averaged power in the pulse is therefore related to the resolution of the pulse amplitude calculation and can be used to estimate the resolution of the beam position measurement of a single bunch. Assuming asynchronous sampling with an uniformly, randomly distributed delay between the sampling clock and the ADC input signal, and assuming the ADC noise to be a

Content from this work may be used under the terms of the CC BY 3.0 licence (© 2020). Any distribution of this work must maintain attribution to the author(s), title of the work, publisher, and DOI

ISBN: 978-3-95450-222-6 ISSN: 2673-5350 doi:10.18429/JACoW-IBIC2020-FRAO02

Content from this work may be used under the terms of the CC BY 3.0 licence (© 2020). Any distribution of this work must maintain attribution to the author(s), title of the work, publisher, and DOI

zero-mean *Gaussian* variable, the expression for the signal-to-noise ratio (SNR) is shown in [9] to be.

$$SNR_{dB} = 10\log_{10}\left(\frac{P_T^2}{\sigma_\epsilon^2 + \sigma_\eta^2}\right) \quad (4)$$

with P_T (see definition Eq. (2)) being the averaged power within the time window T, σ_ϵ^2 the variance of the error introduced by aliasing effects, and σ_η^2 the variance of the error introduced by the ADC noise on the single samples. The two variances are found to be:

$$\sigma_\epsilon^2 = 2(A_{X_k,N}^2 + B_{X_k,N}^2) \quad (5)$$

$$\sigma_\eta^2 = 2\frac{\sigma_\nu^4}{N} + 4\frac{\sigma_\nu^2}{N}P_T \quad (6)$$

with:

$$A_{X_k,N} \doteq \sum_{k=0}^{N-1} |X_k||X_{k-N}| \cdot \cos(\phi_k - \phi_{k-N})$$
$$B_{X_k,N} \doteq \sum_{k=0}^{N-1} |X_k||X_{k-N}| \cdot \sin(\phi_k - \phi_{k-N}) \quad (7)$$

where $X_k = |X_k|\exp(j\phi_k)$ are the coefficients of the Discrete *Fourier* Transformation (DFT) of the signal spectrum, N is the number of samples within the time window T as given by the sampling rate, and σ_ν^2 is the variance of the noise on each sample generated by the ADC.

EXAMPLE: THE LHC EXTRACTION INTERLOCK BPM

Our first example for direct digitization of a bunched beam signal is based on an early prototype of the LHC extraction interlock BPM consolidation project, with details of this system given in [11]. The analysis starts with the signal at the input of the ADC, and explores how the ADC resolution and sampling rate impact the position resolution. Beam studies with raw digitized data taken by two different ADCs have also been acquired, to allow a comparison of the performance estimation obtained through simulations.

The System Architecture

Figure 3 shows a block schematic of the LHC extraction interlock BPM prototype, operating on a pair of vertical stripline BPM electrodes. The analog front-end electronics time-multiplexes the pick-up response from two opposite electrodes of the pick-up into a single acquisition channel, using a 12 ns delay-line. A comb-filter modifies the signal into a 500 MHz burst by combining four replicas of the input signal with $n \times 2$ ns transmission-line delays, see Fig. 4 (left). The analog acquisition electronic then foresees an anti-aliasing low-pass filter and a switchable gain stage before the signal is digitized by an ADC and processed on an FPGA board. Since this system will be used for machine protection purposes, the acquisition chain is designed to be as simple and robust as possible. No automatic gain control (AGC) is permitted to automatically level the signal to match the full scale range of the ADC, and the clocking scheme is independent of the accelerator Radio Frequency (RF), meaning that the sampling clock and pick-up signals are asynchronous.

Application of the Analytic Model

The prototype front-end follows the schematic of Fig. 3, and pre-processes the LHC stripline BPM signal (Fig. 2) to form a burst waveform of four 500 MHz sinusoidal-like oscillations, see Fig. 4, which is subsequenctly digitized by the ADC.

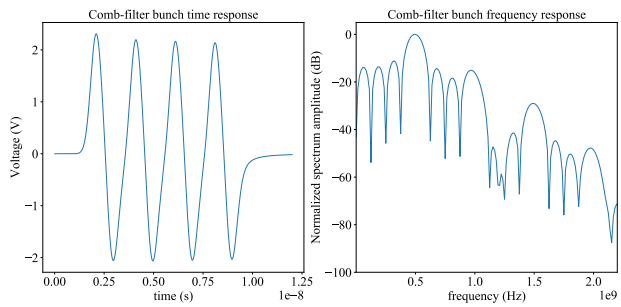

Figure 4: Response of a comb-filter to a single bunch stripline beam position monitor signal (numerical simulation).

The magnitude of the ADC input spectrum, Fig. 4 (right), gives first indications about the ADC requirements in terms of the sampling rate. It peaks at 500 MHz, and most of the spectral power stays below ~1.2 GHz, except for the 3rd harmonic at around 1.5 GHz. Beyond 2 GHz the spectrum magnitudes always stays below -60 dB. Setting -60 dB as the bandwidth limit implies a *Nyquist* rate of 4 GSps. The

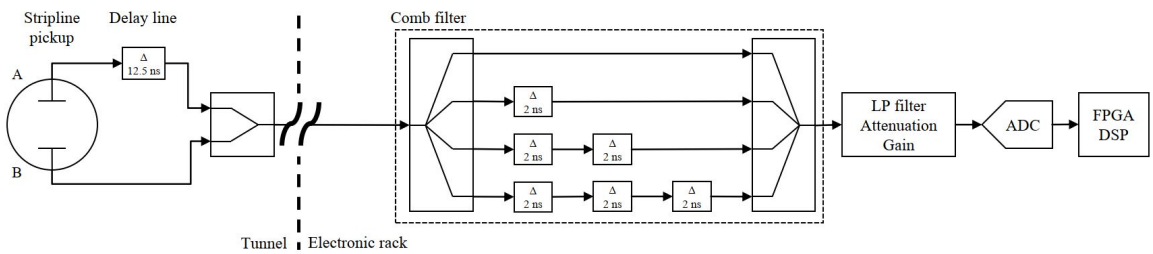

Figure 3: The LHC extraction interlock BPM signal processing scheme [11].

ISBN: 978-3-95450-222-6 ISSN: 2673-5350 doi:10.18429/JACoW-IBIC2020-FRAO02

front-end prototype has been tested with two different ADCs, on two different FMC carrier boards:

- a high-resolution ADC, with 14 nominal bits (9.6 ENOB), maximum sampling rate 3 GSps, here used at 2.6 GSps [12];
- a high-speed ADC, with 12 nominal bits (8.8 ENOB), maximum sampling rate 4 GSps, here used at 3.2 GSps [13].

As shown in [9], the analysis of the errors on the averaged signal power as a function of ADC resolution and sampling rate in the range $0.5 < f_{Nyquist} < 1$ is of particular relevance, which translates to a sampling rate in the range 2 . . . 4 GSps for this particular example. Assuming asynchronous sampling with an uniformly, randomly distributed delay between the sampling clock and the ADC input signal, and assuming the ADC noise to be a zero-mean *Gaussian* variable, the SNR of the averaged power measurement P_T can be expressed as in Eq. (4). In this example the time window T is 12.5 ns and the modulus of the spectrum X_k is shown in Fig. 4, right. Referring to the definition of the Effective Number Of Bits (ENOB), we can express σ_ν^2, the variance of the noise on each sample generated by the ADC, as:

$$\sigma_\nu^2 = \frac{V_{FSR}^2}{12} 2^{-2\mathrm{ENOB}} \tag{8}$$

where V_{FSR} is the full-scale range of the ADC input.

We use the ADC performance P, as defined in Eq. (1), to combine the ADC resolution, given in ENOB, and the maximum sampling rate f_s as a figure of merit for the performance. Based on the specifications of the two ADC chips used for the beam measurements, an average value of $P = 2.05 \cdot 10^{12}$ s^{-1} was found.

By combining Eq. (8) and Eq. (1), the variance of the noise of the ADC as a function of the sampling rate is found to be:

$$\sigma_\nu^2 = \frac{V_{FSR}^2}{12} \frac{f_s^2}{P^2} \tag{9}$$

This allows us to calculate the SNR of the averaged power measurement of the comb-filtered ADC input pulse signal as a function of the sampling rate, while modifying the ADC resolution to keep the performance figure of merit P constant, see Fig. 5.

Figure 5 shows how the SNR is driven by the ADC resolution for sampling frequencies higher than ~2.8 Gsps. At lower rates the aliasing effects dominate, limiting the SNR substantially. For practical beam measurements we expect to observe a better overall performance when using the higher speed ADC, compared to the higher resolution ADC which is limited to operate at 2.6 Gsps sampling rate, always assuming that we utilize the entire input signal range of the ADC.

For this specific application the SNR information is more instructive if related to the single bunch, single pass, position resolution. In a first approximation the smallest detectable beam displacement that the pick-up can resolve is related to the pulse amplitude resolution by means of the pick-up sensitivity.

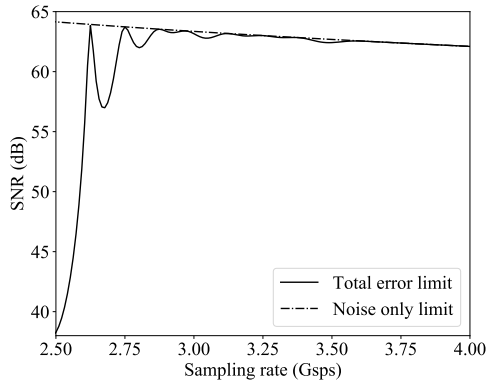

Figure 5: Estimate of the expected SNR for measurement of the averaged power of a comb-filtered pulsed signal as a function of the sampling rate for an ADC of given performance, so with resolution as a function of the sampling rate as in Eq. (9).

Let A be the signal amplitude calculated as the square root of the averaged power P_T, and δ_A the uncertainty on the amplitude measurement, with δ_{P_T} being the uncertainty on the measurement of P_T. We can then write:

$$\frac{A + \delta_A}{A} = \sqrt{1 + \frac{\delta_{P_T}}{P_T}} \tag{10}$$

The uncertainty δ_{P_T} includes the combination of the errors caused by the limited sampling rate and the limited resolution, as derived in [9], and can be expressed as square root of the sum of the two variances, $\delta_{P_T} = \sqrt{\sigma_\epsilon^2 + \sigma_\eta^2}$. If we express the ratio of Eq. (10) in decibel, and divide its value by the pickup sensitivity expressed in decibel per millimeter we get an estimation of the single bunch, single pass, position resolution of the system in millimeters.

This allows us to directly compare the expected performance of the two ADCs used in the beam test prototype. Figure 6 plots Eq. (10), calculated for the comb-filtered bunch signal, as a position resolution referenced to the position sensitivity of the LHC stripline BPM pickup used. The two traces show the estimated resolution for each ADC under consideration for the maximum foreseen bunch intensity in the LHC, $3 \cdot 10^{11}$ charges per bunch (cpb), utilizing two thirds of the ADC's full scale input range. The added dots indicate the specific sampling rate at which each ADC was operated. As expected, the high-resolution ADC, sampling at 2.6 Gsps, is limited by the aliasing effects to a resolution of ~20 µm. The high-speed ADC, with lower resolution, allows us to use sampling rates down to 2.9 Gsps (well below the *Nyquist rate* of 4GSps) without suffering from aliasing limitations, resulting in a position resolution of <15 µm.

Since the LHC extraction interlock BPM signal processing electronics does not foresee a variable gain amplifier, the signals of low intensity bunches will cover only a small fraction of the ADC input range. In this case the ADC noise dominates the measurement uncertainty, see Fig. 7. For both ADCs, the ADC noise dominates the aliasing effects. In

Content from this work may be used under the terms of the CC BY 3.0 licence (© 2020). Any distribution of this work must maintain attribution to the author(s), title of the work, publisher, and DOI

ISBN: 978-3-95450-222-6 ISSN: 2673-5350 doi:10.18429/JACoW-IBIC2020-FRA002

Content from this work may be used under the terms of the CC BY 3.0 licence (© 2020). Any distribution of this work must maintain attribution to the author(s), title of the work, publisher, and DOI

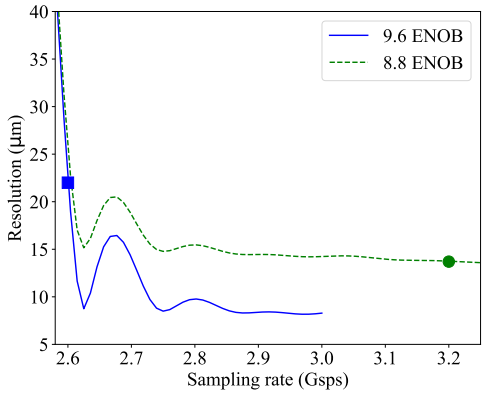

Figure 6: Estimation of the expected resolution of the BPM as a function of the sampling rate for two ADCs with different effective number of bits for a bunch intensity of $3 \cdot 10^{11}$ charges.

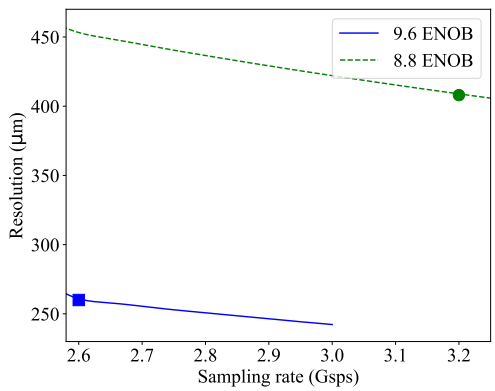

Figure 7: Estimation of the expected resolution of the BPM as a function of the sampling rate for two ADCs with different effective number of bits for a bunch intensity $1 \cdot 10^{10}$ charges.

this case the model predicts that the ADC with higher resolution offers a significantly better performance (resolution <280 µm) as compared to the high-speed ADC (resolution <430 µm).

A Beam-based Study

To verify our ADC performance analysis, we compare this analytical method with the results of both beam measurements and numerical simulation. To ensure the beam measurement is independent on beam position motion, the signal from a single pickup electrode was split and fed to the two inputs of the front-end BPM electronics. Changes in beam intensity and beam position were emulated with a set of attenuators. In parallel, to better characterize the system performance in terms of beam intensity, position and processing parameters, the system was implemented in a simulation framework. Figure 8 shows a typical waveform of a single bunch signal at the input of the ADC, indicating the sampling points of the digitizer, and the corresponding results form the numerical simulation. The analysis of the measured data samples was performed off-line, with the results summarized in Fig. 9. The plot shows the single-shot bunch-by-bunch beam position resolution in micrometers for the two different ADCs as a function of the bunch intensity. The beam intensity was varied, considering that 67 % of the ADC full scale range is sufficient to acquire a maximum bunch intensity with $3 \cdot 10^{11}$ charges per bunch and ±7.5 mm displacement. Each point in the graph represents a beam measurement results with specific acquisition parameters.

As the beam signal level decreases linearly with the beam intensity, and since no gain adjustment was applied, the acquisition of low intensity beam cannot take advantage of the full input range of the ADC. This is reflected by the decrease in the position resolution. The ADC with a higher resolution therefore shows a better performance for low intensity bunches with respect to the high-speed ADC. As predicted by the analytic model, the trend flips when acquiring high intensity bunch signals. The effects of the limited resolution of the converter are less dominant, with the aliasing effects of the lower sample rate ADC becoming more important. The numerical simulation estimates a resolution limit of 22 micrometers for the higher resolution ADC, while the higher speed ADC does not yet suffer from aliasing limitations and reaches 12 micrometer resolution. Both of these

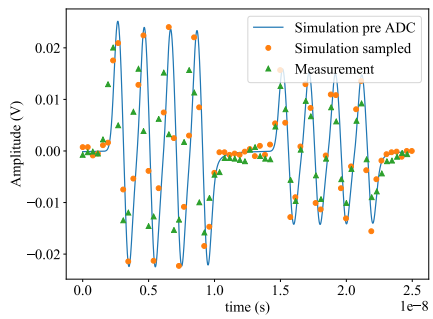

Figure 8: Acquisition with a prototype of the LHC extraction interlock BPM electronics of a pre-processed single bunch signal using the high sampling resolution ADC, compared with the corresponding simulation.

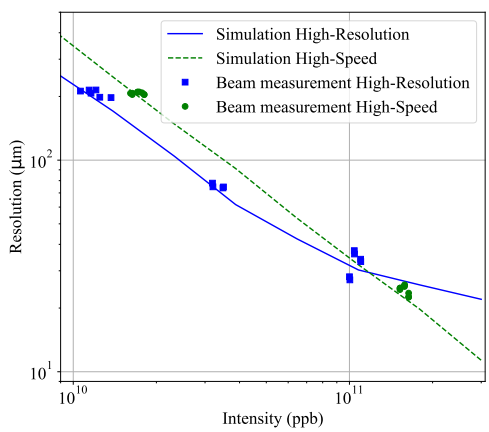

Figure 9: Simulation and beam measurement results of the BPM resolution as a function of the bunch intensity.

ISBN: 978-3-95450-222-6 ISSN: 2673-5350 doi:10.18429/JACoW-IBIC2020-FRAO02

results agree well with the simulation for maximum bunch intensities.

EXAMPLE: SIMULATIONS OF A POSSIBLE FUTURE BPM ACQUISITION UPGRADE FOR THE LHC ORBIT SYSTEM

The previous section demonstrated how the model can help analyse and to understand the effects generated by the ADC performance limits in a given beam instrumentation configuration and to evaluate the resolution of the measured quantity. This analytical approach can therefore help as a design tool for the performance evaluation of future systems, and the selection of the right ADC.

As an example let us take the case of a new BPM read-out system architecture, foreseen to be applied in the frame of a consolidation project for the ~1100 orbit system BPMs of the LHC.

Analog Conditioning

Following the design philosophy of minimizing the number of analog electronics components, time-multiplexing of the pick-up electrodes into a single processing chain is the preferred method. This first part of the BPM read-out architecture is similar to that of the LHC interlock BPM prototype, with the signal from opposing BPM electrodes combined after delaying one of the signals by 12.5 ns (equal to half the minimum 25 ns bunch-to-bunch time distance in the LHC).

To band-limit the bunch signal, and to prepare it for digitization, a low-pass filter is used. For the purpose of this early study a 4th-order *Bessel* low-pass filter was chosen, with a cut-off frequency of 200 MHz found to be the best compromise between bandwidth limitation and response time. This keeps the power leakage between 2 consecutive bunches to < 1 %. As anti-aliasing filter, another *Bessel* low-pass filter of 8th-order was added, with a cut-off frequency of 600 MHz. Figure 10 shows the output of this filter configuration in time and frequency domain for a single, typical LHC bunch passing a button pick-up. As shown in Fig. 10, the signal spectrum amplitude is below -60 dB for frequencies above 725 MHz, which corresponds to a *Nyquist* rate of 1.45 GSps.

Data Transmission Bandwidth Limit

Another constraint that can affect the design of a BPM system is a limit on the bandwidth for the transmitted digitized data. This is actually the case for the next generation read-out electronics for the LHC BPMs, where much of the existing infrastructure has to be re-used, including the number of optical fibers linking the front-end electronics in the tunnel to the processing electronics on the surface. This, and type of radiation hard electro-optical transceivers that have to be used, defines a maximum number of serial data lanes per BPM system and the maximum possible bitrate. This in turn defines the maximum sampling rate at which

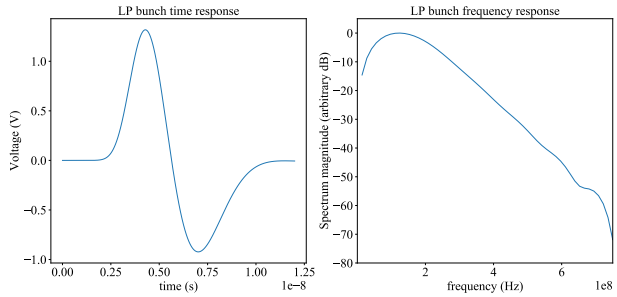

Figure 10: Numerical analysis output response from a single LHC bunch passing a button pick-up, and followed by a *Bessel* 4th-order low-pass filter with a cut-off frequency of 200 MHz and by a *Bessel* 8th-order anti-aliasing filter with a cut-off frequency of 600 MHz.

an ADC can be operated at a given resolution and with a given transmission protocol. In the LHC case, a possible scenario is that only one fiber can be used per BPM, with a maximum of four (so two per processing chain) wavelength multiplexed serial links, each working at a data rate of 10.24 Gbps. This makes a total bandwidth of 20.48 Gbps per processing chain. Considering one of the most popular protocol, the JESD204B standard converter interface [14], samples are transmitted as 16 bit words plus the overhead of 8-bit/10-bit encoding scheme. The resulting maximum sampling rate is:

$$F_{s_{\max}} = \frac{20.48\ \text{Gbps}}{16\ \text{bit} \times (10/8)} = 1.024\ \text{GSps} \qquad (11)$$

Estimation of the Position Resolution

The position sensitivity coefficient used for this study is based on the standard LHC button type BPM. The analytically calculated beam position resolution as function of the sampling rate for a single shot, single bunch measurement, with the analog signal conditioning as described, has been analyzed for a theoretical ADC with fixed performance $P = 4.59 \cdot 10^{12}\ \text{s}^{-1}$, the maximum value found among the converters of Murmann's ADC survey [3] (see Fig. 11).

At the sampling rate imposed by the bandwidth constraint the resolution is limited by aliasing. The theoretical ADC would reach about 5 µm position resolution.

Figure 11 shows also the performance of two commercial ADCs operating close to this optimal point, both reaching less than 9 µm position resolution. One is a nominal 16 bit ADC, 11 ENOB, able to sample up to 1 GSps [15], the other is a nominal 14 bit ADC, 10.1 ENOB, with maximum sampling rate 2.6 GSps [16]. The first reaches 8 µm position resolution sampling at its maximum rate of 1 GSps, the second 8.5 µm limiting its sampling rate at 1.024 GSps. Even though their ENOB values are significantly different, this is a region where aliasing effects are dominant, given them similar performance.

Content from this work may be used under the terms of the CC BY 3.0 licence (© 2020). Any distribution of this work must maintain attribution to the author(s), title of the work, publisher, and DOI

ISBN: 978-3-95450-222-6 ISSN: 2673-5350 doi:10.18429/JACoW-IBIC2020-FRAO02

Content from this work may be used under the terms of the CC BY 3.0 licence (© 2020). Any distribution of this work must maintain attribution to the author(s), title of the work, publisher, and DOI

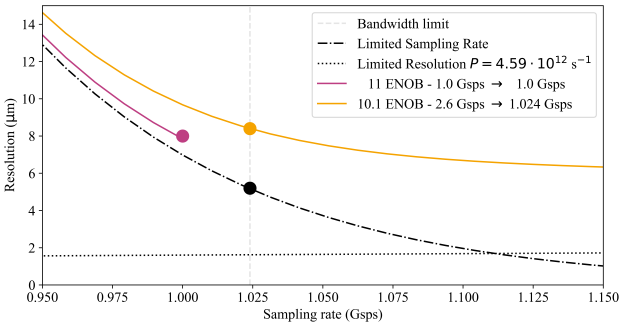

Figure 11: Estimation of the expected position resolution for a single-shot, single bunch position measurement using an LHC button BPM with low-pass filtering, for a fixed performance ADC and for two commercially available ADCs. The dots indicate the sampling points in which each ADC can be operated given the bandwidth limit constraint.

CONCLUSIONS

To achieve the best performance from a direct digitization based architecture it is fundamental to optimize the trade-off between ADC sampling rate and resolution. It has been shown how it is possible to estimate the errors introduced in the energy estimation of a digitized pulsed signal as a function of these parameters to estimate the uncertainty of a specific beam measurement quantity such as position or intensity. The analytic tool presented can facilitate the analysis of the performance of a direct digitization system, and has been benchmarked with both numerical simulations and beam measurements. This analytic approach can also assist in the selection of the ADC when designing a new system. The best choice is often not the highest resolution ADC able to sample at or beyond the *Nyquist* rate, but an ADC with a better resolution at a lower sampling rate.

REFERENCES

[1] R. H. Walden, "Analog-to-digital converter survey and analysis", in *IEEE J. Sel. Areas Commun*, vol. 17, no. 4, pp. 539–550, 1999. doi:10.1109/49.761034

[2] Bin Le, T. W. Rondeau, J. H. Reed and C. W. Bostian, "Analog-to-digital converters,", in *IEEE Signal Processing Magazine*, vol. 22, no. 6, pp. 69-77, Nov. 2005. doi:10.1109/MSP.2005.1550190

[3] B. Murmann, "ADC Performance Survey 1997-2020". http://web.stanford.edu/~murmann/adcsurvey.html

[4] C. E. Shannon, "Communication in the presence of noise", in *Proceedings of the IRE*, Vol. 37, IEEE, 1949, pp. 10–21. doi:10.1109/JRPROC.1949.232969

[5] M. B. Matthews, "On the linear minimum-mean-squared-error estimation of an undersampled wide-sense stationary random process", in *IEEE Trans. Signal Process.*, vol. 48, pp. 272-275, 2000. doi:10.1109/78.815501

[6] A. Kipnis, A. J. Goldsmith, Y. C. Eldar, and T. Weissman, "Distortion-Rate Function of Sub-Nyquist Sampled Gaussian Sources", in *IEEE Transactions on Information Theory*, vol. 62, no. 1, pp. 401-429, Jan. 2016. doi:10.1109/TIT.2015.2485271

[7] E. Mohammadi and F. Marvasti, "Sampling and distortion tradeoffs for bandlimited periodic signals", *2015 International Conference on Sampling Theory and Applications (SampTA)*, Washington, DC, USA, pp. 468-472, 2015. doi:10.1109/SAMPTA.2015.7148935

[8] A. Kipnis, Y. C. Eldar, and A. J. Goldsmith, "Fundamental Distortion Limits of Analog-to-Digital Compression", in *IEEE Transactions on Information Theory*, vol. 64, no. 9, pp. 6013-6033, Sept. 2018. doi:10.1109/TIT.2018.2857822

[9] I. Degl'Innocenti, A. Boccardi, L. Fanucci, and M. Wendt, "Analysis of sampling and noise error on the energy measurement of direct digitally acquired pulsed signals", accepted for publication at *Nuclear Instruments and Methods in Physics Research Section A: Accelerators, Spectrometers, Detectors and Associated Equipment*, 2020, doi:10.1016/j.nima.2020.164571

[10] R. E. Shafer, "Beam position monitoring", in *AIP Conference Proceedings*, vol. 249, p. 601, 1992. doi:10.1063/1.41980

[11] J. Pospisil, O. Bjorkqvist, A. Boccardi, and M. Wendt, "Digital Signal Processing Techniques to Monitor Bunch-by-Bunch Beam Positions in the LHC for Machine Protection Purposes", in *Proc. 6th Int. Beam Instrumentation Conf. (IBIC'17)*, Grand Rapids, MI, USA, Aug. 2017, pp. 146–149. doi:10.18429/JACoW-IBIC2017-TU3AB3

[12] Analog Devices AD9208 Data-sheet, 2017. https://www.analog.com/media/en/technical-documentation/data-sheets/AD9208.pdf

[13] Texas Instrument ADC12J4000 Data-sheet, 2017. http://www.ti.com/lit/ds/symlink/adc12j4000.pdf

[14] JEDEC Standard JESD204B (July 2011). JEDEC Solid State Technology Association. www.jedec.org

[15] Texas Instrument ADS54J60 Data-sheet, 2019. http://www.ti.com/lit/ds/symlink/ads54j60.pdf

[16] Analog Devices AD9689 Data-sheet, 2017. https://www.analog.com/media/en/technical-documentation/data-sheets/AD9689.pdf

ISBN: 978-3-95450-222-6 ISSN: 2673-5350 doi:10.18429/JACoW-IBIC2020-FRAO04

COMMISSIONING OF THE BEAM ENERGY POSITION MONITORING SYSTEM FOR THE SUPERCONDUCTING RIKEN HEAVY-ION LINAC

T. Watanabe*, N. Fukunishi, H. Imao, O. Kamigaito, T. Nishi, K. Ozeki,
N. Sakamoto, A. Uchiyama, Y. Watanabe, K. Yamada, RIKEN, Wako, Japan
T. Toyama, KEK/J-PARC, Tokai, Japan
A. Kamoshida, National Instruments Japan Corporation, Tokyo, Japan
K. Hanamura, Mitsubishi Electric System & Service Co., Ltd., Tokai, Japan
R. Koyama, SHI Accelerator Service Ltd., Wako, Japan

Abstract

Beam commissioning for the RIKEN Heavy-ion Linac (RILAC) upgrade, including the new Superconducting Linac (SRILAC), has been successfully completed. The RILAC upgrade aims at promoting super-heavy element searches and radioactive isotope production for medical use. When the SRILAC beam is accelerated, the beam loss must be reduced to under 1 W/m. To continuously monitor the beam nondestructively, we have developed a new beam energy position monitoring (BEPM) system capable of simultaneously measuring the beam position and energy by measuring the time-of-flight. A great advantage of this system is that it can handle a time-chopped beam by synchronizing the measurement system with the beam-chopping signal. At the start of commissioning, the beam was chopped to 3% duty cycle to protect the SRILAC cavity from beam loss. Even though the beam intensity was 20 enA, we measured the beam position and energy to accuracies of ± 0.1 mm and several 10^{-4} precision, respectively. Here, we present details concerning the BEPM system and commissioning results.

INTRODUCTION

Nihonium (Nh) is a synthetic super-heavy (SH) element with atomic number 113 and is the first element ever discovered in Asia [1]. It's name comes from the word "Nihon", which means "Japan" in Japanese. To promote the research for even heavier synthetic elements and to enhance the production capability of the short-lived radio isotope ^{211}At, which is expected to be useful in cancer therapy [2], an upgrade project of the RIKEN Heavy-ion Linac (RILAC) [3] has begun called the RI Beam Factory (RIBF) project [4, 5]. The project aims to increase the intensities and energies of the heavy ion beams by introducing a superconducting electron cyclotron resonance (ECR) ion source [6] and a superconducting booster named the Superconducting RILAC (SRILAC) [7].

In this scheme, it is crucial to monitor a beam to accelerate it stably. Destructive monitors generate outgassing; if they are used, it becomes difficult to maintain the Q value and surface resistance of the superconducting radio frequency (SRF) cavities over a long period of time. For this reason, we have developed a new beam energy and position monitoring (BEPM) system to continuously monitor the beam nondestructively.

* wtamaki@riken.jp

BEPM SYSTEM FOR THE SRILAC

RILAC and SRILAC

The newly constructed beam transport lines and the SRILAC were installed in February 2020. The existing RILAC and the upgraded facilities are shown in Fig 1. The SRILAC consists of three cryomodules (CM1, CM2, and CM3). CM1 and CM2 each contain four quarter-wavelength resonators (QWR) at 73 MHz and CM3 contains two QWRs. The total acceleration voltage is designed to produce 18 MW with a Q value of 1×10^9. To maintain the ultra-high vacuum ($<10^{-8}$ Pa) and particulate-free conditions, a non-evaporable getter-based differential pumping system was developed and installed upstream and down-stream of the SRILAC [8].

Heavy-ion beams accelerated by the SRILAC are used by the GAs-filled Recoil Ion Separator (GARIS)
Ⅲ to search for SH elements and to produce radioisotopes (RI) for medical use. If further acceleration is necessary in the future, the beams are to be transported to the rear stage Riken Ring Cyclotron (RRC).

Three Types of BEPMs

Depending on the installation location, 3 types of BEPM (Types I, Ⅱ, and Ⅲ) were designed and 11 BEPMs were fabricated [9] by Toyama Co., Ltd. [10]. BEPMs are installed in the centers of the quadrupole magnets (Fig. 1) that are located between the SRF cavities. Photographs of the 3 types

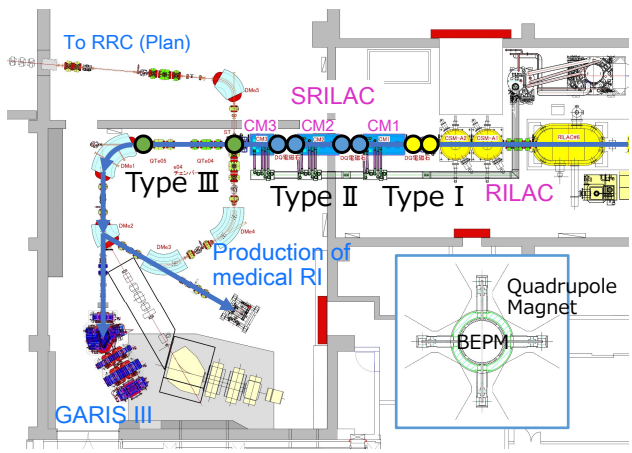

Figure 1: Schematic drawing of the RIKEN Heavy-ion Linac (RILAC), the upgraded Superconducting Linac (SRILAC), and the installation locations of the 3 types of BEPM.

Content from this work may be used under the terms of the CC BY 3.0 licence (© 2020). Any distribution of this work must maintain attribution to the author(s), title of the work, publisher, and DOI

ISBN: 978-3-95450-222-6 ISSN: 2673-5350 doi:10.18429/JACoW-IBIC2020-FRA004

Content from this work may be used under the terms of the CC BY 3.0 licence (© 2020). Any distribution of this work must maintain attribution to the author(s), title of the work, publisher, and DOI

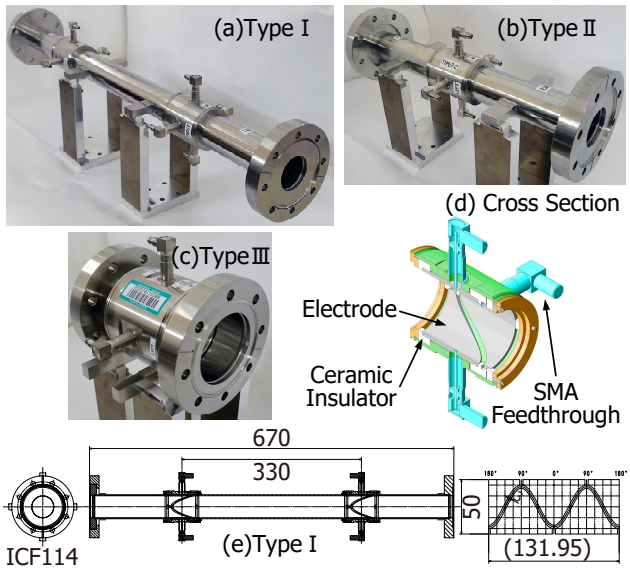

Figure 2: Photographs of the 3 types of BEPM: (a) Type I, (b) Type II, and (c) Type III. (d) Cross section drawing of a BEPM. (e) Schematic drawing of Type I.

of BEPMs and a cross section of a BEPM are shown in Fig. 2, and the mechanical dimensions of each type of BEPM are summarized in Table 1.

By using a parabolic design, the ideal linear response of the quadrupole moments is realized while maintaining good linear position sensitivity [11]. The shape of an electrode is represented by $y = (L/2)\cos 2\theta$, where θ is the angle in the cylindrical coordinate system, y is the longitudinal axis, and L is the length of the electrode. The electrode lengths were determined by taking into account both that the longitudinal distribution of the beam is $\pm 10\%$ of one period and the expansion of the electric field due to the non-affected Lorentz contraction.

Each BEPM has 4 reference planes in the x-axis direction and 8 in the y-axis direction. These reference planes are used for alignment and calibration; they are transferred from the center of the 4 electrodes, for which the mechanical accuracy is within ± 0.05 mm, while that of the other parts is within ± 0.1 mm. To confirm that the mechanical accuracy is maintained within the allowed values, after the welding process is completed, the reference planes are shaped again by using a milling cutter and remeasured by using a 3-D coordinate measuring machine. The vacuum chamber, electrode, and flange are made of super low carbon stainless steel SUS316L, while the fixed and rotational flanges are made of ultra-high vacuum flange ICF114. To provide electrical insulation between each electrode and the vacuum chamber, an alumina ceramic (AS999 [12]) is used, which has a low $\tan\delta$ of 0.5×10^{-4} and a high purity of 99.99%. The signal induced on the electrode by the passing beam is sent outside the vacuum chamber via 50 Ω SMA feed-throughs [13].

Table 1: Mechanical Dimensions (mm) of the 3 Types of BEPM

	Type I	Type II	Type III
Length of chamber	670	360	140
Outside dia. of chamber	58	58	85
Length of electrode	50	50	60
Inner dia. of electrode	40	40	60
Number of BEPMs	2	4	5

Analysis of the Pickup Signal in the Time and Frequency Domains

Before constructing the SRILAC BEPM system, we theoretically estimated the expected pickup signal in the time and frequency domains [14, 15]. Based on these estimations, a prototype BEPM system was designed, fabricated, and installed into the beam transport line at RIBF. By using a 17 eμA beam of $^{238}U^{64+}$ accelerated to 10.5 MeV/u by the RRC, the beam energy and position were measured for several months. The results showed that the agreement between the measured and theoretical values in the frequency domain and the bunch shape in the time domain, was satisfactory and confirmed that the system worked extremely well [16]. After this was established, we investigated the bunched beam signals from the electrostatic pickups of the SRILAC.

The equivalent circuit of an electrostatic pickup is shown in Fig. 3. When charged particles pass by a pickup, an induced voltage $V(t)$ is created over the input-resistance (R) of the amplifier. $V(t)$ is a solution of

$$\frac{dQ(t)}{dt} = \frac{V(t)}{R} + C\frac{dV(t)}{dt}, \quad (1)$$

where C is the total capacitance of the BEPM-electrode, feedthrough, and input of the amplifier. $V(t)$ and charge $Q(t)$ are expressed as $V(t) = V(\omega)\exp(j\omega t)$ and $Q(t) = Q(\omega)\exp(j\omega t)$, respectively. By substituting these equations into Eq. (1), the relationship between the voltage and the angular frequency becomes

$$V(\omega) = \frac{j\omega CR}{1 + j\omega CR}\frac{Q(\omega)}{C}. \quad (2)$$

This circuit forms a high-pass filter with a time constant CR and cut-off frequency (f_c) given by

$$f_c = 1/(2\pi RC). \quad (3)$$

In this case, the cut-off frequency is calculated to be 74 MHz

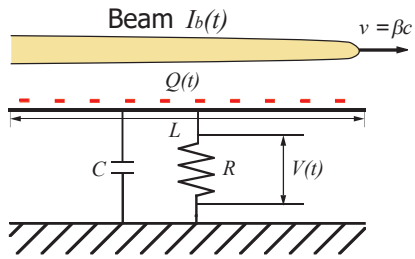

Figure 3: Equivalent circuit for an electrostatic pickup. A beam induces charge $Q(t)$ on the electrodes and voltage $V(t)$ appears on the input-resistance R of the preamplifier, where C is the capacitance of the BEPM-electrodes.

ISBN: 978-3-95450-222-6 ISSN: 2673-5350 doi:10.18429/JACoW-IBIC2020-FRA004

Table 2: Calculation Parameters

β	0.082	($^{51}_{23}V^{13+}$ beam)
N	5.489×10^6	(2.469 pμA)
q	13	Particle charge
T_0	13.699 ns	(f_{rf} = 73 MHz)
σ	1.00 ns	Standard deviation
L	0.06 m	Length of the electrode
$\phi/2\pi$	1/4	Covered ratio by the electrode
R	50 Ω	Input-resistance
G	36.5 dB	Att -3 dB
C	43 pF	Total capacitance of the electrode

from the parameters in Table. 2. It is assumed that the longitudinal distribution of particles in a bunch can expressed by a Gaussian function as follows:

$$I(t) = (qN/\sqrt{2\pi})\sigma \exp(-t^2/2\sigma^2), \quad (4)$$

where q is the particle charge, N is the number of particles in one bunch, and σ is the standard deviation of this Gaussian distribution function. $I(t)$ can be expanded into a Fourier series as

$$I_n = (2qN/T_0) \exp(-n^2\omega_0^2\sigma^2/2), \quad (5)$$

where T_0 is the period of the RF frequency for the RF acceleration cavity and ω_0 is the angular revolution frequency. By using Eq. (2), the coupling impedance Z_n is expressed

$$Z_n = \frac{\phi}{2\pi} \frac{jn\omega_0 R}{(1 + jn\omega_0 RC)} \frac{L}{\beta c}, \quad (6)$$

where L is the length of the electrode, βc is the beam velocity, and ϕ is the azimuth angle over which the electrodes cover the beam. The coefficients of the induced voltage (V_n) can then be obtained by

$$V_n = Z_n I_n. \quad (7)$$

Furthermore, the induced voltage as a function of time ($V(t)$) can then be obtained by

$$V(t) = \sum_{n=-\infty}^{\infty} V_n \exp(jn\omega_0 t). \quad (8)$$

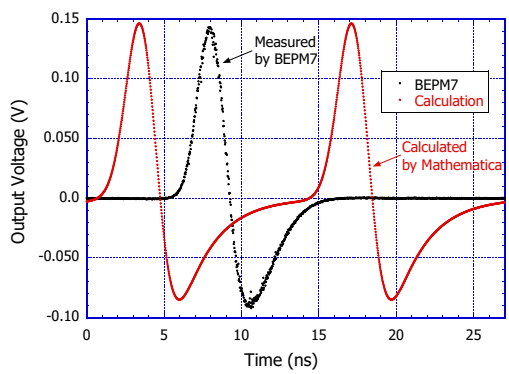

Figure 4: Calculated and measured results of the amplified pickup-voltage in the time domain. Agreement between the measured results and theoretical values is satisfactory.

Figure 4 shows the calculated and measured results of the amplified pickup-voltage in the time domain. The agreement between the measured results and the theoretical values is acceptable. The measured results show only one bunch because the frequency of the pre-accelerator is 36.5 MHz. However, the frequency of the SRILAC is 73 MHz and it has one empty RF bucket. Using the induced voltage V_n from Eq. (7), the pickup-power is given by

$$P_n(dBm) = 10 \log \left(1000 \times GAtt \frac{1}{R} \left(\frac{V_n}{\sqrt{2}} \right)^2 \right), \quad (9)$$

where G is the gain of the amplifier and Att is the attenuation gain of the coaxial cable, which has a length of about 25.3 m.

Figure 5 shows the theoretically calculated results of the amplified pickup-power in the frequency domain. The parameters used in the calculations are tabulated in Table 2.

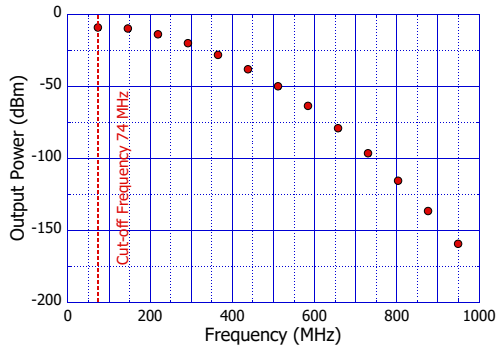

Figure 5: Theoretically calculated results of the amplified pickup-power in the frequency domain.

Improvement of the Noise Figure

We evaluated how a low noise amplifier might improve the noise figure in our system. A noise factor is defined the ratio between the input S_i/N_i and the output S_o/N_o as follows:

$$F = \frac{S_i/N_i}{S_o/N_o}, \quad (10)$$

where S/N is the signal to noise ratio. When amplifiers are connected in cascade, the total noise factor F_T is expressed as

$$F_T = F_1 + \frac{F_2 - 1}{G_1} + \cdots + \frac{F_n - 1}{G_1 \cdot G_2 \cdots G_n} \quad (11)$$

where N_n and G_n are respectively the noise factor and gain of the n-th amplifier. This equation illustrates the important point that the total noise factor is dominated by the performance of the first amplifier, if the amplifier has a high enough gain and low noise floor. Thus, by adapting a low noise amplifier, the total noise factor can be greatly improved. To make the calculation easier, the noise factor is converted to a noise figure (NF) and is expressed in decibels as follows:

$$NF = 10 \log F. \quad (12)$$

The RMS noise voltage V_{nD} of the digitizer PXIe-5160 is 0.14% with a 1-V full-scale range and the band-width is 500 MHz, hence the noise power (P_{nD}) is calculated as fol-

Content from this work may be used under the terms of the CC BY 3.0 licence (© 2020). Any distribution of this work must maintain attribution to the author(s), title of the work, publisher, and DOI

ISBN: 978-3-95450-222-6 ISSN: 2673-5350 doi:10.18429/JACoW-IBIC2020-FRA004

Content from this work may be used under the terms of the CC BY 3.0 licence (© 2020). Any distribution of this work must maintain attribution to the author(s), title of the work, publisher, and DOI

lows:

$$P_{nD} = 10\log(1000 \times (V_n^2/R))/(500 \times 10^6)) = -131\, dBm/Hz. \quad (13)$$

Since the thermal noise figure T_N with a resistance of 50 Ω at a temperature of 290 K is 174 dBm/Hz, the noise figure NF_D of the digitizer is 174 - 131 = 43 dB. If an amplifier with a noise figure NF_A of 2.5 dB and a gain G_A of 36.5 dB are connected to the input of the digitizer, the total noise factor F_T is calculated from Eq. (11) as

$$F_T = NF_A + \frac{NF_d - 1}{G_a} = \log^{-1}[2.5/10] + \frac{\log^{-1}[43/10]}{\log^{-1}[36.5/10]} = 6.24. \quad (14)$$

The total noise figure is calculated to be 8.00 dB by using Eq. (12). Finally, we conclude that the improvement of the noise figure is 43 - 8 = 35 dB/Hz, which yields a great advantage for measurements of weak beams.

Resolution of the Beam Position Measurement

The resolution of the BEPM can be estimated from the total noise figure obtained from the calculation above. Taking into account the bandwidth of 500 MHz, the input noise power P_N is calculated to be -174 + 8 + 10 log (500 × 10^6) = -79 dBm, which corresponds to be 0.025 mV (rms) of input noise voltage V_N. The resolution of the BEPM is estimated by

$$(\delta x) = (D/2) \times (V_N/V_S), \quad (15)$$

where V_S is the induced voltage on the electrostatic pick-up and D is the diameter of the pick-up. By using 165 mV (rms) (see Fig. 4) for V_S, 0.025 mV for V_n, and 40 mm for D, the resolution δx of the BEPM is evaluated to be 0.003 mm from Eq. (15).

Resolution of the Beam Energy Measurement

To evaluate the resolution of the beam energy measurement, we used the time-of-flight (TOF) method, and took into account the following factors. The length measurement error between each BEPM was $\Delta L = \pm 0.5$ mm, as determined by the accuracy of the laser distance meter, the cable length error was $\Delta T_c = 5$ ps and the error of the zero-crossing point error of the digitizer was $\Delta T_z = 5$ ps. The error in β (the ratio of velocity to light velocity) is expressed as follows:

$$\Delta\beta/\beta = \sqrt{(\Delta L/L)^2 + (\Delta T_c/T_{tof})^2 + (\Delta T_z/T_{tof})^2}. \quad (16)$$

Here, by using a length L of 4.0048 m and TOF T_{tof} of 147 ns, $\Delta\beta/\beta$ is then calculated to be 2.6×10^{-4}. From the relationship $\Delta E/E = 2 \times \Delta\beta/\beta$, we conclude that the absolute resolution of the beam energy is 5.1×10^{-4}. The zero-crossing point is precisely obtained by linearly fitting 50 data points within 1 ns around the zero-crossing point.

Amplifiers and Power Supplies

Figure 6 shows pictures of the customized amplifiers and amplifier power supplies [17] and the data -acquisition system. The specifications of the amplifiers and power supplies

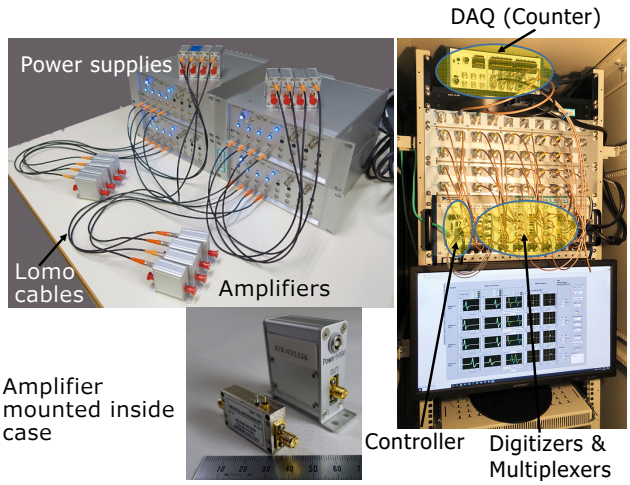

Figure 6: Photographs of the amplifier power supplies, mounted amplifier, and the data -acquisition system (DAQ).

are shown in Table 3. The gains of all the amplifiers are measured in advance and are used by the LabVIEW program for corrections when the beam is measured. The standard deviation of the gains of all the amplifier's was measured to be 0.15 dB. Lemo conector cables, which can be replaced easily in case of failure, are used to supply power to the amplifiers. The power supplies can be remotely turned on and off with a TTL signal and their statuses are monitored. An LED on the front panel turns on when the amplifier is connected. If the supplied current exceeds 140 ± 20 mA in case of failure, the LEDs turn off and the off-status is returned. For the signal cables, we adopted S 07262 BD coaxial cable [20], which has a significant shielding property and a bandwidth of up to 3 GHz.

Table 3: Electrical Specifications of the Amplifiers and Power Supplies

	Amplifier
Model No.	ABL0300-00-3230 [18]
Bandwidth	9 kHz - 3.0 GHz
Noise Figure	2.5 dB typical, 3.0 dB Max @25 °C
Gain	36.5 dB @25 °C
	Amplifier power supply
Model No.	LFS50A-15 [19]
Output Voltage	15 V
Ripple Noise	10 mV_{p-p}

Signal Processing System and Programming

A block diagram of the BEPMs and data -acquisition system is shown in Fig. 7 and electrical specifications of the signal processing devices are shown in Table 4. The amplified pickup signals are sent through coaxial cables to the signal processing devices. The upstream and downstream signals are switched by multiplexers and digitized by the digitizers (PXIe-5160). Although the sampling speed is 1.25 GS/s, by using the random interleave mode, a much higher sampling speed of 50 GS/s is available under the

ISBN: 978-3-95450-222-6 ISSN: 2673-5350 doi:10.18429/JACoW-IBIC2020-FRA004

condition that the signal is repeating continuously. As a result, highly accurate TOF measurements can be realized. The random interleave method achieves a higher sampling rate by operating multiple analog-to-digital converters in parallel.

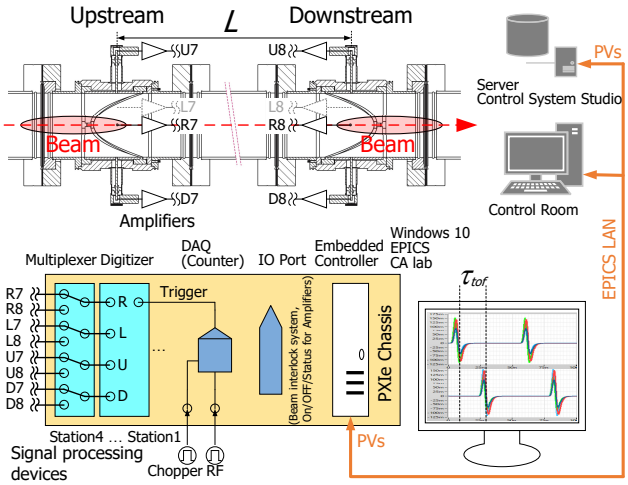

Figure 7: Block diagram of the BEPMs and DAQ.

All the modules are integrated into a PXI express chassis (see Fig. 6). The signal process procedures are controlled by the LabVIEW 2019 graphical programming language and the module drivers are supported by the National Instruments Corporation (Austin, TX, USA) [21]. The obtained data are shared by using CA Lab [22] which is a user-friendly, lightweight, and high performance interface between the LabVIEW program language and the EPICS-based control system. It allows easy reading and writing of EPICS process variables (PV). The BEPM system uses the following PVs: 50 analog inputs, 8 wave-forms, and 13 analog and binary outputs. Currently, measurement results are displayed on a remote desktop. However, once these data are saved, the control system studio, which is an Eclipse-based tool to operate a large-scale control system, can display the results anywhere in the control room.

During the beam tuning procedure, if more than 30 enA of the 0.6 W $^{51}V^{13+}$ beam [23] is lost, the vacuum pressure becomes rapidly worse, increasing from the 10^{-8} Pa to the 10^{-6} Pa range. To avoid this, the beam current should be attenuated to be as weak as possible to avoid vacuum deterioration during the beam tuning procedure and acceleration trial. Since the upstream signal and down-stream signals are switched by the multiplexer, a reference RF signal is required to measure the TOF of the beam. Furthermore, the RF reference signal also needs to be synchronized with the beam chopper signal, because if the measurement was performed while the beam is being chopped, unnecessary null data would be transferred. To address this issue, we introduced a counter that triggers when it reaches the pre-set RF signal. Figure 8 presents a timing chart showing how the data acquisition is triggered at 30 µs after the chopper signal is launched.

Here, the 37th counted RF signal just after the chopper signal is launched triggers the digitizers. The counter works like a field programmable gate array, and the operational procedure is programmed by LabVIEW.

Table 4: Electrical Specifications of the Signal Processing Devices [21]

	Embedded Controller (NI PXIe-8840)
CPU	i7 5700EQ, 2.6 GHz Quad, 8 GB RAM
Transfer rates	8 GB/s
	Digitizer (NI PXIe-5160)
Bandwidth	DC - 500 MHz
Sampling rates	2.5 GS/s (1 ch), 1.25 GS/s (4 ch)
Memory	2 GB
Resolution	10-bit
Channels	4
Transfer rates	600 MB/s
	DAQ (NI PXIe-6341)
IO	16 AI (16-Bit, 500 kS/s), 2 AO, 24 DIO
	DAQ (NI PXIe-6612)
Counter	8-Channel PXI Counter/Time
	Multiplexer (NI PXIe-2746)
Bandwidth	DC - 2.7 GHz
Type	4×1, 4 sets
	PXIe Chassis (NI PXIe-1075)
Slot	18
Transfer rates	4 GB/s

This system is intended to be able to work during SH element searches. The circulating wheel targets are used as shown in Fig. 8; the heavy ion beam is chopped while the target is not irradiated by the beam to avoid radio-activation, temperature increase, and background noise. A photo-sensor detects light emitted through the slit in the wheel frame and creates the chopper signal. Because the BEPM system is synchronized with the chopper signal, precise measurement of the beam position and energy can be realized. Eventually, as beam irradiation of the target continues, some targets

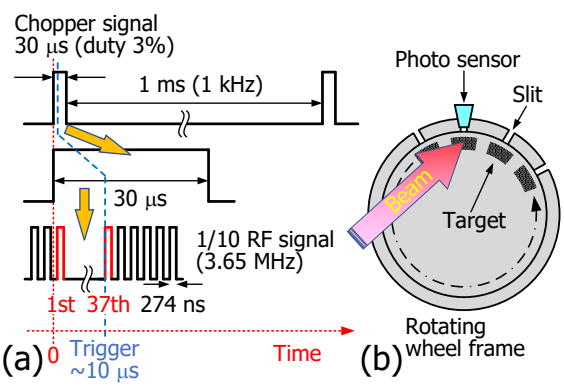

Figure 8: (a) Timing chart showing how the data acquisition is triggered 30 µs after the chopper signal is launched. (b) Circulating wheel target used for the SH element searches. The chopper signal is created by the photo sensor and the slit.

Content from this work may be used under the terms of the CC BY 3.0 licence (© 2020). Any distribution of this work must maintain attribution to the author(s), title of the work, publisher, and DOI

ISBN: 978-3-95450-222-6 ISSN: 2673-5350 doi:10.18429/JACoW-IBIC2020-FRAO04

Content from this work may be used under the terms of the CC BY 3.0 licence (© 2020). Any distribution of this work must maintain attribution to the author(s), title of the work, publisher, and DOI

begin to break down. Since the chopper-off signal is manually masked at the broken target position, the synchronized measurement becomes more important. Presently, it is possible to measure the beam position and beam energy at an intensity of 10 enA by chopping the beam to 1/100.

CALIBRATION OF THE BEPMS

With the goal of measuring the beam position to an overall accuracy of ±0.1 mm, a calibration measurement was performed at the KEK campus in Tokai [24]. A BEPM was connected to a dummy pipe with inner diameter equal to that of one of the BEPMs. Supporting jigs, the dummy pipe, and the BEPM were fixed to an XY stage that could move within the measurement region at 2-mm step intervals. A fixed wire acted as a signal source. If the outputs from the 4 opposing right, left, up, and down electrodes are represented by V_R, V_L, V_U, and V_D, respectively, the horizontal x and vertical y positions of the wire are expressed as follows:

$$\frac{V_R - V_L}{V_R + V_L + V_U + V_D} = \frac{\Delta_x}{\Sigma} \approx f_x(x,y) \approx k_x x,$$
$$\frac{V_U - V_D}{V_R + V_L + V_U + V_D} = \frac{\Delta_y}{\Sigma} \approx f_y(x,y) \approx k_y y. \qquad (17)$$

where $f_x(x,y)$ and $f_y(x,y)$ are 5$^{\text{th}}$-order polynomials of the wire (or beam) position and k is a position sensitivity coefficient. The 1$^{\text{st}}$-order approximations of $f_x(x,y)$ and $f_y(x,y)$ are $k_x x$ and $k_y y$, respectively.

By using the electrode output voltages V_R, V_L, V_U, and V_D, we calculated the values of Δ_x/Σ and Δ_y/Σ from Eq. (17). By fitting these measured data with a 5$^{\text{th}}$-order polynomial, we calculated $f_x(x,y)$ and $f_y(x,y)$, and obtained the calibration coefficients. In Figs. 9(a) and (b), each calculated wire position is plotted based on the calibration coefficients of 5$^{\text{th}}$-order and 1$^{\text{st}}$-order polynomials, respectively. Although Fig. 9(a) demonstrates that the calculated positions are in fairly good agreement with the wire positions, Fig. 9(b) shows that the data mismatching becomes larger the further away the wire is from the center position. Figure 10(a) (enlarged in 10(c)) shows the residuals between the real wire position and the position obtained from the calibrated 5$^{\text{th}}$-order polynomial and Figure 10(b) shows the residuals from the 1$^{\text{st}}$-order polynomial. These results demonstrate that, the residual of 1σ is less than 10 µm when we use the 5$^{\text{th}}$-order

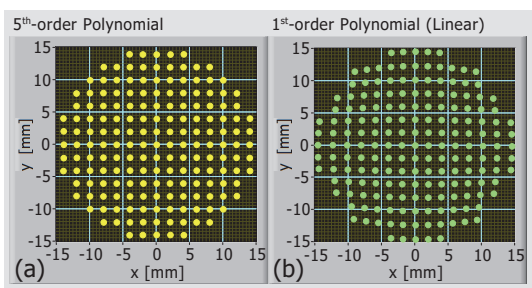

Figure 9: Calculated wire positions plotted by using the calibration coefficients of 5$^{\text{th}}$-order and (b) 1$^{\text{st}}$-order polynomials obtained by the mapping measurements.

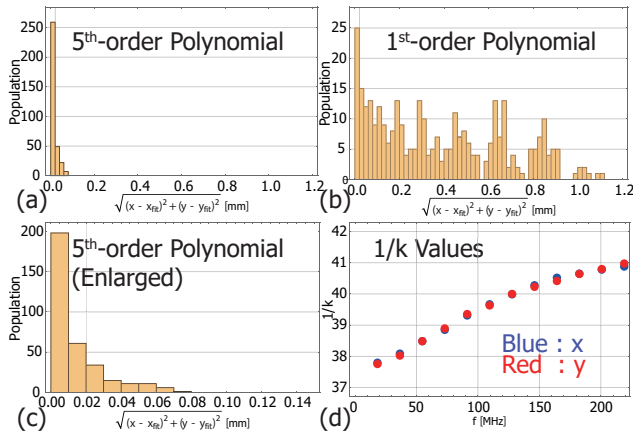

Figure 10: Residuals between the real wire position and the position obtained from the calibrated (a) 5$^{\text{th}}$-order and (b) 1$^{\text{st}}$-order Polynomials. (c) Enlargement of (a). (d) Measured results of the inverse of the position sensitivity coefficients k, which are frequency dependent.

polynomial calibration. In addition, we performed these calibration measurements from 18.25 to 219 MHz in 12 steps of 18.25 MHz intervals. The inverse of the position sensitivity coefficients k of the BEPMs are frequency dependent (Fig. 10(d)). All the 5$^{\text{th}}$-order polynomial calibration coefficients were recorded in tables that the LabVIEW program reads at the time of beam measurement.

COMMISSIONING

Installation of the BEPMs

Since ultrahigh vacuum and particle-free conditions are crucial for SRILAC operation, all the cleaning procedures for the BEPM were done in an ISO class 1 clean room. First, the BEPMs were thoroughly rinsed with ultra-pure water and blow-dried with an ionizing gun [25]. After that, the BEPMs were dried in a vacuum oven at 70°C for 5 days. We continued the blow-drying operation until fewer than 10 particles/s could be detected. Over 3 h was necessary to complete the cleaning procedure for one BEPM. In particular, because long vacuum chambers are present at the ends of the Types I and II BEPMs, they took more time to clean.

To install all the BEPMs between the SRF cavities, half of the quadruple magnets had to be previously positioned, because the BEPMs were to be installed into their center (Figs. 11(a) and (b)). Since the tolerance between the quadrupole magnet and the BEPM is only 1 mm and strength of the feed-through insulator is very weak against external force, careful adjustment of the installation was carried out with the help of laser transits. It is notable that when we installed the BEPMs, we built a temporary ISO class 1 clean room between the SRF cavities. After the installation, the amplifiers connected to the semi-rigid cables and the stiff coaxial signal cables were securely attached to the end faces of the quadrupole magnets by using specially designed jigs (Fig. 11(c)). The Type III BEPM was designed to be fixed separately on the vacuum chamber (Fig. 11(d)) because it is

ISBN: 978-3-95450-222-6 ISSN: 2673-5350 doi:10.18429/JACoW-IBIC2020-FRA004

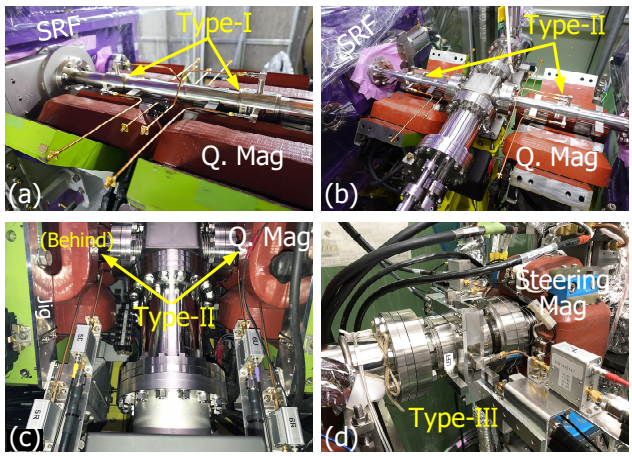

Figure 11: (a) and (b) To install the BEPMs into the center of the quadrupole magnets, half of the quadruple magnets had to be already previously positioned. (c) and (d) After the installation, the amplifiers connected to the semi-rigid cables and the stiff coaxial signal cables were securely attached.

not installed inside the quadrupole magnet. After installation, we measured the alignment errors from the 32 reference planes; their average was 0.08 mm. Each point alignment error data point was recorded in a file that the LabVIEW program uses to correct the beam position at the time of measurement. To measure the TOF precisely, we adjusted the electrical lengths of the 8 coaxial cable sets, totalling 32 cables, to converge within 3 ps. To adjust the cables, we observed the reflected signal caused by a pulser generator with a rapid 1-ns rise time.

Beam Acceleration by the SRILAC

The first $^{40}Ar^{13+}$ beam acceleration test was carried out by using the 9 SRF cavities [7]. Figure 12 shows the displayed results of the BEPM measurements just after the beam was successfully accelerated to 6.2 MeV/u (2020/01/28 21:02). The wave-forms, beam positions, and beam energies at each station are displayed; the value circled in red indicates the final accelerated energy.

The measured beam energy is plotted in Fig. 13 as a function of the phase of the final SRF cavity CM3. In the focusing region, the higher energy beam loses energy, whereas in the defocusing region, the lower energy beam gains energy. This measurement clearly shows us which region we should select to accelerate the beam stably. The phases of the SRF cavities are currently set to -25 degrees. Each phase of an SRF cavity was measured and set in sequence from upstream to down-stream.

Figure 14 shows the relationship between the beam position at BEPM 1 and the vacuum between the CM1 and CM2 (see Fig. 1) when the $^{51}V^{13+}$ beam intensity was increased to 2.5 pμA. From this measurement, we recognized that the vacuum rapidly became worse when the beam position shifted from -1 mm to -2 mm. Therefore, we changed the EPICS interlock system to automatically start the beam attenuator to prevent vacuum deterioration.

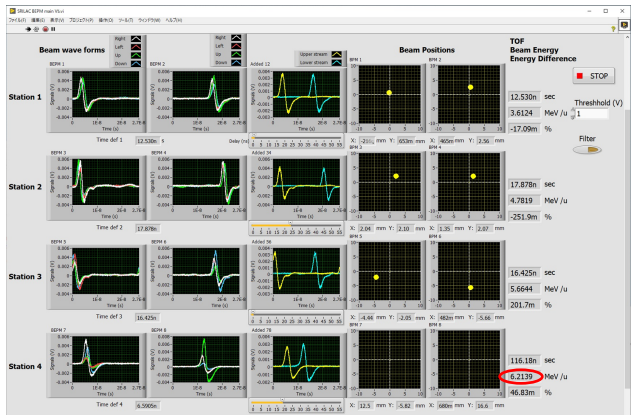

Figure 12: Displayed the BEPM measurement results just after the $^{40}Ar^{13+}$ beam was successfully accelerated to 6.2 MeV/u (2020/01/28 21:02). The positions at station 4 were off scale, which was corrected after the first trial acceleration.

To obtain beam size information from the BEPMs nondestructively, the quadrupole moments are calculated from the following equation and displayed:

$$Q = k_q \times \frac{V_R + V_L - V_U - V_D}{V_R + V_L + V_U + V_D} - < x >^2 + < y >^2 . \quad (18)$$

Currently, we are comparing the calculations to results from the lattice model to obtain the beam emittances ϵ_x and ϵ_y.

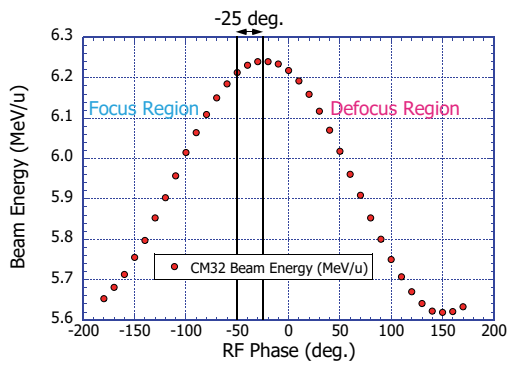

Figure 13: Measured beam energy plotted as a function of the phase of the final SRF cavity CM3.

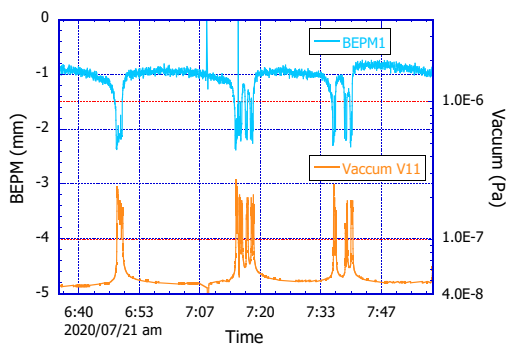

Figure 14: Measured results showing the relationship between the beam position at the BEPM 1 and the vacuum between CM1 and CM2 (see Fig. 1).

Content from this work may be used under the terms of the CC BY 3.0 licence (© 2020). Any distribution of this work must maintain attribution to the author(s), title of the work, publisher, and DOI

ISBN: 978-3-95450-222-6 ISSN: 2673-5350 doi:10.18429/JACoW-IBIC2020-FRAO04

Content from this work may be used under the terms of the CC BY 3.0 licence (© 2020). Any distribution of this work must maintain attribution to the author(s), title of the work, publisher, and DOI

CONCLUSION AND FUTURE OUTLOOK

Beam commissioning for the RIKEN Superconducting Linear Accelerator (SRILAC) has been successfully completed. To continually monitor the beam nondestructively, we have developed a new system (BEPM) to determine simultaneously the beam position and energy by measuring the time-of-flight of the beam. The BEPM system worked extremely to well in determining the phases of the Superconducting Radio Frequency (SRF) cavities and confirming the beam energies and positions, enabling stable beam acceleration.

We are currently working on measurement of the quadrupole moment to obtain the beam size, the beam intensity from the bunched signal, and the TOF using a lock-in amp technique.

REFERENCES

[1] K. Morita *et al.*, "New Result in the Production and Decay of an Isotope, ^{278}113, of the 113th Element", *J. Phys. Soc. Jpn.*, vol. 81, 103201, 2012. doi:10.1143/JPSJ.81.103201

[2] H. Haba, "Production of radioisotopes for targeted radionuclide therapy at RIKEN", *Drug Delivery System*, vol. 35, no.2, pp. 114-120, 2020. doi:10.2745/dds.35.114

[3] M. Odera *et al.*, "Variable frequency heavy-ion linac, RILAC: I. Design, construction and operation of its accelerating structure", *Nucl. Instrum. Methods Phys. Res., Sect. A*, vol. 227, pp. 187–195, 1984. doi:10.1016/0168-9002(84)90121-9

[4] Y. Yano, "The RIKEN RI Beam Factory Project: A status report", *Nucl. Instrum. Methods Phys. Res., Sect. B*, vol. 261, pp. 1009–1013, 2007. doi:10.1016/j.nimb.2007.04.174

[5] H. Okuno *et al.*, "Progress of RIBF accelerators", *Prog. Theor. Exp. Phys.*, vol. 2012, p. 03C002, 2012. doi:10.1093/ptep/pts046

[6] T. Nagatomo *et al.*, "New 28-GHz Superconducting ECR Ion Source for Synthesizing New Super Heavy Elements of Z > 118", in *Proc. ECRIS'18*, Catania, Italy, Sep 2018, pp. 53–57. doi:10.18429/JACoW-ECRIS2018-TUA3

[7] N. Sakamoto *et al.*, "Development of Superconducting Quarter-Wave Resonator and Cryomodule for Low-Beta Ion Accelerators at RIKEN Radioactive Isotope Beam Factory", in *Proc. SRF'19*, Dresden, Germany, Jul. 2019, pp. 750-757. doi:10.18429/JACoW-SRF2019-WETEB1

[8] H. Imao *et al.*, "Non-Evaporative Getter-Based Differential Pumping System for SRILAC at RIBF", in *Proc. SRF'19*, Dresden, Germany, Jul. 2019, pp. 419-423. doi:10.18429/JACoW-SRF2019-TUP013

[9] T. Watanabe *et al.*, in *Proc. of the 15th Annual Meeting of Particle Accelerator Society of Japan*, Aug. 2018, pp. 49-54; http://www.pasj.jp/web_publish/pasj2018/proceedings/index.html

[10] TOYAMA Co., Ltd., http://www.toyama-en.com/

[11] G. Nassibian, "The measurement of the multipole coefficients of a cylindrical charge distribution", CERN-SI-NOTE-EL-70-13, 1970. http://cds.cern.ch/record/358718

[12] Ferrotec Material Technologies Co., http://www.ft-ceramics.co.jp/en/

[13] MARUWA Co., Ltd., https://www.maruwa-g.com/e/

[14] Robert E. Shafer, "Beam position monitoring", *AIP Conference Proceedings*, vol. 249, p. 601, 1992. doi:10.1063/1.41980

[15] T. Watanabe *et al.*, "Beam position monitoring system and COD correction at the cooler synchrotron TARN II", *Nucl. Instrum. Methods Phys. Res., Sect. A*, vol. 381, p. 194, 1996. doi:10.1016/S0168-9002(96)00528-1

[16] T. Watanabe *et al.*, "Development of beam energy and position monitor system at RIBF", in *Proc. of the 14th Annual Meeting of Particle Accelerator Society of Japan*, Aug. 2017, paper WEP091, pp. 1112-1117. http://www.pasj.jp/web_publish/pasj2017/proceedings/PDF/WEP0/WEP091.pdf

[17] Hayashi-Repic Co., https://www.h-repic.co.jp/

[18] Wenteq Microwave Co., http://www.wenteq.com/

[19] Daitron Co., http://www.daitron.co.jp/en/

[20] Huber+Suhner AG, https://www.hubersuhner.com/en

[21] National Instruments Corp., http://www.ni.com/

[22] BESSY CA Lab, https://www.helmholtz-berlin.de/zentrum/locations/it/software/exsteuer/calab/index_en.html

[23] Y. Higurashi *et al.*, RIKEN Accel. Prog. Rep., vol. 51, p. 17, 2018.

[24] T. Watanabe *et al.*, "Calibration for Beam Energy Position Monitor System for Riken Superconducting Acceleration Cavity", in *Proc. IBIC'19*, Sept. 2019, pp. 526-529. doi:10.18429/JACoW-IBIC2019-WEPP007

[25] SIMCO ION, http://www.simcoion.jp/

ISBN: 978-3-95450-222-6 ISSN: 2673-5350 doi:10.18429/JACoW-IBIC2020-FRAO05

HIGH PERFORMANCE DATA ACQUISITION FOR A MODERN ACCELERATOR*

G. Shen, N. Arnold, T. Berenc, J. Carwardine, E. Chandler, T. Fors, T. Madden, D. Paskvan, C. Roehrig, S. Shoaf, S. Veseli, Argonne National Laboratory, Lemont, USA

Abstract

Modern technology provides great potential to acquire large amounts of accelerator data, and the possibility to fine tune the particle beam. The wide use of embedded controllers, like field-programmable gate arrays (FPGA), enables collection of fast data from technical subsystems for monitoring, statistics, diagnostics or fault recording. This also presents a number of challenges related to the data acquisition and data management of accelerator data. As a part of the APS Upgrade project, a general purpose data acquisition (DAQ) system is under active development. The DAQ system interfaces with a number of technical subsystems to provide time-correlated and synchronously sampled data acquisition for commissioning, performance monitoring, troubleshooting and early fault detection. This paper will present the status update for the DAQ system, as well as its use cases at APS.

INTRODUCTION

State-of-the-art embedded controllers (microcontrollers, SoCs, FPGAs, DSPs, etc.) have a plethora of resources to implement a high level of functionality tightly coupled to the technical system equipment. A common use of these resources is to utilize large memory buffers to collect fast data for statistics, diagnostics or fault recording. Each embedded controller may contain several gigabytes of memory for such purposes. This presents a challenge: how does one collect, transfer, and utilize this large amount of data from numerous controllers without affecting normal operations? This challenge must be considered early on in the design cycle of a modern accelerator to ensure the solution is well integrated into the control system.

The original design for the APS-U DAQ system was presented in [1]. This paper describes several updates made during the final design phase.

APS-U DAQ SYSTEM

As presented in [2] and illustrated in Fig. 1, APS-U control system is based on EPICS [3], which is widely used in the accelerator control community. The DAQ system is marked with a red dashed line, and its main components are illustrated in Fig. 2.

Wherever possible DAQ IOCs will directly interface with the technical system hardware where the acquisition is performed. In cases where direct connection to the technical system hardware is not feasible, a system specific "DAQ Front-end" will be used between the technical system and DAQ IOC. Each DAQ IOC will be somewhat customized for a given technical system but will also utilize a common framework for capturing and transferring time-series data. This framework will support the transmission of data across dedicated subnets, either directly to services for continuous data collection, or to services responsible for distribution of data to storage, external services, or applications prepared to accept and analyse this data.

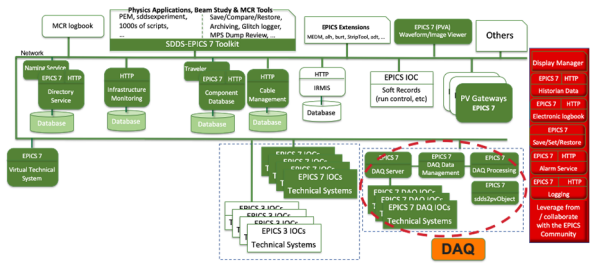

Figure 1: APS-U control system architecture and its DAQ system.

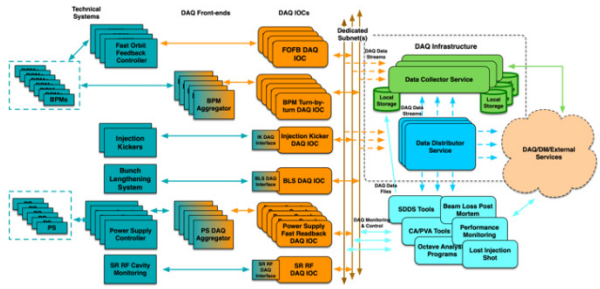

Figure 2: APS-U DAQ system main components.

Key aspects of the Data Acquisition (DAQ) System include:

- Capability to acquire time-correlated synchronously sampled data from several subsystems at various sample rates and correlate this data to within one beam revolution (3.6 µs) or better
- Most DAQ data includes a timestamp for each sample acquired allowing immediate plotting of data from various systems onto a common time-axis
- Support for continuous acquisition or triggered acquisition limited only by available storage
- The ability to route the data to any number of applications
- Use of PV Access [4,5] DAQ objects to encapsulate numerous signals to ensure data synchronicity
- Scalability by partitioning the heavy traffic on dedicated and multiple subnets and servers

* Argonne National Laboratory's work was supported by the U.S. Department of Energy, Office of Science, Office of Basic Energy Sciences, under contract DE-AC02-06CH11357.
† gshen@anl.gov

Content from this work may be used under the terms of the CC BY 3.0 licence (© 2020). Any distribution of this work must maintain attribution to the author(s), title of the work, publisher, and DOI

ISBN: 978-3-95450-222-6 ISSN: 2673-5350 doi:10.18429/JACoW-IBIC2020-FRA005

Content from this work may be used under the terms of the CC BY 3.0 licence (© 2020). Any distribution of this work must maintain attribution to the author(s), title of the work, publisher, and DOI

- Separation from operational systems (networks, processors, servers) to allow troubleshooting & enhancements during user operations

R&D WORK

There has been a significant amount of progress on the DAQ system during the APSU R&D phase. Five prototype DAQ IOCs were deployed, as well as a number of services and utilities for saving, viewing and processing data. This demonstrated time-correlated acquisition across different subsystems with different data sampling frequencies. Figure 3 illustrates an example for DAQ data collected from two different subsystems: BPM turn-by-turn (TBT) and FOFB DAQ systems.

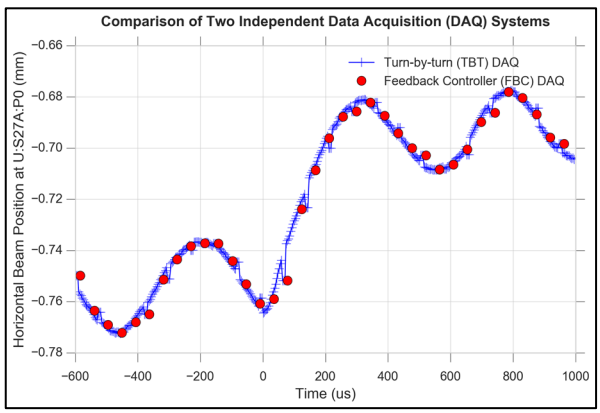

Figure 3: DAQ data example from different subsystems.

In order to provide users with the ability to easily view the DAQ data in real time, we developed an EPICS7 data viewer (see Fig. 4), a scope like application that receives streaming data over EPICS7 PV Access protocol. The viewer allows users to select and display several EPICS7 channels, as well as to perform simple processing in real time (FFT, histogram PSD, etc.).

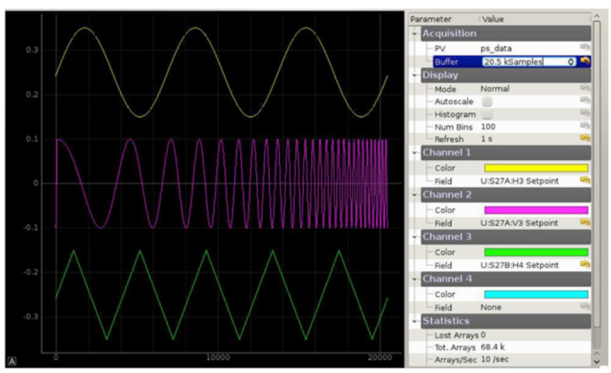

Figure 4: Scope-like-application for APS-U DAQ system.

Over the last few years, these R&D systems have been used extensively for machine studies, diagnostics and troubleshooting. One such example was recent work on the identification and suppression of a troubling 147 Hz vibration source in the APS storage ring. The DAQ system was used to capture 400 channels of continuous data for 20 seconds which was used to identify the sector where the vibration was occurring. Inserting shims to tightly secure a vacuum chamber mount eliminated the vibration [6].

DESIGN UPDATES

One significant architecture change that was made during the final design phase was introduction of the double-sector servers for running turn-by-turn and power supply IOCs. The initial plan involved running a linux-arm TBT DAQ IOC on a micro-TCA FPGA card, and a linux power supplies DAQ IOC hosted on a micro-TCA CPU. The fast orbit feedback IOC was hosted on a linux server. The revised plan calls for hosting all three IOCs on a local linux server (every double-sector), but also requires an FPGA-based data aggregator for both turn-by-turn and power supplies subsystems.

The main advantages of this approach are the common platform used for the three major DAQ subsystems, and also the cost-effectiveness of commodity hardware.

The primary hardware components of the DAQ system are illustrated in Fig. 5. A server will be positioned at each double sector to receive and process the data from three nearby technical systems: Power Supply Fast Monitoring (PS DAQ) data, Fast Orbit Feedback (FOFB) data and BPM TBT data. These double-sector servers isolate much of the "raw data" to local switches and also provide the first level of significant storage for storing long duration acquisitions. Other "one-of" DAQ systems (e.g. LFB, TFB, BLS, …) are connected where most convenient.

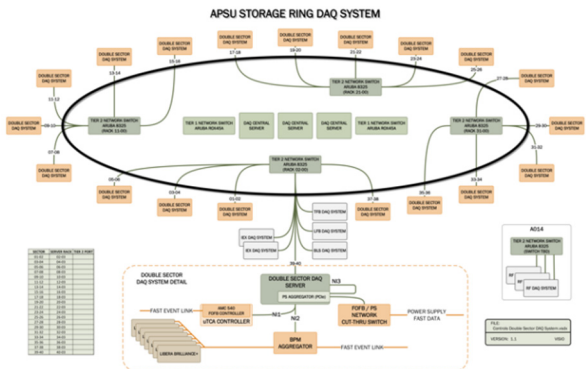

Figure 5: APS-U DAQ hardware architecture.

Additional DAQ servers are in the main Computer Room. These "DAQ Central Servers" are used for data aggregation and user applications.

The components involved with data flow and processing of the DAQ data are numbered & identified in Fig. 6. These are the DAQ interface to the technical system (1), the acquisition and timestamping of the collected data (2), the DAQ IOCs (3), the communication medium and protocols between the IOCs and the services (4), the data collection and distributor services (5), and finally the client API and CLI interfaces for applications that consume the data (6). Also shown is the "processing stack" (7) that illustrates the layers of computing power available for data processing and manipulation. The following

ISBN: 978-3-95450-222-6 ISSN: 2673-5350 doi:10.18429/JACoW-IBIC2020-FRA005

sections give additional details and suggested implementations of these components.

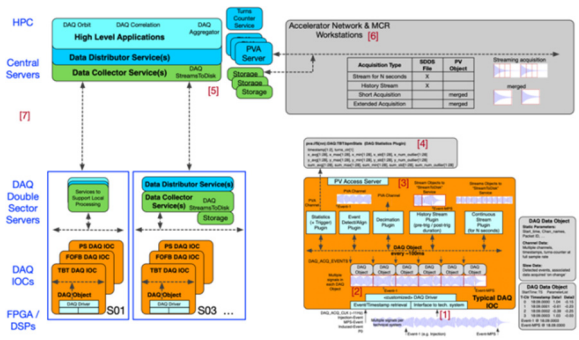

Figure 6: APS-U DAQ system data flow and processing.

As indicated in the bottom-right corner of the Fig. 6, the DAQ IOCs use Area Detector framework [7], which gives us enormous amount of flexibility in terms of processing plugins. The driver gathers data from the technical subsystem, assembles DAQ objects that are then passed through various processing and streaming plugins. The streaming plugins in particular are responsible for actually sending data directly to the data collector service. The history streaming plugins keep circular buffers of data and enable the system to collect data before and after a significant event happens. This can be incredibly useful tool for troubleshooting things like causes of beam dumps or other problems.

Note that all DAQ IOCs have a PVA server that is used to expose DAQ objects on the PV Access channel which can be retrieved using standard EPICS7 clients or APIs.

In addition to various high-level monitoring and processing applications, there are two DAQ services deployed in each double sector, which are 1) data collector service and 2) the distributor service respectively. The data collector service is responsible for storing data to local storage, while the distributor service forwards data to various client applications or other DAQ, data management, or external services.

DATA ACQUISITION MODES

Figure 7 shows a slightly bigger picture of the DAQ IOC and illustrates several DAQ acquisition modes.

The start of each DAQ object is synchronized across IOCs using the fast event system. Each DAQ object contains ~90ms of fast sampled data, slow data that changes infrequently (compared to the fast sampling rate) and static parameters of interest.

The first acquisition mode is continuous streaming of DAQ objects to services and applications. The second one is data acquisition with history, where DAQ objects are stored into a set of circular buffers and streamed to the collector service after a significant preconfigured event happens. The third mode is event based; it involves detecting specific events, aligning data to those events, and presenting this data to clients via designated PV Access channels.

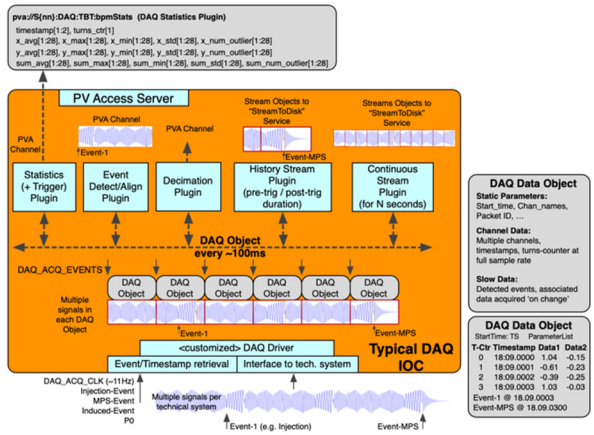

Figure 7: DAQ IOC and acquisition modes.

PERFORMANCE CONSIDERATIONS

As mentioned above, there will be 20 double-sector DAQ servers distributed around the storage ring, each hosting the DAQ IOCs for the turn-by-turn BPM DAQ, the power supply DAQ and the fast orbit feedback DAQ. Because of the numerous channels and fast acquisition, both the turn-by-turn DAQ and power supply DAQ include FPGA-based "aggregators" which receive streams from the technical system hardware and repackage it for efficient processing in the DAQ IOC. Note that just those three double sector subsystems taken together represent more than 13000 channels of data that can be collected simultaneously (see Table 1).

Table 1: Number of Channels of APS-U DAQ System

Technical System DAQ	# of Channels
Fast Orbit Feedback	256 x 20
Power Supply Fast Monitoring	354 x 20
BPM Turn-by-turn	84 (typical) x 20
IX/EX Waveforms	8 x 2
Bunch Lengthening System	9 (typical)
Longitudinal Feedback	1
Transverse Feedback	2
SR RF (current)	6
SR RF (near term)	10 (typical) x 4
SR RF (future)	5 (typical) x 12
Booster RF (5)	14, 10, 10, 8, 8 (typical)
PAR RF (3)	9, 12, 10 (typical)
Total # of Channels	**> 13,000**

Several DAQ systems demand significant performance of the network and server components. Table 2 lists the anticipated data bandwidth for each DAQ system. A series of performance tests have been completed in order to

Content from this work may be used under the terms of the CC BY 3.0 licence (© 2020). Any distribution of this work must maintain attribution to the author(s), title of the work, publisher, and DOI

ISBN: 978-3-95450-222-6 ISSN: 2673-5350 doi:10.18429/JACoW-IBIC2020-FRA005

Content from this work may be used under the terms of the CC BY 3.0 licence (© 2020). Any distribution of this work must maintain attribution to the author(s), title of the work, publisher, and DOI

ensure that all IOCs running on a DAQ double sector server can receive data from the technical systems at maximum rates.

The total double sector data rate is about 144MB/s, while the cumulative data rate for the entire DAQ system is over 3 GB/s. Note that generated Turn-By-Turn data could also include up to 13 additional signals per BPM, or up to 364 signals per double sector that were not counted in the Table 2 analysis. This could potentially result in almost 395 MB/s of additional TBT data per double sector, or almost 8GB/s of data for the entire system.

Table 2: DAQ System Anticipated Data Rates

Technical System DAQ	# of Channels	Sample Rate	Anticipated Data Rate (Per IOC)
Fast Orbit Feedback	256 (x 20)	22.6 kSPS	24MB/s
Power Supply Fast Monitoring	354 (x 20)	22.6 kSPS	32.3MB/s
BPM Turn-by-turn	84 (x 20)	271 kSPS	94MB/s
IX/EX Waveforms	8 (x 2)	4GSPS for 50ns	2.7MB/s (aperiodic)
Bunch Lengthening System	9	2.44MSPS	112.2MB/s
Longitudinal Feedback	1	352 MSPS	48MB/s per acquisition (2 acquisitions/s max)
Transverse Feedback	2	352 MSPS	48MB/s per acquisition x 2 (2 acquisitions/s max)
SR RF	6	271 kSPS	9.2MB/s

HARDWARE CONSIDERATIONS

Aggregators

Two of the DAQ systems, the TBT DAQ and the PS Fast Monitoring DAQ, require "aggregators" between the technical system and the DAQ servers. The platform for these aggregators will be determined during the final design phase.

DAQ Servers

For the purpose of estimating DAQ hardware needs, we assume that each DAQ server supports 1GB/s of combined (read/write) data throughput to/from the local storage. With today's hardware, this should be achievable with a mid-end Linux server: dual 6 physical core CPU with 128GB RAM, at least two 10Gbps networking interfaces, and local SSD storage in a RAID 0+1 (mirrored stripe set) with a PCI Express x4 controller card (each PCI-e lane supports 250MB/s data rate).

CONCLUSIONS

APS-U DAQ is a time-correlated data acquisition system. Among other things, its main features are the ability to acquire data from multiple systems at different sample rates, support for continuous data acquisition, and ability to collect multiple signals within a single IOC. During R&D phase, a significant amount of development has been done, and the system has already seen extensive use during machine studies for diagnostics and troubleshooting.

During final design phase we made several updates to the system design, and we are now actively working towards its deployment into production.

ACKNOWLEDGEMENTS

The authors would like to thank all colleagues at APS facility and APS-U project for their fruitful discussions.

REFERENCES

[1] S. Veseli *et al.*, "Data Acquisition System for the APS Upgrade", in *Proc. ICALEPCS'19,* New York, NY, USA, Oct. 2019, pp. 841-846. doi:10.18429/JACoW-ICALEPCS2019-TUDPP02

[2] G. Shen *et al.*, "High-Level Application Architecture Design for the Aps Upgrade", in *Proc. ICALEPCS'19*, New York, NY, USA, Oct. 2019, pp. 1436-1440. doi:10.18429/JACoW-ICALEPCS2019-WEPHA143

[3] EPICS, https://epics-controls.org

[4] EPICS4 documentation, http://epics-pvdata.sourceforge.net/literature.html

[5] PVA specification, http://epics-pvdata.sourceforge.net/pvAccess_Protocol_Specification.html

[6] L. Emery, pprivate communication, 2018.

[7] Area Detector documentation, http://cars.uchicago.edu/software/epics/areaDetectorDoc.html

ISBN: 978-3-95450-222-6 ISSN: 2673-5350

List of Authors

Bold papercodes indicate primary authors; ~~crossed out~~ papercodes indicate 'no submission'

— A —

Abbott, M.G. THPP23
Ackermann, W. WEPP21
Ady, M. WEPP36
Aggarwal, M. THPP12
Aleksandrov, A.V. THPP20
Alessio, F. ~~THPP02~~
Allaria, E. ~~TUPP31~~
Alves, D. WEPP27
Alves, F. ~~WEPP14~~
Antipov, S.P. WEPP29, WEPP38
Aoyagi, H. **TUPP06**
Arnold, A. ~~WEPP35~~
Arnold, N.D. FRA005
Atkinson, M.P. THPP16
Aurnia, S. ~~TUPP13~~
Avrakhov, P.V. WEPP29, WEPP38

— B —

Baboi, N. ~~**WEPP11**~~
Bachmann, A.-M. **MOA001**
Bahrdt, J. THPP26
Batten, T. ~~**THPP15**~~
Bell, J.C. WEPP16
Belver-Aguilar, C. **TUPP32**
Bence, A. ~~WEPP09~~
Benoist, N. MOA004
Berenc, T.G. FRA005
Berg, W. TUA002
Bergamaschi, M. THPP05
Bett, D.R. **WEPP12**
Bielawski, S. ~~**TUPP15**~~
Bisiach, D. **WEPP01**
Blokland, W. ~~THA002~~, ~~**THPP32**~~
Bobb, L. THPP05
Boccardi, A. WEPP12, FRA002
Bodrov, S. WEPP29
Borland, M. TUA002, THPP25
Boussina, P. TUPP09
Boutachkov, P. ~~TUA004~~
Bouvet, D. TUPP37
Braccini, S. TUPP32
Brill, A.R. WEPP01
Brookes, E.J. **TUPP24**
Broucquart, R. ~~**WEPP02**~~
Bründermann, E. WEA002
Butti, D. THPP33

— C —

Calvey, J.R. TUA002, TUPP23, **THPP25**
Campana, L. TUPP09
Cao, J.S. ~~THPP31~~, ~~FRA006~~
Cao, S.S. **WEPP13**, MOA005
Cao, S.S. TUA001, WEPP03, WEPP24
Cao, S.V. **WEPP06**, WEPP34
Cargnelutti, M. WEPP01
Carwardine, J. FRA005
Carzaniga, T.S. TUPP32
Caspers, F. ~~WEPP18~~
Cavallaro, S. ~~TUPP13~~
Cavanagh, H.V. TUPP24
Cease, H. TUPP10
Chaikovska, I. THPP35
Chandler, E. FRA005
Chapman, L.D. ~~THA003~~
Chen, F.Z. MOA005, TUA001, THPP29, THPP36
Chen, J. MOA005, THPP36
Chen, J. MOA005, **TUA001**, WEPP24, WEPP28
Chen, Y. ~~THPP19~~
Cheng, W.X. TUPP05
Chernyshenko, S. ~~THPP02~~
Chin, M.J. WEPP16, ~~FRA003~~
Clute, T.K. THPP25
Cogan, S. ~~TUPP04~~, ~~TUPP20~~
Condamoor, S. TUPP12
Corbett, W.J. TUPP09, TUPP12
Cosentino, L. ~~TUPP13~~
Curcio, A. ~~**WEA001**~~
Czwalinna, M.K. WEPP21

— D —

Dallin, L.O. ~~THA003~~
Danzeca, S. ~~**FRA001**~~
De Gersem, H. WEPP21
Decker, G. TUA002, TUPP05
Degl'Innocenti, I. **FRA002**
Delerue, N. THPP35
Dewa, H. WEPP31
Di Mitri, S. ~~TUPP31~~
Diamond, J.S. ~~TUPP11~~
Diana, B.F. ~~TUPP13~~
Diaz Cruz, J.A. TUPP17
Dickson, R.W. ~~**THPP13**~~
Ding, K.Z. THPP34
Dobishuk, V. ~~**THPP02**~~
Dölling, R. **WEPP33**
Donegani, E.M. **WEPP07**, **WEPP10**
Dooling, J.C. **TUA002**, TUPP23, THPP25
Doucas, G. ~~WEPP19~~
Downer, M. THA005
Du, Y.Y. ~~THPP31~~, ~~FRA006~~
Du, Z. ~~WEPP18~~
Duarte, H.O.C. ~~**MOA002**~~
Duperrex, P.-A. WEPP05, WEPP15

Content from this work may be used under the terms of the CC BY 3.0 licence (© 2020). Any distribution of this work must maintain attribution to the author(s), title of the work, publisher, and DOI

ISBN: 978-3-95450-222-6 ISSN: 2673-5350

Content from this work may be used under the terms of the CC BY 3.0 licence (© 2020). Any distribution of this work must maintain attribution to the author(s), title of the work, publisher, and DOI

— E —

Eddy, N. ~~TUPP11~~
Edelen, A.L. TUPP17
Edstrom, D.R. TUPP17
El Ajjouri, M. ~~WEPP02~~, ~~WEPP09~~, ~~WEPP14~~
Emery, L. TUAO02, THPP25
Erdmann, M. TUPP10
Evain, C. ~~TUPP15~~
Evtushenko, P.E. ~~WEPP35~~
Ewald, F. MOA004

— F —

Fan, K. THPP22
Fang, W. MOA005
Fanucci, L. FRA002
Farabolini, W. TUPP37
Fedorov, K.V. THPP05
Fedotov, A.E. WEPP29
Feng, C. MOA005
Feng, L. WEPP20, ~~WEPP25~~
Ferianis, M. ~~TUPP31~~
Ferrari, E. ~~TUPP31~~
Fontbonne, J.-M. ~~TUA003~~
Forck, P. WEPP36
Fors, T. FRA005
Friend, M.L. WEPP06, **WEPP34**
Fujita, T. WEPP31
Fukui, T. WEPP31
Fukunishi, N. FRA004
Furia, E. ~~TUPP13~~
Furukawa, Y. TUPP06

— G —

Gagliano, J. THPP25
Gamelin, A. ~~WEPP14~~
Gangwar, R.K. THPP21
Gao, B. MOA005, TUA001, **WEPP03**, WEPP17, THPP36
Gąsior, M. WEPP27
Gavrilov, S.A. WEPP04, WEPP37
Gerth, C. ~~TUPP15~~, ~~WEA004~~
Giangrande, L. THPP04
Giannessi, L. ~~TUPP31~~
Gilardi, A. TUPP37
Gkotse, B. TUPP37
Goetz, A. **THPP33**
Gogolev, S.Yu. ~~TUPP36~~
Gonnin, A. THPP35
Gorokhova, E.I. ~~TUA004~~
Grandsaert, T.J. WEPP07
Grech, L. **WEPP27**
GroSS, M. ~~THPP19~~
Gsponer, A. TUPP32

— H —

Haeffner, P. TUPP32
Hanamura, K. FRA004
Harkay, K.C. TUAO02, TUPP23
Harryman, D.M. TUPP28, **THPP05**
Hartz, M. WEPP34
He, J. ~~TUPP01~~, ~~THPP31~~
Hidaka, Y. ~~TUPP30~~
Hogan, R.B. ~~THPP14~~
Hoyt, J.E. THPP25
Hu, L.X. **THPP34**
Hua, L.F. MOA005
Huang, W.L. MOA003
Hubert, N. WEPP01, ~~WEPP02~~, ~~WEPP09~~, ~~WEPP14~~
Huck, H. THPP26
Huck, M. **THPP26**

— I —

Imao, H. FRA004
Iriso, U. THPP33
Irman, A. THA005

— J —

Jackson, S. WEPP27
Jacobson, B.T. TUPP17
Jalali, B. ~~TUPP15~~
Jiang, R. MOA005, WEPP13, **WEPP28**
Jin, S.S. WEPP26
Jing, C.-J. ~~TUPP34~~
Johansen, E. WEPP33
Jones, B. TUPP24
Jones, O.R. WEPP27, WEPP36
Joshi, V.J. THPP12

— K —

Kalantaryan, D.K. ~~THPP19~~
Kallakuri, P.S. THPP25
Kamigaito, O. FRA004
Kamoshida, A. FRA004
Kang, H.-S. ~~TUPP27~~
Kaplon, J. THPP04
Karataev, P. THPP05
Kieffer, R. THPP05
Kim, C. ~~TUPP27~~, ~~FRCL02~~
Kim, G. ~~TUPP27~~
Knight, E.W. WEPP38
Ko, I.S. ~~TUPP27~~
Ko, J.H. ~~TUPP27~~
Konoplev, I.V. ~~WEPP19~~
Koschitzki, C. ~~THPP19~~
Koshio, Y. WEPP34
Kovalchuk, O.S. THA006
Koyama, R. FRA004
Krasilnikov, M. ~~THPP19~~
Krupa, M. WEPP12
Kube, G. ~~TUPP36~~
Kubytskyi, V. THPP35
Kumar, N. WEPP36
Kuzikov, S.V. **WEPP29**, **WEPP38**

— L —

LaBerge, M. THA005

ISBN: 978-3-95450-222-6 ISSN: 2673-5350

Lahaye, C. ~~TUA003~~
Lai, L.W. WEPP03, **MOA005**, TUA001, WEPP17, **THPP08**, THPP29
Łasocha, K. THPP05, **TUPP28**
Lauth, W. ~~TUPP36~~
Leban, P. TUPP12, WEPP01
Lee, S.H. TUPP05
Leemann, S.C. ~~**THA001**~~
Lefèvre, T. TUPP28, THPP05
Lehmann, C.N. **THPP16**
Leitao, P.V. THPP04
Leng, Y.B. MOA005, TUA001, WEPP03, WEPP13, WEPP24, WEPP28, THA004, THPP08, THPP36
Levens, T.E. WEPP27
Li, C.L. **WEPP20**, ~~**WEPP25**~~
Li, F. MOA003
Li, P. MOA003
Li, X. ~~THPP19~~
Lidia, S.M. ~~TUPP04~~, ~~TUPP08~~, ~~TUPP20~~
Lindberg, R.R. TUA002
Lipka, D. **THPP10**
Lishilin, O. ~~THPP19~~
Liu, A. ~~**TUPP34**~~
Liu, B. WEPP20, ~~WEPP25~~
Liu, F. ~~THPP31~~
Liu, X.Q. WEPP03
Liu, Z. ~~THPP31~~
Lockmann, N.M. ~~**WEA004**~~
Loisch, G. ~~**THPP19**~~
Lorbeer, B. ~~WEPP11~~
Lu, Y.H. ~~THPP31~~
Lumpkin, A.H. **TUPP18**, TUA002, TUPP23, **TUPP17**, WEPP22, **THA005**

— M —

Ma, H.Z. ~~THPP31~~, ~~FRA006~~
Ma, S. ~~**WEPP35**~~
Madden, T.J. FRA005
Maesaka, H. **WEPP31**
Mapelli, A. TUPP37
Marques, S.R. ~~MOA002~~, ~~**FRCL03**~~
Martina, F. **THPP04**
Masaki, M. WEPP31
Mateu, I.M. **TUPP37**
Mazzocchi, F. **WEA002**
Mazzoni, S. **WEPP36**, THPP05, THPP33
Melkumyan, D. ~~THPP19~~
Melnikov, A.A. **WEPP04**
Meng, M. MOA003
Meseck, A. THPP26
Meskova, V. TUPP37
Michalczyk, A. ~~THPP14~~
Minolli, S.M. ~~WEPP02~~
Mirza, S.H. ~~TUA005~~
Molinari, G. TUPP32
Monaco, L. ~~THPP19~~
Monard, H. THPP35
Morataya Campos, D.A. TUPP12
Morrison, L.H. THPP25
Mounet, N. TUPP28
Moutardier, A. THPP35
Müller, A.-S. WEA002
Muggli, P. MOA001

— N —

Nakamura, A. WEPP34
Nakayoshi, K. WEPP34
Navarro Fernandez, A. **TUPP35**
Navrotski, G. TUA002
Ng, A. ~~THPP14~~
Niemczyk, R. ~~THPP19~~
Nishi, T. FRA004
Norum, W.E. WEPP16, ~~FRA003~~
Nosych, A.A. THPP33
Novokshonov, A.I. ~~TUPP36~~

— O —

Okhrimenko, O. ~~THPP02~~
Oppelt, A. ~~THPP19~~
Oprondek, S.M. TUPP10
Ozeki, K. FRA004

— P —

Papazoglou, I. WEPP36
Paroli, B. THPP33
Paskvan, D.R. FRA005
Pasquino, C. WEPP36
Pédeau, D. WEPP01, ~~WEPP02~~, ~~WEPP09~~
Penco, G. ~~TUPP31~~
Penirschke, A. WEPP21, ~~WEPP23~~
Perosa, G. ~~TUPP31~~
Pezzullo, G. TUPP37
Plouviez, E. MOA004
Podobedov, B. ~~**TUPP30**~~
Poirier, S. ~~WEPP02~~
Pons, J.L. MOA004
Portmann, G.J. WEPP16, ~~**FRA003**~~
Potenza, M.A.C. THPP33
Potylitsyn, A. ~~**TUPP36**~~, THPP05
Power, J.G. WEPP38
Preu, S. ~~WEPP23~~
Prieto, P.S. TUPP17
Pugatch, V.M. **THA006**, ~~THPP02~~
Pulvirenti, P.S. ~~TUPP13~~

— Q —

Qiu, R.Y. MOA003

— R —

Rakhman, A. ~~THPP32~~
Ramanathan, M. TUPP10
Ramazanov, D. THA006
Ramirez, C.S. TUPP12
Ravotti, F. TUPP37
Rebernik Ribič, P. ~~TUPP31~~

Content from this work may be used under the terms of the CC BY 3.0 licence (© 2020). Any distribution of this work must maintain attribution to the author(s), title of the work, publisher, and DOI

ISBN: 978-3-95450-222-6 ISSN: 2673-5350

Content from this work may be used under the terms of the CC BY 3.0 licence (© 2020). Any distribution of this work must maintain attribution to the author(s), title of the work, publisher, and DOI

Regensburger, S. ~~WEPP23~~
Rehm, G. THPP23
Reichert, T. ~~TUPP21~~
Reščič, M. ~~**THA002**~~
Richard, C.J. ~~**TUPP08**~~, ~~**TUPP20**~~
Ries, M. THPP26
Roche, B. MOA004
Rodnyi, P. ~~TUA004~~
Roehrig, C. FRA005
Roggli, M. WEPP33
Rohrer, M. WEPP33
Roncarolo, F. TUPP35
Roque da Silva, A.J. ~~**MOOP01**~~
Rossi, A. WEPP36
Roussel, E. ~~TUPP15~~, ~~TUPP31~~
Ruan, J. TUPP17
Ruisard, K.J. **THPP20**
Rule, D.W. THA005
Russo, A.D. ~~TUPP13~~
Ryzhov, A.A. ~~WEPP35~~

— S —

Sadovich, S. WEPP36
Sahu, B.K. THPP21
Saifulin, M. ~~**TUA004**~~
Sajaev, V. TUA002
Sakamoto, N. FRA004
Sakashita, K. WEPP34
Salehilashkajani, A. WEPP36
Sallese, J.M. TUPP37
Salvador, S. ~~TUA003~~
Samadi, N. ~~**THA003**~~
Santucci, R.R. ~~TUPP11~~
Sapinski, M. TUPP35
Scampoli, P. TUPP32
Scarpine, V.E. ~~TUPP11~~
Schaber, J. ~~WEPP35~~
Scheible, B.E.J. **WEPP21**
Scheidt, K.B. MOA004
Scherer, T.A. WEA002
Schippers, J.M. WEPP05, WEPP15
Schlarb, H. WEPP21
Schloegelhofer, A. TUPP28, THPP05
Schmid, M. TUPP32
Schmidt, B. ~~WEA004~~
Schneider, G. WEPP36
Sebek, J.J. TUPP09, TUPP12
Semenov, A. ~~TUPP11~~
Sereno, N. WEPP01
Sertore, D. ~~THPP19~~
Seviour, R. ~~THA002~~
Shane, R. ~~**TUPP04**~~
Shao, J.H. ~~TUPP34~~
Sharma, A. **THPP21**, THPP12
Shea, T.J. WEPP07
Shen, G. **FRA005**
Shen, T. MOA005
Shi, X. ~~THA003~~
Shishlo, A.P. THPP20
Shoaf, S.E. FRA005
Siano, M. THPP33
Sidiropoulou, O. TUPP37
Simon, P. ~~TUA004~~
Singh, R. ~~**TUA005**~~, ~~**TUPP21**~~
Slimmer, D. ~~TUPP11~~
Song, Y. THPP34
Song, Y. **THPP22**
Spampinati, S. ~~TUPP31~~
Spezzani, C. ~~TUPP31~~
Srinivasan, S. **WEPP05**, **WEPP15**
Steffen, B. ~~TUPP15~~
Stepanov, A.N. WEPP29
Stephan, F. ~~THPP19~~
Stevens, J.B. TUA002
Strauß, D. WEA002
Sui, Y.F. ~~THPP31~~, ~~FRA006~~
Sun, B.G. WEPP26
Sun, J.L. **MOA003**
Sun, Y. TUPP23
Sun, Y.P. TUA002
Szwaj, C. ~~TUPP15~~

— T —

Takahashi, S. TUPP06
Takano, S. WEPP31
Tan, Y.E. **THPP11**, THPP16
Taoutaou, F. MOA004
Tavares, D.O. ~~MOA002~~, ~~**FRCL01**~~
Taylor, G. THPP35
Teichert, J. ~~WEPP35~~
Teruzzi, L. THPP33
Thariat, J. ~~TUA003~~
Thomas, C.A. WEPP07
Thurman-Keup, R.M. TUPP17, **WEPP22**
Tian, J.M. MOA003
Tipper, A. **THPP23**
Titov, A.I. **WEPP37**
Torino, L. **MOA004**, THPP33
Toufexis, F. **TUPP09**, **TUPP12**
Toyama, T. FRA004
Trad, G. THPP33
Trautmann, C. ~~TUA004~~
Trovò, M. ~~TUPP31~~

— U —

Uberto, F. MOA004
Uchiyama, A. FRA004
Udrea, S. WEPP36
Ueshima, K. WEPP31

— V —

Valentino, G. WEPP27
Vashchenko, G. ~~THPP19~~
Vecchio, G. ~~**TUPP13**~~
Veness, R. WEPP36

ISBN: 978-3-95450-222-6 ISSN: 2673-5350

Venevtsev, I.D. ~~TUA004~~
Verma, Y. **THPP12**
Veronese, M. ~~**TUPP31**~~
Veseli, S. FRA005
Vetter, S. ~~**WEA003**~~
Vikharev, A.A. WEPP29
Voy, D.C. ~~TUPP11~~
Vukolov, A.V. ~~TUPP36~~

— W —

Walasek-Höhne, B. ~~TUA004~~, ~~TUPP21~~
Wan, J. **THPP36**
Wang, J.G. WEPP26
Wang, L. ~~THPP31~~
Wang, X.T. WEPP20, ~~WEPP25~~
Watanabe, T. **FRA004**
Watanabe, Y. FRA004
Weber, J.M. **WEPP16**, ~~FRA003~~
Wei, S.J. ~~THPP31~~, ~~**FRA006**~~
Wei, Y. ~~WEPP18~~
Weilbach, T. ~~THPP19~~
Welsch, C.P. WEPP36
Wendt, M. WEPP12, FRA002
Wenninger, J. WEPP27
Wermelskirchen, C. TUPP12
Wesch, S. ~~WEA004~~
Westfahl Jr., H. ~~MOOP01~~
Wienands, U. THPP25
Williams, S.D. **THPP35**
Wootton, K.P. TUA002, **TUPP05**, **TUPP10**, TUPP18, **TUPP23**
Wu, F.F. WEPP26
Wu, J.X. ~~WEPP18~~
Wu, T. TUA001
Wu, Y.C. THPP34

— X —

Xiang, R. ~~WEPP35~~
Xiao, A. TUA002
Xu, T.G. MOA003, ~~THPP31~~
Xu, X.Y. **THA004**, TUA001
Xu, Zh.H. MOA003

— Y —

Yadav, R. ~~**WEPP23**~~
Yamada, K. FRA004
Yan, Y.B. MOA005, THPP08
Yang, B.X. TUPP05, TUPP10, TUPP23
Yang, J. ~~THPP31~~, ~~FRA006~~
Yang, T. MOA003
Yang, X. **THPP29**
Ye, K.R. THPP36
Ye, Q. ~~THPP31~~, ~~FRA006~~
Yin, D. ~~THPP31~~
Yu, L. ~~THPP31~~
Yu, L.Y. MOA005, THPP36
Yuan, R.X. MOA005, TUA001, WEPP13, WEPP17
Yue, J.H. ~~TUPP01~~, ~~**THPP31**~~, ~~FRA006~~

— Z —

Zamantzas, C. THPP04
Zeng, L. MOA003
Zhang, H. ~~WEPP19~~
Zhang, H.D. WEPP36
Zhang, N. MOA005, **WEPP17**
Zhang, W.Y. WEPP20, ~~WEPP25~~
Zhang, X.E. ~~THPP31~~, ~~FRA006~~
Zhao, J.X. ~~THPP31~~
Zhao, X.Y. ~~THPP31~~
Zhao, Y. ~~THPP31~~
Zhao, Y. WEPP38
Zhao, Y.K. **WEPP26**
Zhou, F. TUPP17
Zhou, W.M. MOA005, THPP36
Zhou, Y.M. TUA001, **WEPP24**
Zhu, D.C. ~~THPP31~~
Zhu, G. ~~**WEPP18**~~
Žnidarčič, M. TUPP12, WEPP01

Content from this work may be used under the terms of the CC BY 3.0 licence (© 2020). Any distribution of this work must maintain attribution to the author(s), title of the work, publisher, and DOI

ISBN: 978-3-95450-222-6 ISSN: 2673-5350

Content from this work may be used under the terms of the CC BY 3.0 licence (© 2020). Any distribution of this work must maintain attribution to the author(s), title of the work, publisher, and DOI

Institutes List

AAI/ANL
Lemont, Illinois, USA
- Lumpkin, A.H.

AEC
Bern, Switzerland
- Belver-Aguilar, C.
- Braccini, S.
- Carzaniga, T.S.
- Gsponer, A.
- Haeffner, P.
- Scampoli, P.
- Schmid, M.

ALBA-CELLS Synchrotron
Cerdanyola del Vallès, Spain
- Iriso, U.
- Nosych, A.A.
- Torino, L.

ANL
Lemont, Illinois, USA
- Arnold, N.D.
- Berenc, T.G.
- Berg, W.
- Borland, M.
- Brill, A.R.
- Calvey, J.R.
- Carwardine, J.
- Cease, H.
- Chandler, E.
- Cheng, W.X.
- Clute, T.K.
- Decker, G.
- Dooling, J.C.
- Emery, L.
- Erdmann, M.
- Fors, T.
- Gagliano, J.
- Harkay, K.C.
- Hoyt, J.E.
- Kallakuri, P.S.
- Lee, S.H.
- Lindberg, R.R.
- Lumpkin, A.H.
- Madden, T.J.
- Morrison, L.H.
- Navrotski, G.
- Oprondek, S.M.
- Paskvan, D.R.
- Power, J.G.
- Ramanathan, M.
- Roehrig, C.
- Sajaev, V.
- Sereno, N.
- Shao, J.H.
- Shen, G.
- Shi, X.
- Shoaf, S.E.
- Stevens, J.B.
- Sun, Y.P.
- Sun, Y.
- Veseli, S.
- Wienands, U.
- Wootton, K.P.
- Xiao, A.
- Yang, B.X.

AS - ANSTO
Clayton, Australia
- Atkinson, M.P.
- Hogan, R.B.
- Michalczyk, A.
- Ng, A.
- Tan, Y.E.

ASIPP
Hefei, People's Republic of China
- Ding, K.Z.
- Hu, L.X.
- Song, Y.

BNL
Upton, New York, USA
- Hidaka, Y.
- Podobedov, B.

CERN
Geneva, Switzerland
- Ady, M.
- Alessio, F.
- Alves, D.
- Bergamaschi, M.
- Boccardi, A.
- Butti, D.
- Caspers, F.
- Danzeca, S.
- Degl'Innocenti, I.
- Farabolini, W.
- Gąsior, M.
- Giangrande, L.
- Gilardi, A.
- Gkotse, B.
- Goetz, A.
- Grech, L.
- Jackson, S.
- Jones, O.R.
- Kaplon, J.
- Kieffer, R.
- Krupa, M.
- Łasocha, K.
- Lefèvre, T.
- Leitao, P.V.
- Levens, T.E.
- Mapelli, A.
- Martina, F.
- Mateu, I.M.
- Mazzoni, S.
- Meskova, V.
- Mounet, N.
- Navarro Fernandez, A.

ISBN: 978-3-95450-222-6 ISSN: 2673-5350

- Papazoglou, I.
- Pasquino, C.
- Pezzullo, G.
- Ravotti, F.
- Roncarolo, F.
- Rossi, A.
- Sadovich, S.
- Schneider, G.
- Sidiropoulou, O.
- Trad, G.
- Veness, R.
- Wendt, M.
- Wenninger, J.
- Zamantzas, C.

CLS
Saskatoon, Saskatchewan, Canada
- Batten, T.
- Chapman, L.D.
- Dallin, L.O.

CNRS/IN2P3/LPC CAEN
Caen, France
- Lahaye, C.
- Salvador, S.

Cockcroft Institute
Warrington, Cheshire, United Kingdom
- Kumar, N.
- Salehilashkajani, A.
- Welsch, C.P.
- Zhang, H.D.

DESY
Hamburg, Germany
- Baboi, N.
- Chen, Y.
- Czwalinna, M.K.
- Gerth, C.
- Kube, G.
- Lipka, D.
- Lockmann, N.M.
- Lorbeer, B.
- Novokshonov, A.I.
- Schlarb, H.
- Schmidt, B.
- Steffen, B.
- Wesch, S.

DESY Zeuthen
Zeuthen, Germany
- GroSS, M.
- Kalantaryan, D.K.
- Koschitzki, C.
- Krasilnikov, M.
- Li, X.
- Lishilin, O.
- Loisch, G.
- Melkumyan, D.
- Niemczyk, R.
- Oppelt, A.
- Stephan, F.
- Vashchenko, G.
- Weilbach, T.

DLS
Oxfordshire, United Kingdom
- Abbott, M.G.
- Bobb, L.
- Rehm, G.
- Tipper, A.

Elettra-Sincrotrone Trieste S.C.p.A.
Basovizza, Italy
- Allaria, E.
- Di Mitri, S.
- Ferianis, M.
- Giannessi, L.
- Penco, G.
- Rebernik Ribič, P.
- Spampinati, S.
- Spezzani, C.
- Trovò, M.
- Veronese, M.

EPFL
Lausanne, Switzerland
- Bouvet, D.
- Sallese, J.M.

ESRF
Grenoble, France
- Benoist, N.
- Ewald, F.
- Plouviez, E.
- Pons, J.L.
- Roche, B.
- Scheidt, K.B.
- Taoutaou, F.
- Uberto, F.

ESS
Lund, Sweden
- Donegani, E.M.
- Grandsaert, T.J.
- Shea, T.J.
- Thomas, C.A.

Euclid TechLabs, LLC
Solon, Ohio, USA
- Antipov, S.P.
- Avrakhov, P.V.
- Jing, C.-J.
- Knight, E.W.
- Kuzikov, S.V.
- Liu, A.
- Zhao, Y.

Fermilab
Batavia, Illinois, USA
- Diamond, J.S.
- Eddy, N.
- Edstrom, D.R.
- Lumpkin, A.H.
- Prieto, P.S.
- Ruan, J.
- Santucci, R.R.

Content from this work may be used under the terms of the CC BY 3.0 licence (© 2020). Any distribution of this work must maintain attribution to the author(s), title of the work, publisher, and DOI

ISBN: 978-3-95450-222-6 ISSN: 2673-5350

Content from this work may be used under the terms of the CC BY 3.0 licence (© 2020). Any distribution of this work must maintain attribution to the author(s), title of the work, publisher, and DOI

- Scarpine, V.E.
- Semenov, A.
- Slimmer, D.
- Thurman-Keup, R.M.
- Voy, D.C.

FRIB
East Lansing, Michigan, USA
- Cogan, S.
- Lidia, S.M.
- Shane, R.

GOI
St Petersburg, Russia
- Gorokhova, E.I.

GSI
Darmstadt, Germany
- Boutachkov, P.
- Forck, P.
- Mirza, S.H.
- Reichert, T.
- Saifulin, M.
- Sapinski, M.
- Simon, P.
- Singh, R.
- Trautmann, C.
- Udrea, S.
- Walasek-Höhne, B.

HFCIM
HeFei, People's Republic of China
- Wu, Y.C.

Huazhong University of Science and Technology, State Key Laboratory of Advanced Electromagnetic Engineering and Technology,
Hubei, People's Republic of China
- Fan, K.
- Song, Y.

HZB
Berlin, Germany
- Bahrdt, J.
- Huck, H.
- Huck, M.
- Meseck, A.
- Ries, M.

HZDR
Dresden, Germany
- Arnold, A.
- Evtushenko, P.E.
- Irman, A.
- Ma, S.
- Ryzhov, A.A.
- Schaber, J.
- Teichert, J.
- Xiang, R.

I-Tech
Solkan, Slovenia
- Bisiach, D.
- Cargnelutti, M.
- Leban, P.
- Žnidarčič, M.

IAP/RAS
Nizhny Novgorod, Russia
- Bodrov, S.
- Fedotov, A.E.
- Stepanov, A.N.
- Vikharev, A.A.

IHEP
Beijing, People's Republic of China
- Cao, J.S.
- Du, Y.Y.
- He, J.
- Liu, F.
- Liu, Z.
- Lu, Y.H.
- Ma, H.Z.
- Meng, M.
- Sui, Y.F.
- Tian, J.M.
- Wang, L.
- Wei, S.J.
- Xu, T.G.
- Yang, J.
- Ye, Q.
- Yin, D.
- Yu, L.
- Yue, J.H.
- Zeng, L.
- Zhang, X.E.
- Zhao, J.X.
- Zhao, X.Y.
- Zhao, Y.
- Zhu, D.C.

IHEP CSNS
Guangdong Province, People's Republic of China
- Huang, W.L.
- Li, F.
- Li, P.
- Qiu, R.Y.
- Sun, J.L.
- Xu, Zh.H.
- Yang, T.

IIT (ISM)
Dhanbad, Jharkhand, India
- Gangwar, R.K.
- Sharma, A.

IKP
Mainz, Germany
- Lauth, W.

IMP, TU Darmstadt
Darmstadt, Germany
- Preu, S.
- Regensburger, S.
- Yadav, R.

ISBN: 978-3-95450-222-6 ISSN: 2673-5350

IMP/CAS
Lanzhou, People's Republic of China
- Du, Z.
- Wei, Y.
- Wu, J.X.
- Zhu, G.

Indian Institute of Science Education and Research
Mohali, India
- Verma, Y.

INFN/LASA
Segrate (MI), Italy
- Monaco, L.
- Sertore, D.

INFN/LNS
Catania, Italy
- Aurnia, S.
- Cavallaro, S.
- Cosentino, L.
- Diana, B.F.
- Furia, E.
- Pulvirenti, P.S.
- Russo, A.D.
- Vecchio, G.

IUAC
New Delhi, India
- Aggarwal, M.
- Joshi, V.J.
- Sahu, B.K.
- Sharma, A.

Jagiellonian University
Kraków, Poland
- Łasocha, K.

JAI
Oxford, United Kingdom
- Bett, D.R.
- Fedorov, K.V.
- Harryman, D.M.
- Karataev, P.
- Konoplev, I.V.
- Zhang, H.

Japan Synchrotron Radiation Research Institute (JASRI), RIKEN SPring-8 Center
Hyogo, Japan
- Takano, S.

JASRI/SPring-8
Hyogo, Japan
- Aoyagi, H.
- Dewa, H.
- Fujita, T.
- Furukawa, Y.
- Masaki, M.
- Takahashi, S.

Kavli IPMU
Kashiwa, Japan
- Hartz, M.

KEK
Tsukuba, Japan
- Cao, S.V.
- Friend, M.L.
- Nakayoshi, K.
- Sakashita, K.
- Toyama, T.

KIT
Eggenstein-Leopoldshafen, Germany
- Bründermann, E.
- Müller, A.-S.
- Scherer, T.A.

KIT IAM-AWP
Eggenstein Leopoldshafen, Germany
- Mazzocchi, F.
- StrauÃ§, D.

LBNL
Berkeley, California, USA
- Bell, J.C.
- Chin, M.J.
- Leemann, S.C.
- Norum, W.E.
- Portmann, G.J.
- Weber, J.M.

LNLS
Campinas, Brazil
- Duarte, H.O.C.
- Marques, S.R.
- Roque da Silva, A.J.
- Tavares, D.O.
- Westfahl Jr., H.

LPC
Caen, France
- Fontbonne, J.-M.
- Thariat, J.

MIPT
Dolgoprudniy, Moscow Region, Russia
- Gavrilov, S.A.
- Melnikov, A.A.
- Titov, A.I.

Mitsubishi Electric System & Service Co., Ltd
Tsukuba, Japan
- Hanamura, K.

MPI
Muenchen, Germany
- Bachmann, A.-M.
- Muggli, P.

MSU
East Lansing, Michigan, USA
- Richard, C.J.

Naples University Federico II
Napoli, Italy
- Scampoli, P.

Content from this work may be used under the terms of the CC BY 3.0 licence (© 2020). Any distribution of this work must maintain attribution to the author(s), title of the work, publisher, and DOI

ISBN: 978-3-95450-222-6 ISSN: 2673-5350

Content from this work may be used under the terms of the CC BY 3.0 licence (© 2020). Any distribution of this work must maintain attribution to the author(s), title of the work, publisher, and DOI

NASU/INR
Kiev, Ukraine
- Chernyshenko, S.
- Dobishuk, V.
- Kovalchuk, O.S.
- Okhrimenko, O.
- Pugatch, V.M.
- Ramazanov, D.

National Institutes for Quantum and Radiological Science and Technology (QST)
Sayo-cho, Japan
- Ueshima, K.

National Instruments Japan Corporation
MInato-ku, Tokyo, Japan
- Kamoshida, A.

NEXEYA Systems
La Couronne, France
- Minolli, S.M.

NSRC SOLARIS
Kraków, Poland
- Curcio, A.

Okayama University
Okayama, Japan
- Nakamura, A.

Okayama University, Faculty of Science
Okayama City, Japan
- Koshio, Y.

ORNL
Oak Ridge, Tennessee, USA
- Aleksandrov, A.V.
- Blokland, W.
- Dickson, R.W.
- Rakhman, A.
- Ruisard, K.J.
- Shishlo, A.P.

Oxford University, Physics Department
Oxford, Oxon, United Kingdom
- Doucas, G.

PAL
Pohang, Republic of Korea
- Kang, H.-S.
- Kim, C.
- Kim, G.
- Ko, I.S.
- Ko, J.H.

PhLAM/CERCLA
Villeneuve d'Ascq Cedex, France
- Bielawski, S.

PhLAM/CERLA
Villeneuve d'Ascq, France
- Evain, C.
- Roussel, E.
- Szwaj, C.

Private Address
Zhangjiang, Shanghai, People's Republic of China
- Cao, S.S.
- Rule, D.W.

PSI
Villigen PSI, Switzerland
- Duperrex, P.-A.
- Dölling, R.
- Ferrari, E.
- Johansen, E.
- Roggli, M.
- Rohrer, M.
- Samadi, N.
- Schippers, J.M.
- Srinivasan, S.

RAS/INR
Moscow, Russia
- Gavrilov, S.A.
- Melnikov, A.A.
- Titov, A.I.

RIKEN Nishina Center
Wako, Japan
- Fukunishi, N.
- Imao, H.
- Kamigaito, O.
- Nishi, T.
- Ozeki, K.
- Sakamoto, N.
- Uchiyama, A.
- Watanabe, T.
- Watanabe, Y.
- Yamada, K.

RIKEN SPring-8 Center, Innovative Light Sources Division
Hyogo, Japan
- Fukui, T.
- Maesaka, H.

SARI-CAS
Pudong, Shanghai, People's Republic of China
- Feng, L.
- Lai, L.W.
- Liu, B.
- Liu, X.Q.

Shanghai Advanced Research Institute
Pudong, Shanghai, People's Republic of China
- Li, C.L.
- Wang, X.T.
- Zhang, W.Y.

SHI Accelerator Service Ltd.
Tokyo, Japan
- Koyama, R.

SINAP
Shanghai, People's Republic of China
- Cao, S.S.
- Hua, L.F.
- Wan, J.
- Xu, X.Y.
- Yang, X.

ISBN: 978-3-95450-222-6 ISSN: 2673-5350

SLAC
Menlo Park, California, USA
- Boussina, P.
- Campana, L.
- Condamoor, S.
- Corbett, W.J.
- Diaz Cruz, J.A.
- Edelen, A.L.
- Jacobson, B.T.
- Morataya Campos, D.A.
- Ramirez, C.S.
- Sebek, J.J.
- Toufexis, F.
- Vetter, S.
- Wermelskirchen, C.
- Zhou, F.

SOLEIL
Gif-sur-Yvette, France
- Alves, F.
- Bence, A.
- Broucquart, R.
- El Ajjouri, M.
- Gamelin, A.
- Hubert, N.
- Pédeau, D.
- Poirier, S.

SPbPU
St. Petersburg, Russia
- Rodnyi, P.
- Venevtsev, I.D.

SSRF
Shanghai, People's Republic of China
- Cao, S.S.
- Chen, F.Z.
- Chen, J.
- Fang, W.
- Feng, C.
- Gao, B.
- Jiang, R.
- Lai, L.W.
- Leng, Y.B.
- Shen, T.
- Wu, T.
- Xu, X.Y.
- Yan, Y.B.
- Ye, K.R.
- Yu, L.Y.
- Yuan, R.X.
- Zhang, N.
- Zhou, W.M.
- Zhou, Y.M.

STFC/RAL/ISIS
Chilton, Didcot, Oxon, United Kingdom
- Brookes, E.J.
- Cavanagh, H.V.
- Jones, B.

TEMF, TU Darmstadt
Darmstadt, Germany
- Ackermann, W.
- De Gersem, H.

TERA
Novara, Italy
- Molinari, G.

The University of Liverpool
Liverpool, United Kingdom
- Kumar, N.
- Martina, F.
- Salehilashkajani, A.
- Welsch, C.P.
- Zhang, H.D.

The University of Melbourne
Melbourne, Victoria, Australia
- Taylor, G.
- Williams, S.D.

The University of Texas at Austin
Austin, Texas, USA
- Downer, M.
- LaBerge, M.

THM
Friedberg, Germany
- Penirschke, A.
- Scheible, B.E.J.

TPU
Tomsk, Russia
- Gogolev, S.Yu.
- Potylitsyn, A.
- Vukolov, A.V.

TU Dresden
Dresden, Germany
- Schaber, J.

TU Vienna
Wien, Austria
- Schloegelhofer, A.

UCAS
Beijing, People's Republic of China
- Yang, X.

UCLA
Los Angeles, California, USA
- Jalali, B.

Universita' degli Studi di Milano
Milano, Italy
- Paroli, B.

Universita' degli Studi di Milano & INFN
Milano, Italy
- Potenza, M.A.C.
- Siano, M.

University of Chinese Academy of Sciences
Beijing, People's Republic of China
- Xu, X.Y.

Content from this work may be used under the terms of the CC BY 3.0 licence (© 2020). Any distribution of this work must maintain attribution to the author(s), title of the work, publisher, and DOI

ISBN: 978-3-95450-222-6 ISSN: 2673-5350

Content from this work may be used under the terms of the CC BY 3.0 licence (© 2020). Any distribution of this work must maintain attribution to the author(s), title of the work, publisher, and DOI

University of Huddersfield
Huddersfield, United Kingdom
- Reščič, M.
- Seviour, R.

University of Malta, Information and Communication Technology
Msida, Malta
- Valentino, G.

University of Nova Gorica
Nova Gorica, Slovenia
- Rebernik Ribič, P.

University of Queensland
Brisbane, Queensland, Australia
- Lehmann, C.N.

Università degli Studi di Milano
Milano, Italy
- Teruzzi, L.

Università degli Studi di Trieste
Trieste, Italy
- Perosa, G.

Università di Pisa
Pisa, Italy
- Degl'Innocenti, I.
- Fanucci, L.

Université Paris-Saclay, CNRS/IN2P3, IJCLab
Orsay, France
- Chaikovska, I.
- Delerue, N.
- Gonnin, A.
- Kubytskyi, V.
- Monard, H.
- Moutardier, A.

USTC/NSRL
Hefei, Anhui, People's Republic of China
- Jin, S.S.
- Sun, B.G.
- Wang, J.G.
- Wu, F.F.
- Zhao, Y.K.